An experimental study of graphitic carbon nitride-based materials and selected metal-based semiconductors in organic solar cells combined with a computational study of perovskite solar cells

By

Nicholas Rono

Submitted in fulfilment of the academic requirements for the degree of

Doctor of Philosophy

in the School of Chemistry and Physics, University of KwaZulu-Natal, Durban, South Africa.

February 2023

ABSTRACT

Solar energy harvesting technologies have sparked intense scientific attention because solar energy is cleaner, inexhaustible, and can be converted to electricity via the photovoltaic effect with appropriate material systems. Photovoltaic solar cells, which convert solar energy to electricity, have emerged and shown great potential in accessing cheap and clean energy supply. The development of solar cells has evolved into three generations, i.e., first-, second-, and third-generation solar cell devices. Among these solar cell types, third-generation solar cells such as; organic solar cells (OSCs) and perovskites solar cells (PSCs) are under intense scientific analysis because they can provide a cost-effective means of solar energy conversion. Nonetheless, the performance of OSC and PSC devices is limited by several factors, including poor stability, recombination of photogenerated charges, and poor solar harvesting abilities. As a result, there is a need to develop sustainable and commercially viable high-performance OSC and PSC devices. In essence, this research looked into graphitic carbon nitride (g-C_3N_4)-based and related materials from an experimental and computational perspective, in the light of OSC and PSC devices.

It was computationally revealed that heptazine-based g-C_3N_4 is slightly transparent since it allows 47.5% of light to pass through, thus, can facilitate solar harvesting in the active layer of a solar cell. The calculated band gap was established to be 2.87 eV and was indirect, indicating that it can absorb visible light and exhibit a plasmonic effect. The study demonstrated that the Tran–Blaha modified Becke-Johnson (mBJ) exchange-correlation potential, as implemented in WIEN2K computational code, was accurate in calculations compared with the generalised gradient approximation (GGA) of the Perdew-Burke-Ernzerhof (PBE) potential since GGA-PBE underestimated the band gap. The 3-dimensional (3D) heptazine-based g-C_3N_4 model exhibited anisotropic behaviour in all the studied optoelectronic properties, thus, equating to a 2-dimensional (2D) material.

The bulk g-C_3N_4 (B-g-C_3N_4) was exfoliated to nanosheets by two approaches, i.e., thermal etching and liquid exfoliation, and comparatively evaluated with respect to radiant energy harvesting abilities. The thermally exfoliated material (CNNS-TE) exhibited a band gap of 1.89 eV, while liquid exfoliation (CNNS-LE) was 2.59 eV, and

the B-g-C_3N_4 material was 2.17 eV. CNNS-TE showed better photocatalytic degradation of rhodamine B - a model pollutant (about 2.5 times that of B-g-C_3N_4 and CNNS-LE). The enhanced performance of CNNS-TE was attributed to better light harvesting ability due to a lower band gap than the other materials and better charge transfer characteristics due to introducing defects during the thermal etching process.

Furthermore, the CNNS-TE were composited with cadmium sulfide (CdS) particles to form CdS/CNNS-TE composites. The composites were employed as a third component in the active layer of the OSC at 1% wt. composition, together with poly-(3-hexylthiophene) (P3HT):[6,6]-phenyl-C_{61}-butyric acid methyl ester ($PC_{61}BM$) blends. The measured UV intensity of the fabricated devices was highest at the visible light region (about 400-650 nm range), implying that the devices had better light absorption properties in this region. Additionally, with the addition of 5% CdS dopants to CNNS-TE, the device series resistance reduced from 827 Ωcm^2 (for pristine device) to 458 Ωcm^2, but the resistance was unfavourable when the dosage of CdS limit was exceeded further up to 20% concentration. As a result, the best-fabricated device (with 5% CdS/CNNS-TE) exhibited a power conversion efficiency (PCE) of 2.21%, open circuit voltage (V_{oc}) of 0.53 V, short-circuit current density (J_{sc}) of 9.36 $mAcm^{-2}$ and the fill factor (FF) of 46.01%. Therefore, the performance was enhanced by about 50% compared with the undoped device, which showed a PCE of 1.06% thanks to reduced recombination of photogenerated charges and improved electron transfer characteristics.

Besides, the B-g-C_3N_4 was further exfoliated to nanosheets (CNNS-CB) by the chemical blowing approach. The formed nanosheets, i.e., CNNS-CB, were combined with the CdS nanoparticles via a mechanochemical method to construct CdS/CNNS-CB heterostructures. Similarly, CdS/CNNS-CB nanocomposites were then incorporated into the active layer of the OSC device as a third component with the P3HT:$PC_{61}BM$ blend. Remarkably, the device with 10% CdS/CNNS-CB exhibited a PCE of 3.45%, about 183% power conversion enhancement. The study demonstrated that the chemical blowing approach of exfoliation of B-g-C_3N_4 introduced other beneficial defects on the material, thus enhancing performance in a solar cell device compared with the one from thermal etching (CNNS-TE). Nonetheless, the PCE enhancement was ascribed to better light absorption, suppressed fast recombination rates of photogenerated charges, and enhanced charge transfer mechanism.

This study also performed numerical simulations of PSC devices using the one-dimensional Solar Cell Capacitance Simulator (SCAPS-1D). A device with the configuration: glass/FTO/IGZO/$CH_3NH_3PbI_3$/spiro-OMeTAD/Au was numerically simulated. By optimisation of various parameters, such as the thickness of the layer, density of defects and doping densities, the device achieved a modest PCE of 19.95%. In this device, the density of defects of the absorber was very impactful and was kept at 2.5 $\times 10^{14}$ cm^{-3}.

In another investigation, the best electron transport layer (ETL) and hole transport layer (HTL) materials that could be applied in PSCs were evaluated from a lead-free device with a methylammonium tin iodide ($CH_3NH_3SnI_3$) absorber layer. Among the tested ETL materials, WS_2 proved to be the best, probably due to its high electron mobility of about 260 cm^2 V^{-1} s^{-1}. For the HTL materials, 2,2',7,7'-tetrakis[N,N-di(4-methoxyphenyl)amino]-9,9'-spirobifluorene (spiro-OMeTAD), copper(I) oxide (Cu_2O), copper(I) thiocyanate (CuSCN), copper(I) iodide (CuI), and poly(2,5-bis(3-tetradecylthiophen-2-yl)thieno-[3,2-b]thiophene) (D-PBTTT-14) showed relatively higher performance. Generally, the tested devices with the best ETL and HTL materials achieved a PCE of above 16% compared to the primary device with a PCE of 10.47%. Also, devices with formamidinium tin iodide ($HC(NH_2)_2SnI_3$) absorber and WS_2 were simulated to explore further the effects of using different HTL materials (Cu_2O, CuSCN, P3HT and D-PBTTT-14) and improve thermal stability. The device demonstrated exceptional performance of more than 20% at high temperatures ranging from 380 to 420 K but decreased when this limit was exceeded. It was shown that replacing the methyl ammonium component with formamidinium resulted in a more compact material that could withstand high temperatures. The optimised devices with Cu_2O, CuSCN, and D-PBTTT-14 HTL materials achieved remarkable PCEs of more than 21%. In addition, the effects of g-C_3N_4 dopants on ZnO on the performance of a lead-free PSC were evaluated. The study demonstrated that g-C_3N_4 dopants on ZnO ETL enhanced cell performance. This was attributed to better light harvesting properties brought about by g-C_3N_4 and reduced recombination of charges due to the passivation of defects. Nonetheless, the ultimate device with g-C_3N_4/ZnO composites attained a PCE of 22%. The study also showed that cheaper metal back contacts such as Ni, Pt, and Pb can be used in place of expensive Au since the tested devices with these alternative metals attained similar PCEs

compared to that of Au. Moreover, it was elucidated in the study that the PCE of a device comparatively increases as a function of the increasing work function of the metal back contact.

Accordingly, the study offers several strategies for improving the performance of OSC and PSC devices in order to achieve commercially viable and environmentally friendly high-performance solar cells.

PREFACE

The research work presented herein was done at the School of Chemistry and Physics, University of KwaZulu-Natal, Westville Campus, South Africa, from January 2019 to December 2022. The research work was conducted under the supervision of Profs. Joshua K. Kibet, Bice S. Martincigh, and Vincent O. Nyamori. Furthermore, most of the computational work was carried out in 2020 at the Theoretical Physics Laboratory, Faculty of Sciences, University of Tlemcen, Algeria, under the host supervisor, Prof. Abdelkrim E. Merad, courtesy of the academic exchange program (ACADEMY project N° 2017-3052/001-001).

This research work is the author's original work and has not been submitted in any form to any tertiary institution for any degree or diploma. The use of other people's work is appropriately acknowledged.

Signed: Nicholas Rono

Student No: 218087888

Date: 08-February 2023

DECLARATION 1 - PLAGIARISM

I, Nicholas Rono, declare that:

1. The research reported in this thesis, except where otherwise indicated, is my original research.
2. This thesis has not been submitted for any degree or examination at any other University.
3. This thesis does not contain other person's data, pictures, graphs, or other information, unless specifically acknowledged as being sourced from the person.
4. This thesis does not contain other person's writing, unless specifically acknowledged as being sourced from other researchers. Where other written sources have been quoted, then:
    a. Their words have been re-written but, the general information attributed to them has been referenced.
    b. Where their exact words have been used, then their writing has been placed in italics and inside quotation marks and referenced.
5. This thesis does not contain text, graphics or tables copied and pasted from the internet, unless specifically acknowledged, and the source being detailed in the thesis and in the reference's sections.

Signed: Nicholas Rono

Date: 08-February 2023

DECLARATION 2 – PUBLICATION AND CONFERENCE CONTRIBUTIONS

Details of contribution to publications that form part and/or include research presented in this thesis (includes manuscripts in preparation, submitted, *in press* and published articles. The details of the contributions of each author to the experimental and computational work and writing of each publication is specified).

PUBLICATIONS

Publication 1

Nicholas Rono, Joshua K. Kibet, Bice S. Martincigh, and Vincent O. Nyamori **(2021)**. A review of the current status of graphitic carbon nitride. *Critical Reviews in Solid State and Material Sciences.* **46**, 189-217. https://doi.org/10.1080/10408436.2019.1709414

Contributions: I conceptualised and wrote the review paper. Profs. Joshua K. Kibet, Bice S. Martincigh, and Vincent O. Nyamori provided general guidance and proofread the manuscript. Prof. Martincigh restructured the sections of the review.

Publication 2

Nicholas Rono, Abdelkrim E. Merad, Joshua K. Kibet, Bice S. Martincigh, and Vincent O. Nyamori. A first principles study of the optoelectronic properties of heptazine based graphitic carbon nitride. Manuscript in preparation.

Contributions: I conceptualised, optimised the structure of heptazine-based g-C_3N_4, performed first principles calculations on the optoelectronic properties of the model, analysed data, and wrote the manuscript. Profs. Abdelkrim E. Merad, Joshua K. Kibet, Bice S. Martincigh, and Vincent O. Nyamori provided general guidance and proofread the manuscript. Prof. Merad trained me on how to install and use the WIEN2K computational code.

Publication 3

Nicholas Rono, Joshua K. Kibet, Bice S. Martincigh, and Vincent O. Nyamori **(2020)**. A comparative study between thermal etching and liquid exfoliation of bulk graphitic carbon nitride to nanosheets for the photocatalytic degradation of a model environmental

pollutant, Rhodamine B. *Journal of Material Science: Materials Electronics*. **32**, 687–706. https://doi.org/10.1007/s10854-020-04849-8

Contributions: I conceptualised and designed the experiments on the synthesis of bulk g-C_3N_4, and exfolited by two means, i.e. thermal and liquid exfoliation to nanosheets, characterised, analysed, interpreted the data, and wrote the manuscript. Profs. Joshua K. Kibet, Bice S. Martincigh, and Vincent O. Nyamori provided general guidance and proofread the manuscript.

Publication 4

Nicholas Rono, Joshua K. Kibet, Bice S. Martincigh, and Vincent O. Nyamori. Cadmium sulphide doped graphitic carbon nitride nanosheets for improved photon harvesting ability of active layer in organic solar cell. Manuscript in preparation.

Contributions: I conceptualised, planned the experiments, synthesised and characterised CdS/CNNS-TE composites. I fabricated organic solar cell (OSC) devices with the synthesised materials, collect and analysed data and wrote the manuscript. Profs. Joshua K. Kibet, Bice S. Martincigh, and Vincent O. Nyamori provided general guidance and proofread the manuscript.

Publication 5

Nicholas Rono, Joshua K. Kibet, Bice S. Martincigh, and Vincent O. Nyamori. Chemically blown graphitic carbon nitride nanosheets doped with cadmium sulfide nanoparticles for enhanced photon harvesting in organic solar cells. Manuscript in preparation.

Contributions: I conceptualised, planned the experiments on the synthesis and characterisation of CdS/CNNS-CB composites. I fabricated OSC devices with the synthesised materials, collected and analysed data and wrote the manuscript. Profs. Joshua K. Kibet, Bice S. Martincigh, and Vincent O. Nyamori provided general guidance and proofread the manuscript.

Publication 6

Nicholas Rono, Abdelkrim E. Merad, Joshua K. Kibet, Bice S. Martincigh, and Vincent O. Nyamori. Recent advances in the development and simulation of perovskite solar cell devices. Manuscript in preparation.

Contributions: I planned and wrote the review manuscript. Profs. Abdelkrim E. Merad, Joshua K. Kibet, Bice S. Martincigh, and Vincent O. Nyamori provided general guidance and proofread the manuscript.

Publication 7

Nicholas Rono, Abdelkrim E. Merad, Joshua K. Kibet, Bice S. Martincigh, and Vincent O. Nyamori **(2022)**. Simulation of the photovoltaic performance of a perovskite solar cell based on methylammonium lead iodide. *Optical and Quantum Electronics.* **54**, 317. https://doi.org/10.1007/s11082-022-03737-1

Contributions: I conceptualised and modeled a lead-based PSC with the configuration: glass/FTO/IGZO/$CH_3NH_3PbI_3$/spiro-OMeTAD/Au. I did simulations, analysed data, and wrote the manuscript. Profs. Abdelkrim E. Merad, Joshua K. Kibet, Bice S. Martincigh, and Vincent O. Nyamori provided general guidance and proofread the manuscript.

Publication 8

Nicholas Rono, Abdelkrim E. Merad, Joshua K. Kibet, Bice S. Martincigh, and Vincent O. Nyamori **(2021)**. A theoretical investigation of the effect of the hole and electron transport materials on the performance of a lead-free perovskite solar cell based on $CH_3NH_3SnI_3$. *Journal of Computational Electronics:* **20**, 993–1005. https://doi.org/10.1007/s10825-021-01673-z

Contributions: I conceptualised and modeled the lead-free PSC device with the primary configuration: glass/FTO/WS_2/$CH_3NH_3SnI_3$/P3HT/Au. I performed the numerical simulations, analysed the data and wrote the manuscript. Profs. Abdelkrim E. Merad, Joshua K. Kibet, Bice S. Martincigh, and Vincent O. Nyamori provided general guidance and proofread the manuscript.

Publication 9

Nicholas Rono, Abdelkrim E. Merad, Joshua K. Kibet, Bice S. Martincigh, and Vincent O. Nyamori **(2021)**. Optimization of hole transport layer materials for a lead-free perovskite solar cell based on formamidinium tin iodide. *Energy Technology.* **9**, 2100859. https://doi.org/10.1002/ente.202100859

Contributions: I conceptualised and modeled a lead-free PSC with the general configuration: glass/FTO/WS_2/$HC(NH_2)_2SnI_3$/HTL/Au. I carried out simulations, analysed data, and wrote the manuscript. Profs. Abdelkrim E. Merad, Joshua K. Kibet, Bice S. Martincigh, and Vincent O. Nyamori provided general guidance, reviewed and proofread the manuscript.

Publication 10

Nicholas Rono, Abdelkrim E. Merad, Joshua K. Kibet, Bice S. Martincigh, and Vincent O. Nyamori. Graphitic carbon nitride doped zinc oxide as an electron transport layer in a lead-free perovskite solar cell: A SCAPS numerical simulation – Manuscript in preparation.

Contributions: I conceptualised and modeled a lead-free PSC with the general configuration: glass/FTO/ZnO or ZnO/g-C_3N_4/$HC(NH_2)_2SnI_3$/CuSCN/Au. I carried out simulations, analysed data, and wrote the manuscript. Profs. Abdelkrim E. Merad, Joshua K. Kibet, Bice S. Martincigh, and Vincent O. Nyamori provided general guidance, reviewed and proofread the manuscript.

Signed: Nicholas Rono

Student No: 218087888

Date: 08-February 2023

CONFERENCE CONTRIBUTIONS

1. **Flash poster presentation:** Nicholas Rono, Abdelkrim E. Merad, Joshua K. Kibet, Bice S. Martincigh, and Vincent O. Nyamori. A first-principles study of the optoelectronic properties of heptazine-based graphitic carbon nitride. UKZN, College of Agriculture, Engineering and Science. Postgraduate Research and Innovation Symposium, 2021, Westville Campus, South Africa, Online presentation, 9 - 10th December 2021.
2. **Oral presentation:** Nicholas Rono, Abdelkrim E. Merad, Joshua K. Kibet, Bice S. Martincigh, and Vincent O. Nyamori. A theoretical investigation of the effect of the hole and electron transport materials on the performance of a lead-free perovskite solar cell based on $CH_3NH_3SnI_3$. UKZN, Seminar Series. School of Chemistry and Physics, 2021, Westville campus, South Africa, Online presentation, 30th April 2021.
3. **Flash poster presentation:** Nicholas Rono, Abdelkrim E. Merad, Joshua K. Kibet, Bice S. Martincigh, and Vincent O. Nyamori. A first-principles study of the optoelectronic properties of heptazine-based graphitic carbon nitride. The South African Chemical Institute, KwaZulu-Natal Section. Postgraduate Research Colloquium, 2021, Westville Campus, South Africa, Online presentation, 7th July 2021.
4. **Poster Presentation:** Nicholas Rono, Abdelkrim E. Merad, Joshua K. Kibet, Bice S. Martincigh, and Vincent O. Nyamori. Optimization of hole transport layer materials for a lead-free perovskite solar cell based on formamidinium tin iodide. Royal Society of Chemistry. ISF 2021 Young International Solar Fuels Conference, 2021, United Kingdom, Online presentation, 26 - 29th July 2021.
5. **Poster Presentation**: Nicholas Rono, Abdelkrim E. Merad, Joshua K. Kibet, Bice S. Martincigh, and Vincent O. Nyamori. A DFT study of the optoelectronic properties of heptazine-based graphitic carbon nitride. The South African Chemical Institute, KwaZulu-Natal Section. Postgraduate Research Colloquium, 2022, Pietermaritzburg campus, South Africa, Physical meeting, 10th November 2022.
6. **Oral Presentation:** Nicholas Rono, Joshua K. Kibet, Bice S. Martincigh, and Vincent O. Nyamori. Cadmium sulfide doped graphitic carbon nitride nanosheets for improved photon harvesting ability of the active layer in organic solar cells. UKZN, College of Agriculture, Engineering and Science. Postgraduate Research

and Innovation Symposium, 2022, Westville Campus, South Africa, Online presentation, 8 – 9th December 2022.

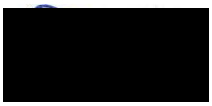

Signed: Nicholas Rono

Date: 08-February 2023

ACKNOWLEDGEMENTS

First and foremost, I would like to wholeheartedly thank and glorify God, almighty, for his providence, care, strength, and good health throughout my entire study period. His profound grace and power made it possible to get this far.

Secondly, I would like to express my sincere gratitude to my main supervisor Prof. Vincent O. Nyamori, for accepting me to join his research group, for his guidance, immense knowledge, invaluable research discussions, and extensive support during my Ph.D. studies.

My sincere appreciation goes to my co-supervisor, Prof. Bice S. Martincigh, for her mentorship, motivation, positive criticisms, moral support, and prompt proofreading of my manuscripts. I am truly grateful. I would also like to express my most profound appreciation to my co-supervisor, Prof. Joshua K. Kibet, for his inspiration, motivation, mentorship, moral support, and timely proofreading of my manuscripts. In addition, I express my sincere gratitude to my host supervisor in Algeria, Prof. Abdelkrim E. Merad, for his invaluable advice, mentorship, research guidance, and warm welcome in his research laboratory. I generally thank all my supervisors for their unwavering support and commitment to my research progress. I am forever grateful.

Besides my supervisors, I greatly appreciate Prof. Stephen O. Olatunji, for his constant motivation and encouragement. He was always keen on my research progress and checked on me in the lab. Much appreciation goes to Prof. Genene Mola and his team for allowing us to fabricate and test solar devices in his lab.

I express my gratitude to the University of KwaZulu-Natal and the School of Chemistry and Physics for admission and for providing all the necessary resources and facilities to pursue my doctoral studies.

Special thanks also go to the administration and technical staff of the School of Chemistry and Physics (Yvonne Gengiah, Usher Bellbhudder, Clementine Dlamini, Renee Naidoo, Unathi Bongoza, Mpho Sehoto, Gregory Moodley, Anita Naidoo, Nundkumar Miller, Samantha Naidoo, Maphumulo Thandeka, Sizwe Zamisa, Soodeyal Shannon and Rama Naidoo), as well as the Microscopy and Microanalysis Unit (MMU) staff (Nelisha Murugan, Vishal Baijnath, Subashen Naidu, and Christopher Phillip) for their patience

and prompt assistance. I do not forget the staff in the Theoretical Physics Laboratory Team (Touileb Yahia and Benmansour N-H) at the University of Tlemcen, Algeria.

I notably accord my thanks to the National Research Foundation (NRF) of South Africa, the University of KwaZulu-Natal (UKZN), the UKZN Nanotechnology Platform, and the Eskom Tertiary Education Support Programme (TESP) for funding this work. In addition, I particularly thank the ACADEMY project N° 2017-3052/001-001 and the coordinator Prof. Latifa Negadi for the opportunity to participate in a one-year mobility exchange program in Algeria.

My deepest gratitude also goes to my colleagues in NanoChemistry and PhysChem Research Groups (Dr. Shoyiga, Dr. Ngidi, Samantha, Regina, Mthokozisi, Caren, Taiwo, Rhoda, John, Pomerai, Tosin, and Opeyemi) for their constant motivation and constructive discussions in the lab.

I would like to express my profound gratitude to my parents, Mr. Timothy K.Toroitich and the late Mrs. Gladys C. Toroitich, my grandfather, Peter Kaptich, and grandmother, Ruth Kenduiywa, for their unfailing, unconditional love, prayers, support, and continuous encouragement throughout my years of study.

I am incredibly grateful to my lovely wife, Mrs. Faith C. Rono, for her love, unwavering support, encouragement, and in particular, for filling the gap in my absence. Without her valuable backing, it would not have been possible to have peace of mind to conduct research far away from home. I am sincerely grateful to my sons, Kelvin Kipkirui and Emanuel Kiprotich, for their love, patience during my absence, laughs, and lovely video calls! I am thankful to my siblings, Susan, Flossy, and Wesley, for supporting me spiritually throughout writing this thesis and my life in general. Special appreciation goes to Uncle Cilas and Festo for their prayers, motivation, and financial support toward my study and aspirations. I am also grateful to my other family members (cousins, aunts, in-laws, and uncles), the “Braii family” in Durban, and friends who have supported me along the way.

Finally, I would like to thank everyone who has played a significant role in my study career whom I didn’t mention in this humble note of gratitude.

DEDICATION

This thesis is dedicated to my beloved late grandmother Mrs. Ester Kaptich and my late mother, Mrs. Gladys Toroitich. Although they were an inspiration and worked tirelessly to support me in furthering my education, they were unable to see me achieving this level of education. This is meant for you.

With humility, gratitude, and love, I also dedicate this thesis to my dad, Mr. Timothy K.Toroitich, my dear wife, Mrs. Faith C. Rono, my siblings, Susan, Flossy, and Wesley, and my sons, Kelvin, and Emanuel, for their sacrifices and support throughout my academic journey.

LIST OF ABBREVIATIONS

Abbreviation	Full meaning
//	zz-direction
⊥	xx-direction
0D	Zero dimension
1D	One dimension
2D	Two dimensions
3D	Three dimensions
a.u.	Arbitrary unit
AFORS-HET	Automat for simulation of heterostructures
AM	Air mass
ATR	Attenuated total reflectance
BET	Brunauer-Emmett-Teller
B-g-C_3N_4	Bulk graphitic carbon nitride
BHJ	Bulk heterojunction
BHJ OSC	Bulk heterojunction organic solar cell
BJH	Barrett-Joyner-Halenda
BP	Black phosphorus
BQ	Benzoquinone
C	Capacitance

CB	Chemical blowing exfoliation
CB	Conduction band
CBM	Conduction band minimum
CD	Carbon dot
CdS/CNNS-CB	Cadmium sulfide doped graphitic carbon nitride nanosheets from Chemical blowing exfoliation
CdS/CNNS-TE	Cadmium sulfide doped graphitic carbon nitride nanosheets from thermal exfoliation
CIGS	Copper-indium-gallium-selenide
CN	g-C_3N_4
CNNS-CB	Graphitic carbon nitride nanosheets from chemical blowing exfoliation
CNNS-LE	Graphitic carbon nitride nanosheets from liquid exfoliation
CNNS-TE	Graphitic carbon nitride nanosheets from thermal exfoliation
CNS	Sulphur mediated graphitic carbon nitride
CNT	Carbon nanotube
CP	Ciprofloxacin
CQD	Carbon quantum dot
CV	Cyclic voltammetry
DFT	Density functional theory

DMSO	Dimethyl sulfoxide
DOE	Department of energy
DOS	Density of state
D-PBTTT-14	Poly(2,5-bis(3-tetradecylthiophen-2-yl)thieno-[3,2-b]thiophene)
DSSC	Dye-sensitised solar cell
$EDAI_2$	Ethylenediammonium diiodide
EDX	Energy dispersive X-ray spectroscopy
E_F	Fermi energy level
E_g	Optical band gap
EIS	Electrochemical impedance spectroscopy
ETL	Electron transport layer
ETM	Electron transporting material
FA	Formamidinium
FEM	Finite element method
FF	Fill factor
FP-LAPW+lo	Full potential-linearised augmented plane wave plus the local orbital
FRET	Fluorescence resonance energy transfer
FTIR	Fourier-transform infrared spectroscopy
FTO	Florine doped tin-oxide

GA	Guanidinium
g-C_3N_4	Graphitic carbon nitride
g-C_3N_4 QD	Graphitic carbon nitride quantum dot
GCE	Glassy carbon electrode
GGA	Generalised gradient approximation
GPVDM	General-purpose photovoltaic device model
HOMO	Highest occupied molecular orbital
HR-TEM	High resolution-transmission electron microscopy
HSC	Hydrogen storage capacity
HTL	Hole transport layer
HTM	Hole transporting material
ICL	Interconnecting layer
ICP-OES	Inductively coupled plasma-optical emission spectrometer
I_D/I_G	Ratio of the area under D-band and G-band peaks
IGZO	Indium gallium zinc oxide
IPA	Isopropyl alcohol
ITO	Indium doped tin oxide
J_{sc}	Short-circuit current density

KS	Khon-Sham
LE	Liquid exfoliation
LUMO	Lowest unoccupied molecular orbital
MA	Methylammonium
MB	Methylene blue
mBJ	Modified Becke-Johnson
MDMO-PPV	Poly[2-methoxy-5-(3,7-dimethyloctyloxy)-1,4-phenylen]-*alt*-(vinylene)
MPCS	Mesoporous carbon sphere
N_a	Density of p-type doping
N_c	Effective density of state at conduction band
N_d	Density of n-type doping
NREL	National renewable energy laboratory
N_t	Density of defects
N_v	Effective density of state at valence band
OSC	Organic solar cell
P3HT	Poly-(3-hexylthiophene)
PBE	Perdew-Burke-Ernzerhof
PC1D	Personal computer one-dimensional
$PC_{61}BM$	[6,6]-phenyl-C_{61}-butyric acid methyl ester

PCE	Power conversion efficiency
PEDOT:PSS	Poly(3,4-ethylenedioxythiophene):poly(4-styrenesulfonate)
PEI	Poly(ethyleneimine)
PHCl	Phenylhydrazine hydrochloride
PL	Photoluminescence
PMMA	Poly(methyl methacrylate)
PMMA/SB	Poly(methyl methacrylate)/styrene-butadiene
PNDIT-F3N	Poly[(9,9-bis(3′-(*N*,*N*-dimethylamino)propyl)-2,7-fluorene)-alt-5,5′-bis(2,2′-thiophene)-2,6-naphthalene-1,4,5,8-tetracaboxylic-*N*,*N*′-di(2-ethylhexyl)imide]
PPPDE	1-[N-(2-Hydroxyethyl)-4′-piperidyl]-3-(4′-piperidyl) propane
PSC	Perovskite solar cell
PXRD	Powder X-ray diffraction
QE	Quantum efficiency
R_{ct}	Charge transfer resistance
rGO	Reduced graphene oxide
RhB	Rhodamine B
RMT	Muffin-tin spheres
Rs	Series resistance

R_s	Solution resistance
SAED	Selected area electron diffraction
SCAPS-1D	One-dimensional Solar Cell Capacitance Simulator
SCF	Self-consistent field cycle
SCLC	Space charge limited current
SEM	Scanning electron microscopy
spiro-OMeTAD	2,2',7,7'-tetrakis[N,N-di(4-methoxyphenyl)amino]-9,9'-spirobifluorene
TC	Tetracycline
TE	Thermal etching exfoliation
TEM	Transmission electron microscopy
TEOA	Tri-ethanolamine
TGA	Thermal gravimetric analysis
TSC	Tandem solar cell
UV-DRS	UV-diffuse reflectance spectroscopy
UV-Vis	Ultraviolet-visible
VB	Valence band
VBM	Valence band maximum
V_{oc}	Open-circuit voltage
W	Warburg

wxAMPS	wx-analysis of microelectronic and photonic structures
ε_r	Relative dielectric permittivity
μ_n	Mobility of electrons
μ_p	Mobility of holes
χ	Electron affinity

LIST OF FIGURES

LIST OF TABLES

TABLE OF CONTENTS

CHAPTER TWO

A review of the current status of graphitic carbon nitride

CHAPTER THREE

A theoretical study of the optoelectronic properties of heptazine-based graphitic carbon nitride

CHAPTER FOUR

A comparative study between thermal etching and liquid exfoliation of bulk graphitic carbon nitride to nanosheets for solar harvesting applications

CHAPTER FIVE

Cadmium sulfide-doped graphitic carbon nitride nanosheets for improved photon harvesting of the active layer in organic solar cells

CHAPTER SIX

Chemically blown graphitic carbon nitride nanosheets doped with cadmium sulfide nanoparticles for enhanced photon harvesting in organic solar cells

CHAPTER SEVEN

Recent advances in the development and simulation of perovskite solar cell devices

CHAPTER EIGHT

Simulation of the photovoltaic performance of a perovskite solar cell based on methylammonium lead iodide

CHAPTER NINE

A theoretical investigation of the effect of the hole and electron transport materials on the performance of a lead-free perovskite solar cell based on $CH_3NH_3SnI_3$

CHAPTER TEN

Optimisation of hole transport layer materials for a lead-free perovskite solar cell based on formamidinium tin iodide

CHAPTER ELEVEN

Graphitic carbon nitride doped zinc oxide as an electron transport layer in a lead-free perovskite solar cell: A SCAPS numerical simulation

CHAPTER TWELVE

Conclusions and future work

APPENDICES

CHAPTER ONE

Introduction

Rapid globalisation and industrialisation have globally augmented energy demands beyond the currently available supply. The extensive use of fossil fuels has posed severe pressure on their availability and, thus, the risk of depletion. Moreover, environmental pollution impacts due to the utilisation of fossil fuels have escalated and necessitated the exploration of clean, cheap, and sustainable energy sources [1]. Renewable energy sources that have been explored include wind, geothermal, solar, solar thermal, hydropower, hydrogen, and tidal energies [2]. Among these energy sources, solar energy is the most abundant, clean, and can offer unlimited use in the presence of sunlight [3]. Photovoltaic devices, also called solar cells, convert photon energy to electricity by the photovoltaic effect, a phenomenon first demonstrated in 1839 by Alexandre-Edmond Becquerel [4]. This remarkable discovery has formed the basis for the historical development of solar cell devices. The first single-crystal silicon solar cell device, with a power conversion efficiency (PCE) of 6%, was first fabricated in 1954 by Chapin et al. [5]. Over the years, the development of solar cells has progressively increased due to the high demand for clean and sustainable energy supplies. Therefore, solar cells are categorised into three generations, i.e., first, second and third generations, based on the time, PCE and the nature of materials used to make them.

The first-generation solar cells were made from monocrystalline or polycrystalline silicon wafers [1]. Monocrystalline silicon solar cells exhibit a high PCE of about 24% and are stable at elevated temperatures, while polycrystalline silicon devices show a comparatively lower PCE of about 14% [6] and cannot withstand high operation temperatures [7]. Practically, monocrystalline silicon solar cell devices are expensive since pure silicon is required; therefore, polycrystalline silicon devices are preferred due to ease of fabrication and low cost [6]. Nevertheless, silicon-based solar cells still dominate today's market, contributing to about 86% of the world's photovoltaic market [7] because they exhibit high PCE, long lifespan, are non-toxic, resistant to corrosion, are lightweight, and are stable at relatively high temperatures compared with other solar cells.

The second-generation solar cells emerged with a focus on reducing the high cost of using pure silicon. These are made by depositing a thin layer of amorphous silicon on a

substrate (glass or other layers) to fabricate thin-film solar cells [1]. Also referred to as non-crystalline/amorphous silicon solar cells, second-generation solar devices utilise less silicon semiconductor material, thus, saving on the cost of production. Furthermore, other classes of second-generation solar cells used cadmium telluride (CdTe) [8], copper, and indium-based semiconductors as light-absorbing materials [9]. The devices with CdTe became attractive because of low fabrication cost, but it was not environmentally friendly due to the toxicity of cadmium. Therefore, other better materials were explored to reduce the bottlenecks associated with the use of cadmium.

On the other hand, copper-indium-gallium-selenide (CIGS) devices exhibit better performance and low levels of cadmium when compared with CdTe devices. Generally, second-generation solar cells are cheaper than first-generation solar cells due to lower production costs but exhibit lower PCE. Thus, the need to develop solar cell devices that are cheap, easy to fabricate, environmentally benign, and with high performance.

New frontiers of solar harvesters have been advanced to replace silicon, indium, and cadmium-based solar cells. These include organic solar cells (OSCs), dye-sensitised solar cells (DSSCs), tandem solar cells (TSCs), and perovskite solar cells (PSCs), which belong to the third-generation solar cell category [10, 11]. The new solar cell devices are flexible, cheap, and light and can be fabricated using solution preparation methods with low power consumption [12, 13]. These third-generation devices are under intensive investigation from experimental and theoretical approaches [14, 15] geared towards performance enhancement and commercialisation. Presently, the third-generation solar cells are less commercialised, but promising strides to take them to the market are underway.

1.1 Third-generation solar cells

The third-generation solar cells have received much scientific attention because of ease of fabrication, low cost, and that they can incorporate environmentally friendly materials such as carbonaceous materials, organic dyes, conductive polymers, and perovskites. The details of third-generation solar cells are discussed in the following sections.

1.1.1 Organic solar cells

Fundamentally, the organic solar cell is a type of photovoltaic cell which uses organic polymers. These polymers have conductive properties and are, therefore, able to transfer

electrical currents [16]. Typical OSCs have the following parts: the anode, the photoactive layer, the hole transport layer (HTL), and the cathode (transparent substrate) [17, 18]. The photoactive layer can either be a bilayer junction (donor and acceptor components form layers) or a bulk hetero-junction (BHJ) (donor and acceptor components are mixed), as shown in Figure 1.1 [19, 20].

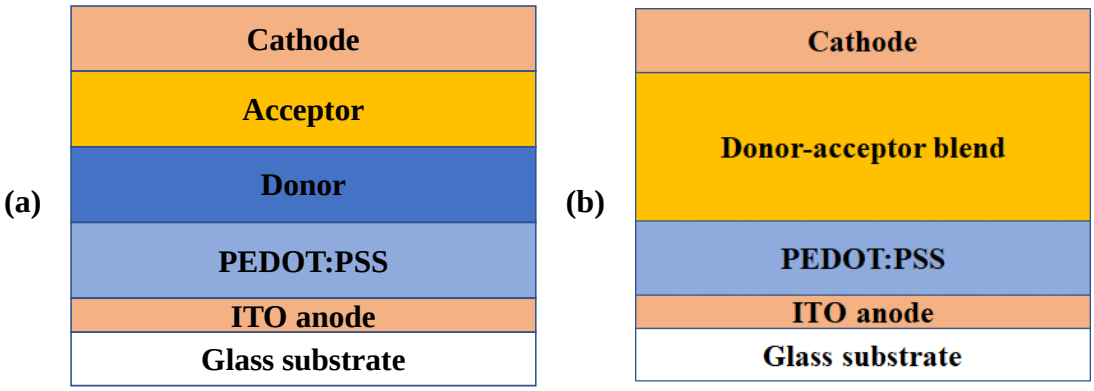

Figure 1.1: A schematic diagram of a typical bilayer (a) and (b) BHJ OSC [20]

In OSCs, light energy causes electron transfer from the donor component to the acceptor component, i.e., charge separation [21]. The main challenge is to prevent the recombination of charges and to transfer them to the respective electrodes (anode and cathode) [22-24]. In bilayer cells, the chances of charge recombination are low because electrons travel to the electrode layer of the n-type material, and holes travel to the electrode layer of the p-type material. On the contrary, recombination for BHJ OSCs can be occur between the donor and the acceptor layers because of interfacial defects which entice charges, thus, causing recombination [25, 26].

The attractive attributes of OSCs include the use of materials that are lightweight, biodegradable and fabricated through solution preparation methods with low power consumption [27-29]. During the fabrication of OSCs, composites can be deposited in a single step but via many ways, for instance, spin-coating, inkjet printing, and roller casting [30]. Hence, the flexibility in making them. However, OSCs suffer from low efficiency; therefore, there is a need to engineer devices with better performance. For over 20 years, most OSCs contained fullerenes as acceptors, but this has changed, and OSCs without fullerene have been technologically advanced [31]. The PCE of non-fullerene OSCs has reached over 13%, which is better than that for OSCs with fullerene [17]. The performance of any photovoltaic device is dependent on the short-circuit

current (J_{sc}), fill factor (FF), and open-circuit voltage (V_{oc}). When the values of these parameters are high at maximum power, the performance of a device is also high [32]. Accordingly, organic solar cells with high PCE are continually fabricated. Nevertheless, most organic solar cells suffer the problem of recombination of charges, hence, reducing the magnitude of the photogenerated current. Therefore it is important to incorporate materials which are efficient in separation of charges.

1.1.2 Perovskite solar cells

The PSCs are potentially more efficient than silicon-based solar cells because of their robust charge transfer efficiency [33]. The PCE of PSCs has lately increased from 3.8% to above 23% [34, 35]. Semiconducting organic-inorganic hybrid perovskites have attractive optoelectronic properties such as a direct energy band gap, long carrier lifetimes, strong optical absorption, long charge diffusion length, and hole and electron transfer capabilities [35]. Recently, researchers have attempted to improve the PCE of PSCs cells through enhanced charge transfer at interfaces, selection of suitable PSC component materials, proper band alignment, defect engineering, and, more so, computational modelling of devices.

Despite these strategies that have been put forward, there are serious challenges facing the commercialisation of PSCs, namely, the stability of devices when exposed to light, humidity, high temperature, and toxicity of lead [36]. In order to eliminate or reduce the effects of lead, other metals such as Pt, Sn, and Ge have been used to replace toxic lead in the cationic part of the perovskite absorber [37]. Among the group of lead alternatives, Sn has been chiefly tested because it has similar chemical properties as lead [38]. Therefore, lead-free or lead-less PSCs have emerged, though their performance is still lower than their lead-based counterparts [39]. For instability issues, encapsulation and replacement of unstable components of perovskite materials have been carried out [40]. For instance, the thermally unstable methylammonium part of the perovskite has been replaced with the formamidinium cation; thus, a more compact perovskite structure is formed [41].

1.1.2.1 Interface engineering in PSCs

The efficacy of charge transfer at interfaces is essential in any PSC cell because the photogenerated holes and electrons must be separated and selectively transported to the respective electrodes effectively to enable the flow of electric current. Therefore, hole-transporting materials (HTM) and electron-transporting materials (ETM) are essential components of solar cells. The ETM/perovskite/HTM architecture is necessary for electron-hole separation in solar cells. The electron transfer efficiency at the perovskite/ETM interface and hole transfer at the perovskite/HTM interface significantly contribute to the overall efficiency of PSCs [35, 42]. The influence of perovskite/ETM and HTM interfaces goes beyond efficient charge transfer. Recent studies have shown that hysteresis in PSCs (decrease in cell performance when measurements are done in the increasing or decreasing electric bias regime) can significantly be reduced by adequately engineering interfacial materials [43]. Additionally, interfacial materials offer extra support for crystal growth and also act as moisture protection barriers [44]. Recently, Liu et al. [45] fabricated a PSC with graphitic carbon nitride quantum dots (g-C_3N_4QD) at the SnO_2 electron transport layer and perovskite absorber, i.e., SnO_2/perovskite interface. Incorporating g-C_3N_4QD facilitated effective crystal growth of the perovskite and reduced defects, thus, leading to less recombination of photogenerated charges because g-C_3N_4QD can cross-link and offer a smooth surface.

1.1.3 Dye-sensitised solar cells

As shown in Figure 1.2, a typical DSSC is a photoelectrochemical device that consists of the following: (i) a photoanode made up of an oxide layer (normally, TiO_2 is deposited on a transparent conductive glass substrate, such as fluorine-doped tin oxide (FTO)) (ii) a monolayer of dye molecules on the surface of the TiO_2 layer which absorbs optical photons and produces excited electrons; (iii) an electrolyte containing a redox couple (typically, I^-/I_3^-) in an organic solvent which receives electrons from the counter electrode and is reduced causing regeneration of the dye, and (iv) a platinised conductive glass substrate which serves as a counter electrode [46].

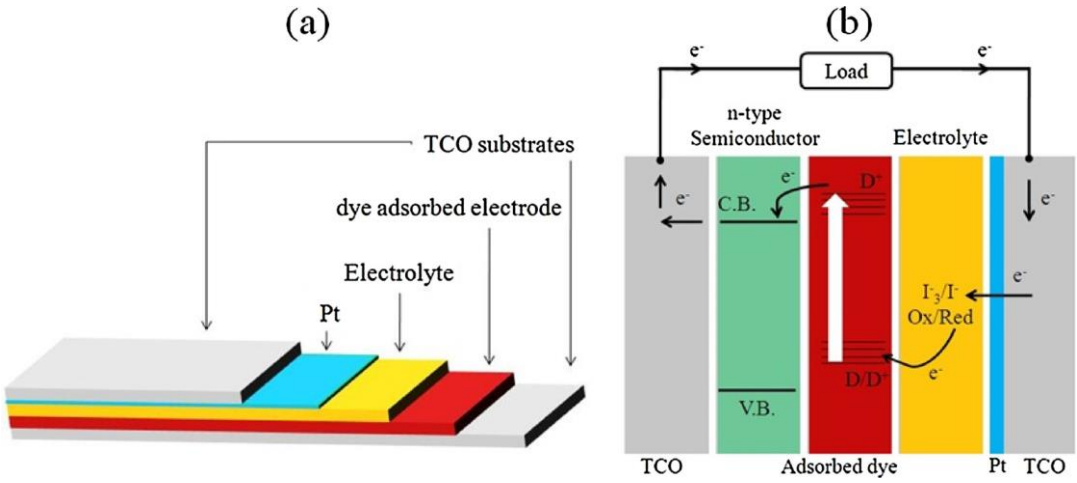

Figure 1.2: (a) A typical DSSC design and (b) an illustration of the working principle [46]

Figure 2b shows the working mechanism of a DSSC. When light energy falls on the cell, the dye molecules absorb the photons, and excited electrons are generated and injected into the conduction band of the TiO_2, which are transferred to the cathode and flow through the external circuit to the platinised FTO counter electrode. The redox couple electrolyte attracts electrons from the counter electrode and is itself reduced, and the reduced part of the electrolyte replenishes the photo-oxidised dye. During the regular operation of DSSCs, the liquid electrolyte evaporates over time, limiting the performance of these cells because of increased operating temperatures [47]. To mitigate this challenge, scientists have attempted to address this issue by replacing the electrolyte with a solid hole transport material (HTM) and, therefore, giving rise to the current solid-state dye-sensitized solar cells (ssDSSCs) [48]. The working principle of the ssDSSCs is essentially similar to the OSCs, and PSCs already described; however, the unique feature is that the absorber is still a dye in this case. Recently Jahantigh et al. [49] numerically simulated ssDSSCs, and the device achieved a PCE of 17.72%.

1.1.4 Tandem solar cells

In an effort to attain higher efficiency in photovoltaic cells, tandem-structured cells have been fabricated. The cell is formed by stacking two or more sub-cells together, either the active layer or the hole transport layer [50-54]. The PCE can be significantly improved with tandem solar cells due to reduced thermal losses, enhanced optical absorption of broad-range light, and transmission loss [55].

Dürr et al. [54] constructed a tandem DSSC with two dyes, i.e., a red dye in the upper compartment and a black dye in the lower section. The device exhibited a PCE of 10.5% and a good J_{sc} of 21.1 mA cm^{-2}. Recently, Hosseinnezhad et al. [56] designed a perovskite/DSSC tandem solar cell. In this design, the top was the perovskite section, and the bottom was the DSSC section. When an organic dye was used in the DSSC (lower compartment), the device achieved a PCE of about 8.77%, and N719 dye achieved a relatively higher PCE of 10.54%.

Cheng et al. [55] designed a tandem OSC with non-fullerene acceptors in the back sub-cell (Figure 1.3). They reported an attractive PCE value of 13.3% in the lab and a certified PCE value of 11.5% by the national renewable energy laboratory (NREL).

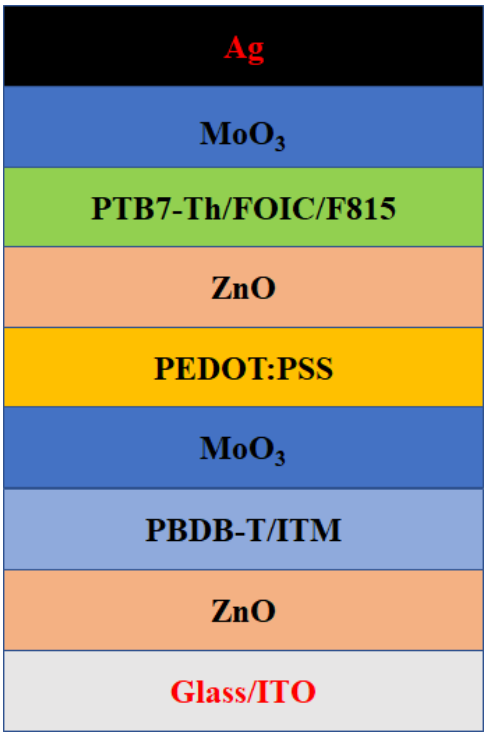

Figure 1.3: A typical tandem OSC device [55]

Thermal losses are also very common in the devices; for instance, OSC has inherent defects of thermalisation losses and transmission losses due to under-utilisation of absorbed radiation [57, 58]. In the tandem design, the rear cell with a narrow band gap active layer can absorb low energy photons while the front cell with a wide band gap active layer can absorb a photon of high energy; therefore, low and high energy radiation is absorbed effectively and in turn results in high PCE values [58].

In addition to incorporating the best active layers in the tandem solar cell, developing an interconnecting layer (ICL) is also essential in attaining high power conversion efficiencies [57, 59]. Typically, an ICL consists of a pair of hole transport layer (HTL) and electron transport layer (ETL) materials and forms an ohmic contact between the sub-cells [60]. The ICL is responsible for charge extraction and, hence, less recombination [59, 61]. Zhang et al. [62] prepared through the solution process an ICL consisting of poly[(9,9-bis(3′-(*N*,*N*-dimethylamino)propyl)-2,7-fluorene)-alt-5,5′-bis(2,2′-thiophene)-2,6-naphthalene-1,4,5,8-tetracaboxylic-*N*,*N*′-di(2-ethylhexyl)imide] (PNDIT-F3N) merged with poly(ethyleneimine) (PEI) as the ETL. At the same time, with poly(3,4-ethylenedioxythiophene): polystyrene sulfonate (PEDOT:PSS) as the HTL, a remarkable PCE value of 12.6% was reported for the developed tandem organic cell because of incorporation of ICL.

Another attractive plus point of tandem OSCs is their reduced photocurrent, and resulting low power losses. Basically, the V_{oc} is the sum of the V_{oc} of the sub-cell in series, and the J_{sc} is restricted by the low J_{sc} of the sub-cells. Therefore, by ohms law, $P = I^2R_s$, where P is the power, I is the current and R_s is the resistance; if the current is diminished, power losses will also reduce.

1.2 Efficiency parameters of a photovoltaic cell

The power conversion efficiency (PCE) of a photovoltaic cell is determined by three parameters, namely, J_{sc}, V_{oc}, and FF [63-65]. For example, in an OSC, the maximum V_{oc} is obtained by calculating the energy difference between the highest occupied molecular orbital (HOMO) for the donor component and the lowest unoccupied molecular orbital (LUMO) for the acceptor component [16, 63]. In practice, theoretically, the maximum Voc value obtained is larger than the experimental one due to energy losses occurring at the interfaces between photoactive layers and electrodes [63]. Moreover, J_{sc} depends mainly on the absorption spectrum of the photoactive layer [66]. For instance, poly(3-hexylthiophene) (P3HT) exhibits a much higher efficiency than poly[2-methoxy-5-(3,7-dimethyloctyloxy)-1,4-phenylen]-*alt*-(vinylene) (MDMO-PPV) because of their different absorption spectra. For example, P3HT absorbs light from about 380 to 670 nm while MDMO-PPV absorbs from 350 to 570 nm [20]. Another important parameter is the FF, for which good transport characteristics of a material are important [65]. For example,

the mobility of very good charge carriers in polyconjugated polymers always ranges between 10^{-3} to 10^{-1} cm^2 V^{-1} s^{-1} [20]. The overall efficiency parameters of the photovoltaic cell can be illustrated in Equation 1.

$$\eta = \frac{p_m}{p_{in}} = \frac{(J_{sc} \times V_{oc} \times FF)}{P_{in}} \quad \text{Equation (1)}$$

Here, η is the efficiency, p_m is the output power, and p_{in} is the input power. These parameters are crucial and depend on the properties of the material. Therefore, simulations can help optimise what could otherwise have been difficult to achieve experimentally.

1.3 Factors affecting the performance of solar cells

The PCE of solar cells is decreased by a number of factors hence, limiting their practical application and commercialisation. The main factors are; the recombination of charges [67], improper band alignment between the layers [68], chemical and physical degradation of cells [69], and thermal losses [70]. The recombination of photogenerated charges in solar cells can arise through the presence of amphoteric defects in the absorber material or interfacial defects. These defects of the absorber act as Shockley-Read-Hall non-radiative centres, which trap charges and thus recombine [67]. Also, recombination can occur at the interfaces between the absorber and HTL or ETL [71], but it has been shown theoretically by Sobayel et al. [72] that amphoteric defects are worse than interfacial defects. For instance, the electrons should be injected effectively into the conduction band of the ETL from the absorber; therefore, the excitons will not recombine [73]. The interfacial recombination has been shown to reduce by introducing a passivation layer at interfaces. When Peng et al. [74] used an ultrathin passivation layer comprising of poly(methyl methacrylate): [6,6]-phenyl-C_{61}-butyric acid methyl ester (PMMA:PCBM); the device showed improved V_{oc} and a high PCE of 20%. With regard to OSCs, photogenerated charges can recombine at the BHJ and induce charges that can also recombine at the electrodes [75, 76]. Introducing a thin interfacial layer between the donor and acceptor material can lead to high PCE of BHJ-OSCs [77].

Similarly, improving the morphological characteristics of the active layer also reduces the recombination of photogenerated charges [78]. Chemical and physical degradation of materials used in solar cells is also a barrier to achieving high efficiency; for instance,

polymers degrade because of contact with water and oxygen [79-81]. Water vapour in the air can diffuse into the active layer causing chemical degradation, or water molecules could be present during fabrication and cause degradation in the process. This explains why the humidity of the surroundings should be as low as possible during thin film solar cell fabrication. Similarly, oxygen can react with polymer semiconductors with the aid of light [82]. For instance, PEDOT:PSS as the HTL is known to be hygroscopic, hence, can absorb water, causing degeneration of the HTL [69]. To mitigate this, encapsulation and choice of better materials reduce this setback [79]. Chang et al. [59] encapsulated a tandem PSC. The device showed outstanding long-term stability (91% of its PCE for a period of 9300 hours in air.

1.4 Computational modelling of solar cells

Computational modelling has gained more scientific interest in the photovoltaic community in the recent past [83, 84]. This arises because computational studies aid in studying device aspects in detail that would otherwise be inaccessible from experimental perspectives. The availability of state-of-the-art computational software/simulators, such as solar cell capacitance simulator (SCAPS) [85, 86], SILVACO ATLAS [87], general-purpose photovoltaic device model (GPVDM) [88], and wx-analysis of microelectronic and photonic structures (wxAMPS) [89], facilitate these studies. These computational aids have been utilised to model and study the physics of solar cell devices. The basic photovoltaic parameters, i.e., PCE, FF, J_{sc}, V_{oc}, and quantum efficiency (QE), are explored with respect to a particular device. Various factors affecting the performance of the device can be elucidated from the simulation. Azri et al. [90] simulated the performance of different electron and hole transport materials in a PSC device with the help of the SCAPS-1D simulator. With the tested ETL materials, zinc oxide (ZnO) and titanium dioxide (TiO_2) were found to be more suitable, while for the HTL, copper(I) thiocyanate (CuSCN) showed better performance. Additionally, tungsten disulfide (WS_2), with a high electron-transport mobility (about 260 $cm^2\ V^{-1}\ s^{-1}$) and a band gap of 1.36 eV, has proved to be a cheap and effective ETL material [91]. Sobayel et al. [72] simulated a PSC with a device configuration of FTO/WS_2/$CH_3NH_3PbI_3$−xClx/2,2′,7,7′-tetrakis (N, N′-di-p-methoxyphenyl amine)-9,9-spirobifluorene (Spiro-OMeTAD)/Ni with SCAPS-1D in which WS_2 as the ETL and the cell exhibited a remarkable PCE of 25.70%. By implementing the aforementioned strategies, the performance of OSC and

PSC devices has significantly improved. However, the performance of the best-performing devices has not yet reached the theoretical Shockley-Queisser limit efficiency of more than 31%. As a result, more concerted efforts are required to improve the performance of solar cell devices and propel the anticipated commercialisation.

1.5 Problem statement

The conversion of solar energy to electricity via the photovoltaic effect is a critical step in the solar energy harvesting process. Although solar energy is the world's most abundant, clean energy source, harvesting and converting it to valuable forms remains a challenge due to the low performance of available materials and technologies, high costs, and environmental concerns. Presently, OSC and PSC devices have been identified as better alternatives to expensive silicon-based devices because of their low production cost, use of cheap and environmentally friendly materials, and relatively promising high performance. However, the efficacy of the OSC and PSC devices is still low compared to commercially available silicon-based devices. Therefore, there is a need to enhance their performance from experimental and computational approaches, which can propel commercialisation. This study focuses on improving the performance of OSC and PSC devices by selection and utilisation of effective materials, optimisation of various cell parameters (such as density of defects, doping densities, and materials), and testing of different device configurations, the introduction of dopants to various device layers, and enhancement the stability of devices.

1.6 Aim and objectives

The aim of the study was to develop and provide insights into graphitic carbon nitride-based and other selected metal-based semiconductors for efficient solar harvesting in OSCs and PSCs, in addition, to theoretically studying the performance of PSCs so as to provide insights and directions for improvement of solar cell devices.

The aim of the research was achieved by undertaking the following specific objectives:

- To investigate the experimentally elusive optoelectronic properties of heptazine-based g-C_3N_4 by computational techniques.
- To study the effect of the exfoliation method (thermal (CNNS-TE) and liquid (CNNS-LE)) on the solar harvesting properties of g-C_3N_4 nanosheets.

- To synthesize and characterise cadmium sulphide and g-C_3N_4 nanosheets (from thermal etching exfoliation method) composites (CdS/CNNS-TE) and incorporate as a third component in P3HT:PCBM photoactive layer blends of the bulk heterojunction organic solar cell (BHJ-OSC).
- To introduce cadmium sulphide and g-C_3N_4 nanosheets (from chemical blowing exfoliation method) (CdS/CNNS-CB) composites into the photoactive layer of the BHJ-OSC and evaluate the device's photovoltaic performance.
- To optimise the performance of a lead-based PSC with the configurations: glass/FTO/IGZO/$CH_3NH_3PbI_3$/spiro-OMETAD/Au and examine the effect of changing various cell parameters such as density of defects, doping densities, and external operating temperature.
- To perform computational simulations on a lead-free PSC with the primary cell configuration: glass/FTO/WS_2/$CH_3NH_3SnI_3$/P3HT/Au and investigate the effect of using different ETL materials (TiO_2, IGZO, SnO_2, ZnO and PCBM) and HTL materials (spiro-OMeTAD, Cu_2O, CuSCN, CuI, and D-PBTTT-14) as well as different back contact metal (Ag, Cu, Ni, and Pt) on the device's performance.
- To perform numerical simulations of a lead-free PSC with the general configuration: glass/FTO/WS_2/$HC(NH_2)_2SnI_3$/HTL/Au and carry out performance optimisation for devices with different HTL materials (copper(I) oxide (Cu_2O) and copper(I) thiocyanate (CuSCN), and organic poly(2,5-bis(3-tetradecylthiophen-2-yl)thieno-[3,2-b]thiophene) (D-PBTTT-14) and poly(3-hexylthiophene-2,5-diyl) (P3HT)) and explore the thermal stabilities.
- To carry out computational modelling of a lead-free PSC with the configuration: glass/FTO/ETL/$HC(NH_2)_2SnI_3$/CuSCN/Au with pure ZnO or doped with g-C_3N_4 ETL materials and investigate the effects of g-C_3N_4 dopant on the overall device performance.

1.7 Thesis synopsis

This thesis presents original research work from experimental and computational approaches undertaken to improve the performance of OSCs and PSCs. The thesis is in two main parts, i.e., the OSC and PSC device sections. Therefore, in the thesis, there are two literature reviews, one in chapter two and the other in chapter seven, covering the literature of the respective study sections. The chapters are presented in manuscript/paper format with uniform style irrespective of the journal styles where it was published/or yet to be submitted to, except for chapters one and twelve. The chapter outlines are presented as follows:

Chapter 1

This chapter provides a general background on OSCs, PSCs and DSSCs, the challenges and prospects of performance enhancement, and the numerical simulation of the physics of solar devices. The motivation, general aim, and specific objectives of the study are also presented in this chapter and the thesis synopsis.

Chapter 2

This chapter presents a literature review of the current status of g-C_3N_4 and its composites (synthesis, morphologies, and characterisation) and its various applications, such as in photocatalysis, sensing, energy storage, and, in particular, solar cells, in which currently there very limited literature. It also presents an overview of computational studies performed on g-C_3N_4 and its various composites. Most of this chapter has been published in *Critical Reviews in Solid State and Material Sciences.* **46**, 189-217.

Chapter 3

This chapter details the computational study undertaken on the g-C_3N_4 nanomaterial with the WIEN2K computational code. The chapter describes the optoelectronic properties of g-C_3N_4, such as band gap, the density of states, optical absorption, reflectivity, dielectric constant, and absorption coefficient. Moreover, the chapter discusses the anisotropic behaviour of heptazine-based g-C_3N_4 for the optical properties investigated. The chapter illustrates the potential application of g-C_3N_4 in optoelectronic devices such as solar cells.

Chapter 4

This chapter presents an experimental comparative study of exfoliation methods, i.e., thermal etching and liquid exfoliation, as applied to bulk g-C_3N_4. The properties of the materials from the two exfoliation methods, in particular with regard to light-harvesting capabilities, are investigated. The photocatalytic characteristics of the materials derived from the two approaches were tested on the degradation of a model pollutant (Rhodamine B). In essence, the thermal etching approach resulted in a better photoactive material than liquid exfoliation. The contents of this chapter were published in the *Journal of Material Science: Materials Electronics*. **32**, 687–706.

Chapter 5

This chapter details the synthesis and characterisation of a cadmium sulfide-doped graphitic carbon nitride nanosheet composite (CdS/CNNS-TE). The CNNS-TE materials were synthesised from the thermal etching method of exfoliation of bulk g-C_3N_4. The composite was incorporated as a third component in the active (P3HT:PCBM) layer of the fabricated BHJ-OSCs, and the performance was evaluated. The PCE of the devices was significantly improved relative to the pristine device (without the dopants).

Chapter 6

The synthesis and evaluation of cadmium sulfide-doped g-C_3N_4 nanosheet (from the chemical blowing exfoliation technique) (CdS/CNNS-CB) composite are covered in this chapter. The advantages of employing CNNS-CB with the chemical blowing exfoliation technique are emphasised. The chapter addresses how the performance of the manufactured BHJ-OSCs can be improved by introducing composites to the photoactive layer. The enhanced performance of the doped devices was attributed to enhanced light harvesting, enhanced charge transfer, and reduced photogenerated charge recombination as a result of the inclusion of the dopant (third component).

Chapter 7

This chapter presents a literature review on PSCs and the numerical simulations of PSCs. In this review, various PSC configurations are highlighted, and the detailed operation of PSCs is presented. Moreover, the challenges facing the commercialisation of PSCs and the different remedies investigated so far are pointed out. Additionally, the section focuses on the detailed operation of numerical simulators (fundamental equations) and

the advantages and disadvantages of some selected simulators. Finally, the prospects of enhancing PSC performance are highlighted.

Chapter 8

This chapter reports the numerical simulation of a lead-based PSC with a general architecture: glass/FTO/IGZO/$CH_3NH_3PbI_3$/spiro-OMeTAD/Au. The effect of changing various parameters and materials (density of defects, thicknesses of components, doping densities of absorber, HTL, and ETL) on the overall performance of the cell is elucidated and presented. The effect of external working temperature conditions of the device and the use of different back contacts are detailed. The device shown in this chapter gave a PCE of 19.97%, and most of this chapter was published in the journal of *Optical and Quantum Electronics.* **54**, 317.

Chapter 9

This chapter reports on optimising the ETL and HTL materials in a lead-free perovskite solar cell with methylammonium tin iodide as the absorber. The effect of using different ETL and HTL materials on the performance of the device is highlighted. Other parameters that affect the performance of the device were also highlighted. Overall, the best ETL (WS_2) and HTL (CuSCN) were identified, and the best PCE achieved was 22.25%. Most of this chapter was published in the *Journal of Computational Electronics:* **20**, 993–1005.

Chapter 10

This chapter describes the computational study of a lead-free perovskite solar cell with WS_2 material as the ETL. Different HTL materials comprising inorganic copper(I) oxide (Cu_2O) and copper(I) thiocyanate (CuSCN), and organic poly(2,5-bis(3-tetradecylthiophen-2-yl)thieno-[3,2-b]thiophene) (D-PBTTT-14) and poly(3-hexylthiophene-2,5-diyl) (P3HT) were tested, and their performance was evaluated. The best device yielded an appreciable PCE above 21% and showed better thermal stability due to the formamidinium part of the perovskite absorber. The better performance for the devices was attributed to the high electron mobility of WS_2, forming an ideal ETL in all the tested devices except for the device with the P3HT HTL. The contents of this chapter are published in *Energy Technology*. **9**, 2100859.

Chapter 11

This chapter describes the computational modelling of lead-free PSCs. The physics of the devices are discussed and presented. The effect of using ZnO doped with g-C_3N_4 (ZnO/g-C_3N_4) as an ETL is investigated. As the concentration of g-C_3N_4 dopant in the devices increased, so did their performance. The optimised lead-free device showed a PCE of 22.23%.

Chapter 12

This chapter provides an in-depth summary of the entire thesis. The key findings of the current study are summarised, as well as suggestions and recommendations for future work are highlighted. Furthermore, it emphasizes the importance of computational tools in studying materials and simulating solar cell devices, which leads to a better understanding and performance enhancement. In general, it emphasises the importance of research in generating new knowledge in material science and solar harvesting applications such as solar cells.

References

[1] A.S. Arul Prishya, L. Chopra, Manikanika, Comprehensive review on uses of silicon dioxide in solar cell. Mater. Today: Proc., (2022). https://doi.org/10.1016/j.matpr.2022.09.348.

[2] T.-Z. Ang, M. Salem, M. Kamarol, H.S. Das, M.A. Nazari, N. Prabaharan, A comprehensive study of renewable energy sources: Classifications, challenges and suggestions. Energy Strategy Rev. **43**, 100939 (2022). https://doi.org/10.1016/j.esr.2022.100939.

[3] J. Khan, M.H. Arsalan, Solar power technologies for sustainable electricity generation – A review. Renew. Sustain. Energy Rev. **55**, 414-425 (2016). https://doi.org/10.1016/j.rser.2015.10.135.

[4] M. Becquerel, Mémoire sur les effets électriques produits sous l'influence des rayons solaires. C. R. Acad. Sci. Paris ou CRAS. **9**, 561-567 (1839).

[5] D.M. Chapin, C.S. Fuller, G.L. Pearson, A new silicon p-n junction photocell for converting solar radiation into electrical power. J. Appl. Phys. **25**, 676-677 (1954). https://doi.org/10.1063/1.1721711.

[6] T. Saga, Advances in crystalline silicon solar cell technology for industrial mass production. NPG Asia Mater. **2**, 96-102 (2010). https://doi.org/10.1038/asiamat.2010.82.

[7] M. Mrinalini, N. Islavath, S. Prasanthkumar, L. Giribabu, Stipulating low production cost solar cells all set to retail…! Chem. Rec. **19**, 661-674 (2019). https://doi.org/10.1002/tcr.201800106.

[8] R.N. Castellano, Solar panel processing, Archives contemporaines. Paris, France, 2010.

[9] K. Vijayan, S.P. Vijayachamundeeswari, K. Sivaperuman, N. Ahsan, T. Logu, Y. Okada, A review on advancements, challenges, and prospective of copper and non-copper based thin-film solar cells using facile spray pyrolysis technique. Solar Energy. **234**, 81-102 (2022). https://doi.org/10.1016/j.solener.2022.01.070.

[10] M. Krebs-Moberg, M. Pitz, T.L. Dorsette, S.H. Gheewala, Third generation of photovoltaic panels: A life cycle assessment. Renew. Energy. **164**, 556-565 (2021). https://doi.org/10.1016/j.renene.2020.09.054.

[11] E. Mirabi, F. Akrami Abarghuie, R. Arazi, Integration of buildings with third-generation photovoltaic solar cells: A review. Clean Energy. **5**, 505-526 (2021). https://doi.org/10.1093/ce/zkab031.

[12] A.W.Y. Ho-Baillie, H.G.J. Sullivan, T.A. Bannerman, H.P. Talathi, J. Bing, S. Tang, A. Xu, D. Bhattacharyya, I.H. Cairns, D.R. McKenzie, Deployment opportunities for space photovoltaics and the prospects for perovskite solar cells. Adv. Mater. Technol. **7**, 2101059 (2022). https://doi.org/10.1002/admt.202101059.

[13] Y. Bensouda, D. Barrit, Mini-review on all-inorganic lead-based perovskite solar cells: Challenges and opportunities for production and upscaling. Emergent Mater. **5**, 207-225 (2022). https://doi.org/10.1007/s42247-022-00364-0.

[14] A.P. Kirk, Solar photovoltaic cells: Photons to electricity, Academic Press. USA, 2014.

[15] S. Nema, R. Nema, G. Agnihotri, Matlab/simulink based study of photovoltaic cells/modules/array and their experimental verification. Int. J. Energy Environ. **1**, 487-500 (2010).

[16] F.A. Larrain, C. Fuentes-Hernandez, W.-F. Chou, V.A. Rodriguez-Toro, T.-Y. Huang, M.F. Toney, B. Kippelen, Stable solvent for solution-based electrical doping of semiconducting polymer films and its application to organic solar cells. Energy Environ. Sci. **11**, 2216-2224 (2018). https://doi.org/10.1039/C8EE00811F.

[17] J. Hou, O. Inganäs, R.H. Friend, F. Gao, Organic solar cells based on non-fullerene acceptors. Nat. Mater. **17**, 119 (2018). https://doi.org/10.1038/nmat5063.

[18] T.A. Amollo, G.T. Mola, V.O. Nyamori, Polymer solar cells with reduced graphene oxide–germanium quantum dots nanocomposite in the hole transport layer. J Mater Sci: Mater Electron. **29**, 7820–7831 (2018). https://doi.org/10.1007/s10854-018-8781-1.

[19] J. Zhang, H.S. Tan, X. Guo, A. Facchetti, H. Yan, Material insights and challenges for non-fullerene organic solar cells based on small molecular acceptors. Nat. Energy. **3**, 720–731 (2018). https://doi.org/10.1038/s41560-018-0181-5.

[20] P. Troshin, R. Lyubovskaya, V. Razumov, Organic solar cells: structure, materials, critical characteristics, and outlook. Nanotechnol. Russ. **3**, 242 (2008). https://doi.org/10.1134/S1995078008050029.

[21] W. Li, L. Ye, S. Li, H. Yao, H. Ade, J. Hou, A high-efficiency organic solar cell enabled by the strong intramolecular electron push–pull effect of the nonfullerene acceptor. Adv. Mater. **30**, 1707170 (2018). https://doi.org/10.1002/adma.201707170.

[22] M.C. Heiber, T. Okubo, S.-J. Ko, B.R. Luginbuhl, N.A. Ran, M. Wang, H. Wang, M.A. Uddin, H.Y. Woo, G.C. Bazan, Measuring the competition between bimolecular charge recombination and charge transport in organic solar cells under operating conditions. Energy Environ. Sci. **11**, 3019-3032 (2018). https://doi.org/10.1039/C8EE01559G.

[23] M.Z. Rahman, K. Davey, S.-Z. Qiao, Carbon, nitrogen and phosphorus containing metal-free photocatalysts for hydrogen production: progress and challenges. J. Mater. Chem. A. **6**, 1305-1322 (2018). https://doi.org/10.1039/C7TA10404A

[24] S.M. Menke, N.A. Ran, G.C. Bazan, R.H. Friend, Understanding energy loss in organic solar cells: toward a new efficiency regime. Joule. **2**, 25-35 (2018). https://doi.org/10.1016/j.joule.2017.09.020.

[25] H. Cha, S. Wheeler, S. Holliday, S.D. Dimitrov, A. Wadsworth, H.H. Lee, D. Baran, I. McCulloch, J.R. Durrant, Influence of blend morphology and energetics on charge separation and recombination dynamics in organic solar cells incorporating a nonfullerene acceptor. Adv. Funct. Mater. **28**, 1704389 (2018). https://doi.org/10.1002/adfm.201704389.

[26] D. Baran, N. Gasparini, A. Wadsworth, C.H. Tan, N. Wehbe, X. Song, Z. Hamid, W. Zhang, M. Neophytou, T. Kirchartz, Robust nonfullerene solar cells

approaching unity external quantum efficiency enabled by suppression of geminate recombination. Nat. Commun. **9**, 2059 (2018). https://doi.org/10.1038/s41467-018-04502-3.

[27] B.Y. Wang, T.H. Yoo, J.W. Lim, B.I. Sang, D.S. Lim, W.K. Choi, D.K. Hwang, Y.J. Oh, Enhanced light scattering and trapping effect of Ag nanowire mesh electrode for high efficient flexible organic solar cell. Small. **11**, 1905-1911 (2015). https://doi.org/10.1002/smll.201402161.

[28] E. Jeong, G. Zhao, M. Song, S.M. Yu, J. Rha, J. Shin, Y.-R. Cho, J. Yun, Simultaneous improvements in self-cleaning and light-trapping abilities of polymer substrates for flexible organic solar cells. J. Mater. Chem. A. **6**, 2379-2387 (2018). https://doi.org/10.1039/C7TA09351A.

[29] J. Zhao, Y. Li, G. Yang, K. Jiang, H. Lin, H. Ade, W. Ma, H. Yan, Efficient organic solar cells processed from hydrocarbon solvents. Nat. Energy. **1**, 15027 (2016). https://doi.org/10.1038/nenergy.2015.27.

[30] B.C. Thompson, J.M. Fréchet, Polymer–fullerene composite solar cells. Angew. Chem. Int. Ed. **47**, 58-77 (2008). https://doi.org/10.1002/anie.200702506.

[31] H. Fu, Z. Wang, Y. Sun, Polymer donors for high-performance non-fullerene organic solar cells. Angew. Chem. Int. Ed. **58**, 4442-4453 (2019). https://doi.org/10.1002/anie.201806291.

[32] W. Ma, C. Yang, X. Gong, K. Lee, A.J. Heeger, Thermally stable, efficient polymer solar cells with nanoscale control of the interpenetrating network morphology. Adv. Funct. Mater. **15**, 1617-1622 (2005). https://doi.org/10.1002/adfm.200500211.

[33] M.A. Green, Corrigendum to 'Solar cell efficiency tables (version 49)'[Prog. Photovolt: Res. Appl. 2017; 25: 3–13]. Prog. Photovolt.: Res. Appl. **4**, 333-334 (2017). https://doi.org/10.1002/pip.2876.

[34] P. Wang, R. Li, B. Chen, F. Hou, J. Zhang, Y. Zhao, X. Zhang, Gradient energy alignment engineering for planar perovskite solar cells with efficiency over 23%. Adv. Mater. **32**, 1905766 (2020). https://doi.org/10.1002/adma.201905766.

[35] S. Yang, W. Fu, Z. Zhang, H. Chen, C.-Z. Li, Recent advances in perovskite solar cells: Efficiency, stability and lead-free perovskite. J. Mater. Chem. A, (2017). https://doi.org/10.1039/C7TA00366H

[36] Y. Cheng, Y. Peng, A.K.-Y. Jen, H.-L. Yip, Development and challenges of metal halide perovskite solar modules. Sol. RRL. **6**, 2100545 (2022). https://doi.org/10.1002/solr.202100545.

[37] Q. Zhang, F. Hao, J. Li, Y. Zhou, Y. Wei, H. Lin, Perovskite solar cells: must lead be replaced – and can it be done? Sci Technol Adv Mater. **19**, 425-442 (2018). https://doi.org/10.1080/14686996.2018.1460176.

[38] G. Schileo, G. Grancini, Lead or no lead? Availability, toxicity, sustainability and environmental impact of lead-free perovskite solar cells. J. Mater. Chem. C **9**,67-76 (2021). https://doi.org/10.1039/D0TC04552G.

[39] W. Ke, M.G. Kanatzidis, Prospects for low-toxicity lead-free perovskite solar cells. Nat. Commun. **10**, 965 (2019). https://doi.org/10.1038/s41467-019-08918-3.

[40] S.S. Dipta, A. Uddin, Stability issues of perovskite solar cells: A critical review. Energy Technol. **9**, 2100560 (2021). https://doi.org/10.1002/ente.202100560.

[41] A. Amat, E. Mosconi, E. Ronca, C. Quarti, P. Umari, M.K. Nazeeruddin, M. Grätzel, F. De Angelis, Cation-induced band-gap tuning in organohalide perovskites: Interplay of spin–orbit coupling and octahedra tilting. Nano Lett. **14**, 3608-3616 (2014). https://doi.org/10.1021/nl5012992.

[42] E. Mosconi, E. Ronca, F. De Angelis, First-principles investigation of the TiO_2/organohalide perovskites interface: The role of interfacial chlorine. J. Phys. Chem. Lett. **5**, 2619-2625 (2014). https://doi.org/10.1021/jz501127k.

[43] L. Yang, A.T. Barrows, D.G. Lidzey, T. Wang, Recent progress and challenges of organometal halide perovskite solar cells. Rep. Prog. Phys. **79**, 026501 (2016). https://doi.org/10.1088/0034-4885/79/2/026501.

[44] A. Akbari, J. Hashemi, E. Mosconi, F. De Angelis, M. Hakala, First principles modelling of perovskite solar cells based on TiO_2 and Al_2O_3: Stability and interfacial electronic structure. J. Mater. Chem. A. **5**, 2339-2345 (2017). https://doi.org/10.1039/C6TA08874K.

[45] P. Liu, Y. Sun, S. Wang, H. Zhang, Y. Gong, F. Li, Y. Shi, Y. Du, X. Li, S.-s. Guo, Q. Tai, C. Wang, X.-Z. Zhao, Two dimensional graphitic carbon nitride quantum dots modified perovskite solar cells and photodetectors with high performances. J. Power Sources. **451**, 227825 (2020). https://doi.org/10.1016/j.jpowsour.2020.227825.

[46] M. Mehrabian, S. Dalir, Numerical simulation of highly efficient dye sensitized solar cell by replacing the liquid electrolyte with a semiconductor solid layer. Optik. **169**, 214-223 (2018). https://doi.org/10.1016/j.ijleo.2018.05.059.

[47] S. Mahalingam, A. Nugroho, D. Floresyona, K.S. Lau, A. Manap, C.H. Chia, N. Afandi, Bio and non-bio materials-based quasi-solid state electrolytes in DSSC: A review. Int J Energy Res. . **46**, 5399-5422 (2022). https://doi.org/10.1002/er.7541.

[48] Y. Luo, L. Yang, J. Zhang, Photoelectrochemical polymerization for solid-state dye-sensitized solar cells. Macromol. Rapid Commun. **43**, 2100762 (2022). https://doi.org/10.1002/marc.202100762.

[49] F. Jahantigh, M.J. Safikhani, The effect of HTM on the performance of solid-state dye-sanitized solar cells (SDSSCs): A SCAPS-1D simulation study. J. Appl. Phys A. **125**, 276 (2019). https://doi.org/10.1007/s00339-019-2582-0.

[50] B.A. Ek, T.S. Gershon, S. Guha, O. Gunawan, T.K. Todorov, Transparent conducting oxide as top-electrode in perovskite solar cell by non-sputtering process. 2018, Google Patents.

[51] L. Steier, S. Holliday, A bright outlook on organic photoelectrochemical cells for water splitting. J. Mater. Chem. A. **6**, 21809-21826 (2018). https://doi.org/10.1039/C8TA07036A.

[52] T. Ameri, G. Dennler, C. Lungenschmied, C.J. Brabec, Organic tandem solar cells: A review. Energy Environ. Sci. **2**, 347-363 (2009). https://doi.org/10.1039/B817952B.

[53] J. You, L. Dou, K. Yoshimura, T. Kato, K. Ohya, T. Moriarty, K. Emery, C.-C. Chen, J. Gao, G. Li, A polymer tandem solar cell with 10.6% power conversion efficiency. Nat Commun. **4**, 1446 (2013). https://doi.org/10.1038/ncomms2411.

[54] M. Dürr, A. Bamedi, A. Yasuda, G. Nelles, Tandem dye-sensitized solar cell for improved power conversion efficiencies. Appl. Phys. Lett. **84**, 3397-3399 (2004). https://doi.org/10.1063/1.1723685.

[55] P. Cheng, Y. Liu, S.-Y. Chang, T. Li, P. Sun, R. Wang, H.-W. Cheng, T. Huang, L. Meng, S. Nuryyeva, Efficient tandem organic photovoltaics with tunable rear sub-cells. Joule. **3**, 432-442 (2018). https://doi.org/10.1016/j.joule.2018.11.011.

[56] M. Hosseinnezhad, Enhanced performance of dye-sensitized solar cells using perovskite/DSSCs tandem design. J. Electron. Mater. **48**, 5403-5408 (2019). https://doi.org/10.1007/s11664-019-07272-w.

[57] A.R. bin Mohd Yusoff, D. Kim, H.P. Kim, F.K. Shneider, W.J. da Silva, J. Jang, A high efficiency solution processed polymer inverted triple-junction solar cell exhibiting a power conversion efficiency of 11.83%. Energy Environ. Sci. **8**, 303-316 (2015). https://doi.org/10.1039/C4EE03048F.

[58] J. You, L. Dou, K. Yoshimura, T. Kato, K. Ohya, T. Moriarty, K. Emery, C.-C. Chen, J. Gao, G. Li, Y. Yang, A polymer tandem solar cell with 10.6% power conversion efficiency. Nat. Commun. **4**, 1446 (2013). https://doi.org/10.1038/ncomms2411.

[59] C.-Y. Chang, B.-C. Tsai, Y.-C. Hsiao, M.-Z. Lin, H.-F. Meng, Solution-processed conductive interconnecting layer for highly-efficient and long-term stable monolithic perovskite tandem solar cells. Nano Energy. **55**, 354-367 (2019). https://doi.org/10.1016/j.nanoen.2018.10.014.

[60] J. You, L. Dou, Z. Hong, G. Li, Y. Yang, Recent trends in polymer tandem solar cells research. Prog. Polym. Sci. **38**, 1909-1928 (2013). https://doi.org/10.1016/j.progpolymsci.2013.04.005.

[61] L. Meng, Y. Zhang, X. Wan, C. Li, X. Zhang, Y. Wang, X. Ke, Z. Xiao, L. Ding, R. Xia, Organic and solution-processed tandem solar cells with 17.3% efficiency. Science. **361**, 1094-1098 (2018). https://doi.org/10.1126/science.aat2612.

[62] K. Zhang, B. Fan, R. Xia, X. Liu, Z. Hu, H. Gu, S. Liu, H.L. Yip, L. Ying, F. Huang, Highly efficient tandem organic solar cell enabled by environmentally friendly solvent processed polymeric interconnecting layer. Adv. Energy Mater. **8**, 1703180 (2018). https://doi.org/10.1002/aenm.201703180.

[63] Z. Zheng, Q. Hu, S. Zhang, D. Zhang, J. Wang, S. Xie, R. Wang, Y. Qin, W. Li, L. Hong, A highly efficient non-fullerene organic solar cell with a fill factor over 0.80 enabled by a fine-tuned hole-transporting layer. Adv. Mater. **30**, 1801801 (2018). https://doi.org/10.1002/adma.201801801.

[64] X. Xu, T. Yu, Z. Bi, W. Ma, Y. Li, Q. Peng, Realizing over 13% efficiency in green-solvent-processed nonfullerene organic solar cells enabled by 1, 3, 4-thiadiazole-based wide-bandgap copolymers. Adv. Mater. **30**, 1703973 (2018). https://doi.org/10.1002/adma.201703973.

[65] Z. He, C. Zhong, X. Huang, W.Y. Wong, H. Wu, L. Chen, S. Su, Y. Cao, Simultaneous enhancement of open-circuit voltage, short-circuit current density, and fill factor in polymer solar cells. Adv. Mater. **23**, 4636-4643 (2011). https://doi.org/10.1002/adma.201103006.

[66] D. Liu, B. Kan, X. Ke, N. Zheng, Z. Xie, D. Lu, Y. Liu, Extended conjugation length of nonfullerene acceptors with improved planarity via noncovalent interactions for high-performance organic solar cells. Adv. Energy Mater. **8**, 1801618 (2018). https://doi.org/10.1002/aenm.201801618.

[67] J. Chen, N.G. Park, Causes and solutions of recombination in perovskite solar cells. Adv. Mater. **31**, 1803019 (2019). https://doi.org/10.1002/adma.201803019.

[68] K. Lu, Y. Lei, R. Qi, J. Liu, X. Yang, Z. Jia, R. Liu, Y. Xiang, Z. Zheng, Fermi level alignment by copper doping for efficient ITO/perovskite junction solar cells. J. Mater. Chem. A. **5**, 25211-25219 (2017). https://doi.org/10.1039/C7TA07828E.

[69] S.K. Gupta, S. Banerjee, A. Singh, L.S. Pali, A. Garg, Modeling of degradation in normal and inverted OSC devices. Sol. Energy Mater. Sol. Cells. **191**, 329-338 (2019). https://doi.org/10.1016/j.solmat.2018.11.039.

[70] A. Le Bris, J.-F. Guillemoles, Hot carrier solar cells: Achievable efficiency accounting for heat losses in the absorber and through contacts. Appl. Phys. Lett. **97**, 113506 (2010). https://doi.org/10.1063/1.3489405.

[71] Y. Tu, X. Yang, R. Su, D. Luo, Y. Cao, L. Zhao, T. Liu, W. Yang, Y. Zhang, Z. Xu, Diboron-assisted interfacial defect control strategy for highly efficient planar perovskite solar cells. Adv. Mater. **30**, 1805085 (2018). https://doi.org/10.1002/adma.201805085.

[72] K. Sobayel, M. Akhtaruzzaman, K. Rahman, M. Ferdaous, Z.A. Al-Mutairi, H.F. Alharbi, N.H. Alharthi, M.R. Karim, S. Hasmady, N. Amin, A comprehensive defect study of tungsten disulfide (WS_2) as electron transport layer in perovskite solar cells by numerical simulation. Results Phys. **12**, 1097-1103 (2019). https://doi.org/10.1016/j.rinp.2018.12.049.

[73] K.H. Wong, K. Ananthanarayanan, J. Luther, P. Balaya, Origin of hole selectivity and the role of defects in low-temperature solution-processed molybdenum oxide interfacial layer for organic solar cells. J. Phys. Chem. C. **116**, 16346-16351 (2012). https://doi.org/10.1021/jp303679y.

[74] J. Peng, Y. Wu, W. Ye, D.A. Jacobs, H. Shen, X. Fu, Y. Wan, T. Duong, N. Wu, C. Barugkin, H.T. Nguyen, D. Zhong, J. Li, T. Lu, Y. Liu, M.N. Lockrey, K.J. Weber, K.R. Catchpole, T.P. White, Interface passivation using ultrathin polymer–fullerene films for high-efficiency perovskite solar cells with negligible hysteresis. Energy Environ. Sci. **10**, 1792-1800 (2017). https://doi.org/10.1039/C7EE01096F.

[75] A. Rahimi Chatri, S. Torabi, V.M. Le Corre, L.J.A. Koster, Impact of electrodes on recombination in bulk heterojunction organic solar cells. ACS Appl. Mater. Interfaces. **10**, 12013-12020 (2018). https://doi.org/10.1021/acsami.7b19234.

[76] J. Brauer, M. Causa, N. Banerji, Charge generation and recombination in organic solar cells, in *Nanostructured materials for type III photovoltaics*. 2017. p. 226-267.

[77] T. Heidel, D. Hochbaum, J. Sussman, V. Singh, M. Bahlke, I. Hiromi, J. Lee, M. Baldo, Reducing recombination losses in planar organic photovoltaic cells using multiple step charge separation. J. Appl. Phys. **109**, 104502 (2011). https://doi.org/10.1063/1.3585863.

[78] K. Zhu, T.B. Vinzant, N.R. Neale, A.J. Frank, Removing structural disorder from oriented TiO_2 nanotube arrays: Reducing the dimensionality of transport and recombination in dye-sensitized solar cells. Nano Lett. **7**, 3739-3746 (2007). https://doi.org/10.1021/nl072145a.

[79] M. Jørgensen, K. Norrman, F.C. Krebs, Stability/degradation of polymer solar cells. Sol. Energy Mater Sol. Cells. **92**, 686-714 (2008). https://doi.org/10.1016/j.solmat.2008.01.005.

[80] K. Norrman, M.V. Madsen, S.A. Gevorgyan, F.C. Krebs, Degradation patterns in water and oxygen of an inverted polymer solar cell. J. Am. Chem. Soc. **132**, 16883-16892 (2010). https://doi.org/10.1021/ja106299g.

[81] K. Kawano, R. Pacios, D. Poplavskyy, J. Nelson, D.D. Bradley, J.R. Durrant, Degradation of organic solar cells due to air exposure. Sol. Energy Mater Sol. Cells. **90**, 3520-3530 (2006). https://doi.org/10.1016/j.solmat.2006.06.041.

[82] I. Borazan, A study about lifetime of photovoltaic fibers. Sol. Energy Mater Sol. Cells. **192**, 52-56 (2019). https://doi.org/10.1016/j.solmat.2018.12.003.

[83] S. Naqvi, A. Patra, Hole transport materials for perovskite solar cells: A computational study. Mater. Chem. Phys. **258**, 123863 (2021). https://doi.org/10.1016/j.matchemphys.2020.123863.

[84] H. Sabzyan, F. Ghaderi, Computational study of iron perovskite $CH_3NH_3FeI_3$ as an alternative to the lead perovskite $CH_3NH_3PbI_3$ for application in solar cells. J. Phys.: Condens. Matter. **32**, 465501 (2020). https://doi.org/10.1088/1361-648x/ab9b4f.

[85] N.F. Ramli, S. Sepeai, N.F.M. Rostan, N.A. Ludin, M.A. Ibrahim, M.A.M. Teridi, S.H. Zaidi. Model development of monolithic tandem silicon-perovskite solar cell by SCAPS simulation. in *AIP Conference Proceedings*. 2017. AIP Publishing LLC. https://doi.org/10.1063/1.4982178.

[86] N. Rono, A.E. Merad, J.K. Kibet, B.S. Martincigh, V.O. Nyamori, A theoretical investigation of the effect of the hole and electron transport materials on the performance of a lead-free perovskite solar cell based on $CH_3NH_3SnI_3$. J. Comput. Electron. **20**, 993-1005 (2021). https://doi.org/10.1007/s10825-021-01673-z.

[87] S. Michael, A novel approach for the modeling of advanced photovoltaic devices using the SILVACO/ATLAS virtual wafer fabrication tools. Sol. Energy Mater. Sol. Cells. **87**, 771-784 (2005). https://doi.org/10.1016/j.solmat.2004.07.050.

[88] A. Hima, A. Khechekhouche, I. Kemerchou, N. Lakhdar, B. Benhaoua, F. Rogti, I. Telli, A. Saadoun, GPVDM simulation of layer thickness effect on power conversion efficiency of $CH_3NH_3PbI_3$ based planar heterojunction solar cell. Int. J. Energetica. **3** (2018). https://www.ijeca.info.

[89] S. Yaşar, S. Kahraman, S. Çetinkaya, Ş. Apaydın, İ. Bilican, İ. Uluer, Numerical thickness optimization study of CIGS based solar cells with wxAMPS. Optik. **127**, 8827-8835 (2016). https://doi.org/10.1016/j.ijleo.2016.06.094.

[90] F. Azri, A. Meftah, N. Sengouga, A. Meftah, Electron and hole transport layers optimization by numerical simulation of a perovskite solar cell. Sol. Energy. **181**, 372-378 (2019). https://doi.org/10.1016/j.solener.2019.02.017.

[91] P.P. Hankare, A.H. Manikshete, D.J. Sathe, P.A. Chate, A.A. Patil, K.M. Garadkar, WS_2 thin films: Optoelectronic characterization. J. Alloys Compd. **479**, 657-660 (2009). https://doi.org/10.1016/j.jallcom.2009.01.024.

CHAPTER TWO

CRITICAL REVIEWS IN SOLID STATE AND MATERIALS SCIENCES
2021, VOL. 46, NO. 3, 189–217
https://doi.org/10.1080/10408436.2019.1709414

REVIEW

A review of the current status of graphitic carbon nitride

Nicholas Rono[a], Joshua K. Kibet[b], Bice S. Martincigh[a], and Vincent O. Nyamori[a]

[a]School of Chemistry and Physics, University of KwaZulu-Natal, Durban, South Africa; [b]Chemistry Department, Egerton University, Egerton, Kenya

ABSTRACT

Graphitic carbon nitride (g-C_3N_4) has become an important material because of its attractive optoelectronic properties. It has been applied in various fields such as photovoltaics, biosensing, and photocatalysis. As an analog of graphene, it has layers which can be transformed into different morphologies including nanosheets, nanotubes, and quantum dots. Pristine g-C_3N_4 exhibits a low specific surface area and a high rate of recombination of photogenerated charges. Therefore, modification is required in order to improve its properties, for instance, by doping it with other atoms and transforming it into another morphology. In this review, the synthesis, modifications, and applications of g-C_3N_4 are evaluated. The use of theoretical strategies to understand various properties of g-C_3N_4 and its composites is highlighted. Moreover, the current status on the application of g-C_3N_4 is explored. Ultimately, this review will shed more light on the uses and modifications of g-C_3N_4 for future applications.

KEYWORDS

graphitic carbon nitride; composites; photocatalysis; photovoltaics; density functional theory

Table of contents

CONTACT Vincent O. Nyamori Nyamori@ukzn.ac.za
Color versions of one or more of the figures in the article can be found online at www.tandfonline.com/bsms.

CHAPTER TWO

A review of the current status of graphitic carbon nitride

Nicholas Rono,[a] Joshua K. Kibet,[b] Bice S. Martincigh[a] and Vincent O. Nyamori[a]*

[a]School of Chemistry and Physics, University of KwaZulu-Natal, Westville Campus, Private Bag X54001, Durban, 4000, South Africa

[b]Chemistry Department, Egerton University, Njoro Campus, P.O. Box 536-20115, Egerton, Kenya

*Corresponding author: E-mail: Nyamori@ukzn.ac.za, Tel: +27312608256

Abstract

Graphitic carbon nitride (g-C_3N_4) has become an important material because of its attractive optoelectronic properties. It has been applied in various fields such as photovoltaics, biosensing, and photocatalysis. As an analogue of graphene, it has layers which can be transformed into different morphologies including nanosheets, nanotubes and quantum dots. Pristine g-C_3N_4 exhibits a low specific surface area and a high rate of recombination of photogenerated charges. Therefore, modification is required in order to improve its properties, for instance, by doping it with other atoms and transforming it into another morphology. In this review, the synthesis, modifications and applications of g-C_3N_4 are evaluated. The use of theoretical strategies to understand various properties of g-C_3N_4 and its composites is highlighted. Moreover, the current status on the application of g-C_3N_4 is explored. Ultimately, this review will shed more light on the uses and modifications of g-C_3N_4 for future applications.

Keywords

graphitic carbon nitride; morphologies; doping; composites; photocatalysis; photovoltaics; density functional theory

2.1 Introduction

Globally, the demand for sustainable and clean energy, together with environmental degradation challenges, have caused mounting concern to the nanoscience community, environmentalists, policymakers, economists and many other parties [1, 2]. This has arisen from the exponential depletion of other sources of energy, such as fossil fuels, which are also not environmentally-friendly [3]. The combustion of fossil fuels to produce energy has caused environmental damage, global warming and climate change [4-6]. Similarly, the use of metal-based photocatalysts, such as titanium dioxide [7], cadmium sulfide [8] and platinum [9], are not environmentally benign. Accordingly, solar energy conversion is promising in offering the best solution to these challenges [10-12] and, therefore, solar technologies have attracted a great deal of scientific attention because they are believed to be sustainable, clean and offer unlimited use in the presence of solar energy [13]. There is therefore a quest for green and environmentally-friendly nanostructured materials that can harness solar energy and convert it into useful forms, such as electricity [11], as well as driving photo-initiated reactions for synthesis and environmental clean-up [14].

One such material that has attracted much attention is graphitic carbon nitride (g-C_3N_4). Its favourable attributes include its tuneable optoelectronic properties and the fact that it is a metal-free semiconductor [15-17]. It has been applied in a number of fields, including photocatalysis [18], sensing [19, 20], and photovoltaics [21] because it exhibits better performance as well as being environmentally benign [22-24]. Photocatalytic g-C_3N_4-based materials synergistically remove pollutants from the environment, by means of adsorption as well as photocatalysis, and hence have wide application in pollutant degradation [25]. Similarly, in photovoltaics, this material has a relatively low band gap (approx. 2.7 eV), which allows for the absorption of more light leading to an increased rate of generation of photocharges, and as a result, more electrons will be available in the conduction band to drive photo-reactions [26]. As well-established sensors, g-C_3N_4-based materials have advantages such as high sensitivity and selectivity of analytes, high surface area and chemical stability [27].

Graphitic carbon nitride has been synthesised through various routes, but in essence bulk g-C_3N_4 has been obtained by pyrolysis of any nitrogen-rich precursor, such as melamine

[28], thiourea [29], urea [30] and cyanamide [31]. Unfortunately, bulk g-C_3N_4 exhibits poor electronic properties such as a high rate of recombination of photogenerated electrons and holes, small specific surface area and low quantum yield [25, 32]. This is because of its structural defects which arise due to stacking of the layers leading to a low specific surface area and a high recombination rate of photogenerated charges [33]. To circumvent these challenges, exfoliation has been utilised to achieve materials with large specific surface areas and thus increased surfaces for reactions, and low recombination rates of photogenerated charges due to reduced diffusion path lengths leading to improved electronic properties for various applications [34].

Bulk g-C_3N_4 is analogous to graphene in that it consists of layers which are held together by weak van der Waals forces of attraction, thus it is possible to exfoliate these layers into nanosheets [35]. Exfoliation methods, such as liquid phase exfoliation [36, 37], thermal etching exfoliation [38, 39], ultrasonic-assisted exfoliation [40], chemical blowing [41] and chemical (utilising strong acids) exfoliation [42] have been utilised to achieve nanostructured materials with few sheets of g-C_3N_4. Although many efforts have been dedicated to effectively exfoliate bulk g-C_3N_4 into sheets, there is still a challenge in achieving a good yield, controlled morphology and ultrathin nanosheets, thus the need for more research in this area [43, 44]. Once bulk g-C_3N_4 (three dimensional) is transformed into nanosheets (two dimensional) [45] it can be transformed into different morphologies, such as nanorods/nanotubes (one-dimensional) [46] and quantum dots (zero-dimensional) [47, 48], which find application in industrial processes and energy harvesting. Tubular g-C_3N_4 has been achieved through hard, soft and self-templating methods [49], quantum dots have been obtained by hydrothermal etching means [25] and, recently, honeycomb-structured g-C_3N_4 was prepared by a salt-template-assisted strategy via a one-step process [50].

In addition to exfoliation, other efforts to enhance the optoelectronic properties of g-C_3N_4 have been tested; these include, construction of heterojunctions [51], coupling with carbonaceous materials [52, 53] and introduction of structural defects [54]. Two-dimensional g-C_3N_4 has been utilised in constructing heterojunctions with other materials [55]. Hitherto, heterojunctions consisting of 0D/2D [44, 56], 1D/2D, and 2D/2D [41, 57] systems have emerged. Huang et al.[44] proposed the current trends in merging 0D with 2D g-C_3N_4 to form 0D/2D composites with enhanced photocatalytic performance.

Similarly, Ong [58] reviewed the 2D/2D interface of g-C_3N_4 with other 2D nanomaterials. Undoubtedly, construction of heterojunctions, such as type II [56, 59], Schottky [60], and Z-schemes [61, 62], enhance photo-driven reactions by reducing the diffusion path length of charges, lowering the recombination rate of photogenerated charges, and increasing the surface area of the photocatalyst. Furthermore, to intrinsically modify g-C_3N_4, Niu et al. [54] introduced defects on g-C_3N_4, by subjecting it to heat and this enhances its photocatalytic activity. To further improve the electronic properties of g-C_3N_4, doping with other materials, including nitrogen [63], boron [64], bismuth [65], and phosphorus [66], has been performed.

Most studies have been carried out on the use of g-C_3N_4 as a photocatalyst [15, 67-69]. Wang et al. [70] were the first to report the use of graphitic carbon nitride as a visible light photocatalyst for splitting water and, since then, more studies have been conducted on the photocatalytic nature of this material.[71] Chen et al. [72] reported the assimilation of g-C_3N_4 dots in the active layer of bulk heterojunction (BHJ) polymer solar cells (PSCs) and the power conversion efficiency (PCE) of the cell was significantly improved. However, it is worth noting that the use of g-C_3N_4 in polymer solar cells is very narrow in the literature [72]. This could be apparently attributed to the fact that, although g-C_3N_4 has good light absorption capabilities due to its low band gap energy (2.7 eV), it has limited electronic conductivity [73, 74] as a result of the high recombination rate of photogenerated charges, which limits its application in organic solar cells. Therefore, modifications to this material must be sustained to improve its properties. Nevertheless, the material is low-cost, lightweight and easy to process and has a tuneable band gap structure; it is promising in a wide range of applications including photovoltaics, sensing and photocatalysis. This review highlights current progress made on the synthesis and modifications of g-C_3N_4. Furthermore, an application of a computational strategy for the study of g-C_3N_4 is presented.

2.2 Structures of graphitic carbon nitride

Graphitic carbon nitride is formed by polymerisation of cheap nitrogen-containing precursors, such as melamine. A polymer of C_3N_4 was first reported in the 1830s and since then much work has been carried out to determine how different synthetic procedures affect the product formed in terms of its reactivity and morphology.

2.2.1. Geometrical structure

The precise architecture of g-C_3N_4 consists of two main units, namely, tri-s-triazine (C_6N_7) and s-triazine (C_3N_3) rings, as presented in Figure 2.1 [75, 76]. Tri-s-triazine has been established to be more stable under ambient conditions [77]. Density functional theory (DFT) calculations on the two main units of g-C_3N_4 have also shown that tri-s-triazine is the most stable thermodynamically [75, 78]. Theoretically, it has been reported that the ideal surface area of a monolayer sheet can be increased up to about 2500 m^2 g^{-1} [79].

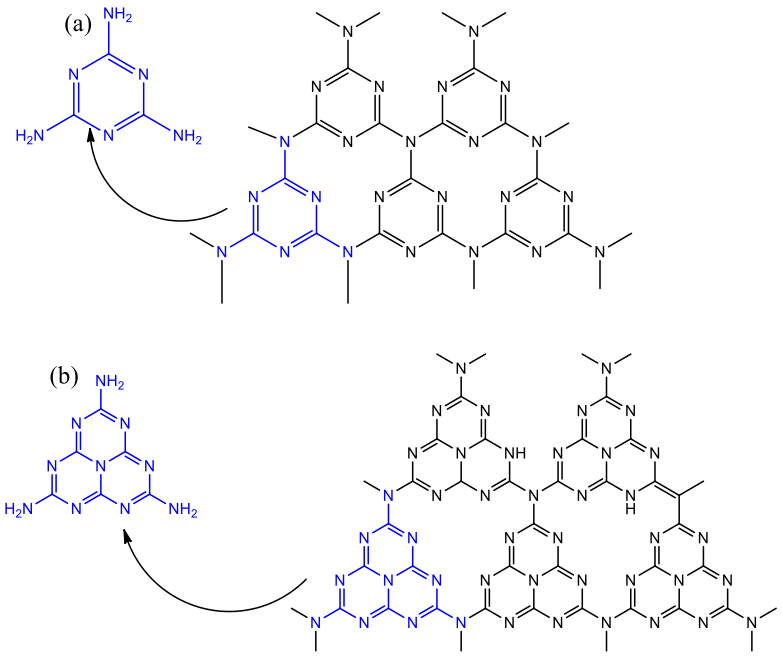

Figure 2.1: (a) s-Triazine and (b) tri-s-triazine-based structures of g-C_3N_4 [76]

Graphene, which is similar to g-C_3N_4, is largely studied and popular [72]. Typically, it has a 2D sheet of sp^2-hybridised carbons [80] while g-C_3N_4 has π-conjugated graphitic planes produced through sp^2-hybridisation of carbon as well as nitrogen atoms [81]. Fina et al. [82] studied the three dimensional (3D) structure of g-C_3N_4 by using both powder X-ray diffraction (PXRD) and neutron diffraction strategies. They showed that the as-prepared g-C_3N_4 exhibits a 3D configuration with mis-alignment of tri-s-triazine based-layers (A-B configuration and not A-A configuration). The layers mis-align so as to avoid the repulsive forces of π-electrons in adjacent layers.

2.2.2. Electronic structure

Graphitic carbon nitride has become a centre of discussion because of its unique electronic properties and potential applications [83]. It contains carbon and nitrogen which are sp^2 hybridised forming a π-conjugated delocalized system. The lone pair of electrons from nitrogen is responsible for the formation of the lone pair valence band and, hence, the band structure [84]. The combination of the lone pair state and π-bonding stabilises the lone pair position, thus it is worth noting that it is the lone pair of nitrogen which is pivotal in the electronic structure of g-C_3N_4 [85]. The material is an n-type semiconductor [29]. Theoretical strategies involving DFT calculations predicted that the valence band consists of nitrogen P_z orbitals while the conduction band consists of carbon P_z orbitals, thus carbon atoms acts as points where reduction takes place and nitrogen atoms as points where oxidation takes place [86]. As a photocatalyst, g-C_3N_4 has the ability to separate holes and electrons. The band gap of 2.7 eV enables it to absorb sunlight and, thus, it can be used for purification of water, hydrogen generation and solar cell applications [84, 87]. Figure 2.2 shows a representation of the charge transfer in g-C_3N_4.

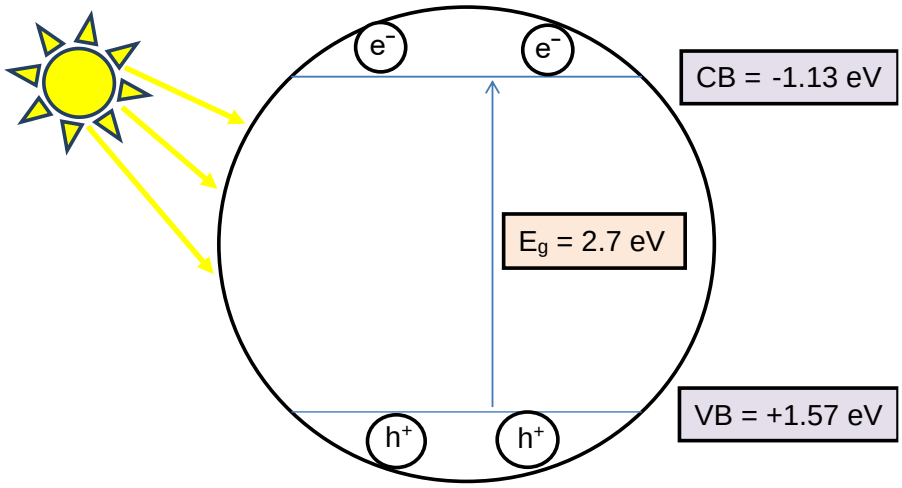

Figure 2.2: A typical charge transfer scheme for g-C_3N_4

2.3 Different morphologies of graphitic carbon nitride

In this section, the different morphologies of g-C_3N_4 and their preparation methods will be discussed. Graphitic carbon nitride can be transformed into various forms such as nanosheets, nanotubes, nanowires, quantum dots and 3D g-C_3N_4.

2.3.1 Bulk material

Bulk g-C_3N_4 has a three-dimensional structure and is similar to graphite. Typically, bulk g-C_3N_4 is synthesised by pyrolysis of nitrogen-rich precursors such as melamine, dicyandiamide, thiourea or urea [88]. Bulk g-C_3N_4, characterised by a band gap of 2.7 eV, suffers from a low specific surface area due to stacking of layers during polycondensation, a poor quantum yield because of limited or no electronic transition, and a high rate of recombination of photogenerated holes and electrons [89-91]. To circumvent these drawbacks, many attempts have been made to improve its photocatalytic properties. This includes exfoliation of bulk g-C_3N_4 into nanosheets, nanotubes and quantum dots; doping of g-C_3N_4 with other elements, or adding g-C_3N_4 to other materials to form nanocomposites [91-93].

2.3.2 Nanosheets

As previously pointed out, bulk g-C_3N_4 consists of a layered and planar structure just like graphite [94]. Nitrogen and carbon atoms are held together by covalent bonds, but between the layers, weak van der Waals forces of attraction exist [95]. The layers can separate into 2D nanosheets when sufficient energy is provided to break the van der Waals forces of attraction between the layers of g-C_3N_4 in a suitable solvent [96]. Yang et al. [45] prepared g-C_3N_4 nanosheets by simple liquid-phase exfoliation of bulk g-C_3N_4 and the resultant nanosheets exhibited a band gap energy of 2.65 eV.

Niu et al. [97] prepared g-C_3N_4 nanosheets by thermal oxidation etching of bulk g-C_3N_4 in air. Interestingly, the resulting g-C_3N_4 nanosheets had a large band gap (approx. 2.9 eV), high specific surface area (approx. 306 m^2 g^{-1}) and improved electron transport as compared with bulk g-C_3N_4 due to high quantum confinement [97, 98].

2.3.2.1 Exfoliation of bulk material into nanosheets

Owing to the presence of strong covalent bonds between the carbon and nitrogen atoms and weak van der Waals forces of attraction between the layers of bulk g-C_3N_4, exfoliation of the layers is possible [24, 97, 99]. Various methods, such as chemical exfoliation (utilising strong acids), thermal exfoliation, liquid ultrasonic exfoliation and chemical blowing (utilising blowing agents) have been used in "peeling off" bulk g-C_3N_4. This section discusses these methods in detail. However, some exfoliation processes,

such as ultrasonication-assisted solution and chemical etching processes, are time-consuming and utilise corrosive reagents such as hydrochloric acid and sulfuric acid and, therefore, are not considered green [100, 101].

2.3.2.1.1 Chemical exfoliation

During chemical exfoliation, reagents such as concentrated sulfuric, nitric and hydrochloric acids have been utilised. Xu et al. [102] synthesized g-C_3N_4 nanosheets through a chemical exfoliation method. Typically, they thermally decomposed dicyandiamide at a temperature of 500 °C and the resulting as-prepared bulk g-C_3N_4 was mixed with concentrated sulfuric acid. Water was added to the mixture followed by sonication. The final product was exfoliated g-C_3N_4 nanosheets. Ideally, with the aid of the sonication process, concentrated sulfuric acid intercalates between the layers of bulk g-C_3N_4 and reacts with water to produce heat which then breaks the van der Waals forces of attraction between the layers, the sonic energy dismembers the broken bulk g-C_3N_4 into monolayer nanosheet exfoliates. The schematic process is illustrated in Figure 2.3. Moreover, Zhang et al. [103] used both concentrated nitric and hydrochloric acids to exfoliate bulk g-C_3N_4 and compared the yields and performance in the photo-reduction of Cr(VI). Both acids produced very similar results. The yield was 41 and 40% respectively with respect to the original melamine.

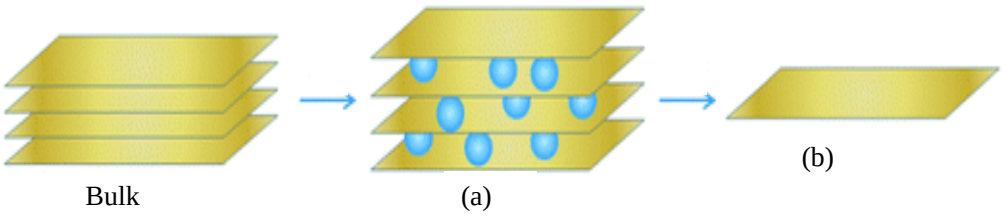

Figure 2.3: A representation of the chemical exfoliation of bulk g-C_3N_4 in which (a) bulk g-C_3N_4 is intercalated with sulfuric acid and (b) an exfoliated g-C_3N_4 nanosheet is formed [102]

It was noted that the exfoliation process was dependent on the concentration of sulfuric acid. At low acid concentration bulk g-C_3N_4 was only exfoliated to a small extent. Ma and co-workers [104] exfoliated bulk g-C_3N_4 to a few nanosheets of g-C_3N_4 by using nitric acid. Nitric acid was added to bulk g-C_3N_4, water was added, and thereafter the mixture was sonicated. The product was a few layers of g-C_3N_4 which exhibited a

specific surface area of 179.5 m^2 g^{-1} while bulk g-C_3N_4 had a specific surface area of 17.4 m^2 g^{-1}. The nanosheets showed better photocatalytic performance than bulk g-C_3N_4. Essentially, the two morphologies of g-C_3N_4 were compared for the photocatalytic degradation of methylene blue and hydrogen generation by splitting the water molecule. Figure 2.4 illustrates clearly that nanosheets of g-C_3N_4 were far better in photodegradation as well as in water splitting processes than bulk g-C_3N_4.

Although this strategy of exfoliation of bulk g-C_3N_4 results in nanosheets with high surface areas, it presents significant disadvantages, such as low yield, poor controllability, long and tedious processes, and utilises corrosive acids or liquids, and hence is not considered a green process.

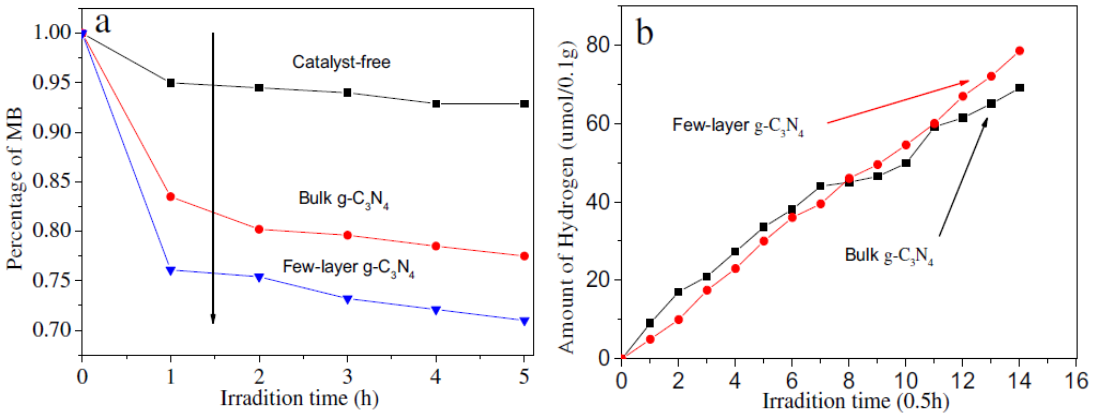

Figure 2.4: (a) Photodegradation of methylene blue (MB) and (b) hydrogen generation by photo-splitting of water by g-C_3N_4 as catalyst [104]

2.3.2.1.2 Thermal exfoliation

In general, thermal exfoliation is carried out by subjecting bulk g-C_3N_4 to heat which breaks the weak van der Waals forces of attraction between the layers resulting in exfoliation [23, 105]. Ideally, during the heating process, hydrogen attached to the tri-s-triazine or s-triazine units reacts with oxygen, thus forming a gas, and as this gas escapes it forms pores in the bulk material and as sheets are also formed [106]. Consequently, the resulting g-C_3N_4 nanosheets will be associated with a high surface area and also pore volumes, thereby enhancing the porosity. Challagulla and co-workers [105] used both thermal and chemical etching of bulk g-C_3N_4 to form nanosheets for the photocatalytic reduction of nitrobenzene. Bulk g-C_3N_4 was thermally etched by subjecting it to a temperature of 500 °C for 2 hours in air. The product had a Brunauer–Emmett–Teller

(BET) surface area of 216.3 m^2 g^{-1}. Additionally, the chemical etching used was similar to the one adopted by Xu et al. [102] and the BET surface area for the obtained nanosheets was 95.5 m^2 g^{-1}. Recently, Fu et al. [107] synthesised g-C_3N_4 nanosheets by thermal etching of melamine and used it to make a two dimensional (2D) composite containing WO_3/g-C_3N_4 for improved photocatalysis of water to yield hydrogen.

In summary, this method offers advantages such as low cost, absence of solvents, fast and time-efficient, high yield, and it introduces beneficial structural defects on the resulting nanosheets. However, this method results in a material with low crystallinity and relatively low surface area.

2.3.2.1.3 Liquid exfoliation

In liquid exfoliation, an appropriate liquid is added to bulk g-C_3N_4 and the mixture is ultrasonicated so as to exfoliate g-C_3N_4 [34, 108, 109]. Yuan et al. [34] prepared g-C_3N_4 via the liquid exfoliation method: bulk g-C_3N_4 was first obtained by thermal decomposition of urea, this was then dispersed in N-methylpyrrolidone, and thereafter ultrasonication was carried out to obtain g-C_3N_4. The nanosheets were combined with MoS_2 to form a composite for photocatalytic hydrogen generation.

Similarly, Hatamie et al. [19] prepared thin nanosheets of g-C_3N_4 by the liquid exfoliation approach. Initially, bulk g-C_3N_4 was prepared by thermal decomposition of melamine and the resulting material was exfoliated with deionised water and sonication. Figure 2.5 depicts the exfoliation process.

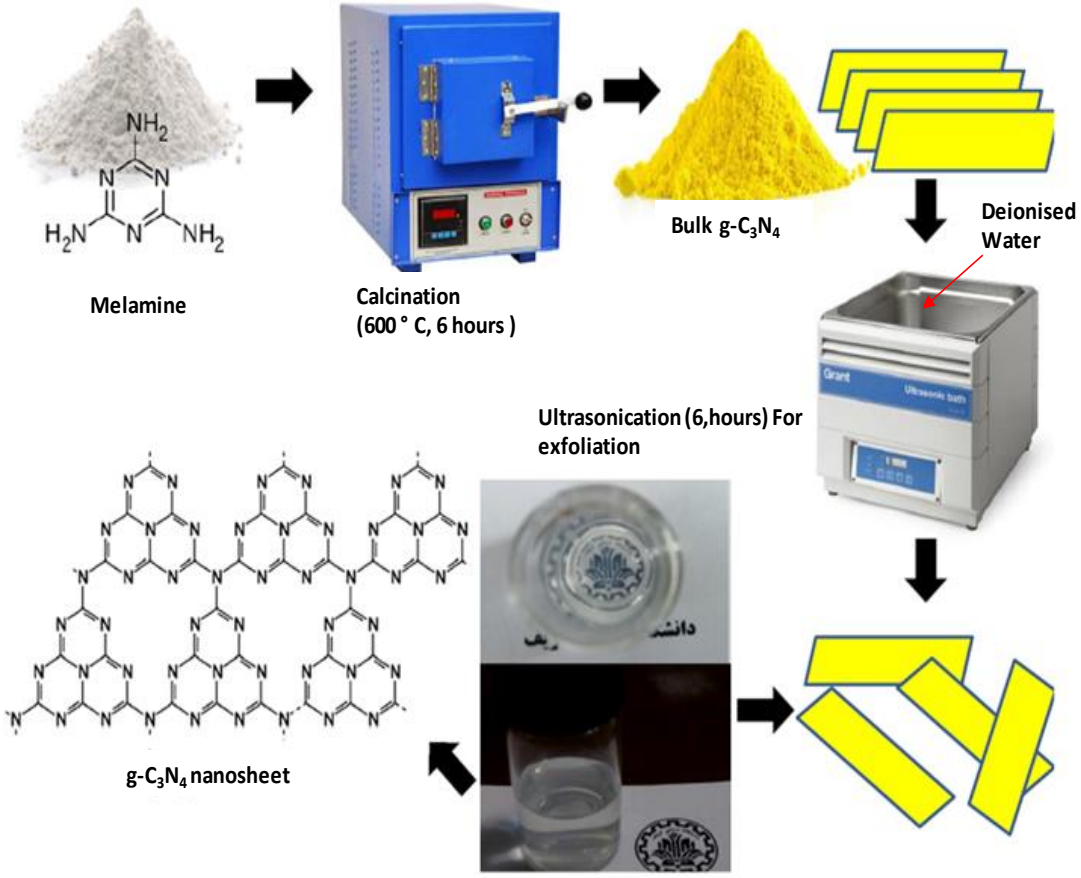

Figure 2.5: A typical liquid exfoliation process of bulk g-C_3N_4 to nanosheets [19]

Also, Huang et al. [110] synthesised g-C_3N_4 nanosheets with water as the exfoliating liquid during ultrasonication. Bulk g-C_3N_4 was prepared by thermal etching of melamine, after which it was exfoliated by ultrasonication for 10 hours. The bulk and nanosheets obtained had specific surface areas of 8.66 and 26.48 m^2 g^{-1} respectively. Remarkably, nanosheets showed better performance on photoreduction of carbon dioxide.

In this regard, liquid exfoliation has inherent advantages: water as a green solvent can be used, and nanosheets with a high surface area and relatively high crystallinity can be formed, which are critical properties in photo-driven reactions. However, the demerits of this method may include tedious operations such as sonication, long preparation cycles, and high cost and low yields.

2.3.2.1.4 Chemical blowing

In this approach, appropriate blowing agents, for example, ammonium chloride [111] and magnesium carbonate [112], are selected because they can release gases when subjected to heat. The gases escape into the layered material, such as bulk g-C_3N_4, resulting in layer

separation [113]. Yan et al. [112] synthesised flake-like porous g-C_3N_4 with superior photocatalytic activity by a chemical blowing strategy. Typically, a mixture of melamine and magnesium carbonate was heated in which magnesium carbonate decomposed to produce carbon dioxide gas that separated the nanosheet layers of bulk g-C_3N_4. Moreover, the CO_2 gas formed prevented further polymerisation of tri-s-triazine units.

Similarly, Ye et al. [113] heated a mixture of ammonium chloride (NH_4Cl) and melamine at a temperature of 520 °C for 4 hours. During the reaction, NH_4Cl released ammonia gas, which blew off the layers of bulk g-C_3N_4 and at the same time prevented the polymerisation of CN frameworks. The melamine acted as a precursor for the formation of bulk g-C_3N_4. Accordingly, the nanosheets obtained from this strategy exhibited enhanced photocatalytic degradation of rhodamine B.

More recently, Zhang et al. [41] constructed a Z-scheme heterojunction consisting of a 2D/2D BiOBr/CDs/g-C_3N_4 nanocomposite. The g-C_3N_4 nanosheets incorporated in this composite were judiciously prepared by heating a melamine/ammonium chloride mixture, a typical example of a chemical blowing method, where NH_4Cl acted as a blowing agent and melamine was the g-C_3N_4 source.

Generally, this strategy offers a single-step process which saves time, and agglomeration of nanosheets is significantly reduced. Further, a more porous structure is formed which provides more sites for reactions to take place. In contrast, the main challenge with regard to this approach is the selection of an appropriate blowing agent which will not affect the optoelectronic properties of the resulting nanosheets.

2.3.3 Nanotubes

Hollow/tubular g-C_3N_4-structured materials, conventionally known as graphitic carbon nitride nanotubes, [114] exhibit a one dimensional (1D) morphology with unique characteristics, such as enhanced visible light absorption, large specific surface area, fast electron transport and a lower rate of recombination of photogenerated electron-hole pairs [88, 108].

Generally, the major preparation methods for g-C_3N_4 nanotubes are hard-, soft- and self-templating methods [83, 88]. During the hard-templating strategy, an appropriate template with the desired structure is utilised, the g-C_3N_4 precursor interacts with it as it

is pyrolysed and after removal of the template, the g-C_3N_4 gains an opposite replica morphology of the used template [115]. Silica has been widely used as a template because it is less toxic and usually removed afterwards by using hydrogen fluoride [116] or ammonium bifluoride (NH_4HF_2) [83]. However, the use of these solutions is not environmentally benign because they are corrosive and toxic. Wang et al. [115] prepared mesoporous g-C_3N_4 by using calcium carbonate as a hard template which was later removed with hydrochloric acid. The resulting mesoporous g-C_3N_4 nanotubes had a BET surface area of 38.6 $m^2\ g^{-1}$ and an increased photocurrent of 4.2 times more than the bulk under a -0.2 V biasing.

Similarly, in the soft-templating approach, surfactants (such as Triton X-100 and pluronic P123) are used as soft templates [117]. Graphitic carbon nitride precursors such as melamine and dicyandiamide are combined and polymerised together with the template so as to achieve a g-C_3N_4 material with the desired structure [118]. Fundamentally, the choice of the template is crucial, because in most cases, the template is thermally degraded before the formation of g-C_3N_4 [83]. Yan [119] prepared porous g-C_3N_4 via a soft-templating strategy by employing melamine as a g-C_3N_4 precursor and pluronic P123 as the surfactant. The mesoporous g-C_3N_4 obtained exhibited a BET surface area of 90 $m^2\ g^{-1}$ and enhanced photocatalytic hydrogen production.

As an example of the self-templating approach, Mo and co-workers [88] reported for the first time the preparation of graphitic carbon nitride nanotubes by using melamine as the only precursor. The process was acid-alkali free and used the slow in-situ conversion of a portion of melamine to cyanuric acid. The unchanged portion of melamine and the converted part were then pyrolysed together to obtain g-C_3N_4 nanotubes with a high number of nitrogen defects. Liu et al. [120] synthesised tubular graphitic carbon nitride (g-C_3N_4) from melamine and also bulk g-C_3N_4 for comparison and then used them to make composites with ZIF-8 nanoclusters for CO_2 solar conversion to fuel.

Wang et al. [121] reported a convenient method for synthesising graphitic carbon nitride in bulk, nanosheets, nanoribbons and quantum dots. Bulk g-C_3N_4 was prepared by thermal etching of urea. The as-obtained bulk g-C_3N_4 was subjected to heat to achieve g-C_3N_4 nanosheets, these were then treated with acid (acid etching) to access nanorods,

and the nanorods were hydrothermally cut to obtain quantum dots. Figure 2.6 summarises the processes used to achieve g-C_3N_4 quantum dots from the bulk.

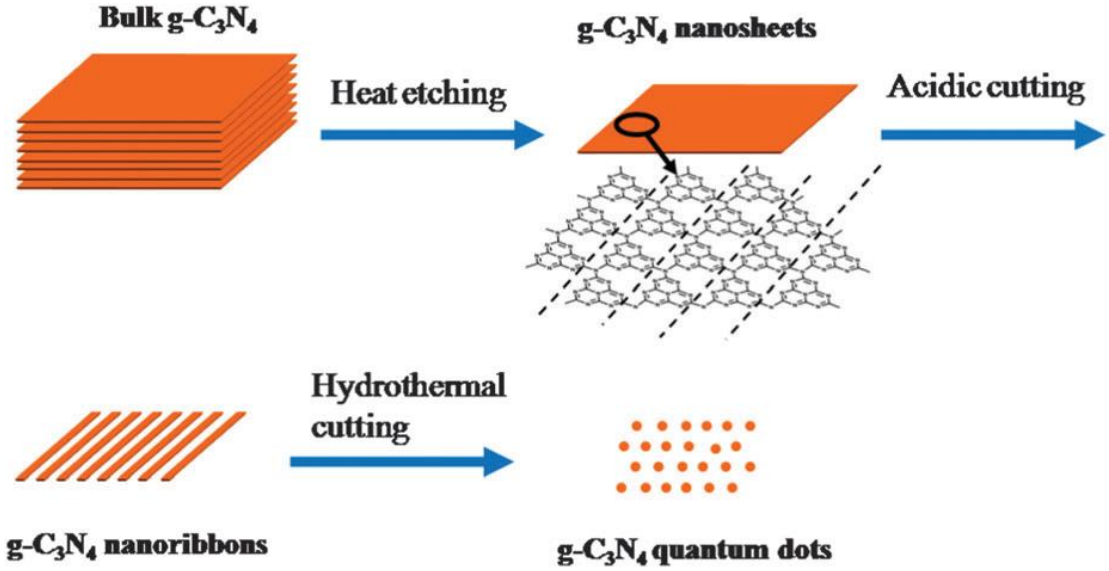

Figure 2.6: A scheme showing a systematic process of obtaining nanosheets, nanoribbons and quantum dots of g-C_3N_4 from the bulk [121]

2.3.4 Nanowires

Nanowires are one dimensional rod-like g-C_3N_4 which have lately gained a lot of scientific attention because of their high surface area to volume ratio and, hence, more sites for reactions [122]. In order to improve the surface area of mesoporous carbon spheres (MPCs), Oh et al. [122] fabricated a composite comprising of g-C_3N_4 nanowires and impregnated it with MPCs to form a 3D composite structure. Due to its increased surface area, the composite was shown to portray better electrochemical properties than graphene, carbon nanotubes, and activated carbon materials used as electrical double layer capacitors.

More recently, Tang et al. [123] constructed a composite consisting of g-C_3N_4 nanowires as the substrate for conducting poly(3,4-ethylenedioxythiophene):poly(4-styrenesulfonate) (PEDOT:PSS). The resultant 3D material showed good capacitive properties (202 F g^{-1}), recyclability and flexibility. Similarly, to further increase the surface area of g-C_3N_4, Xie et al. [124] prepared nanowires by polycondensation of a solvothermally pre-treated cyanuric acid-melamine mixture precursor at 500 °C for two hours. The product formed nanowires which showed enhanced photocatalytic

degradation of methylene blue under visible light irradiation because of the increased number of sites for reactions to occur in the nanostructured material.

2.3.5 Quantum dots

Graphitic carbon nitride quantum dots (g-CNQDs) with zero-dimensional structure (0D) have gained more and more attention because of their attractive properties such as chemical stability, bright fluorescence, large specific surface area, biocompatibility and moderate band gap [125]. Quantum dots of g-C_3N_4 have been synthesised through different routes. Lin and co-workers [126] first prepared bulk g-C_3N_4 by thermal heating of melamine to a temperature of 550 °C, and then the resultant bulk g-C_3N_4 was etched with a mixture of concentrated sulfuric and nitric acids. Figure 2.7 shows typical transmission electron microscope (TEM) images of bulk g-C_3N_4 and g-CNQDs. The g-CNQDs have been applied as fluorescent probes for environmental and biological detection because of their ability to fluoresce, and the fact that they are thermally stable, nontoxic, water-soluble and biocompatible [67, 127].

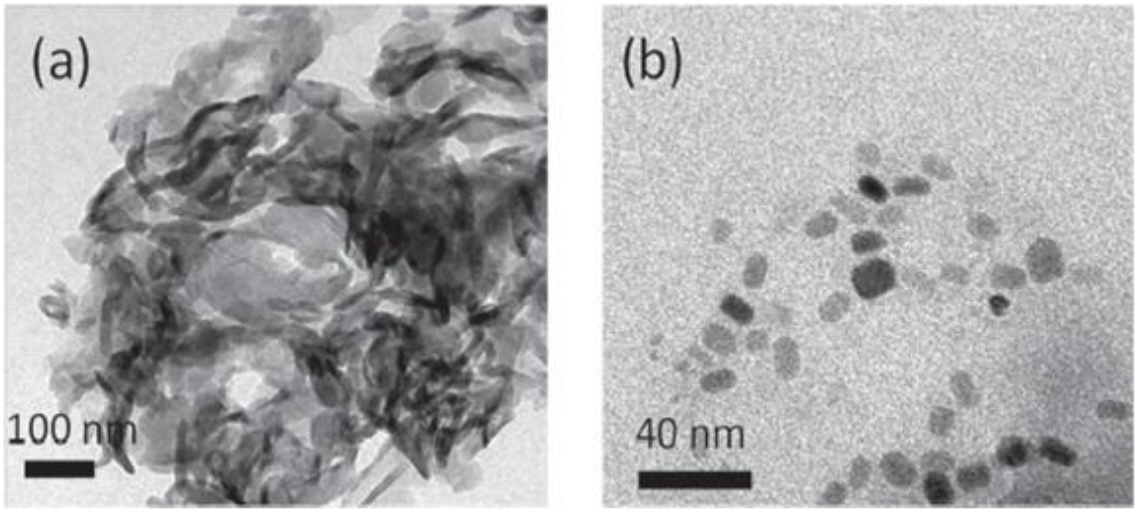

Figure 2.7: Typical TEM images of (a) bulk g-C_3N_4 and (b) g-C_3N_4 quantum dots [72]

2.3.6 3-D g-C_3N_4

Although graphitic carbon nitride has been applied in many fields such as photocatalysis, it still faces a number of drawbacks such as high recombination rates of charges, low surface area and poor light absorption capabilities. In an attempt to increase the surface area of this material, Liang et al. [128] designed a macroporous 3D g-C_3N_4 by judiciously

using melamine sponge as a template and carried out a one-step polymerisation of melamine sponge soaked in urea. The resultant product was directly cut into different 3D shapes containing g-C_3N_4. Basically, melamine and urea are precursors of g-C_3N_4, hence this method resulted in a macroscopic 3D g-C_3N_4 with enhanced photocatalytic hydrogen production.

Wang et al. [129] prepared a mesoporous 3D g-C_3N_4 by way of using silica as a template after optimising the self-polymerisation reaction conditions. The subsequent 3D g-C_3N_4 was 6.5 times superior to bulk g-C_3N_4 when utilised in photocatalytic hydrogen evolution. The 3D architecture offers more sites for the photoreaction to take place and better light absorption. Similarly, Luo et al. [38] synthesised 3D g-C_3N_4 with tremendous photocatalytic hydrogen evolution, i.e. 29.5 times more than for pristine g-C_3N_4. Typically, bulk g-C_3N_4 was acid-treated while the other samples were untreated; both acid-treated and untreated samples were calcined. Interestingly, the acid-treated material portrayed a porous 3D structure and, hence, an increased surface area, and improved light absorption characteristics.

Fan et al. [130] designed a remarkable 3D nanoneedle g-C_3N_4 nano-enzyme. With the basic law of electrostatics which infers that charges are concentrated at sharp points, the as-prepared nanoneedle allowed the concentration of charges at the tip, thus activating hydrogen peroxide to hydroxyl radicals ($^{\bullet}OH$). Consequently, the $^{\bullet}OH$ radicals caused effective peroxidase-like oxidation of 3,3′,5,5′-tetramethylbenzidine.

2.4 Modifications to improve efficiency

As a way of improving the photoelectronic properties of g-C_3N_4, doping, construction of heterojunctions, coupling with carbonaceous materials, and introduction of defects have been carried out to obtain different morphologies with improved properties. In this section, these modifications of g-C_3N_4, including the formation of composites, are discussed in detail.

2.4.1 Doping

Graphitic carbon nitride has been doped to enhance its photo-electronic properties [131]. The idea behind doping relies on the fact that g-C_3N_4 is layered and possesses cavities that can accommodate heteroatoms, hence causing changes in the electronic band structure (band gap) and, thus, the visible light absorption [84, 132]. Kamal et al. [133] doped g-C_3N_4 with boron and used it to make a composite with $NiFe_2O_4$; the resultant B-CN/$NiFe_2O_4$ composite showed an improved photocatalytic effect for the degradation of methylene blue. Wang et al. [134] doped g-C_3N_4 with cobalt and the resultant doped g-C_3N_4 was used as a heterogeneous catalyst to trigger the photocatalytic effect of peroxymonosulfate for the degradation of organic pollutants.

Graphitic carbon nitride can also be doped with sulfur which has a lower electronegativity than nitrogen [135, 136]. Liu et al. [84] doped g-C_3N_4 with sulfur and the doped material exhibited an attractive photoreactivity based on both theoretical and experimental characterisation. Yan et al. [137] doped g-C_3N_4 with boron and compared the doped material with pristine g-C_3N_4. The materials were used in the photodegradation of rhodamine B and methyl orange; strikingly, the doped g-C_3N_4 showed a better photodegradation effect than pristine g-C_3N_4. Boron as the dopant increased the adsorption of rhodamine B, and, hence, there was better contact between the g-C_3N_4 photocatalyst and the pollutant. This enhanced the degradation rate. Additionally, boron caused a slight decrease in the band gap thereby encouraging more light absorption.

The photocatalytic efficacy of g-C_3N_4 has been enhanced by altering the structural texture, and electronic and optical properties. Zhu et al. [138] doped g-C_3N_4 with phosphorus via thermolysis of both melamine and organophosphonic acid without a template involved. A flower-like nanostructured catalyst was formed and this was applied in the photolysis of water to produce hydrogen (Figure 2.8). The integration of phosphorus into the g-C_3N_4 skeleton changes the optoelectronic properties and improves the electronic properties. The phosphorous-doped flower-like g-C_3N_4 exhibited a large surface area with many active sites and improved optoelectronic properties. More recently, Yang et al. [139] also prepared a similar (3D) phosphorus-doped mesoporous flower-like g-C_3N_4 catalyst and used it for the same photocatalytic splitting of water; their results corroborate those of

Zhu et al. [138] The phosphorus atoms slow down the recombination rate of photogenerated holes and electrons and thus improve the efficiency of the photocatalyst.

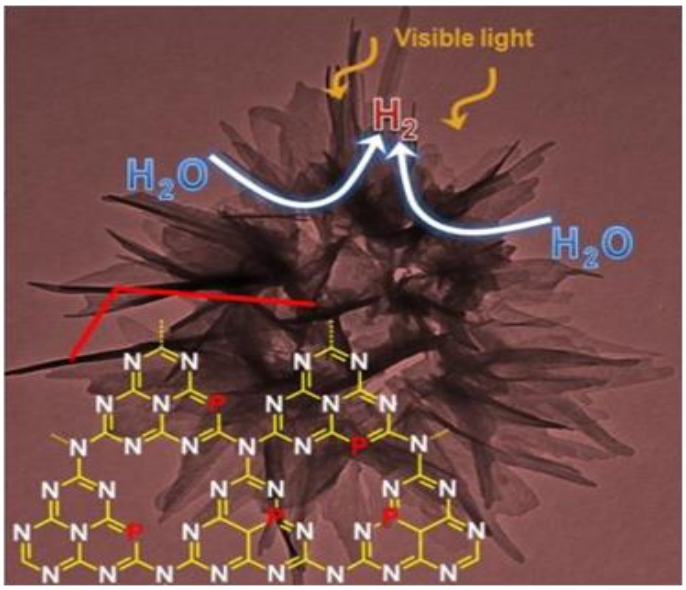

Figure 2.8: A graphical representation of flower-like nanostructured phosphorus doped g-C_3N_4 used in the photolysis of water to yield hydrogen [138]

2.4.2 Constructing heterojunctions

As a way of minimising problems such as poor separation of photogenerated charges and low light absorption behaviour of g-C_3N_4, the construction of heterojunctions has become necessary. With a heterojunction, the band gap energy can be significantly reduced and therefore light absorption as well as charge transfer will be increased. So far, the following types of heterojunctions have been constructed: Z-scheme heterojunctions [61, 140], type II heterojunctions [58, 59] and Schottky junctions [60] as presented in Figure 2.9.

More recently, Zhang et al. [41] constructed a Z-scheme heterojunction system made up of 2D/2D BiOBr/carbon dots (CDs)/g-C_3N_4. The composite showed improved performance when used to photodegrade ciprofloxacin (CIP) and tetracycline (TC). This was attributed to the fact that the surface area of the composite was greatly increased and, hence, there were more sites for the reaction; additionally, light absorption was extended to the visible region and also to the near infrared region.

Additionally, Zhang et al. [59] designed a type II heterojunction between sulfur mediated g-C_3N_4 (CNS) and pristine g-C_3N_4 (CN). This system resulted in appropriate band alignment and facilitated charge transfer. Ideally, the gradient established between the conduction band (CB) of CN and CNS can drive the movement of photogenerated electrons from CN to CNS. Similarly, photo-induced holes also migrate from CNS to CN. This process hinders recombination of photogenerated charges which is considered crucial in photoreactions. Photocatalytic hydrogen production was greatly improved for the CN/CNS heterojunctions.

Another exciting junction which can be constructed is the Schottky junction in which a noble metal and g-C_3N_4 are combined and the resulting interface allows for better charge transfer due to reduced recombination [51]. In most cases the metals used to construct such a junction are plasmonic metals such as Au, Ag, Pd, Pt, Rh and Ir. Basically, plasmonic metals are added to 2D g-C_3N_4, where the metal will absorb electromagnetic radiation leading to excitation of electrons with sufficient energy to overcome the Schottky barrier. The hot electrons will migrate to the conduction band (CB) of the semiconductor thus causing reduction of a nearby species. For instance, Mo et al. [141] designed a nanocomposite containing plasmonic gold nanoparticles and g-C_3N_4 nanosheets which showed improved performance in photocatalytic hydrogen generation (cf. Figure 2.9).

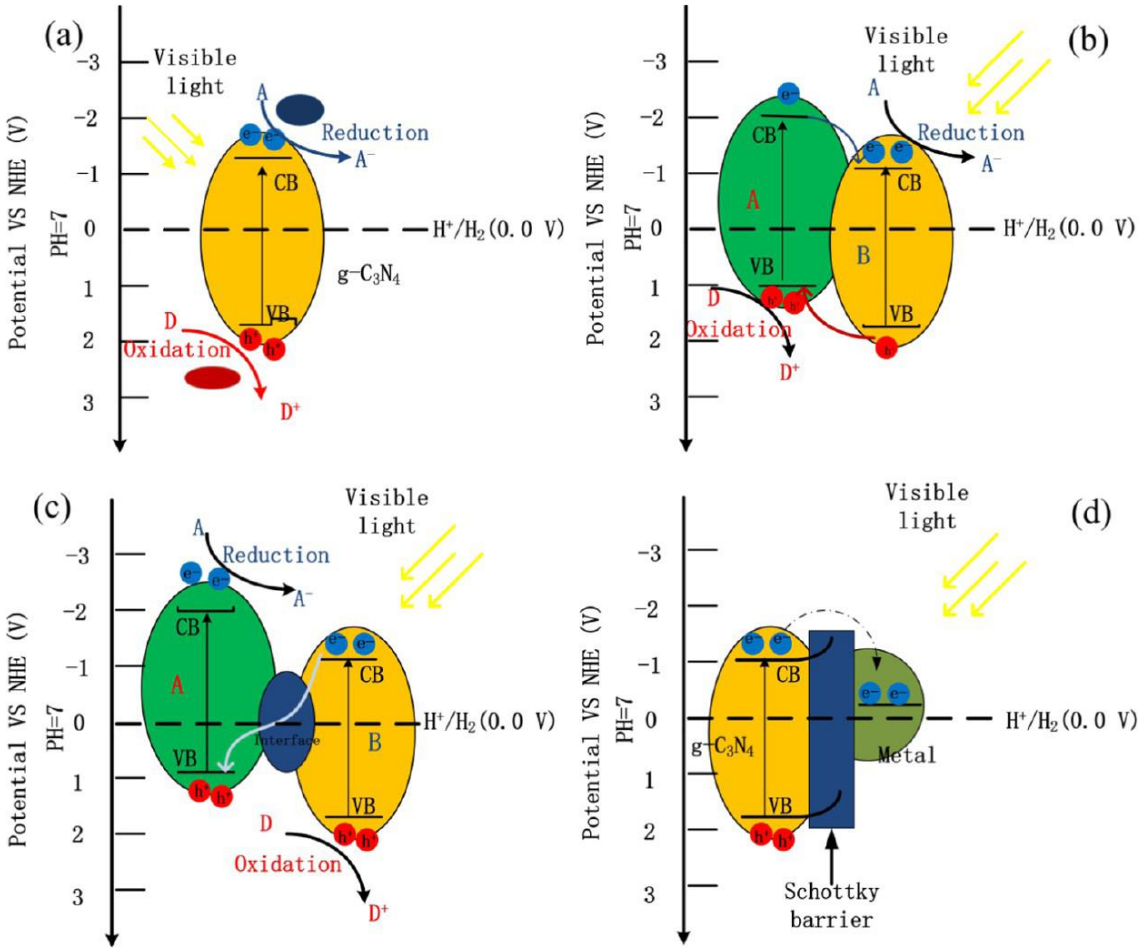

Figure 2.9: (a) A typical photocatalytic mechanism of pure g-C_3N_4, (b) schematic photoinduced charge transfer in a type II heterojunction, (c) Z-scheme heterojunction, and (d) Schottky junction [51]

2.4.3 Coupling with carbonaceous materials

In order to improve its optoelectronic performance, g-C_3N_4 has been coupled with carbonaceous materials such as carbon nanotubes, graphene and fullerenes [142]. These materials have attractive properties such as high surface area, thermal and chemical stabilities, and are environmentally benign with high conductivity characteristics.

Gong et al. [52] combined multi-walled carbon nanotubes and cyanamide precursors to form a g-C_3N_4/carbon nanotube (CN/CNT) composite after calcination. The composite exhibited synergistic effects while the inherent electrical conductivity was due to the presence of highly conducting CNTs. Meanwhile, composites with a high proportion of

g-C_3N_4 exhibited better optoelectronic activity while those with a greater proportion of CNTs were excellent in oxygen reduction.

Moreover, Li et al. [142] prepared a porous carbon/carbon nitride composite with enhanced photocatalytic degradation of methylene blue (MB) because of the synergistic effects of both carbon and carbon nitride, such as better light absorption efficiency, enhanced adsorption and improved charge separation. Fundamentally, porous carbon materials can serve as supports for catalysts and can at the same time perform as real catalysts by activating species like H_2O_2 to yield free radicals such as $^{\bullet}OH$ [53].

2.4.4 Introduction of defects

A while ago, the introduction of defects into g-C_3N_4 gained a lot of scientific attention because these defects tune the structure as well as the electronic band gap energy of this material. Niu et al. [54] subjected bulk g-C_3N_4 to thermal treatment and this resulted in the formation of nanosheets with structural defects. The nanosheets displayed extended light absorption capabilities and better photocatalytic performance during hydrogen evolution. Fundamentally, heat breaks the van der Waals forces of attraction between the layers of g-C_3N_4 while at the same time pores are generated in it, resulting in the formation of porous nanosheets. Furthermore, the electronic structure and charge transfer efficiency of the material was tuned accordingly. Similarly, Zhang et al. [143] modified g-C_3N_4 by way of heating a mixture of dicyandiamide and ammonium chloride at 550 °C for 4 hours. The resultant nanosheets showed a remarkable photo-driven catalytic hydrogen evolution. Thermal treatment introduced numerous defects on the engineered electronic structure thus extending the light absorption efficiency of the material. Moreover, the structural alterations on the surface, exposed more sites for reactions to take place. Ultimately, the synergistic effects of both the modified electronic band structure and altered morphology resulted in a superior photocatalyst.

Yang et al. [50] modified both the morphology and electronic band structure of g-C_3N_4 by calcining a mixture of sodium chloride and dicyandiamide. Sodium chloride acted as a salt template over which a honey-comb structure of g-C_3N_4 was formed. Due to multiple internal reflections within this unique structure, red-shifted band edges were formed. Therefore, the photocatalytic hydrogen evolution by as-prepared g-C_3N_4 was tremendously increased.

The remarkable advantages of the introduction of defects includes both morphological and electronic band structure modifications. The synergistic effects of both modifications yield better charge separation, light absorption (red-shift) and high surface areas, which are fundamental in photo-driven reactions.

2.5 Applications

Due to the appealing properties of g-C_3N_4, such as biodegradability, sustainability, appropriate tuneable narrow band gap and electron-rich properties, it has been applied in a range of fields including photocatalysis, sensing, energy storage and solar cells. In this section, the typical applications of g-C_3N_4 will be discussed.

2.5.1 Photocatalysis

The ability of g-C_3N_4 to harvest solar energy due to its band gap suitability has made possible its application as a photocatalyst [144, 145]. Although bulk g-C_3N_4 has restrictions of absorbing only blue light (450 nm), because of a relatively wide band gap (approx. 2.7 eV), low surface area, and fast rate of charge recombination, different modifications have been carried out to improve and optimise light absorption. These include copolymerisation, doping and dye-sensitisation. Graphitic carbon nitride photocatalysts have typically been applied in two main areas: for the degradation of pollutants and for splitting water to form H_2 and O_2.

Jiang et al. [63] doped g-C_3N_4 nanosheets with nitrogen and used the resultant material in the degradation of tetracycline. They compared it with undoped bulk g-C_3N_4. The N-doped g-C_3N_4 nanosheets showed improved photocatalytic properties for the degradation of tetracycline as well as improved stability. Owing to nanosheet development, the surface area was increased and, hence, there were more active sites in addition to the reduction in the rate of recombination of charges. Figure 2.10 shows the photocatalytic activity of bulk g-C_3N_4 (DCN), N-doped bulk g-C_3N_4 (NDCN-4), g-C_3N_4 nanosheets (DCN-S) and N-doped g-C_3N_4 nanosheets (NDCN-4S) on the degradation of tetracycline. It is clearly evident that NDCN-4S and DCN-S exhibited greater photocatalytic activity than DCN and NDCN-4 because of the increased surface area and low recombination rate of charges as a result of exfoliation of bulk g-C_3N_4 into nanosheets and also doping [94].

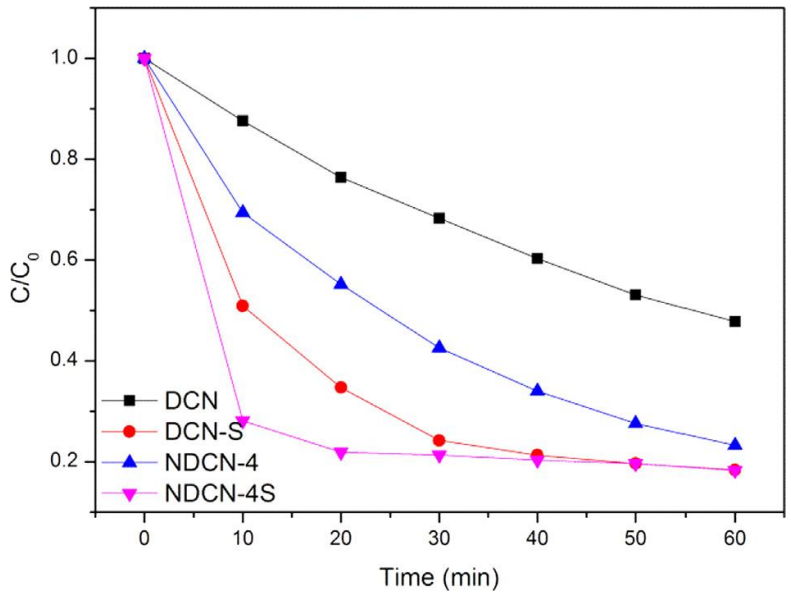

Figure 2.10: Effects of altering bulk g-C_3N_4 into nanosheets on the photocatalytic destruction of tetracycline where DCN is bulk g-C_3N_4, NDCN-4N is N-doped bulk g-C_3N_4, DCN-S is g-C_3N_4 nanosheets and NDCN-4S is N-doped g-C_3N_4 nanosheets [63]

Titanium dioxide (TiO_2) based materials have been widely used as photocatalysts and for solar energy conversion because of their stability and excellent photocatalytic properties [146]. However, the use of TiO_2 for degrading pollutants in the atmosphere is restricted by a number of factors. For instance, TiO_2 powders in air can pose serious health problems to humans and animals when inhaled and, also, they are non-recyclable [147, 148]. Therefore, appropriate clean materials with excellent practical applications are necessary to remove pollutants from the atmosphere. In addition, bismuth-based photocatalysts have also been utilised in photocatalysis. For instance, Li et al. [61] constructed a Z-scheme heterojunction composite between $Bi_2Fe_4O_9$ and Bi_2WO_6 which displayed an enhanced photocatalytic effect on the degradation of rhodamine B when compared with the individual photocatalyst components. Similarly, Li et al. [140] designed a AgI/$Bi_{24}O_{31}Cl_{10}$ composite and this yielded a remarkable photo-reduction of Cr(VI) and photo-oxidation of tetracycline (TC). Interestingly, bismuth-based photocatalysts are also very effective and compete equally with pristine g-C_3N_4.

Since its successful exfoliation some time in 2014, black phosphorus has gained scientific attention because of its attractive photocatalytic features [149]. Analogous, to g-C_3N_4, black phosphorus (BP) has a tuneable band gap, high surface area, better optoelectronic properties and is naturally metal free. In contrast, black phosphorus has a band gap

between 0.3-1.5 eV thus enabling it to absorb more visible light than g-C_3N_4 with a band gap of 2.7 eV [56]. In order to capitalise on synergism, Lei et al. [56] engineered a 0D-2D (BP quantum dot/g-C_3N_4) nanocomposite which exhibited remarkable photocatalytic hydrogen production because of the synergistic contribution of both BP quantum dots and 2D g-C_3N_4 nanosheets.

Huang et al. [150] prepared protonated ultrathin graphitic carbon nitride/titanium dioxide nanocomposites (pCN/TiO_2) for NO photodegradation. Pristine TiO_2 was also prepared for comparison. The films were placed on glass substrates and TiO_2 acted as a chemical glue. The pCN/TiO_2 films exhibited a high separation of charges. NO removal was monitored by means of electron spin resonance spectroscopy in which the spectra showed the presence of $O_2^{\bullet -}$ and $^{\bullet}OH$ radicals.

Xu et al. [151] synthesised a C-doped ZrO_2/g-C_3N_4/Ni_2P (C-ZrO_2/g-C_3N_4/Ni_2P) composite based on the UiO-66-NH_2 material for the evolution of hydrogen from splitting of water. Hydrogen evolution when C-ZrO_2/g-C_3N_4/20%Ni_2P was used was 10.04 mmol g^{-1} h^{-1} and for C-ZrO_2/20%Ni_2P the hydrogen evolved was 0.90 mmol g^{-1} h^{-1}. This clearly shows that the incorporation of g-C_3N_4 was very effective in splitting water, i.e. ten times more. This was associated with the improved charge separation by C-ZrO_2 and g-C_3N_4. The Ni_2P-co-catalyst also accelerates the surface reaction.

Cheng et al. [152] prepared a tungsten trioxide/graphitic carbon nitride composite (WO_3/g-C_3N_4) and used it for the photocatalytic production of hydrogen. The composite showed enhanced photocatalytic production of hydrogen at a rate of 400 μmol h^{-1} g_{cat}^{-1} while pristine g-C_3N_4 only produced approximately 27 μmol h^{-1} g_{cat}^{-1}. Pristine Ag_3PO_4 is known to be a photocatalyst, however, it suffers from low stability.[153] Xu et al. [154] prepared a g-C_3N_4/Ag_3PO_4 nanocomposite via a precipitation method. The composite showed enhanced photocatalytic splitting of water as well as degradation of pollutants and this is because of increased dispersion of nanomaterials, improved optical properties and low recombination rate of holes-electrons, which is due to the synergistic effect of both materials. Similarly, Zhou et al. [155] synthesized a AgCl/Ag_3PO_4/g-C_3N_4 composite with very high photocatalytic effect for the degradation of sulfamethoxazole. The reactive species were holes and chloride ions and, hence, the effectiveness could be

attributed to synergism. Table 2.1 lists more photocatalytic applications of g-C_3N_4 materials.

Table 2.1: Some selected photocatalytic applications of g-C_3N_4

Form of g-C_3N_4	Specific photocatalytic application	Specific surface area/m^2 g^{-1}	Reference
N-doped g-C_3N_4	Tetracycline degradation	74.79	[63]
P-doped g-C_3N_4	Hydrogen evolution	235.85	[139]
rGO/g-C_3N_4	Rhodamine B and methyl orange degradation		[144]
g-C_3N_4 nanosheets	Hydrogen generation	31.1	[100]
TiO_2/g-C_3N_4	Tetracycline degradation	51.87	[101]
g-C_3N_4	Hydrogen generation		[79]
WO_3/g-C_3N_4	Hydrogen generation		[152]
Au/g-C_3N_4	Degradation of bisphenol A		[18]

2.5.1.1. Magnetic photocatalysts

The assimilation of photocatalysts and magnetic materials has captivated a great deal of scientific interest [156, 157]. Magnetic photocatalysts are preferred because of their ability to be recovered and recycled [158, 159]. Additionally, and apart from their magnetic property, Fe_3O_4 materials have been utilised in composites with photocatalysts because they have other very attractive properties such as low toxicity, environmentally benign and compatibility with other materials [160, 161]. Hence, graphitic carbon nitride photocatalysts with magnetic materials have emerged and been applied in some areas, however, this is still limited in application. Incorporation of magnetic materials began in 2013 and since then the number of publications reported in this area have gradually risen [15]. Jia et al. [156] prepared a g-C_3N_4/Fe_3O_4 composite for the photodegradation of the dye rhodamine B and the composite showed an attractive efficiency in the destruction of the pollutant under visible light irradiation as well as being magnetically separable. The specific surface area of the composite was increased, hence availing large facets for

reaction. Figure 2.11 shows the nitrogen adsorption–desorption isotherms of Fe_3O_4, g-C_3N_4 and Fe_3O_4/g-C_3N_4 indicating that the composite has a large BET surface area and, therefore, more reaction sites [156].

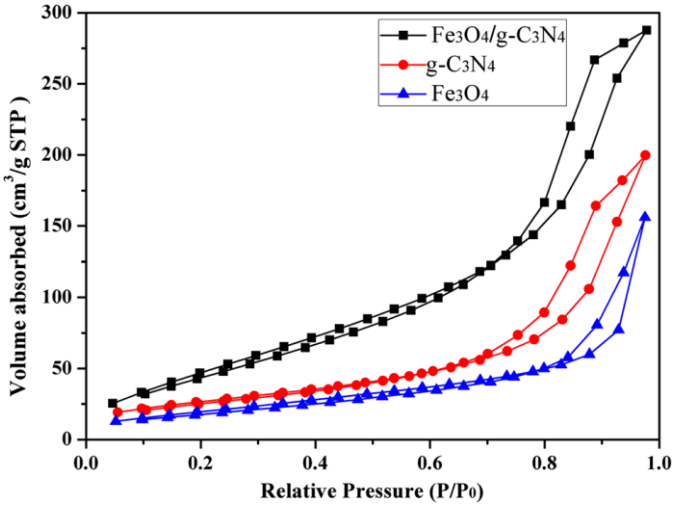

Figure 2.11: Nitrogen adsorption–desorption isotherms for Fe_3O_4/g-C_3N_4 nanocomposites, g-C_3N_4 and Fe_3O_4 [156]

2.5.2 Sensors

Recently, Zhang and co-workers [162] developed a sensor based on a g-C_3N_4 nanosheet–MnO_2 composite (Figure 2.12). The composite was fast and selective in the detection of glutathione in living cells and aqueous solutions. The g-C_3N_4 nanosheets were applied here because of their high fluorescence quantum yield and high specific surface area. When glutathione is added to the composite, MnO_2 is reduced to Mn^{2+}, this leads to the removal of fluorescence resonance energy transfer (FRET) from the g-C_3N_4 nanosheets and, hence, the inherent fluorescence is regained. Another additional advantage of this composite is its portrayed low cytotoxicity.

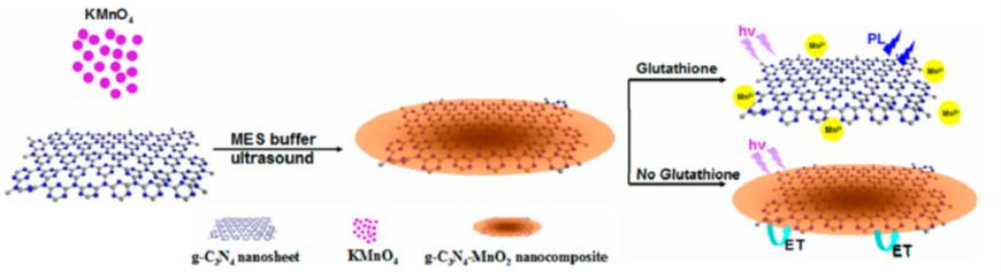

Figure 2.12: A representation of the g-C_3N_4–MnO_2 nanocomposite for sensing of glutathione [162]

Chen et al. [163] used graphitic carbon nitride quantum dots (g-CNQDs) directly to detect hydroquinone in the environment (aquatic and air systems). Typically, hydroquinone quenches the fluorescence of g-CNQDs indirectly. On the other hand, quinone was formed by catalytic oxidation of hydroquinone by horseradish peroxidase in the presence of hydrogen peroxide. The resultant quinone also quenches the g-CNQDs. A remarkably low detection limit of 0.04 μM was recorded and the linear range was 0.5–11.6 μM. On other hand, Lai et al. [164] fabricated an aptasensor for detection of mercury ions in which the electrochemical sensor is composed of a glassy carbon electrode modified with sulfur-nitrogen and co-doped mesoporous carbon. The lowest detection limit for this sensor was 0.45 pM with a linear range between 0.001-1000 nM. More applications of g-C_3N_4 as a sensor or as a detector are presented in Table 2.2.

Table 2.2: Use of g-C_3N_4 for sensing or detection applications

Form of g-C_3N_4	**Specific use of g-C_3N_4**	**Reference**
g-C_3N_4 nanosheets	Detection of lead ions	[19]
g-C_3N_4 nanosheets	Potentiometric sensor-silver ions carrier	[20]
g-C_3N_4 nanosheets	Detection of Cu^{2+} ions and photocatalysis	[24]
P-doped g-C_3N_4	Photochemical aptasensing	[66]
g-C_3N_4 quantum dots	Detection of mercury and iodide ions	[47]
Oxygen and sulphur-doped g-C_3N_4 quantum dots	Detection of mercury(II) ions and bioimaging	[48]
g-C_3N_4 quantum dots and Bi_2MoO_6	Photoelectrochemical detection of copper ions	[89]
g-C_3N_4 nanosheets	Bioimaging	[94]
g-C_3N_4 nanosheets	Fluorescence detection of ascorbic acid	[109]
g-C_3N_4 quantum dots	Selective glucose sensor	[125]
Oxygen and sulphur doped g-C_3N_4 quantum dots	Fluorescence detection of copper and silver ions and biothiols	[127]
g-C_3N_4 nanosheet-MnO_2	Fluorescence sensor for intracellular imaging of glutathione	[162]

2.5.3 Energy storage

Graphitic carbon nitride has the ability to be used as an energy store. Wu et al. [165] reported theoretically that lithium with a high density can be intercalated into a triangular space between nitrogen in the triazine units of g-C_3N_4. Through a first principles approach involving DFT calculations, it was shown that the interaction between lithium atoms and the spaces within nitrogen is very strong and can be utilised to store energy. Lithium-decorated graphitic carbon nitride can be used as both a cathode and an anode in lithium-based batteries and can be used to store hydrogen [166] since the adsorption energy for hydrogen with lithium is ideal for hydrogen sorption. Mahdizadeh et al. [166] recently also showed computationally that palladium intercalated g-C_3N_4 can effectively be used for hydrogen energy storage. The theoretical volumetric hydrogen storage capacity (HSC), for instance, for g-C_3N_4 (with interlayer spacing d = 8 Å) went past the Department of Energy (DOE) target of 30 g H_2 L^{-1} at 177 K and 5.7 MPa.

2.5.4 Photovoltaic cells

Few studies have reported the incorporation of g-C_3N_4 in solar cells and, in particular, organic solar cells, though it has great potential in this field if applied. Chen et al. [72] for the first time, incorporated g-CNQDs into an inverted bulk heterojunction-polymer solar cell (BHJ-PSC) (Figure 2.13 (a)). The power conversion efficiency (PCE) was significantly enhanced. For instance, when the poly(3-hexylthiophene-2,5-diyl):[6,6]-phenyl-C_{61}-butyric acid methyl ester (P3HT:$PC_{61}BM$) active layer polymer cell was doped with g-CNQDs the PCE value was increased to ≈17.5% from 4.23%. When poly(4,8-bis-alkyloxybenzo(l,2-b:4,5-b′)dithiophene-2,6-diylalt-(alkylthieno(3,4-b)thiophene-2-carboxylate)-2,6-diyl):[6,6]-phenyl C_{71}-butyric acid methyl ester (PBDTTT-C:$PC_{71}BM$) was doped with g-C_3N_4 QDs the efficiency improved from 6.36 to 11.6%, and finally for poly [4,8-bis(5-(2-ethylhexyl)thiophen-2-yl)benzo[1,2-b:4,5-b′]dithiophene-co-3-fluorothieno[3,4-b]thiophene-2-carboxylate] (PTB7-Th):$PC_{71}BM$ doped with g-C_3N_4 QDs it improved from 9.18 to 11.8%. The current density-voltage curves for the P3HT:$PC_{61}BM$ solar cell doped with either bulk g-C_3N_4 or g-C_3N_4 QDs are illustrated in Figures 2.13 (b), (c), and (d). Fundamentally, g-CNQDs increased the short-circuit current (J_{sc}) and improved the interfacial layer contact between the active layer and hole transport layer and, hence, enhanced the PCE values.

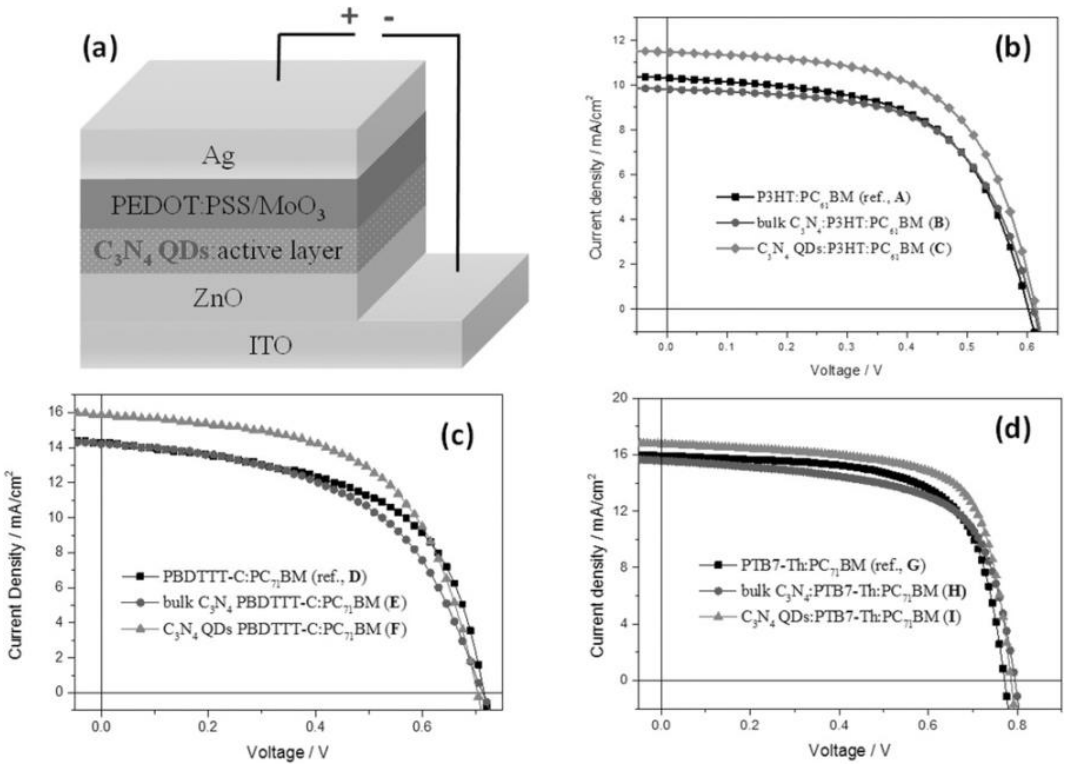

Figure 2.13: (a) An inverted bulk heterojunction polymer solar cell consisting of ITO/ZnO/C_3N_4:active layer/PEDOT:PSS (or MoO_3)/Ag. (b), (c) and (d) are current density-voltage curves for undoped and bulk g-C_3N_4 or C_3N_4 QDs doped ITO/ZnO/C_3N_4:P3HT:$PC_{61}BM$/PEDOT:PSS/Ag, undoped and bulk g-C_3N_4 or C_3N_4 QDs doped ITO/ZnO/C_3N_4:PBDTTT-C:$PC_{71}BM$/MoO_3/Ag and undoped and bulk g-C_3N_4 or C_3N_4 QDs doped ITO/ZnO/C_3N_4:PBT_7-Th:$PC_{71}BM$/MoO_3/Ag respectively [72]

Although this is the first report on the use of graphitic carbon nitride quantum dots in polymer cells, it shows that g-C_3N_4 has great potential to be incorporated into more polymer cells. Therefore, more future research should be conducted in this area.

In summary, despite all the above highlighted applications, the following challenges still limit g-C_3N_4 applications in many areas: (i) high recombination rate of photogenerated charges due to low quantum confinement, (ii) low surface areas due to lack of an ideal method for the exfoliation of g-C_3N_4 to perfect monolayers, (iii) inappropriate light absorption due to difficulty in tuning the band gap energy, and (iv) inherent low electrical conductivity.

2.6 Computational studies

Computational strategies are very important in studying the properties, mode of action, and synthetic routes of various nanomaterials including g-C_3N_4. Nonetheless, computational simulation of g-C_3N_4 is scarce in literature and this opens a rich area for further research. Theoretical calculations are conducted to mimic actual models in order to estimate and compliment experimental data. Consequently, quantum mechanical computational methods, such as density functional theory (DFT), have become indispensable when studying electronic and atomistic properties such as band gap energies, electron transfer at interfaces and crystalline structures [167, 168]. Quantum mechanics simulations give a more detailed description of a system, however, it is used for small systems with limited degrees of freedom and not in solution phases [169]. Previously, experimental spectroscopy and ab initio calculations on g-C_3N_4 systems have been explored and found that the band gap energy depends on the stacking configuration and more importantly on the lattice constant of the material [170]. Generally, the conduction band is comprised only of p_z states and the band gap is governed by the position of these states, thus the band gap is susceptible to stress and the stacking configuration adopted by the system and may experiences large variations, while the valence band experiences only small shifts upon changes dictated by the geometry of the system [170, 171].

Moreover, DFT calculations have mainly been performed by using the Gaussian 09 computational platform with the hybrid Becke three-parameter, Lee-Yang-Parr (B3LYP) exchange-correlation functional and the 6-31G* basis set [172-175]. An understanding of the energy gap between the highest occupied molecular orbital (HOMO) and the lowest unoccupied molecular orbital (LUMO) is essential in determining the efficiency of polymer solar cells for example [172]. Generally, optimised structures are used in calculations: to ensure that this is achieved the calculation is run and the phonon frequency obtained is checked to see if it is free from any imaginary frequencies [176, 177]. The simulated data from DFT calculations on the values of HOMO and LUMO, and hence the band gap, are compared with the experimental values obtained from cyclic voltammetry (CV) or UV-visible spectroscopy [178].

Zhu et al. [179] predicted the feasibility of using g-C_3N_4 for destruction of nitrogen monoxide through theoretical calculations before performing the experiments. It was found from the calculations that the N-O bond can be broken suddenly if NO is adsorbed to the tri-s-triazine section and not onto the surface of carbon, as acclaimed before, as shown in Figure 2.14. The computed adsorption energy between NO and g-C_3N_4 was −338.5 kJ mol^{-1} portraying a strong interaction. After adsorption the NO bond length increases and, thus, is weakened and breaks as shown in Figure 2.14.

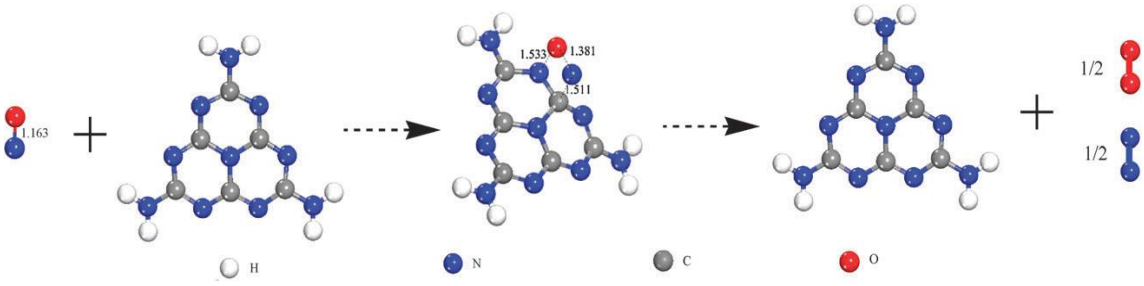

Figure 2.14: Theoretical decomposition process of NO with g-C_3N_4 as a catalyst [179]

Algara-Siller et al. [180] deduced the structure and band gap of triazine-based g-C_3N_4, both from experiments and DFT calculations. The results obtained are depicted in Figure 2.15. The actual structure of triazine-based g-C_3N_4 is corrugated and not planer. The calculated and experimental (UV-Vis and XPS) band gap of triazine-based g-C_3N_4 ranged between 1.6-2.0 eV. The DFT calculation corroborates the experimental values obtained.

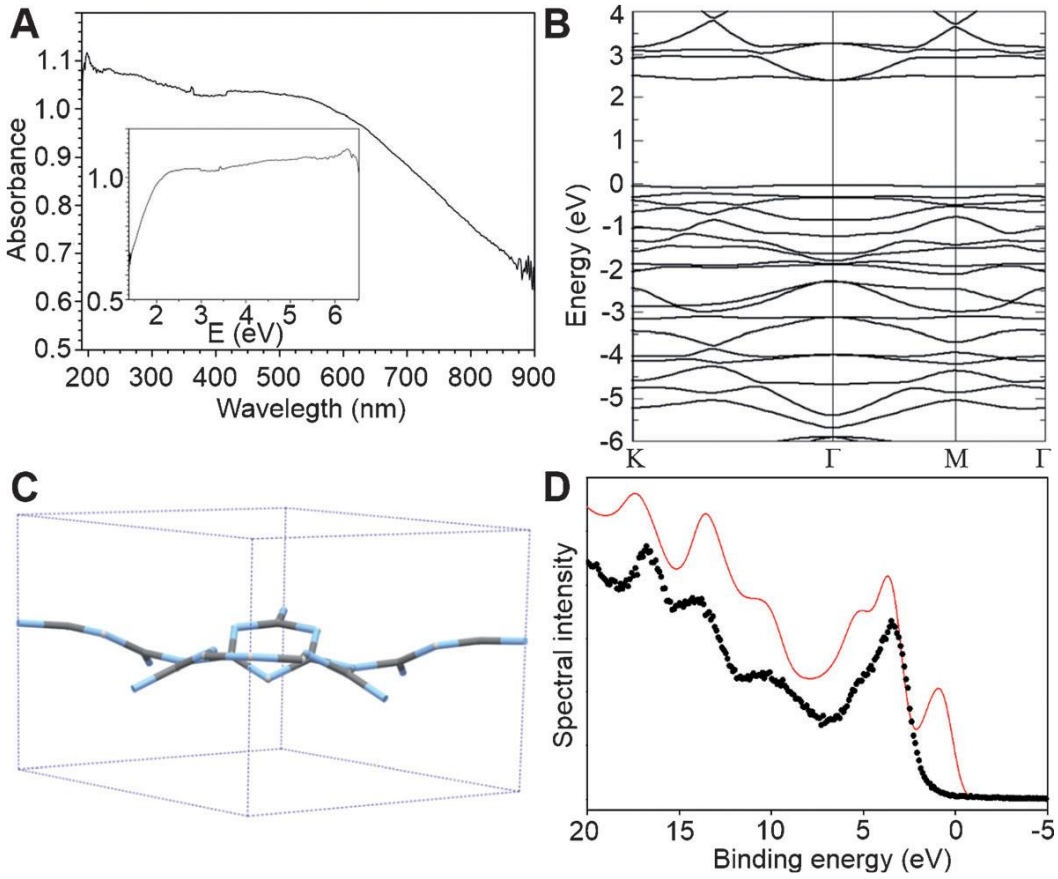

Figure 2.15: (a) Triazine-based g-C_3N_4 UV/Vis diffuse-reflectance spectrum and Kubelka–Munk plot. (b) Mono-sheet calculated band structure of triazine-based g-C_3N_4. (c) Corrugated structure of triazine-based g-C_3N_4 obtained from DFT calculations, and (d) XPS spectrum of the triazine-based g-C_3N_4 valence band region (black) and theoretically calculated XPS graph for the equilibrium structure (red) [180]

Similarly, Wang et al. [171] computed the band gap energy of the most stable phase of g-C_3N_4 theoretically; the computed band gap was 2.87 eV. This value was consistent with the experimentally determined optical band gap of as-prepared g-C_3N_4 samples. Theoretically, it was shown that during polycondensation at different temperatures, phases of g-C_3N_4, which are thermodynamically dissimilar, exist and the stable phase exhibits a direct band gap (2.87 eV) which is very close to the experimental value. These results indicate that there is a correlation between temperature and band gap because an increase in temperature leads to an increase in the proportion of material undergoing phase changes.

Zhu et al. [181] studied carbon dioxide adsorption on g-C_3N_4 by means of DFT calculations. It was determined that the adsorption energies for the models used were

negative which implied that the reaction was exothermic. Cui et al. [182] used DFT calculations to study the effect of doping g-C_3N_4 nanosheets with oxygen. Oxygen-doping resulted in the delocalisation of the HOMO-LUMO and, thus, increased the carrier mobility and also increased the number of facets for the reaction and, hence, the separation of charges.

Wu et al. [183] used the state-of-the-art hybrid functional HSE06 for the calculation of band dispersions and the electronic density of state (DOS) of three nanoribbons with widths 1.61, 2.23 and 2.84 nm, and the corresponding band gap energies of 3.06, 2.73, and 2.71 eV, respectively, were estimated [183]. The results obtained show a predominant optical transition within the tri-s-triazine unit of the polymer, with a bathochromic shift originating from a progressively increasing degree of polymerisation [184]. Moreover, the band gap energy of crystallised g-C_3N_4 nanoribbons decreases with increasing degree of polymerisation of the molecular strand resulting in polymeric g-C_3N_4 which is reported to exhibit a red-shift at higher polycondensation temperature [183, 184]. Remarkably, quantum chemical calculations show that the width of the molecular strand has an important impact on the electronic structure of polymerised and crystallised g-C_3N_4 nanoribbons, suggesting that the electronic structure depends on the structure of g-C_3N_4 [183].

The optical properties and condensation degree (structure) of molecular polymeric g-C_3N_4 has also been found to depend strongly on the process temperature [183]. Nano g-C_3N_4 nanosheets [183, 185], nanoribbons [186] and quantum dots [187], exhibit large specific surface areas, hence shortening the diffusion distance of charge carriers (electrons and holes), and significantly enhancing the performance of g-C_3N_4 as a photocatalyst [187].

By means of density functional theory (DFT) computations, the catalytic performance of a series of single metal atoms supported on graphitic carbon nitride (g-C_3N_4) for nitrogen reduction reactions (NRR) has been evaluated by Zhang et al. [188] Additionally, the use of g-C_3N_4 as a substrate to anchor metal catalysts offers several merits, such as maintaining metal atoms in their neutral state and accumulation of surface polarisation charges on metal atoms, thus providing more accurate evidence for the identification of catalytically active sites [189-191]. Generally, computational calculations assist

significantly in estimation of the band gap energies of semiconductors, and they can also be used for the calculation of the HOMO-LUMO band gap of polymers.

2.6.1 Theoretical estimation of HOMO-LUMO band gap of carbon nitride oligomers and polymers

In a typical computational calculation of the band gaps of polymers, such as g-C_3N_4, a sequence of oligomers (repeating units) is used to represent the entire polymer, and hence DFT computations are possible [177]. The characteristics of the oligomer are extrapolated to represent the entire polymer and this is the most widely accepted estimation [192]. Two main steps are important in the calculation of HOMO-LUMO band gap energies: first oligomer structures are optimised and, secondly, the band gaps of the optimised structure are obtained. Notably, the energy gap is the difference between the HOMO value and the LUMO value [193]. Zade and Bendikov [192] reported how to predict the band gap of a conducting polymer from oligomers by extrapolation of the linear graph of the HOMO-LUMO band gap against the reciprocal of the number of monomers. The band gaps of oligomers of oligothiophene, -pyrrole, -furan, -paraphenylene and -3,4-ethylenedioxythiophene (EDOT) were studied by DFT [194, 195]. It was noted that long oligomers (≥ 20 oligomers) should be used such that a significantly accurate prediction is obtained (Figure 2.16). Remarkably, it has been shown that the existence of C≡N and C=O can significantly narrow down the HOMO–LUMO gap whereas the presence of O−H can slightly enhance the band gap energy [196]. These differences can be attributed to the different electronic properties among the functional groups: O−H is electron-donating, while C≡N and C=O are electron-withdrawing functional groups. Thus, graphitic carbon nitride substituted with electron-withdrawing groups could be an important milestone towards achieving scientific and industrial applications [196].

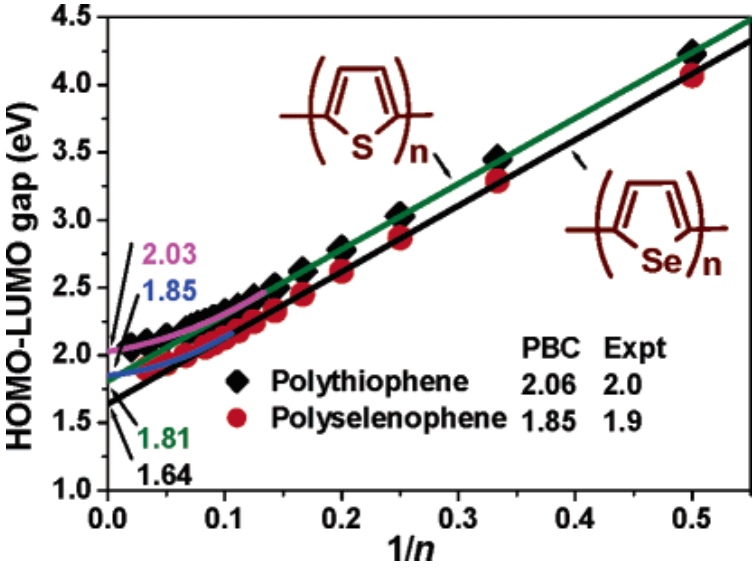

Figure 2.16: A typical linear extrapolation curve for polythiophene and polyselenophene HOMO-LUMO gaps with both theoretical and experimental values [192]

Recently, Mestiri and co-workers [197] reported the modelling of copolymers for organic solar cell applications based on 2,2'-(1,4-phenylene)bis(quinazolin-4(3H)imine) (PBQI) using both DFT and time-dependent density functional theory (TD-DFT). The optoelectronic properties of thiophene-alt-PBQI (TH-PBQI) and N-vinylcarbazole-alt-PBQI (VK-PBQI) copolymers were first examined and later the copolymer polycyclopentadithiophene-alt-(2,2'-(1,4-phenylene)bis(quinazolin-4(3H)-imine)) (CPDT-PBQI), which was constructed by joining two successive 3-thiophene units by means of a carbon bridge, was assessed. The electronic and optical properties were examined by both DFT and TD-DFT in order to understand the electronic properties of PBQI. The HOMO-LUMO energies were computed and found to be −5.76 and −2.11 eV respectively, and the band gap was 3.64 eV as illustrated in Figure 2.17.

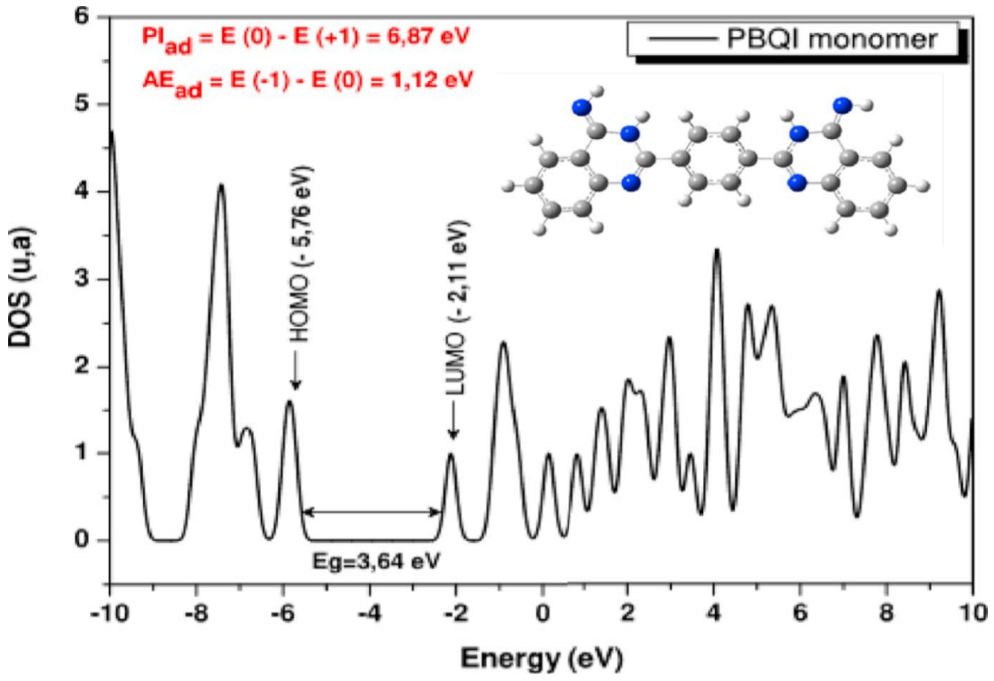

Figure 2.17: Density of state (DOS) of geometrically optimised PBQI monomer [197]

Time-dependent density functional theory (TD-DFT) is used to determine ground state energies and oscillator strengths [198]. The TD-DFT method provides an exact solution to the time-dependent Schrödinger equation [199]. The calculation is routinely performed on optimised structures. Figure 2.18 shows the absorption spectrum achieved from TD-DFT simulation of the CPDT-PBQI copolymer modelled by Mestiri et al. [197] with the 6-31g (d) basis set. Moreover, DFT in conjunction with Chemissian computational software, can be used to model electron density maps as well as HOMO-LUMO band gap energies of nanomaterial building blocks (oligomers) [193, 195].

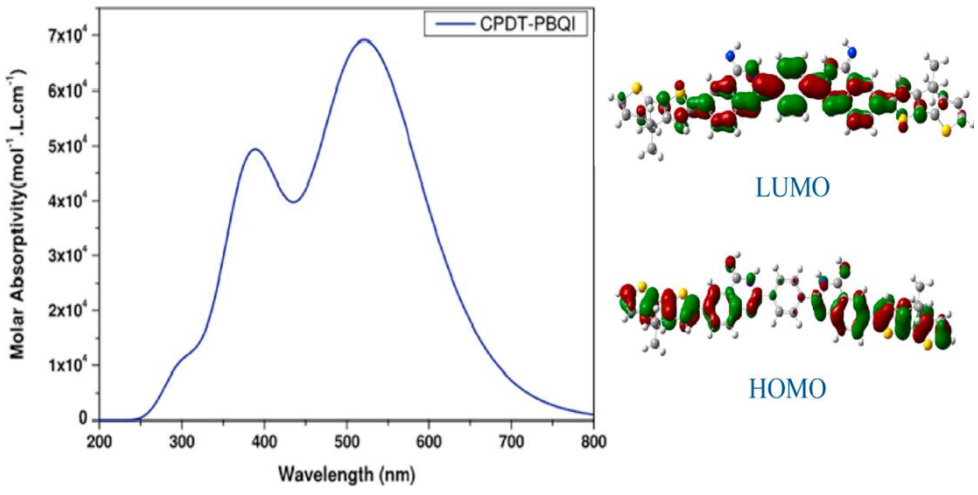

Figure 2.18: Optical absorption of CPDT-PBQI copolymer [197]

For comparison purposes, the HOMO-LUMO band gap should be estimated both experimentally and theoretically. Experimentally HOMO-LUMO gaps can be measured by both cyclic voltammetry (CV) [200] and photoelectron spectroscopy in air (PES) [201, 202]. PES measurement can be done on solid thin films, where the work function is determined, and this corresponds to the HOMO. The LUMO is calculated by adding the HOMO values to the band gap energy obtained by UV-Vis absorbance spectroscopy [201]. Similarly, CV measurements can be performed to determine the HOMO energy and the values obtained are added to the band gap values obtained by UV-VIS absorbance spectroscopy to determine the LUMO energies as well [202].

2.7 Summary and outlook

The trends in solar technology have shifted to the use of environmentally benign materials. In this review, we have examined the current trends in the utilisation of g-C_3N_4 in various applications such as biosensing, photocatalysis as well as photovoltaics. Moreover, the synthesis as well as enhancement of the photo-performance of g-C_3N_4 has been highlighted. In essence, g-C_3N_4 is a metal-free semiconductor with a tuneable band gap, high thermal and chemical stability, and attractive electronic properties. Graphitic carbon nitride has a band gap of ~ 2.7 eV and it is able to absorb UV radiation. The exfoliation processes of g-C_3N_4, doping, and amalgamation with other materials to form composites, can result in better optoelectronic properties of the material and the composites portray synergistic properties.

Pristine g-C_3N_4 exhibits a low specific surface area and high rate of recombination of the photogenerated holes and electrons. Consequently, bulk g-C_3N_4 has been transformed to nanosheets, nanorods, and quantum dots, as a way of increasing the surface area and, thus, introducing more active sites for reactions and high quantum confinement. Although considerable efforts have been made so far in this area, the challenge still lies in the recombination of photogenerated charges and, therefore, there is a need to incorporate theoretical and experimental perspectives. Moreover, an understanding of the charge transfer process in composites is still lacking in the literature. Similarly, little has been reported on the use of this material in organic solar cells and, hence, the need to expand this area in the existing body of knowledge so as to improve solar harvesting. The application of computational tools in studying g-C_3N_4 is very important because it saves

on time and gives more insight into various properties and is also helpful in the proper tuning of the material.

This review will be of great importance to material scientists and nanotechnologists interested in seeking materials for various photovoltaic and sensing applications, and environmentalists who require better materials for degradation of pollutants. Finally, the authors believe that more research needs to be performed on g-C_3N_4 to expand its potential applications.

Acknowledgements

The authors are grateful for the research support received from the National Research Foundation of South Africa and the University of KwaZulu-Natal Nanotechnology Platform.

References

[1] B. Usher, Renewable energy: A primer for the twenty-first century, ed.Columbia University Press. New York, 2019.

[2] M. Huq, Science, Technology and Development: North-South Co-operation, ed.Routledge. New York 2020.

[3] T. Bradford, Solar revolution: The economic transformation of the global energy industry, ed.MIT Press. London, England 2008.

[4] P.G.V. Sampaio, M.O.A. González, Photovoltaic solar energy: Conceptual framework. Renew. Sustain. Energy Rev. **74**, 590-601 (2017). https://doi.org/10.1016/j.rser.2017.02.081.

[5] C. Pelletier, Y. Rogaume, L. Dieckhoff, G. Bardeau, M.-N. Pons, A. Dufour, Effect of combustion technology and biogenic CO_2 impact factor on global warming potential of wood-to-heat chains. Appl. Energy. **235**, 1381-1388 (2019). https://doi.org/10.1016/j.apenergy.2018.11.060.

[6] A. du Plessis, Climate Change: Current Drivers, Observations and Impacts on the Globe's Natural and Human Systems, in Water as an Inescapable Risk. 2019, Springer: Switzerland. p. 27-53.

[7] Q. Xiang, J. Yu, M. Jaroniec, Synergetic effect of MoS_2 and graphene as cocatalysts for enhanced photocatalytic H_2 production activity of TiO_2 nanoparticles. J. Am. Chem. Soc. **134**, 6575-6578 (2012). https://doi.org/10.1021/ja302846n.

[8] A. Petala, D.I. Kondarides, Photocatalytic hydrogen production over mixed Cd-Zn sulfide catalysts promoted with nickel or nickel phosphide. Catal. Today, (2019). https://doi.org/10.1016/j.cattod.2019.03.036.

[9] H. Yoshida, R. Yamada, T. Yoshida, Platinum cocatalyst loaded on calcium titanate photocatalyst for water splitting in a flow of water vapor. ChemSusChem, (2019). https://doi.org/10.1002/cssc.201802799.

[10] E. Kabir, P. Kumar, S. Kumar, A.A. Adelodun, K.-H. Kim, Solar energy: Potential and future prospects. Renew. Sustain. Energy Rev. **82**, 894-900 (2018). https://doi.org/10.1016/j.rser.2017.09.094.

[11] M. Al Shafeey, A.M. Harb. Photovoltaic as a promising solution for peak demands and energy cost reduction in Jordan. in Renewable Energy Congress (IREC), 2018 9th International. 2018. IEEE. https://doi.org/10.1109/IREC.2018.8362570.

[12] P.F. Varadi, F. Wouters, A.R. Hoffman, The Sun Is Rising in Africa and the Middle East: On the Road to a Solar Energy Future, ed.CRC Press. Florida, USA2018.

[13] P.V. Kamat, Meeting the clean energy demand: Nanostructure architectures for solar energy conversion. J. Phys. Chem. C. **111**, 2834-2860 (2007). https://doi.org/10.1021/jp066952u.

[14] C. Guruge, S.Y. Rfaish, C. Byrd, S. Yang, A.K. Starrett, E. Guisbert, N. Nesnas, Caged proline in photoinitiated organocatalysis. J. Org. Chem., (2019). https://doi.org/10.1021/acs.joc.9b00220.

[15] M. Mousavi, A. Habibi-Yangjeh, S.R. Pouran, Review on magnetically separable graphitic carbon nitride-based nanocomposites as promising visible-light-driven photocatalysts. J. Mater. Sci. Mater. Electron. **29**, 1719-1747 (2018). https://doi.org/10.1007/s10854-017-8166-x.

[16] Y. Li, Z. Ruan, Y. He, J. Li, K. Li, Y. Jiang, X. Xu, Y. Yuan, K. Lin, In situfabrication of hierarchically porous g-C_3N_4 and understanding on its enhanced photocatalytic activity based on energy absorption. Appl. Catal. B: Environ. **236**, 64-75 (2018). https://doi.org/10.1016/j.apcatb.2018.04.082.

[17] Y.-Y. Li, S.-F. Ma, B.-X. Zhou, W.-Q. Huang, X. Fan, X. Li, K. Li, G.-F. Huang, Hydroxy-carbonate-assisted synthesis of high porous graphitic carbon nitride with broken of hydrogen bonds as a highly efficient visible-light-driven photocatalyst. J. Phys. D: Appl. Phys. **52**, 105502 (2019). https://doi.org/10.1088/1361-6463/aaf84a.

[18] C.H. Hak, L.C. Sim, K.H. Leong, Y.H. Chin, P. Saravanan. Sunlight photodeposition of gold nanoparticles onto graphitic carbon nitride (g-C_3N_4) and application towards the degradation of bisphenol A. in IOP Conf. Ser. Mater. Sci. Eng. 2018. IOP Publishing. https://doi.org/10.1088/1757-899X/409/1/012008.

[19] A. Hatamie, P. Jalilian, E. Rezvani, A. Kakavand, A. Simchi, Fast and ultra-sensitive voltammetric detection of lead ions by two-dimensional graphitic carbon nitride (g-C_3N_4) nanolayers as glassy carbon electrode modifier. Measurement. **134**, 679-687 (2019). https://doi.org/10.1016/j.measurement.2018.10.082.

[20] T. Alizadeh, F. Rafie, An innovative application of graphitic carbon nitride (g-C_3N_4) nano-sheets as silver ion carrier in a solid state potentiometric sensor. Mater. Chem. Phys. **227**, 176-183 (2019). https://doi.org/10.1016/j.matchemphys.2019.01.060.

[21] M. Afshari, M. Dinari, M.M. Momeni, Ultrasonic irradiation preparation of graphitic-C_3N_4/polyaniline nanocomposites as counter electrodes for dye-sensitized

solar cells. Ultrason Sonochem. **42**, 631-639 (2018). https://doi.org/10.1016/j.ultsonch.2017.12.023.

[22] J. Li, D. Wu, J. Iocozzia, H. Du, X. Liu, Y. Yuan, W. Zhou, Z. Li, Z. Xue, Z. Lin, Achieving efficient incorporation of π-electrons into graphitic carbon nitride for markedly improved hydrogen generation. Angew. Chem. **131**, 2007-2011 (2018). https://doi.org/10.1002/ange.201813117.

[23] S. Sun, J. Li, J. Cui, X. Gou, Q. Yang, Y. Jiang, S. Liang, Z. Yang, Simultaneously engineering K-doping and exfoliation into graphitic carbon nitride (g-C_3N_4) for enhanced photocatalytic hydrogen production. Int. J. Hydrog. Energy. **44**, 778-787 (2019). https://doi.org/10.1016/j.ijhydene.2018.11.019.

[24] H. Xu, J. Yan, X. She, L. Xu, J. Xia, Y. Xu, Y. Song, L. Huang, H. Li, Graphene-analogue carbon nitride: novel exfoliation synthesis and its application in photocatalysis and photoelectrochemical selective detection of trace amount of Cu^{2+}. Nanoscale. **6**, 1406-1415 (2014). https://doi.org/10.1039/C3NR04759H.

[25] K. Li, F.-Y. Su, W.-D. Zhang, Modification of g-C_3N_4 nanosheets by carbon quantum dots for highly efficient photocatalytic generation of hydrogen. Appl. Surf. Sci. . **375**, 110-117 (2016). https://doi.org/10.1016/j.apsusc.2016.03.025.

[26] G. Liao, Y. Gong, L. Zhang, H. Gao, G.-J. Yang, B. Fang, Semiconductor polymeric graphitic carbon nitride photocatalysts: The "holy grail" for the photocatalytic hydrogen evolution reaction under visible light. Energy Environ. Sci., 2080-2147 (2019). https://doi.org/10.1039/C9EE00717B

[27] C. Cheng, Y. Huang, X. Tian, B. Zheng, Y. Li, H. Yuan, D. Xiao, S. Xie, M.M. Choi, Electrogenerated chemiluminescence behavior of graphite-like carbon nitride and its application in selective sensing Cu^{2+}. Anal. Chem. **84**, 4754-4759 (2012). https://doi.org/10.1021/ac300205w.

[28] M. Bellardita, E.I. García-López, G. Marcì, I. Krivtsov, J.R. García, L. Palmisano, Selective photocatalytic oxidation of aromatic alcohols in water by using P-doped g-C_3N_4. Appl. Catal. B: Environ. **220**, 222-233 (2018). https://doi.org/10.1016/j.apcatb.2017.08.033.

[29] S. Hua, D. Qu, L. An, W. Jiang, Y. Wen, X. Wang, Z. Sun, Highly efficient p-type Cu_3P/n-type g-C_3N_4 photocatalyst through Z-scheme charge transfer route. Appl. Catal. B: Environ. **240**, 253-261 (2019). https://doi.org/10.1016/j.apcatb.2018.09.010.

[30] J.-G. Kim, S.-M. Park, M.E. Lee, E.E. Kwon, K. Baek, Photocatalytic co-oxidation of As (III) and Orange G using urea-derived g-C_3N_4 and persulfate. Chemosphere. **212**, 193-199 (2018). https://doi.org/10.1016/j.chemosphere.2018.08.081.

[31] M. Inagaki, T. Tsumura, T. Kinumoto, M. Toyoda, Graphitic carbon nitrides (g-C_3N_4) with comparative discussion to carbon materials. Carbon. **141**, 580-607 (2018). https://doi.org/10.1016/j.carbon.2018.09.082.

[32] C. Ye, J.-X. Li, Z.-J. Li, X.-B. Li, X.-B. Fan, L.-P. Zhang, B. Chen, C.-H. Tung, L.-Z. Wu, Enhanced driving force and charge separation efficiency of protonated g-C_3N_4 for photocatalytic O_2 evolution. ACS Catal. **5**, 6973-6979 (2015). https://doi.org/10.1021/acscatal.5b02185.

[33] S. Kang, L. Zhang, M. He, Y. Zheng, L. Cui, D. Sun, B. Hu, " Alternated cooling and heating" strategy enables rapid fabrication of highly-crystalline g-C_3N_4 nanosheets for efficient photocatalytic water purification under visible light irradiation. Carbon. **137**, 19-30 (2018). https://doi.org/10.1016/j.carbon.2018.05.010.

[34] Y.-J. Yuan, Z. Shen, S. Wu, Y. Su, L. Pei, Z. Ji, M. Ding, W. Bai, Y. Chen, Z.-T. Yu, Liquid exfoliation of g-C_3N_4 nanosheets to construct 2D-2D MoS_2/g-C_3N_4 photocatalyst for enhanced photocatalytic H_2 production activity. Appl. Catal. B: Environ. **246**, 120-128 (2019). https://doi.org/10.1016/j.apcatb.2019.01.043.

[35] S. Liu, Z. Guo, X. Zeng, X. Meng, H. Sun, Y. Wan, G. Zuo, Self assembly and controlled drug release of a nano-laminated graphite carbon nitride/methotrexate complex. J. Mater. Sci.: Mater. Med. **29**, 116 (2018). https://doi.org/10.1007/s10856-018-6128-3.

[36] S. Ouédraogo, B. Chouchene, C. Desmarets, T. Gries, L. Balan, R. Fournet, G. Medjahdi, K. Bayo, R. Schneider, Copper octacarboxyphthalocyanine as sensitizer of graphitic carbon nitride for efficient dye degradation under visible light irradiation. Appl. Catal. A: Gen. **563**, 127-136 (2018). https://doi.org/10.1016/j.apcata.2018.06.036.

[37] J. Cui, D. Qi, X. Wang, Research on the techniques of ultrasound-assisted liquid-phase peeling, thermal oxidation peeling and acid-base chemical peeling for ultra-thin graphite carbon nitride nanosheets. Ultrason Sonochem. **48**, 181-187 (2018). https://doi.org/10.1016/j.ultsonch.2018.05.020.

[38] B. Luo, R. Song, J. Geng, D. Jing, Y. Zhang, Facile preparation with high yield of a 3D porous graphitic carbon nitride for dramatically enhanced photocatalytic H_2 evolution under visible light. Appl. Catal. B: Environ. **238**, 294-301 (2018). https://doi.org/10.1016/j.apcatb.2018.07.039.

[39] K. Zhu, Y. Lv, J. Liu, W. Wang, C. Wang, P. Wang, A. Meng, Z. Li, Q. Li, Explosive thermal exfoliation of intercalated graphitic carbon nitride for enhanced photocatalytic degradation properties. Ceram. Int. **45**, 3643-3647 (2019). https://doi.org/10.1016/j.ceramint.2018.11.025.

[40] J. Wang, Z. Yang, W. Yao, X. Gao, D. Tao, Defects modified in the exfoliation of g-C_3N_4 nanosheets via a self-assembly process for improved hydrogen evolution performance. Appl. Catal. B: Environ. **238**, 629-637 (2018). https://doi.org/10.1016/j.apcatb.2018.07.017.

[41] M. Zhang, C. Lai, B. Li, D. Huang, G. Zeng, P. Xu, L. Qin, S. Liu, X. Liu, H. Yi, Rational design 2D/2D BiOBr/CDs/g-C_3N_4 Z-scheme heterojunction photocatalyst with carbon dots as solid-state electron mediators for enhanced visible and NIR photocatalytic activity: Kinetics, intermediates, and mechanism insight. J. Catal. **369**, 469-481 (2019). https://doi.org/10.1016/j.jcat.2018.11.029.

[42] A. Sett, D. Das, D. Banerjee, U. Ghorai, N. Das, B. Das, K. Chattopadhyay, 1D–2D hybrids as efficient optoelectronic materials: a study on graphitic carbon nitride nanosheets wrapped with zinc oxide rods. Dalton Trans. **47**, 4501-4507 (2018). https://doi.org/10.1039/C8DT00016F

[43] H. Wang, L. Fang, S. Hu, Y. Pei, W. Ma, A green and facile method to prepare graphitic carbon nitride nanosheets with outstanding photocatalytic H_2O_2 production ability via NaClO hydrothermal treatment. New J. Chem. . **42**, 18335-18341 (2018). https://doi.org/10.1039/C8NJ03044H

[44] D. Huang, Z. Li, G. Zeng, C. Zhou, W. Xue, X. Gong, X. Yan, S. Chen, W. Wang, M. Cheng, Megamerger in photocatalytic field: 2D g-C_3N_4 nanosheets serve as support of 0D nanomaterials for improving photocatalytic performance. Appl. Catal. B: Environ. **240**, 153-173 (2018). https://doi.org/10.1016/j.apcatb.2018.08.071.

[45] S. Yang, Y. Gong, J. Zhang, L. Zhan, L. Ma, Z. Fang, R. Vajtai, X. Wang, P.M. Ajayan, Exfoliated graphitic carbon nitride nanosheets as efficient catalysts for hydrogen evolution under visible light. Adv. Mater. **25**, 2452-2456 (2013). https://doi.org/10.1002/adma.201204453.

[46] Q. Guo, Y. Xie, X. Wang, S. Zhang, T. Hou, S. Lv, Synthesis of carbon nitride nanotubes with the C_3N_4 stoichiometry via a benzene-thermal process at low temperatures. ChemComm, 26-27 (2004). https://doi.org/10.1039/B311390F

[47] S. Barman, M. Sadhukhan, Facile bulk production of highly blue fluorescent graphitic carbon nitride quantum dots and their application as highly selective and sensitive sensors for the detection of mercuric and iodide ions in aqueous media. J. Mater. Chem. A. **22**, 21832-21837 (2012). https://doi.org/10.1039/C2JM35501A

[48] Y.-C. Lu, J. Chen, A.-J. Wang, N. Bao, J.-J. Feng, W. Wang, L. Shao, Facile synthesis of oxygen and sulfur co-doped graphitic carbon nitride fluorescent quantum dots and their application for mercury (II) detection and bioimaging. J. Mater. Chem. C. **3**, 73-78 (2015). https://doi.org/10.1039/C4TC02111H.

[49] W.-J. Ong, L.-L. Tan, Y.H. Ng, S.-T. Yong, S.-P. Chai, Graphitic carbon nitride (g-C_3N_4)-based photocatalysts for artificial photosynthesis and environmental remediation: are we a step closer to achieving sustainability? Chem. Rev. **116**, 7159-7329 (2016). https://doi.org/10.1021/acs.chemrev.6b00075.

[50] F. Yang, D. Liu, Y. Li, L. Cheng, J. Ye, Salt-template-assisted construction of honeycomb-like structured g-C_3N_4 with tunable band structure for enhanced photocatalytic H_2 production. Appl. Catal. B: Environ. **240**, 64-71 (2019). https://doi.org/10.1016/j.apcatb.2018.08.072.

[51] D. Huang, X. Yan, M. Yan, G. Zeng, C. Zhou, J. Wan, M. Cheng, W. Xue, interfaces, Graphitic carbon nitride-based heterojunction photoactive nanocomposites: Applications and mechanism insight. ACS Appl. Mater. Interfaces. **10**, 21035-21055 (2018). https://doi.org/10.1021/acsami.8b03620.

[52] Y. Gong, J. Wang, Z. Wei, P. Zhang, H. Li, Y. Wang, Combination of carbon nitride and carbon nanotubes: Synergistic catalysts for energy conversion. ChemSusChem. **7**, 2303-2309 (2014). https://doi.org/10.1002/cssc.201402078.

[53] D. Huang, H. Luo, C. Zhang, G. Zeng, C. Lai, M. Cheng, R. Wang, R. Deng, W. Xue, X. Gong, Nonnegligible role of biomass types and its compositions on the formation of persistent free radicals in biochar: Insight into the influences on fenton-like process. Chem. Eng. J. **361**, 353-363 (2019). https://doi.org/10.1016/j.cej.2018.12.098.

[54] P. Niu, M. Qiao, Y. Li, L. Huang, T. Zhai, Distinctive defects engineering in graphitic carbon nitride for greatly extended visible light photocatalytic hydrogen evolution. Nano Energy. **44**, 73-81 (2018). https://doi.org/10.1016/j.nanoen.2017.11.059.

[55] A. Akhundi, A. Habibi-Yangjeh, M. Abitorabi, S. Rahim Pouran, Review on photocatalytic conversion of carbon dioxide to value-added compounds and renewable fuels by graphitic carbon nitride-based photocatalysts. Catal. Rev., 1-34 (2019). https://doi.org/10.1080/01614940.2019.1654224.

[56] W. Lei, Y. Mi, R. Feng, P. Liu, S. Hu, J. Yu, X. Liu, J.A. Rodriguez, J.-o. Wang, L. Zheng, Hybrid 0D–2D black phosphorus quantum dots–graphitic carbon nitride nanosheets for efficient hydrogen evolution. Nano Energy. **50**, 552-561 (2018). https://doi.org/10.1016/j.nanoen.2018.06.001.

[57] Z. Zhang, J. Huang, M. Zhang, Q. Yuan, B. Dong, Ultrathin hexagonal SnS_2 nanosheets coupled with g-C_3N_4 nanosheets as 2D/2D heterojunction photocatalysts toward high photocatalytic activity. Appl. Catal. B: Environ. **163**, 298-305 (2015). https://doi.org/10.1016/j.apcatb.2014.08.013.

[58] W.-J. Ong, 2D/2D graphitic carbon nitride (g-C_3N_4) heterojunction nanocomposites for photocatalysis: why does face-to-face interface matter? Front. Mater. Sci. **4**, 1-11 (2017). https://doi.org/10.3389/fmats.2017.00011.

[59] J. Zhang, M. Zhang, R.Q. Sun, X. Wang, A facile band alignment of polymeric carbon nitride semiconductors to construct isotype heterojunctions. Angew. Chem. Int. Ed. . **51**, 10145-10149 (2012). https://doi.org/10.1039/C5EE01895A

[60] Z. Chen, Y. Yu, X. She, K. Xia, Z. Mo, H. Chen, Y. Song, J. Huang, H. Li, H. Xu, Constructing schottky junction between 2D semiconductor and metallic nickel phosphide for highly efficient catalytic hydrogen evolution. Appl. Surf. Sci., (2019). https://doi.org/10.1016/j.apsusc.2019.07.270.

[61] B. Li, C. Lai, G. Zeng, L. Qin, H. Yi, D. Huang, C. Zhou, X. Liu, M. Cheng, P. Xu, Facile hydrothermal synthesis of Z-scheme Bi_2Fe4O_9/Bi_2WO_6 heterojunction photocatalyst with enhanced visible light photocatalytic activity. ACS Appl. Mater. Interfaces. **10**, 18824-18836 (2018). https://doi.org/10.1021/acsami.8b06128.

[62] D. Huang, S. Chen, G. Zeng, X. Gong, C. Zhou, M. Cheng, W. Xue, X. Yan, J. Li, Artificial Z-scheme photocatalytic system: What have been done and where to go? Coord. Chem. Rev. **385**, 44-80 (2019). https://doi.org/10.1016/j.ccr.2018.12.013.

[63] L. Jiang, X. Yuan, G. Zeng, J. Liang, Z. Wu, H. Yu, D. Mo, H. Wang, Z. Xiao, C. Zhou, Nitrogen self-doped g-C_3N_4 nanosheets with tunable band structures for enhanced photocatalytic tetracycline degradation. J. Colloid Interface Sci. **536**, 17-29 (2019). https://doi.org/10.1016/j.jcis.2018.10.033.

[64] J. Wei, W. Shen, J. Zhao, C. Zhang, Y. Zhou, H. Liu, Boron doped g-C_3N_4 as an effective metal-free solid base catalyst in Knoevenagel condensation. Catal. Today. **316**, 199-205 (2018). https://doi.org/10.1016/j.cattod.2018.02.041.

[65] Y. Li, K. Lv, W. Ho, Z. Zhao, Y. Huang, Enhanced visible-light photo-oxidation of nitric oxide using bismuth-coupled graphitic carbon nitride composite

heterostructures. Chinese J. Catal. **38**, 321-329 (2017). https://doi.org/10.1016/S1872-2067(16)62573-1.

[66] B. Peng, L. Tang, G. Zeng, S. Fang, X. Ouyang, B. Long, Y. Zhou, Y. Deng, Y. Liu, J. Wang, Self-powered photoelectrochemical aptasensor based on phosphorus doped porous ultrathin g-C_3N_4 nanosheets enhanced by surface plasmon resonance effect. Biosens. Bioelectron. **121**, 19-26 (2018). https://doi.org/10.1016/j.bios.2018.08.042.

[67] X. Wang, S. Jiang, X. Huo, R. Xia, E. Muhire, M. Gao, Facile preparation of a TiO_2 quantum dot/graphitic carbon nitride heterojunction with highly efficient photocatalytic activity. Nanotechnology. **29**, 205702 (2018). https://doi.org/10.1088/1361-6528/aab1be.

[68] M. Volokh, G. Peng, J. Barrio, M. Shalom, Carbon nitride materials for water splitting photoelectrochemical cells. Angew. Chem. Int. Ed. **57**, 1186-1192 (2018). https://doi.org/10.1002/anie.201806514.

[69] H. Kasap, R. Godin, C. Jeay Bizot, D.S. Achilleos, X. Fang, J.R. Durrant, E. Reisner, Interfacial engineering of a carbon nitride-graphene oxide-molecular Ni catalyst hybrid for enhanced photocatalytic activity. ACS Catal. **8**, 6914-6926 (2018). https://doi.org/10.1021/acscatal.8b01969.

[70] X. Wang, K. Maeda, A. Thomas, K. Takanabe, G. Xin, J.M. Carlsson, K. Domen, M. Antonietti, A metal-free polymeric photocatalyst for hydrogen production from water under visible light. Nat. Mater. **8**, 76 (2009). https://doi.org/10.1088/1361-6528/aab1be.

[71] S. Yan, Z. Li, Z. Zou, Photodegradation performance of g-C_3N_4 fabricated by directly heating melamine. Langmuir. **25**, 10397-10401 (2009). https://doi.org/10.1021/la900923z.

[72] X. Chen, Q. Liu, Q. Wu, P. Du, J. Zhu, S. Dai, S. Yang, Incorporating graphitic carbon nitride (g-C_3N_4) quantum dots into bulk-heterojunction polymer solar cells leads to efficiency enhancement. Adv. Funct. Mater. **26**, 1719-1728 (2016). https://doi.org/10.1002/adfm.201505321.

[73] J. Tian, Q. Liu, A.M. Asiri, K.A. Alamry, X. Sun, Ultrathin graphitic C_3N_4 nanosheets/graphene composites: Efficient organic electrocatalyst for oxygen evolution reaction. ChemSusChem. **7**, 2125-2130 (2014). https://doi.org/10.1002/cssc.201402118.

[74] Y. Luo, Y. Yan, S. Zheng, H. Xue, H. Pang, Graphitic carbon nitride based materials for electrochemical energy storage. J. Mater. Chem. A **7**,901-924 (2019). https://doi.org/10.1039/C8TA08464E

[75] S. Sun, S. Gu, J. Sun, F. Xia, G. Chen, First principles investigation of the electronic properties of graphitic carbon nitride with different building block and sheet staggered arrangement. J. Alloys Compd. **735**, 131-139 (2018). https://doi.org/10.1016/j.jallcom.2017.11.061.

[76] S. Zhang, P. Gu, R. Ma, C. Luo, T. Wen, G. Zhao, W. Cheng, X. Wang, Recent developments in fabrication and structure regulation of visible-light-driven g-C_3N_4-

based photocatalysts towards water purification: A critical review. Catal. Today, (2018). https://doi.org/10.1016/j.cattod.2018.09.013.

[77] E. Kroke, M. Schwarz, E. Horath-Bordon, P. Kroll, B. Noll, A.D. Norman, Tri-s-triazine derivatives. Part I. from trichloro-tri-s-triazine to graphitic C_3N_4 structures. New J. Chem. **26**, 508-512 (2002). https://doi.org/10.1039/B111062B

[78] A. Wang, C. Wang, L. Fu, W. Wong-Ng, Y. Lan, Recent advances of graphitic carbon nitride-based structures and applications in catalyst, sensing, imaging, and LEDs. Nanomicro Lett **9**,47 (2017). https://doi.org/10.1007/s40820-017-0148-2.

[79] S. Cao, J. Yu, G-C_3N_4-based photocatalysts for hydrogen generation. J. Phys. Chem. Lett. **5**, 2101-2107 (2014). https://doi.org/10.1021/jz500546b.

[80] H. Sun, S. Liu, G. Zhou, H.M. Ang, M.O. Tadé, S. Wang, Reduced graphene oxide for catalytic oxidation of aqueous organic pollutants. ACS Appl. Mater. Interfaces. **4**, 5466-5471 (2012). https://doi.org/10.1021/am301372d.

[81] M. Wu, J. Zhang, C. Liu, Y. Gong, R. Wang, B. He, H. Wang, Rational design and fabrication of noble-metal-free NixP cocatalyst embedded 3D N-TiO2/g-C_3N_4 heterojunctions with enhanced photocatalytic hydrogen evolution. ChemCatChem. **10**, 3069-3077 (2018). https://doi.org/10.1002/cctc.201800197.

[82] F. Fina, S.K. Callear, G.M. Carins, J.T. Irvine, Structural investigation of graphitic carbon nitride via XRD and neutron diffraction. Chem. Mater. **27**, 2612-2618 (2015). https://doi.org/10.1021/acs.chemmater.5b00411.

[83] Y. Zheng, J. Liu, J. Liang, M. Jaroniec, S.Z. Qiao, Graphitic carbon nitride materials: controllable synthesis and applications in fuel cells and photocatalysis. Energy Environ. Sci. **5**, 6717-6731 (2012). https://doi.org/10.1039/C2EE03479D

[84] G. Liu, P. Niu, C. Sun, S.C. Smith, Z. Chen, G.Q. Lu, H.-M. Cheng, Unique electronic structure induced high photoreactivity of sulfur-doped graphitic C_3N_4. J. Am. Chem. Soc. . **132**, 11642-11648 (2010). https://doi.org/10.1021/ja103798k.

[85] G. Dong, Y. Zhang, Q. Pan, J. Qiu, A fantastic graphitic carbon nitride (g-C_3N_4) material: Electronic structure, photocatalytic and photoelectronic properties. J. Photochem. Photobiol. C: Photochem. Rev. **20**, 33-50 (2014). https://doi.org/10.1016/j.jphotochemrev.2014.04.002.

[86] M.Z. Rahman, K. Davey, C.B. Mullins, Tuning the intrinsic properties of carbon nitride for high quantum yield photocatalytic hydrogen production. Adv. Sci. **5**, 1800820 (2018). https://doi.org/10.1002/advs.201800820.

[87] Y. Zhang, T. Mori, J. Ye, Polymeric carbon nitrides: Semiconducting properties and emerging applications in photocatalysis and photoelectrochemical energy conversion. Sci. Adv. Mater. **4**, 282-291 (2012). https://doi.org/10.1166/sam.2012.1283.

[88] Z. Mo, H. Xu, Z. Chen, X. She, Y. Song, J. Wu, P. Yan, L. Xu, Y. Lei, S. Yuan, Self-assembled synthesis of defect-engineered graphitic carbon nitride nanotubes for efficient conversion of solar energy. Appl. Catal. B: Environ. **225**, 154-161 (2018). https://doi.org/10.1016/j.apcatb.2017.11.041.

[89] S. Chen, N. Hao, D. Jiang, X. Zhang, Z. Zhou, Y. Zhang, K. Wang, Graphitic carbon nitride quantum dots in situ coupling to Bi_2MoO_6 nanohybrids with enhanced

charge transfer performance and photoelectrochemical detection of copper ion. J. Electroanal. Chem. **787**, 66-71 (2017). https://doi.org/10.1016/j.jelechem.2017.01.042.

[90] J. Gao, Y. Wang, S. Zhou, W. Lin, Y. Kong, A facile one-step synthesis of Fe-doped g-C_3N_4 nanosheets and their improved visible-light photocatalytic performance. ChemCatChem. **9**, 1708-1715 (2017). https://doi/pdf/10.1002/cctc.201700492.

[91] Z. Mao, J. Chen, Y. Yang, D. Wang, L. Bie, B.D. Fahlman, Novel g-C_3N_4/CoO nanocomposites with significantly enhanced visible-light photocatalytic activity for H_2 evolution. ACS Appl. Mater. Interfaces. **9**, 12427-12435 (2017). https://doi.org/10.1021/acsami.7b00370.

[92] P. Xia, B. Zhu, B. Cheng, J. Yu, J. Xu, 2D/2D g-C_3N_4/MnO_2 nanocomposite as a direct Z-scheme photocatalyst for enhanced photocatalytic activity. ACS Sustain. Chem. Eng. **6**, 965-973 (2017). https://doi.org/10.1021/acssuschemeng.7b03289.

[93] Y. Deng, L. Tang, G. Zeng, Z. Zhu, M. Yan, Y. Zhou, J. Wang, Y. Liu, J. Wang, Insight into highly efficient simultaneous photocatalytic removal of Cr(VI) and 2,4-diclorophenol under visible light irradiation by phosphorus doped porous ultrathin g-C_3N_4 nanosheets from aqueous media: Performance and reaction mechanism. Appl. Catal. B: Environ. **203**, 343-354 (2017). https://doi.org/10.1016/j.apcatb.2016.10.046.

[94] X. Zhang, X. Xie, H. Wang, J. Zhang, B. Pan, Y. Xie, Enhanced photoresponsive ultrathin graphitic-phase C_3N_4 nanosheets for bioimaging. J. Am. Chem. Soc. **135**, 18-21 (2012). https://doi.org/10.1021/ja308249k.

[95] X. Du, G. Zou, Z. Wang, X. Wang, A scalable chemical route to soluble acidified graphitic carbon nitride: An ideal precursor for isolated ultrathin g-C_3N_4 nanosheets. Nanoscale. **7**, 8701-8706 (2015). https://doi.org/10.1039/C5NR00665A

[96] S. Ye, R. Wang, M.-Z. Wu, Y.-P. Yuan, A review on g-C_3N_4 for photocatalytic water splitting and CO_2 reduction. Appl. Surf. Sci. **358**, 15-27 (2015). https://doi.org/10.1016/j.apsusc.2015.08.173.

[97] P. Niu, L. Zhang, G. Liu, H.M. Cheng, Graphene-like carbon nitride nanosheets for improved photocatalytic activities. Adv. Funct. Mater. **22**, 4763-4770 (2012). https://doi.org/10.1002/adfm.201200922.

[98] Y. Hou, Z. Wen, S. Cui, X. Guo, J. Chen, Constructing 2D porous graphitic C_3N_4 nanosheets/nitrogen-doped graphene/layered MoS_2 ternary nanojunction with enhanced photoelectrochemical activity. Adv. Mater. **25**, 6291-6297 (2013). https://doi.org/10.1002/adma.201303116.

[99] Y. Zhang, T. Mori, L. Niu, J. Ye, Non-covalent doping of graphitic carbon nitride polymer with graphene: Controlled electronic structure and enhanced optoelectronic conversion. Energy Environ. Sci. **4**, 4517-4521 (2011). https://doi.org/10.1039/C1EE01400E

[100] L.J. Fang, Y.H. Li, P.F. Liu, D.P. Wang, H.D. Zeng, X.L. Wang, H.G. Yang, Facile fabrication of large-aspect-ratio g-C_3N_4 nanosheets for enhanced photocatalytic

hydrogen evolution. ACS Sustain. Chem. Eng. **5**, 2039-2043 (2017). https://doi.org/10.1021/acssuschemeng.6b02721.

[101] W. Wang, J. Fang, S. Shao, M. Lai, C. Lu, Compact and uniform TiO_2 g-C_3N_4 core-shell quantum heterojunction for photocatalytic degradation of tetracycline antibiotics. Appl. Catal. B: Environ. **217**, 57-64 (2017). https://doi.org/10.1016/j.apcatb.2017.05.037.

[102] J. Xu, L. Zhang, R. Shi, Y. Zhu, Chemical exfoliation of graphitic carbon nitride for efficient heterogeneous photocatalysis. J. Mater. Chem. A. **1**, 14766-14772 (2013). https://doi.org/10.1039/C3TA13188B.

[103] Y. Zhang, Q. Zhang, Q. Shi, Z. Cai, Z. Yang, Acid-treated g-C_3N_4 with improved photocatalytic performance in the reduction of aqueous Cr (VI) under visible-light. Sep. Purif. Technol. **142**, 251-257 (2015). https://doi.org/10.1016/j.seppur.2014.12.041.

[104] Y. Ma, E. Liu, X. Hu, C. Tang, J. Wan, J. Li, J. Fan, A simple process to prepare few-layer g-C_3N_4 nanosheets with enhanced photocatalytic activities. Appl. Surf. Sci. **358**, 246-251 (2015). https://doi.org/10.1016/j.apsusc.2015.08.174.

[105] S. Challagulla, S. Payra, C. Chakraborty, S. Roy, Determination of band edges and their influences on photocatalytic reduction of nitrobenzene by bulk and exfoliated g-C_3N_4. Phys. Chem. Chem. **21**, 3174-3183 (2019). https://doi.org/10.1039/C8CP06855K.

[106] G. Lei, Y. Cao, W. Zhao, Z. Dai, L. Shen, Y. Xiao, L. Jiang, Exfoliation of graphitic carbon nitride for enhanced oxidative desulfurization: A facile and general strategy. ACS Sustain. Chem. Eng. **7**, 4941-4950 (2019). https://doi.org/10.1021/acssuschemeng.8b05553.

[107] J. Fu, Q. Xu, J. Low, C. Jiang, J. Yu, Ultrathin 2D/2D WO_3/g-C_3N_4 step-scheme H_2-production photocatalyst. Appl. Catal. B: Environ. **243**, 556-565 (2019). https://doi.org/10.1016/j.apcatb.2018.11.011.

[108] R. Li, Y. Ren, P. Zhao, J. Wang, J. Liu, Y. Zhang, Graphitic carbon nitride (g-C_3N_4) nanosheets functionalized composite membrane with self-cleaning and antibacterial performance. J. Hazard. Mater. **365**, 606-614 (2019). https://doi.org/10.1016/j.jhazmat.2018.11.033.

[109] S. Wang, g-C_3N_4 nanosheets as "on-off-on" selective fluorescence biosensor to detect ascorbic acid via redox reaction. J. Alloys Compd. **770**, 952-958 (2019). https://doi.org/10.1016/j.jallcom.2018.08.182.

[110] Y. Huang, Y. Wang, Y. Bi, J. Jin, M.F. Ehsan, M. Fu, T. He, Preparation of 2D hydroxyl-rich carbon nitride nanosheets for photocatalytic reduction of CO_2. RSC Adv. **5**, 33254-33261 (2015). https://doi.org/10.1039/C5RA04227E

[111] S.N. Talapaneni, J.H. Lee, S.H. Je, O. Buyukcakir, T.w. Kwon, K. Polychronopoulou, J.W. Choi, A. Coskun, Chemical blowing approach for ultramicroporous carbon nitride frameworks and their applications in gas and energy storage. Adv. Funct. Mater. **27**, 1604658 (2017). https://doi.org/10.1002/adfm.201604658.

[112] J. Yan, X. Han, X. Zheng, J. Qian, J. Liu, X. Dong, F. Xi, One-step template/chemical blowing route to synthesize flake-like porous carbon nitride photocatalyst. Mater. Res. Bull. **94**, 423-427 (2017). https://doi.org/10.1016/j.materresbull.2017.06.022.

[113] B. Ye, X. Han, M. Yan, H. Zhang, F. Xi, X. Dong, J. Liu, Fabrication of metal-free two dimensional/two dimensional homojunction photocatalyst using various carbon nitride nanosheets as building blocks. J. Colloid Interface Sci. **507**, 209-216 (2017). https://doi.org/10.1016/j.jcis.2017.08.002.

[114] F. He, G. Chen, J. Miao, Z. Wang, D. Su, S. Liu, W. Cai, L. Zhang, S. Hao, B. Liu, Sulfur-mediated self-templating synthesis of tapered C-PAN/g-C_3N_4 composite nanotubes toward efficient photocatalytic H_2 evolution. ACS Energy Lett. **1**, 969-975 (2016). https://doi.org/10.1021/acsenergylett.6b00398.

[115] J. Wang, C. Zhang, Y. Shen, Z. Zhou, J. Yu, Y. Li, W. Wei, S. Liu, Y. Zhang, Environment-friendly preparation of porous graphite-phase polymeric carbon nitride using calcium carbonate as templates, and enhanced photoelectrochemical activity. J. Mater. Chem. A **3**,5126-5131 (2015). https://doi.org/10.1039/C4TA06778A

[116] H.H. Refsgaard, P.M. Brockhoff, B. Jensen, Free polyunsaturated fatty acids cause taste deterioration of salmon during frozen storage. J. Agric. Food Chem. **48**, 3280-3285 (2000). https://doi.org/10.1021/jf000021c.

[117] Y. Wang, X. Wang, M. Antonietti, Y. Zhang, Facile one-pot synthesis of nanoporous carbon nitride solids by using soft templates. ChemSusChem **3**,435-439 (2010). https://doi.org/10.1002/cssc.200900284.

[118] Z. Yang, Y. Zhang, Z. Schnepp, Soft and hard templating of graphitic carbon nitride. J. Mater. Chem. A. **3**, 14081-14092 (2015). https://doi.org/10.1039/C5TA02156A

[119] H. Yan, Soft-templating synthesis of mesoporous graphitic carbon nitride with enhanced photocatalytic H_2 evolution under visible light. ChemComm. **48**, 3430-3432 (2012). https://doi.org/10.1039/C2CC00001F

[120] S. Liu, F. Chen, S. Li, X. Peng, Y. Xiong, Enhanced photocatalytic conversion of greenhouse gas CO_2 into solar fuels over g-C_3N_4 nanotubes with decorated transparent ZIF-8 nanoclusters. Appl. Catal. B: Environ. **211**, 1-10 (2017). https://doi.org/10.1016/j.apcatb.2017.04.009.

[121] W. Wang, C.Y. Jimmy, Z. Shen, D.K. Chan, T. Gu, g-C_3N_4 quantum dots: Direct synthesis, upconversion properties and photocatalytic application. ChemComm. **50**, 10148-10150 (2014). https://doi.org/10.1039/C4CC02543A.

[122] T. Oh, M. Kim, J. Choi, J. Kim, Design of graphitic carbon nitride nanowires with captured mesoporous carbon spheres for EDLC electrode materials. Ionics. **24**, 3957-3965 (2018). https://doi.org/10.1007/s11581-018-2544-0.

[123] Z. Tang, X. Zhang, L. Duan, A. Wu, W. Lü, Three-dimensional carbon nitride nanowire scaffold for flexible supercapacitors. Nanoscale Res. Lett. **14**, 98 (2019). https://doi.org/10.1186/s11671-019-2932-z.

[124] M. Xie, W. Wei, Z. Jiang, Y. Xu, J. Xie, Carbon nitride nanowires/nanofibers: a novel template-free synthesis from a cyanuric chloride–melamine precursor towards enhanced adsorption and visible-light photocatalytic performance. Ceram. Int. **42**, 4158-4170 (2016). https://doi.org/10.1016/j.ceramint.2015.11.089.

[125] Y.-L.T. Ngo, W.M. Choi, J.S. Chung, S.H. Hur, Highly biocompatible phenylboronic acid-functionalized graphitic carbon nitride quantum dots for the selective glucose sensor. Sens. Actuators B Chem. **282**, 36-44 (2019). https://doi.org/10.1016/j.snb.2018.11.031.

[126] X. Lin, D. Xu, R. Zhao, Y. Xi, L. Zhao, M. Song, H. Zhai, G. Che, L. Chang, Highly efficient photocatalytic activity of g-C_3N_4 quantum dots (CNQDs)/Ag/Bi_2MoO_6 nanoheterostructure under visible light. Sep. Purif. Technol. . **178**, 163-168 (2017). https://doi.org/10.1016/j.seppur.2017.01.020.

[127] H. Wang, Q. Lu, M. Li, H. Li, Y. Liu, H. Li, Y. Zhang, S. Yao, Electrochemically prepared oxygen and sulfur co-doped graphitic carbon nitride quantum dots for fluorescence determination of copper and silver ions and biothiols. Anal. Chim. Acta. **1027**, 121-129 (2018). https://doi.org/10.1016/j.aca.2018.03.063.

[128] Q. Liang, Z. Li, X. Yu, Z.H. Huang, F. Kang, Q.H. Yang, Macroscopic 3D porous graphitic carbon nitride monolith for enhanced photocatalytic hydrogen evolution. Adv. Mater. **27**, 4634-4639 (2015). https://doi.org/10.1002/adma.201502057.

[129] X. Wang, K. Maeda, X. Chen, K. Takanabe, K. Domen, Y. Hou, X. Fu, M. Antonietti, Polymer semiconductors for artificial photosynthesis: Hydrogen evolution by mesoporous graphitic carbon nitride with visible light. J. Am. Chem. Soc. **131**, 1680-1681 (2009). https://doi.org/10.1088/1361-6528/aab1be.

[130] Y. Fan, W. Zhang, Y. Liu, Z. Zeng, X. Quan, H. Zhao, 3D branched crystal carbon citride with enhanced Intrinsic peroxidase-like activity: A hypersensitive platform for colorimetric detection. ACS Appl. Mater. Interfaces. **11**, 17467-17474 (2019). https://doi.org/10.1021/acsami.9b04320.

[131] Z.-H. Sheng, L. Shao, J.-J. Chen, W.-J. Bao, F.-B. Wang, X.-H. Xia, Catalyst-free synthesis of nitrogen-doped graphene via thermal annealing graphite oxide with melamine and its excellent electrocatalysis. ACS Nano. **5**, 4350-4358 (2011). https://doi.org/10.1021/nn103584t.

[132] J. Wen, J. Xie, X. Chen, X. Li, A review on g-C_3N_4-based photocatalysts. Appl. Surf. Sci. **391**, 72-123 (2017). https://doi.org/10.1016/j.apsusc.2016.07.030.

[133] S. Kamal, S. Balu, S. Palanisamy, K. Uma, V. Velusamy, T.C. Yang, Synthesis of boron doped C_3N_4/$NiFe_2O_4$ nanocomposite: An enhanced visible light photocatalyst for the degradation of methylene blue. Results Phys. **12**, 1238-1244 (2019). https://doi.org/10.1016/j.rinp.2019.01.004.

[134] L. Wang, X. Guo, Y. Chen, S. Ai, H. Ding, Cobalt-doped g-C_3N_4 as a heterogeneous catalyst for photo-assisted activation of peroxymonosulfate for the degradation of organic contaminants. Appl. Surf. Sci. **467**, 954-962 (2019). https://doi.org/10.1016/j.apsusc.2018.10.262.

[135] J. Chen, Z. Hong, Y. Chen, B. Lin, B. Gao, One-step synthesis of sulfur-doped and nitrogen-deficient g-C_3N_4 photocatalyst for enhanced hydrogen evolution under

visible light. Mater. Lett. **145**, 129-132 (2015). https://doi.org/10.1016/j.matlet.2015.01.073.

[136] S. Stolbov, S. Zuluaga, Sulfur doping effects on the electronic and geometric structures of graphitic carbon nitride photocatalyst: insights from first principles. J. Condens. Matter Phys. **25**, 085507 (2013). https://doi.org/10.1088/0953-8984/25/8/085507.

[137] S. Yan, Z. Li, Z. Zou, Photodegradation of rhodamine B and methyl orange over boron-doped g-C_3N_4 under visible light irradiation. Langmuir. **26**, 3894-3901 (2010). https://doi.org/10.1021/la904023j.

[138] Y.-P. Zhu, T.-Z. Ren, Z.-Y. Yuan, Mesoporous phosphorus-doped g-C_3N_4 nanostructured flowers with superior photocatalytic hydrogen evolution performance. ACS Appl. Mater. Interfaces. **7**, 16850-16856 (2015). https://doi.org/10.1021/acsami.5b04947.

[139] H. Yang, Y. Zhou, Y. Wang, S. Hu, B. Wang, Q. Liao, H. Li, J. Bao, G. Ge, S. Jia, Three-dimensional flower-like phosphorus-doped g-C_3N_4 with a high surface area for visible-light photocatalytic hydrogen evolution. J. Mater. Chem. A. **6**, 16485-16494 (2018). https://doi.org/10.1039/C8TA05723K.

[140] B. Li, C. Lai, P. Xu, G. Zeng, D. Huang, L. Qin, H. Yi, M. Cheng, L. Wang, F. Huang, Facile synthesis of bismuth oxyhalogen-based Z-scheme photocatalyst for visible-light-driven pollutant removal: Kinetics, degradation pathways and mechanism. J. Clean. Prod. **225**, 898-912 (2019). https://doi.org/10.1016/j.jclepro.2019.04.012.

[141] Z. Mo, H. Xu, Z. Chen, X. She, Y. Song, P. Yan, Y. Xu, Y. Lei, S. Yuan, H. Li, Gold/monolayer graphitic carbon nitride plasmonic photocatalyst for ultrafast electron transfer in solar-to-hydrogen energy conversion. Chinese J. Catal. **39**, 760-770 (2018). https://doi.org/10.1016/S1872-2067(17)62978-4.

[142] Y. Li, M. Meng, C. Ji, S. Teng, L. Gao, R. Qu, Z. Yang, C. Sun, Y. Zhang, Soft-template synthesis of hybrid carbon and carbon nitride composites with enhanced photocatalytic activity for the degradation of methylene blue under visible light. Environ. Prog. Sustain. Energy. **35**, 1-16 (2019). https://doi.org/10.1002/ep.13186.

[143] D. Zhang, Y. Guo, Z. Zhao, Porous defect-modified graphitic carbon nitride via a facile one-step approach with significantly enhanced photocatalytic hydrogen evolution under visible light irradiation. Appl. Catal. B: Environ. **226**, 1-9 (2018). https://doi.org/10.1016/j.apcatb.2017.12.044.

[144] X. Zhao, D. Pan, X. Chen, R. Li, T. Jiang, W. Wang, G. Li, D.Y. Leung, g-C_3N_4 photoanode for photoelectrocatalytic synergistic pollutant degradation and hydrogen evolution. Appl. Surf. Sci. **467**, 658-665 (2019). https://doi.org/10.1016/j.apsusc.2018.10.090.

[145] M. Shen, L. Zhang, J. Shi, Converting CO_2 into fuels by graphitic carbon nitride-based photocatalysts. Nanotechnology. **29**, 412001 (2018). https://doi.org/10.1088/1361-6528/aad4c8.

[146] M.S. Mahmoud, E. Ahmed, A. Farghali, A. Zaki, E.A. Abdelghani, N.A. Barakat, Influence of Mn, Cu, and Cd–doping for titanium oxide nanotubes on the

photocatalytic activity toward water splitting under visible light irradiation. Colloids Surf. A Physicochem. Eng. Asp. . **554**, 100-109 (2018). https://doi.org/10.1016/j.colsurfa.2018.06.039.

[147] R.I. Benmessaoud, Human and eco-toxicological impacts of organometallic halide perovskites. 2017, EPFL.

[148] S.A. Younis, E.M. El-Fawal, P. Serp, Nano-wastes and the Environment: Potential Challenges and Opportunities of Nano-waste Management Paradigm for Greener Nanotechnologies. Handbook of Environmental Materials Management, 1-72 (2018).

[149] B. Li, C. Lai, G. Zeng, D. Huang, L. Qin, M. Zhang, M. Cheng, X. Liu, H. Yi, C. Zhou, Black Phosphorus, a rising star 2D nanomaterial in the post-graphene era: Synthesis, properties, modifications, and photocatalysis applications. Small. **15**, 1804565 (2019). https://doi.org/10.1002/smll.201804565.

[150] Y. Huang, P. Wang, Z. Wang, Y. Rao, J.-j. Cao, S. Pu, W. Ho, S.C. Lee, Protonated g-C_3N_4/Ti^{3+} self-doped TiO_2 nanocomposite films: Room-temperature preparation, hydrophilicity, and application for photocatalytic NO_x removal. Appl. Catal. B: Environ. **240**, 122-131 (2019). https://doi.org/10.1016/j.apcatb.2018.08.078.

[151] J. Xu, J. Gao, Y. Qi, C. Wang, L. Wang, Anchoring Ni_2P on the UiO-66-NH_2/g-C_3N_4-derived C-doped ZrO2/g-C_3N_4 heterostructure: highly efficient photocatalysts for H_2 production from water splitting. ChemCatChem. **10**, 3327-3335 (2018). https://doi.org/10.1002/cctc.201800353.

[152] C. Cheng, J. Shi, Y. Hu, L. Guo, WO_3/g-C_3N_4 composites: One-pot preparation and enhanced photocatalytic H_2 production under visible-light irradiation. Nanotechnology. **28**, 164002 (2017). https://doi.org/10.1088/1361-6528/aa651a.

[153] Y. Xie, G. Alexander, R. Schwartzman, N. Singh, M. Torjman, M. Goldberg, I. Wainer, R. Moaddel, Development and validation of a sensitive LC–MS/MS method for the determination of d-serine in human plasma. J. Pharm. Biomed. **89**, 1-5 (2014). https://doi.org/10.1016/j.jpba.2013.10.028.

[154] H. Xu, H. Zhao, Y. Song, W. Yan, Y. Xu, H. Li, L. Huang, S. Yin, Y. Li, Q. Zhang, g-C_3N_4/Ag_3PO_4 composites with synergistic effect for increased photocatalytic activity under the visible light irradiation. Mater Sci Semicond Process. **39**, 726-734 (2015). https://doi.org/10.1016/j.mssp.2015.04.013.

[155] L. Zhou, W. Zhang, L. Chen, H. Deng, J. Wan, A novel ternary visible-light-driven photocatalyst AgCl/Ag_3PO_4/g-C_3N_4: Synthesis, characterization, photocatalytic activity for antibiotic degradation and mechanism analysis. Catal. Commun. **100**, 191-195 (2017). https://doi.org/10.1016/j.catcom.2017.06.049.

[156] X. Jia, R. Dai, Y. Sun, H. Song, X. Wu, One-step hydrothermal synthesis of Fe_3O_4/gC_3N_4 nanocomposites with improved photocatalytic activities. J. Mater. Sci. Mater. Electron. . **27**, 3791-3798 (2016). https://doi.org/10.1007/s10854-015-4224-4.

[157] M. Duan, J.G. Shapter, W. Qi, S. Yang, G. Gao, Recent progress in magnetic nanoparticles: Synthesis, properties, and applications. Nanotechnology. **29**, 452001 (2018). https://doi.org/10.1088/1361-6528/aadcec.

[158] T. Xie, H. Li, C. Liu, J. Yang, T. Xiao, L. Xu, Magnetic photocatalyst $BiVO_4$/Mn-Zn ferrite/reduced graphene oxide: Synthesis strategy and its highly photocatalytic activity. Nanomaterials. **8**, 380 (2018). https://doi.org/10.3390/nano8060380.

[159] A. Akhundi, A. Habibi-Yangjeh, High performance magnetically recoverable g-C_3N_4/Fe_3O_4/Ag/Ag_2SO_3 plasmonic photocatalyst for enhanced photocatalytic degradation of water pollutants. Adv. Powder Technol. **28**, 565-574 (2017). https://doi.org/10.1016/j.apt.2016.10.025.

[160] T. Peik-See, A. Pandikumar, L.H. Ngee, H.N. Ming, C.C. Hua, Magnetically separable reduced graphene oxide/iron oxide nanocomposite materials for environmental remediation. Catal. Sci. Technol. **4**, 4396-4405 (2014). https://doi.org/10.1039/C4CY00806E.

[161] G. Simonsen, M. Strand, G. Øye, Potential applications of magnetic nanoparticles within separation in the petroleum industry. J. Pet. Sci. **165**, 488-495 (2018). https://doi.org/10.1016/j.petrol.2018.02.048.

[162] X.-L. Zhang, C. Zheng, S.-S. Guo, J. Li, H.-H. Yang, G. Chen, Turn-on fluorescence sensor for intracellular imaging of glutathione using g-C_3N_4 nanosheet–MnO_2 sandwich nanocomposite. Anal. Chem. **86**, 3426-3434 (2014). https://doi.org/10.1021/ac500336f.

[163] J. Chen, Y. Gao, X. Hu, Y. Xu, X. Lu, Detection of hydroquinone with a novel fluorescence probe based on the enzymatic reaction of graphite phase carbon nitride quantum dots. Talanta. **194**, 493-500 (2019). https://doi.org/10.1016/j.talanta.2018.09.111.

[164] C. Lai, S. Liu, C. Zhang, G. Zeng, D. Huang, L. Qin, X. Liu, H. Yi, R. Wang, F. Huang, Electrochemical aptasensor based on sulfur–nitrogen codoped ordered mesoporous carbon and thymine–Hg^{2+}–thymine mismatch structure for Hg^{2+} detection. ACS Sens. . **3**, 2566-2573 (2018). https://doi.org/10.1021/acssensors.8b00926.

[165] M. Wu, Q. Wang, Q. Sun, P. Jena, Functionalized graphitic carbon nitride for efficient energy storage. J. Phys. Chem. C. **117**, 6055-6059 (2013). https://doi.org/10.1021/jp311972f.

[166] S.J. Mahdizadeh, E.K. Goharshadi, Hydrogen storage on graphitic carbon nitride and its palladium nanocomposites: A multiscale computational approach. Int. J. Hydrog. Energy. **44**, 8325-8340 (2019). https://doi.org/10.1016/j.ijhydene.2019.02.071.

[167] A. Akbari, J. Hashemi, E. Mosconi, F. De Angelis, M. Hakala, First principles modelling of perovskite solar cells based on TiO_2 and Al_2O_3: Stability and interfacial electronic structure. J. Mater. Chem. A. **5**, 2339-2345 (2017). https://doi.org/10.1039/C6TA08874K.

[168] E. Mosconi, E. Ronca, F. De Angelis, First-principles investigation of the TiO_2/organohalide perovskites interface: The role of interfacial chlorine. J. Phys. Chem. Lett. **5**, 2619-2625 (2014). https://doi.org/10.1021/jz501127k.

[169] M. Ramezanpour, S. Leung, K. Delgado-Magnero, B. Bashe, J. Thewalt, D. Tieleman, Computational and experimental approaches for investigating

nanoparticle-based drug delivery systems. Biochim. Biophys. Acta - Biomembr. **1858**, 1688-1709 (2016). https://doi.org/10.1016/j.bbamem.2016.02.028.

[170] S. Zuluaga, L.-H. Liu, N. Shafiq, S.M. Rupich, J.-F. Veyan, Y.J. Chabal, T. Thonhauser, Structural band-gap tuning in g-C_3N_4. Phys. Chem. Chem. . **17**, 957-962 (2015). https://doi.org/10.1039/C4CP05164E

[171] J. Wang, D. Hao, J. Ye, N. Umezawa, Determination of crystal structure of graphitic carbon nitride: Ab initio evolutionary search and experimental validation. Chem. Mater. **29**, 2694-2707 (2017). https://doi.org/10.1021/acs.chemmater.6b02969.

[172] Z. Ma, E. Wang, M.E. Jarvid, P. Henriksson, O. Inganäs, F. Zhang, M.R. Andersson, Synthesis and characterization of benzodithiophene–isoindigo polymers for solar cells. J. Mater. Chem. A. **22**, 2306-2314 (2012). https://doi.org/10.1039/C1JM14940G

[173] S. Tretiak, K. Igumenshchev, V. Chernyak, Exciton sizes of conducting polymers predicted by time-dependent density functional theory. Phys. Rev. B. **71**, 033201 (2005). https://doi.org/10.1103/PhysRevB.71.033201.

[174] L. Zhang, Q. Zhang, H. Ren, H. Yan, J. Zhang, H. Zhang, J. Gu, Calculation of band gap in long alkyl-substituted heterocyclic-thiophene-conjugated polymers with electron donor–acceptor fragment. Sol. Energy Mater Sol. Cells. **92**, 581-587 (2008). https://doi.org/10.1016/j.solmat.2007.12.010.

[175] J. You, L. Dou, K. Yoshimura, T. Kato, K. Ohya, T. Moriarty, K. Emery, C.-C. Chen, J. Gao, G. Li, A polymer tandem solar cell with 10.6% power conversion efficiency. Nat. Commun. **4**, 1446 (2013). https://doi.org/10.1038/ncomms2411.

[176] D. Hashemi, X. Ma, R. Ansari, J. Kim, J. Kieffer, Design principles for the energy level tuning in donor/acceptor conjugated polymers. Phys. Chem. Chem. Phys. **21**, 789-799 (2018). https://doi.org/10.1039/C8CP03341B

[177] U. Salzner, P. Pickup, R. Poirier, J. Lagowski, Accurate method for obtaining band gaps in conducting polymers using a DFT/hybrid approach. J. Phys. Chem. A. **102**, 2572-2578 (1998). https://doi.org/10.1021/jp971652l.

[178] H. Zhou, L. Yang, A.C. Stuart, S.C. Price, S. Liu, W. You, Development of fluorinated benzothiadiazole as a structural unit for a polymer solar cell of 7% efficiency. Angew. Chem. Int. Ed. **50**, 2995-2998 (2011). https://doi.org/10.1002/ange.201005451.

[179] J. Zhu, Y. Wei, W. Chen, Z. Zhao, A. Thomas, Graphitic carbon nitride as a metal-free catalyst for NO decomposition. ChemComm. **46**, 6965-6967 (2010). https://doi.org/10.1039/C0CC01432J

[180] G. Algara-Siller, N. Severin, S.Y. Chong, T. Björkman, R.G. Palgrave, A. Laybourn, M. Antonietti, Y.Z. Khimyak, A.V. Krasheninnikov, J.P. Rabe, Triazine-based graphitic carbon nitride: A two-dimensional semiconductor. Angew. Chem. **126**, 7580-7585 (2014). https://doi.org/10.1002/anie.201402191.

[181] B. Zhu, L. Zhang, D. Xu, B. Cheng, J. Yu, Adsorption investigation of CO_2 on g-C_3N_4 surface by DFT calculation. J. CO_2 Util. **21**, 327-335 (2017). https://doi.org/10.1016/j.jcou.2017.07.021.

[182] J. Cui, S. Liang, X. Wang, J. Zhang, First principle modeling of oxygen-doped monolayer graphitic carbon nitride. Mater. Chem. Phys. . **161**, 194-200 (2015). https://doi.org/10.1016/j.matchemphys.2015.05.036.

[183] H.Z. Wu, Q.H. Zhong, S. Bandaru, J. Liu, W.M. Lau, L.L. Li, Z. Wang, Exploring the formation and electronic structure properties of the g-C_3N_4 nanoribbon with density functional theory. J. Condens. Matter Phys. **30**, 155303 (2018). https://doi.org/10.1088/1361-648X/aab2ca.

[184] T. Tyborski, C. Merschjann, S. Orthmann, F. Yang, M.C. Lux-Steiner, T. Schedel-Niedrig, Tunable optical transition in polymeric carbon nitrides synthesized via bulk thermal condensation. J. Condens. Matter Phys. **24**, 162201 (2012). https://doi.org/10.1088/0953-8984/24/16/162201.

[185] Z. Teng, H. Lv, C. Wang, H. Xue, H. Pang, G. Wang, Bandgap engineering of ultrathin graphene-like carbon nitride nanosheets with controllable oxygenous functionalization. Carbon. **113**, 63-75 (2017). https://doi.org/10.1016/j.carbon.2016.11.030.

[186] Y. Zhao, F. Zhao, X. Wang, C. Xu, Z. Zhang, G. Shi, L. Qu, Graphitic carbon nitride nanoribbons: graphene-assisted formation and synergic function for highly efficient hydrogen evolution. Angew. Chem. Int. Ed. **53**, 13934-9 (2014). 10.1002/anie.201409080.

[187] W. Wang, J.C. Yu, Z. Shen, D.K.L. Chan, T. Gu, g-C_3N_4 quantum dots: Direct synthesis, upconversion properties and photocatalytic application. ChemComm. **50**, 10148-10150 (2014). https://doi.org/10.1039/C4CC02543A.

[188] J. Zhang, Y. Chen, X. Wang, Two-dimensional covalent carbon nitride nanosheets: Synthesis, functionalization, and applications. Energy Environ. Sci. **8**, 3092-3108 (2015). https://doi.org/10.1039/C5EE01895A

[189] G. Gao, Y. Jiao, E.R. Waclawik, A. Du, Single atom (Pd/Pt) supported on graphitic carbon nitride as an efficient photocatalyst for visible-light reduction of carbon dioxide. J. Am. Chem. Soc. . **138**, 6292-6297 (2016). https://doi.org/10.1021/jacs.6b02692.

[190] X. Li, P. Cui, W. Zhong, J. Li, X. Wang, Z. Wang, J. Jiang, Graphitic carbon nitride supported single-atom catalysts for efficient oxygen evolution reaction. ChemComm. **52**, 13233-13236 (2016). https://doi.org/10.1039/C6CC07049C.

[191] L. Zhang, W. Zhao, W. Zhang, J. Chen, Z. Hu, gt-C_3N_4 coordinated single atom as an efficient electrocatalyst for nitrogen reduction reaction. Nano Res. **12**, 1181-1186 (2019). https://doi.org/10.1007/s12274-019-2378-8.

[192] S.S. Zade, M. Bendikov, From oligomers to polymer: Convergence in the HOMO−LUMO gaps of conjugated oligomers. Org. Lett. **8**, 5243-5246 (2006). https://doi.org/10.1021/ol062030y.

[193] C. Kurgat, J. Kibet, P. Cheplogoi, Molecular modeling of major tobacco alkaloids in mainstream cigarette smoke. Chem. Cent. J. **10**, 43 (2016). https://doi.org/10.1186/s13065-016-0189-5.

[194] T. Hussain, M. Hankel, D.J. Searles, Computational evaluation of lithium-functionalized carbon nitride (g-C_6N_8) monolayer as an efficient hydrogen storage

material. J. Phys. Chem. C. **120**, 25180-25188 (2016). https://doi.org/10.1021/acs.jpcc.6b06182.

[195] L.M. Ombaka, P.G. Ndungu, J. Kibet, V.O. Nyamori, The effect of pyridinic-and pyrrolic-nitrogen in nitrogen-doped carbon nanotubes used as support for Pd-catalyzed nitroarene reduction: an experimental and theoretical study. J. Mater. Sci. **52**, 10751-10765 (2017). https://doi.org/10.1007/s10853-017-1241-0.

[196] H. Li, Z. Zhang, Y. Liu, W. Cen, X. Luo, Functional group effects on the HOMO-LUMO gap of g-C_3N_4. Nanomaterials **8**,589 (2018). https://doi.org/10.3390/nano8080589.

[197] T. Mestiri, S. Ghomrasni, D. Khlaifia, K. Alimi, DFT modeling of new (2, 2'-(1, 4-phenylene) bis (quinazolin-4 (3H)-imine)(PBQI) based copolymers for photovoltaic applications. Physica B Condens. Matter. **544**, 1-9 (2018). https://doi.org/10.1016/j.physb.2018.05.009.

[198] D. Guillaumont, S. Nakamura, Calculation of the absorption wavelength of dyes using time-dependent density-functional theory (TD-DFT). Dyes Pigm. **46**, 85-92 (2000). https://doi.org/10.1016/S0143-7208(00)00030-9.

[199] C. Adamo, D. Jacquemin, The calculations of excited-state properties with time-dependent density functional theory. Chem. Soc. Rev. **42**, 845-856 (2013). https://doi.org/10.1039/C2CS35394F

[200] S.K. Haram, A. Kshirsagar, Y.D. Gujarathi, P.P. Ingole, O.A. Nene, G.B. Markad, S.P. Nanavati, Quantum confinement in CdTe quantum dots: Investigation through cyclic voltammetry supported by density functional theory (DFT). J. Phys. Chem. C. **115**, 6243-6249 (2011). https://doi.org/10.1021/jp111463f.

[201] J.H. Snook, L.A. Samuelson, J. Kumar, Y.-G. Kim, J.E. Whitten, Ultraviolet photoelectron spectroscopy of nanocrystalline TiO_2 films sensitized with (2,2′-bipyridyl) ruthenium (II) dyes for photovoltaic applications. Org. Electron. **6**, 55-64 (2005). https://doi.org/10.1016/j.orgel.2005.03.001.

[202] A. Agarwal, A.K. Hundal, J.-Y. Chen, A. Bilic, W. Xiang, S.V. Bhosale, J.-L. Li, R.A. Evans, A. Gupta, Direct connection of an amine to oligothiophene to generate push-pull chromophores for organic photovoltaic applications. Dyes Pigm. **162**, 315-323 (2019). https://doi.org/10.1016/j.dyepig.2018.10.048.

CHAPTER THREE

A theoretical study of the optoelectronic properties of heptazine-based graphitic carbon nitride

Nicholas Rono,[a] Abdelkrim E. Merad,[b] Joshua K. Kibet,[c] Bice S. Martincigh[a] and Vincent O. Nyamori[a]*

[a]School of Chemistry and Physics, University of KwaZulu-Natal, Westville Campus, Private Bag X54001, Durban, 4000, South Africa

[b]Solid State Physics Team, Theoretical Physics Laboratory, Faculty of Sciences, A Belkaid University, Box 119, 13000, Tlemcen, Algeria

[c]Chemistry Department, Egerton University, Njoro Campus, P.O. Box 536-20115, Egerton, Kenya

*Corresponding author: E-mail: Nyamori@ukzn.ac.za, Tel: +27312608256

Abstract

Graphitic carbon nitride (g-C_3N_4) is a promising metal-free semiconductor that has attracted extensive attention because of its attractive attributes, such as tunable band gap, as well as chemical and thermal stabilities. Despite these attractive features, other properties, particularly optoelectronic properties, have not been exhaustively explored. Herein, we report the optoelectronic properties of a three-dimensional (3D) heptazine-based graphitic carbon nitride (g-C_3N_4). First-principle density functional theory (DFT) calculations were performed with a full-potential linearised augmented plane wave coupled to the local orbital (FP-LAPW+lo) method as implemented in the Wien2k computational code. The generalised gradient approximation (GGA) of the Perdew-Burke-Ernzerhof (PBE) and the modified Becke-Johnson (mBJ) exchange-correlation potentials were used, and the results were compared. Optoelectronic properties, such as electronic band gap, dielectric constant (real and imaginary parts), reflectivity, optical conductivity, refractive index, and the absorption coefficient of heptazine-based g-C_3N_4, were investigated both in the perpendicular (⊥) and parallel (//) directions of the incident photons. In essence, the model exhibited anisotropic behaviour since the examined properties were generally insensitive to the // incident photons compared to the ⊥ incident

photons. The mBJ calculations gave a band gap energy of 2.87 eV, which was in good agreement with experimental values, although the GGA-PBE method underestimated this energy (1.16 eV). The real part of the dielectric constant exhibited a maximum at 3.0 for the GGA-PBE and 4.04 eV for the mBJ potential for the ⊥ incident photons, whereas the // incident photons were inconsequential. The GGA-PBE and mBJ methods determined that the reflectivity of the material was about 52.5%, implying that it is slightly opaque. Additionally, the optical conductivity for the ⊥ incident photons started in the visible light region, i.e. at 1.8 and 2.75 eV for the GGA-PBE and mBJ methods, respectively, whereas for the // incident photons, the conductivity started at higher energies. Generally, the anisotropic behaviour was more pronounced when the mBJ potential was used. These findings are important for the advancement of optoelectronic applications of heptazine-based g-C_3N_4.

Keywords: Anisotropy; dielectric constant; optoelectronic; Wien2k; heptazine; graphitic carbon nitride

3.1 Introduction

Graphitic carbon nitride (g-C_3N_4) is a promising metal-free semiconductor that has attracted immense attention due to its attractive attributes, such as tuneable band gap, and thermal and chemical stabilities [1]. The g-C_3N_4 material has been applied in several fields, such as tribological engineering [2], photocatalysis [3], sensors [4, 5], and photovoltaics [6, 7]. Bulk g-C_3N_4 is easily synthesised from thermal polycondensation of nitrogen-containing precursors, such as melamine, urea, and dicyandiamide [8, 9], via cheap and scalable processes. In essence, g-C_3N_4 has two basic tectonic units, i.e. s-triazine- and heptazine (tri-s-triazine)-based g-C_3N_4 [10]. Previously, it has been established from density functional theory (DFT) that heptazine-based g-C_3N_4 is more stable than triazine-based g-C_3N_4 [11]. For this reason, heptazine-based g-C_3N_4 has been extensively studied both theoretically and experimentally by many researchers [12, 13]. Moreover, in photocatalysis, semiconductors with an indirect bandgap have been reported to be more effective than those with a direct band gap [14]; therefore, the heptazine form of g-C_3N_4 with an indirect band gap has become very useful in the field of optoelectronics compared with triazine-based g-C_3N_4 with a direct bandgap [15].

Studies have revealed that three-dimensional (3D) heptazine-based g-C_3N_4 can have several possible configurations, including graphite-like planar or buckled A-A and A-B stacking configurations [16, 17]. Tyborski et al. [17] combined computational and experimental X-ray diffraction (XRD) strategies to explore the proper structure of 3D g-C_3N_4. They concluded that g-C_3N_4 could comprise buckled or flat A-A polymeric g-C_3N_4. With regard to the most stable configuration of heptazine-based g-C_3N_4 nanosheets, which is a two-dimensional (2D) material, Gao et al. [18] theoretically showed that corrugated forms of heptazine-based g-C_3N_4 are energetically and dynamically more stable than planar nanosheets due to the repulsion caused by neighbouring nitrogen atoms [11]. However, the main challenge is confirming which configuration of bulk g-C_3N_4 with a 3D structure is more favourable energetically because, experimentally, it is difficult to obtain pure g-C_3N_4 with a high degree of crystallinity [19, 20]. Nevertheless, two noticeable peaks at $2\theta = 13.04°$ and 27.25° are observed in the diffractograms from experimental XRD results [1, 21]. The former peak is attributed to in-plane repeated units with an interplane distance of approximately 6.788 Å, and the latter corresponds to the interlayer spacing of 3.25 Å between g-C_3N_4 layers

[9], therefore, providing insights that heptazine units are more predominant in the synthesised products. Computationally, heptazine-based g-C_3N_4 has a hexagonal crystal structure with a lattice parameter "a" = 7.13 Å, which is close to an in-plane distance of the repeated units of 6.788 Å as deduced from experiments [19].

Even though heptazine-based g-C_3N_4 has been extensively studied both experimentally and computationally, most of its optical and electronic properties have not been fully elucidated, thus impeding its application in optoelectronic and nanotechnologies. Therefore, it is of interest to further investigate its optoelectronic properties to advance its applications in potential fields, such as photovoltaics, where it is scarcely applied. In this study, the electronic and optical properties of heptazine-based g-C_3N_4 have been computationally investigated with the Wien2K computational platform. Calculated properties, such as the dielectric constant (real and imaginary parts), absorption, refractive index, reflectivity, and conductivity, have been derived from two computational approaches: the generalised gradient approximation (GGA) of the Perdew-Burke-Ernzerhof (PBE) exchange-correlation functional and the modified Becke-Johnson (mBJ) exchange-correlation potential, and compared.

3.2 Computational details

In this study, the electronic and optical properties of heptazine-based graphitic carbon nitride were investigated. Our first-principle calculations based on density functional theory (DFT), were carried out using the full potential linearised augmented plane wave plus the local orbital (FP-LAPW+lo) method [22], as implemented in the Wien2K package [23]. In this approach, the Khon-Sham (KS) equations are solved within two regions, i.e. sphere muffin tin (the region around the nucleus) and interstitial spaces (regions between the muffin tins) [24]. The structural properties were calculated with the generalised gradient approximation (GGA) of the Perdew-Burke-Ernzerhof (PBE) exchange-correlation functional (GGA-PBE) [25]. The electronic and optical properties were calculated using both the generalised gradient approximation (GGA-PBE) and the Tran–Blaha modified Becke-Johnson (mBJ) exchange-correlation potential [26, 27], and the results were compared.

Tran and Blaha introduced the latter potential, which is known to reproduce experimental band gap values for a range of semiconductors and insulators [24, 25]; thus, it was used in this work.

The mBJ exchange-correlation potential, $v_{x,\sigma}^{mBJ}(r)$, is expressed, according to Equation 1:

$$v_{x,\sigma}^{mBJ}(r) = c\, v_{x,\sigma}^{BR}(r) + (3c-2)\frac{1}{\pi}\sqrt{\frac{5}{6}}\sqrt{\frac{t_\sigma(r)}{\rho_\sigma(r)}} \qquad \text{Equation (1)}$$

where $v_{x,\sigma}^{BR}$ is the Becke Roussel potential [27, 28], r is the coordinate vector of the reference electron, $t_\sigma(r)$ is the kinetic-energy density, $\rho_\sigma(r)$ is the electron density, and the c parameter is given by Equation 2:

$$c = \alpha + \beta\left(\frac{1}{V_{cell}}\int_{cell}\frac{|\nabla\rho(r)|}{\rho(r)}d^3(r)\right)^{1/2} \qquad \text{Equation (2)}$$

where $\alpha = -0.012$, $\beta = 1.023$ bohr$^{1/2}$ (as was obtained from fitting experimental results) [29], and V_{cell} is the unit cell volume.

On the other hand, the GGA-PBE exchange-correlation potential reproduces the band gap of metallic materials well but underestimates by half the band gap of semiconductors from the experimental values [29].

The three-dimensional (3D) structure of heptazine-based g-C_3N_4 with the A-A stacking configuration of Tyborski et al. [16] was considered in this work. The reasons for the choice of this model are as follows: (i) heptazine-based g-C_3N_4 has been identified as the most abundant product during the actual synthesis process and not triazine-based forms of g-C_3N_4 [30], (ii) theoretically, it has been well-established that heptazine units are energetically favoured over triazine building units of g-C_3N_4, and (iii) the XRD data of the A-A stacking configuration matches with our previous experimental two theta values [20]. In our experiment, two prominent peaks at about $2\theta = 13.2°$ and 27.4°, corresponding to the (001) and (002) crystal planes, respectively, were observed. In essence, the strong peak at $2\theta = 13.2°$ with interlayer spacing d = 0.337 nm was attributed to the in-plane structural stacking motif of heptazine tectonic units (tri-s-triazine units), and the latter at 27.4° with an interplanar spacing d = 0.167 nm was attributed to the interlayer stacking of aromatic rings in the sample. Therefore, this model was of

significance in our present study. The supercell model under investigation was of dimension 1 × 1 × 1, with 14 atoms (6 C and 8 N), space group No. 174 p-6, and the lattice parameters: a = b = 6.950 Å, c = 3.2750 Å, α = β = 90°, γ = 120°. In order to obtain a relaxed structure, energy minimisation optimisation based on c/a was carried out. The Monkhorst-pack k-points mesh with 8 × 8 × 15 divisions of reciprocal lattice vectors in the irreducible part of the Brillouin zone was used [31]. All structural optimisation calculations were carried out on this mesh and were sufficient to give an accurate minimum energy, which was less than 10^{-4} Rydberg (Ry), where the self-consistent field cycles (SCF) calculation was considered to have converged. The Fourier charge density G_{max} was set to be 12 (Ry), while the atomic radii of the muffin-tin spheres (RMT) were 1.29 and 1.23 a.u. for nitrogen (N) and carbon (C) atoms, respectively. The optical and electronic properties were performed on a denser mesh with 5000 K-points. Ideally, a denser k-point mesh is crucial because it reduces the parasitic effects in calculating various properties of the material [31-33].

The optical properties of the heptazine system were deduced using a complex dielectric function $\varepsilon(\omega) = \varepsilon_1(\omega) + \varepsilon_2(\omega)$, where $\varepsilon_1(\omega)$ is the real part, and $\varepsilon_2(\omega)$ is the imaginary part. The real part, $\varepsilon_1(\omega)$, as determined by the Kramers–Kronig transformation, links the two parts of the dielectric constant [29, 34]. The imaginary part is directly associated with the material's electronic band structure and is derived from the momentum matrix elements between the occupied and unoccupied electronic levels [35]. The dielectric constant can be used to determine more optical properties such as the absorption coefficient α(ω), the refractive index n(ω), and the reflectivity R(ω). The related equation for each property is expressed in Equations 3-5.

The optical absorption can be calculated from the formula [36]:

$$\alpha(\omega) = \sqrt{2\omega}\left[\sqrt{\varepsilon_1^2(\omega) + \varepsilon_2^2(\omega)} \quad + \varepsilon_1(\omega)\right]^{1/2} \qquad \text{Equation (3)}$$

while the refractive index of the material can be calculated from Equation 4,

$$n(\omega) = \left[\frac{\varepsilon_1(\omega)}{2} \quad + \frac{\sqrt{\varepsilon_1^2(\omega)+\varepsilon_2^2(\omega)}}{2}\right]^{1/2} \qquad \text{Equation (4)}$$

and the reflectivity can be calculated directly from Fresnel's formula (Equation 5) [36]:

$$R(\omega) = \left|\frac{1-n(\omega)}{1+n(\omega)}\right|^2 \quad \text{Equation (5)}$$

3.3 Results and discussion

In this section, the structural optimisation and the optical properties of the model are presented.

3.3.1 Structural optimisation and geometrical properties

In order to obtain a relaxed structure with optimised lattice parameters, the optimisation process was carried out via the energy minimisation approach. In principle, the total energy as a function of c/a of the unit cell was calculated. Figure 3.1 shows a graph of energy as a function of the c/a ratio; the lowest point of the curve represents the lowest energy (ground state energy) (-18137.064 eV) and is related to optimised lattice parameters. The optimised crystal lattice parameters were found to be: a = b = 7.062 Å, c = 3.172 Å, α = β = 90°, γ = 120°. These constants are consistent with the experimental values obtained from XRD measurements [9, 20] and other theoretical reported values [17]. The different viewpoints of the A-A stacking configuration of heptazine-based g-C_3N_4 are shown in Figure 3.2.

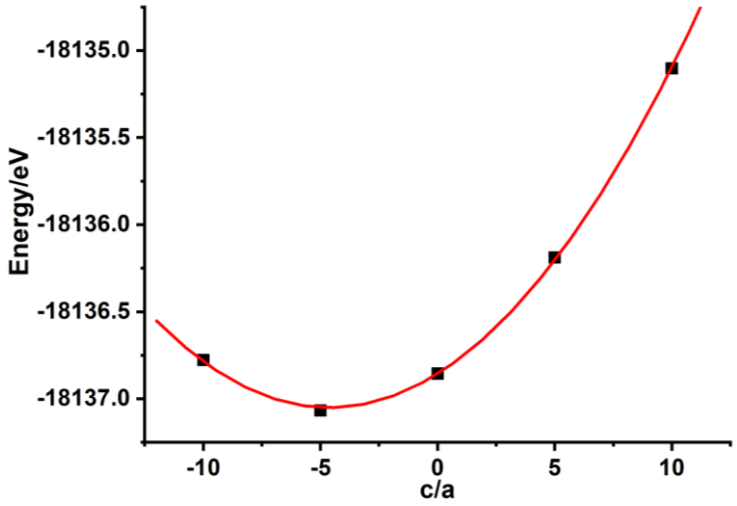

Figure 3.1: The energy versus c/a ratio optimisation curve for a heptazine-based g-C_3N_4 supercell

(a)

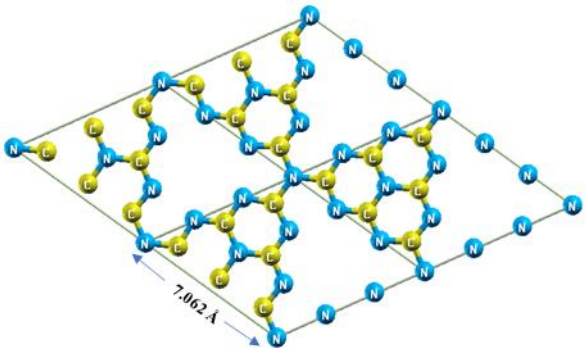

(b)

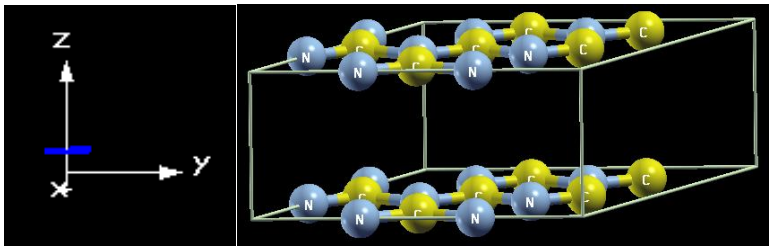

Figure 3.2: Geometrical structures of optimised bulk heptazine-based g-C_3N_4 supercells: (a) 2 × 2 top view, and (b) 1 × 1 × 1 side view

3.3.2 Electronic properties

The electronic band structure of heptazine-based g-C_3N_4 was calculated using both the GGA-PBE and mBJ exchange-correlation potentials, and the corresponding band structures are presented in Figure 3.3. The dotted line represents the Fermi level, whose energy is 0 eV. Essentially, the symmetry points were obtained directly from the WIEN2K graphical diagrams and used in labelling the plotted graphs. The band gap energy was found to be 1.16 eV from the GGA-PBE calculation (Figure 3.3a) and 2.87 eV for the mBJ exchange-correlation potential (Figure 3.3b). As pointed out earlier, the classical GGA-PBE method underestimates the band gap in semiconductor materials, and as confirmed here, the band gap obtained using GGA-PBE is lower than the one obtained from the newly developed mBJ exchange-correlation potential. More precisely, the band gap energy (2.87 eV) for heptazine-based g-C_3N_4 calculated using the mBJ potential agrees with the experimental band gap value of about 2.7 eV [20].

Furthermore, Figures 3.3a and 3.3b show that both the valence band maximum (VBM) and the conduction band minimum (CBM) are not located at the same point, indicating that the semiconductor material has an indirect band gap, and phonon absorption effect can be experienced. Thus, radiative recombination of holes and electrons is minimal [37].

Reducing the recombination of photogenerated charges is a significant property in photocatalysis and solar cell applications where a low recombination of photogenerated charges is required.

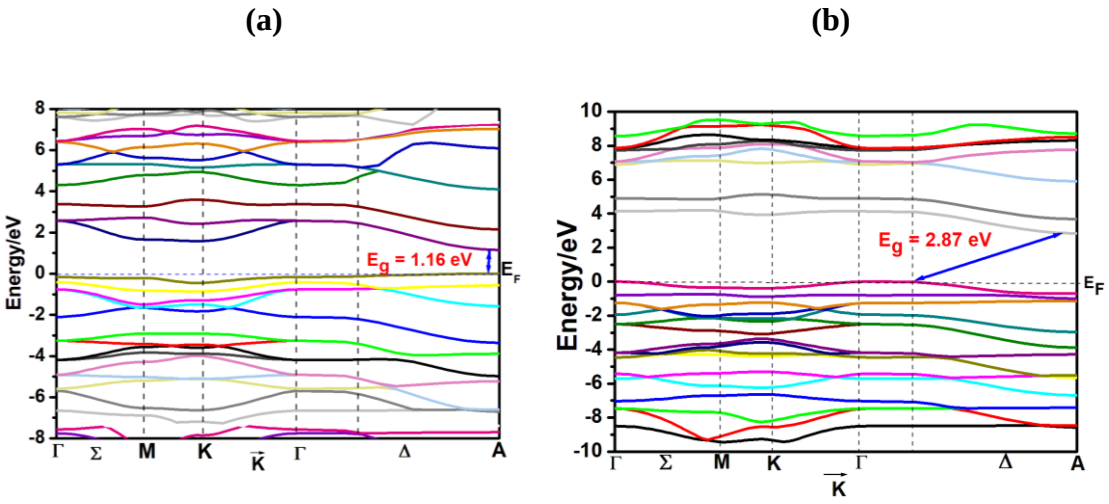

Figure 3.3: The band structure of heptazine-based g-C_3N_4 calculated from (a) GGA-PBE and (b) mBJ exchange-correlation potentials. The dotted line at 0 eV shows the Fermi level

The density of state (DOS) calculation was carried out to establish the elemental orbital contribution in forming the valence and conduction bands. Figure 3.4 shows the total and partial density of states of bulk heptazine-based-g-C_3N_4 calculated using the GGA-PBE (Figure 3.4a) and mBJ approaches (Figure 3.4b). It can be observed that the band gap obtained from GGA-PBE was small and is related to the band structure of the material (see Figure 3.3a). In the case of the mBJ calculation (Figure 3.4b), the band gap is directly related to the band structure (see Figure 3.3b); and was relatively more significant than the GGA band gap. Typically, from the two (mBJ and GGA-PBE) approaches, the conduction band minimum (CBM) is primarily dominated by nitrogen than the valence band minimum (VBM), but this phenomenon is more pronounced with the GGA-PBE approach.

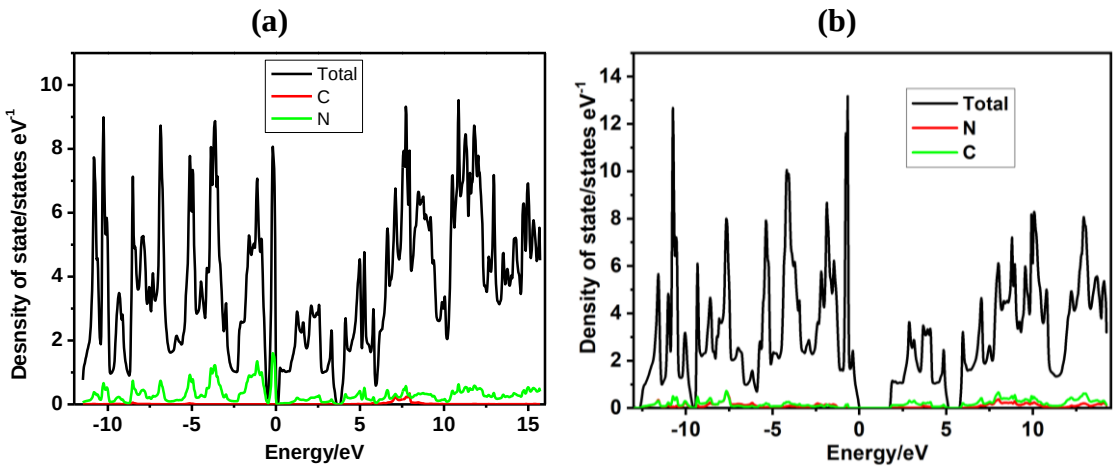

Figure 3.4: Total and partial density of states of bulk heptazine-based g-C_3N_4 calculated by using the (a) GGA-PBE and (b) mBJ potentials

In order to study in detail the contribution of each atom on the DOS, the partial DOS of nitrogen and carbon obtained from the mBJ potential was evaluated (Figure 3.5). Clearly, for carbon and nitrogen atoms, it can be seen that the CBM and VBM are mainly dominated by C-2p states (Figure 3.5a) and the N-2p states (Figure 3.5b), respectively, and these results are in agreement with findings reported elsewhere [38]. In essence, there is hybridisation between C-2p and N-2p states, which results in the formation of covalent bonds [39].

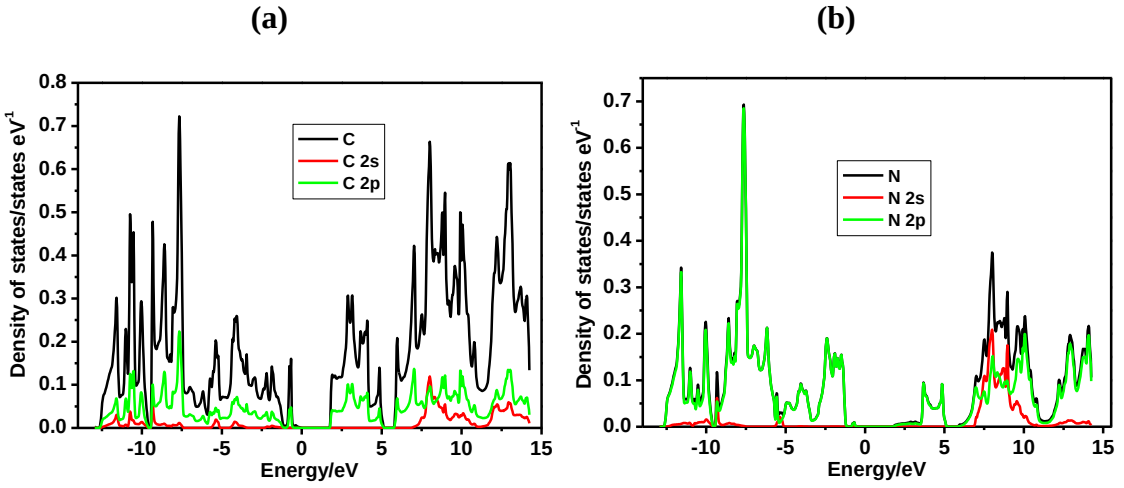

Figure 3.5: Partial DOS of bulk heptazine-based g-C_3N_4 calculated from the mBJ potential for (a) carbon and (b) nitrogen atoms

Figure 3.6 shows the electron charge density contour for heptazine-based g-C_3N_4. As can be seen, the nitrogen atoms attract valence electrons relative to the carbon atoms because

nitrogen (3.04) is more electronegative than carbon (2.55). At the centre of the ring, there is a region with a low charge density.

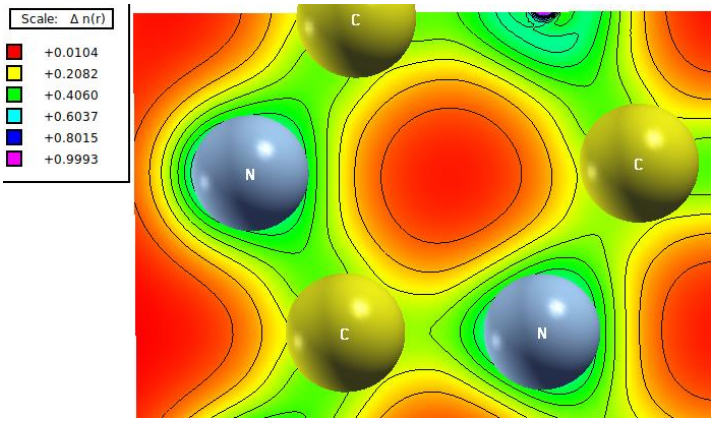

Figure 3.6: The 2D electron charge density for heptazine-based-g-C_3N_4

3.3.3 Optical properties

Graphitic carbon nitride is a material with good optoelectronic properties. In this section, the optical properties, such as dielectric constant, reflectivity, refractive index, and optical conductivity, are investigated using the GGA-PBE and mBJ computational approaches, and the results are compared. Heptazine-based g-C_3N_4 with hexagonal symmetry is expected to exhibit anisotropic behaviour in all the calculated linear optical properties. Therefore, the optical properties were calculated in both perpendicular (⊥), denoted as xx-direction, and parallel (//), denoted as zz-direction, directions of the electromagnetic radiation incident with respect to the z-axis.

3.3.3.1 The real and the imaginary dielectric function

Figure 3.7 shows the real and imaginary parts of the dielectric constant both from GGA-PBE and mBJ calculations. In general, the two approximations (GGA-PBE and mBJ) exhibited similar results for both real and imaginary parts of the dielectric constant in both the ⊥ (xx-direction) and // (zz-direction) directions of the incident photons. However, some distinct characteristics exist in the Figures (cf. Figures 3.7). The static permittivity ε_o ($\varepsilon_1 = h\upsilon = 0$) for GGA-PBE was 6.87 (Figure 3.7a), and when mBJ was used, this value reduced to 4.27 (Figure 3.7c) for the ⊥ incident photon. The maximum dielectric constant was observed at 3.0 eV ($\varepsilon_1 = 15.65$) for GGA-PBE (Figure 3.7a), while for the mBJ calculation, it was observed at 4.04 eV ($\varepsilon_1 = 11.17$) (Figure 3.7c) for the ⊥

incident photons. Figure 3.7 shows that the real and imaginary dielectric representation did not respond to the // incident photons. The imaginary part of the dielectric constant (Figure 3.7b and Figure 3.7d) for both approximations shows that the dielectric constant was significant for only ⊥ incident light photons with energy below 12.0 eV. It is important to note that the maximum dielectric function peak for GGA-PBE at 3.18 eV (ε_2 = 15.55) (Figure 3.7b) was greater than that of mBJ at 4.29 eV (ε_2 = 13.47) (Figure 3.7d) in the ⊥ photon incident direction. The anisotropic behaviour in the real and imaginary parts of the dielectric constant disappears at about 12.0 eV in both approximations. The plasmon energies (i.e. energy at which the real part of the dielectric function becomes negative) [40] for heptazine-based g-C_3N_4 were observed at 3.48 and 4.73 eV for GGA-PBE (Figure 3.7a), whereas for mBJ, they were observed at 4.55 and 5.5 eV (Figure 3.7c).

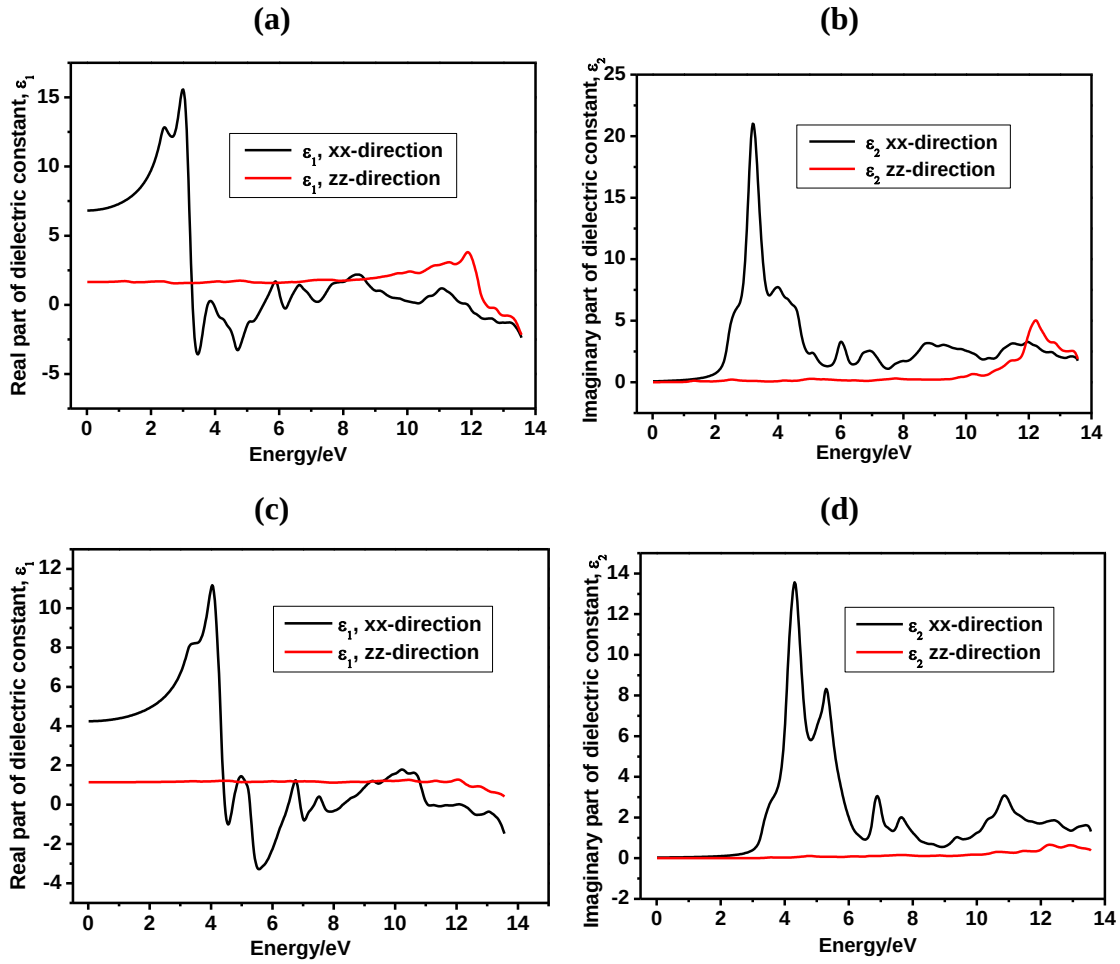

Figure 3.7: The variation of the real and imaginary parts of the dielectric function of heptazine-based g-C_3N_4 as a function of the energy of the incident electromagnetic radiations, calculated from the (a) and (b) GGA-PBE approximation and (c) and (d) mBJ

approach. The letters xx and zz stand for the ⊥ and // directions of the incident electromagnetic radiation, respectively

3.3.3.2 The optical absorption

Figure 3.8 shows the absorption phenomena of our model heptazine-based g-C_3N_4 supercell computed by using Equation 3. Figure 3.8a (GGA-PBE calculation) shows that the material's absorption behaviour begins at 2.05 eV (visible region) and 4.75 eV (ultraviolet region) for the ⊥ and // incident electromagnetic radiation, correspondingly. The maximum absorption was observed at 3.34 eV, which is in good agreement with experimental observation data [21], and 4.72 eV ($\alpha = 101.01 \times 10^4$ cm^{-1}) for the ⊥ incident photons, while for the // incident photons the maximum was observed at 12.36 eV ($\alpha = 180 \times 10^4$ cm^{-1}). The anisotropic behaviour of the model with regard to absorption vanished at 4.75 eV.

Similarly, from mBJ calculations (Figure 3.8b), the absorption behaviour began at 6.5 eV and dropped off at 12.94 eV. It can be seen from the mBJ calculations (Figure 3.8b) that the absorption of our model started at about 2.10 eV and 6.5 eV with regard to the ⊥ and the // incident electromagnetic radiation, respectively. Additionally, at higher energy (above 6.5 eV), the disappearance of the anisotropic behaviour was more pronounced with the GGA-PBE method than with the mBJ method. In general, our model was insensitive to the // incident electromagnetic radiation up to about 5 eV in both GGA-PBE and mBJ approximations. Moreover, it can be concluded that the material absorbs electromagnetic radiation of more than 2 eV, implying that the absorption is mainly in the visible range towards the UV region. Since the material can absorb photons from within a wide range of the electromagnetic spectrum, it can be used for photocatalytic and photovoltaic applications.

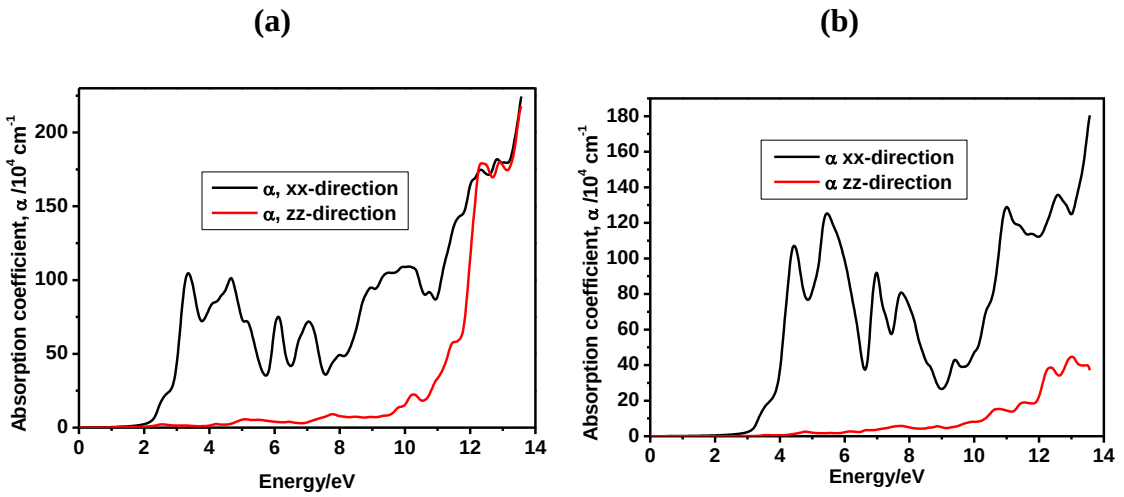

Figure 3.8: Variation of the optical absorption of heptazine-based g-C_3N_4 as a function of the energy of the incident electromagnetic radiation, calculated from (a) the GGA-PBE approximation and (b) the mBJ approach. The letters xx and zz stand for the ⊥ and // directions of the incident electromagnetic radiation, respectively

3.3.3.3. The refractive index

Figure 3.9 reports the refractive index (n) of heptazine-based g-C_3N_4 obtained from the GGA-PBE and mBJ approximations computed using Equation 4. Figure 3.9a (GGA-PBE) shows that the static refractive indices (refractive index at zero energy) for ⊥ and the // direction polarization were 2.61 and 1.29, respectively. Furthermore, the maximum refractive index observed at 3.05 eV (visible region) was 4.24 for the ⊥ photon incidence direction and 2.08 at 12.01 eV (n = 2.08) for the // polarisation direction. The anisotropic behaviour of the material vanished at 12.0 eV.

Similarly, from Figure 3.9b (mBJ graph), the static refractive indices for both the ⊥ and the // photon incidence were 2.06 and 1.05, respectively. The maximum refractive index observed at 4.11 eV was 3.51 for the ⊥ direction, and at 12.10 eV, the refractive index was 1.16 for the // direction. At higher photon energy above 12.0 eV, the anisotropic character disappeared but was more pronounced when the GGA-PBE potential was used. The maximum refractive indices along the // direction were observed at 11.93 eV (n = 2.09) for GGA-PBE (Figure 3.9a) and 12.10 eV (n = 1.16) for mBJ (Figure 3.9b). The refractive index character of the material was insensitive to the // incident photons. In general, a higher refractive index is undesirable because more of the incident light will be

reflected away, thus, limiting power conversion efficiency (PCE) in a photovoltaic solar cell.

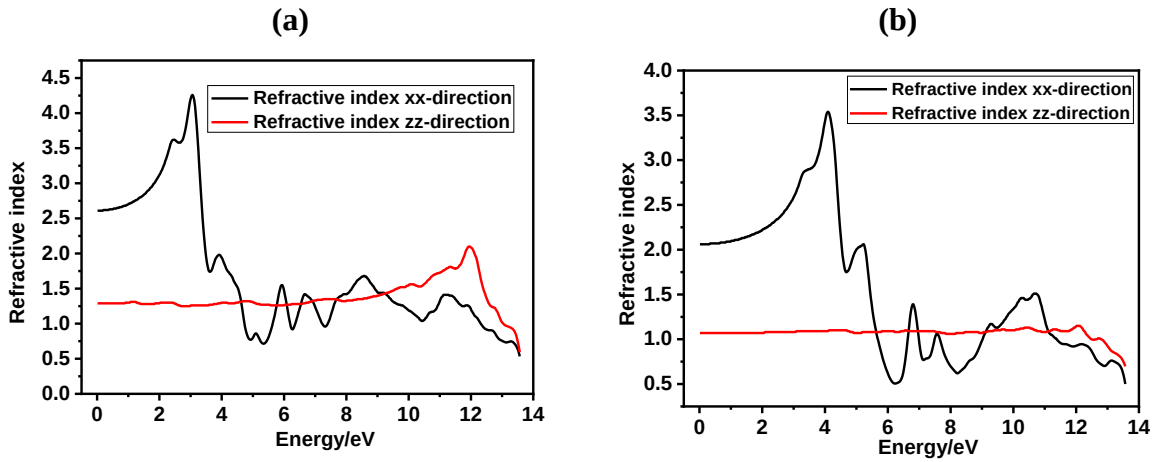

Figure 3.9: Variation of the refractive index of heptazine-based g-C_3N_4 as a function of the energy of the incident electromagnetic radiation as calculated from (a) the GGA-PBE approximation and (b) the mBJ approach. The letters xx and zz stand for the ⊥ and // directions of the incident electromagnetic radiation, respectively

3.3.3.4 The reflectivity of the material

Figure 3.10 depicts the reflectivity of the material calculated from the GGA-PBE and mBJ exchange-correlation potentials from zero to 13.5 eV by using Equation 5. From Figure 3.10a (GGA-PBE), a maximum reflectivity for the ⊥ incident electromagnetic radiation was observed at 3.34 eV (visible region), with a percentage reflectivity of about 52.5%, followed by another peak at 4.75 eV with a percentage reflectivity of 51.44%. A minimum reflectivity was observed at 7.55 eV of about 5%, implying that the material is transparent. The material exhibited anisotropic reflectivity behaviour at low energy values, but this phenomenon vanished above 10.15 eV. Notably, reflectivity along the zz-direction (the // incident photons) was apparently very low at photon energies below 10.15 eV but increased at higher energies. This could be ascribed to the fact that in our 3D model, there was no matter along the z lattice parameter to interact with light; thus, it can be equated to a 2-dimensional model.

Figure 3.10b shows the reflectivity calculated using the mBJ approximation method. The maximum reflectivity of heptazine-based g-C_3N_4 at 5.93 eV was about 52.5%, followed by a peak at 4.41eV approximated at 44% for the ⊥ incident electromagnetic radiation,

indicating that the material is slightly opaque as opposed to the results obtained from GGA. Therefore, the material exhibited more pronounced anisotropic characteristics. The slight transparency of about 52% of the material is crucial since it will allow radiant energy to penetrate the inner layers of an optical device, especially the active layer of a solar cell. The anisotropic behaviour vanished beyond 12.3 eV, and the reflectivity for the // polarization was about 2% above this energy value. This indicates that the reflectivity was insensitive to the // incident photon direction. The two intense peaks at 3.34 and 4.70 eV observed (for GGA-PBE and the // incident photons) match the plasmon energies of heptazine-based g-C_3N_4, where the real part of the dielectric function is negative for energies of 3.48 and 4.73 eV, respectively (Figure 3.7a). Similarly, from the mBJ graph, the two intense peaks at 4.41 and 5.938 eV for the xx-incident radiation in the reflectivity graphs match very well with the material's plasmon energies of 4.55 and 5.5 eV in the real part of the dielectric constant for the ⊥ electromagnetic incident radiation.

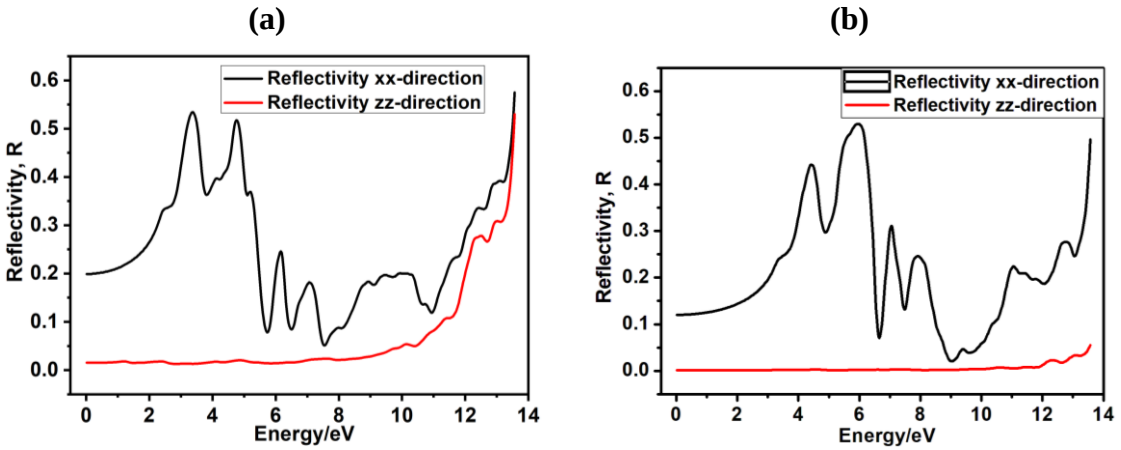

Figure 3.10: Variation of reflectivity of heptazine-based g-C_3N_4 as a function of the energy of the incident electromagnetic radiation, calculated from (a) the GGA-PBE approximation and (b) the mBJ approach. The letters xx and zz stand for the ⊥ and // directions of the incident electromagnetic radiation, respectively

3.3.3.5 The optical conductivity

Since g-C_3N_4 is a promising semiconductor, it is informative to investigate its optical conductivity. Basically, graphitic carbon nitride is a semiconductor with a band gap of about 2.7 eV [20]. Figure 3.11 illustrates the variation of the optical conductivity as a function of the incident photons' energy in the ⊥ and the // directions, calculated from the

two approximations. As can be observed, the optical conductivities determined from the two methods (GGA-PBE and mBJ) did not start at zero energy, indicating that the material is a semiconductor with relatively high conductivity and is not gapless as for graphene. For GGA-PBE (Figure 11a), the conductivity starts at about 1.8 eV, and the maximum conductivity was achieved at 3.22 eV ($\sigma = 8.18 \times 10^{15}\ \Omega^{-1}\ cm^{-1}$) (visible region) with respect to the ⊥ incident photons, while for the // incident photons, the conductivity starts at the higher energy of about 9.4 eV. The maximum conductivity was 12.218 eV ($\sigma = 7.34 \times 10^{15}\ \Omega^{-1}\ cm^{-1}$) for the // direction of incidence of the electromagnetic radiation, which is inconsequential in an optical device.

In the case of the mBJ calculations (Figure 3.11b), the conductivity started at 2.745 eV (visible region) and achieved a maximum at 4.309 eV ($\sigma = 7.07 \times 10^{15}\ \Omega^{-1}\ cm^{-1}$) (ultraviolet region) when the electromagnetic radiation was incident in the ⊥ direction. On the other hand, for the // direction, the conductivity starts at a higher energy of about 10.10 eV but at a very low intensity. The anisotropic behaviour of the material is more pronounced when the mBJ approximation is used than the GGA-PBE approximation. Notably, the optical conductivity for the material for both methods did not start at zero because there exists an energy gap in the material. However, it exhibited a maximum in the visible light region; thus, better electron transfer characteristics are displayed in this region.

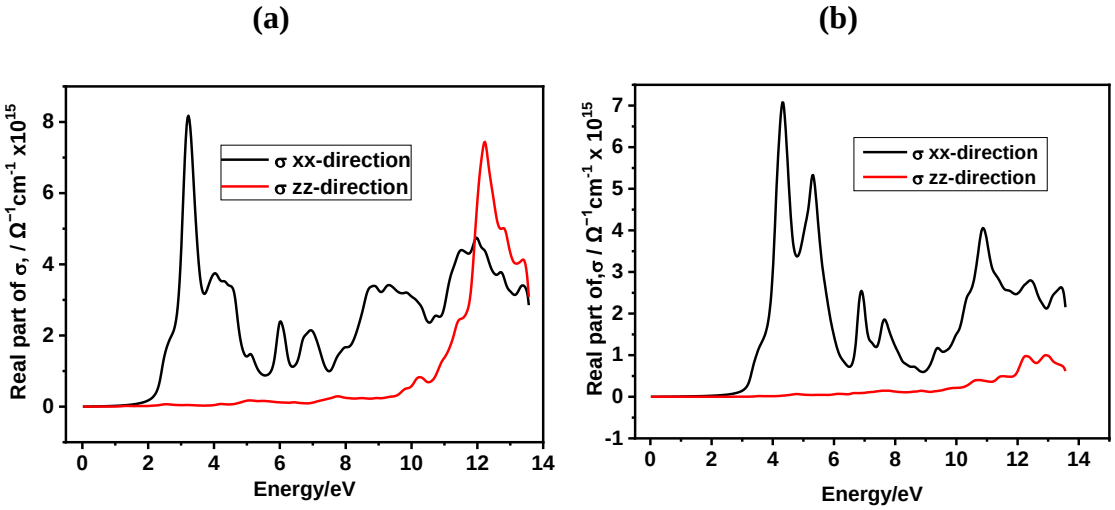

Figure 3.11: Variation of the optical conductivity of heptazine-based g-C_3N_4 as a function of the energy of the incident electromagnetic radiations calculated from (a) the

GGA-PBE approximation and (b) the mBJ approach. The letters xx and zz stand for the ⊥ and // directions of the incident electromagnetic radiation, respectively

In summary, the calculated static dielectric constant, refractive index, and reflectivity for the ⊥ direction of the incident electromagnetic radiation are shown in Table 3.1. Also, the band gap energies are presented.

Table 3.1: The calculated optoelectronic properties of heptazine-based g-C_3N_4 from the GGA and mBJ methods obtained for the ⊥ direction of the incident photons

Method	Band gap/eV	Static dielectric constant, $\varepsilon_1(0)$	Static refractive index, n(0)	Static reflectivity index, R(0)	Plasmon energies/eV
GGA-PBE	1.16	6.87	2.61	0.19	3.48, 4.73
mBJ	2.87	4.27	2.06	0.12	4.55, 5.5

3.4 Conclusions

The optoelectronic properties of heptazine-based g-C_3N_4 have been studied using first-principle calculations with a full-potential linearised augmented plane wave plus the local orbital (FP-LAPW+lo) method. The GGA-PBE and mBJ exchange-correlation potentials were employed in the calculations. Our results showed that the mBJ approach produced a band gap energy of 2.87 eV, which is in good agreement with experimental data [20], while the GGA-PBE method underestimates the band gap (1.16 eV) of the material. The material's anisotropic behaviour was exhibited at energies lower than 12.0 eV for the calculated optical properties for both GGA-PBE and mBJ approaches. Nevertheless, the optical dielectric constants, absorption, conductivity, reflectivity, and refraction were more pronounced for the ⊥ direction of incident photons than along the // direction of incidence for both the GGA-PBE and mBJ approximations. The static permittivity was 6.87 eV for the GGA-PBE approach but decreased to 4.27 eV when the mBJ method was employed for the ⊥ direction of the incident photons.

Similarly, the static refractive index was 2.61 eV (for GGA-PBE) and decreased to 2.06 eV (for mBJ) for the ⊥ direction of incident photons. Moreover, the reflectivity results from both approaches generally show that the material is moderately transparent, i.e.,

about 52% of light is reflected back in the ⊥ direction of incident radiation. The reflectivity due to the // direction of the incident electromagnetic radiation was inconsequential. The optical absorption begins in the visible light region of the electromagnetic spectrum, as observed in the two numerical methods (GGA-PBE and mBJ), indicating that the material has a response in the visible region (for the ⊥ photon direction). For the incident photons, the maximum conductivities were 3.22 (GGA-PBE) and 4.39 eV (mBJ). The results of this work provide more insights into the optoelectronic properties of heptazine-based g-C_3N_4 and indicate suitable avenues for applying the material in photovoltaic, photocatalytic, and nanoelectronics technologies.

Acknowledgements

NR is appreciative of the ACADEMY project N° 2017-3052/001-001 for an academic mobility scholarship to the University of Tlemcen, Algeria, where this work was carried out at the Theoretical Physics Laboratory (TPL). AEM is indebted to DGRSDT and MHESR of Algeria for financial support under the PRFU research project N° B00L02UN130120180011. The authors are grateful for the financial support provided by the National Research Foundation (NRF) of South Africa, under grant numbers 103979 and 109580; the University of KwaZulu-Natal (UKZN), the UKZN Nanotechnology Platform, and the Eskom Tertiary Education Support Programme (TESP).

References

[1] T. Fidan, M. Torabfam, Q. Saleem, C. Wang, H. Kurt, M. Yüce, J. Tang, M.K. Bayazit, Functionalized graphitic carbon nitrides for environmental and sensing applications. Adv. Energy Sustain.Res. **2**, 2000073 (2021). https://doi.org/10.1002/aesr.202000073.

[2] C. Duan, D. Yuan, Z. Yang, S. Li, L. Tao, Q. Wang, T. Wang, High wear-resistant performance of thermosetting polyimide reinforced by graphitic carbon nitride (g-C_3N_4) under high temperature. Compos. Part A Appl. Sci. Manuf. . **113**, 200-208 (2018). https://doi.org/10.1016/j.compositesa.2018.07.008.

[3] R. Zhang, X. Zhang, S. Liu, J. Tong, F. Kong, N. Sun, X. Han, Y. Zhang, Enhanced photocatalytic activity and optical response mechanism of porous graphitic carbon nitride (g-C_3N_4) nanosheets. Mater. Res. Bull. **140**, 111263 (2021). https://doi.org/10.1016/j.materresbull.2021.111263.

[4] L. Mao, X. Xue, X. Xu, W. Wen, M.-M. Chen, X. Zhang, S. Wang, Heterostructured CuO-g-C_3N_4 nanocomposites as a highly efficient photocathode for

photoelectrochemical aflatoxin B1 sensing. Sens. Actuators B Chem. **329**, 129146 (2021). https://doi.org/10.1016/j.snb.2020.129146.

[5] Jigyasa, H. Singh, J.K. Rajput, Graphitic carbon nitride nanosheets (g-C_3N_4 NS) as dual responsive template for fluorescent sensing as well as degradation of food colorants. Food Chem. **343**, 128451 (2021). https://doi.org/10.1016/j.foodchem.2020.128451.

[6] X. Chen, Q. Liu, Q. Wu, P. Du, J. Zhu, S. Dai, S. Yang, Incorporating graphitic carbon nitride (g-C_3N_4) quantum dots into bulk-heterojunction polymer solar cells leads to efficiency enhancement. Adv. Funct. Mater. **26**, 1719-1728 (2016). https://doi.org/10.1002/adfm.201505321.

[7] J. Chen, H. Dong, L. Zhang, J. Li, F. Jia, B. Jiao, J. Xu, X. Hou, J. Liu, Z. Wu, Graphitic carbon nitride doped SnO_2 enabling efficient perovskite solar cells with PCEs exceeding 22%. J. Mater. Chem. A. **8**, 2644-2653 (2020). https://doi.org/10.1039/C9TA11344D.

[8] T.K.A. Nguyen, T.-T. Pham, H. Nguyen-Phu, E.W. Shin, The effect of graphitic carbon nitride precursors on the photocatalytic dye degradation of water-dispersible graphitic carbon nitride photocatalysts. Appl. Surf. Sci. **537**, 148027 (2021). https://doi.org/10.1016/j.apsusc.2020.148027.

[9] E. Alwin, W. Nowicki, R. Wojcieszak, M. Zieliński, M. Pietrowski, Elucidating the structure of the graphitic carbon nitride nanomaterials via X-ray photoelectron spectroscopy and X-ray powder diffraction techniques. Dalton Trans. **49**, 12805-12813 (2020). https://doi.org/10.1039/D0DT02325F.

[10] M. Ghashghaee, Z. Azizi, M. Ghambarian, Conductivity tuning of charged triazine and heptazine graphitic carbon nitride (g-C_3N_4) quantum dots via nonmetal (B, O, S, P) doping: DFT calculations. J. Phys. Chem. Solids. **141**, 109422 (2020). https://doi.org/10.1016/j.jpcs.2020.109422.

[11] J. Gracia, P. Kroll, Corrugated layered heptazine-based carbon nitride: the lowest energy modifications of g-C_3N_4 ground state. J. Mater. Chem. **19**, 3013-3019 (2009). https://doi.org/10.1039/B821568E.

[12] B. Zhu, L. Zhang, B. Cheng, J. Yu, First-principle calculation study of tri-s-triazine-based g-C_3N_4: A review. Appl. Catal. B: Environ. **224**, 983-999 (2018). https://doi.org/10.1016/j.apcatb.2017.11.025.

[13] X. Li, J. Xiong, X. Gao, J. Huang, Z. Feng, Z. Chen, Y. Zhu, Recent advances in 3D g-C_3N_4 composite photocatalysts for photocatalytic water splitting, degradation of pollutants and CO_2 reduction. J. Alloys Compd. **802**, 196-209 (2019). https://doi.org/10.1016/j.jallcom.2019.06.185.

[14] J. Zhang, P. Zhou, J. Liu, J. Yu, New understanding of the difference of photocatalytic activity among anatase, rutile and brookite TiO_2. Phys. Chem. Chem. **16**, 20382-20386 (2014). https://doi.org/10.1039/C4CP02201G.

[15] H. Zhang, X. Zuo, H. Tang, G. Li, Z. Zhou, Origin of photoactivity in graphitic carbon nitride and strategies for enhancement of photocatalytic efficiency: Insights from first-principles computations. Phys. Chem. Chem. **17**, 6280-6288 (2015). https://doi.org/10.1039/C4CP05288A.

[16] F. Fina, S.K. Callear, G.M. Carins, J.T.S. Irvine, Structural investigation of graphitic carbon nitride via XRD and neutron diffraction. Chem. Mater. **27**, 2612-2618 (2015). https://doi.org/10.1021/acs.chemmater.5b00411.

[17] T. Tyborski, C. Merschjann, S. Orthmann, F. Yang, M.C. Lux-Steiner, T. Schedel-Niedrig, Crystal structure of polymeric carbon nitride and the determination of its process-temperature-induced modifications. J. Condens. Matter Phys. **25**, 395402 (2013). https://doi.org/10.1088/0953-8984/25/39/395402.

[18] Q. Gao, X. Zhuang, S. Hu, Z. Hu, Corrugation matters: Structure models of single layer heptazine-based graphitic carbon nitride from first-principles studies. J. Phys. Chem. C. **124**, 4644-4651 (2020). https://doi.org/10.1021/acs.jpcc.0c00411.

[19] J. Wang, D. Hao, J. Ye, N. Umezawa, Determination of crystal structure of graphitic carbon nitride: Ab Initio evolutionary search and experimental validation. Chem. Mater. **29**, 2694-2707 (2017). https://doi.org/10.1021/acs.chemmater.6b02969.

[20] N. Rono, J.K. Kibet, B.S. Martincigh, V.O. Nyamori, A comparative study between thermal etching and liquid exfoliation of bulk graphitic carbon nitride to nanosheets for the photocatalytic degradation of a model environmental pollutant, rhodamine B. J. Mater. Sci.: Mater. Electron. **32**, 687-706 (2021). https://doi.org/10.1007/s10854-020-04849-8.

[21] S. Fujita, H. Habuchi, S. Takagi, H. Takikawa, Optical properties of graphitic carbon nitride films prepared by evaporation. Diam. Relat. Mater. **65**, 83-86 (2016). https://doi.org/10.1016/j.diamond.2016.02.008.

[22] P. Blaha, K. Schwarz, F. Tran, R. Laskowski, G.K. Madsen, L.D. Marks, WIEN2k: An APW+ lo program for calculating the properties of solids. J. Chem. Phys. **152**, 074101 (2020). https://doi.org/10.1063/1.5143061.

[23] P. Blaha, K. Schwarz, G.K. Madsen, D. Kvasnicka, Luitz, WIEN2K: An augmented plane wave+ local orbitals program for calculating crystal properties. J. Chem. Phys., (2001). https://doi.org/10.1063/1.5143061.

[24] O.K. Andersen, Linear methods in band theory. Phys. Rev. B **12**, 3060-3083 (1975). https://doi.org/10.1103/PhysRevB.12.3060.

[25] J.P. Perdew, K. Burke, M. Ernzerhof, Generalized gradient approximation made simple. Phys. Rev. Lett. **77**, 3865-3868 (1996). https://doi.org/10.1103/PhysRevLett.77.3865.

[26] F. Tran, P. Blaha, Accurate band gaps of semiconductors and insulators with a semilocal exchange-correlation potential. Phys. Rev. Lett. **102**, 226401 (2009). https://doi.org/10.1103/PhysRevLett.102.226401.

[27] A.D. Becke, E.R. Johnson, A simple effective potential for exchange. J. Chem. Phys. **124**, 221101 (2006). https://doi.org/10.1063/1.2213970.

[28] A.D. Becke, M.R. Roussel, Exchange holes in inhomogeneous systems: A coordinate-space model. Phys. Rev. A. **39**, 3761-3767 (1989). https://doi.org/10.1103/PhysRevA.39.3761.

[29] H.I. Berrezoug, A.E. Merad, M. Aillerie, A. Zerga, First principle study of structural stability, electronic structure and optical properties of Ga doped ZnO with different

concentrations. Mater. Res. Express. **4**, 035901 (2017). https://doi.org/10.1088/2053-1591/aa6076.

[30] T. Narkbuakaew, P. Sujaridworakun, Synthesis of tri-s-triazine based g-C_3N_4 photocatalyst for cationic rhodamine B degradation under visible light. Top. Catal. **63**, 1086-1096 (2020). https://doi.org/10.1007/s11244-020-01375-z.

[31] H.J. Monkhorst, J.D. Pack, Special points for Brillouin-zone integrations. Phys. Rev. B. **13**, 5188 (1976). https://doi.org/10.1103/PhysRevB.13.5188.

[32] P. Blaha, K. Schwarz, F. Tran, R. Laskowski, G.K.H. Madsen, L.D. Marks, WIEN2k: An APW+lo program for calculating the properties of solids. J. Chem. Phys. **152**, 074101 (2020). https://doi.org/10.1063/1.5143061.

[33] F. Ghalouci, L. Ghalouci, M. Safer, F. Belkheir, F. Djali. Study of the stoichiometry effect on the interaction of hexagonal HgSe with electromagnetic radiation. in *ICREEC 2019*. 2020. Singapore: Springer Singapore. https://doi.org/10.1007/978-981-15-5444-5_34.

[34] H.I. Berrezoug, A.E. Merad, A. Zerga, Z.S. Hassoun, Simulation and Modeling of Structural Stability, Electronic Structure and Optical Properties of ZnO. Energy Procedia. **74**, 1517-1524 (2015). https://doi.org/10.1016/j.egypro.2015.07.711.

[35] Y.G. Zhang, G.B. Zhang, Y.X. Wang, First-principles study of the electronic structure and optical properties of Ce-doped ZnO. J. Appl. Phys. **109**, 063510 (2011). https://doi.org/10.1063/1.3561436.

[36] M.L. Ould Ne, A. Abbassi, A.G. El Hachimi, A. Benyoussef, H. Ez-Zahraouy, A. El Kenz, Electronic optical, properties and widening band gap of graphene with Ge doping. Opt. Quantum Electron. **49**, 218 (2017). https://doi.org/10.1007/s11082-017-1024-5.

[37] J. Kangsabanik, M.K. Svendsen, A. Taghizadeh, A. Crovetto, K.S. Thygesen, Indirect band gap semiconductors for thin-film photovoltaics: High-throughput calculation of phonon-assisted absorption. J. Am. Chem. Soc. **144**, 19872-19883 (2022). https://doi.org/10.1021/jacs.2c07567.

[38] J. Liu, Effect of phosphorus doping on electronic structure and photocatalytic performance of g-C_3N_4: Insights from hybrid density functional calculation. J. Alloys Compd. **672**, 271-276 (2016). https://doi.org/10.1016/j.jallcom.2016.02.094.

[39] D. Ghosh, G. Periyasamy, S.K. Pati, Transition metal embedded two-dimensional C_3N_4–graphene nanocomposite: A multifunctional material. J. Phys. Chem. C. **118**, 15487-15494 (2014). https://doi.org/10.1021/jp503367v.

[40] M. Houmad, H. Zaari, A. Benyoussef, A. El Kenz, H. Ez-Zahraouy, Optical conductivity enhancement and band gap opening with silicon doped graphene. Carbon. **94**, 1021-1027 (2015). https://doi.org/10.1016/j.carbon.2015.07.033.

CHAPTER FOUR

J Mater Sci: Mater Electron

A comparative study between thermal etching and liquid exfoliation of bulk graphitic carbon nitride to nanosheets for the photocatalytic degradation of a model environmental pollutant, Rhodamine B

Nicholas Rono[1], Joshua K. Kibet[2,*], Bice S. Martincigh[1], and Vincent O. Nyamori[1]

[1] School of Chemistry and Physics, University of KwaZulu-Natal, Westville Campus, Private Bag X54001, Durban 4000, South Africa
[2] Department of Chemistry, Egerton University, Njoro, P.O. Box 536-20115, Egerton, Kenya

Received: 12 June 2020
Accepted: 5 November 2020

ABSTRACT

Graphitic carbon nitride (g-C_3N_4) is a metal-free photoactive material which has gained significant interest in the advancement of electronic and optical devices because of its attractive optoelectronic properties, such as tuneable band gap, and suitable chemical and thermal stability. This material has been utilized in a range of applications including photocatalysis, biosensing and photovoltaics. Bulk g-C_3N_4 (B-g-C_3N_4) has been shown to exhibit low photo-efficiency due to its low specific surface area and high rate of recombination of photo-generated charges; thus, there is a need for its exfoliation. Also, the type of exfoliation method utilized is crucial. In this work, two exfoliation methods of g-C_3N_4, namely, liquid and thermal etching exfoliation, were investigated. Both methods successfully produced g-C_3N_4 nanosheets, but those synthesized by liquid exfoliation (CNNS-LE) had a much larger specific surface area of 41.68 $m^2\ g^{-1}$ than those prepared by thermal exfoliation (CNNS-TE) (14.76 $m^2\ g^{-1}$) or the parent B-g-C_3N_4 (3.22 $m^2\ g^{-1}$). The band gap energies of B-g-C_3N_4, CNNS-LE and CNNS-TE were found to be 2.71, 2.59 and 1.89 eV, respectively. Graphitic carbon nitride nanosheets prepared by thermal exfoliation (CNNS-TE) were found to be 2.5 times more effective in the photo-degradation of Rhodamine B than B-g-C_3N_4 and CNNS-LE. This is attributed to the positive effect of their porous structure, which gives rise to effective separation of charges, and their extended light absorption properties. Thus, thermal treatment introduces structural defects and electronic modifications that result in an enhanced photocatalytic performance. Consequently, thermal etching is effective in exfoliation of B-g-C_3N_4 to form a material suitable for photo-driven applications.

Address correspondence to E-mail: jkibet@egerton.ac.ke

https://doi.org/10.1007/s10854-020-04849-8
Published online: 21 November 2020

CHAPTER FOUR

A comparative study between thermal etching and liquid exfoliation of bulk graphitic carbon nitride to nanosheets for solar harvesting applications

Nicholas Rono[a], Joshua K. Kibet*[b], Bice S. Martincigh[a] and Vincent O. Nyamori[a]

[a]School of Chemistry and Physics, University of KwaZulu-Natal, Westville Campus, Private Bag X54001, Durban, 4000, South Africa

[b]Department of Chemistry, Egerton University, Njoro, P.O. Box 536-20115, Egerton, Kenya

*Corresponding author: E-mail: jkibet@egerton.ac.ke Tel: +254 720 352 437

Abstract

Graphitic carbon nitride (g-C_3N_4) is a metal-free photoactive material which has gained significant interest in the advancement of electronic and optical devices because of its attractive optoelectronic properties, such as tuneable band gap, and suitable chemical and thermal stability. This material has been utilised in a range of applications including photocatalysis, biosensing and photovoltaics. Bulk g-C_3N_4 (B-g-C_3N_4) has been shown to exhibit low photo-efficiency due to its low specific surface area, and high rate of recombination of photogenerated charges, thus, there is a need for its exfoliation. Also, the type of exfoliation method utilised is crucial. In this work, two exfoliation methods of g-C_3N_4, namely, liquid and thermal etching exfoliation, were investigated. Both methods successfully produced g-C_3N_4 nanosheets but those synthesised by liquid exfoliation (CNNS-LE) had a much larger specific surface area of 41.68 $m^2\ g^{-1}$ than those prepared by thermal exfoliation (CNNS-TE) (14.76 $m^2\ g^{-1}$) or the parent B-g-C_3N_4 (3.22 $m^2\ g^{-1}$). The band gap energies of B-g-C_3N_4, CNNS-LE and CNNS-TE were found to be 2.71, 2.59 and 1.89 eV, respectively. Graphitic carbon nitride nanosheets prepared by thermal exfoliation (CNNS-TE) were found to be 2.5 times more effective in the photo-degradation of Rhodamine B than B-g-C_3N_4 and CNNS-LE. This is attributed to the positive effect of their porous structure, which gives rise to effective separation of charges and its extended light absorption properties. Thus, thermal treatment introduces structural

defects and electronic modifications that result in an enhanced photocatalytic performance. Consequently, thermal etching is effective in exfoliation of B-g-C_3N_4 to form a material suitable for photo-driven applications.

Keywords: Exfoliation; graphic carbon nitride; band gap; photocatalysis

4.1 Introduction

Rapid population growth as well as industrial development has led to increased pollution that has lately approached a crisis point [1-3]. In particular, detrimental by-products from fossil fuel combustion as a source of energy [4-6] have been released into the natural environment precipitating pollution, global warming and climate change, and threatening the lives of flora and fauna [7, 8]. To mitigate against these effects, solar energy has been identified as one of the most versatile methods to degrade environmental pollutants in various environments such as water systems, soil, and wetlands [9]. Solar energy is currently used in various fields such as photovoltaics [10], photo-sensors [11] and photocatalysis [12, 13].

The quest to photo-degrade pollutants in the environment has encouraged researchers to constantly search for materials which are environmentally benign and efficient in solar energy conversion [14]. In the recent past, silicon [15], cadmium telluride [16], and copper [17] and indium-based [18, 19] semiconductors have been the most promising light-absorbing materials, but they have various drawbacks; for instance, titanium dioxide [20], silicon [21] and indium [22] are relatively expensive, while cadmium is a well-established cancer-initiating agent [23]. For this reason, graphitic carbon nitride (g-C_3N_4) has emerged as a better alternative because of its attractive optoelectronic properties, suitable chemical and conducive thermal stability, lower cost and toxicity [24], and its favourable metal-free nature. Moreover, it has a reasonable tuneable band gap [25, 26].

Typical bulk g-C_3N_4 suffers from a low surface area and a high rate of recombination of photogenerated charges [26], thus, it is limited in solar energy harvesting and conversion. To enhance the performance of bulk g-C_3N_4, various modifications, such as doping [27, 28] and exfoliation [29] to nanosheets, have been carried out. The exfoliated nanosheets have been shown to exhibit better performance in a range of applications such as the photocatalytic degradation of pollutants [30], hydrogen production [25, 31] and biosensing [32]. This is because the nanosheets possess a high surface area, high quantum confinement, and short diffusion distances for the photogenerated charges, and these properties improve the efficiency relative to bulk g-C_3N_4 [33].

Currently, many attempts have been made to exfoliate bulk g-C_3N_4 to nanosheets with extended light absorption properties [34]. The methods that have been explored include

liquid exfoliation [35, 36], chemical blowing [37] and thermal etching [38]. Hatamie et al. [39] used liquid exfoliation to prepare nanosheets that showed a fluorescence peak at 456 nm under an excitation wavelength of 355 nm. These nanosheets were efficient for fluorosensing metronidazole in biological and drug samples. Recently, Iqbal et al. [40] showed that bulk g-C_3N_4 can be thermally exfoliated, because the bonds between the layers can be broken by heat, and the consequential nanosheets exhibit better performance in photocatalytic hydrogen production as a result of their extended light absorption edges. Papailias et al. [41] exfoliated bulk g-C_3N_4 via both thermal etching and chemical exfoliation with the aid of concentrated sulphuric acid. Interestingly, both methods resulted in nanosheets that were more effective in the photocatalytic degradation of NO_x. However, nanosheets from chemical exfoliation showed superior photocatalytic activity than those from thermal etching. This was ascribed to the favourable band gap edges, increased superoxide anion radical formation and the larger pore volume of the chemically exfoliated material.

The introduction of defects in materials has gained significant attention in various fields such as photocatalysis and electrocatalysis, among others, because defects have been shown to modulate the properties of materials [26]. For instance, in g-C_3N_4 photocatalyst material, defects such as cyano groups and nitrogen vacancies have been introduced by heating the precursors at elevated controlled-temperatures [42, 43]. This allows for the modulation of the material's electronic band structure, surface area, and charge carrier transfer mechanism [43]. Recently, Liang et al. [42] through thermal treatment of bulk g-C_3N_4, prepared g-C_3N_4 nanosheets with nitrogen defects (vacancies) and high quantum confinement. These two features synergistically resulted in a more superior photocatalyst (almost 6 times better) during hydrogen production than the bulk. This was due to increased surface area, better charge transport and better light absorption caused by conduction band position adjustment. Moreover, Liang et al. [44] established that an increase in nitrogen vacancies (defects) could influence the negative shift of the conduction band potential, and this results in enhanced light absorption. In order to modify the morphology and benefit from the surface area enhancement, Shi et al. [45] employed a hard templating strategy to prepare g-C_3N_4 nanosheets. In this case, spherically shaped silica was used as a hard template, and spherical porous g-C_3N_4 was formed. The resulting photocatalysts exhibited high surface area and stability and, thus,

enhanced photo-hydrogen generation and photo-degradation of rhodamine B (RhB) when compared with bulk g-C_3N_4.

Herein, we have compared two exfoliation methods of bulk g-C_3N_4; namely, thermal etching and liquid exfoliation. The resulting nanosheets, with reference to the bulk, were characterized and evaluated in the photocatalytic degradation of a model pollutant, RhB. Rhodamine B is a synthetic organic dye which can form reactive oxygen species (ROS) when exposed to light. The reactive oxygen species have detrimental health effects, for instance, Safitri et al. [46] demonstrated that, with increasing doses, RhB can trigger lipid peroxidation and cervical epithelial cell proliferation in mice. Thus, as a potential carcinogenic compound, RhB concentrations in the environment and food substances should be monitored and removed [47].

From the characteristics observed, the advantages and disadvantages of each exfoliation method were deduced. The two methods are facile, environmentally friendly and do not utilize any corrosive acids. Nonetheless, the thermal exfoliation synthetic route resulted in a better photocatalyst. This is attributed to the formation of nanosheets with a porous structure which enhanced cross-plane diffusion, and thereby promoted charge and mass transfer; the narrower band gap energy which facilitated better light absorption; the lower rate of recombination of photogenerated charges and the smaller electron transfer resistance that enhanced electrical transfer. These properties are considered critical in the application of nanomaterials in energy and optical devices. To the best of our knowledge, this is the first time these two exfoliation techniques have been compared in detail with regards to their characteristics and the performance of the resulting materials.

4.2 Experimental

4.2.1 Chemicals

Melamine (CAS No. 108-78-1), carbon paste (CAS No. 7440-05-3) and potassium ferricyanide (CAS No. 13746-66-2) were purchased from Merck (South Africa), while Rhodamine B (CAS No. 81-88-9), potassium chloride (99%) (CAS No. 7447-40-7), isopropyl alcohol (IPA) (CAS No. 67-63-0), tri-ethanolamine (TEOA) (CAS No. 102-71-6) and p-benzoquinone (BQ) (CAS No. 106-51-4) were purchased from Sigma Aldrich (South Africa). All the chemicals were of analytical grade and were used without further

treatment. Deionised water was collected from a Millipore Milli-Q Elix 5 UV water purification system with a resistivity of 18.2 MΩ cm at 20 °C.

4.2.2 Synthesis of bulk graphitic carbon nitride

Bulk g-C_3N_4 was synthesised by conventional polycondensation of melamine [48]. Typically, melamine (10 g) was placed in an open ceramic crucible and transferred to a muffle furnace. The contents of the crucible were heated, at a rate of 5 °C min^{-1}, from room temperature to 550 °C and maintained at that temperature for 4 hours. Thereafter, the crucible, and its contents, was allowed to cool to room temperature. Bulk g-C_3N_4 was formed as a yellow solid and labelled B-g-C_3N_4. The as-formed B-g-C_3N_4 was ground with a pestle and mortar and kept in sample vials.

4.2.3 Liquid exfoliation of B-g-C_3N_4

B-g-C_3N_4 was exfoliated to nanosheets via liquid exfoliation as previously reported with some modifications [39, 49-53]. The as-prepared B-g-C_3N_4 (100 mg) was dispersed in 100 mL of deionised water in a round-bottomed flask and sonicated for 14 hours in a 400 W ultrasonic water bath operating at 50 °C. The resulting dispersion was centrifuged at 6000 rpm for 15 minutes to remove unexfoliated B-g-C_3N_4. A colloidal solution was obtained which contained g-C_3N_4 nanosheets. This solution was dried at 80 °C in an oven and the product (g-C_3N_4 nanosheets) was denoted CNNS-LE.

4.2.4 Thermal exfoliation of B-g-C_3N_4

A thermal etching method was employed as described by Iqbal et al. [40] but with some adjustments of the conditions. As-prepared B-g-C_3N_4 (0.5 g) was placed in quartz glass boat. The boat was placed inside a quartz tube in a tube furnace of a chemical vapour deposition (CVD) reactor. A stream of nitrogen gas was allowed to flow through the reactor for a few minutes to flush the system and ensure inertness. The sample was then heated to a temperature of 600 °C (at a rate of 10 °C min^{-1}) and maintained at this temperature for two hours. Thereafter, the reactor was left to cool naturally under a flow of nitrogen to room temperature, after which the gas flow was discontinued. A brown-yellow product (g-C_3N_4 nanosheets) was obtained and denoted CNNS-TE.

4.2.5 Characterisation of the catalysts

Powder X-ray diffraction (XRD) analyses of the samples were conducted with a Bruker AXS D8 Advance powder X-ray diffractometer equipped with Cu-Kα radiation (λ = 1.5406 Å) at 40 kV and 40 mA. UV–Visible diffuse reflectance spectra were recorded with a PerkinElmer Lambda 35 UV–visible spectrophotometer fitted with a Labsphere integrating sphere. The photoluminescence spectra were recorded with a PerkinElmer LS 55 spectrofluorimeter at an excitation wavelength of 325 nm. The structure and morphology of the catalysts was investigated by means of scanning electron microscopy (SEM, Carl Zeiss Ultra Plus fitted with an energy dispersive Oxford X-max detector), with an operating voltage of 30 kV, and transmission electron microscopy (TEM, JEOL JEM 1010) operating at both normal and high resolution (HRTEM) modes and with an operating voltage of 200 kV. The images were taken at different magnifications until well resolved micrographs were obtained. Before TEM analysis, the samples were prepared as follows: powdered samples were dispersed in ethanol and sonicated for 15 minutes, and thereafter, the sample holder (grid) was dipped into the dispersion. The sample holder was removed and dried under a UV lamp and then inserted into the TEM sample port for imaging. The Fourier transform infrared (FTIR) spectra were acquired with a PerkinElmer Spectrum 100 FTIR spectrometer fitted with an attenuated total reflectance (ATR) sampling accessory. Elemental analysis was carried out with an Elementar vario EL cube CHNSO elemental analyser. The thermal stability of the samples was determined with a TA Instruments Q series thermal analyser (Q600) in air. The Brunauer–Emmett–Teller (BET) specific surface areas and porosities were determined from N_2 adsorption-desorption isotherms at 77 K with a Micromeritics TriStar II surface area and porosity analyser. The surface structural defects were analysed with a Renishaw inVia Raman microscope.

4.2.6 Electrochemical measurements

The electrochemical measurements were carried out with a Metrohm 797 VA Computrace electrochemistry workstation. A three-electrode system consisting of a reference, counter and working electrode was employed. The working electrodes were made by modifying glassy carbon electrodes (GCE) with the respective photocatalysts (B-g-C_3N_4, CNNS-LE and CNNS-TE). The modification typically involved the following: ethanol (600 μL)

was added to a mixture containing 10 mg photocatalyst and 3 mg carbon paste (binder), and thereafter sonicated for 10 minutes. The resulting dispersion was drop-casted with a micro-pipette onto a clean glassy carbon electrode and allowed to dry overnight. A platinum wire was used as a counter electrode, while Ag/AgCl was used as the reference electrode. Additionally, 1 M KCl was used as the electrolyte. The system was purged for five minutes with nitrogen gas to drive off dissolved oxygen in the solution that would otherwise interfere with the redox activity of the working electrode during measurements. Cyclic voltammetry measurements (CV) were run at a voltage sweep rate of 100 mV s^{-1}, over a potential range of -0.6 to 0.6 V for four cycles with the last three cycles being recorded. Furthermore, electrochemical impedance spectroscopy (EIS) measurements were performed with a CH Instruments CHI660E electrochemical workstation, also with the same three electrode system. The electrolyte used was 5 mM $[Fe(CN)_6]^{4-/3-}$ solution (a standard negative redox probe) containing 0.1 M KCl at a voltage frequency range of 1 Hz to 100 kHz and 5 mV amplitude.

4.2.7 Photocatalytic activity experiment

The experiment was carried out at the University of KwaZulu-Natal in Durban, South Africa (-29.81694° N, 30.94492° E, 200 m above sea level) and the intensity of solar radiation on that particular day was 843 ± 2 W m^{-2}, and the temperature was 26 °C. An aqueous solution of RhB (5 mg L^{-1}) was prepared, and its UV-visible absorption spectrum was recorded with a Shimadzu UV-3600 double beam UV-visible-NIR spectrophotometer. The B-g-C_3N_4, CNNS-LE and CNNS-TE photocatalysts (5 mg) were separately weighed into respectively labelled Petri-dishes and, thereafter, RhB solution (5 mL) was added. As a reference, Petri-dishes containing RhB solution without catalyst were also prepared. Separate Petri-dishes were prepared for each data point. All solutions were judiciously covered with aluminium foil, to avoid any photo-degradation that could be caused by either daylight or laboratory lights, and allowed to stand for 60 minutes in order to attain adsorption-desorption equilibrium for the samples containing the catalysts [38]. The prepared solutions were simultaneously exposed to the sun for the photo-degradation studies. Petri-dishes containing the samples were collected and taken for analysis at intervals of 10 minutes, for a total period of 60 minutes. Before spectral analysis, the solution was centrifuged at 6000 rpm for 10 minutes and the supernatant

filtered through a 0.45 μm syringe filter to remove the catalyst. The absorbance of the filtrate at a λ_{max} of 553 nm was measured. The percentage degradation of RhB at a given time was calculated from Equation (1) [54]:

$$(A_o - A_t)/A_o \times 100\ \% \qquad \text{Equation (1)}$$

where A_0 is the initial absorbance of RhB before exposure to sunlight and A_t is the absorbance of RhB at any given time t. Finally, the best performing photocatalyst was recovered and the above procedure was repeated under the same conditions for three more cyclic runs in order to ascertain its stability.

4.3 Results and discussion

B-g-C_3N_4 and the nanosheets prepared by liquid exfoliation and thermal etching were first characterised before being tested for their ability to photo-degrade the model pollutant – Rhodamine B.

4.3.1 Morphology and dimensions

The surface morphology and dimensions of the prepared samples was investigated by both scanning electron microscopy (SEM) and transmission electron microscopy (TEM), and the images acquired are shown in Figures 4.1 and 4.2. From the SEM images (Figure 4.1) it can be seen that B-g-C_3N_4 (Figure 4.1a) contains large blocks of particles with a rough surface that have dimensions ranging between 200-500 nm. These relatively large sizes could be attributed to stacking of layers of g-C_3N_4 formed during the high temperature polycondensation of melamine. Evidently, in Figure 4.1b, CNNS-TE exhibits a porous structure with relatively smaller particles (20-50 nm), and the layers are apparently loose, possibly because during the thermal etching process of B-g-C_3N_4 to form CNNS-TE nanosheets under nitrogen, the weak van der Waals forces of attraction between the layers were broken. Simultaneously, the layers separated and corrosion occurred on the nanosheets resulting in a porous surface [55].

On the other hand, the SEM and TEM images of the CNNS-LE nanosheets in Figures 4.1 and 4.2, respectively, revealed particles of sizes between 50-100 nm in a characteristically disordered planar morphology, but these were not as porous as those for CNNS-TE which depicted circular dislocations and boundaries (Figure 4.1b). The disordered planar morphology exhibited by the CNNS-LE nanosheets can be attributed to breakdown of

van der Waals forces of attraction between layers by sonic wave energy dissipated by the sonicator during liquid exfoliation and, thus, the layers were separated and no defects were noted on the surface [39]. Based on these results, B-g-C_3N_4 was successfully exfoliated to nanosheets via thermal etching and liquid exfoliation processes.

Moreover, the thickness of the CNNS-TE nanosheet was estimated from the size distribution profile of the selected area of the TEM image (Figure 4.3b). From point A to point B in Figure 4.3a, the intensity decreased because the number of electrons striking the detector decreased as the number of sheets (thickness) increased, suggesting that the bulk material was exfoliated to a few sheets, which possibly stacked on each other in the CNNS-TE material.

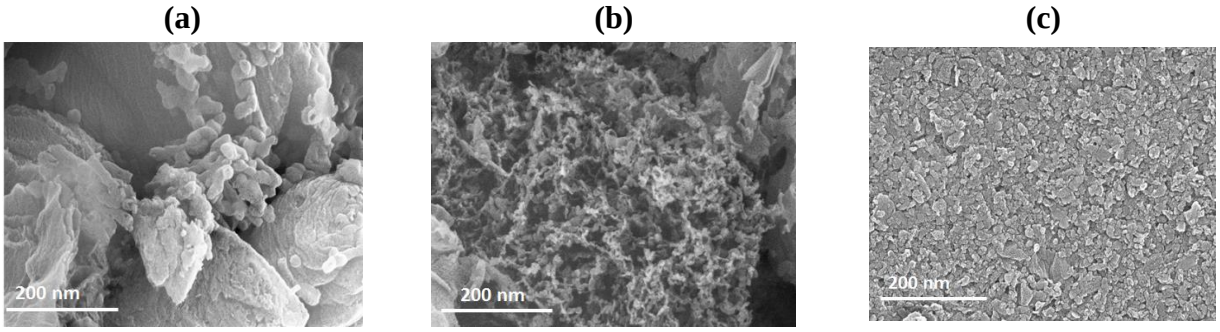

Figure 4.1: SEM images of (a) B-g-C_3N_4, (b) CNNS-TE nanosheets and (c) CNNS-LE nanosheets

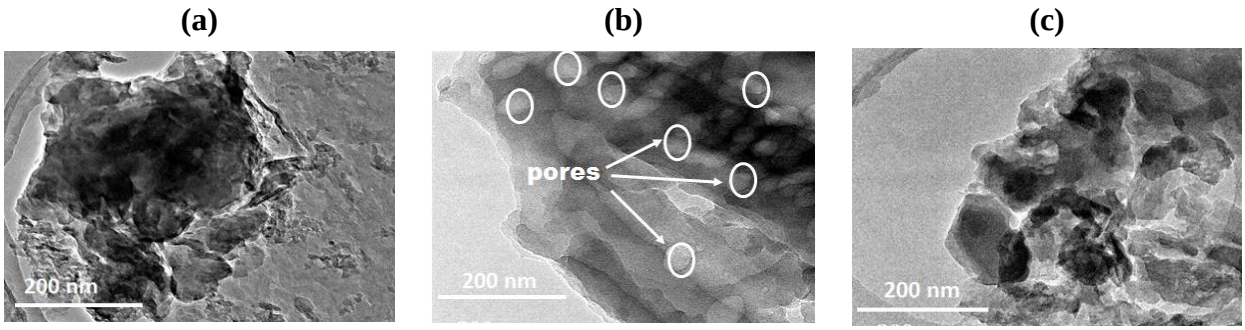

Figure 4.2: TEM images of (a) B-g-C_3N_4, (b) CNNS-TE nanosheets and (c) CNNS-LE nanosheets

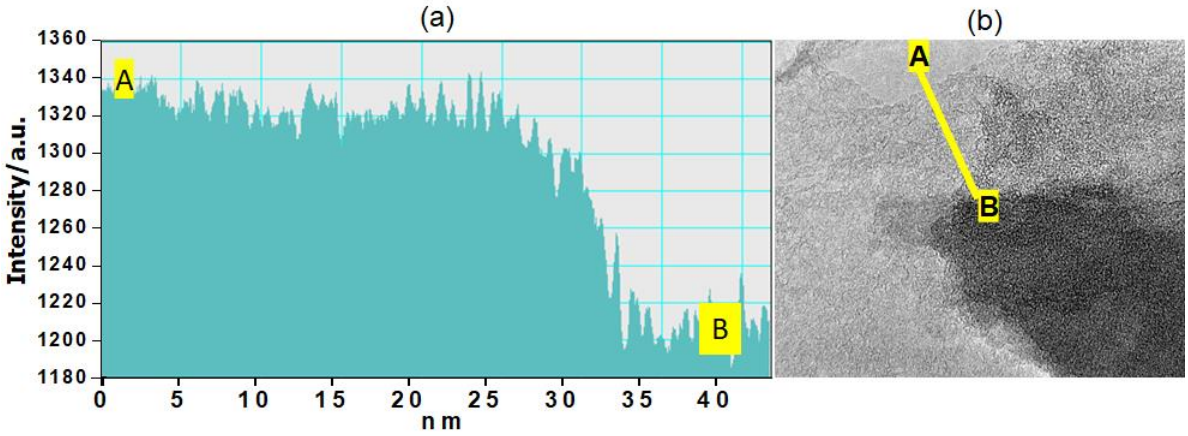

Figure 4.3: (a) A typical intensity profile showing the lattice calculation and (b) the corresponding TEM image showing the distance profiled (A-B) for the CNNS-TE nanosheets

4.3.2 Structural analysis

The crystal structures of the prepared samples were examined by powder XRD, and the diffractograms are presented in Figure 4.4a. Clearly, the diffractograms contain two characteristic peaks, i.e. at around $2\theta = 27.4°$ and 13.2°, corresponding to interlayer spacings of 0.167 and 0.337 nm, respectively. The interlayer spacing was calculated from Bragg's law, $n\lambda = 2d\sin\theta$. The diffraction peak at 27.4° is indexed to the (002) plane and corresponds to interlayer stacking of conjugated aromatic systems, while the peak at 13.2° is indexed to the (100) plane and corresponds to in-plane structural packing motifs of tri-s-triazine units of g-C_3N_4 [52]. In the case of CNNS-LE, the peak for the (002) plane was intense, sharp and shifted from 27.4 to 27.7°. This can be attributed to the increased crystallinity and decreased interlayer distances between the CNNS-LE nanosheets. For the CNNS-TE nanosheets, this peak was shorter and broader, and experienced a shift from 27.4° to 27.2°, corresponding to an increase in the interlayer spacing. The increase in interlayer spacing may be attributed to buckling of the nanosheets as a result of high temperature pyrolysis, thus making the material more amorphous [40].

To further confirm the structures of the prepared samples, HRTEM analysis was carried out and the results are reported in Figure 4.4b. Both B-g-C_3N_4 and CNNS-TE nanosheets showed amorphous diffraction patterns for a material in powder form, while the CNNS-LE nanosheets were somewhat crystalline as evidenced by spots in circles – a characteristic of crystalline materials in powder form.

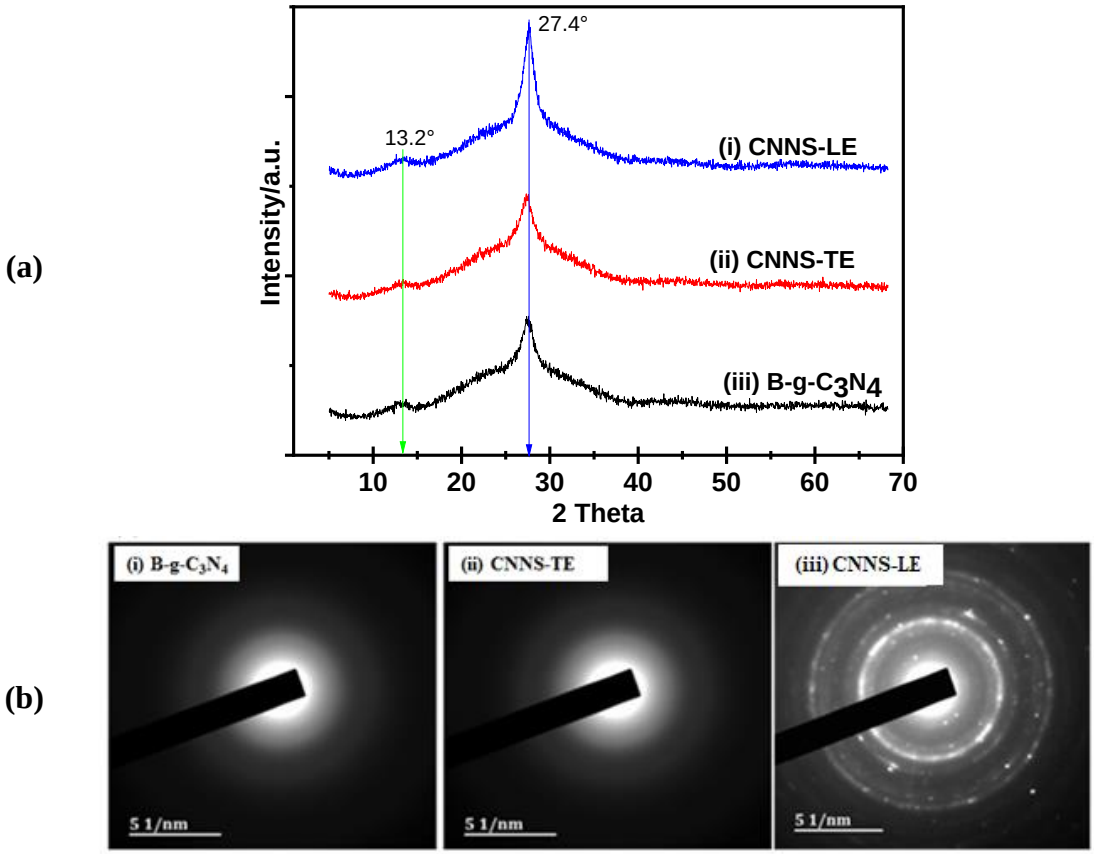

Figure 4.4: (a) Powder X-ray diffractograms of CNNS-TE, CNNS-LE and B-g-C_3N_4, and (b) the selected area electron diffraction (SAED) micrographs for (i) B-g-C_3N_4, (ii) CNNS-TE and (iii) CNNS-LE

4.3.3 Surface area and porosity

The Brunauer-Emmett-Teller (BET) surface area and Barrett-Joyner-Halenda (BJH) porosity measurements were determined from nitrogen adsorption-desorption isotherms at 77 K and are presented in Figure 4.5. All the samples displayed type IV isotherms and type H3 hysteresis loops (Figure 4.5a) indicating that multilayer adsorption occurred and was accompanied by capillary condensation in the nanomaterials [56]. The BET surface areas of B-g-C_3N_4, CNNS-LE and CNNS-TE were 3.22, 41.68 and 14.76 m^2 g^{-1}, respectively. This clearly indicates that, after successful exfoliation of B-g-C_3N_4 via the two means, the surface area was greatly increased. The BET surface of CNNS-LE of 41.68 m^2 g^{-1} coincides with what has been previously reported for such nanosheets obtained via liquid exfoliation [57]. The BJH pore volumes (Figure 4.5b) also followed the same pattern as the BET surface areas with CNNS-LE having the largest pore volume

of 0.12 cm^3 g^{-1}, while CNNS-TE and B-g-C_3N_4 had smaller pore volumes of 0.09 and 0.03 cm^3 g^{-1}, correspondingly. Generally, both B-g-C_3N_4 and CNNS-TE were macroporous and CNNS-LE was mesoporous. These results are in agreement with what was observed in the corresponding SEM and TEM images in Figures. 4.1 and 4.2.

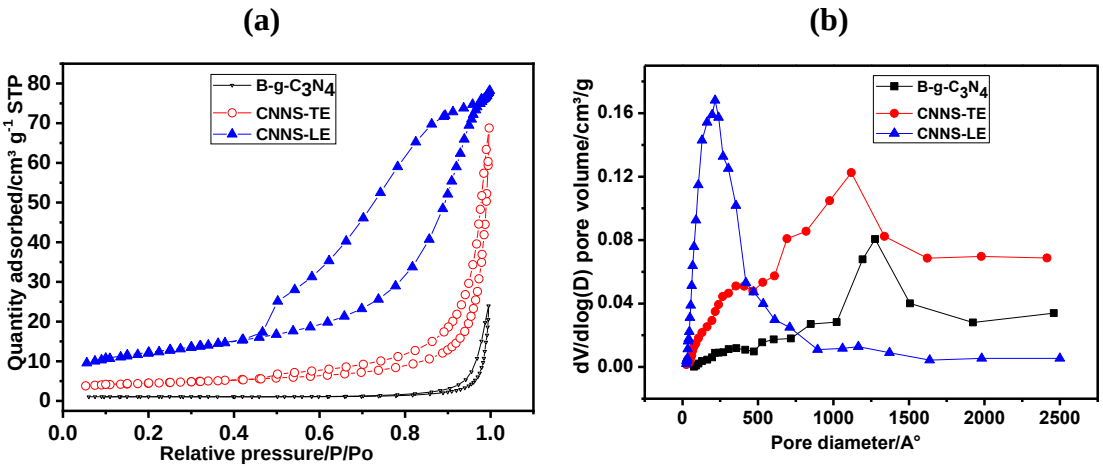

Figure 4.5: (a) BET nitrogen adsorption-desorption isotherms and (b) the BJH pore volumes of B-g-C_3N_4, CNNS-TE and CNNS-LE

4.3.4 Chemical structure

Fourier transform infrared spectroscopy (FTIR) was used to determine the chemical structures of the as-prepared samples (B-g-C_3N_4, CNNS-LE and CNNS-TE) and melamine (the starting precursor) as shown in Figure 4.6a. It should be noted that melamine has slightly different functional groups from the rest of the synthesised materials and, hence, the differences in the absorption peaks observed. The characteristic spectrum of B-g-C_3N_4 was the same as for the nanosheets, CNNS-TE and CNNS-LE, implying that when the bulk was exfoliated to nanosheets the basic chemical structure remained unchanged [55]. The peaks observed between 3500-3000 cm^{-1} represent N-H/O-H stretching vibration bands, indicating that presence of NH or NH_2 in the nanosheets, and can also be attributed to the presence of surface adsorbed water molecules [26, 58]. The peak at around 2170 cm^{-1} is associated with the terminal cyano group [35, 38, 39], while the set of peaks at 1700-900 cm^{-1} are attributed to the breathing modes of s-triazine derivatives [59]. Additionally, the peak at about 815 cm^{-1} is be linked to the breathing mode of tri-s-triazine units [35, 60].

Figure 4.6b shows the Raman spectra of the samples with the characteristic D and G bands centred at 1406 and 1564 cm^{-1}, respectively. These characteristic peaks are in accordance with previous reports [61]. In essence, the ratio of the intensities of the D and G bands (I_D/I_G) provides information on the degree of graphitisation of the materials [62]. The calculated ratios (I_D/I_G) of B-g-C_3N_4, CNNS-LE and CNNS-TE were 1.13, 1.29 and 1.17, respectively. CNNS-LE and CNNS-TE exhibited higher I_D/I_G ratios than the B-g-C_3N_4, indicating that the nanosheets possess more structural defects as a result of the liquid and thermal exfoliation treatments, respectively. The Raman spectra for the nanosheets and the bulk g-C_3N_4 material were similar, implying that, the basic structure of the bulk material was maintained, even after exfoliation, as was also observed in the infrared spectra.

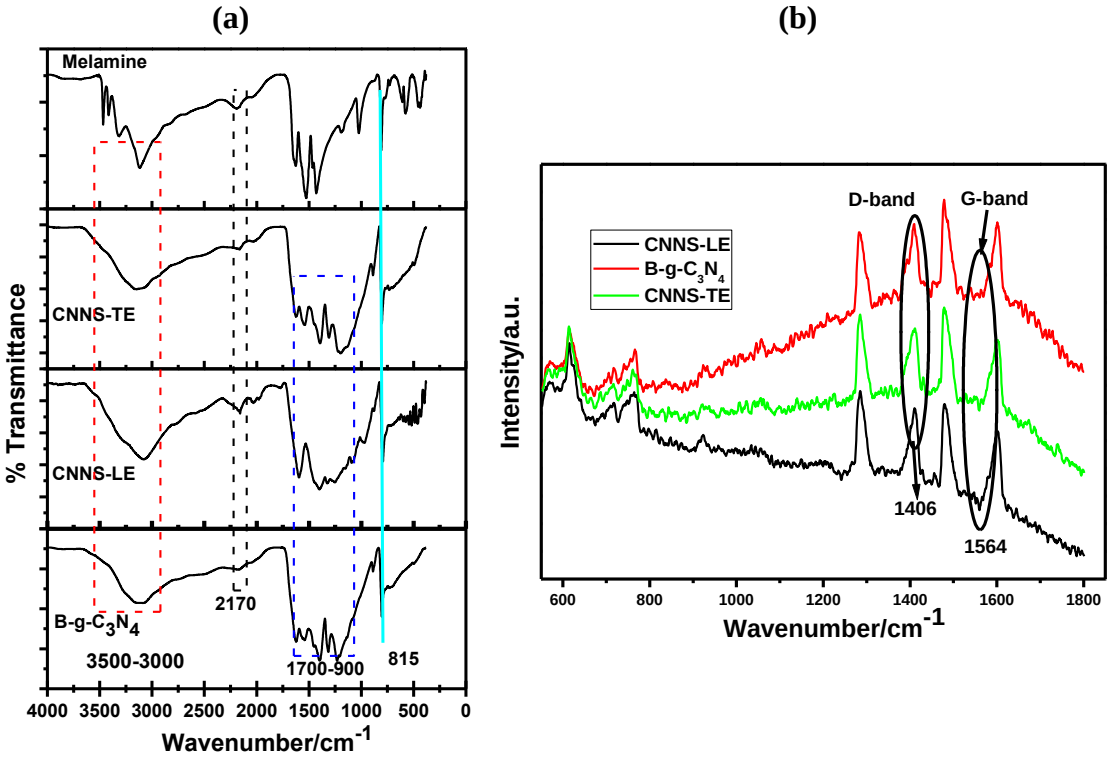

Figure 4.6: (a) FTIR spectra of melamine, CNNS-TE, CNNS-LE and B-g-C_3N_4 and (b) Raman spectra of the photocatalysts obtained with an excitation wavelength of 785 nm

4.3.5 Thermal stability

The thermal stability of the materials was investigated in an atmosphere of air. The resulting thermograms are shown in Figure 4.7. As can be observed from Figure 4.7a, the initial weight loss that was noted between 50 and 150 °C may be due to the loss of water that had adsorbed on the surface of the samples. The sharp weight loss that occurred between 450 and 630 °C may be attributed to the decomposition of the samples to CO_x and NO_x as a result of oxidation and, subsequently, the horizontal portion (no mass loss) of the graph suggests that all the materials have been converted to char as residual mass [63]. The specific decomposition temperatures of B-g-C_3N_4, CNNS-LE and CNNS-TE were 622, 615 and 583 °C, in that order (Figure 4.7b). The CNNS-TE nanosheets had the lowest thermal stability, followed by the CNNS-LE nanosheets, while B-g-C_3N_4 had the highest thermal stability. Generally, the as-prepared materials are thermally stable below 580°C and, thus, stable for photocatalytic and photovoltaic applications.

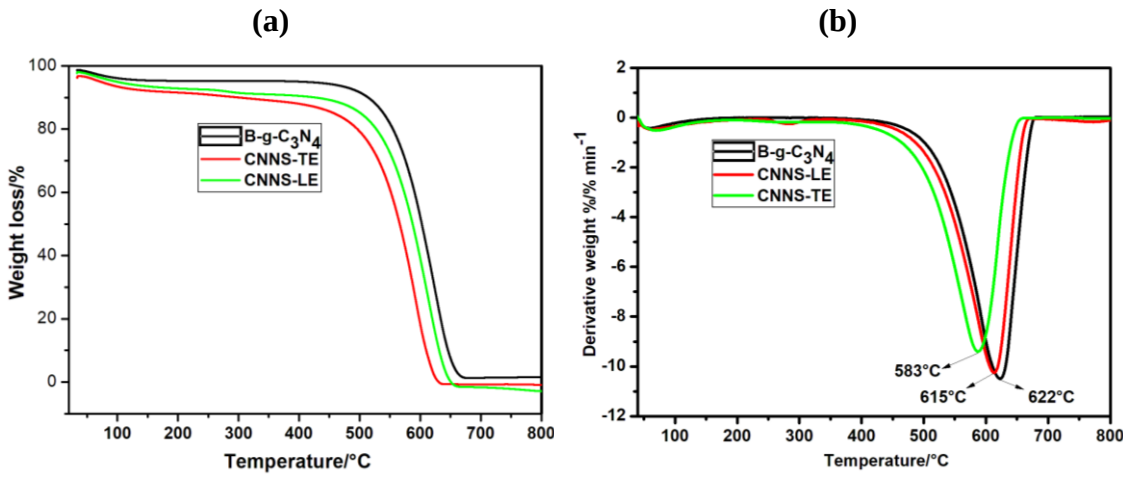

Figure 4.7: (a) TGA thermograms for B-g-C_3N_4, CNNS-LE and CNNS-TE measured under air and (b) the corresponding derivative thermograms

4.3.6 Chemical composition

The chemical composition of the photocatalysts was determined with an Elementar CHNSO elemental analyser and the results are presented in Table 4.1. As can be noted from Table 4.1, all the materials have approximately the same carbon/nitrogen ratio (C/N) of 0.57 implying that not all of the material fully polymerised to yield pure graphitic carbon nitride (C/N = 0.64). However, the nanosheets obtained from liquid exfoliation exhibited a larger oxygen content of 19.81% than B-g-C_3N_4 and CNNS-TE, probably because they were synthesised in water by ultrasonication which could have functionalised the edges of the tri-s-triazine units.

Table 4.1: Elemental composition of B-g-C_3N_4, CNNS-LE and CNNS-TE obtained from elemental analysis

Photocatalyst	C/%	N/%	O/%	H/%	C/N
B-g-C_3N_4	31.98	53.77	9.55	2.20	0.59
CNNS-LE	23.77	41.69	19.81	2.43	0.57
CNNS-TE	33.00	58.18	10.65	2.22	0.57

4.3.7 Electrochemical properties

The electrochemical characteristics of the prepared samples were measured by means of cyclic voltammetry and the voltammograms are shown in Figure 4.8. B-g-C_3N_4 did not show any redox peaks (Figure 4.8a), while both CNNS-LE and CNNS-TE photocatalysts showed quasi-redox behaviour (Figure 4.8b). The nanosheets from the CNNS-TE sample exhibited superior electrochemical behaviour than those from liquid exfoliation and this is because they had a better current response. This could have contributed to their better photocatalytic performance (see Section 3.10).

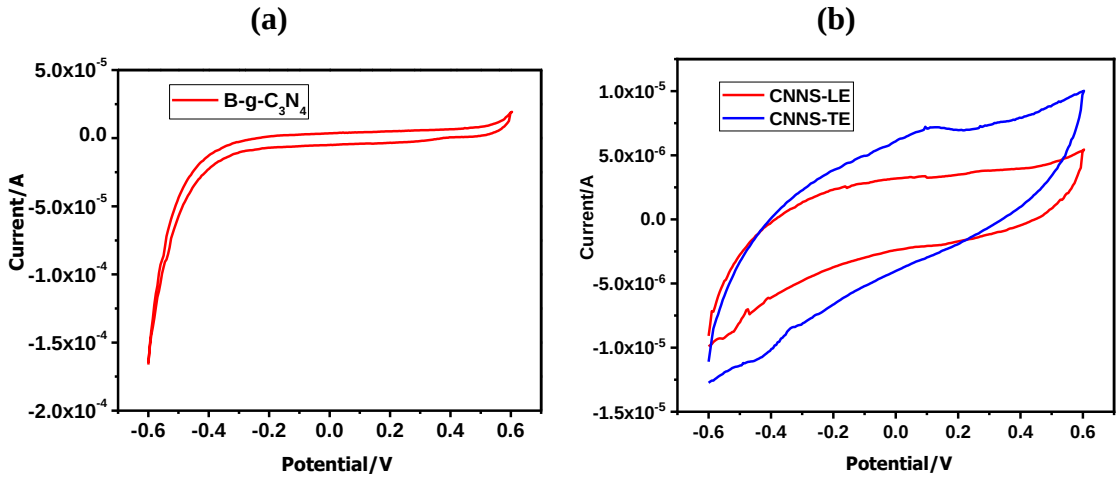

Figure 4.8: Cyclic voltammograms of (a) B-g-C_3N_4/GCE and (b) CNNS-TE/GCE and CNNS-LE/GCE in 1 M KCl, recorded over a potential range of -0.6 to 0.6 V with a sweep scan rate of 100 mV s^{-1}

In addition, electrochemical impedance spectroscopy was also carried out to investigate the charge transfer rates of the materials. Figure 4.9 shows the Nyquist plots of the modified electrodes (B-g-C_3N_4/GCE, CNNS-TE/GCE and CNNS-LE/GCE) in $Fe(CN)_6^{4-/3-}$ solutions. Generally, the semi-circular part of the Nyquist plot at the high frequency region indicates the electron transfer limiting process while the linear part at the low frequency region indicates the diffusion-controlled process [64]. The diameter of the semi-circle is proportional to the charge transfer resistance (R_{ct}) [65]. All the measured samples showed a semi-circle and a linear part implying that there were competing processes, i.e. electron transfer and diffusion-controlled processes. CNNS-TE showed the smallest semicircle diameter suggesting that it had better electrical conductivity (i.e.

lowest electron transfer resistance) than CNNS-LE and B-g-C_3N_4. Meanwhile, B-g-C_3N_4 had the largest semi-circle and, hence, low electron transfer properties.

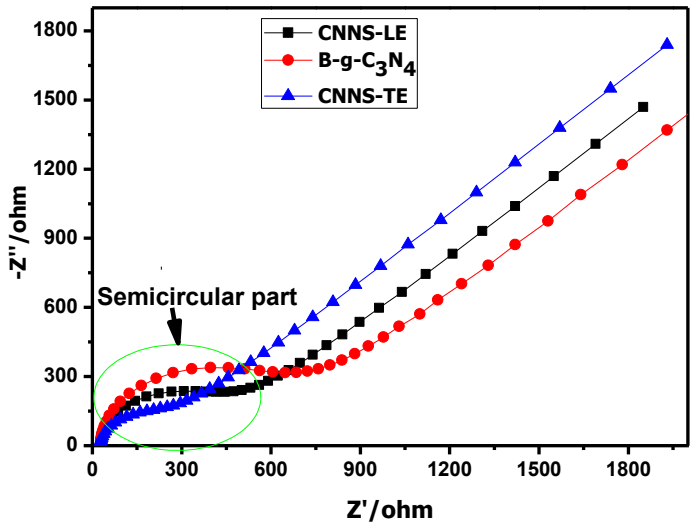

Figure 4.9: Nyquist plots for B-g-C_3N_4/GCE, CNNS-TE/GCE and CNNS-LE/GCE in $Fe(CN)_6^{4-/3-}$ solutions

4.3.8 Optical properties and band structure

The optical properties of the prepared samples were investigated by means of UV-visible-diffuse reflectance spectroscopy (UV-Vis-DRS) as shown in Figure 4.10a. Generally, B-g-C_3N_4 exhibited the lowest intensity whereas the nanosheets obtained via thermal etching (CNNS-TE) showed the highest intensity. It can be observed that the CNNS-LE nanosheets exhibited a slight blue shift (381 to 378 nm) relative to the bulk probably because of reduced conjugation length and increased quantum confinement, which is due to the increased surface area as a result of liquid exfoliation [66]. In contrast, CNNS-TE showed a significant red shift (381 to 386 nm) in comparison with B-g-C_3N_4 and this may be attributed to the high temperature intrinsic-modification of the porous nanosheets, formed during the thermal etching process under nitrogen. This defect-related extra light absorption band edge is in agreement with other trends reported for g-C_3N_4 nanosheets synthesised via thermal etching of bulk graphitic carbon nitride under argon [67]. Additionally, CNNS-TE showed an absorption band "shoulder" between 450 and 550 nm, thus absorbing more light in the visible region. This is consistent with reports by other authors [68].

With the consideration that graphitic carbon nitride is a material with a direct allowed transition [69], the transformed Kubelka-Munk plot $((\alpha h\nu)^{1/2}/eV^{1/2}$ against E/eV) [70] was used to calculate the band gap energy as presented in Figure 4.10b. B-g-C_3N_4 had a band gap of 2.71 eV (Table 4.2) which corroborates with other values reported previously [71], while CNNS-LE and CNNS-TE had band gaps of 2.59 and 1.89 eV, respectively (Table 4.2). Thus, CNNS-TE can absorb more visible light than CNNS-LE and B-g-C_3N_4, as depicted by the respective gradually decreasing band gap values. This shows that as the B-g-C_3N_4 material was exfoliated to nanosheets, the band gap energy decreased and the resulting nanosheets showed extended light absorption edges; a property that is crucial in light-driven photocatalytic and photovoltaic activities [26]. Clearly, it can be noted that CNNS-TE is a better visible light photocatalyst than CNNS-LE because its light absorption edges are more extended towards the visible region (lowest band gap) of the electromagnetic spectrum and, thus, the thermal etching method can be a promising route to exfoliate B-g-C_3N_4 to nanosheets for the purpose of photocatalysis.

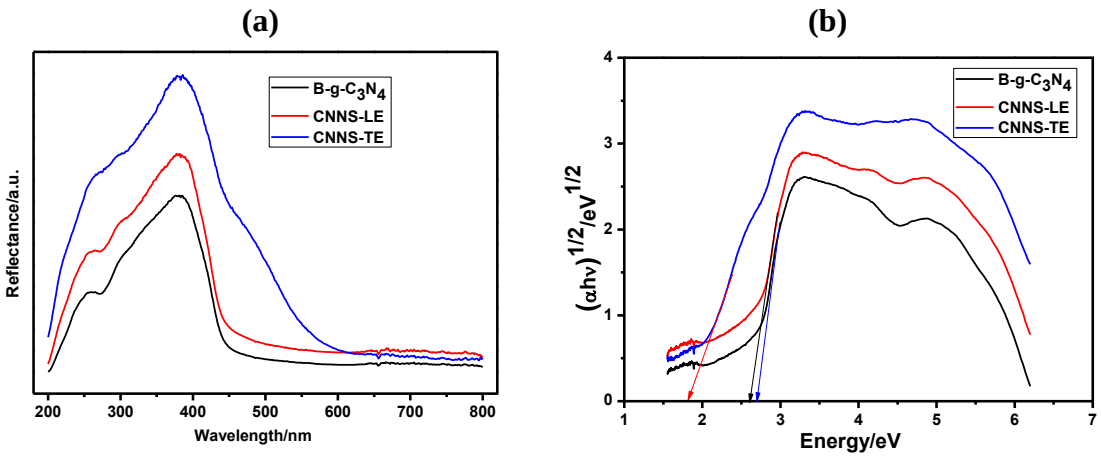

Figure 4.10: (a) UV-visible diffuse reflectance spectra of B-g-C_3N_4, CNNS-LE and CNNS-TE and (b) transformed Kubelka-Munk plots $((\alpha h\nu)^{1/2}/eV^{1/2}$ versus E/eV) for the corresponding materials

Table 4.2: Optical and textural properties of the prepared samples

Photocatalyst	Band gap energy/eV	Valence band potential/eV	Conduction band potential/eV	BET surface area/m^2 g^{-1}	BJH pore volume/cm^3 g^{-1}
B-g-C_3N_4	2.71	1.59	-1.13	3.22	0.03
CNNS-LE	2.59	1.52	-1.07	41.68	0.12
CNNS-TE	1.89	1.17	-0.71	14.76	0.09

4.3.9 Band potentials and rate of recombination of photocharges

The valence band potentials E_{VB} and conduction band potentials E_{CB} of the photocatalysts were calculated from the Butler and Ginley equations (Equations 2 and 3) [72, 73]:

$$E_{VB} = \chi - E_e + 0.5E_g \qquad \text{Equation (2)}$$

$$E_{CB} = E_{VB} - E_g \qquad \text{Equation (3)}$$

where E_g is the energy gap (band gap) calculated from the Kubelka-Munk plot, χ is the electronegativity of the semiconductor and is 4.73 eV for g-C_3N_4 [74], and E_e is the energy of free electrons on the hydrogen scale (approx. 4.5 eV). The calculated values for the conduction band (CB) and the valence band (VB) potentials for the photocatalysts, B-g-

C_3N_4, CNNS-LE and CNNS-TE, are summarised in Table 4.2. The VB and CB potentials of B-g-C_3N_4 were 1.59 eV and -1.13 eV, respectively. To further confirm the positions of the CBs and VBs of the materials, Mott Schottky analysis [75] (Figure 4.11a) was carried out. The estimated CBs for B-g-C_3N_4, CNNS-LE and CNNS-TE were: -1.18, -1.15 and -0.85 V (vs. Ag/AgCl), respectively. The VB positions for B-g-C_3N_4, CNNS-LE and CNNS-TE, were then calculated from the band gap obtained from UV-visible-DRS and were found to be: +1.53, +1.44 and +1.04 V (vs. Ag/AgCl), correspondingly, which are close to the values listed in Table 4.2. These results are in agreement with previous reports [74]. CNNS-TE had the lowest energy band gap and this could have contributed to its enhanced photocatalytic performance (see Section 4.3.10). Fundamentally, heat treatment results in modification of the morphology and electronic band structure of the material.

In order to investigate the rate of recombination of photogenerated charges, i.e., the charge separation efficiency, of the prepared photocatalysts, photoluminescence (PL) spectra were measured (Figure 4.11b). Practically, B-g-C_3N_4 had the highest PL intensity, followed by CNNS-LE and then CNNS-TE in descending order. This implies that the rate of recombination of photogenerated charges was highest in B-g-C_3N_4 and least in CNNS-TE. Remarkably, CNNS-TE (with the lowest intensity) showed a greatly suppressed recombination rate of photogenerated charge carriers.

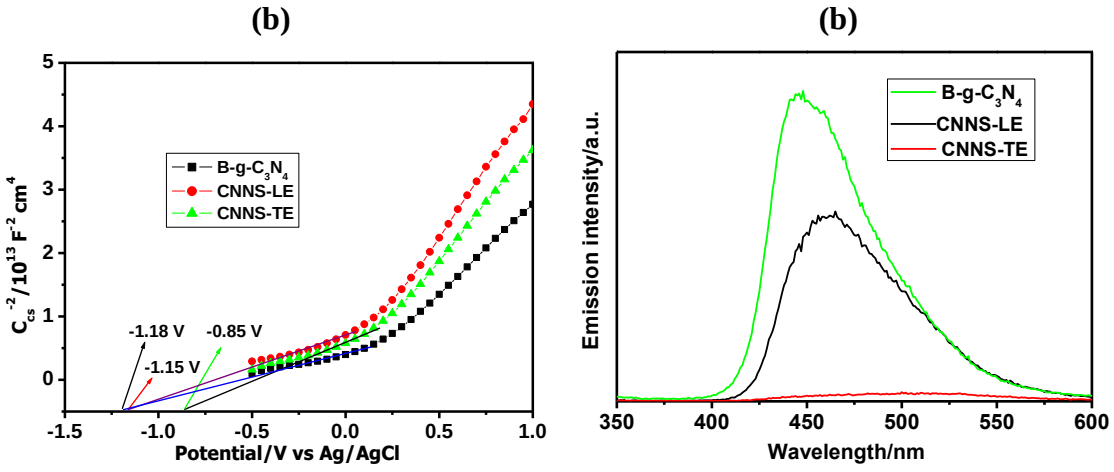

Figure 4.11: (a) Mott-Schottky plots measured at 1 kHz in 5 mM $[Fe(CN)6]^{4-/3-}$ solution, and (b) photoluminescence spectra of the as-synthesised photocatalysts

4.3.10 Photocatalytic activity

To evaluate the photocatalytic activities of the prepared catalysts, photocatalytic experiments were conducted under solar irradiance to mimic the actual conditions under which photocatalysts operate in the destruction of pollutants. In this experiment, RhB was used as a model pollutant at an initial concentration of 5 mg L^{-1}. Figure 4.12 illustrates the adsorption-degradation profile of the RhB solution. As depicted, for the first 60 minutes, adsorption of RhB on the surface of the catalyst took place in the dark, and CNNS-TE and CNNS-LE photocatalysts showed higher adsorption than the bulk B-g-C_3N_4. This could be attributed to the larger surface areas of the exfoliated products compared with the bulk and, thus, more exposed active sites for adsorption. All the catalysts (B-g-C_3N_4, CNNS-LE and CNNS-TE) showed significant degradation of the model pollutant (RhB) with increasing time of solar exposure as reported in Figure 4.12.

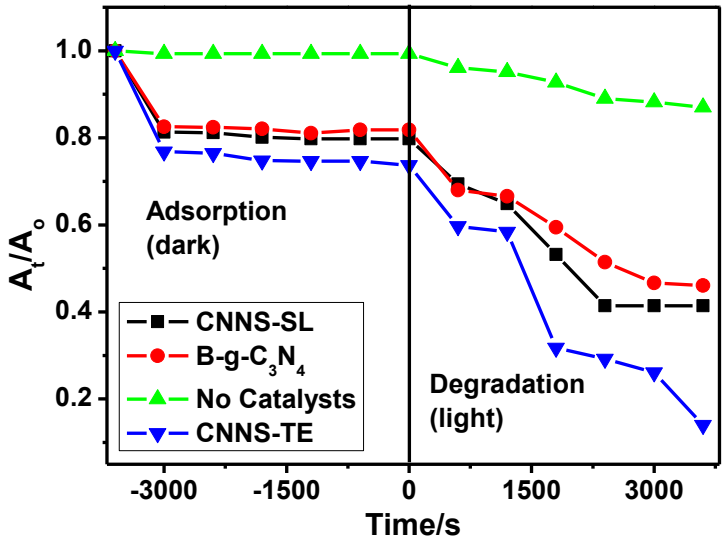

Figure 4.12: Photocatalytic performance of B-g-C_3N_4, g-C_3N_4 nanosheets obtained from thermal etching (CNNS-TE), g-C_3N_4 nanosheets from liquid exfoliation (CNNS-LE) and self-degradation of RhB without a catalyst for 60 minutes

From the graph in Figure 4.12, it can be observed that the CNNS-TE photocatalyst showed an excellent photocatalytic degradation activity of about 86% of the pollutant in 60 minutes, while CNNS-LE nanosheets and B-g-C_3N_4 degraded the same model pollutant by about 59 and 54%, respectively, within the same time period. The remarkable photocatalytic performance of CNNS-TE could be attributed to the fact that during thermal etching structural defects formed that modified the electronic band

structure (lowering the band gap energy) and thus enhanced light absorption [25, 40]. Furthermore, CNNS-TE had the lowest rate of recombination of photogenerated charges (Figure 4.11), and hence a high photo-activity. Although it is widely expected that the photocatalyst with the highest surface area would perform better in photocatalysis due to an increased number of reactions sites and increased quantum confinement and thus low recombination of photogenerated charges, this was not the case here. In this case, CNNS-LE with the largest surface area of 41.68 m^2 g^{-1}, did not perform better than CNNS-TE which had a much lower surface area of 14.76 m^2 g^{-1}. Similar observations were reported by Zhang et al. [25]. This observation gives insight to the fact that in addition to the specific surface area which plays a critical role in photo-activity, other factors such as the light-harvesting ability of a material (band gap) and the separation of photogenerated charges are also important in photocatalytic activity [25].

From the elemental analysis results (Table 4.1) it was shown that CNNS-LE had the largest oxygen content (19.81%) relative to the other catalysts. Thus, it is likely that the edges of the tri-s-triazine units of the CNNS-LE nanosheets were functionalized with more oxygen-containing groups during the ultra-sonication process in water, and, hence, causing a reduction in the number of nitrogen vacancies which could have otherwise caused re-organisation of charges in the CN-skeleton [76].

In order to ascertain the stability of CNNS-TE, a recycling experiment was carried out. As shown in Figure 4.13a, the photoactivity of the catalyst was maintained even after the fourth cycle with only approximately 0.4% activity lost. The stability of the photocatalysts was further confirmed by performing powder XRD analyses of the photocatalyst after use and the diffractograms obtained before and after were compared. Figure 4.13b shows the diffractogram of the CNNS-TE photocatalyst after use. As can be seen, the photocatalysts exhibited similar diffractograms as the initial photocatalyst (before use) (Figure 4.4a), implying that the chemical structures of the catalysts were not affected after use, thus, stable.

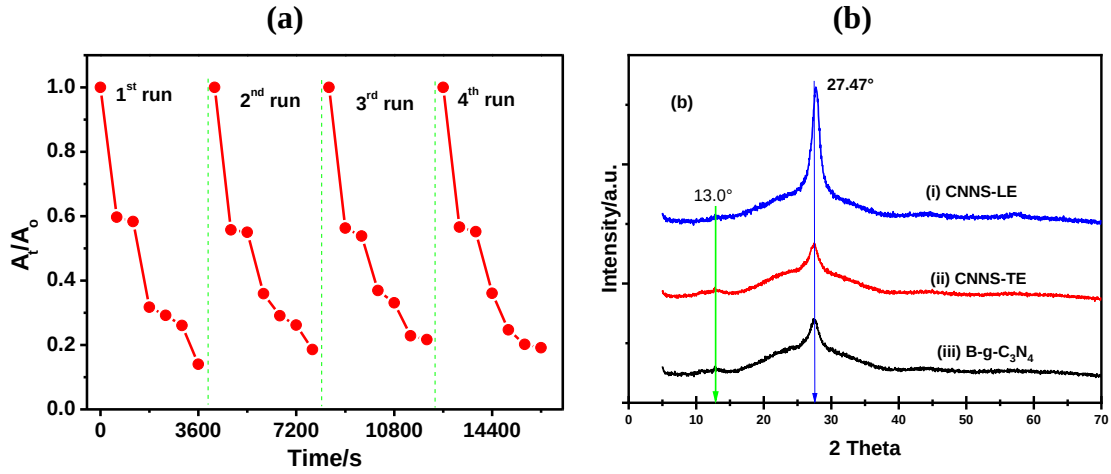

Figure 4.13: (a) Cycling runs for the CNNS-TE photocatalyst for the degradation of RhB solution under solar irradiation, (b) Powder X-ray diffractograms of CNNS-TE, CNNS-LE and B-g-C_3N_4 after use

Table 4.3 shows a comparison between photocatalytic performances of the as-prepared nanosheets with other similar nanosheets prepared in previously published work. The as-prepared photocatalysts showed comparable activities with other similar photocatalysts.

Table 4.3: Comparison of photocatalytic degradation performance of CNNS-TE and CNNS-LE with recently published results

Photocatalyst	Light source	Exfoliation method	Pollutant	Degradation/%	Degradation time/min	Reference
g-C_3N_4 with nitrogen defects	visible	Thermal etching	RhB	95	30	[44]
spherical mesoporous g-C_3N_4	visible	Hard template and thermal etching	RhB	95	20	[45]
graphene-like C_3N_4	visible	Liquid	MB*	94.5	25	[77]
g-C_3N_4 CNNS	visible	Liquid	RhB	49	120	[78]
CNNS-LE	sunlight	Liquid	RhB	59	60	This work
CNNS-TE	sunlight	Thermal etching	RhB	86	60	This work

*MB – methylene blue

4.3.11 Kinetics and mechanism of photo-degradation of Rhodamine B

To monitor the kinetics of the photodegradation of RhB by the catalysts and self-degradation, the pseudo-first-order reaction (Equation 4) was applied [79]:

$$\ln (A_t/A_o) = -kt \qquad \text{Equation (4)}$$

where A_o is the initial absorbance of RhB, A_t is the absorbance of RhB at any time t after solar radiation exposure, k is the pseudo-first-order rate constant, and t is the time in seconds.

Figure 4.14 shows the linear fit of ln (A_t/A_o) as a function of time. In this case, it is evident that the photo-degradation of RhB is consistent with pseudo-first-order reaction kinetics. Ideally, the slope of the graph gives the rate constant, therefore, the calculated rate constants k, for the B-g-C_3N_4, CNNS-LE and CNNS-TE catalysts were, 0.17, 0.21 and 0.44 s^{-1}, respectively. These values are consistent with what was reported for g-C_3N_4 [78]. The rate constant for the self-degradation of RhB was very low with a value of 0.008 s^{-1}.

The rate of degradation of RhB by CNNS-TE was found to be 2.5 times higher than that of B-g-C_3N_4 and CNNS-LE, and remarkably 54 times faster than that of the self-degradation of RhB. This may be attributed to the fact the CNNS-TE possesses the lowest band gap energy according to the results presented in Table 4.2. Also, the low rate of recombination of photogenerated charges and favourable porous morphology may also be responsible for these observations. Hence, it can be noted that the thermal treatment of B-g-C_3N_4 to give CNNS-TE resulted in the intrinsic modification of the electronic band structure of the material resulting in increased efficiency. More importantly, the macroporous structure provided cross-plane diffusion channels which enhance charge transfer as well as mass transfer, and, hence, the observed enhanced photocatalytic efficiency.

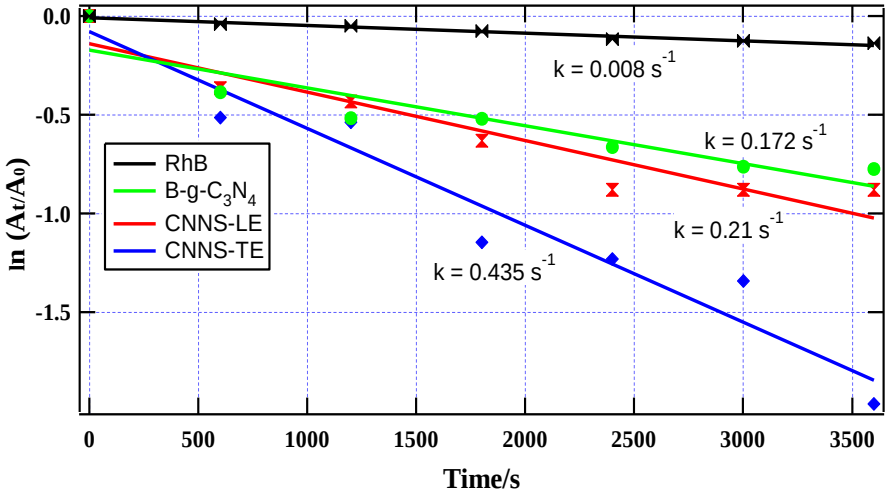

Figure 4.14: Pseudo-first-order kinetics plots for the degradation of RhB by B-g-C_3N_4, CNNS-LE and CNNS-TE photocatalysts, and self-degradation of RhB solution under solar exposure

To determine the active species in the photodegradation mechanism of RhB by the CNNS-TE photocatalyst, trapping experiments were performed. Typically, isopropyl alcohol (IPA), tri-ethanolamine (TEOA) and p-benzoquinone (BQ) were introduced as scavengers for photogenerated hydroxyl radicals ($^{\bullet}OH$), holes (h^+) and superoxide anion ($O_2^{\bullet-}$), respectively. As reported in Figure 4.15, photo-degradation of RhB, by CNNS-TE was considerably inhibited by the presence of scavenger solutions, while in the absence of scavengers the percentage photo-degradation of RhB was the highest. Among the scavengers, the rate of degradation declined in the following order: TEOA < IPA < BQ. Accordingly, it was evident that holes were actively involved in the photodegradation process of Rhodamine B followed by hydroxyl and superoxide anion radicals, respectively.

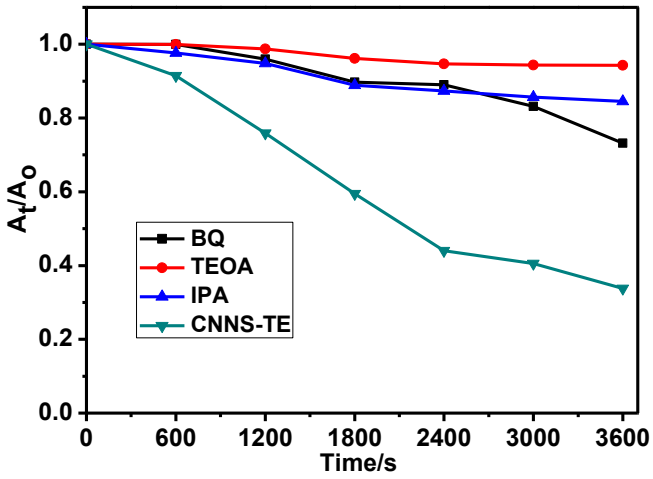

Figure 4.15: Degradation of the model pollutant RhB by CNNS-TE catalyst in the absence and presence of scavengers

Based on the results reported in Figure 4.15, a plausible mechanism for the photocatalytic degradation of RhB by CNNS-TE was proposed. When CNNS-TE was exposed to sunlight, the electrons in the valence band (VB) were excited and promoted to the conduction band (CB), while at the same time, holes (h^+) were left at the VB. Ideally, photogenerated electrons in the CB can be scavenged by surrounding oxygen molecules (O_2) to form superoxide radical anions ($O_2^{\cdot-}$), while photogenerated holes (h^+) at the VB react with attached water molecules (H_2O) to form hydrogen ions (H^+) and hydroxyl radicals ($^{\cdot}OH$) [79]. Consequently, hydrogen ions can protonate $O_2^{\cdot-}$ to form $^{\cdot}OOH$ radicals, which can also react with electrons to form hydrogen peroxide (H_2O_2). Hydrogen peroxide (H_2O_2) can undergo reduction and yield hydroxide ions (OH^-) and hydroxyl radicals ($^{\cdot}OH$). The photogenerated active species ($^{\cdot}OH$, $O_2^{\cdot-}$, $^{\cdot}OOH$) then participate in the degradation of RhB to carbon dioxide and water as reported by [80]. The possible reactions involved in the degradation of RhB can be summarised as shown in Equations 5-12.

$$g\text{-}C_3N_4 + h\nu \rightarrow h^+ + e^- \qquad \text{Equation (5)}$$

$$e^- + O_2 \rightarrow O_2^{\cdot-} \qquad \text{Equation (6)}$$

$$h^+ + H_2O \rightarrow h^+ + {}^{\cdot}OH \qquad \text{Equation (7)}$$

$$h^+ + O_2^{\cdot-} \rightarrow {}^{\cdot}OOH \qquad \text{Equation (8)}$$

$$e^- + OH^- \rightarrow {}^{\cdot}OH \qquad \text{Equation (9)}$$

$^{\bullet}OOH + h^{+} + e^{-} \rightarrow H_2O_2$ Equation (10)

$H_2O_2 + e^{-} \rightarrow {}^{\bullet}OH + OH^{-}$ Equation (11)

$^{\bullet}OH + O_2^{\bullet -} + {}^{\bullet}OOH + RhB \rightarrow$ mineralised products ($CO_2 + H_2O$) Equation (12)

Therefore, the superior photocatalytic activity of CNNS-TE is attributed to the ease of generation of photo-charges as a result of the energy low band gap and its associated low rate of recombination of charges.

4.4 Conclusions

This study has shown that graphitic carbon nitride can be successfully exfoliated by two green methods, namely, liquid and thermal exfoliation, as evidenced by BET, TEM, XRD and SEM analyses. The resulting nanosheets exhibited extended light absorption band edges, increased surface areas and better photocatalytic activities in the degradation of rhodamine B in the presence of sunlight than bulk B-g-C_3N_4. Although nanosheets from both of the exfoliation methods exhibited larger surface areas than bulk graphitic carbon nitride, significant differences between them exist. CNNS-TE exhibited the following characteristics: less thermal stability, better electrochemical conductivity, smaller energy band gap, lower rate of recombination of photogenerated charges, less oxygen content and a more porous structure. In contrast, CNNS-LE exhibited a relatively higher thermal stability, lower electrochemical conductivity, larger energy band gap, higher rate of recombination of photogenerated charges, more oxygen content, and somewhat more crystalline structure than its counterpart, CNNS-TE nanosheets. Thus, the excellent photocatalytic degradation of RhB exhibited by CNNS-TE (86%) can be attributed to the lower rate of recombination of photogenerated charges, low energy band gap, and better electrochemical conductivity. Moreover, the macro-porous structure exhibited cross-plane diffusion channels which facilitated charge and mass transfer processes, thus increasing the photocatalytic activity. These results show that heat modifies the morphology and intrinsic electronic structure of the semiconductor which boosts the photocatalytic performance of the CNNS-TE photo-catalyst. In general, thermal exfoliation can offer a relatively cheaper and more facile route of exfoliating g-C_3N_4 with better photocatalytic activity, while liquid exfoliation requires long tedious cycles but

results in the formation of nanosheets with high surface areas, and more oxygen functional groups which may have greater potential applications in other fields.

Acknowledgement

The authors are grateful for research support provided by the National Research Foundation of South Africa, under grant numbers 103979 and 109580; the University of KwaZulu-Natal (UKZN), the UKZN Nanotechnology Platform, and the Eskom Tertiary Education Support Programme (TESP).

References

[1] L. Han, W. Zhou, W. Li, Y. Qian, Urbanization strategy and environmental changes: An insight with relationship between population change and fine particulate pollution. Sci Total Environ. **642**, 789-799 (2018). https://doi.org/10.1016/j.scitotenv.2018.06.094.

[2] A.S. Goudie, Human impact on the natural environment, (John Wiley and Sons, New Jersey2018).

[3] P.J. Landrigan, R. Fuller, N.J. Acosta, O. Adeyi, R. Arnold, A.B. Baldé, R. Bertollini, S. Bose-O'Reilly, J.I. Boufford, P.N. Breysse, The Lancet Commission on pollution and health. The Lancet. **391**, 462-512 (2018). https://doi.org/10.1016/S0140-6736(17)32345-0.

[4] V. Smil, Energy in world history, (Routledge, London, United Kingdom2019).

[5] B.D. Fahlman, What Is "Materials Chemistry"?, in Materials Chemistry. 2018, Springer: Dordrecht. p. 1-21.

[6] H. Li, K. Wang, Y. Sun, C.T. Lollar, J. Li, H.-C. Zhou, Recent advances in gas storage and separation using metal–organic frameworks. Mater Today. **21**, 108-121 (2018). https://doi.org/10.1016/j.mattod.2017.07.006.

[7] S.A. Sarkodie, S. Adams, Renewable energy, nuclear energy, and environmental pollution: Accounting for political institutional quality in South Africa. Sci Total Environ. **643**, 1590-1601 (2018). https://doi.org/10.1016/j.scitotenv.2018.06.320.

[8] A. Gu, F. Teng, X. Feng, Effects of pollution control measures on carbon emission reduction in China: Evidence from the 11th and 12th five-year plans. Clim Policy. **18**, 198-209 (2018). https://doi.org/10.1080/14693062.2016.1258629.

[9] E. Kabir, P. Kumar, S. Kumar, A.A. Adelodun, K.-H. Kim, Solar energy: Potential and future prospects. Renew Sustain Energy Rev. **82**, 894-900 (2018). https://doi.org/10.1016/j.rser.2017.09.094.

[10] I. Hadar, T.B. Song, W. Ke, M.G. Kanatzidis, Modern processing and insights on selenium solar cells: The world's first photovoltaic device. J Adv Energy Mater. **9**, 1802766 (2019). https://doi.org/10.1002/aenm.201802766.

[11] M. Sakata, M. Iwaya, T. Takeuchi, S. Kamiyama, I. Akasaki, High photosensitivity AlGaN/GaInN/GaN heterojunction field-effect transistor type visible photosensors. Jpn J Appl Phys. **58**, SCCC22 (2019). https://doi.org/10.7567/1347-4065/ab0f20.

[12] J. Xu, M. Shalom, Conjugated carbon nitride as an emerging luminescent material: quantum dots, thin films and their applications in imaging, sensing, optoelectronic devices and photoelectrochemistry. ChemPhotoChem. **3**, 170-179 (2019). https://doi.org/10.1002/cptc.201800256.

[13] C.B. Ong, L.Y. Ng, A.W. Mohammad, A review of ZnO nanoparticles as solar photocatalysts: synthesis, mechanisms and applications. Renew Sustain Energy Rev. **81**, 536-551 (2018). https://doi.org/10.1016/j.rser.2017.08.020.

[14] Z. Komeily-Nia, M. Montazer, P. Heidarian, B. Nasri-Nasrabadi, Smart photoactive soft materials for environmental cleaning and energy production through incorporation of nanophotocatalyst on polymers and textiles. Polym Adv Technol. **30**, 235-253 (2019). https://doi.org/10.1002/pat.4480.

[15] F.-Q. Zhang, Y. Hu, R.-N. Sun, H. Fu, K.-Q. Peng, Gold-sensitized silicon/ZnO core/shell nanowire array for solar water splitting. Front Chem. **7**, 206 (2019). https://doi.org/10.3389/fchem.2019.00206.

[16] I.J. Peter, S. Dhinakaran, K. Ramachandran, P. Nithiananthi. Performance of TiO_2/CdS/Bi_2S_3 heterostructure based semiconductor sensitized solar cell. in AIP Conference Proceedings. 2019. AIP Publishing. https://doi.org/10.1063/1.5113396.

[17] Z. Guo, X. Ming, G. Wang, B. Hou, X. Liu, T. Mei, J. Li, J. Wang, X. Wang, Super-hydrophilic copper sulfide films as light absorbers for efficient solar steam generation under one sun illumination. J Semicond Sci Technol. **33**, 025008 (2018). https://doi.org/10.1088/1361-6641/aaa323.

[18] P.J. Sellin, Recent advances in compound semiconductor radiation detectors. Nucl Instrum Methods Phys Res. **513**, 332-339 (2003). https://doi.org/10.1016/j.nima.2003.08.058.

[19] S.K. Kurinec, Emerging photovoltaic materials: Silicon and beyond, (John Wiley and Sons. New Jersey2018).

[20] Q. Xiang, J. Yu, M. Jaroniec, Synergetic effect of MoS_2 and graphene as cocatalysts for enhanced photocatalytic H_2 production activity of TiO_2 nanoparticles. J Am Chem Soc. **134**, 6575-6578 (2012). https://doi.org/10.1021/ja302846n.

[21] G. Gautier, Micro fuel cells based on silicon materials, in Portable hydrogen energy systems. 2018, Elsevier: Cambridge. p. 107-123.

[22] N. Patni, P. Sharma, S.G. Pillai, Newer approach of using alternatives to (indium doped) metal electrodes, dyes and electrolytes in dye sensitized solar cell. Mater Res Express. **5**, 045509 (2018). https://doi.org/10.1088/2053-1591/aaad37.

[23] A. Hartwig, Cadmium and its impact on genomic stability, in Cadmium Interaction with Animal Cells. 2018, Springer: Cham. p. 107-125.

[24] Z. Wang, M. Murugananthan, Y. Zhang, Graphitic carbon nitride based photocatalysis for redox conversion of arsenic (III) and chromium (VI) in acid aqueous solution. Appl Catal B Environ. **248**, 349-356 (2019). https://doi.org/10.1016/j.apcatb.2019.02.041.

[25] D. Zhang, Y. Guo, Z. Zhao, Porous defect-modified graphitic carbon nitride via a facile one-step approach with significantly enhanced photocatalytic hydrogen evolution under visible light irradiation. Appl Catal B Environ. **226**, 1-9 (2018). https://doi.org/10.1016/j.apcatb.2017.12.044.

[26] P. Niu, M. Qiao, Y. Li, L. Huang, T. Zhai, Distinctive defects engineering in graphitic carbon nitride for greatly extended visible light photocatalytic hydrogen evolution. Nano Energy. **44**, 73-81 (2018). https://doi.org/10.1016/j.nanoen.2017.11.059.

[27] N. Tian, H. Huang, X. Du, F. Dong, Y. Zhang, Rational nanostructure design of graphitic carbon nitride for photocatalytic applications. J Mater Chem A. **7**, 11584-11612 (2019). https://doi.org/10.1039/C9TA01819K.

[28] Y. Zhou, W. Lv, B. Zhu, F. Tong, J. Pan, J. Bai, Q. Zhou, H. Qin, Template-free one-step synthesis of g-C_3N_4 nanosheets with simultaneous porous network and S-doping for remarkable visible-light-driven hydrogen evolution. ACS Sustain Chem Eng. **7**, 5801-5807 (2019). https://doi.org/10.1021/acssuschemeng.8b05374.

[29] L. Cui, Y. Liu, X. Fang, C. Yin, S. Li, D. Sun, S. Kang, Scalable and clean exfoliation of graphitic carbon nitride in NaClO solution: Enriched surface active sites for enhanced photocatalytic H_2 evolution. Green Chem. **20**, 1354-1361 (2018). https://doi.org/10.1039/C7GC03704J.

[30] M. Mousavi, A. Habibi-Yangjeh, M. Abitorabi, Fabrication of novel magnetically separable nanocomposites using graphitic carbon nitride, silver phosphate and silver chloride and their applications in photocatalytic removal of different pollutants using visible-light irradiation. J Colloid Interface Sci. **480**, 218-231 (2016). https://doi.org/10.1016/j.jcis.2016.07.021.

[31] G. Liao, Y. Gong, L. Zhang, H. Gao, G.-J. Yang, B. Fang, Semiconductor polymeric graphitic carbon nitride photocatalysts: The "holy grail" for the photocatalytic hydrogen evolution reaction under visible light. Energy Environ Sci. **12**, 2080-2147 (2019). https://doi.org/10.1039/C9EE00717B.

[32] J. Tian, Q. Liu, C. Ge, Z. Xing, A.M. Asiri, A.O. Al-Youbi, X. Sun, Ultrathin graphitic carbon nitride nanosheets: A low-cost, green, and highly efficient electrocatalyst toward the reduction of hydrogen peroxide and its glucose biosensing application. Nanoscale. **5**, 8921-8924 (2013). https://doi.org/10.1039/C3NR02031B.

[33] S.P. Pattnaik, A. Behera, S. Martha, R. Acharya, K. Parida, Facile synthesis of exfoliated graphitic carbon nitride for photocatalytic degradation of ciprofloxacin under solar irradiation. J Mater Sci. **54**, 5726-5742 (2019). https://doi.org/10.1007/s10853-018-03266-x.

[34] H. Wang, L. Fang, S. Hu, Y. Pei, W. Ma, A green and facile method to prepare graphitic carbon nitride nanosheets with outstanding photocatalytic H_2O_2 production ability via NaClO hydrothermal treatment. New J Chem. **42**, 18335-18341 (2018). https://doi.org/10.1039/C8NJ03044H.

[35] S. Yang, Y. Gong, J. Zhang, L. Zhan, L. Ma, Z. Fang, R. Vajtai, X. Wang, P.M. Ajayan, Exfoliated graphitic carbon nitride nanosheets as efficient catalysts for

hydrogen evolution under visible light. Adv Mater. **25**, 2452-2456 (2013). https://doi.org/10.1002/adma.201204453.

[36] J. Ran, T.Y. Ma, G. Gao, X.-W. Du, S.Z. Qiao, Porous P-doped graphitic carbon nitride nanosheets for synergistically enhanced visible-light photocatalytic H_2 production. Energy Environ Sci. **8**, 3708-3717 (2015). https://doi.org/10.1039/C5EE02650D.

[37] J. Yan, X. Han, X. Zheng, J. Qian, J. Liu, X. Dong, F. Xi, One-step template/chemical blowing route to synthesize flake-like porous carbon nitride photocatalyst. Mater Res Bull. **94**, 423-427 (2017). https://doi.org/10.1016/j.materresbull.2017.06.022.

[38] Y. Wang, H. Cai, F. Qian, Y. Li, J. Yu, X. Yang, M. Bao, X. Li, Facile one-step synthesis of onion-like carbon modified ultrathin g-C_3N_4 2D nanosheets with enhanced visible-light photocatalytic performance. J Colloid Interface Sci. **533**, 47-58 (2019). https://doi.org/10.1016/j.jcis.2018.08.039.

[39] A. Hatamie, F. Marahel, A. Sharifat, Green synthesis of graphitic carbon nitride nanosheet (g-C_3N_4) and using it as a label-free fluorosensor for detection of metronidazole via quenching of the fluorescence. Talanta. **176**, 518-525 (2018). https://doi.org/10.1016/j.talanta.2017.08.059.

[40] W. Iqbal, B. Qiu, Q. Zhu, M. Xing, J. Zhang, Self-modified breaking hydrogen bonds to highly crystalline graphitic carbon nitrides nanosheets for drastically enhanced hydrogen production. Appl Catal B Environ. **232**, 306-313 (2018). https://doi.org/10.1016/j.apcatb.2018.03.072.

[41] I. Papailias, N. Todorova, T. Giannakopoulou, N. Ioannidis, N. Boukos, C.P. Athanasekou, D. Dimotikali, C. Trapalis, Chemical vs thermal exfoliation of g-C_3N_4 for NO_x removal under visible light irradiation. Appl Catal B Environ. **239**, 16-26 (2018). https://doi.org/10.1016/j.apcatb.2018.07.078.

[42] L. Liang, L. Shi, F. Wang, H. Wang, P. Yan, Y. Cong, L. Yao, Z. Yang, W. Qi, g-C_3N_4 nano-fragments as highly efficient hydrogen evolution photocatalysts: Boosting effect of nitrogen vacancy. Appl catal A-Gen. **599**, 117618 (2020). https://doi.org/10.1016/j.apcata.2020.117618.

[43] H. Liu, S. Ma, L. Shao, H. Liu, Q. Gao, B. Li, H. Fu, S. Fu, H. Ye, F. Zhao, J. Zhou, Defective engineering in graphitic carbon nitride nanosheet for efficient photocatalytic pathogenic bacteria disinfection. Appl catal B-environ. **261**, 118201 (2020). https://doi.org/10.1016/j.apcatb.2019.118201.

[44] L. Liang, L. Shi, F. Wang, L. Yao, Y. Zhang, W. Qi, Synthesis and photo-catalytic activity of porous g-C_3N_4: Promotion effect of nitrogen vacancy in H_2 evolution and pollutant degradation reactions. Int. J. Hydrog. Energy. **44**, 16315-16326 (2019). https://doi.org/10.1016/j.ijhydene.2019.05.001.

[45] L. Shi, F. Wang, J. Sun, The preparation of spherical mesoporous g-C_3N_4 with highly improved photocatalytic performance for H_2 production and rhodamine B degradation. Mater. Res. Bull. **113**, 115-121 (2019). https://doi.org/10.1016/j.materresbull.2019.01.028.

[46] Y.A. Safitri, I.W.A. Indrawan, S. Winarsih, Rhodamine B induces oxidative stress and cervical epithelial cell proliferation in the uterus. Toxicol. Rep. **2**, 1434-1436 (2015). https://doi.org/10.1016/j.toxrep.2015.08.013.

[47] Y. Huang, D. Wang, W. Liu, L. Zheng, Y. Wang, X. Liu, M. Fan, Z. Gong, Rapid screening of rhodamine B in food by hydrogel solid-phase extraction coupled with direct fluorescence detection. Food Chem. **316**, 126378 (2020). https://doi.org/10.1016/j.foodchem.2020.126378.

[48] Z. Zeng, X. Quan, H. Yu, S. Chen, Y. Zhang, H. Zhao, S. Zhang, Carbon nitride with electron storage property: Enhanced exciton dissociation for high-efficient photocatalysis. Appl Catal B Environ. **236**, 99-106 (2018). https://doi.org/10.1016/j.apcatb.2018.05.003.

[49] J. Tian, Q. Liu, A.M. Asiri, A.H. Qusti, A.O. Al-Youbi, X. Sun, Ultrathin graphitic carbon nitride nanosheets: A novel peroxidase mimetic, Fe doping-mediated catalytic performance enhancement and application to rapid, highly sensitive optical detection of glucose. Nanoscale. **5**, 11604-11609 (2013). https://doi.org/10.1039/C3NR03693F.

[50] Y. Huang, Y. Wang, Y. Bi, J. Jin, M.F. Ehsan, M. Fu, T. He, Preparation of 2D hydroxyl-rich carbon nitride nanosheets for photocatalytic reduction of CO_2. RSC Adv. **5**, 33254-33261 (2015). https://doi.org/10.1039/C5RA04227E.

[51] H. Huang, R. Chen, J. Ma, L. Yan, Y. Zhao, Y. Wang, W. Zhang, J. Fan, X. Chen, Graphitic carbon nitride solid nanofilms for selective and recyclable sensing of Cu^{2+} and Ag^{+} in water and serum. ChemComm. **50**, 15415-15418 (2014). https://doi.org/10.1039/C4CC06659F.

[52] Y. Lou, Y. Shi, S. Liu, J. He, Y. Li, L. Tao, L. Zeng, H. Long, Q. Wen, J. Li, Preparation of ultrathin graphitic carbon nitride nanosheet and its application to a tunable multi-wavelength mode-locked fiber laser. Opt Mater. **86**, 382-386 (2018). https://doi.org/10.1016/j.optmat.2018.10.037.

[53] J. Tian, Q. Liu, A.M. Asiri, A.O. Al-Youbi, X. Sun, Ultrathin graphitic carbon nitride nanosheet: A highly efficient fluorosensor for rapid, ultrasensitive detection of Cu^{2+}. Anal chem. **85**, 5595-5599 (2013). https://doi.org/10.1021/ac400924j.

[54] G. Sharma, D.D. Dionysiou, S. Sharma, A. Kumar, H. Ala'a, M. Naushad, F.J. Stadler, Highly efficient Sr/Ce/activated carbon bimetallic nanocomposite for photoinduced degradation of rhodamine B. Catal Today. **335**, 437-451 (2019). https://doi.org/10.1016/j.cattod.2019.03.063.

[55] J. Lu, Y. Wang, J. Huang, L. Cao, J. Li, G. Hai, Z. Bai, One-step synthesis of g-C_3N_4 hierarchical porous structure nanosheets with dramatic ultraviolet light photocatalytic activity. Mater Sci Eng B. **214**, 19-25 (2016). https://doi.org/10.1016/j.mseb.2016.08.003.

[56] M. Kruk, M. Jaroniec, Gas adsorption characterization of ordered organic−inorganic nanocomposite materials. Chem Mater. **13**, 3169-3183 (2001). https://doi.org/10.1021/cm0101069.

[57] A. Hatamie, P. Jalilian, E. Rezvani, A. Kakavand, A. Simchi, Fast and ultra-sensitive voltammetric detection of lead ions by two-dimensional graphitic carbon nitride (g-

C_3N_4) nanolayers as glassy carbon electrode modifier. Measurement. **134**, 679-687 (2019). https://doi.org/10.1016/j.measurement.2018.10.082.

[58] H. Zhao, H. Yu, X. Quan, S. Chen, Y. Zhang, H. Zhao, H. Wang, Fabrication of atomic single layer graphitic-C_3N_4 and its high performance of photocatalytic disinfection under visible light irradiation. Appl Catal B Environ. **152**, 46-50 (2014). https://doi.org/10.1016/j.apcatb.2014.01.023.

[59] R. Li, Y. Ren, P. Zhao, J. Wang, J. Liu, Y. Zhang, Graphitic carbon nitride (g-C_3N_4) nanosheets functionalized composite membrane with self-cleaning and antibacterial performance. J Hazard Mater. **365**, 606-614 (2019). https://doi.org/10.1016/j.jhazmat.2018.11.033.

[60] Y. Yu, Q. Zhou, J. Wang, The ultra-rapid synthesis of 2D graphitic carbon nitride nanosheets via direct microwave heating for field emission. ChemComm. **52**, 3396-3399 (2016). https://doi.org/10.1039/C5CC10258H.

[61] S. Balu, Y.-L. Chen, T.C.K. Yang, J.-N. Chen, S.-W. Chen, Effect of ultrasound-induced hydroxylation and exfoliation on P90–TiO_2/g-C_3N_4 hybrids with enhanced optoelectronic properties for visible-light photocatalysis and electrochemical sensing. Ceram. Int. **46**, 18002-18018 (2020). https://doi.org/10.1016/j.ceramint.2020.04.115.

[62] A.C. Ferrari, J. Robertson, Interpretation of Raman spectra of disordered and amorphous carbon. Phys. Rev. B. **61**, 14095 (2000). https://doi.org/10.1103/PhysRevB.61.14095.

[63] X. Li, J. Zhang, L. Shen, Y. Ma, W. Lei, Q. Cui, G. Zou, Preparation and characterization of graphitic carbon nitride through pyrolysis of melamine. Appl Phys A. **94**, 387-392 (2009). https://doi.org/10.1007/s00339-008-4816-4.

[64] H. Begum, M.S. Ahmed, S. Jeon, New approach for porous chitosan–graphene matrix preparation through enhanced amidation for synergic detection of dopamine and uric acid. ACS Omega. **2**, 3043-3054 (2017). https://doi.org/10.1021/acsomega.7b00331.

[65] Y. Wang, W. Cao, L. Wang, Q. Zhuang, Y. Ni, Electrochemical determination of 2,4,6-trinitrophenol using a hybrid film composed of a copper-based metal organic framework and electroreduced graphene oxide. Microchim Acta. **185**, 315 (2018). https://doi.org/10.1007/s00604-018-2857-8.

[66] J. Xu, L. Zhang, R. Shi, Y. Zhu, Chemical exfoliation of graphitic carbon nitride for efficient heterogeneous photocatalysis. J Mater Chem A. **1**, 14766-14772 (2013). https://doi.org/10.1039/C3TA13188B.

[67] Y. Kang, Y. Yang, L.C. Yin, X. Kang, L. Wang, G. Liu, H.M. Cheng, Selective breaking of hydrogen bonds of layered carbon nitride for visible light photocatalysis. Adv Mater. **28**, 6471-6477 (2016). https://doi.org/10.1002/adma.201601567.

[68] Y. Wang, X. Wang, M. Antonietti, Polymeric graphitic carbon nitride as a heterogeneous organocatalyst:From photochemistry to multipurpose catalysis to sustainable chemistry. Angew Chem. **51**, 68-89 (2012). https://doi.org/10.1002/anie.201101182.

[69] C.R. Dhas, R. Venkatesh, K. Jothivenkatachalam, A. Nithya, B.S. Benjamin, A.M.E. Raj, K. Jeyadheepan, C. Sanjeeviraja, Visible light driven photocatalytic degradation of Rhodamine B and direct red using cobalt oxide nanoparticles. Ceram Int. **41**, 9301-9313 (2015). https://doi.org/10.1016/j.ceramint.2015.03.238.

[70] Y. Zhang, J. Zhou, W. Cai, J. Zhou, Z. Li, Enhanced photocatalytic performance and degradation pathway of Rhodamine B over hierarchical double-shelled zinc nickel oxide hollow sphere heterojunction. Appl Surf Sci. **430**, 549-560 (2018). https://doi.org/10.1016/j.apsusc.2017.06.325.

[71] S. Cao, J. Low, J. Yu, M. Jaroniec, Polymeric photocatalysts based on graphitic carbon nitride. Adv Mater. **27**, 2150-2176 (2015). https://doi.org/10.1002/adma.201500033.

[72] K. Vignesh, M. Kang, Facile synthesis, characterization and recyclable photocatalytic activity of Ag_2WO_4/g-C_3N_4. Mater Sci Eng B. **199**, 30-36 (2015). https://doi.org/10.1016/j.mseb.2015.04.009.

[73] B. Zhu, P. Xia, Y. Li, W. Ho, J. Yu, Fabrication and photocatalytic activity enhanced mechanism of direct Z-scheme g-C_3N_4/Ag_2WO_4 photocatalyst. Appl Surf Sci. **391**, 175-183 (2017). https://doi.org/10.1016/j.apsusc.2016.07.104.

[74] Y. Sun, W. Zhang, T. Xiong, Z. Zhao, F. Dong, R. Wang, W.-K. Ho, Growth of BiOBr nanosheets on C_3N_4 nanosheets to construct two-dimensional nanojunctions with enhanced photoreactivity for NO removal. J Colloid Interface Sci. **418**, 317-323 (2014). https://doi.org/10.1016/j.jcis.2013.12.037.

[75] K. He, J. Xie, M. Li, X. Li, In situ one-pot fabrication of g-C_3N_4 nanosheets/NiS cocatalyst heterojunction with intimate interfaces for efficient visible light photocatalytic H_2 generation. Appl. Surf. Sci. **430**, 208-217 (2018). https://doi.org/10.1016/j.apsusc.2017.08.191.

[76] X. Kang, Y. Kang, X. Hong, Z. Sun, C. Zhen, C. Hu, G. Liu, H. Cheng, Improving the photocatalytic activity of graphitic carbon nitride by thermal treatment in a high-pressure hydrogen atmosphere. Pro Nat Sci-Mater. **28**, 183-188 (2018). https://doi.org/10.1016/j.pnsc.2018.02.006.

[77] X. She, H. Xu, Y. Xu, J. Yan, J. Xia, L. Xu, Y. Song, Y. Jiang, Q. Zhang, H. Li, Exfoliated graphene-like carbon nitride in organic solvents: enhanced photocatalytic activity and highly selective and sensitive sensor for the detection of trace amounts of Cu^{2+}. J. Mater. Chem. A. **2**, 2563-2570 (2014). https://doi.org/10.1039/C3TA13768F.

[78] J. Yan, X. Han, J. Qian, J. Liu, X. Dong, F. Xi, Preparation of 2D graphitic carbon nitride nanosheets by a green exfoliation approach and the enhanced photocatalytic performance. J. Mater. Sci. **52**, 13091-13102 (2017). https://doi.org/10.1007/s10853-017-1419-5.

[79] Q.I. Rahman, M. Ahmad, S.K. Misra, M. Lohani, Effective photocatalytic degradation of rhodamine B dye by ZnO nanoparticles. Mater Lett. **91**, 170-174 (2013). https://doi.org/10.1016/j.matlet.2012.09.044.

[80] T. Wu, G. Liu, J. Zhao, H. Hidaka, N. Serpone, Photoassisted degradation of dye pollutants. V. Self-photosensitized oxidative transformation of rhodamine B under

visible light irradiation in aqueous TiO_2 dispersions. J Phys Chem B. **102**, 5845-5851 (1998). https://doi.org/10.1021/jp980922c.

CHAPTER FIVE

Cadmium sulfide-doped graphitic carbon nitride nanosheets for improved photon harvesting of the active layer in organic solar cells

Nicholas Rono,[a] Joshua K. Kibet,[b] Bice S. Martincigh[a] and Vincent O. Nyamori[a]*

[a]School of Chemistry and Physics, University of KwaZulu-Natal, Westville Campus, Private Bag X54001, Durban, 4000, South Africa

[b]Chemistry Department, Egerton University, Njoro Campus, P.O. Box 536-20115, Egerton, Kenya

*Corresponding author: E-mail: Nyamori@ukzn.ac.za, Tel: +27312608256

Abstract

In the present work, graphitic carbon nitride nanosheets (CNNS) from thermal etching (TE) method of exfoliation of bulk graphitic carbon nitride (B-g-C_3N_4) i.e., CNNS-TE loaded with cadmium sulfide (CdS) nanoparticles were prepared by a facile mechanochemical approach. The as-prepared materials were introduced as a third component in the active layer of bulk heterojunction organic solar cells (BHJ-OSCs) to enhance light-harvesting properties and induce better separation and transport mechanisms of photogenerated charges. The active layer of the pristine (undoped) device was composed of poly(3-hexylthiophene) (P3HT) and [6,6]-phenyl-C_{61}-butyric acid methyl ester ($PC_{61}BM$) blends. With the incorporation of the nanocomposites into the P3HT:$PC_{61}BM$ active layer blends, the best device with 5% CdS/CNNS-TE exhibited a power conversion efficiency (PCE) of 2.21%, which was a 50% power conversion enhancement compared with the pristine device. The augmented PCE was attributed to better light absorption, faster transport, and suppressed recombination of photogenerated charges in the doped active layer. These impressive attributes resulted from the formation of a heterostructure between CdS and CNNS-TE with effective charge transfer characteristics. The results of this work will provide an efficient way of improving the performance of organic solar cells (OSCs) and lead to potential commercialisation.

Keywords: Power conversion efficiency; OSC; photoactive layer; graphitic carbon nitride; thermal etching

5.1 Introduction

Solar energy harvesting and its utilisation have recently gained significant scientific attention since this form of energy is inexhaustible and clean [1, 2]. Photovoltaic devices, such as solar cells, convert radiant energy to electric energy via a photovoltaic process [3]. Recently, bulk heterojunction (BHJ) organic solar cells (OSCs) have emerged as attractive device designs in OSCs [4, 5]. This is because they offer a large interfacial area between the donor and acceptor materials, thus reducing the rate of recombination of photogenerated charges and improving charge transport mechanisms [6, 7]. The power conversion efficiency (PCE) has been gradually enhanced to above 18% for solution-processable BHJ-OSCs due to suppressed recombination rates of photogenerated charges using materials with better charge transport characteristics [8, 9].

In a BHJ-OSC, the photoactive layer (absorber layer) is a crucial component of the cell because it absorbs light, and the excitons are generated and separated [10, 11]. Polymer-fullerenes blends, such as poly(3-hexylthiophene) (P3HT) and [6,6]-phenyl C_{61}-butyric acid methyl ester ($PC_{61}BM$), have mainly been used as active layer materials [12]. Although they show promising performance, they suffer from poor stability [13], high recombination of photogenerated charges (due to short diffusion lengths) [14], and ineffective light-harvesting ability [15]. Therefore, modification of an effective active layer is essential for enhancing the performance of devices. Introducing a third component into a donor-acceptor active layer has become an important strategy for boosting the performance of OSCs [16, 17]. Essentially, including a third component can lead to improved chemical and thermal stability, better light absorption, and suppressed intrinsic and interfacial recombination of excitons of the photoactive layer.

Graphitic carbon nitride (g-C_3N_4) has emerged as a promising semiconductor material to be incorporated into OSCs devices [18]. This is because the g-C_3N_4 semiconductor has a tuneable band gap of 2.7 eV, better light absorption, and a metal-free nature, and thus, is crucial in solar harvesting applications [19, 20]. Presently, several modification strategies have been employed on the g-C_3N_4 material in order to optimise its properties. These include exfoliation of bulk g-C_3N_4 to nanosheets, transformation into various morphologies such as nanorods, nanosheets, quantum dots, nanotubes, nanowires, and 3D-g-C_3N_4, doping with metals or non-metals (Ag, Cu, N, B), and coupling with other

materials such as carbonaceous materials (graphene, activated carbon) and semiconductors (CdS, ZnO, WO_3 and TiO_2, and BP) [21]. These modifications, especially the formation of heterostructures, have reduced the rate of recombination of electron-hole pairs and enhanced charge transfer characteristics [22]. Recently, Pareek et al. [23] introduced graphitic carbon nitride quantum dots (g-C_3N_4 QDs) into the active layer of OSCs with a P3HT:PC_{71}BM blend. The doped device exhibited a performance of 40% better than the pristine device. This was attributed to Förster resonance energy transfer (FRET) between the active polymer blends and g-C_3N_4 QDs, which led to the improved light-harvesting ability of the device. Chen et al. [18] investigated the effect of g-C_3N_4 QDs on the performance of OSCs. The devices with g-C_3N_4 QDs in the active layer as dopants performed better than the undoped devices. For example, a device with a poly(3-hexylthiophene-2,5-diyl):[6,6]-phenyl-C_{61}-butyric acid methyl ester (P3HT:PC_{61}BM) active layer achieved a PCE of 4.23% which represented a 17.5% enhancement compared with the undoped device.

Meanwhile, Soh et al. [24] modified the TiO_2 electron transport layer (ETL) by doping it with g-C_3N_4/Ag nanocomposites. Remarkably, the resultant device with the modified ETL exhibited a 30% PCE enhancement relative to the pristine device because of improved charge extraction, smooth surface, and thus the better interface between the absorber and the ETL, effective electron extraction, and suppressed recombination of photogenerated charges. Notably, it is important to note that only a few works have reported the incorporation of g-C_3N_4 or its composites in the active layer of OSCs. Therefore, it is necessary to explore more potential applications of g-C_3N_4-based nanomaterials in OSCs so as to enhance the PCE for commercialisation.

Herein, cadmium sulfide/graphitic carbon nitride nanosheets (CdS/CNNS-TE) nanocomposites were synthesised by a facile mechanochemical approach and introduced into the active layer (with P3HT:PC_{61}BM blends) of OSCs as a third component. Various devices with as-prepared samples were fabricated and tested under AM 1.5 solar illumination. For comparison, a pristine device with only P3HT:PC_{61}BM blend in the active layer was also fabricated. The effect of dopants on the photovoltaic performance of the OSCs was critically examined. Additionally, the optical properties of the fabricated devices were also investigated.

5.2 Experimental

The chemical, materials, and characterisation of the prepared samples are presented and discussed in this section.

5.2.1 Materials and chemicals

Melamine (99%) (CAS No. 99 108-78-1), cadmium nitrate tetrahydrate ($Cd(NO_3)_2.4H_2O$ (98%) (CAS No. 10022-68-1), sodium sulfide (Na_2S) (≥98.0%) (CAS No. 1313-82-2), lithium fluoride (LiF) (≥99.98%) (CAS No. 7789-24-4), poly-(3-hexylthiophene) (P3HT) (99%) (CAS No. 1693-86-3), poly-(3,4-ethylene dioxythiophene):poly-(styrene-sulfonate) (PEDOT:PSS) (99%) (CAS No. 155090-83-8), [6,6]-phenyl-C_{61}-butyric acid methyl ester ($PC_{61}BM$) (>99.5%) (CAS No. 160848-22-6), dichloromethane (DCM) (≥99.8%) (CAS No. 75-09-2), chloroform (≥99%) (CAS No. 67-66-3), ethanol (95.0%) (CAS No. 64-17-5), nitric acid (≥65%) (CAS No. 7697-37-2), potassium ferricyanide (99%) (CAS No. 13746-66-2), hydrochloric acid (37%) (CAS No. 7647-01-0) and indium tin oxide (ITO) (CAS No. 50926-11-9) glass substrates (surface resistivity 8-12 Ω sq^{-1}) were purchased from Sigma Aldrich (South Africa). All the chemicals were of analytical grade and were used without further treatment. Deionised water was from a Millipore Milli-Q Elix 5 UV water purification system with a resistivity of 18.2 MΩ cm at 20 °C.

5.2.2 Synthesis of bulk graphitic carbon nitride

Bulk g-C_3N_4 was synthesised by conventional polycondensation of melamine. Melamine (10 g) was typically placed in an open ceramic crucible and transferred to a muffle furnace. The contents of the crucible were heated at a rate of 5 °C min^{-1} to 550 °C and maintained for 4 h. After that, it was allowed to cool to room temperature. Bulk g-C_3N_4 was formed as a yellow solid and labelled B-g-C_3N_4. The as-formed B-g-C_3N_4 was ground and kept in sample vials.

5.2.3 Synthesis of g-C_3N_4 nanosheets

A thermal etching method was employed as described by Iqbal et al. [25] but with slight condition modifications. As-prepared B-g-C_3N_4 (0.5 g) was placed in a quartz glass boat. The boat was placed inside a quartz tube in a tube furnace. A stream of nitrogen gas was passed through the reactor for a few minutes to flush the system and ensure inertness.

The sample was then heated to a temperature of 600 °C (at a rate of 10 °C min^{-1}) and maintained for 2 h. Subsequently, the reactor was left to cool naturally under a flow of nitrogen to room temperature, after which the gas flow was discontinued. A brown-yellow product (g-C_3N_4 nanosheets) was obtained and denoted CNNS-TE.

5.2.4 Synthesis of cadmium sulfide nanoparticles

Cadmium sulfide (CdS) nanoparticles were synthesised by a chemical precipitation method [26] using equimolar solutions of cadmium nitrate and sodium sulfide as precursors. In the synthesis process, 100 ml of 0.1 M of sodium sulfide solution was added dropwise to 100 ml of 0.1 M cadmium nitrate solution in a beaker with continuous stirring. The gradual colour transition of the reaction mixture was from pale yellow to deep yellow after the completion of the reaction. The yellow precipitate formed was washed severally by centrifugation with distilled water and absolute ethanol consecutively, followed by oven-drying at a temperature of 90 °C for 5 h.

5.2.5 Synthesis of CdS/CNNS-TE heterostructure

The 5% CdS/CNNS-TE heterostructure was prepared by a facile mechanochemical approach. Typically, CdS (0.005 g) and CNNS-TE (0.095 g) powders were mixed homogenously in an agar mortar. The mixture was dispersed in deionised water and sonicated for 1 hour in an ultrasonic bath. After which, the dispersion was oven-dried overnight at a temperature of 90 °C before characterisation. A similar process was performed to obtain CdS/CNNS-TE ratios of 10% and 20%. For comparison, CdS and CNNS-TE were used as-prepared.

5.2.6 Characterisation of the photoactive materials

The structure and morphology of the photoactive materials and spin-coated substrates were investigated with scanning electron microscopy (SEM, Carl Zeiss Ultra Plus) fitted with an EDS (Oxford X-max) detector and a high-resolution transmission electron microscope (TEM, JEOL, JEM 1010) operating at both standard and high resolution (HRTEM) modes at 200 KV. The crystal structure analysis of the samples was conducted with a BRUKER AXS D8 Advance powder X-ray diffractometer with Cu-Kα radiation (λ = 1.5406 Å) at 40 kV and 40 mA. UV–Vis diffuse reflectance spectra (UV-DRS) were

recorded with a PerkinElmer Lambda 35 UV–visible spectrophotometer fitted with a Labsphere integrating sphere. The photoluminescence spectra (PL) of the samples were recorded with a PerkinElmer LS 55 spectrofluorometer at an excitation wavelength of 325 nm. The chemical structure was investigated using a PerkinElmer Spectrum 100 Fourier transform infrared (FTIR) spectrometer fitted with an attenuated total reflectance (ATR) sampling accessory. The thermal stability of the samples was determined with a TA Instruments Q series thermal analyser (Q600) in air. The elemental composition of the samples was determined using energy-dispersive X-ray (SEM-EDX) spectroscopy. For the samples containing cadmium, a PerkinElmer Optima 5300 DV inductively coupled plasma-optical emission spectrometer (ICP-OES) was used to quantify the cadmium content present in the samples. A Shimadzu UV-3600 double-beam UV-Vis-NIR spectrophotometer was used to record the optical absorption and transmittance spectra of the samples and fabricated devices. Electrochemical impedance spectroscopy (EIS) and Mott–Schottky measurements were performed with a three-electrode cell containing a - working, reference, and counter electrodes using a CHI 660E electrochemical workstation. Basically, the counter electrode was a platinum wire, while the reference electrode was an electrode with Ag/AgCl solution, and the working electrode was a modified glassy carbon electrode (GCE). The electrolyte used in the experiment was 1M KCl.

5.2.7 Fabrication of organic solar cells and their characterisation

The organic solar cell with the following configuration: ITO/PEDOT:PSS/P3HT:$PC_{61}BM$ or doped-P3HT:$PC_{61}BM$/LiF/Al (Figure 5.1) was fabricated under ambient conditions under 35% humidity. Typically, ITO glass with surface resistivity of 15 Ω sq^{-1} with dimensions 30 mm × 30 mm was masked halfway with a tape, and the exposed part was etched with a hot mixture of conc. hydrochloric acid, conc. nitric acid, and water at respective volume concentration ratios of 48%:48%:4%. The etched substrate was ultrasonically and consecutively cleaned with deionised water, acetone, and isopropanol for 10 minutes, then dried in a furnace for 20 minutes at a temperature of 120 °C. The PEDOT:PSS precursor solution (20 mg in 100 mL DCM) was spin-coated on the cleaned and dry substrate at 3500 rpm for 30 seconds before drying again in an oven at a temperature of 120 °C for 20 minutes. The absorber

layer precursor solution was made by mixing P3HT and $PC_{61}BM$ in a ratio of 1:1 in 500 µL chloroform for the pristine device. For other devices with dopant materials, 1% by mass of each material, i.e., CdS, 5% CdS/CNNS-TE, 10% CdS/CNNS-TE, 20% CdS/CNNS-TE, and CNNS-TE were added to the P3HT:$PC_{61}BM$ mixture and 500 µL DCM was added and magnetically stirred at a temperature of 40 °C for 3 hours to ascertain that the material mixes well with P3HT:$PC_{61}BM$. The respective precursor solutions were spin-coated on the annealed PEDOT:PSS layer at a rate of 1200 rpm for 40 seconds and annealed under nitrogen at a temperature of 120 °C for 10 minutes. The device was covered judiciously and transferred to a deposition chamber, where the electron transport layer was deposited on the metal back contact. A lithium fluoride (LiF) electron transport layer with a thickness of 0.5 nm, and an aluminium layer of 100 nm, was deposited at a pressure of 10^{-6} mbar. Lastly, the device was immediately annealed under nitrogen gas in a tube furnace for 5 minutes. The device performance measurement was carried out using a Keithley (HP2420) source meter with an AM 1.5 global solar simulator (model SS50AAA), with illumination light intensity kept at 100 mW cm^{-2}. The measured effective area of the devices was 0.02 cm^2.

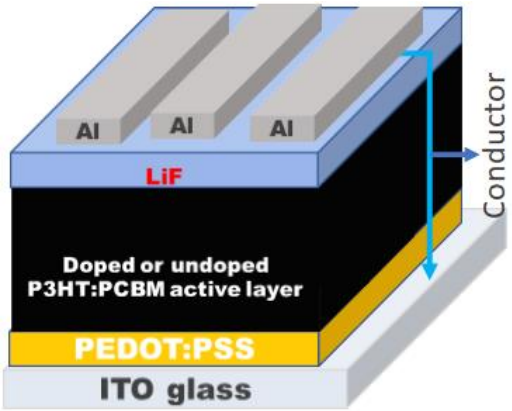

Figure 5.1: Basic structure of the device under investigation

5.3 Results and discussion

CdS/CNNS samples were prepared and characterised using various techniques and later incorporated into the active layer of an OSC

5.3.1 Material characterisation

5.3.1.1 Surface morphology and microstructure

The surface morphology and microstructure of the as-prepared samples were examined with scanning electron microscopy (SEM) and transmission electron microscopy (TEM). The acquired images are presented in Figures 5.2 and 5.3, and also in Supporting Information Figures S5.1 and S5.2. The SEM image of CNNS-TE exhibits a porous structure with disordered sheet-like structures (Figure 5.2a). The porous structure formation could be because the weak van der Waals forces of attraction between the layers were broken during the thermal etching process, and defects were introduced in the layers of the g-C_3N_4 material. From Figure 5.2b, 5% CdS/CNNS-TE showed coarse particles of dimensions ranging between 40 and 50 nm on porous sheets. Also, the SEM images of 10% CdS/CNNS-TE (Figure S5.1 (a)) and 20% CdS/CNNS-TE (Figure S5.1 (b)) showed small, agglomerated particles on porous sheets and these were very conspicuous in 20% CdS/CNNS-TE, implying that CdS nanoparticles were deposited on the CNNS-TE layers. Moreover, as depicted in Figure 5.2c, the CdS showed flake-like particles with a relatively rough morphology.

Figure 5.3 shows the TEM images of the samples. CNNS-TE (Figure 5.3a) clearly portrayed layers comprising a few transparent sheets stacked on each other, suggesting that bulk g-C_3N_4 material was successfully exfoliated to sheets during the thermal etching process. Meanwhile, from Figure 5.3b, a 5% CdS/CNNS-TE sample showed agglomerated particles (5-10 nm) which were randomly anchored on CNNS-TE sheets. Additionally, for both 10% CdS/CNNS-TE (Figure 5.S2 (e)) and 20% CdS/CNNS-TE (Figure S5.2 (f)) samples, the CdS nanoparticles were anchored on the CNNS-sheets, indicating a strong interaction between the CdS nanoparticles and CNNS-TE nanosheets. Figure 5.3c revealed evenly dispersed spherical CdS nanoparticles (5-10 nm) occasioned by agglomeration. To further investigate the microstructure of as-prepared samples, the interlayer spacings, i.e., the d-spacings, were explored from high-resolution transmission electron microscopy (HRTEM), and the images are presented in Figure 5.3 (d) and (f) and Figures S5.1 (c) and (d). The measured d-spacings were: 0.344, 0.338, 0.334, and 0.338 nm for 5% CdS/CNNS-TE, 10% CdS/CNNS-TE, 20% CdS/CNNS-TE and CdS samples, respectively. The estimated d-spacing of about 0.34 nm of CdS-based samples

obtained here corresponds to the peak at 2θ = 26.48° measured from powder XRD and represents the (111) crystal plane (see Section 5.3.1.2). Notably, the CNNS-TE material in Figure 5.3d did not show any lattice fringes, indicating that the material could be amorphous rather than crystalline; thus, lattice fringes were diffuse. Since there was no diffraction pattern formation in the CNNS-TE sample, the observed d-spacing in the composites can only be attributed to the presence of CdS nanoparticles.

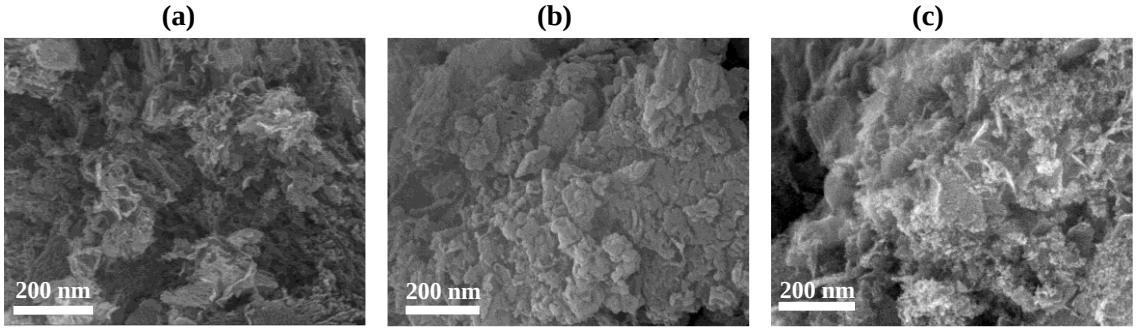

Figure 5.2: SEM images of (a) CNNS-TE, (b) 5% CdS/CNNS-TE and (c) CdS samples

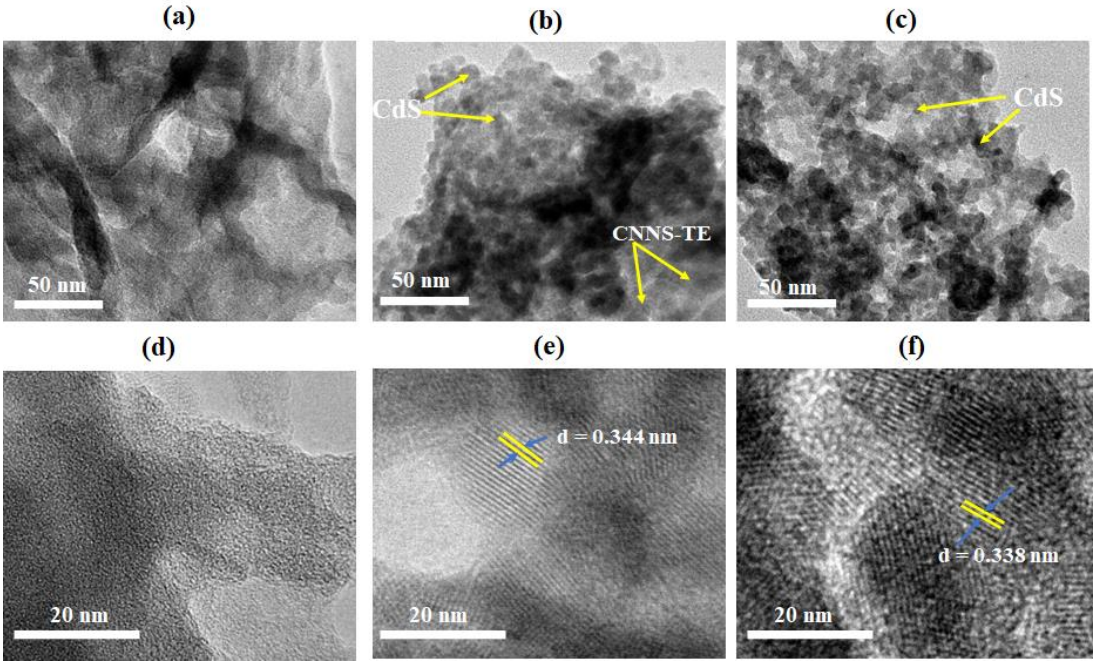

Figure 5.3: TEM images of (a) CNNS-TE, (b) 5% CdS/CNNS-TE and (c) CdS samples, and HRTEM images of (d) CNNS-TE, (e) 5% CdS/CNNS-TE and (f) CdS samples

5.3.1.2 Crystal structure

Figure 5.4a shows the powder X-ray diffractograms for as-prepared samples. As depicted in Figure 5.4a, the pristine CNNS-TE sample showed a different XRD pattern from the

samples with CdS nanoparticles, indicating that it has a unique basic structure. For the CNNS-TE sample, two intense peaks at 2θ = 13.2° and 27.3° are observed and correspond to the (001) and (002) crystal planes of g-C_3N_4, respectively. In essence, the strong peak at 2θ = 13.2° with interlayer spacing d = 0.337 nm is attributed to the in-plane structural stacking motif of heptazine tectonic units (tri-s-triazine units), whereas the peak at 27.3° with interplanar spacing d = 0.168 nm is attributed to the interlayer stacking of aromatic rings in the samples. The diffraction pattern related to CdS samples exhibited peaks at 2θ = 23.40, 26.48, 30.24, 36.24, 43.68, 49.82, and 50.08°, corresponding to the (100), (111), (020), (102), (202), (103), (112), and (311) planes of CdS. The CdS-based diffractograms match the cubic crystal structure of the CdS (Hawleyite) phase, with JCPDS number: 96-101-126 and space group F-4 3m [27]. With the incorporation of CdS dopants into the CNNS-TE material, the peak intensity at 27° decreased and shifted to a lower 2θ angle of about 26.48 (Figure 5.4a). Similarly, by considering pure CdS samples, there was a shift in position for the peak centred 2θ = 26.48° to 26.8, 26.38, and 26.56° for 5% CdS/CNNS-TE, 10% CdS/CNNS-TE and 20% CdS/CNNS-TE, respectively. The shift could be attributed to the formation of a composite material.

To further confirm the crystal structure of as-prepared samples, the selected area electron diffraction (SAED) micrographs were obtained from high-resolution transmission electron microscopy (HRTEM) analysis (Figure 5.4b and Figures S5.2 (a) and (b)). As depicted in Figure 5.4b (i), the CNNS-TE sample showed an amorphous diffraction pattern, i.e., a diffuse, continuous disc shape without any discernible spots or rings. These results confirm the absence of lattice fringes witnessed in Figure 5.3d.

Figures 5.4b (ii) and (iii) of the 5% CdS/CNNS-TE and CdS samples, respectively, exhibited the crystalline structure of a material in powder form since the dots around the rings were observed in the SAED micrographs. Similar observations were also made in Figure S5.2 (a) and (b) for 10% CdS/CNNS-TE and 20% CdS/CNNS-TE, respectively. The spots in 5% CdS/CNNS-TE samples were few compared with the other CdS-based samples (see Figure 5.4b (ii) and (iii) and Figure S5.2 (a) and (b)), implying that 10% CdS/CNNS-TE, 20% CdS/CNNS-TE, and CdS, respectively, were more crystalline than 5% CdS/CNNS-TE. Generally, the crystallinity in the samples was due to the presence of the CdS dopants and could aid photo-driven reactions.

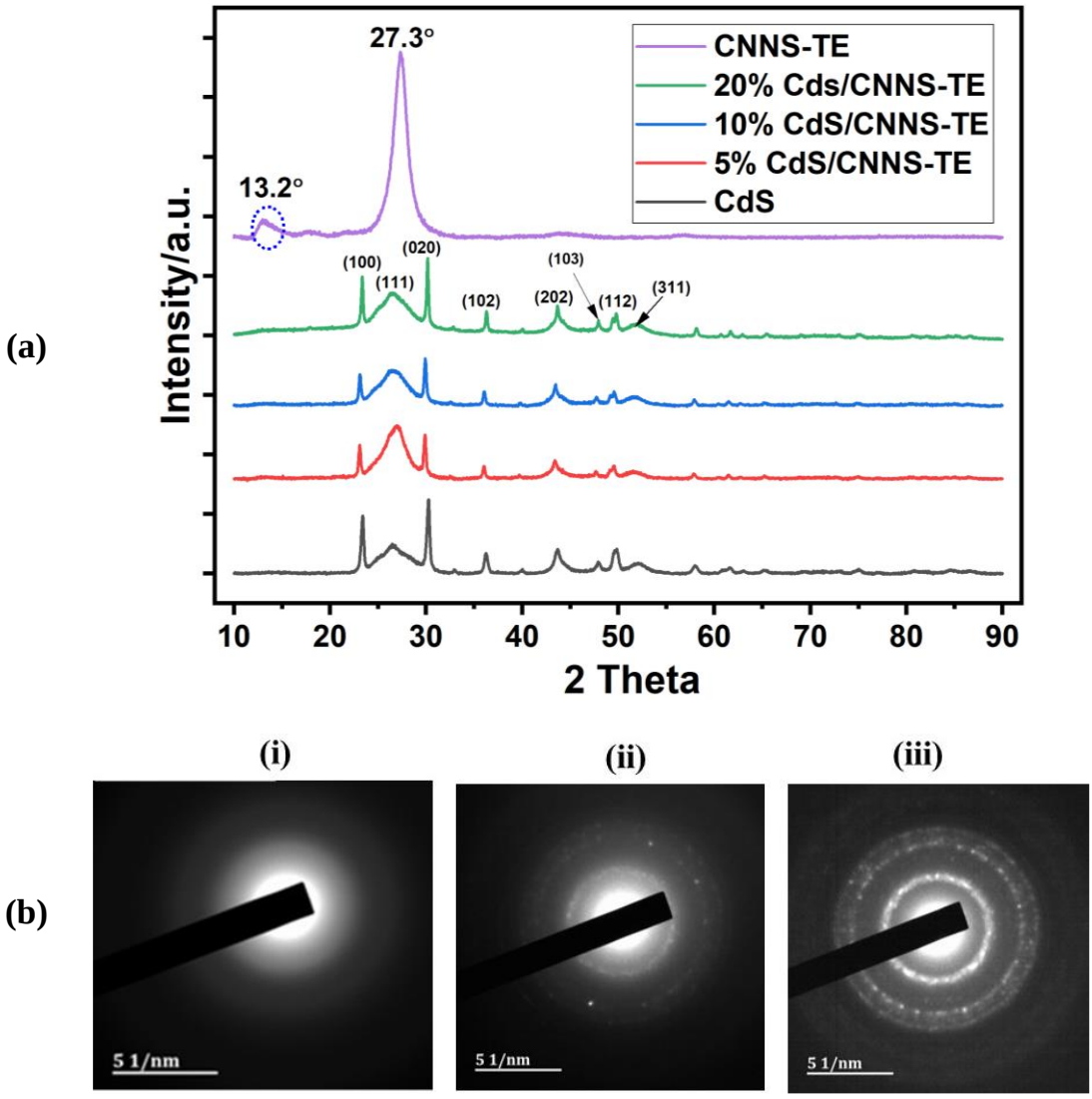

Figure 5.4: (a) Powder X-ray diffractograms for pure CdS, CNNS-TE, and CdS/CNNS-TE composites. (b) Selected area diffraction (SAED) patterns of (i) CNNS-TE, (ii) 5% CdS/CNNS-TE and (iii) CdS samples

5.3.1.3 Chemical structure

Fourier transform infrared spectroscopy (FTIR) was carried out to identify the chemical structures in the as-prepared samples, and the spectra are shown in Figure 5.5. For CNNS-TE and CdS/CNNS-TE nanocomposite samples, the peaks at around 3639-2540 cm^{-1} are assigned to N-H or hydroxyl group stretching vibrations, indicating that some NH_2 groups and also adsorbed surface water may be present in the samples. The conspicuous peak at 2173 cm^{-1} could represent the presence of the cyano group (-C≡N), and the bands at around 1681-938 cm^{-1} are assigned to the presence of C-N or C=N

heterocycles in samples. It can be observed that the number of bands was reduced in the CdS/CNNS-TE samples when compared with the undoped CNNS-TE.

This implies that the basic structure of CNNS-TE was slightly changed when forming composites with CdS, whilst the common band at 802 cm^{-1} was assigned to the breathing modes of triazine units in samples with CNNS-TE. For the CdS sample, the peaks in the fingerprint region, i.e., 632 and 424 cm^{-1}, can be attributed to the Cd-S bond stretching vibration. These bands in the fingerprint region were missing for the CNNS-TE and CdS/CNNS-TE nanocomposites, possibly due to the low CdS loading.

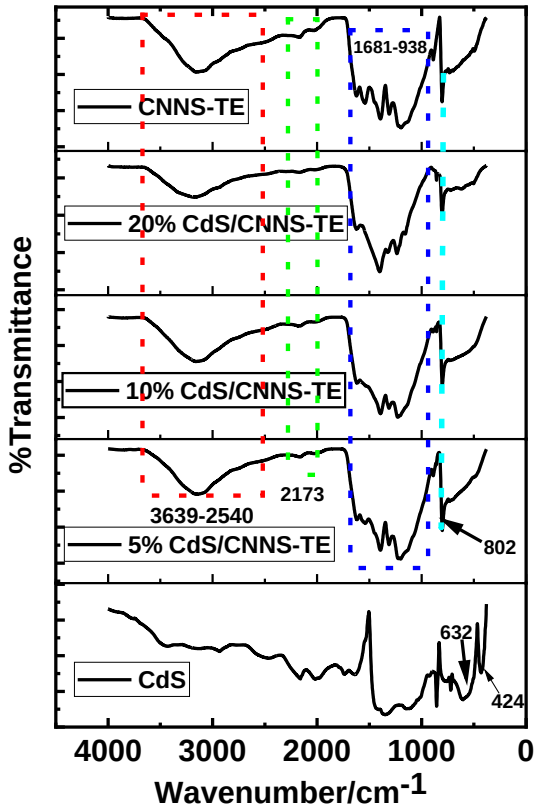

Figure 5.5: ATR-FTIR spectra for CdS, 5% CdS/CNNS-TE, 10% CdS/CNNS-TE, 20% CdS/CNNS-TE, and CNNS-TE samples

5.3.1.4 Elemental composition

The elemental composition of the samples was elucidated by scanning electron microscopy-energy dispersive X-ray analysis (SEM-EDX) (Table 5.1). The nanocomposite samples showed that nitrogen, oxygen, carbon, sulfur, and cadmium were present in their respective proportions. Additionally, for samples with Cd present, inductively coupled plasma-optical emission spectrometry (ICP-OES) analysis was

further carried out (see Table 5.1). The amount of Cd measured from ICP-OES in the samples was related to the proportions of the initial precursor ratios but appreciably higher than the amount determined from SEM-EDX. The difference in the amount of Cd from the two approaches could be ascribed to the fact that SEM-EDX only acquires data from a small section of the sample, but ICP-OES determines the bulk composition of the sample and, thus, is more representative. To further confirm the distribution of elements in the samples, SEM-EDX mapping was carried out. Figures 5.6 (a)-(c) and Figures S5.2 (c) and (d) show that expected elements in CNNS, 5% CdS/CNNS-TE, 10% CdS/CNNS-TE, 20% CdS/CNNS-TE and CdS samples were present and evenly distributed.

Table 5.1: Elemental composition of as-prepared samples

Sample	C/%	N/%	O/%	S/%	Cd/%	Cd*/%
CdS	-	-	-	14.74	85.26	86.34
5% CdS/CNNS-TE	42.28	48.98	3.81	0.79	4.14	16.04
10% CdS/CNNS-TE	35.24	45.54	4.83	2.10	12.28	51.39
20% CdS/CNNS-TE	21.98	21.09	4.98	7.23	44.71	61.56
CNNS-TE	46.94	46.89	6.19	-	-	-

*Weight percentage of Cd from ICP-OES analysis

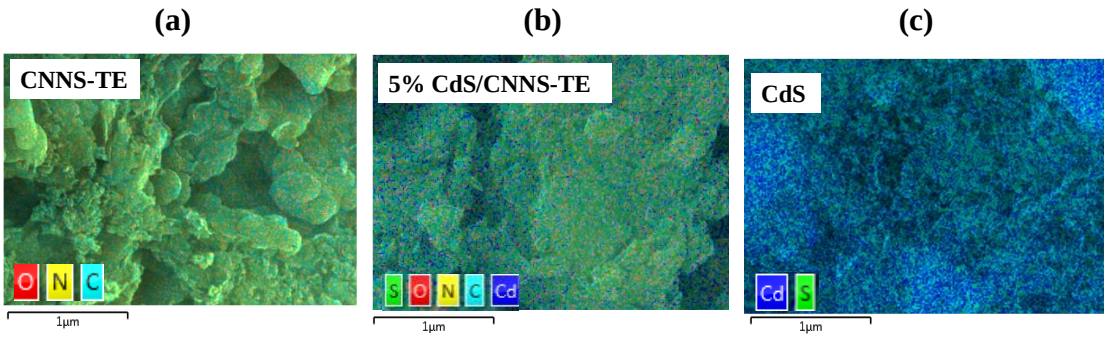

Figure 5.6: The elemental distribution maps for as-prepared (a) CNNS-TE, (b) 5% CdS/CNNS-TE and (c) CdS materials obtained from energy dispersive X-ray spectroscopy

5.3.1.5 Charge transfer characteristics

Electrochemical impedance spectroscopy (EIS) was carried out to understand the charge transfer characteristics of the prepared samples. Figure 5.7 shows the Nyquist plots and the equivalent circuit (inset) of the modified electrodes with the as-prepared samples. The charge transfer at the high-frequency region was due to the electron transfer limiting process since the curve presents a semi-circular-shaped part. Furthermore, the charge transfer at the lower frequency region was a diffusion-controlled process since the curve was linear in this region [28]. The CNNS-TE sample shows the biggest semi-circle, implying that electron transfer was ineffective in this electrode compared with the CdS and CdS/CNNS-TE composites. Furthermore, equivalent circuits were simulated, and the electrochemical parameters were extracted, as shown in Table 5.2. Basically, the lower the charge transfer resistance (R_{ct}), the better the electrode in terms of charge transfer mechanisms. From Table 5.2, the CNNS-TE sample gave the highest R_{ct} value of 128.4 Ω, supporting the already observed biggest semi-circle in the Nyquist plot (see Figure 5.7). Generally, this value significantly reduced from 128.4 to 0.001 Ω when CdS dopants were added; this can be attributed to an improvement of the charge transfer mechanism due to the formation of CdS/CNNS-TE heterojunctions. From this observation, it could be deduced that CdS particles play a vital role in the electron charge transfer process.

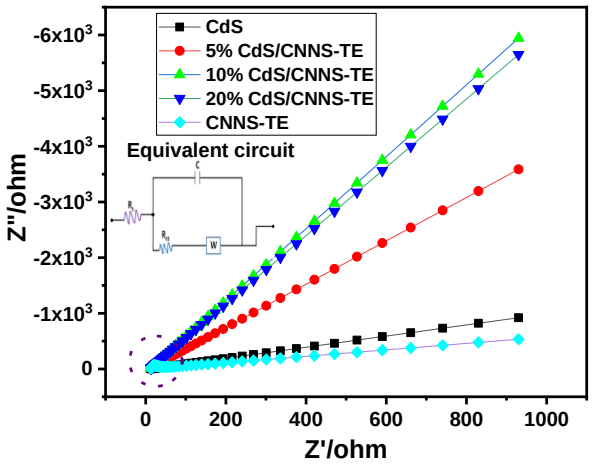

Figure 5.7: Nyquist plots for CdS, 5% CdS/CNNS-TE, 10% CdS/CNNS-TE, 20% CdS/CNNS-TE, and CNNS-TE samples carried out in $Fe(CN)_6^{4-/3-}$ solutions

Table 5.2: The electrochemical parameters of as-prepared samples

Electrode	Solution resistance (Rs)/Ω cm^2	Capacitance (C)/F	R_{ct}/Ω	Warburg (W)/ Ω $s^{-1/2}$
CdS/GCE	9.65	1.00×10^{-12}	0.001	3.06×10^{-4}
5% CdS/CNNS-TE/GCE	5.78	9.85×10^{-8}	122.7	7.87×10^{-5}
10% CdS/CNNS-TE/GCE	2.13	9.31×10^{-8}	17.42	4.75×10^{-5}
20% CdS/CNNS-TE/GCE	2.64	1.07×10^{-3}	0.001	4.99×10^{-5}
CNNS-TE/GCE	5.98	1.91×10^{-7}	128.4	5.29×10^{-4}

GCE is the glassy carbon electrode

5.3.1.6 Thermal stability

The thermal stability of the as-prepared photoactive materials was investigated by thermal analysis under air, and the results are presented in Figure 5.8. Figure 5.8a shows the thermal decomposition profile of the photoactive materials. The slight initial mass loss (about 5%) between 90 and 100 °C could be attributed to the loss of adsorbed water in the sample. As expected, the CdS experienced no mass loss because it is thermally stable up to a temperature greater than 1000 °C, which was not explored during the analysis. The drastic mass loss that occurred at around 390 °C for the other samples (5% CdS/CNNS-TE, 10% CdS/CNNS-TE, 20% CdS/CNNS-TE, and CNNS-TE) could be attributed to the conversion of carbon nitride in the composites to carbon dioxide (CO_2) and nitrogen oxides (NO_x). However, the nanocomposites exhibited different residual mass losses, i.e., the residual masses for 5% CdS/CNNS-TE, 10% CdS/CNNS-TE, and 20% CdS/CNNS-TE were about 16.40, 30.76, and 47.86%, respectively. To further confirm the amount of Cd in the samples, the values of residual masses, i.e., for CdS obtained here, were compared to those reported from ICP-OES measurements (see Table 5.1). Accordingly, the residual mass of 5% CdS/CNNS (16.40%) agrees well with the ICP-OES value of 16.04%; however, deviations were noted for the 10% CdS/CNNS-TE (51.39%) and 20% CdS/CNNS-TE (61.51%) samples. Nevertheless, the increase in residual mass was related to the amount of stable CdS nanoparticles present in the composite, i.e., the more Cd ratio in the sample, the more the residual mass and vice-

versa. Moreover, there was no residual mass in CNNS-TE because it is composed of carbon, nitrogen, and some oxygen; thus, it exhibited complete combustion. Derivative thermograms were plotted to ascertain the specific decomposition temperatures (Figure 5.8b). The specific decomposition temperatures for 5% CdS/CNNS-TE, 10% CdS/CNNS-TE, 20% CdS/CNNS-TE, and CNNS-TE were 609, 598, 570, and 614 °C, respectively. Generally, the as-prepared nanocomposites were stable below 570 °C and can, therefore, be stable at similar elevated temperature regimes, such as in solar cell devices.

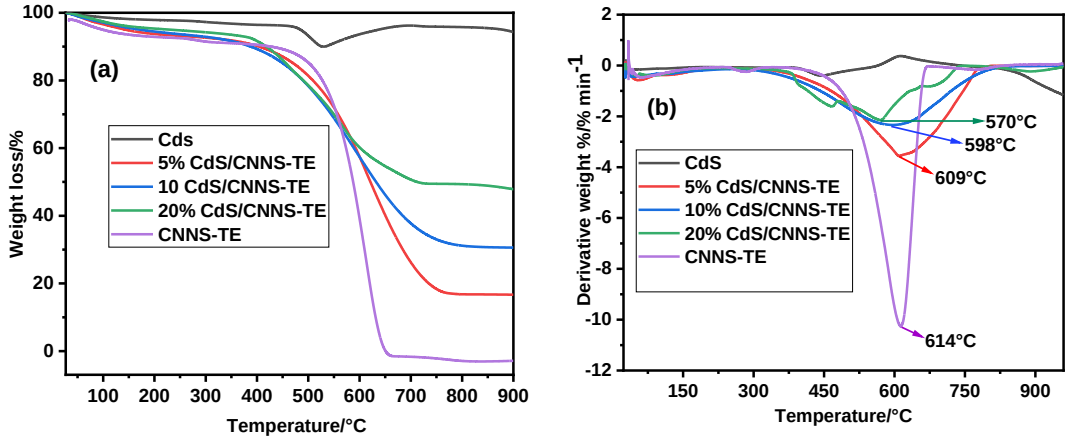

Figure 5.8: (a) TGA thermograms and (b) the corresponding derivative graphs for CdS, 5% CdS/CNNS-TE, 10% CdS/CNNS-TE, 20% CdS/CNNS-TE, and CNNS-TE, carried out under air

5.3.1.7 Optical properties and band structure

Figure 5.9 shows the UV-diffuse reflectance spectra (UV-DRS) of as-prepared samples. As depicted in Figure 5.9a, the maximum absorption for CNNS-TE and CdS nanomaterials was observed at about 380 and 495 nm, respectively. The CNNS-TE showed an absorption shoulder, which gradually extended to a longer wavelength (visible region). The spectra for CdS/CNNS-TE samples extended light absorption (redshift), especially at the longer wavelengths between 558-643 nm, when compared with the CNNS-TE and CdS samples. This implies that when the heterostructures were formed, the resulting composites exhibited better light absorption, especially in the visible region. Furthermore, the band gap energies of the samples were calculated from the transformed Kubelka-Munk plot $((\alpha h\nu)^{1/2}/eV^{1/2}$ vs. E/eV) as presented in Figure 5.9b. The estimated band gap values are reported in Table 5.3. In general, the band gap values of the

nanocomposites (5% CdS/CNNS-TE and 10% CdS/CNNS-TE) were lower than for pure CdS and CNNS-TE nanomaterials, except for the 20% CdS/CNNS sample. This shows that when the CdS nanoparticles were introduced to the CNNS-TE, the band gap was reduced due to intrinsic electronic modification, which aids in more light absorption.

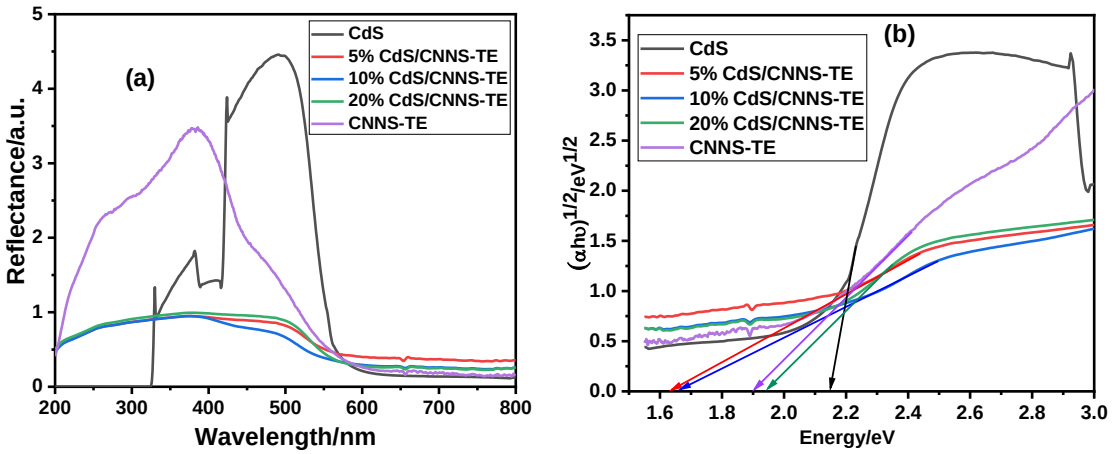

Figure 5.9: The UV-Visible reflectance and transformed Kubelka-Munk spectra of pure CdS, CNNS-TE, and CdS/CNNS-TE composites with different CdS loadings

5.3.1.8 Position of band potentials and rate of separation of photogenerated charges

To determine the positions of the valence band (VB) and conduction band (CB) potentials for the samples, the Butler and Ginley equations were used (Equations (1) and (2)):

$$E_{VB} = \chi - E_e + 0.5E_g \qquad \text{Equation (1)}$$

$$E_{CB} = E_{VB} - E_g \qquad \text{Equation (2)}$$

Where, E_g is the energy gap (band gap) calculated from the Kubelka-Munk plot, χ is the electronegativity of the semiconductor, which is 4.73 eV for g-C_3N_4 [29], and E_e is the energy of free electrons on the hydrogen scale which is approximately 4.5 eV. The calculated values of VB and CB are presented in Table 5.3. The values for CdS and CNNS-TE agree with other previous data [30].

Table 5.3: The optical properties of the as-prepared photoactive materials

Photoactive material	Band gap energy/eV	Valence band potential/eV	Conduction band potential/eV
CdS	2.14	1.30	-0.84
5% CdS/CNNS-TE	1.62	1.04	-0.58
10% CdS/CNNS-TE	1.65	1.06	-0.59
20% CdS/CNNS-TE	1.94	1.20	-0.74
CNNS-TE	1.89	1.18	-0.71

To further investigate the position of band potentials, Mott-Schottky measurements (Figure 5.10a) were carried out. The CBs were estimated by extrapolating the linear part of the curve to intercept the x-axis [29]. Therefore, the estimated CBs for CdS, 5% CdS/CNNS-TE, 10% CdS/CNNS-TE, 20% CdS/CNNS-TE, and CNNS-TE were: 0.53, 0.38, -0.26, -0.17 and 0.53 V (vs. Ag/AgCl), correspondingly. Additionally, the VBs were calculated from the previously estimated CBs and band gap energies (from Table 5.3). The calculated VBs for CdS, 5% CdS/CNNS-TE, 10% CdS/CNNS-TE, 20% CdS/CNNS-TE, and CNNS-TE were: +2.67, +2.00, +1.39, +1.77 and +2.42 V (vs. Ag/AgCl), respectively. Generally, the VB values of 5% CdS/CNNS-TE, 10% CdS/CNNS-TE, and 20% CdS/CNNS-TE samples were less than that of CNNS-TE, implying that there could exist a strong interaction between CNNS-TE and CdS dopant, that downshifted the VB edge of CNNS-TE material.

The charge separation efficiency of as-prepared materials was evaluated using photoluminescence (PL) measurements (Figure 5.10b). The undoped CNNS-TE sample exhibited high intensity, implying a high charge recombination of photogenerated charges. With the addition of CdS nanoparticles as dopants, the intensities significantly decreased as a function of increasing the CdS dose in the samples. For instance, the intensity of 5% CdS/CNNS-TE nanocomposites was lower than for the undoped CNNS-TE, whereas the 10% CdS/CNNS-TE, 20% CdS-CNNS-TE and CdS nanoparticle samples were the lowest according to Figure 5.10b. Generally, the recombination of photogenerated charges was significantly suppressed when CNNS-TE was doped with CdS nanoparticles, and this could be attributed to proper band alignment between CNNS-TE and CdS nanomaterials, thus, imparting better charge transfer characteristics, which could be beneficial in photo-driven applications.

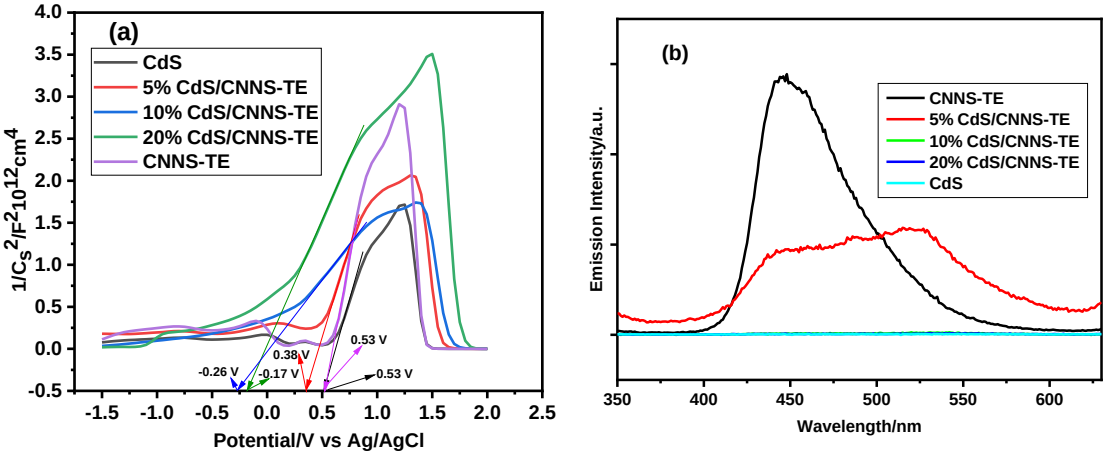

Figure 5.10: (a) Mott-Schottky plots measured at 1 kHz in 5 mM $[Fe(CN)_6]^{4-/3-}$ solution and (b) PL spectra for as-prepared photoactive materials

5.3.2 Device characterisation and measurements

This section discusses the various devices characterisation and their photovoltaic application.

5.3.2.1 Film morphology of the active layers of fabricated devices

Figure 5.11 shows SEM images of doped and undoped P3HT:$PC_{61}BM$ active layer films. The pristine, 5% CdS/CNNS-TE, and 10% CdS/CNNS-TE films exhibited relatively smooth morphologies and were somewhat similar. On the other hand, films with CdS, and 20% CdS/CNNS-TE showed a rather rough morphology, probably due to more CdS nanoparticle concentration. Remarkably, the film with only CNNS-TE showed a smooth morphology, which could be beneficial in charge transport characteristics in the devices.

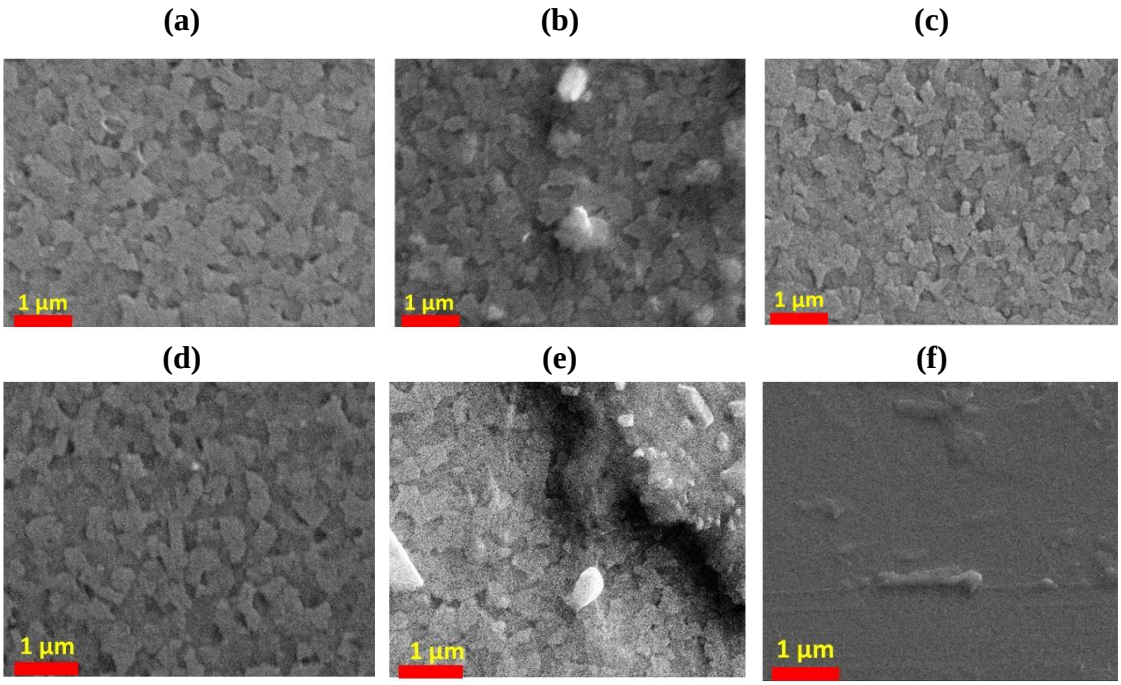

Figure 5.11: SEM images showing film morphology of doped and undoped active layers: (a) pristine, (b) CdS, (c) 5% CdS/CNNS-TE, (d) 10% CdS/CNNS-TE, (e) 20% CdS/CNNS-TE and (f) CNNS-TE

5.3.2.2 Optical absorption and transmittance

A solar cell device's optical absorption properties are critical since the amount of light absorbed determines the number of photogenerated charges. Figure 5.12a shows the UV-Visible spectra of the devices with or without (pristine) dopants in the active layer, P3HT:$PC_{61}BM$ blends. As can be observed, the devices with CNNS-TE, CdS, 5% CdS/CNNS-TE, 10% CdS/CNNS-TE, and 20% CdS/CNNS-TE nanoparticles showed the highest light absorption compared with the pristine material. This resulted in high performance in the respective devices because of enhanced photon absorption characteristics of the active layer brought about by the dopants. The absorbance of the devices increased from about 400 nm to a maximum of 520 nm and then extended towards the 600 nm range, implying that a significant portion of the visible light in the electromagnetic spectrum was harvested. Figure 5.12b shows the optical transmittance of the devices; as presented, the optical transmittance of the pristine device was the highest when compared with the doped devices. Nevertheless, there was still about 40%

light transmission in the doped devices, which is critical in the device's overall performance.

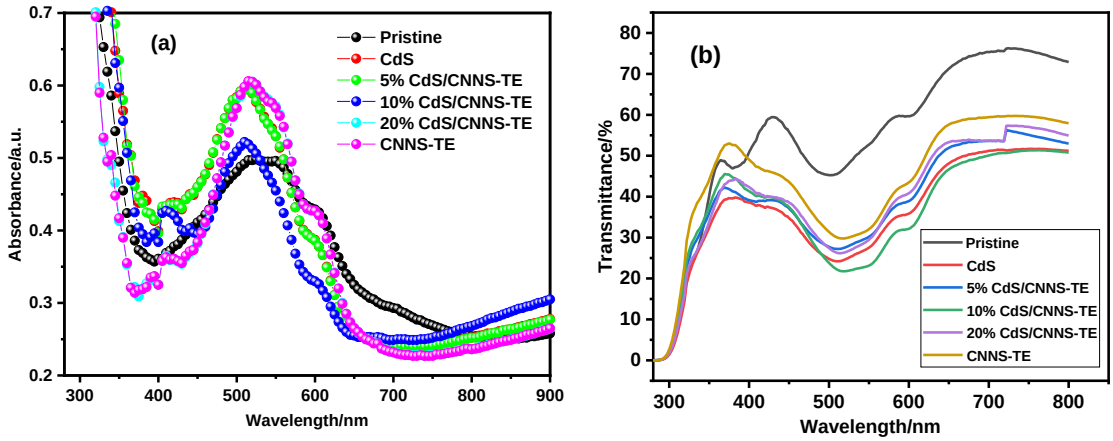

Figure 5.12: (a) UV-Vis absorption and (b) optical transmission spectra of fabricated pristine and doped BHJ-OSC devices

5.3.2.3 Photovoltaic characteristics

The photovoltaic performance, as well as the characterisation of the fabricated devices, is presented in this section. Figure 5.13 shows the current-voltage (J-V) curves of the device with or without the dopants in the active layer. On the other hand, Table 5.4 shows the measured photovoltaic parameters for each device, i.e., power conversion efficiency (PCE), fill factor (FF), short circuit current density (J_{sc}), open-circuit voltage (V_{oc}), and series resistance (R_s). The J-V curve shows that the current density increases when the dopants are introduced into the active layer of the device compared with the pristine device. In essence, the performance of the doped devices was higher than that of the pristine device, as shown in Table 5.4. The series resistance of the undoped device decreased from 827 to 458 Ω cm^2 because of the addition of dopants (CNNS-TE, CdS, 5% CdS/CNNS-TE, 10% CdS/CNNS-TE, and 20% CdS/CNNS-TE). Remarkably, the best-performing device with 5% CdS/CNNS-TE nanoparticles achieved a PCE = 2.21%, J_{sc} = 9.36 mA cm^{-2}, FF = 46.01%, and V_{oc} = 0.53 V. The performance was twofold better than that of the pristine device (PCE = 1.06). This observation can be attributed to better charge separation and transport mechanisms, and also the enhanced light harvesting ability due to the presence of an effective heterojunction between the CdS and CNNS-TE nanomaterials. On the other hand, except for pristine, 10% CdS/CNNS-TE and 20% CdS/CNNS-TE gave lower performance than the other tested samples (see Table 5.4).

This could be attributed to the high series resistance exhibited by the two devices, thus impeding the current flow in these devices and, therefore, low performance.

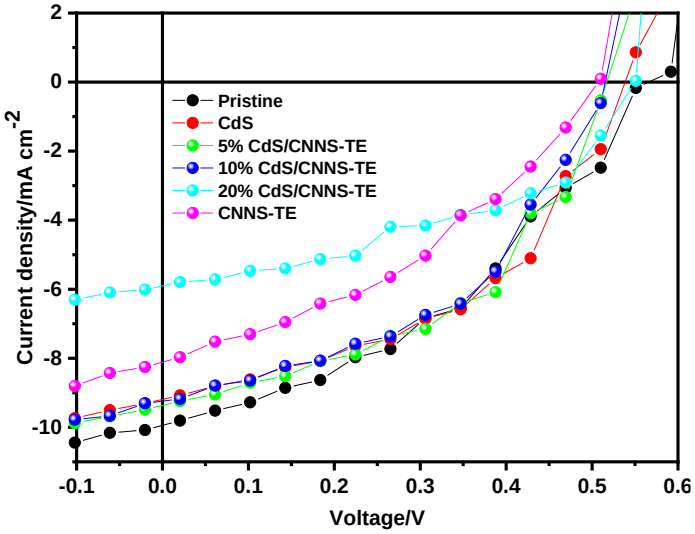

Figure 5.13: J-V characteristic curves of solar cell devices fabricated with P3HT:$PC_{61}BM$ active layer blends and various nanoparticles at 1wt.% concentration

Table 5.4: The photovoltaic parameters of BHJ-OSC devices fabricated with or without different nanoparticles

P3HT:$PC_{61}BM$:NPs	V_{oc}/V	J_{sc}/mA cm^{-2}	FF/%	PCE/%	R_s/Ω cm^2
Pristine	0.55	9.01	37.58	1.06	827
CdS	0.53	8.24	45.97	1.92	548
5% CdS/CNNS-TE	0.53	9.36	46.01	2.21	458
10% CdS/CNNS-TE	0.48	7.57	36.10	1.60	628
20% CdS/CNNS-TE	0.54	7.44	44.35	1.58	820
CNNS-TE	0.54	8.37	40.44	1.69	751

5.3.2.4 Charge transport characteristics

Photovoltaic measurements in the dark were also performed to elucidate the charge transport characteristics of fabricated devices and are presented in Figure 5.14. The space charge limited current (SCLC) method was utilised to determine the charge transport mechanism in the active layer of photovoltaic devices [31]. Figure 5.14a shows the J-V curves for devices on a log scale, where this kind of curve exhibits diode characteristics.

As observed, the curves obey Ohms law ($J \propto V$) at low voltages as it drops down before a further drastic drop where the filling of trap states occurs in the material. Thereafter, the curve becomes asymptotic before rising again to a maximum (SCLC regime). Basically, in the SCLC regime, all traps in the material have already been filled, and the current derived from the device is solely dependent on the bulk properties of the absorber system. Accordingly, several models have been developed and tested to describe the transport phenomenon of semiconductors at the SCLC regimes. As a result, fundamental transport parameters in semiconductor materials, such as mobility and field activation factors, have been determined [32]. Therefore, in this case, the Mott-Gurney law (Equation 3) coupled with the field-dependent equation in the form of $\mu = \mu_{\circ} exp\left(\gamma\sqrt{E}\right)$ was employed to describe the SCLC regime in the system. Basically, Mott-Gurney law defines the SCLC of a material when an electric field is applied, and with the absence of charge traps, provided that the electrode-semiconductor contact obeys Ohm's law [32]. The law can be expressed as Equation 3:

$$J = \frac{9}{8}\varepsilon\varepsilon_{\circ}\mu_{\circ}\frac{V^2}{L^3} exp\left(0.89\gamma\sqrt{\frac{V}{L}}\right) \qquad \text{Equation (3)}$$

where ε is the relative permittivity of the material, $\varepsilon_{\circ}$ is the permittivity of free space, $\mu_{\circ}$ is the low-field mobility, γ is the field activation factor, V is the applied voltage which can be corrected by subtracting built-in voltage (V_{bi}), and L is the thickness of the absorber layer. The experimental SCLC data obtained from taking J-V measurements in the dark conditions were fitted into Equation 3, which showed a good agreement with experimental data, as depicted in Figure 5.14b. The values of zero-field mobilities and field activation factors attained from the fitted data are presented in Table 5.5. From Table 5.5, the zero-field mobility of the doped active layers was one order higher than that of the pristine device. This indicates that the charge mobilities were enhanced after incorporating dopants, which could have reduced the recombination of the photogenerated charges.

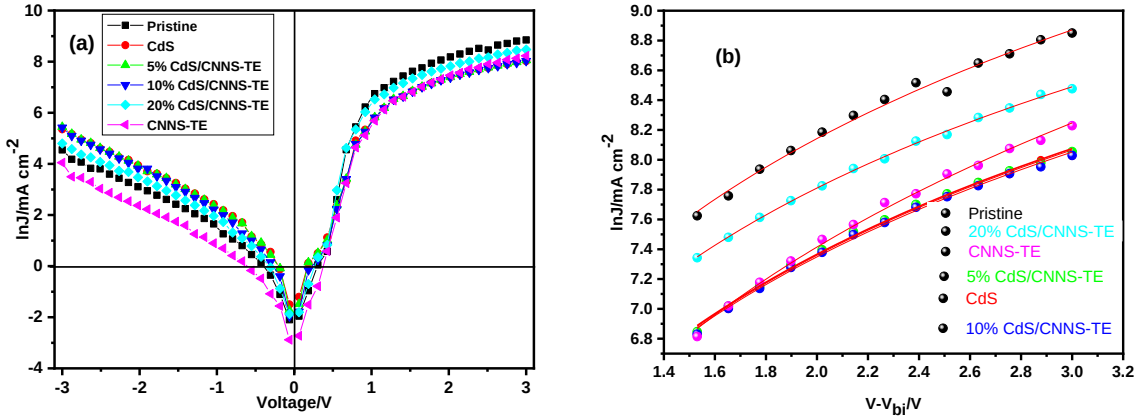

Figure 5.14: (a) J-V dark curves with different nanoparticles and (b) the SCLC achieved from several BHJ-OSC devices fitted to Equation (3)

Table 5.5: The charge carrier transport parameters of BHJ-OSCs based on the undoped and doped photoactive layer with different nanoparticles at 1 wt.% concentration

P3HT:$PC_{61}BM$:Nanoparticles	**μ_o (Zero-field mobility)/$cm^2 S^{-1} V^{-1}$**	**γ (Field activation factor)/$cm V^{-1}$**
Pristine (without dopants)	2.1621×10^{-4}	-1.5225×10^{-4}
CdS	1.0914×10^{-3}	-7.6931×10^{-4}
5% CdS/CNNS-TE	1.0861×10^{-3}	-7.6553×10^{-4}
10% CdS/CNNS-TE	1.0961×10^{-3}	-7.7265×10^{-4}
20% CdS/CNNS-TE	1.9349×10^{-3}	-1.3639×10^{-4}
CNNS-TE	6.5790×10^{-3}	-4.6373×10^{-4}

5.4 Conclusion

Cadmium sulfide (CdS) nanocomposites were successfully prepared and incorporated as a third component in P3HT:$PC_{61}BM$ active layer blends. For comparison, reference devices with only CdS and CNNS-TE nanoparticles were also fabricated. With the incorporation of the 5% CdS/CNNS-TE nanocomposite as the dopant in the active layer, the best device achieved a PCE of 2.21%, which was over 50% power conversion enhancement when compared with the pristine device, which reached a PCE of 1.06%. The better performance of 5% CdS/CNNS-TE nanocomposite was attributed to better

charge transfer mechanisms, low recombination, better light absorption (due to the lowest band gap (1.62 eV)), and low series resistance in the device due to the formation of an effective heterojunction between CdS and CNNS-TE materials. Additionally, the CNNS-TE in the composites could have assisted in photon harvesting and the formation of a smooth film morphology, thus enhancing charge transfer and suppressing charge recombination processes. The use of CdS/CNNS-TE nanocomposites in this work is envisaged to expand the potential power conversion enhancement in BHJ-OSCs, thus, paving the way for their production and commercialisation.

Acknowledgements

The authors are thankful for the financial support provided by the National Research Foundation (NRF) of South Africa, under grant numbers 103979 and 109580; the University of KwaZulu-Natal (UKZN), the UKZN Nanotechnology Platform, and the Eskom Tertiary Education Support Programme (TESP). Finally, the authors are very grateful to Professor Genene Mola and his team at the UKZN-PMB campus for using facilities in their laboratory to fabricate devices.

Conflict of interest

The authors declare no conflict of interest.

References

[1] J. Gong, C. Li, M.R. Wasielewski, Advances in solar energy conversion. Chem. Soc. Rev. **48**, 1862-1864 (2019). https://doi.org/10.1039/C9CS90020A.

[2] N. Novas, R.M. Garcia, J.M. Camacho, A. Alcayde, Advances in solar energy towards efficient and sustainable energy. Sustainability. **13**, 6295 (2021). https://doi.org/10.3390/su13116295.

[3] L. Wang, L. Huang, W.C. Tan, X. Feng, L. Chen, X. Huang, K.-W. Ang, 2D Photovoltaic devices: Progress and prospects. Small methods. **2**, 1700294 (2018). https://doi.org/10.1002/smtd.201700294.

[4] N. Terenti, G.-I. Giurgi, L. Szolga, I. Stroia, A. Terec, I. Grosu, A.P. Crișan, Effect of the terminal acceptor unit on the performance of non-fullerene indacenodithiophene acceptors in organic solar cells. Molecules. **27**, 1229 (2022). https://doi.org/10.3390/molecules27041229.

[5] I. Litzov, C. Brabec, Development of efficient and stable inverted bulk heterojunction (BHJ) solar cells using different metal oxide interfaces. Materials. **6**, 5796-5820 (2013). https://doi.org/10.3390/ma6125796.

[6] Y. Liang, L. Yu, A new class of semiconducting polymers for bulk heterojunction solar cells with exceptionally high performance. Acc. Chem. Res. **43**, 1227-1236 (2010). https://doi.org/10.1021/ar1000296.

[7] W. Huang, P. Cheng, Y. Yang, G. Li, Y. Yang, High-performance organic bulk-heterojunction solar cells based on multiple-donor or multiple-acceptor components. Adv. Mater. **30**, 1705706 (2018). https://doi.org/10.1002/adma.201705706.

[8] J. Song, L. Zhu, C. Li, J. Xu, H. Wu, X. Zhang, Y. Zhang, Z. Tang, F. Liu, Y. Sun, High-efficiency organic solar cells with low voltage loss induced by solvent additive strategy. Matter. **4**, 2542-2552 (2021). https://doi.org/10.1016/j.matt.2021.06.010.

[9] A. Labiod, O.A. Ibraikulov, S. Dabos-Seignon, S. Ferry, B. Heinrich, S. Méry, S. Fall, H.J. Tchognia Nkuissi, T. Heiser, C. Cabanetos, N. Leclerc, e.P. Lévêque, Photo-degradation in bulk heterojunction organic solar cells using a fullerene or a non-fullerene derivative electron acceptor. Org. Electron. **107**, 106549 (2022). https://doi.org/10.1016/j.orgel.2022.106549.

[10] D.D.Y. Setsoafia, K.S. Ram, H.M. Rad, D. Ompong, N.K. Elumalai, J. Singh, Optimizing device structure of PTB7-Th:PNDI-T10 bulk heterojunction polymer solar cells by enhancing optical absorption. Energies. **15**, 711 (2022). https://doi.org/10.3390/en15030711.

[11] Y. Yan, Y. Zhang, W.A. Memon, M. Wang, X. Zhang, Z. Wei, The role of entropy gains in the exciton separation in organic solar cells. Macromol. Rapid Commun. **n/a**, 2100903 (2022). https://doi.org/10.1002/marc.202100903.

[12] S. Obuchovsky, M. Levin, A. Levitsky, G.L. Frey, Morphology visualization of P3HT:Fullerene blends by using subsurface atomic layer deposition. Org. Electron. **49**, 234-241 (2017). https://doi.org/10.1016/j.orgel.2017.06.050.

[13] F. Brioua, M. Remram, R. Nechache, H. Bourouina, Electrical and optical modeling of poly(3-hexylthiophene):[6,6]-phenyl-C_{61} butyric acid methyl ester P3HT–PCBM bulk heterojunction solar cells. Appl. Phys. A. **123**, 704 (2017). https://doi.org/10.1007/s00339-017-1288-4.

[14] M.W. Dlamini, G.T. Mola, Near-field enhanced performance of organic photovoltaic cells. Phys. B: Condens. Matter. **552**, 78-83 (2019). https://doi.org/10.1016/j.physb.2018.09.027.

[15] J.N. Ike, M.S.G. Hamed, G.T. Mola, Effective energy harvesting in thin film organic solar cells using Ni:Zn as bimetallic nanoparticles. J. Phys. Chem. Solids. **161**, 110405 (2022). https://doi.org/10.1016/j.jpcs.2021.110405.

[16] J. Lee, S.M. Lee, S. Chen, T. Kumari, S.-H. Kang, Y. Cho, C. Yang, Organic photovoltaics with multiple donor–acceptor pairs. Adv. Mater. **31**, 1804762 (2019). https://doi.org/10.1002/adma.201804762.

[17] D. Li, L. Zhu, X. Liu, W. Xiao, J. Yang, R. Ma, L. Ding, F. Liu, C. Duan, M. Fahlman, Q. Bao, Enhanced and balanced charge transport boosting ternary solar cells over 17% efficiency. Adv. Mater. **32**, 2002344 (2020). https://doi.org/10.1002/adma.202002344.

[18] X. Chen, Q. Liu, Q. Wu, P. Du, J. Zhu, S. Dai, S. Yang, Incorporating graphitic carbon nitride (g-C_3N_4) quantum dots into bulk-heterojunction polymer solar cells leads to efficiency enhancement. Adv. Funct. Mater. **26**, 1719-1728 (2016). https://doi.org/10.1002/adfm.201505321.

[19] G. Mamba, A.K. Mishra, Graphitic carbon nitride (g-C_3N_4) nanocomposites: A new and exciting generation of visible light driven photocatalysts for environmental pollution remediation. Appl. Catal. B: Environ. **198**, 347-377 (2016). https://doi.org/10.1016/j.apcatb.2016.05.052.

[20] D.S. Pattanayak, D. Pal, J. Mishra, C. Thakur, Noble metal–free doped graphitic carbon nitride (g-C_3N_4) for efficient photodegradation of antibiotics: Progress, limitations, and future directions. Environ. Sci. Pollut. Res., (2022). https://doi.org/10.1007/s11356-022-20170-9.

[21] N. Rono, J.K. Kibet, B.S. Martincigh, V.O. Nyamori, A review of the current status of graphitic carbon nitride. Crit. Rev. Solid State Mater. Sci. **46**, 189-217 (2021). https://doi.org/10.1080/10408436.2019.1709414.

[22] X. Li, J. Zhang, Y. Huo, K. Dai, S. Li, S. Chen, Two-dimensional sulfur- and chlorine-codoped g-C_3N_4/CdSe-amine heterostructures nanocomposite with effective interfacial charge transfer and mechanism insight. Appl. Catal. B Environ. **280**, 119452 (2021). https://doi.org/10.1016/j.apcatb.2020.119452.

[23] S. Pareek, S. Waheed, A. Rana, P. Sharma, S. Karak, Graphitic carbon nitride quantum dots (g-C_3N_4 QDs) to improve photovoltaic performance of polymer solar cell by combining Förster resonance energy transfer (FRET) and morphological effects. Nano Express. **1**, 010057 (2020). https://doi.org/10.1088/2632-959X/ab9b2f.

[24] M.F. Soh, M.F.M. Noh, N.A. Mohamed, J. Safaei, N.N. Rosli, E.L. Lim, C.C. Yap, M.A.M. Teridi, Incorporation of g-C_3N_4/Ag dopant in TiO_2 as electron transport layer for organic solar cells. Mater. Lett. **253**, 117-120 (2019). https://doi.org/10.1016/j.matlet.2019.06.052.

[25] W. Iqbal, B. Qiu, Q. Zhu, M. Xing, J. Zhang, Self-modified breaking hydrogen bonds to highly crystalline graphitic carbon nitrides nanosheets for drastically enhanced hydrogen production. Appl Catal B Environ. **232**, 306-313 (2018). https://doi.org/10.1016/j.apcatb.2018.03.072.

[26] Z.R. Khan, M. Zulfequar, M.S. Khan, Chemical synthesis of CdS nanoparticles and their optical and dielectric studies. J. Mater. Sci. **46**, 5412-5416 (2011). 10.1007/s10853-011-5481-0.

[27] P. Baláž, M. Baláž, E. Dutková, A. Zorkovská, J. Kováč, P. Hronec, J. Kováč, M. Čaplovičová, J. Mojžiš, G. Mojžišová, A. Eliyas, N.G. Kostova, CdS/ZnS nanocomposites: From mechanochemical synthesis to cytotoxicity issues. Mater. Sci. Eng. C. **58**, 1016-1023 (2016). https://doi.org/10.1016/j.msec.2015.09.040.

[28] H. Begum, M.S. Ahmed, S. Jeon, New approach for porous chitosan–graphene matrix preparation through enhanced amidation for synergic detection of dopamine and uric acid. ACS Omega. **2**, 3043-3054 (2017). https://doi.org/10.1021/acsomega.7b00331.

[29] Y. Sun, W. Zhang, T. Xiong, Z. Zhao, F. Dong, R. Wang, W.-K. Ho, Growth of BiOBr nanosheets on C_3N_4 nanosheets to construct two-dimensional nanojunctions with enhanced photoreactivity for NO removal. J. Colloid. Interface Sci. **418**, 317-323 (2014). https://doi.org/10.1016/j.jcis.2013.12.037.

[30] Y. Zou, J. Shi, D. Ma, Z. Fan, L. Cheng, D. Sun, Z. Wang, C. Niu, CdS quantum dots decorated ultrathin WS_2/g-C_3N_4 2D/2D heterojunction nanosheets for highly efficient photocatalytic hydrogen production under visible light. ChemSusChem. **11**, 245-253 (2018). https://doi.org/10.1002/cssc.201800053.

[31] F. Lmai, S. Ezairi, A. Azouz, Optical properties influence of the polarization and the temperature on heterojunction organic solar cell. Optik. **262**, 169295 (2022). https://doi.org/10.1016/j.ijleo.2022.169295.

[32] G. Tessema, Charge transport across bulk heterojunction organic thin film. Appl. Phys. A. **106**, 53-57 (2012). https://doi.org/10.1007/s00339-011-6676-6.

CHAPTER SIX

Chemically blown graphitic carbon nitride nanosheets doped with cadmium sulfide nanoparticles for enhanced photon harvesting in organic solar cells

Nicholas Rono,[a] Bice Martincigh,[a] Joshua K. Kibet[b] and Vincent O. Nyamori[a]*

[a]School of Chemistry and Physics, University of KwaZulu-Natal, Westville Campus

Private Bag X54001, Durban 4000, South Africa

[b]Egerton University, Njoro Campus, Chemistry Department, PO Box 536-20115, Egerton, Kenya

*Corresponding author: E-mail: Nyamori@ukzn.ac.za, Tel: +27312608256

Abstract

Solar harvesting is crucial in a bulk heterojunction organic solar cell (BHJ-OSC) because it determines the number of photogenerated charges in the absorber layer of an OSC and hence, the performance. In this work, graphitic carbon nitride (g-C_3N_4) nanosheets (CNNS) from the chemical blowing (CB) method of exfoliation of bulk g-C_3N_4 (CNNS-CB) were doped with cadmium sulfide (CdS) nanoparticles to form CdS/CNNS-CB composites. The CdS/CNNS-CB composites were incorporated into the active layer of a BHJ-OSC as a third component together with poly(3-hexylthiophene) (P3HT) and [6,6]-phenyl C_{61}-butyric acid methyl ester (PCBM) blends. It was envisaged that the CdS/CNNS-CB materials would assist in the light-harvesting and passivation of bulk defects, thus, suppressing the recombination of photogenerated charges and improving the charge transfer in the active layer of the OSC device. The results demonstrated that the CNNS-CB formed an intimate heterostructure with CdS nanoparticles, with an improved light-harvesting ability (low band gap), suppressed rate of recombination of photogenerated charges, and enhanced charge carrier mobility. Consequently, the best-performing device was achieved by utilising a 10% CdS/CNNS-CB sample in the P3HT:PC_{61}BM active layer as a dopant. The champion device achieved the best power conversion efficiency (PCE) of 3.45%, which was about 183% performance enhancement relative to the pristine device, which had a PCE of 1.89%. The augmented performance

exhibited by the best device (with 10% CdS/CNNS-CB) was credited to better light-harvesting ability, suppressed recombination of photogenerated charges, and improved charge transport characteristics, due to the incorporation of the 10% CdS/CNNS-CB heterostructure. Our results are envisaged to provide effective avenues for the improvement of the performance of OSCs by modification of the active layer with g-C_3N_4-based materials.

Keywords: Chemical blowing; OSC; graphitic carbon nitride; absorber layer; PCE

6.1 Introduction

Organic solar cells (OSCs) that convert light energy to electricity via photovoltaic technology have been extensively researched because of their attractive features, such as low cost [1], ease of fabrication, lightweight [2], and semi-transparent characteristics [3]. The power conversion efficiency (PCE) of OSCs has reached over 18% [4] through various modifications, such as device structure optimisation [5], use of effective materials [6], and tunning of the components [7] of the device. Despite the various modifications that have been advanced, the performance of OSCs still faces several drawbacks, such as low performance, when compared with commercially available silicon-based solar cells [4] and their inorganic counterparts (perovskite solar cells) [8]. They are hampered by issues of poor stability, a high rate of recombination of photogenerated charges, and poor light-harvesting and incident photon to electron conversion [9].

To improve the performance of OSC, the modification of particularly the active layer has been performed [10]. Basically, the active layer is essential because when light energy falls on the device, it is absorbed and used in the generation of excitons [7]. Therefore, the effectiveness of the active layer in solar harvesting in this process is vital in realising a high PCE. Recently, dopants have been introduced into the active layer, typically comprising poly(3-hexylthiophene) (P3HT) and [6,6]-phenyl C_{61}-butyric acid methyl ester (PCBM) blends as a third component [11, 12]. The reasons for doping the active layer include the improvement of photon absorption, charge transfer mechanism, and impediment of recombination of photogenerated charges. Shin et al. [13] introduced graphene quantum dots (GQDs) into the active layer, and the device's performance increased from a PCE of 3.56 to 4.23%, indicating that the GQDs play a crucial role in the device's performance.

Graphitic carbon nitride (g-C_3N_4) is a metal-free semiconductor material with a tuneable band gap that exhibits high thermal and chemical stabilities [14, 15]. By considering these attractive attributes, g-C_3N_4 has shown great potential in solar cell applications. However, the application of this material in photo-driven applications such as solar cells is restricted by the fast recombination of photogenerated charges and low electrical conductivity [15]. In order to improve the properties of g-C_3N_4, modifications such as composite formation [16], morphological adjustment, and introduction of defects have

been carried out [17]. Defect engineering on g-C_3N_4 has gained significant attention because defects are believed to cause electronic band structure modulation [18], which is beneficial in solar-driven processes, such as photovoltaics and photocatalysis. Therefore, the thermal etching method of exfoliation of g-C_3N_4 could lead to a better material compared with other exfoliation routes that do not introduce defects [19]. Moreover, the doping of g-C_3N_4 could aid in band structure modulation [20]. Therefore, it is essential to explore various ways of forming effective g-C_3N_4-based composites to capitalise on their promising optoelectronic properties in devices like OSCs.

Herein, we report the preparation of graphitic carbon nitride nanosheets (CNNS-CB) from the chemical blowing method of exfoliation doped with cadmium sulfide nanoparticles (CdS) to form a composite (CdS/CNNS-CB) that was incorporated in the active layer of an OSC. The reference cell was fabricated with only P3HT:PC_{61}BM blends in the active layer, while the doped devices were fabricated with the incorporation of as-prepared materials as a third component in the P3HT:PC_{61}BM active layer blends. The effect of dopants on the photovoltaic performance of the cells was investigated and discussed. By taking advantage of the formation of a heterostructure between the CNNS-CB and CdS materials, it was envisaged that incorporating the CdS/CNNS-CB heterostructure dopants into the active layer would enhance photon harvesting, suppress recombination of photogenerated charges, and improve the charge transfer process. Additionally, the photovoltaic characteristics of the fabricated cells were measured and studied in dark conditions to explore the charge transfer characteristics in the devices. Finally, the optical absorption of devices was examined and evaluated. The results of this work are expected to present a new strategy for the performance enhancement of OSCs by incorporating doped g-C_3N_4-based materials.

6.2 Experimental

6.2.1 Chemicals

Melamine (99%) (CAS No. 99 108-78-1), ammonium chloride (NH_4Cl) (≥99.5%) (12125-02-9), cadmium nitrate tetrahydrate ($Cd(NO_3)_2.4H_2O$ (98%) (CAS No. 10022-68-1), sodium sulfide (Na_2S) (≥98.0%) (CAS No. 1313-82-2), lithium fluoride (LiF) (≥99.98%) (CAS No. 7789-24-4), poly-(3-hexylthiophene) (P3HT) (99%) (CAS No.

1693-86-3), poly-(3,4-ethylene dioxythiophene):poly-(styrene-sulfonate) (PEDOT:PSS) (99%) (CAS No. 155090-83-8), [6,6]-phenyl-C_{61}-butyric acid methyl ester ($PC_{61}BM$) (>99.5%) (CAS No. 160848-22-6), dichloromethane (DCM) (≥99.8%) (CAS No. 75-09-2), chloroform (≥99%) (CAS No. 67-66-3), ethanol (95.0%) (CAS No. 64-17-5), nitric acid (≥65%) (CAS No. 7697-37-2), potassium ferricyanide (99%) (CAS No. 13746-66-2), hydrochloric acid (37%) (CAS No. 7647-01-0) and indium tin oxide (ITO) (CAS No. 50926-11-9) glass substrates with surface resistivity of 15 Ω sq^{-1} were bought from Sigma Aldrich Ltd (South Africa). All the chemicals were used as obtained without further treatment. Deionised water with a resistivity of 18.2 MΩ cm at 20 °C was obtained from a Millipore Milli-Q Elix 5 UV water purification system.

6.2.2 Synthesis of photoactive materials

Firstly, bulk g-C_3N_4 was synthesised by polycondensation of a nitrogen-rich melamine precursor. Melamine (5 g) was typically placed in an open ceramic crucible and transferred to a muffle furnace. The contents of the crucible were heated at a rate of 5 °C min^{-1} to 550 °C and kept for 4 hours in the furnace. After that, it was allowed to cool to room temperature. Bulk g-C_3N_4 was formed as a yellow solid and was labelled B-g-C_3N_4.

Secondly, bulk g-C_3N_4 (2.0 g) and a chemical blowing agent, ammonium chloride (1 g), were homogenously mixed in an agar mortar to form a precursor. The mixture was then calcined in a tube furnace at a ramping rate of 5 °C min^{-1} up to 600 °C and continued at this temperature for 2 hours under a constant stream of nitrogen gas. Graphitic carbon nitride nanosheets formed and were then labelled CNNS-CB. On the other hand, cadmium sulfide (CdS) nanoparticles were prepared via a chemical precipitation method [21] with slight modifications. In brief, 100 mL 0.1 M of sodium sulfide solution was added dropwise to 100 mL of 0.1 M cadmium nitrate solution under vigorous magnetic stirring until a deep yellow precipitate was formed. The precipitate was filtered and washed consecutively with water and ethanol, and later oven-dried at 90 °C for 5 h.

Finally, in order to construct the CdS/CNNS-CB heterostructure, a mechanochemical approach was employed to combine the CdS and CNNS-CB materials. In this process, for example, to form a 10% CdS/CNNS-CB composite, 0.01 g of CdS and 0.09 g of CNNS-CB powders were ultrasonically dispersed in 40 mL of deionised water for 1 hour. The resulting dispersant was kept overnight in a drying oven set at 90 °C. The dried as-

prepared samples were labelled and stored in amber glass vials for characterisation and application.

6.2.3 Characterisation of photoactive materials

The micro and crystal structures of as-prepared samples were investigated by using both normal (TEM, JEOL, JEM 1010) and high-resolution transmission electron microscopy (HRTEM) operated at 200 kV. The surface morphology of as-prepared samples was investigated by means of scanning electron microscopy (SEM, Carl Zeiss Ultra Plus), fitted with an energy dispersive spectroscopy (EDS) (Oxford X-max) detector. The elements present in the samples were identified, quantified, and mapped using an energy-dispersive X-ray analysis (EDX) system available in the SEM instrument. The crystallinity of the samples was explored with a BRUKER AXS D8 Advance powder X-ray diffractometer with Cu-Kα radiation (λ = 1.5406 Å) at 40 kV and 40 mA. The optical properties, such as UV–vis diffuse reflectance spectra, were investigated with a PerkinElmer Lambda 35 UV–Visible spectrophotometer fitted with a Labsphere integrating sphere and $BaSO_4$ as the reference. The measurement of the rate of recombination of photogenerated charges (photoluminescence spectra (PL)) was recorded with a PerkinElmer LS 55 spectrofluorometer and the excitation wavelength was kept at 325 nm. The functional groups present in the samples were elucidated using a PerkinElmer Spectrum 100, Fourier transform infrared (FTIR) spectrometer coupled with an attenuated total reflectance (ATR) sampling accessory. Finally, thermogravimetric analysis (TGA) of the samples was carried out in air with a TA instruments Q series thermal analyser (Q600).

6.2.4 Fabrication of organic solar cells and their characterisation

The devices with an active surface area of 0.02 cm^2 were fabricated under ambient conditions. First, an indium tin oxide (ITO) (surface resistivity, 15 $\Omega\ sq^{-1}$) glass substrate was cut into 30 mm × 30 mm square pieces. The ITO glass was then etched with concentrated acids, i.e. conc. hydrochloric acid and conc. nitric acid, and sequentially cleaned with deionised water, acetone, and isopropanol for 10 minutes by ultrasonication. The substrates were oven-dried at a temperature of 120 °C for 20 minutes. An OSC with the following general architecture was fabricated:

ITO/PEDOT:PSS/P3HT:PC61BM/LiF/Al (Figure 6.1). The hole transport layer (HTL), PEDOT:PSS, was deposited on the substrates by a spin-coating technique. Typically, PEDOT:PSS solution with a concentration of 20 mg in 100 mL DCM was spin-coated at 3500 rpm for 30 s and then oven-dried at a temperature of 120 °C for 20 minutes. In order to prepare the active layer solution, P3HT and $PC_{61}BM$ photoactive materials were mixed in a ratio of 1:1 and homogeneously dispersed in 500 µL chloroform. For the solution with as-synthesised materials (CdS, 5% CdS/CNNS-CB, 10% CdS/CNNS-CB, 20% CdS/CNNS-CB, and CNNS-CB) as dopants, 1 wt.% of the respective nanomaterials was added to the P3HT:$PC_{61}BM$ active layer blend solution and magnetically stirred for 3 h. The as-prepared active layer solution was spin-coated on the dried PEDOT:PSS layer at a rate of 1200 rpm for 40 s. The samples were annealed in a tube furnace under a constant flow of nitrogen with a temperature set at 120 °C for 10 minutes. Layers of 0.5 nm-thick lithium fluoride and 100 nm-thick aluminium were sequentially deposited by thermal evaporation on the active layer at a pressure of 10^{-6} mbar. The current density versus voltage (J-V) characteristics of the fabricated devices was measured using a Keithley (HP2420) source meter with a solar simulator (Photo Emission Tech., Inc., model SS50AAA) at AM 1.5 global under 1 sun. The illumination intensity of the simulator was 100 mW cm^{-2}. The optical properties of the devices were investigated with a Shimadzu UV-3600 double-beam UV-Vis-NIR spectrophotometer.

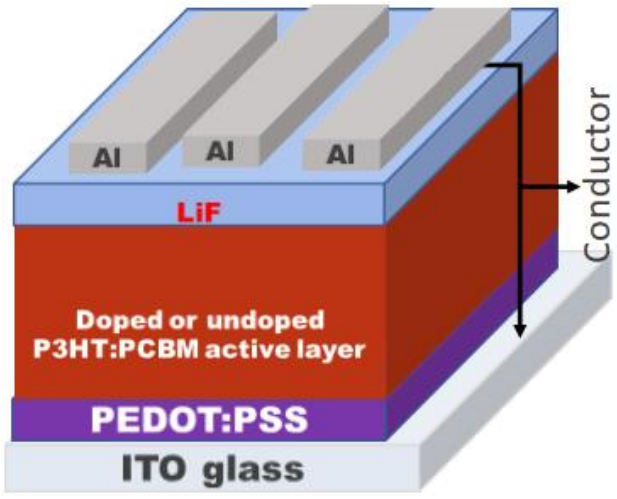

Figure 6.1: General device structure of the fabricated OSC

6.3 Results and discussion

In this section, the characterisation of prepared samples and devices is presented and discussed in detail.

6.3.1 Material characterisation

The two pristine materials, CdS and CNNS-CB, together with three CdS/CNNS-CB heterostructures, were investigated.

6.3.1.1 Morphology and structure

In order to investigate the surface morphology and structure of the as-prepared samples, SEM and TEM analyses were carried out. Figure 6.2 and Supporting Information Figures S6.1 (a) and (b) show the SEM micrographs of the samples, while Figures 6.2 and Supporting Information Figures S6.1, (c), (d), (e), and (f) are the TEM micrographs. The SEM image of the CNNS-CB sample presents blocks with rough surfaces and some fissures/cracks (Figure 6.2a); this could be attributed to the fact that, during the chemical blowing process, the blowing gas was escaping, thus, forming fissures on the surface of the material as exfoliation takes place. Also, a similar morphology was noted for sample 5% CdS/CNNS-CB in Supporting Information Figure S6.1(a), possibly due to more CNNS-CB components in the composite. Meanwhile, the 10% CdS/CNNS-CB sample in Figure 6.2b exhibited a porous structure with smaller particles with dimensions of about 60-80 nm on rough blocks of particles. Additionally, a similar observation was noted for the 20% CdS/CNNS-CB sample in Supporting Information Figure S6.1 (b). On the other hand, the SEM image of the CdS (Figure 6.2c) sample showed a porous structure with disordered flake-like particles.

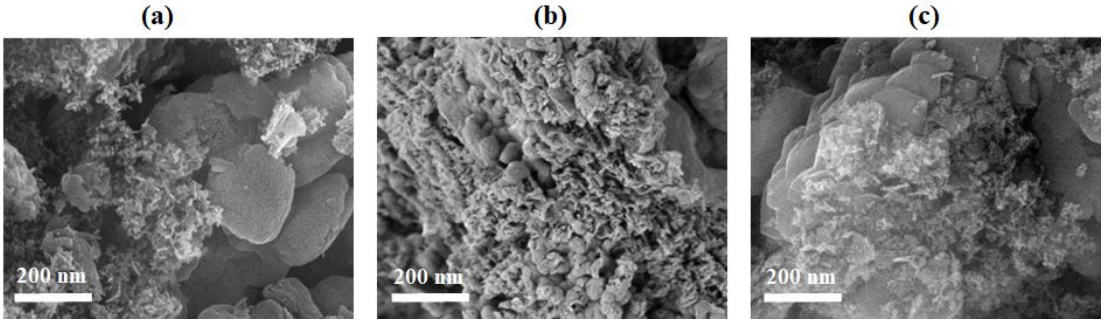

Figure 6.2: SEM images of (a) CNNS-CB, (b) 10% CdS/CNNS-CB and (c) CdS samples

Moreover, the microstructure of the samples was explored with TEM. Clearly, the CNNS-CB showed transparent sheets with pores occasioned by some stacking (seen as dark regions) (Figure 6.3a), implying that the exfoliation of the B-g-C_3N_4 material took place during the chemical process and the sheets were formed with pores, probably created by the escaping blowing gas. The 10% CdS/CNNS-CB sample in Figure 6.3b showed small particles with dimensions of about 5 nm on the porous transparent sheets, indicating that the CdS nanoparticles were deposited on the exfoliated CNNS-CB nanosheets during composite formation. Moreover, the 5% CdS/CNNS-CB (Supporting Information Figure S6.1, c) and 20% CdS/CNNS-CB CB (Supporting Information Figure S6.1, d) samples depicted the same observation, i.e., some small particles anchored on the CNNS-CB nanosheets. The CdS sample (Figure 6.3c) showed disordered, non-uniformly dispersed particles with dimensions of about 5-10 nm, and the particles could have slightly agglomerated because some regions of the micrograph were darker, implying more particles were sitting on each other; thus, the beam of electrons from the microscope could not pass through.

To further explore the microstructure of the samples, an HRTEM image of the samples was obtained. Figure 6.3d show the HRTEM image of the CNNS-CB sample. Clearly, lattice fringes were not observed during the analysis, indicating that the material could be amorphous and, therefore, presenting a diffuse kind of diffraction pattern. Notably, the samples with CdS particles showed distinct diffraction patterns, showing that the crystallinity was due to CdS nanoparticles and not the CNNS-CB component in the composite. Nonetheless, the calculated d-pacing for 5% CdS/CNNS-CB (Supporting Information Figure S6.1, (e)), 10% CdS/CNNS-CB (Figure 6.3e), 20% CdS/CNNS-CB (Supporting Information Figure S6.1, (d)) and CdS (Figure 6.3f) nanomaterials were: 0.336, 0.362, 0.330 and 0.388 nm, respectively. Generally, the d-spacing of the CdS nanoparticles decreased with the incorporation of CNNS-CB, suggesting that CdS strongly interacted with CNNS-CB during composite formation.

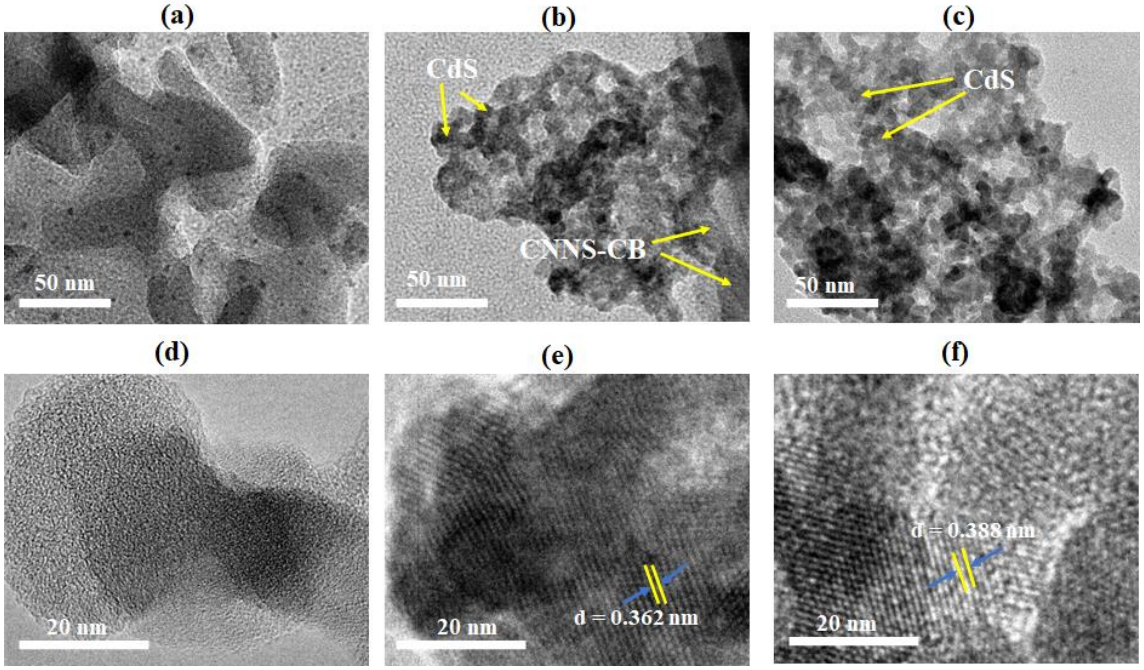

Figure 6.3: TEM images of (a) CNNS-CB, (b) 10% CdS/CNNS-CB, and (c) CdS samples, and HRTEM images of (d) CNNS-CB, (e) 10% CdS/CNNS-CB, and (f) CdS samples

6.3.1.2 Crystal structure analysis

The crystal structures of the as-prepared photoactive materials were determined by powder X-ray diffractometry and are presented in Figure 6.4a. The diffractograms show that the pure CNNS-CB sample gave a distinct diffractogram compared with CdS and CdS/CNNS-CB composites. CNNS-CB showed two characteristic peaks at about 2θ = 13.1 and 27.5°, which correspond to the (001) and (002) crystal planes of g-C_3N_4, respectively [22]. For samples with pure CdS and as dopant, diffraction peaks at 2θ = 23.40, 26.48, 30.24, 36.24, 43.68, 49.82, and 50.08°, were observed and identified to match the (100), (111), (020), (102), (202), (103), (112), and (311) planes of cubic hawleyite phase CdS, respectively. From the diffractograms, the peak at 2θ = 13.1° disappeared in the CdS/CNNS composites, implying that the interlayer spacing of CNNS-CB was significantly reduced with the introduction of CdS dopants. Additionally, the intensity of the characteristic intense peak at 2θ = 27.5° for CNNS-CB was decreased considerably due to an increase in the CdS dopant concentration. On the other hand, CdS samples present a distinct diffractogram compared with the CdS/CNNS-CB composites. Generally, the intensity of the peaks in the CdS sample decreased due to the increased

CNNS-CB concentration in the doped sample. The observed disappearance of some peaks and the changes in the intensity of the characteristic peak in the composites, when compared with the pure materials, suggest that composites that possess unique characteristics from the individual components were formed.

To further explore the crystal character of the materials, selected area diffraction (SAED) micrographs were acquired from the HRTEM analysis and are presented in Figure 6.4b. As can be seen, the CNNS-CB sample (Figure 6.4b, (i)) exhibited a diffuse, disc-shaped, without spots, micrograph - a characteristic of an amorphous material in powder form. The CdS (Figure 6.4b, (iii)) and CdS/CNNS-CB ((Figure 6.4b, (ii)) and (Supporting Information Figures S6.2a, (i) and (ii)) generally showed some crystallinity ascribed to the CdS nanoparticles in the samples.

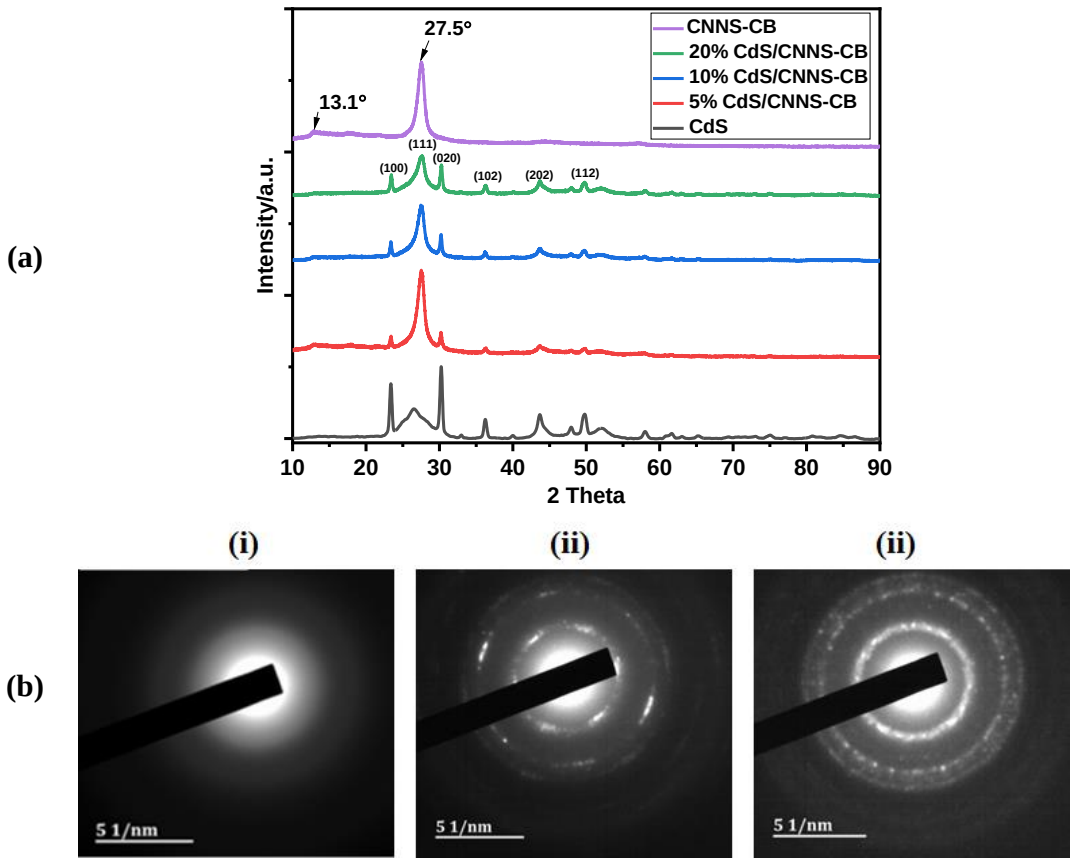

Figure 6.4: (a) Powder X-ray diffractograms for as-prepared materials. (b) Selected area diffraction (SAED) patterns of (i) CNNS-CB, (ii) 10% CdS/CNNS-CB and (iii) CdS samples

6.3.1.3 Chemical structure and composition

In order to identify the chemical structures in the as-prepared samples, Fourier transform infrared spectroscopy (FTIR) was carried out, and the results are presented in Figure 6.5. The CdS spectrum presented a distinct pattern when compared with the CNNS-CB samples. The peaks at around 3477-2890 cm^{-1} were assigned to either N-H or hydroxyl group stretching vibrations and were ascribed to the presence of the NH_2 functional group and adsorbed water in the samples, respectively [23]. Meanwhile, a peak at 2151 cm^{-1} was assigned to the cyano group (-C≡N) that may be present in the samples with the CNNS-CB component [24]. The bands at around 1700-1011 cm^{-1} were assigned to C-N or C=N heterocycles in the CNNS-CB-based samples [25]. Also, the band at 806 cm^{-1}, which was missing in the CdS sample, was attributed to the out-of-plane bending vibration of tri-s-triazine (heptazine) or s-triazine (triazine) units in the CNNS-CB-based samples [26]. Finally, for the CdS sample, the peak at 624 cm^{-1} in the fingerprint region was assigned to the Cd-S stretching vibration [27].

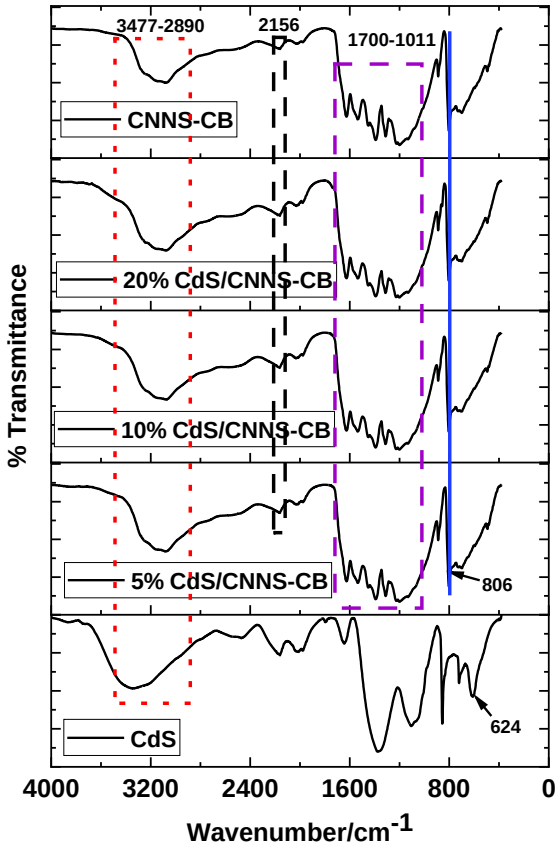

Figure 6.5: ATR-FTIR spectra for as-prepared samples

Furthermore, the elemental composition and distribution of the samples were investigated using SEM-EDX. The elemental composition graph, table (inset), and the mapping images of the samples are presented in Figure 6.6 and Supporting Information Figures S6.2 (b) and (c). As depicted in Figure 6.6a, C, N, and O elements were present in the CNNS-CB sample, and nitrogen was in a large proportion (58.48%) in the sample (Figure 6.6a inset). For the composites, in Figure 6.6b and Supporting Information Figures S6.2 (b) and (c), it was observed that all the elements (C, N, O, S and Cd) present in CNNS-CB and CdS were represented. This suggests that there was a successful formation of the composites. Cadmium (Cd) was evenly distributed especially in 5% CdS/CNNS-CB and 20% CdS/CNNS-CB (Supporting Information Figures S6.2 (b) and (c), respectively). Figure 6.6c shows that only Cd and S were present in the as-prepared CdS sample.

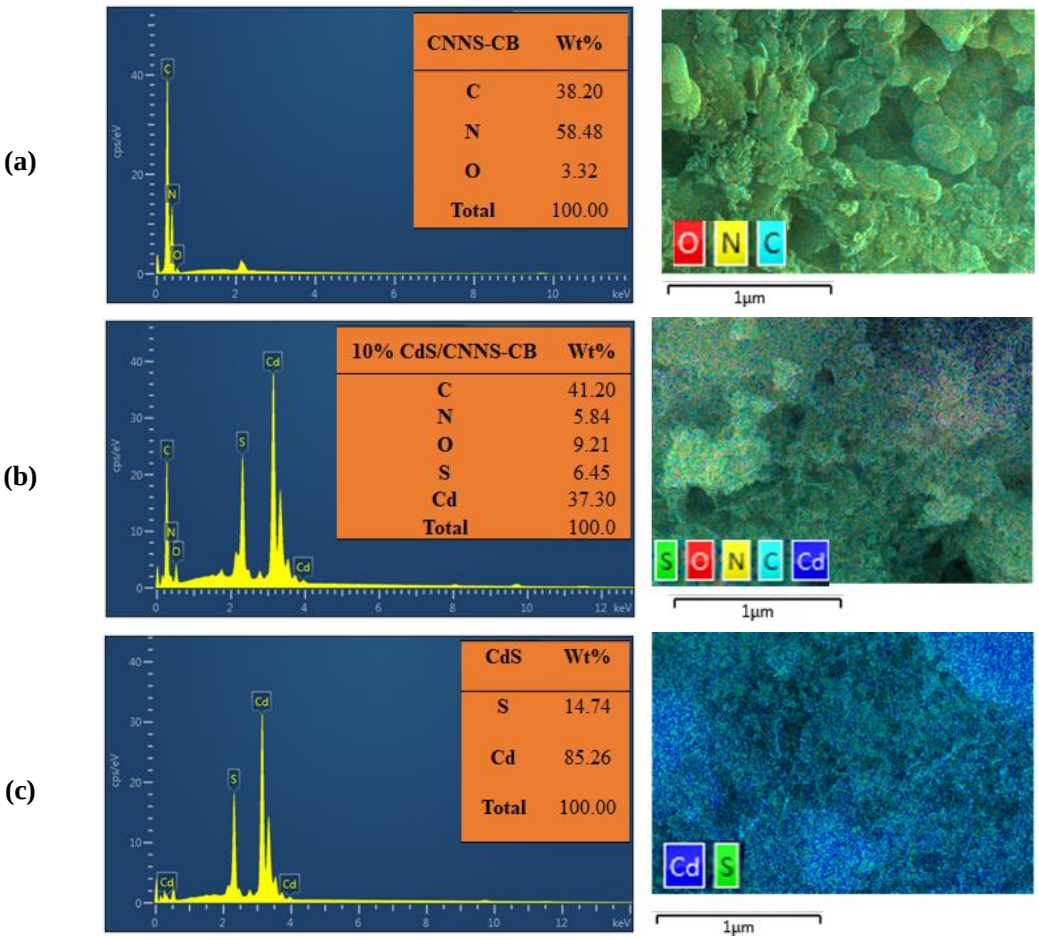

Figure 6.6: SEM-EDX elemental composition graph, composition table (inset), and the corresponding mapping images for (a) CNNS-CB, (b) 10% CdS/CNNS-CB and (c) CdS samples

6.3.1.4 Rate of recombination of photogenerated charges

The rate of recombination of photogenerated charges is crucial in photo-driven devices such as solar cells, where a material exhibiting a low recombination rate is desirable. Figure 6.7 show the PL spectra of the as-prepared samples excited at a wavelength of 410 nm. The CNNS-CB sample exhibited the highest intensity compared with the other materials, implying that the rate of recombination of photogenerated charges was highest in this sample. Nevertheless, the intensity of the CNNS-CB generally decreased significantly due to the introduction of the CdS dopant. Overall, the PL intensity of the composites and CdS was lower than that of the pure CNNS-CB material, thus, indicating lower recombination rates of photogenerated charges in CdS and the composites materials, which can be helpful in solar cell applications. Moreover, the CNNS-CB sample exhibited a red-shift as a function of increasing the CdS dose, indicating that the introduction of the CdS dopant probably modulated the band structure (band gap), thus the red-shift.

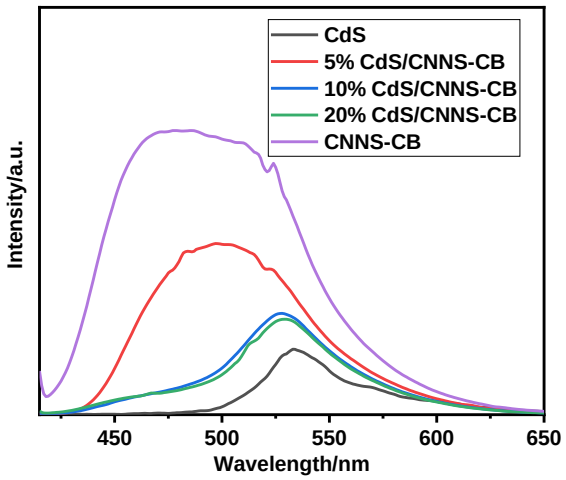

Figure 6.7: Photoluminescence spectra for as-prepared samples at an excitation wavelength of 410 nm

6.3.1.5 Optical properties and band structure

In order to determine the optical properties of as-prepared samples, UV-diffuse reflectance spectroscopy (UV-DRS) was carried out, and the spectra obtained are depicted in Figure 6.8. From Figure 6.8a, CdS exhibited the highest optical absorption at a wavelength of about 490 nm. Although with the incorporation of CNNS-CB, the intensity of the CdS decreased significantly, the absorption edge of the composites (5% CdS/CNNS-CB, 10% CdS/CNNS-CB, and 20% CdS/CNNS-CB) was extended towards longer wavelengths (red shift). The red shift experienced in the composites could be attributed to proper band alignment that resulted from intrinsic band structure modification in the composites, which is beneficial in solar-driven applications. The CNNS intensity was the lowest but extended towards the visible light region, as shown in Figure 6.8a.

The band structure of the photoactive materials was determined by the estimation of the band gap energies from the transformed Kubelka-Munk $((\alpha h\nu)^{1/2}/eV^{1/2}$ vs E/eV) plot (Figure 6.8b). The calculated band gap values are presented in Table 6.1. The band gap energies for CdS, 5% CdS/CNNS-CB, 10% CdS/CNNS-CB, 20% CdS/CNNS-CB, and CNNS-CB samples were: 2.14, 2.07, 1.99, 2.03, and 2.09 eV, respectively. The 10% CdS/CNNS-CB sample exhibited the lowest band gap, probably due to the formation of a heterostructure between CNNS-CB and CdS with a modified band structure, thus a low band gap value. Essentially, a low band gap is beneficial since the material would absorb more light, especially in the visible region of the electromagnetic spectrum. Moreover, the positions of the conduction band (CB) and the valence band (VB) were estimated by using the already calculated band gap energies (from the Kubelka-Munk plots) in the Butler and Ginley equations (Equations (1) and (2))

$$E_{VB} = \chi - E_e + 0.5E_g \qquad \text{Equation (1)}$$

$$E_{CB} = E_{VB} - E_g \qquad \text{Equation (2)}$$

where E_g is the energy gap (band gap) calculated from the Kubelka-Munk plot, χ is the electronegativity of the semiconductor and is 4.73 eV for g-C_3N_4 [28], and E_e is the energy of free electrons on the hydrogen scale (approx. 4.5 eV). The calculated values of the VB and CB are illustrated in Table 6.1. The VBs and CBs values of the CNNS-CB sample

changed significantly when the CdS dopant was introduced, suggesting that new materials were formed during composite formation.

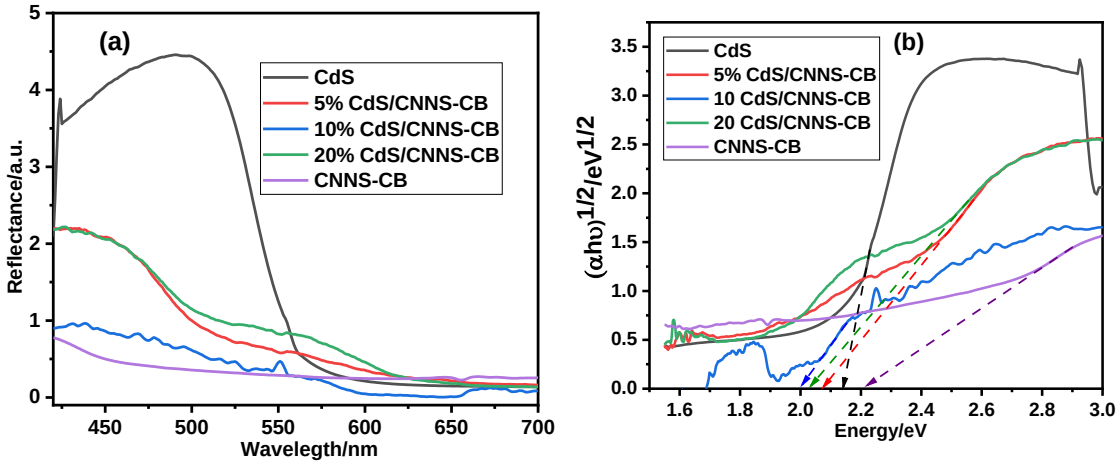

Figure 6.8: (a) The UV-Visible diffuse reflectance spectra and (b) transformed Kubelka-Munk plots for as-prepared pure CdS, CNNS-CB, and CdS/CNNS-CB composites samples

Table 6.1: Optical properties of the as-prepared samples

Material	Band gap energy/eV	Valence band potential/eV	Conduction band potential/eV
CdS	2.14	1.30	-0.84
5% CdS/CNNS-CB	2.07	1.27	-0.8
10% CdS/CNNS-CB	1.99	1.23	-0.76
20% CdS/CNNS-CB	2.03	1.25	-0.78
CNNS-CB	2.09	1.28	-0.81

6.3.1.6 Thermal stability

Figure 6.9 shows the thermograms of the as-prepared samples investigated under air. Figure 6.9a show the weight loss as a function of temperature for the materials, between a temperature of 27 and 968 °C. The initial mass loss of about 2% experienced by the samples from the initial temperature to about 200 °C was ascribed to the loss of adsorbed water in the samples. The drastic mass loss for the CNNS-CB, 5% CdS/CNNS-CB, 10%

CdS/CNNS-CB, and 20% CdS/CNNS-CB samples that occurred at a temperature around 500 - 750 °C was linked to the thermal decomposition of the g-C_3N_4 framework, to release CO_2 and oxides of nitrogen (NO_x). The CdS sample, as expected, experienced no mass loss because of its high thermal stability of above 1000 °C. Furthermore, the residual masses for 5% CdS/CNNS-CB, 10% CdS/CNNS-CB, and 20% CdS/CNNS-CB composites were 5.76, 10.94, and 17.95%, respectively. The residual masses obtained were attributed to the remaining mass of thermally stable CdS in the samples. Notably, the respective residual masses of the composites agreed with the proportion of CdS incorporated in the CNNS-CB before forming the composites via a mechanochemical approach (refer to Section 6.2.2). The specific decomposition temperatures of the samples were deduced from the derivative curves presented in Figure 6.9b. The exact thermal decomposition temperature for 5% CdS/CNNS-CB, 10% CdS/CNNS-CB, 20% CdS/CNNS-CB, and CNNS-CB were found to be: 711, 697, 706, and 707 °C, correspondingly. It can be noted that the CNNS-CB-based samples experience high thermal stability (stable up to 690 °C), which is desirable in photo-driven applications.

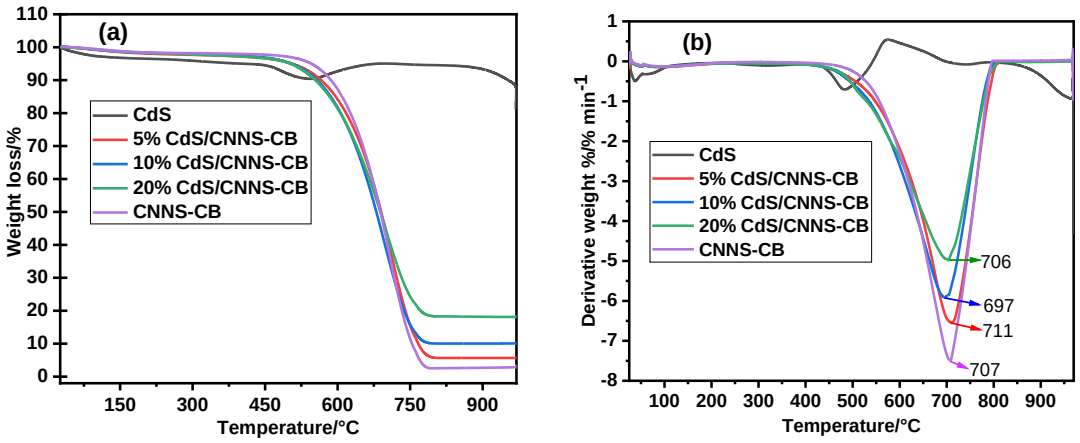

Figure 6.9: (a) TGA thermograms and (b) the corresponding derivative graphs for as-prepared pure CdS, CNNS-CB, and CdS/CNNS-CB composite samples, performed under air conditions

6.3.2 Device characterisation and measurements

The performance of the fabricated devices was evaluated and is presented in this section in terms of photovoltaic parameters, i.e., PCE, open circuit voltage (V_{oc}), short circuit current density (J_{sc}), fill factor (FF), and series resistance (Rs).

6.3.2.1 Optical absorption of the devices

In order to ascertain the light-harvesting ability of the fabricated devices, optical absorption spectra were obtained. Figure 6.10 shows the optical absorption of devices with or without the dopants in the active layer. As can be observed, the absorbance of all devices was highest in the region between 450-600 nm of the electromagnetic spectrum, an indication that they can absorb visible light, which is the most abundant in solar radiation. The absorption maximum centred at around 512 nm can be ascribed to the absorbance of a common P3HT:PC_{61}BM polymer blend utilised in all devices. Remarkably, the absorption intensity of the doped devices was higher than that of the undoped cell (pristine), and this was attributed to the enhanced light harvesting ability brought about by the dopants in the active layers.

Furthermore, for only doped devices, the absorption shoulder at around 600 nm (which was missing in the spectrum of the pristine device) extended towards a longer wavelength (Figure 6.10). The introduction of dopants could have led to the red shift, which is beneficial in OSCs. The OSC with the 10% CdS/CNNS-CB exhibited the highest absorption in the visible region when compared with its counterparts. This can be ascribed to its lowest band gap energy (see Table 6.1), which facilitates the absorption of more visible light. Essentially, the greater the light-harvesting capability of a device, the more improved should be its photovoltaic performance.

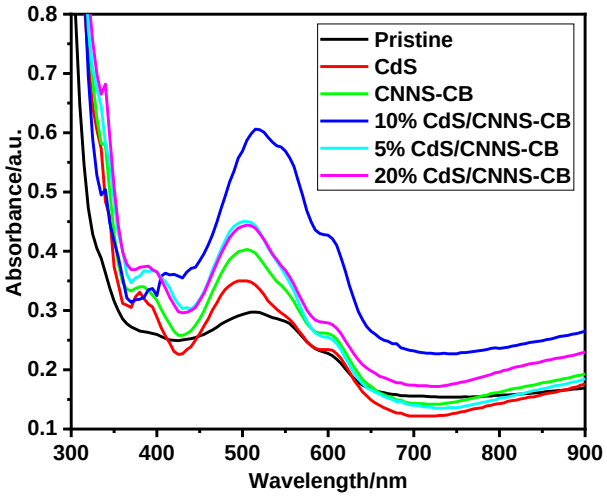

Figure 6.10: Optical absorption spectra of the fabricated OSC devices

6.3.2.2 Photovoltaic characteristics of devices

The photovoltaic performance of the fabricated devices was evaluated by carrying out current-versus-voltage (J-V) measurements. Figure 6.11 shows the J-V curves for the devices with or without the dopants in the active layer with P3HT:$PC_{61}BM$ polymer blends. Moreover, the extracted photovoltaic parameters (PCE, J_{sc}, FF, $V_{oc,}$ and R_s) of the devices are presented in Table 6.2. From the J-V curves (Figure 6.11), the devices offer different characteristics, particularly the magnitudes of the photogenerated currents. In essence, devices with dopants in the active layer showed appreciable enhanced photogenerated current densities (Table 6.2). The improvement in the high current generation could be attributed to better light absorption due to the incorporation of dopants in the active layer, which in turn assisted in the extraction of more excitons. This was also observed in the UV-Vis spectra of the OSC devices (Figure 6.10). The 10% CdS/CNNS-CB composite device exhibited the highest PCE of 3.45%, J_{sc} of 12.57 mA cm^{-2}, and FF of 55.26% (Table 6.2). The remarkable PCE of 3.45% was 182% greater than that of the pristine device, with a PCE of 1.89%. The improvement in performance for this particular device (10% CdS/CNNS-CB) could be ascribed to better light absorption due to the low band gap, thus high photocurrent current generation, low recombination of photogenerated charges, and enhanced charge transfer characteristics (due to the low series resistance). The poorer performance of the pristine device, i.e., PCE of 1.89%, could be linked to its highest series resistance of 838 Ω cm^2, as shown in Table 6.2. The high resistance could result from the high recombination rate of

photogenerated charges and poor light-harvesting characteristics. It can be observed that the devices with CNNS-CB components (Table 6.2) showed a relatively low series resistance of less than 600 Ω cm^2; this could imply that the CNNS-CB could aid in the passivation of bulk defects and facilitate a fast charge transfer process in the devices [29].

Nonetheless, the devices with 5% CdS/CNNS-CB and 20% CdS/CNNS-CB showed appreciably high PCEs of 2.74 and 2.70%, respectively. The relatively high performance could be credited to relatively high J_{sc} (above 10 mA cm^{-2}) and FF values (above 50%). Notably, the slight difference in their performance could be due to the fact that J_{sc} and FF in 20% CdS/CNNS-CB devices slightly dropped, probably due to an increase in CdS dopant concentration beyond the optimum 10%. Generally, the performance of doped devices with CdS/CNNS-CB composites was higher than that of individual CdS and CNNS-CB, implying that there was a significant synergistic effect in the composites.

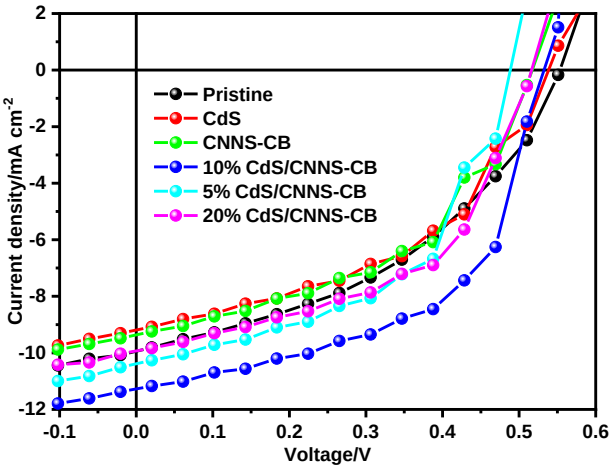

Figure 6.11: The current-voltage characteristic of OSC devices fabricated with P3HT:PC_{61}BM active layer blends with various dopants at 1.0 wt.% concentration

Table 6.2: Photovoltaic parameters of the fabricated OSC devices

P3HT:$PC_{61}BM$:Nanoparticles	V_{oc}/V	J_{sc}/mA cm^{-2}	FF/%	PCE/%	R_s/Ω cm^2
Pristine	0.57	10.03	39.43	1.89	838
CdS	0.53	8.24	49.97	1.92	698
CNNS-CB	0.53	10.03	46.01	2.36	582
5% CdS/CNNS-CB	0.50	10.95	51.74	2.74	536
10% CdS/CNNS-CB	0.54	12.57	55.26	3.45	511
20% CdS/CNNS-CB	0.50	10.49	50.60	2.70	567

6.3.2.3 Charge transport characteristics

Device charge transport characteristics are an important property to measure in an OSC since they give an indication of the mobility of charge carriers in the device. In order to investigate the charge transfer properties of the fabricated devices, space charge limited current (SCLC) measurements were made under dark conditions [30]. In the dark, charge generation is impeded due to the absence of light, and trap states are filled in the material. Figure 6.12 shows the J-V curves taken in the dark for the fabricated devices on a log scale. As can be seen, from Figure 6.12a, the J-V curves manifest a diode-like behaviour. The graph can be divided into three regions; the first part is at low voltage. Here, the curve obeys Ohms law; the second part is evidenced by a sudden dip where all the trap states have been filled; and the third region is where the curve becomes asymptotic before reaching a maximum. This is the SCLC regime, where the current extracted from the device is dependent only on the bulk properties of the active layer. Consequently, the Mott–Gurney law can be utilised to explain the SCLC of a given system, with the condition that the Ohmic contact exists between the electrode and semiconductor [30, 31]. Therefore, the Mott–Gurney law can be expressed as

$$J = \frac{9}{8}\varepsilon\varepsilon_{\circ}\mu_{\circ}\frac{V^2}{L^3}exp\left(0.89\gamma\sqrt{\frac{V}{L}}\right) \qquad \text{Equation (3)}$$

where ε is the relative permittivity of the material, $\varepsilon_{\circ}$ is the permittivity of free space, $\mu_{\circ}$ is the low-field mobility, γ is the field activation factor, V is the applied voltage, V_{bi}, is

the built-in voltage, and L is the thickness of the active layer. In order to obtain the values of zero field mobility and the field activation factor, the data acquired from the SCLC measurement in the dark was fitted into Equation 3. The fitting graph was plotted and is presented in Figure 6.12b. As can be observed, the experimental data fit well with Equation 3. Meanwhile, Table 6.3 depicts the zero field mobilities obtained and the field activation factors of devices. Clearly, the effect of dopants on μ_o, the transport parameter, was significant. From Table 6.3, the device with CdS exhibited the highest carrier mobility, μ_o of 7.2080×10^{-3} $cm^2 S^{-1} V^{-1}$ at a field activation factor of -9.5347×10^{-4} cm V^{-1}, while the pristine device showed the lowest value of 2.1514×10^{-4} $cm^2 S^{-1} V^{-1}$, at a γ value of -1.3677×10^{-4} cm V^{-1}, implying that CdS nanoparticles can facilitate a fast charge transport mechanism in the OSC. Generally, the values of μ_o, the transport parameter, increased by order of magnitude with the incorporation of dopants into the active layer of the respective devices compared with the pristine materials. Nonetheless, the values of the field activation factor, γ, apparently remained unchanged as a function of doping.

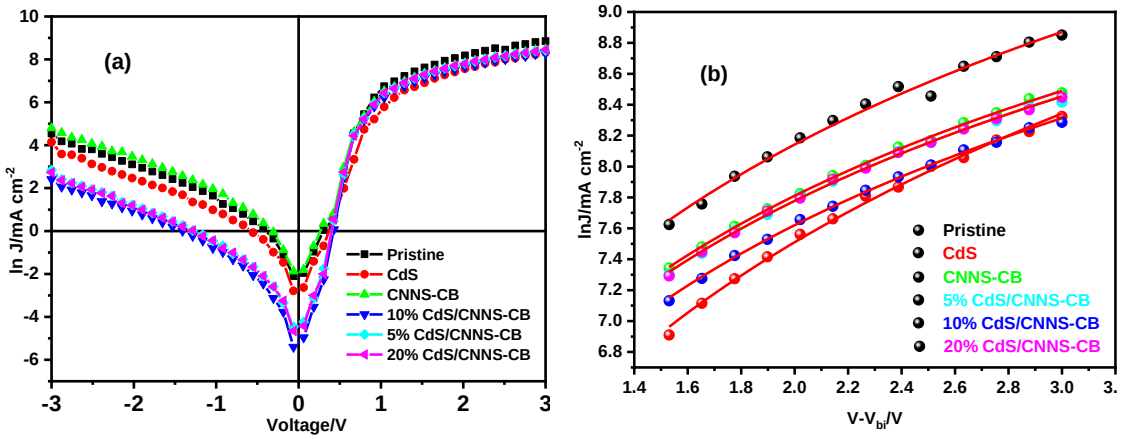

Figure 6.12: The current-voltage characteristics measured in the dark for devices with different nanoparticles (a) and (b) the SCLC achieved from the fabricated OSC devices, and a fit based on Equation (3)

Table 6.3: The charge carrier mobility parameters for the fabricated OSCs

P3HT:$PC_{61}BM$:Nanoparticles	μ_o (Zero-field mobility)/cm^2 S^{-1} V^{-1}	γ (Field activation factor)/cm V^{-1}
Pristine	2.1514×10^{-4}	-1.3677×10^{-4}
Cds	7.2080×10^{-3}	-9.5347×10^{-4}
CNNS-CB	1.9359×10^{-3}	-4.5823×10^{-4}
5% Cds/CNNS-CB	1.8990×10^{-3}	-1.2252×10^{-4}
10% Cds/CNNS-CB	1.4998×10^{-3}	-1.2009×10^{-4}
20% Cds/CNNS-CB	1.9272×10^{-3}	-1.2307×10^{-4}

6.4 Conclusion

Graphitic carbon nitride nanosheets (CNNS-CB) from the chemical blowing method of exfoliation of bulk g-C_3N_4 were synthesised and successfully doped with cadmium sulfide nanoparticles. The as-prepared materials were suitably incorporated into the active layer of an organic solar cell (OSC) with poly(3-hexylthiophene) (P3HT) and [6,6]-phenyl C_{61}-butyric acid methyl ester (PCBM) polymer blends as a dopant. The introduction of dopants in the active layer was aimed towards the improvement of photon harvesting, charge transport, and suppression of fast charge recombination in the active layer of an OSC, thus, yielding high performance. From the results obtained, it was established that the CNNS-CB material exhibited an amorphous structure with defects probably caused by escaping blowing gases during the synthesis process. Basically, a porous structure can aid in the creation of cross-plane diffusion channels for effective charge and mass transfer processes. The introduction of defects in the CNNS-CB material is believed to have led to intrinsic modulation of the band structure, leading to the exhibited low band gap (of about 2.09 eV) formation, which was effective in the light-harvesting process. In view of this, the band gap reduction in the composites was linked more to the presence of the CNNS-CB component, thus, aiding light-harvesting. Moreover, the CdS nanoparticles formed were somewhat crystalline and, therefore, could be responsible for the crystallinity observed in the composites. Also, the CdS sample showed the lowest rate of recombination of photogenerated charges; therefore, it was

deduced that CdS could have aided in suppressing the fast recombination of photogenerated charges in the composites.

Consequently, the as-prepared CdS/CNNS-CB composites showed better light absorption due to a reduced band gap and suppressed recombination of photogenerated charges (relatively low photoluminescence intensity), ascribed to the existence of a synergistic effect between the CNNS-CB and CdS materials. Remarkably, by incorporating 10% CdS/CNNS-CB as a dopant in the active layer of the OSC, our device attained an optimal PCE of 3.45%, which was a power conversion enhancement of about 183% compared with that of the pristine device (PCE = 1.89%). The best performance was ascribed to better light-harvesting properties, the reduced recombination rate of photogenerated charges, and enhanced charge mobility compared with the undoped device. However, it was noted that a large dose of CdS in the sample was detrimental to the PCE of the device. Therefore, CdS concentrations should be kept optimally low for improved performance and, by extension, for environmental concerns. This work demonstrates a potential avenue for improving the performance of OSC in the near future.

Acknowledgements

The authors are appreciative of the financial support provided by the National Research Foundation (NRF) of South Africa, under grant numbers 103979 and 109580; the University of KwaZulu-Natal (UKZN), the UKZN Nanotechnology Platform, and the Eskom Tertiary Education Support Programme (TESP). Finally, the authors are very thankful to Professor Genene Mola and his team at the UKZN-PMB campus for using facilities in their laboratory to fabricate devices.

Conflict of interest

The authors declare no conflict of interest.

References

[1] R. Ma, C. Yan, J. Yu, T. Liu, H. Liu, Y. Li, J. Chen, Z. Luo, B. Tang, X. Lu, G. Li, H. Yan, High-efficiency ternary organic solar cells with a good figure-of-merit enabled by two low-cost donor polymers. ACS Energy Lett. **7**, 2547-2556 (2022). https://doi.org/10.1021/acsenergylett.2c01364.

[2] O.A. Abdulrazzaq, V. Saini, S. Bourdo, E. Dervishi, A.S. Biris, Organic solar cells: A review of materials, limitations, and possibilities for improvement. Part. Sci. Technol. **31**, 427-442 (2013). https://doi.org/10.1080/02726351.2013.769470.

[3] Z. Hu, J. Wang, X. Ma, J. Gao, C. Xu, K. Yang, Z. Wang, J. Zhang, F. Zhang, A critical review on semitransparent organic solar cells. Nano Energy. **78**, 105376 (2020). https://doi.org/10.1016/j.nanoen.2020.105376.

[4] K. Jin, Z. Xiao, L. Ding, 18.69% PCE from organic solar cells. J. Semicond. **42**, 060502 (2021). https://doi.org/10.1088/1674-4926/42/6/060502.

[5] R. Zhou, Z. Jiang, C. Yang, J. Yu, J. Feng, M.A. Adil, D. Deng, W. Zou, J. Zhang, K. Lu, W. Ma, F. Gao, Z. Wei, All-small-molecule organic solar cells with over 14% efficiency by optimizing hierarchical morphologies. Nat. Commun. **10**, 5393 (2019). https://doi.org/10.1038/s41467-019-13292-1.

[6] S.D. Dimitrov, Z. Huang, F. Deledalle, C.B. Nielsen, B.C. Schroeder, R.S. Ashraf, S. Shoaee, I. McCulloch, J.R. Durrant, Towards optimisation of photocurrent from fullerene excitons in organic solar cells. Energy Environ. Sci. **7**, 1037-1043 (2014). https://doi.org/10.1039/C3EE42607F

[7] C. Cui, Y. Li, Morphology optimization of photoactive layers in organic solar cells. Aggregate. **2**, e31 (2021). https://doi.org/10.1002/agt2.31.

[8] C. Ma, N.-G. Park, A realistic methodology for 30% efficient perovskite solar cells. Chem. **6**, 1254-1264 (2020). https://doi.org/10.1016/j.chempr.2020.04.013.

[9] S.R. Cowan, N. Banerji, W.L. Leong, A.J. Heeger, Charge formation, recombination, and sweep-out dynamics in organic solar cells. Adv. Funct. Mater. **22**, 1116-1128 (2012). https://doi.org/10.1002/adfm.201101632.

[10] M. Riede, D. Spoltore, K. Leo, Organic solar cells—The path to commercial success. Adv. Energy Mater. **11**, 2002653 (2021). https://doi.org/10.1002/aenm.202002653.

[11] P. Mahendia, G. Chauhan, H. Wadhwa, G. Kandhol, S. Mahendia, R. Srivastava, O.P. Sinha, T.D. Clemons, S. Kumar, Study of induced structural, optical and electrochemical properties of poly(3-hexylthiophene) (P3HT), [6,6]-phenyl-C_{61}-butyric-acid-methyl-ester (PCBM) and their blend as an effect of graphene doping. J. Phys. Chem. Solids. **148**, 109644 (2021). https://doi.org/10.1016/j.jpcs.2020.109644.

[12] A.T. Mallajosyula, S.S.K. Iyer, B. Mazhari, Increasing the efficiency of charge extraction limited poly-(3-hexylthiophene):[6,6] phenyl C_{61}-butyric acid methyl ester solar cells using single walled carbon nanotubes with metallic characteristics. J. Appl. Phys. **109**, 124908 (2011). https://doi.org/10.1063/1.3598081.

[13] D.H. Shin, C.W. Jang, J.S. Ko, S.-H. Choi, Enhancement of efficiency and stability in organic solar cells by employing MoS_2 transport layer, graphene electrode, and

graphene quantum dots-added active layer. Appl. Surf. Sci. **538**, 148155 (2021). https://doi.org/10.1016/j.apsusc.2020.148155.

[14] Z. Zhao, Y. Sun, F. Dong, Graphitic carbon nitride based nanocomposites: A review. Nanoscale. **7**, 15-37 (2015). https://doi.org/10.1039/C4NR03008G

[15] N. Rono, J.K. Kibet, B.S. Martincigh, V.O. Nyamori, A review of the current status of graphitic carbon nitride. Crit. Rev. Solid State Mater. Sci. **46**, 189-217 (2021). https://doi.org/10.1080/10408436.2019.1709414.

[16] D. Lu, P. Fang, W. Wu, J. Ding, L. Jiang, X. Zhao, C. Li, M. Yang, Y. Li, D. Wang, Solvothermal-assisted synthesis of self-assembling TiO_2 nanorods on large graphitic carbon nitride sheets with their anti-recombination in the photocatalytic removal of Cr(VI) and rhodamine B under visible light irradiation. Nanoscale. **9**, 3231-3245 (2017). https://doi.org/10.1039/C6NR09137G.

[17] N. Rono, J.K. Kibet, B.S. Martincigh, V.O. Nyamori, A comparative study between thermal etching and liquid exfoliation of bulk graphitic carbon nitride to nanosheets for the photocatalytic degradation of a model environmental pollutant, Rhodamine B. J. Mater. Sci. Mater. **32**, 687-706 (2021). https://doi.org/10.1007/s10854-020-04849-8.

[18] H. Liu, S. Ma, L. Shao, H. Liu, Q. Gao, B. Li, H. Fu, S. Fu, H. Ye, F. Zhao, J. Zhou, Defective engineering in graphitic carbon nitride nanosheet for efficient photocatalytic pathogenic bacteria disinfection. Appl. Catal. B: Environ. **261**, 118201 (2020). https://doi.org/10.1016/j.apcatb.2019.118201.

[19] P. Niu, M. Qiao, Y. Li, L. Huang, T. Zhai, Distinctive defects engineering in graphitic carbon nitride for greatly extended visible light photocatalytic hydrogen evolution. Nano Energy. **44**, 73-81 (2018). https://doi.org/10.1016/j.nanoen.2017.11.059.

[20] Y. Jiang, Z. Sun, C. Tang, Y. Zhou, L. Zeng, L. Huang, Enhancement of photocatalytic hydrogen evolution activity of porous oxygen doped g-C_3N_4 with nitrogen defects induced by changing electron transition. Appl. Catal. B: Environ. **240**, 30-38 (2019). https://doi.org/10.1016/j.apcatb.2018.08.059.

[21] Z.R. Khan, M. Zulfequar, M.S. Khan, Chemical synthesis of CdS nanoparticles and their optical and dielectric studies. J. Mater. Sci. **46**, 5412-5416 (2011). 10.1007/s10853-011-5481-0.

[22] J. Wang, D. Hao, J. Ye, N. Umezawa, Determination of crystal structure of graphitic carbon nitride: Ab initio evolutionary search and experimental validation. Chem. Mater. **29**, 2694-2707 (2017). https://doi.org/10.1021/acs.chemmater.6b02969.

[23] G. Liu, G. Zhao, W. Zhou, Y. Liu, H. Pang, H. Zhang, D. Hao, X. Meng, P. Li, T. Kako, J. Ye, In situ bond modulation of graphitic carbon nitride to construct p–n homojunctions for enhanced photocatalytic hydrogen production. Adv. Funct. Mater. **26**, 6822-6829 (2016). https://doi.org/10.1002/adfm.201602779.

[24] S. Yang, Y. Gong, J. Zhang, L. Zhan, L. Ma, Z. Fang, R. Vajtai, X. Wang, P.M. Ajayan, Exfoliated graphitic carbon nitride nanosheets as efficient catalysts for hydrogen evolution under visible light. Adv. Mater. **25**, 2452-2456 (2013). https://doi.org/10.1002/adma.201204453.

[25] Y. Shi, Z. Gui, B. Yu, R.K.K. Yuen, B. Wang, Y. Hu, Graphite-like carbon nitride and functionalized layered double hydroxide filled polypropylene-grafted maleic anhydride nanocomposites: Comparison in flame retardancy, and thermal, mechanical and UV-shielding properties. Compos. B. Eng. **79**, 277-284 (2015). https://doi.org/10.1016/j.compositesb.2015.04.046.

[26] B.V. Lotsch, M. Döblinger, J. Sehnert, L. Seyfarth, J. Senker, O. Oeckler, W. Schnick, Unmasking melon by a complementary approach employing electron diffraction, solid-state nmr spectroscopy, and theoretical calculations—structural characterization of a carbon nitride polymer. Eur. J. Chem. **13**, 4969-4980 (2007). https://doi.org/10.1002/chem.200601759.

[27] M. Cui, Y. Xin, R. Song, Q. Sun, X. Wang, D. Lu, Fluorescence sensor for bovine serum albumin detection based on the aggregation and release of CdS QDs within CMC. Cellulose. **27**, 1621-1633 (2020). https://doi.org/10.1007/s10570-019-02865-4.

[28] Y. Sun, W. Zhang, T. Xiong, Z. Zhao, F. Dong, R. Wang, W.-K. Ho, Growth of BiOBr nanosheets on C_3N_4 nanosheets to construct two-dimensional nanojunctions with enhanced photoreactivity for NO removal. J. Colloid Interface Sci. **418**, 317-323 (2014). https://doi.org/10.1016/j.jcis.2013.12.037.

[29] P. Liu, Y. Sun, S. Wang, H. Zhang, Y. Gong, F. Li, Y. Shi, Y. Du, X. Li, S.-s. Guo, Q. Tai, C. Wang, X.-Z. Zhao, Two dimensional graphitic carbon nitride quantum dots modified perovskite solar cells and photodetectors with high performances. J. Power Sources. **451**, 227825 (2020). https://doi.org/10.1016/j.jpowsour.2020.227825.

[30] Z. Xu, J.P. Madalaimuthu, J.B. Slowik, R. Meitzner, A. Anand, S. Alam, H. Corte, S. Stumpf, U.S. Schubert, H. Hoppe, Compatible solution-processed interface materials for improved efficiency of polymer solar cells. Adv. Mater. Interfaces 2201740 (2022). https://doi.org/10.1002/admi.202201740.

[31] G. Tessema, Charge transport across bulk heterojunction organic thin film. Appl. Phys. A. **106**, 53-57 (2012). https://doi.org/10.1007/s00339-011-6676-6.

CHAPTER SEVEN

Recent advances in the development and simulation of perovskite solar cell devices

Nicholas Rono,[a] Abdelkrim E. Merad,[b] Joshua K. Kibet,[c] Bice S. Martincigh[a] and Vincent O. Nyamori[a]*

[a]School of Chemistry and Physics, University of KwaZulu-Natal, Westville Campus, Private Bag X54001, Durban, 4000, South Africa

[b]Solid State Physics Team, Theoretical Physics Laboratory, Faculty of Sciences, A Belkaid University, Box 119, 13000, Tlemcen, Algeria

[c]Chemistry Department, Egerton University, Njoro Campus, P.O. Box 536-20115, Egerton, Kenya

*Corresponding author: E-mail: Nyamori@ukzn.ac.za, Tel: +27312608256

Abstract

Recently, perovskite solar cells (PSCs) have gained enormous scientific attention because of their high-power conversion efficiency (PCE) of above 25%, ease of fabrication, and relatively low cost. Consequently, PSCs are promising to replace the expensive silicon-based solar cells. However, despite their attractive attributes, PSCs still face numerous challenges, such as low stability, interfacial and bulk recombination of photogenerated charges, and lead toxicity, thus, hindering their commercialisation. In this review, various configurations of the devices and the challenges facing PSCs have been highlighted. The current state-of-the-art computational modelling simulators are presented and extensively discussed. In addition, the utilisation of simulators in studying the physics of the devices has been exemplified. The advantages and shortcomings of various simulators in simulations of PSC devices have been pointed out. Overall, this review will shed more light on the theoretical and experimental future fabrication strategies of PSCs and easing hurdles for better performances and envisaged commercialisation.

Keywords: Numerical simulation; electron transport layer; perovskite solar cells; power conversion efficiency; hole transport layer; lead-free

7.1 Introduction

Globally, technological advancement and ever-rising population growth have led to substantial energy demands. Consequently, available fossil fuels are on the verge of depletion because of overutilisation in various sectors of world economies. In essence, industrialisation has been embraced by many countries because it is known to boost economic growth but requires a high amount of energy, which has accelerated the utilisation of non-renewable sources [1]. The excessive use of these forms of energy has led to pollution of the environment and global warming effects because of the emission of greenhouse gases such as carbon dioxide, methane, and oxides of nitrogen (NO_x), and many others, thus causing climate change [2]. To mitigate these effects, scientists are exploring renewable potential energy sources such as geothermal, wind, and solar to replace non-renewable sources [3, 4]. Among these packs of energy sources, solar energy has been identified to be more promising. Thus, many efforts have been put forward to harvest it both at industrial and laboratory scales. Towards this end, photovoltaic technologies have attracted much scientific attention and technologies towards converting solar energy directly to other forms [5]. According to the American Society for Testing and Materials, the solar energy reaching the earth's surface is air mass 1.5G (AM 1.5G) and air mass 1.5D (AM 1.5D), as depicted in Figure 7.1. For instance, the power densities for these spectral irradiances, AM 1.5G is about 1000 W m^{-2}, and AM 1.5D is about 900 W m^{-2} [6-8]. The spectral irradiance AM 1.5G is relevant to photovoltaics, and AM 1.5D is appropriate for solar concentrators [8]. Solar energy irradiance has not been fully tapped globally either by solar thermal technology or photovoltaic conversions [9]. Generally, photovoltaic conversions of solar energy entail the following essential processes which must take place simultaneously in order to convert solar energy into useful electric current: (i) absorption of solar radiations using appropriate materials, (ii) generation of electron-hole pairs, (iii) separation of charge carriers (holes and electrons) to avoid recombination, and (iv) transfer of photogenerated holes and electrons to the respective electrodes [10-12]. The effectiveness of a device in the conversion of solar energy to electricity solely depends on these four basic processes and, therefore, efforts to engineer devices with high power conversion efficiencies (PCE) is still ongoing to optimise the above processes.

Basically, a perovskite material has the following general cubic structure $AB^{2+}X_3$ (ABX_3) [13], where A, B and X are atoms of distinct elements. A and B are metallic cations, while X is non-metallic anion such as a halogen. An A cation is always larger size than the other B and X elements. Other perovskites derivative structures include: $A_2B^{4+}X_6$ such as K_2PtCl_6 [14]; $A_3B_2{}^{3+}X_9$, for example $Rb_3Bi_2I_9$ [15]; and $A_2B^{1+}B^{3+}X_6$ [16], a typical example of which is $Cs_2AgBiBr_6$ films [17].

The inorganic-organic hybrid perovskites belonging to the third-generation solar cells have been utilised to generate cost-effective devices for solar energy conversions [18, 19]. This is because perovskites have attractive inherent properties such as better light absorption capabilities, tuneable band gaps, easy and cheap fabrication routes, and high charge carrier mobilities [20, 21]. At present, the PCE of organo-lead perovskite solar cells (PSCs) has reached over 25% within ten years since its inception in 2009 by Kojima et al. [22]; however, this performance is still far from the theoretical Shockley–Queisser limit efficiency which is about a PCE of over 31% [8]. Although lead-based perovskites have exhibited good PCE, there are two main limitations of this kind of perovskite: stability issues and toxicity of lead, which limits their commercialisation [23, 24]. A new class of lead-free or lead-less perovskite alternatives have emerged; for example, tin (Sn) [25], antimony [26, 27], and germanium [28]-based perovskites have been tested because they are believed to be environmentally friendly [29, 30].

In order to boost the performance of photovoltaic devices, different approaches have been proposed, which include experimentally engineering devices [31], computational studies of PSC materials [32, 33] and, in particular, device modelling and simulations [34, 35]. Device modelling and simulations have made impressive strides, as witnessed by the significant rise in the number of publications on these topics.

This review highlights the principle of operation, various configurations, and the challenges facing PSCs. Moreover, the current state-of-the-art modelling simulators and techniques are critically reviewed. The critical parameters that influence the overall performance of a PSC are illustrated regarding how they can be achieved using numerical simulators. In essence, the effects of thicknesses of various layers, doping concentration, density of defects, different hole transport (HTL) and electron transport layer (ETL) materials, operating temperatures, different metal work functions, and different configurations on overall photovoltaic performance are presented.

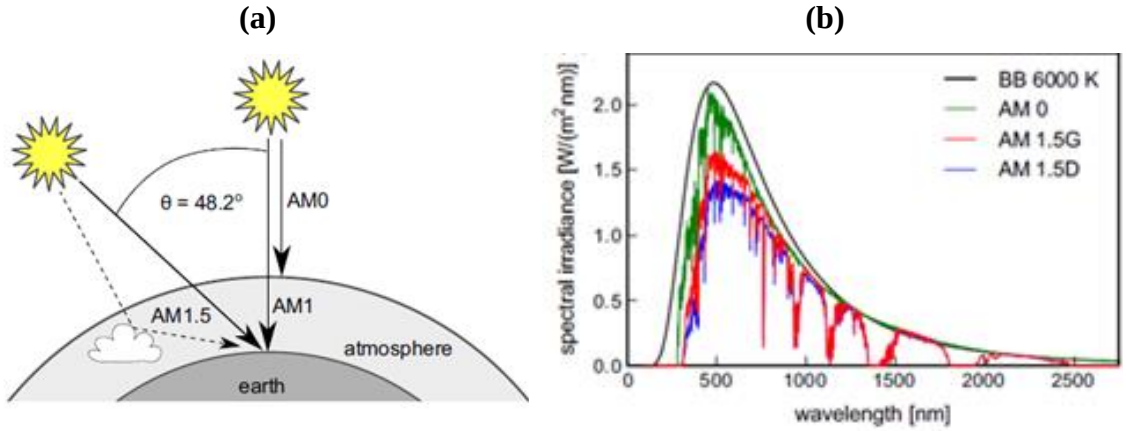

Figure 7.1: (a) Schematic representation of the spectral irradiance for direct sunlight, AM 1.5D (solid arrow), direct scattered sunlight, AM 1.5G (solid and dashed arrow), and sunlight outside the earth's atmosphere (AM 0), and (b) Spectral irradiance spectra as per standard American Society for Testing and Materials with the spectrum of the black body obtained by Shockley and Queisser at a surface temperature of 6000 K [8]

7.2 The structure, working principle, and configurations of PSCs

A PSC generally consists of an absorber (perovskite) layer sandwiched by the HTL and ETL, which are also connected to charge collectors, i.e., anode and cathode [36], as shown in Figure 7.2a. The cathode is normally a glass substrate coated with conductive indium-tin-oxide (ITO) or fluorine-tin-oxide (FTO), and the anode is a metal conductor such as Al, Au, Pt, and Ag [37]. The role of the ETL in the device is to transport photogenerated electrons from the absorber to the anode and block the holes. The attributes of an effective ETL material are the highest occupied molecular orbital (HOMO), also referred to as the valence band (VB) in semiconductors, and the lowest unoccupied molecular orbital (LUMO), also called the conduction band (CB) in semiconductors, must be slightly higher than that of the absorber. Additionally, it must be transparent to allow light to pass through, have high electron mobility, and have better band alignment with the absorber [37]. The commonly used ETLs include indium gallium zinc oxide (IGZO), [6,6]-phenyl-C_{61}-butyric acid methyl ester (PCBM), SnO_2, TiO_2, ZnO [38], and ZnOS [39]. On the other hand, the HTL is responsible for collecting holes from the absorber and transporting them to the cathode while blocking the electrons. Ideally, the HOMO of the HTL must be slightly higher than that of the perovskite absorber and have high hole mobility for it to perform effectively. Some typical examples of HTLs used include 2,2',7,7'-

tetrakis[N,N-di(4-methoxyphenyl)amino]-9,9'-spirobifluorene (spiro-OMeTAD), copper(I) oxide (Cu_2O), copper(I) thiocyanate (CuSCN), copper(I) iodide (CuI), and poly(2,5-bis(3-tetradecylthiophen-2-yl)thieno-[3,2-b]thiophene) (D-PBTTT-14) [40]. The perovskite absorber layer primarily absorbs radiation from the sun, thus, generating excitons and separating charges. Finally, the separated charges flow to the external circuit as an electric current [41, 42]. Figure 7.2b illustrates the principle of operation of a typical PSC device. Notably, the charge separation process of charges is crucial as far as the PCE of the cell is concerned.

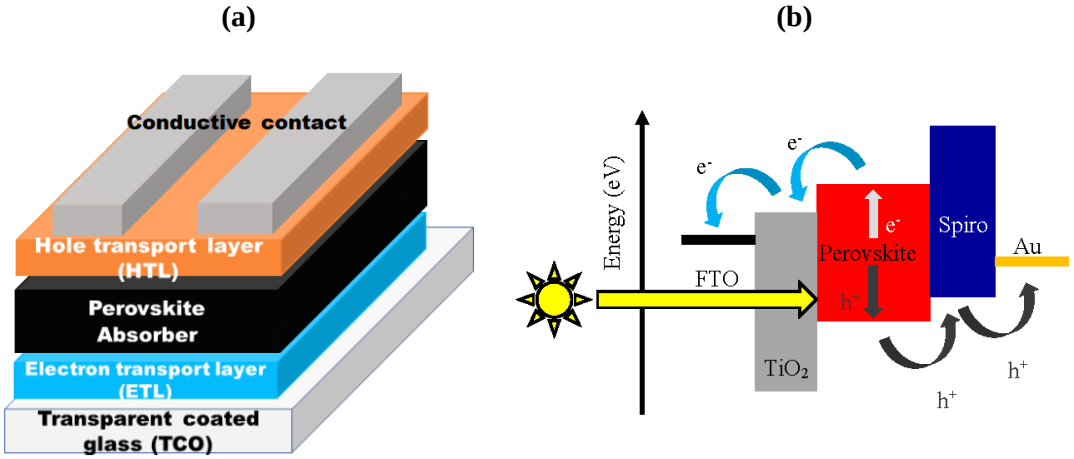

Figure 7.2: (a) The general structure of a typical PSC and (b) the working principle [43]

Generally, a PSC can be classified as n-i-p (regular) (Figure 7.3a) or p-i-n (inverted) (Figure 7.3b), depending on which part of the device receives illumination. For instance, if the ETL part receives direct sunlight, it is a n-i-p (conventional) design. On the other hand, if the light is received directly from the HTL side, it is classified as p-i-n (inverted). These two significant classes of PSCs and their components are illustrated in Figure 7.3. Typically, the *n* part is the electron transport layer, while the *i* parts is the absorber, and *p* is the hole transport layer.

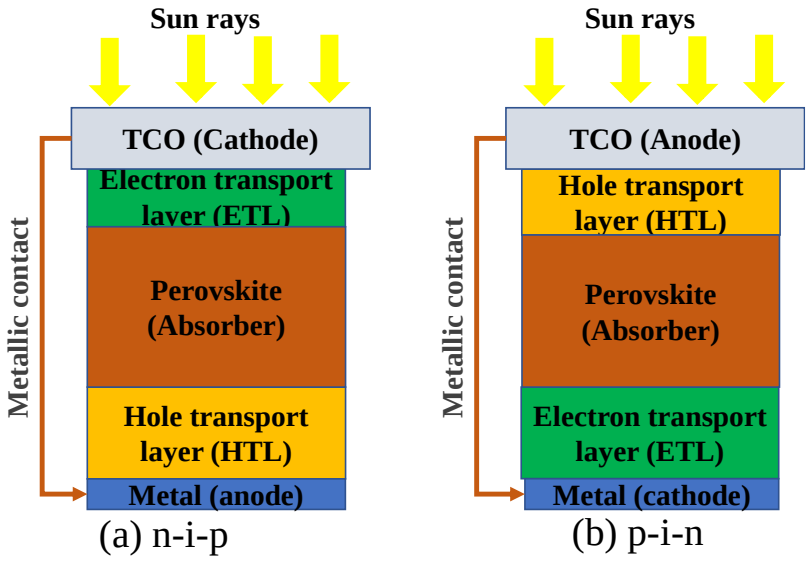

Figure 7.3: Basic configurations of PSCs (a) n-i-p (regular) and (b) p-i-n (inverted)

These two configurations can be further classified as mesoscopic or planar PSCs [44]. The mesoscopic structure is formed when mesoscopic (mp) metal oxides such as mp-TiO_2 or mp-Al_2O_3 are added together with the perovskite material in the absorber layer. On the other hand, the planar configuration has only the compact perovskite layer; therefore, the PSC configurations can be mesoscopic or planar n-i-p or mesoscopic or planar p-i-n. Figure 7.4 shows all four configurations of PSCs.

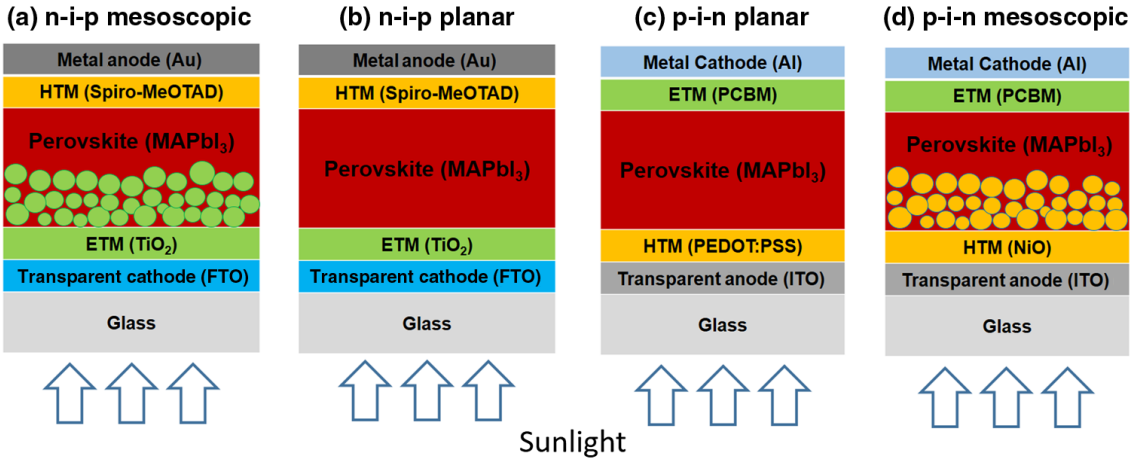

Figure 7.4: Typical configurations of PSCs [45]

7.2.1 Other PSCs configurations

Recently, other unique structures have emerged, i.e., ETL-free and HTL-free PSCs. This has been inspired by the need to take PSCs from the laboratory to the market; therefore, less costly devices must be fabricated.

7.2.1.1 The electron transport layer-free configuration

Typically, PSCs require the ETL layer to reduce photogenerated charge recombination and attain high open-circuit voltage (V_{oc}), thus, high performance. Nevertheless, ETL-free perovskites have recently gained significant scientific interest because the design eliminates ETLs such as SnO_2, ZnO, and TiO_2, which require high-temperature fabrication procedures [31,32] and are not cost-effective [46] and thus, hinder the commercialisation of PSCs. Huang et al. [47] simulated a planar PSC without the inclusion of an ETL by using the SCAPS-1D solar cell simulator, and the device exhibited a modest PCE of over 19%. The simulation results showed that the front part of the device must be carefully designed since the FTO/perovskite interface density of defects has a significant effect on the PCE of the device greater than the perovskite/HTL interface. Therefore, the passivation of the FTO/perovskite interface could significantly reduce the density of defects, thus reducing charge recombination. More recently, Huang et al. [46] fabricated a high-performance ETL-free PSC illustrated in Figure 7.5 through an interface engineering strategy. In essence, a thin layer of a small molecule, such as 1-[N-(2-hydroxyethyl)-4′-piperidyl]-3-(4′-piperidyl) propane (PPPDE), was inserted at the interface between the FTO and the perovskite to passivate the density of defects and reduce recombination. The device exhibited a reasonable PCE of 19.71%, which was 31% more than the pristine device without the small molecule thin interfacial layer.

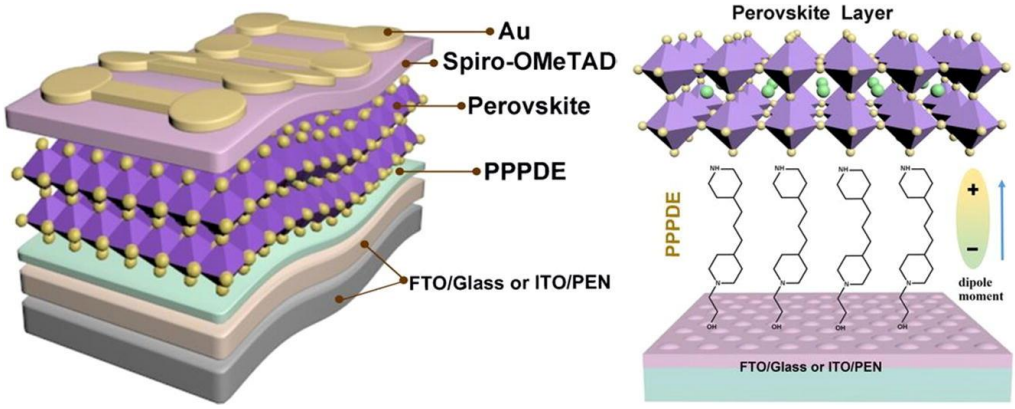

Figure 7.5: A typical ETL-free PSC [46]

7.2.1.2 The hole transport-free PSC

Recently, HTL-free PSCs have emerged as an interesting architecture in PSC fabrication [39, 48]. This has been propelled by the fact that perovskite materials have both long diffusion lengths [49], which can transfer charge effectively and ambipolar behaviour [50]; therefore, they can serve very well in transport and charge separation without the need for HTL material. Additionally, the materials commonly used for making HTLs, such as, spiro-OMeTAD [51] and poly(3,4-ethylenedioxythiophene) polystyrene sulfonate (PEDOT:PSS) [52, 53], are expensive, presenting high cost in the fabrication of PSCs; therefore, the need for HTL-free devices is essential [54, 55]. Recently, Chen et al. [56] fabricated a PSC without a HTL material (Figure 7.6). Typically, carbon was used as an electrode back contact to replace expensive metal back contacts. Three carbon sources, i.e., carbon nanocoil (CNC), graphene, and multiwalled carbon nanotubes (MWCNTs), were investigated as the carbon source. From the results, MWCNTs performance was better than the other chosen forms of carbons. The HTL-free device demonstrated a decent PCE of about 11%.

Similarly, Taheri-Ledari et al. [42] designed an HTL-free PSC with a ternary ETL consisting of reduced graphene oxide (RGO), ZnO nanorods, and copper indium sulfide quantum dots ($CuInS_2$ QDs). It was established that the ETL layer optimisation caused a high device performance of 15.74%. Generally, for an HTL-free PSC, ETL layer optimisation, passivation of ETL/perovskite, and a smooth and thick perovskite layer (to reduce shunt resistance) are essential for the realisation of the high performance of the device.

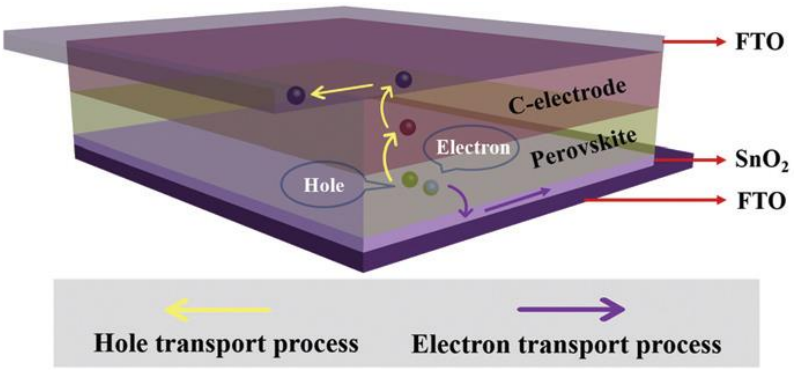

Figure 7.6: A typical HTL-free PSC [56]

7.2.1.3 The tandem PSC

A tandem solar cell (TSC) consists of two or more single-junction solar cells coupled together or with different light-absorbing layers with different band gaps [57]. Ideally, the PCE of such devices exceeds the theoretical Shockley-Queisser limit of 45% [58]. In this configuration, the absorber with a larger band gap lies above the one with a lower band gap energy to receive light with a shorter wavelength. On the other hand, a lower band gap will receive light with longer wavelengths. The idea is for the two absorbers to receive a wider spectral range and reduce spectral losses; thus, more sunlight is converted to electricity. To optimise the PCE, Duha et al. [59] proposed a TSC with methylammonium germanium iodide ($MAGeI_3$) and formamidinium tin iodide ($FASnI_3$) absorbers (Figure 7.7) which was constructed theoretically with the aid of SCAPS-1D. The PCE of the tandem device was 30.85%. Basically, for a TSC, the sub-cells are treated as two cells in a series connection. This implies that the voltages of each sub-cell are different, and thus, the voltage in the tandem device is the sum of the individual voltages of each sub-cell. In contrast, the current across the sub-cells is the same;, thus, the overall current of the tandem PSC. In the SCAPS-1D simulator, a multijunction device cannot be simulated at once. Therefore, each sub-cell is simulated separately [60].

More recently, Farhadi et al. [61] simulated the effect of different ETL and HTL materials on the performance of a tandem PSC with methylammonium lead iodide ($MAPbI_3$) and methylammonium tin iodide ($MASnI_3$) as absorber layers. The device achieved a PCE of 30.88% after optimisation.

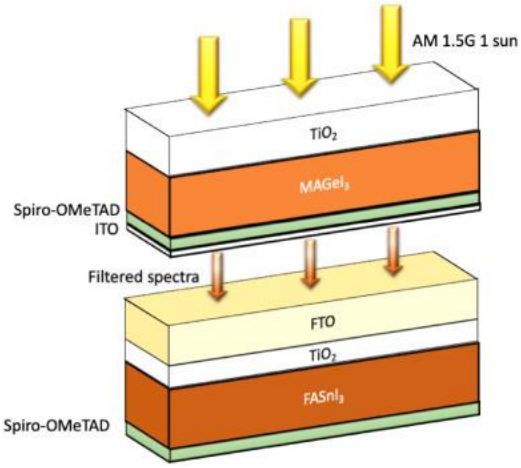

Figure 7.7: Tandem PSC device [59]

7.3 Factors limiting the performance and commercialisation of PSCs

The PCE of solar cells is decreased by a number of factors, hence, limiting their practical application and consequent commercialisation. The main factors include recombination of photogenerated charges [62], improper band alignment between the layers [63], chemical and physical degradation (stability issues) of the cell [64, 65], thermal losses [66, 67], and toxicity of lead.

7.3.1 The recombination of photogenerated charges

The recombination of photogenerated charges in solar cells can arise because of the presence of amphoteric defects in the absorber material or interfacial defects. The defects of the absorber act as Shockley-Read-Hall non-radiative centres, which trap charges, and thus cause recombination [62]. Also, at the interfaces between the absorber and HTL or ETL, recombination can occur [68], but it has been shown theoretically by Sobayel et al. [34] that amphoteric defects are worse than interfacial defects. For instance, the electrons should be injected effectively to the conduction band of the ETL from the absorber, so suitable band alignment should exist similarly for the HTL; therefore, the exciton recombination is minimised [69]. Through the introduction of a passivation layer at interfaces, the interfacial recombination has been shown to be reduced. Peng et al. [70] used an ultrathin passivation layer comprising of poly(methyl methacrylate): [6,6]-phenyl-C_{61}-butyric acid methyl ester (PMMA:PCBM), and the device showed an improved open circuit voltage and an optimal PCE of 20%. He et al. [71] designed a sandwich-like electron transport layer for a PSC with carbon quantum dots (CQDs) in between two tin oxide (SnO_2) layers, as shown in Figure 7.8. Essentially, in the engineered ETL, the bottom SnO_2 passivates the defects of the FTO layer, and at the FTO/SnO_2 interface, the charge recombination is greatly reduced. The CQDs caused enhanced optical transparency, a charge carrier transfer mechanism, and hole blocking/electron transport at the ETL. Overall, the hysteresis loss was reduced, and thus, the PCE of the PSC was significantly augmented.

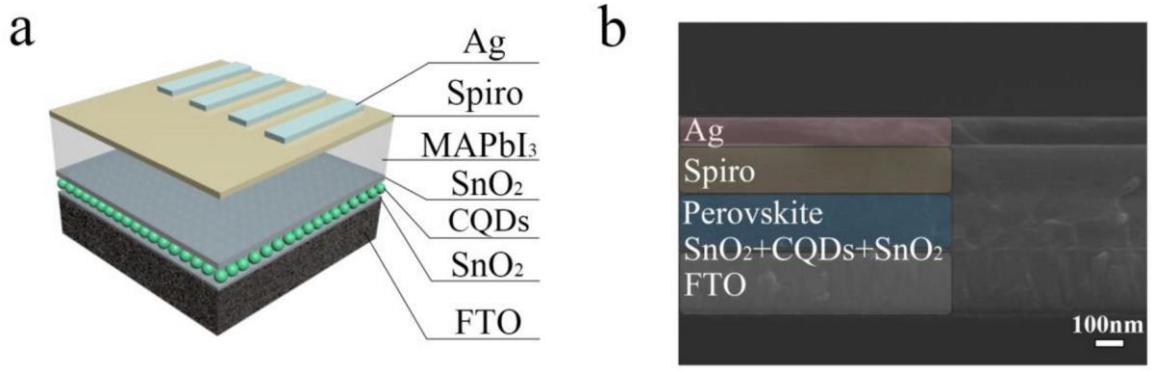

Figure 7.8: (a) A typical schematic representation of the layers of a PSC with a passivating layer of CQDs and (b) a corresponding cross-sectional SEM image showing the sandwich-like designed ETL [71]

Similarly, Liu et al. [72] inserted a graphitic carbon nitride quantum dot (g-CNQD) layer between the SnO_2 ETL and perovskite layer materials in a PSC with the following architecture: FTO/SnO_2/g-CNQD/Perovskite/Spiro-OMETAD/Au (Figure 7.9, inset). The g-CNQDs helped modify the interface and achieve a smooth surface for forming the perovskite layer with high crystallinity. Additionally, the g-CNQDs aided in suppressing the recombination rate of photogenerated charges by passivating the defects and high grain boundaries.

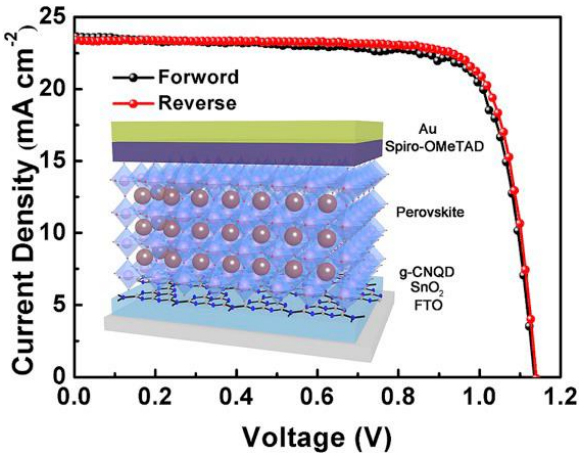

Figure 7.9: A typical current-voltage curve for a PSC (inset) with g-CNQDs as passivating agent [72]

7.3.2 Stability issues

Chemical and physical degradation of materials used in solar cells is also a barrier to achieving high efficiency [64]. When degradation occurs, the structure of the device will ultimately collapse and the performance is greatly reduced [73]. Basically, PSC components degrade due to exposure to moisture [74], heat [75], ultraviolet light, and oxygen [76].

7.3.2.1 Moisture

Water vapour in the air can diffuse into the PSC device, causing chemical degradation or water molecules could be present during fabrication and cause degradation in the PSC. This explains why during the actual fabrication process of PSCs, the humidity of the surroundings should be as low as possible. Normally, the fabrication process is carried out in a glovebox under inert conditions, such as a continuous flow of N_2 or Ar gases [77]. Generally, the perovskite layer can first degrade to its components, and thereafter, the constituents react with water [20]. For instance, PEDOT:PSS as the HTL is known to be hygroscopic; hence, it can absorb water, thus causing the degeneration of the HTL [78]. However, some researchers infer that a particular level of humidity is required to facilitate the formation of perovskite materials, and therefore, much discussion is ongoing on this aspect [79]. Lin et al. [80] prepared caesium lead halide perovskites ($CsPbI_2Br$) in the presence of water and dimethyl sulfoxide (DMSO), and it was shown that uniform $CsPbI_2Br$ films (with the grain size of about 4.4 μm) were formed. Ideally, an appropriate amount of water was essential in forming the cubic perovskite phase, and the PCE of the device was 16.47%.

7.3.2.2 Presence of light and oxygen

Essentially, oxygen-induced PSC deterioration occurs in the presence of light [81]. This is because oxygen reacts with photogenerated electrons to form superoxide ($O_2^{\cdot-}$), active species [82]. These species can now react with the components of the PSCs and, thus, cause degradation [83]. Bryant et al. [84] demonstrated that oxygen in the presence of light caused the rapid degradation of $MAPbI_3$, and the device posted a low performance. Moreover, the moisture induced-degradation was not severe as the light oxygen-induced degradation. Meanwhile, Aristidou et al. [85] combined computational and experimental strategies to investigate the mechanisms involved during oxygen photo-induced

degradation of PSCs. The fast oxygen diffusion into the PSC was associated with forming the reactive oxygen species, superoxide.

To counteract the stability issue, Wang et al. [86] introduced phenylhydrazine hydrochloride (PHCl) into the perovskite material to reduce Sn^{4+} and also to retard the degradation rate of formamidinium tin iodide ($FASnI_3$), and the device PCE was 11.4%. Ideally, the PHCl possesses hydrazino and phenyl groups which are reducing agents and hydrophobic, respectively.

To mitigate these extrinsic instability issues, encapsulation and choice of better materials can reduce these setbacks [87]. Mohammadi et al. [88] encapsulated the PSCs with a bilayer material, poly(methyl methacrylate)/styrene-butadiene (PMMA/SB) to cut off oxygen and moisture. The device maintained about 80% of the initial power at 85 °C and 85% humidity for a period of 100 hours. Moreover, the devices exhibited a slight PCE reduction of about 5% when subjected to −15 °C for 6 h and about ∼20% when dipped in HCl (37%) for 90 min of an initial PCE. Chang et al. [89] encapsulated a tandem PSC. The device showed outstanding long-term stability and posted 91% of its PCE after 9300 h in air.

7.3.2.3 Thermal effects

Apart from the moisture and oxygen factors already discussed, thermal instability also occurs in the device during operation. It is believed that the temperature of the device rises to twice that of the surrounding temperature; this negatively affects the efficiency of the cell [90]. The presence of moisture and heat can accelerate the degradation of the cell, thus, reducing its performance. High temperatures affect mainly the perovskite and HTL components of the device. The commonly used methylammonium (MA) $[CH_3NH_3]^+$-based perovskite has been established to be unstable due to the organic component, namely, the $[CH_3NH_3]^+$ cation [91]. More importantly, to mitigate this thermal instability, various cations, such as formamidinium (FA), have been used to replace the organic $[CH_3NH_3]^+$ component in the perovskite material, and a more stable structure is usually formed [92].

7.3.3 Toxicity of lead

The toxicity of lead has greatly hampered the commercialisation of PSCs, despite the fact that lead-based PSCs still show robust PCE values [29]. Researchers have made many attempts to reduce the amount of lead (lead-less) or eliminate lead (lead-free) in PSCs [93, 94]. Basically, there are two main approaches to lead reduction in PSCs, i.e., the chemical lead reduction approach and the physical lead reduction approach [95], where the amounts of lead in PSCs are significantly reduced without compromising much on the PCE of the device. These two approaches can be summarised in Figure 7.10.

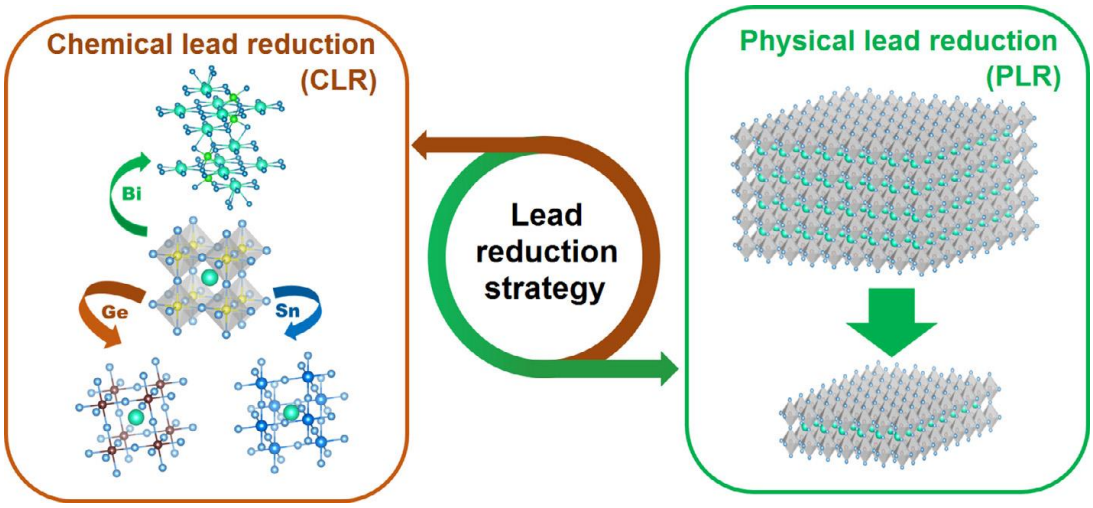

Figure 7.10: The concept of the reduction approaches of lead in PSCs [95]

7.3.3.1 The chemical reduction of lead

This involves the chemical replacement of lead with other elements, such as germanium (Ge), antimony (Sb), bismuth (Bi), and tin (Sn) [93, 96], in the PSCs. Among these potential elements that can be used to replace Pb, Sn has been established to be more suitable [93, 97]. This is because Sn has similar properties to Pb, and therefore, Sn-based PSCs have emerged. However, they are limited by poor stability [98] and low performance compared with their Pb counterparts [99]. The low stability is attributed to the ease of oxidation of Sn^{2+} to Sn^{4+} in air [92] and, therefore, suitable reducing agents, such as SnF_2 [97, 100], have been incorporated into the perovskite as an additive. Recently, Jokar et al. [101] prepared a tin-based PSC with a mixture of nonpolar organic guanidinium (GA^+) and FA as a cation and 1% of ethylenediammonium diiodide ($EDAI_2$) additive. Essentially, the device stability was enhanced by incorporating FA instead of

the unstable MA cation. The unencapsulated device was stable for more than six hours with a PCE of 8.3%. Wang et al. [102] compared the performance of a device with different metal dichalcogens, molybdenum disulfide (MoS_2), tungsten disulfide (WS_2), and tungsten diselenide (WSe_2), as $FASnI_3$ perovskite growth templates. The surfaces of these dichalcogenides are smooth and reduce defects. In this case, the metal dichalcogens acted as interfacial passivation agents between the NiO_x ETL and the absorber. The device with WSe_2 exhibited a record performance of about 10.47% compared to the other dichalcogens. Although this approach is being utilised currently, it is not sufficient, since the devices still post low performance and poor stability issues. Therefore, other methods need to be investigated.

7.3.3.2 Physical lead reduction

In this approach, the amount of lead in the perovskite is greatly reduced by the additon of other materials in which a "lead-less" perovskite is formed. Also, the physical lead reduction can involve incorporating optical spacer layer materials to reduce the amounts of lead but not compromise the PCE of the device [95]. Zheng et al. [95] conducted a theoretical study by simulating the transfer matrix model (TMM) as implemented in the MATLAB computational suite. An optical space was introduced in the PSC device, and the PCE was reduced to only 96% from the original performance, while the amount of lead used was reduced by 70% without much interference to performance. In order to reduce the amount of lead in the perovskite, Zhang et al. [103] prepared a lead-less PSC by the addition of strontium (Sr) (10 mol% strontium chloride precursor) to the PbI_2 precursor solution. The device exhibited better light absorption, charge extraction, and low recombination rates of charges overall, and the device showed a decent PCE of 15.64%. Soleimanioun et al. [104] synthesised methylammonium-zinc-lead iodide ($MAZn_{0.2}Pb_{0.8}I_3$), a lead-less perovskite, and compared its stability with that of pristine $MAPbI_3$. After 60 days of ageing, $MAZn_{0.2}Pb_{0.8}I_3$ proved more stable than $MAPbI_3$ since there was no significant change in the UV spectrum (Figure 7.11) after that period, while for $MAPbI_3$, the change was significant due to degradation leading to the formation of PbI_3.

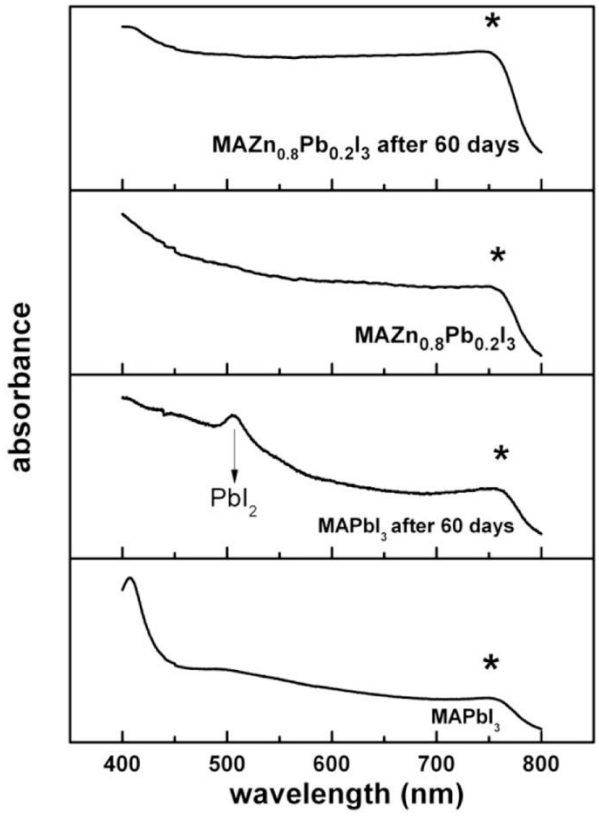

Figure 7.11: The UV-visible spectra of 60-day aged $MAZn_{0.2}Pb_{0.8}I_3$ and $MAPbI_3$ perovskite materials [104]

7.4 Solar cell device modelling and simulations

In this section, the various solar cell simulators that can be used to model PSCs are presented and discussed with regard to their merits and limitations. The fundamental equations being solved during the simulation process are also presented.

7.4.1 Fundamental simulation equations

In a semiconductor material, the charge transfer is governed by three basic equations: (1) the Poisson equation, which shows the relationship between the electric potential (E) and the charge concentration (ρ) in a semiconductor, (2) drift and diffusion current equations where the drift is due to the electric field and the diffusion term is due to the difference in electron concentration or holes, and (3) the continuity equation which represents the rate of generation and recombination of charges [38]. Therefore, the Poisson equation can be expressed as:

$$\frac{\partial^2 \psi}{\partial^2 x} = -\frac{\partial E}{\partial x} = -\frac{\rho}{\varepsilon_s} = -\frac{q}{\varepsilon_s}[p - n + N_D^+(x) - N_A^-(x) \pm N_{def}(x)] \quad \text{Equation (1)}$$

Here, ψ is the electrostatic potential, ε_s is the relative static permittivity of free space, q is the elementary charge, n is the electron density, p is the hole density, N_D^+ is the density of the ionised donors, N_A^- is the density of ionised acceptors, and N_{def} is the defect density of the acceptor or donor [105]. The drift-diffusion current equations are expressed in Equations (2) and (3) for the electrons and holes, respectively.

$$j_n = D_n \frac{dn}{dx} + \mu_n n \frac{d\emptyset}{dx} \quad \text{Equation (2)}$$

$$j_p = D_p \frac{dn}{dx} + \mu_p p \frac{d\emptyset}{dx} \quad \text{Equation (3)}$$

where D_n is the electron diffusion coefficient, μ_n is the electron mobility, D_p is the hole diffusion coefficient, μ_p is the hole mobility and $\emptyset$ is the electrostatic potential [106]. The equations of continuity for electrons and holes are presented as Equations (4) and (5), respectively.

$$\frac{\partial j_n}{\partial x} + G - U_n(n,p) = 0 \quad \text{Equation (4)}$$

$$-\frac{\partial j_p}{\partial x} + G - U_p(n,p) = 0 \quad \text{Equation (5)}$$

where j_n is the electron current density, j_p is the hole current density, $U_{n,p}$ is the net recombination rate, and *G* is the generation rate [38, 105, 107].

Presently, state-of-the-art simulators have been developed and can model solar cells in 1, 2 and 3-dimensional configurations. Consequently, the simulators that will be discussed herein numerically solve Equations (1)-(5) in one dimension (1-D), and this includes the solar cell capacitance simulator (SCAPS) [108], SILVACO ATLAS [109], general-purpose photovoltaic device model (GPVDM) [105], and wx-analysis of microelectronic and photonic structures (wxAMPS) [110]. The simulators can give the recombination profiles of charges, photovoltaic parameters, i.e., open circuit voltage (V_{oc}), fill factor (FF) current density (J_{sc}) and PCE, band diagrams and many other parameters of the modelled cell.

7.4.2 Solar cell simulators

Solar cell simulators are computational software that aid in solving the fundamental solar cell equations described above and give solutions in the form of graphs and basic photovoltaic parameters. In this section, various simulators, such as SCAP-1D, SILVACO ATLAS, wxAMPS, and the GPVDM, are described.

7.4.2.1 Solar cell capacitance simulator-1 dimensional

The SCAPS-1D software is freely available and was developed by Professor Marc Burgelman and his team at the University of Ghent [111]. This simulation software numerically solves the three basic equations of semiconductors under steady-state conditions. It can generate data on the recombination rates of charges, band alignment, quantum efficiency, photovoltaic parameters, and current densities of a model solar cell device. Typically, to carry out simulations, the basic input properties of materials are obtained from previously published papers and keyed into the software input section. Table 7.1 shows typical input parameters for a device gathered from previous reports.

Table 7.1: Some input parameters for various materials required by SCAPS-1D

Parameter	FTO [112]	WS_2 (ETL) [113]	$CH_3NH_3SnI_3$ (absorber) [106]	P3HT (HTL) [38]
Thickness, d (μm)	0.05	0.5	0.5	1.0
Band gap, E_g (eV)	3.5	1.87	1.31	1.85
Affinity, χ (eV)	4.0	4.3	4.17	3.1
Dielectric Permittivity (relative), ε_r	9.0	11.9	8.2	3.4
Effective density of state at CB, N_c (cm^{-3})	2.2×10^{18}	1.0×10^{18}	1.0×10^{18}	1.0×10^{22}
Effective density of state at VB, N_v (cm^{-3})	1.8×10^{19}	2.4×10^{19}	1.0×10^{18}	1.0×10^{22}
Mobility of electrons, μ_n ($cm^2 V^{-1} s^{-1}$)	20.0	260	1.6	1.0×10^{-4}
Mobility of holes, μ_p ($cm^2 V^{-1} s^{-1}$)	10.0	51	1.6	1.0×10^{-3}
Density of n-type doping, N_D (cm^{-3})	1.0×10^{19}	1.1×10^{19}	0.0	0.0
Density of p-type doping, N_A (cm^{-3})	0.0	0.0	3.3×10^{18} [113]	3.17×10^{13}
Density of defects, N_t (cm^{-3})	0.0	1.2×10^{11}	1.5×10^{17} (varied)	1.0×10^{14}

The model cell is built by adding layers together, with each layer having specific basic parameters. The input and modelling section of the software is shown in Figure 7.12.

Figure 7. 12: A typical SCAPS-1D solar cell modelling panel

The software can allow variation of various parameters, which include the density of defects, doping densities, thicknesses, operating temperature, and many other properties regarding the cell. This modelling software provides more options to input parameters and is easy to manipulate and install. Although SCAPS-1D is sufficiently accurate for devices without any transverse dependency, it is limited when calculations involve other dimensions. For instance, in the device needs the inclusion of plasmonic material, then a two- or three-dimensional problem has to be solved, which is not accessible in SCAPS-1D. However, because of the fact that the software can only take seven layers, it is limiting in modelling devices that require more layers above seven.

7.4.2.2 The wx-analysis of microelectronic and photonic structures

The wxAMPS is a one-dimensional free software that can model any two-terminal device, such as a diode, solar cell, sensor, and photodiode. The algorithm behind this software is the three basic semiconductor equations described in Section 7.4.1. It is an improved version of the analysis of microelectronic and photonic structures (AMPS), which was developed by Professor Stephen Fonash and his co-workers at Pennsylvania State University [114, 115].

The new software developed at the University of Illinois exhibits better simulation capabilities, easy data entry, and enhanced visualisation. Figure 7.13 shows the combined graphical user interface for wxAMPS. Because of the availability of many layers, it can also be used to simulate graded solar cells with ease [115]. The input parameters are the same as for SCAPS-1D (see Table 7.1), and the software can simulate the recombination profiles, photovoltaic parameters, and the occupation probability of deep defects. The advantages of wxAMPS are that it can do the job in batches and can get materials properties from compatible "WIKI" database [116]. However, the software can only solve one-dimensional problems.

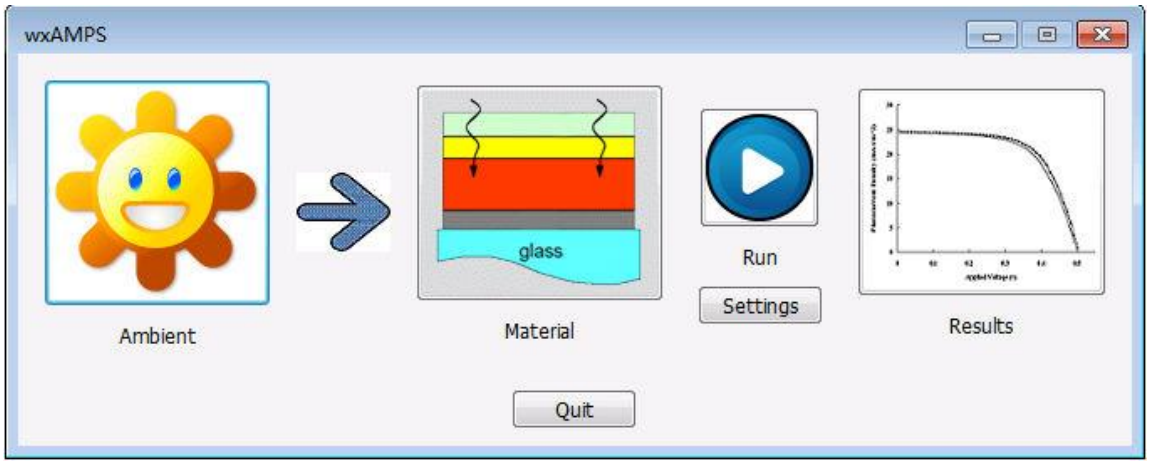

Figure 7.13: The main graphical user interface of wxAMPS [117]

7.4.2.3 The general-purpose photovoltaic device model

The GPVDM is another new powerful modelling software that is used to simulate one-dimensional (1-D) thin-film devices, such as organic solar cells (OSCs), PSCs, organic light-emitting diodes (OLEDS), and field emission effect transistors (OFETs), as shown in the new simulation window in Figure 7.14. This model is being developed by MacKenzie and his team at the University of Nottingham, UK [118].

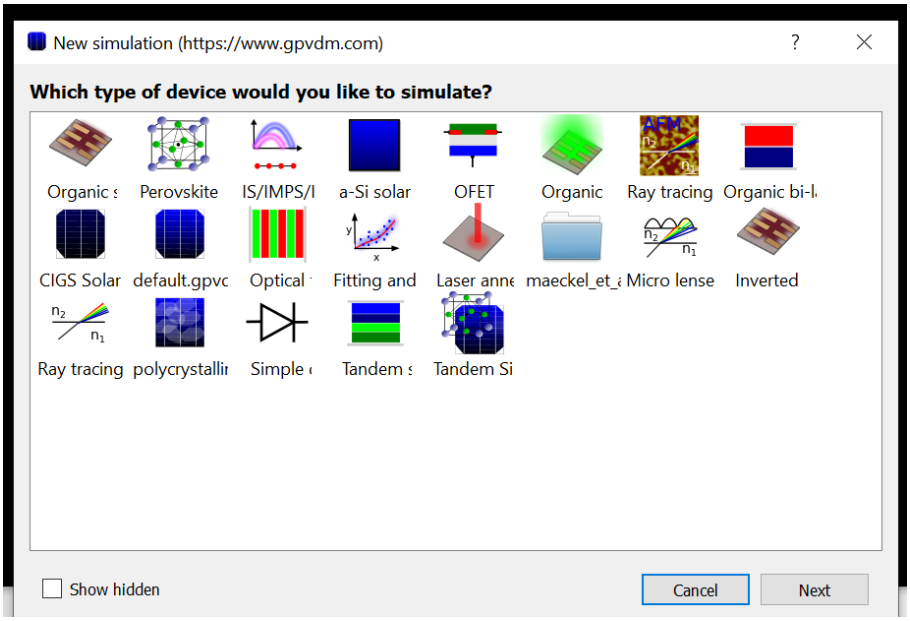

Figure 7.14: GPVDM new simulation window showing possible devices that can be simulated

Because the model has two coupled solvers, i.e., electrical and optical, it can simulate the electrical and optical characteristics of the device. It also solves the three basic device equations under a steady state in a time domain. Currently, the 2D and 3D models are under development and in different languages, so as to avert the problems associated with the use of 1D and single language (english), respectively. The input data is inserted into the model at the layer editor pop-up window as depicted in Figure 7.15, and the electrical parameters of materials are collected from previous literature sources, and utilised to build the structure of the device [118].

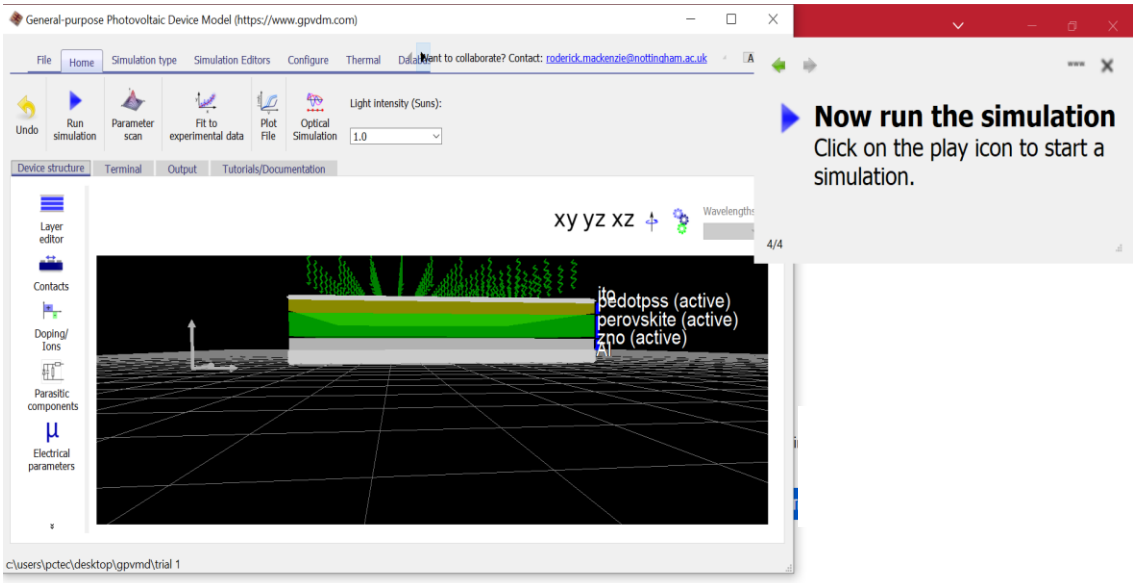

Figure 7.15: GPVDM user interface for building the device and entering electrical input data

7.4.2.4 SILVACO ATLAS

The ATLAS solar cell simulator by SILVACO International is a powerful modelling tool that extracts the electrical characteristics of a physical structure [119]. The simulation of charge transport is done in a 2D grid system called a mesh. The following material parameters are essential in the construction of a model solar cell and simulation: band gap energy, dielectric permittivity, electron and hole state densities, electron, and hole mobilities, electron affinity, radiative recombination rate, doping levels of holes transport and electron transport materials, and layer thickness. Moreover, the critical material optical file containing the wavelength-dependent refractive index, n, and extinction coefficient, k, must also be available. More importantly, the mesh is divided into regions, each material, including electrodes, is assigned into respective parts, then the illumination light spectrum is specified, and thereafter, simulation is initiated. Figure 7.16 shows a typical solar cell constructed by using SILVACO ATLAS software.

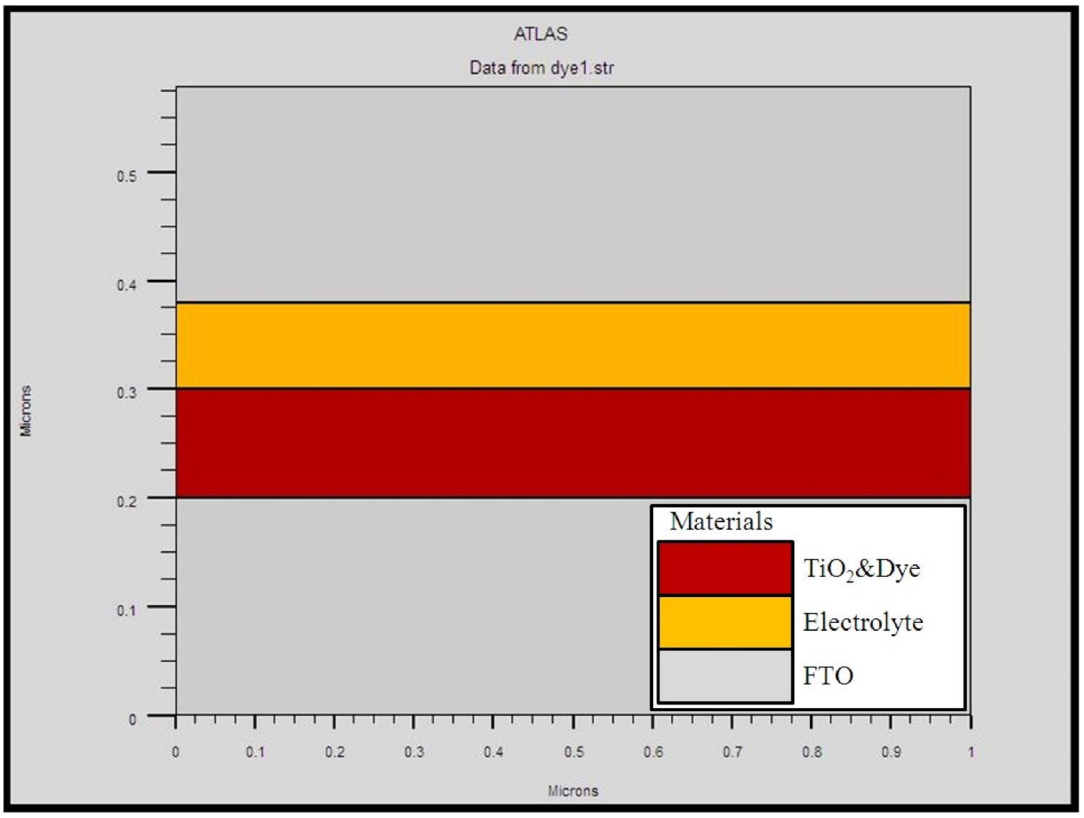

Figure 7.16: A typical solar cell structure in SILVACO ATLAS code [120]

For accurate simulations, the "LUMINOUS" optoelectronic module, also available in ATLAS, is engaged to model electron-hole pair generation accurately. The LUMINOUS uses the optical refractive index for optical tracing in the device. Simultaneously, the extinction coefficient is used to determine the rate of the electron-hole pair generation process in each mesh. These two important simulations give rise to wavelength-dependent photogeneration in the entire cell. The advantage of this model is that monochromatic light or complex spectrum sources, for example, AM0, can be set. Because of the availability of different models, a solar cell engineer can have an opportunity to choose which specific available model to use for a particular set of materials, such as organic and inorganic materials. This unique feature is not available in all other simulators, such as SCAPS, GPVDM and wxAMPS, and thus offers an advantage. Finally, this simulator can give a variety of output results, such as I-V characteristics, spectral response, electrostatic fields, etc. The simulator has been shown to yield results consistent with experiments [106, 121]. While SILVACO Atlas is very powerful, it is not a freely available software to download, thus limiting its access by many researchers. Some other available simulators are presented in Table 7.2.

Table 7.2: Some other solar cell simulators

Simulator	Method	Dimension	Reference
3D-Finite element method (FEM) technique	Numerical	3D	[122]
Automat for simulation of heterostructures (AFORS-HET)	Numerical	1D	[123]
COMSOL Multiphysics	Numerical	3D	[124]
A personal computer one-dimensional (PC1D)	Numerical	1D	[125]

7.5 Applications of solar cell simulators in modelling solar cells

Solar cell simulators have been applied in the discovery of solutions and insights to solar cell challenges which limit their performances and commercialisation. Simulations allow for manipulation of the models, and more information that could have otherwise not been easily obtained from experiments is accessed within a short period of time. In many aspects, simulators have been used in: screening of appropriate materials for respective components of the cell, giving insights on the effects of tuning the intrinsic properties of each component, evaluation of the external temperature working conditions, effects of changing back contacts, and overall performance of the cells. In this section, these specific aspects will be discussed regarding different simulators and solar cells.

7.5.1 Screening of suitable materials for solar cell components

In order to optimise the performance of a solar cell, a proper choice of suitable materials that serve as the hole transport layer, electron transport layer, absorber, and back contact electrodes, should be made. Recently, Arzi et al. [38] investigated the effect of different ETLs and HTLs by using SCAPS-1D, on the performance of the primary n-i-p cell with the ITO/PEDOT:PSS/$CH_3NH_3GeI_3$/IGZO/Ag configuration. An optimal PCE of 23% was achieved when titanium oxide (TiO_2) and ZnO were inserted as the ETL. Other selected and tested ETLs were: [6,6]-phenyl-C_{61}-butyric acid methyl ester (PCBM), indium gallium zinc oxide (IGZO), and SnO_2. The enhanced performance seen when TiO_2

and ZnO were used could be attributed to their proper band alignment between the conduction bands of the ETL and the LUMO of the perovskite. Similarly, among the tested HTLs, i.e., poly(3-hexylthiophene-2,5-diyl) (P3HT), Spiro-OMeTAD, CuSCN, CuI and nickel(II) oxide (NiO), the best performance was achieved with the utilisation of the CuSCN HTL material, also attributed to the favourable band alignment with the perovskite material. Lately, various perovskite designs have emerged, and they are geared towards performance improvement. Hima et al. [106] compared the performance of two perovskites, i.e., $CH_3NH_3PbI_3$ and $CH_3NH_3SnI_3$, by inserting them separately into a general structure: TiO_2/perovskite/spiro-OMeTAD layers. A theoretical simulation was performed with SILVACO ATLAS software, and the cell with the $CH_3NH_3PbI_3$ perovskite exhibited a higher PCE of 18.16%, and the other perovskite, $CH_3NH_3SnI_3$, achieved 9.56%. The high performance of $CH_3NH_3PbI_3$ could be attributed to better band alignment between the perovskite and both ETL and HTL materials. Hossain et al. [126] modelled a PSC and screened various HTL using both wxAMPS and SCAPS software, whereby Cu_2O performed much better than other suggested HTLs (spiro-OMETAD, NiO, CuI, CuSCN), and the device achieved a PCE of above 24% because the Cu_2O HTL had very high hole mobilities of 256 $cm^2\ V^{-1}\ s^{-1}$ as compared with the other tested HTLs.

7.5.2 Tuning the intrinsic properties of solar cell components

The intrinsic properties of cell component materials, such as doping densities, the density of defects, and layer thickness, play a very important role as far as the power conversion of a solar cell is concerned. Therefore, it is paramount to search for optimum levels that would give enhanced PCE. This is possible and feasible while using the simulators to guide experiments for commercial production. Practically, adjusting the intrinsic properties of the materials to suit the purpose can be an expensive enterprise; therefore, simulations are inevitable before real practice [127]. Patel [128] recently simulated a lead-free PSC (glass/FTO/TiO_2/$CH_3NH_3SnI_3$/Cu_2O/metal back contact) with the SCAPs solar cell simulator. The effect of intrinsic properties, such as thicknesses, acceptor concentration, and the density of the absorber defects, on the overall performance of the device, was investigated. The best possible thickness was 500 nm, and the optimum density of the absorber defects was about $10^{14}\ cm^{-3}$. After optimising these parameters, the device exhibited J_{sc} of 40.14 mA cm^{-2}, V_{oc} of 0.93 V, FF of 75.78%, and PCE of 28.39%. In order to optimise the performance of the eco-friendly unleaded PSC, Jayan

et al. [129] first computed the bandgap and absorption spectra of the absorber layer with the aid of WIEN2K computational software. The information from the WIEN2K density functional theory (DFT) software was injected into the SCAPS simulator, and after optimisation, the device with the FTO/ZnO/$CsPbI_3$/$CuSbS_2$/Se configuration achieved a PCE of 15.6%. Also, it was deduced that Se could be used as an alternative to expensive Au as the back contact.

7.5.3 Selection of metal back contact

The choice of appropriate metal back contact for a PSC is crucial. The typically used metal back contacts include metals like Au, Pt, Ag, Cu, Ni, and Pd [130, 131]. Au and Ag have been widely used among these metals because of their high PCE [132]. Gold, in particular, does not react with the perovskite material [132], gold is expensive, and Ag is unstable, thus limiting their practical use in devices despite their high performances. Also, more environmentally friendly materials, such as carbon nanotubes [133], have been tested for potential use as back contacts so as to reduce the pollution effects caused by the utilisation of metals. Inspired by these challenges, researchers have devoted more efforts to exploring other potential back contacts, both experimentally and computationally. Rono et al. [40] investigated theoretically the effect of different metal back contacts on the performance of a lead-free PSC with the general architecture: glass/FTO/WS_2/$HC(NH_2)_2SnI_3$/HTL/metal back contact. The metal back contacts tested and their work functions were Pt (5.65 eV), Pd (5.3 eV), Ni (5.0 eV), Ag (4.7 eV), Au (5.05 eV), and Cu (4.65 eV). Generally, a metal with a high metal work functions performed better, and it was evident that expensive Au can be replaced with cheaper alternatives, such as Pt, Pd, Ni, and Ag, since they exhibited similar PCE values. Figure 7.17 shows the effects of various metals back contacts on the photovoltaic parameters: PCE, V_{oc}, J_{sc} and FF.

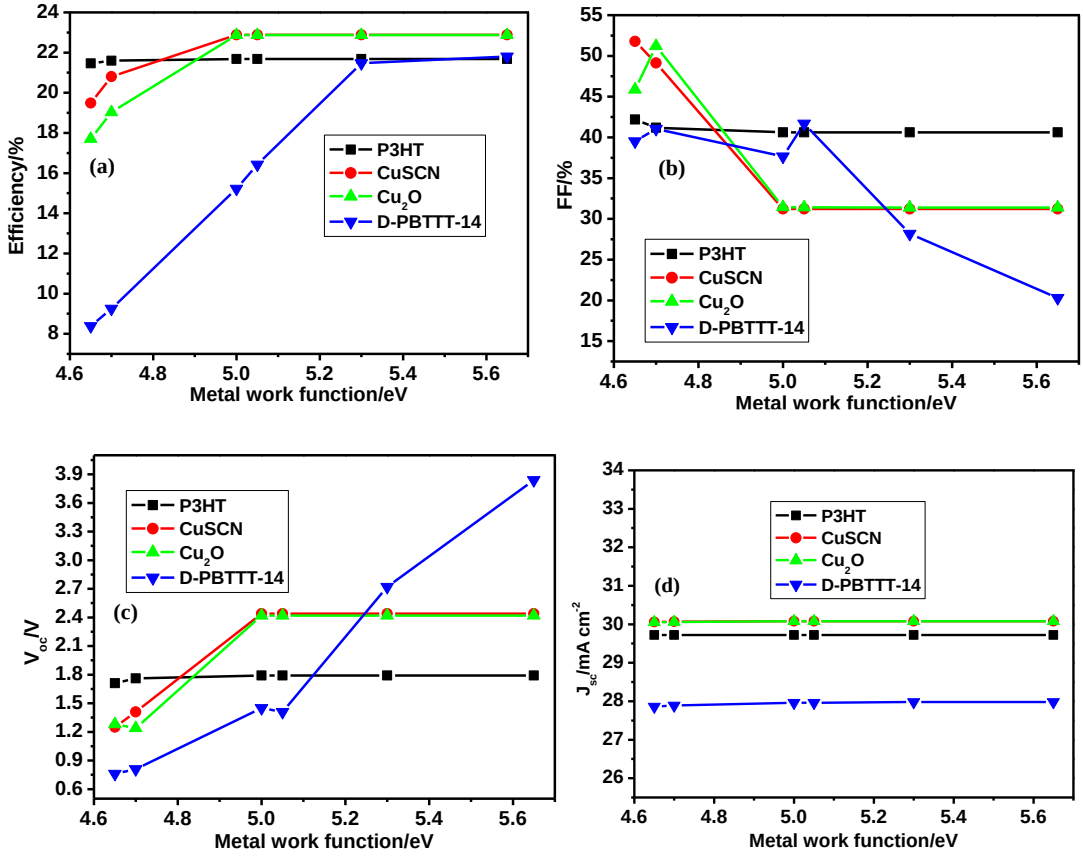

Figure 7.17: Effects of various metal back contacts on the photovoltaic parameters of a PSC [40]

Similarly, Jayan et al. [132] investigated, by using the SCAPS simulator, the effect of different metal work functions on the performance of the PSC configuration: FTO/PCBM/$MASnI_3$/CuI/metal back contact. Evidently, the V_{oc} increases for metals such as Ag, Cu, and Fe, but no significant change was observed for metals with high work functions (W, Ni, Pd, Pt, and Se). More importantly, this study established that the PCE increased with increasing metal work function but remained unchanged for metals with high work functions. This corroborates the experimental results obtained by Behrouznejad et al. [131].

7.5.4 Effects of external temperature working conditions

The external working temperature affects the performance of the device and its structural stability. This is because solar panels are normally exposed outside of buildings for instance, on top of roofs or on windows. Consequently, state-of-art simulators, such as SCAPS-1D, SILVACO ATLAS and wxAMPS, have been used to simulate the

performance of PSCs operating under different temperature conditions. Meng et al. [134] demonstrated the effect of heat on the mixed cation perovskite (FAPbI3)1−xMAPb(Br3−yCly)x devices experimentally. The performance of the devices decreased with an increase in temperature from 25 to 250 °C, and this could be attributed to the decomposition of the MA part of the perovskite material to PbI_2. Similarly, there was an increase in the defect density from 3.87×10^{17} cm^{-3} to 9.03×10^{17} cm^{-3}. Generally, the density of defects and deformation stress in the device increases with an increase in temperature leading to an overall low device performance [132]. Kanoun et al. [112] simulated the performance of a $MAGeI_3$-based PSC and investigated the effect of temperature between 300 to 500 K for devices with common ETL and different HTL materials. The change in photovoltaic performance is shown in Figure 7.18. The V_{oc} slightly increased as a function of the increase in temperature. This is attributed to a decrease in the band gap of the perovskite absorber material. This agrees well with the experimental results reported by Meng et al. [134]. On the other hand, the V_{oc}, which is believed to be the most temperature-affected parameter, decreases with an increase in temperature.

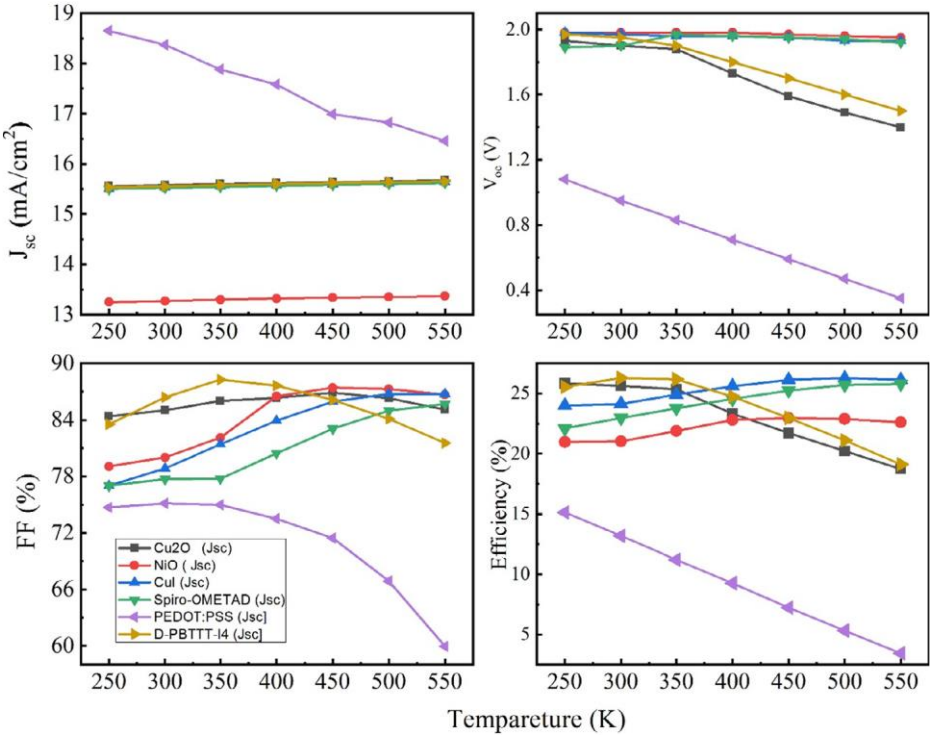

Figure 7.18: The variation of photovoltaic parameters for $MAGeI_3$-based devices with, a common ETL but different HTLs as a function of temperature [112]

7.6 Summary and outlook

The development of PSCs has gained tremendous momentum since its commencement in 2009 because of their potential to convert light energy into electricity. The current PCE of a PSC has reached over 25%, thus, significantly competing with silicon-based solar cells, which are relatively expensive. In this review, various fabrication strategies, such as physical or chemical reduction of toxic lead, passivation of the interfacial and bulk defects, and proper choice of device components, have been highlighted. These modifications have greatly improved the PCE, stability and helped to reduce the toxicity of lead. So far, few strides towards the commercialisation of PSCs have been made, though there is still more to be done.

More importantly, advanced computational modelling of devices and materials has recently gained much attention in photovoltaic research. In essence, numerical simulations of PSCs have been discussed to explore the physics of PSC devices. Basically, the main semiconductor equations (the continuity equations of holes and electrons, and Poisons equations) are solved by various one or multi-dimensional simulators.

Furthermore, the typical simulators utilised in the study of PSC devices as regards the photovoltaic parameters (PCE, FF, V_{oc}, and J_{sc}) and other fundamental properties, such as the thickness of components, back contacts, the density of defects, and doping of the materials, among other characteristics of PSCs, have been extensively discussed. Presently, the development of a number of simulators, such as SCAP-1D, SILVACO ALTAS, and GPVDM, have made simulations of the devices possible, and the results of the simulators often agree with experimental results. Finally, this review is envisaged to aid in the removal of barriers in the fabrication of PSCs with better performance, high stability, and less toxicity, and that be of great importance to nanotechnologists in the field of photovoltaic devices.

Acknowledgements

The authors are thankful for the financial support provided by the National Research Foundation (NRF) of South Africa, under grant numbers 103979 and 109580; the University of KwaZulu-Natal (UKZN), the UKZN Nanotechnology Platform, and the Eskom Tertiary Education Support Programme (TESP).

Conflict of interest

The authors declare no conflict of interest.

References

[1] S. Kappenthuler, S. Seeger, Addressing global environmental megatrends by decoupling the causal chain through floating infrastructure. Futures. **113**, 102420 (2019). https://doi.org/10.1016/j.futures.2019.04.007.

[2] M.L. Khandekar, T.S. Murty, P. Chittibabu, The global warming debate: A review of the state of science. Pure Appl. Geophys. **162**, 1557-1586 (2005). https://doi.org/10.1007/s00024-005-2683-x.

[3] M.D. Leonard, E.E. Michaelides, D.N. Michaelides, Substitution of coal power plants with renewable energy sources – Shift of the power demand and energy storage. Energy Convers. Manag. **164**, 27-35 (2018). https://doi.org/10.1016/j.enconman.2018.02.083.

[4] S.K. Chandy, Tapping renewable energy sources in contemporary india; Issues and challenges. Invertis J. Renew. Energy. **10**, 1-6 (2020). https://doi.org/10.5958/2454-7611.2020.00001.6.

[5] J. Khan, M.H. Arsalan, Solar power technologies for sustainable electricity generation – A review. Renew. Sust. Energ. Rev. **55**, 414-425 (2016). https://doi.org/10.1016/j.rser.2015.10.135.

[6] M. Grätzel, Photovoltaic and photoelectrochemical conversion of solar energy. Philos. Transact. A Math. Phys. Eng. Sci. **365**, 993-1005 (2007). https://doi.org/10.1098/rsta.2006.1963.

[7] K. Mertens, Photovoltaics: Fundamentals, Technology, and Practice, John Wiley and Sons. West Sussex, United Kingdom, 2018.

[8] S. Rühle, Tabulated values of the Shockley–Queisser limit for single junction solar cells. Sol. Energy. **130**, 139-147 (2016). https://doi.org/10.1016/j.solener.2016.02.015.

[9] A.K. Bhattacharjee, N. Kutkut, I. Batarseh, Review of multi port converters for solar and energy storage integration. IEEE Trans. Power Electron. **34**, 1431 - 1445 (2018). https://doi.org/10.1109/TPEL.2018.2830788.

[10] H. Yang, Z. Jin, D. Liu, K. Fan, G. Wang, Visible light harvesting and spatial charge separation over the creative Ni/CdS/Co_3O_4 photocatalyst. J. Phys. Chem. C **122**, 10430-10441 (2018). https://doi.org/10.1021/acs.jpcc.8b01666.

[11] J.d.S. de Souza, L.O.M. de Andrade, A.V. Müller, A.S. Polo, Nanomaterials for solar energy conversion: Dye-sensitized solar cells based on ruthenium(II) tris-heteroleptic compounds or natural dyes, in *Nanoenergy*. 2018, Springer. p. 69-106.

[12] E. Dickinson, Solar Energy Technology Handbook: 0, CRC Press. Boca Raton, Florida, USA, 2018.

[13] A.B.A. Schippers, V. Brandwijk, E.W. Gorter, Derivation and discussion of crystal structures of compounds ABX_3 and A_2BX_6: Part I. Derivation of the structures. J. Solid State Chem. **6**, 479-492 (1973). https://doi.org/10.1016/S0022-4596(73)80004-0.

[14] M. Faizan, X. Wang, S.A.M. Abdelmohsen, K.C. Bhamu, S. Sappati, A. Laref, N. Muhammad, M. Mushtaq, A.M.M. Abdelbacki, R. Khenata, Understanding the electronic structure and optical properties of vacancy-ordered double perovskite A_2BX_6 for optoelectronic applications. Energy and Fuels. **36**, 7065-7074 (2022). https://doi.org/10.1021/acs.energyfuels.2c00341.

[15] M. Xia, J.-H. Yuan, G. Niu, X. Du, L. Yin, W. Pan, J. Luo, Z. Li, H. Zhao, K.-H. Xue, X. Miao, J. Tang, Unveiling the structural descriptor of $A_3B_2X_9$ perovskite derivatives toward x-ray detectors with low detection limit and high stability. Adv. Funct. Mater. . **30**, 1910648 (2020). https://doi.org/10.1002/adfm.201910648.

[16] M.L. Tarlton, S. Skanthakumar, V. Vallet, R.E. Wilson, Hexanitrato complexes and hybrid double perovskites of Am^{3+} and Cm^{3+}. ChemComm. **58**, 11997-12000 (2022). https://doi.org/10.1039/D2CC05162A.

[17] V. Huynh, Advances in lead-free perovskite phototransistors. (2020). http://hdl.handle.net/1773/46243.

[18] A. Mutalikdesai, S.K. Ramasesha, Emerging solar technologies: Perovskite solar cell. Resonance. **22**, 1061-1083 (2017). https://doi.org/10.1007/s12045-017-0571-1.

[19] F. Giordano, A. Abate, J.P. Correa Baena, M. Saliba, T. Matsui, S.H. Im, S.M. Zakeeruddin, M.K. Nazeeruddin, A. Hagfeldt, M. Graetzel, Enhanced electronic properties in mesoporous TiO_2 via lithium doping for high-efficiency perovskite solar cells. Nat. Commun. **7**, 10379 (2016). https://doi.org/10.1038/ncomms10379.

[20] I. Mesquita, L. Andrade, A. Mendes, Perovskite solar cells: Materials, configurations and stability. Renew. Sust. Energ. Rev. **82**, 2471-2489 (2018). https://doi.org/10.1016/j.rser.2017.09.011.

[21] S.A. Olaleru, J.K. Kirui, D. Wamwangi, K.T. Roro, B. Mwakikunga, Perovskite solar cells: The new epoch in photovoltaics. Solar. Energy. **196**, 295-309 (2020). https://doi.org/10.1016/j.solener.2019.12.025.

[22] A. Kojima, K. Teshima, Y. Shirai, T. Miyasaka, Organometal halide perovskites as visible-light sensitizers for photovoltaic cells. J. Am. Chem. Soc. **131**, 6050-6051 (2009). https://doi.org/10.1021/ja809598r.

[23] F. Igbari, Z.K. Wang, L.S. Liao, Progress of lead-free halide double perovskites. Adv. Energy Mater. **9**, 1803150 (2019). https://doi.org/10.1002/aenm.201803150.

[24] D. Wang, M. Wright, N.K. Elumalai, A. Uddin, Stability of perovskite solar cells. Sol. Energy Mater Sol. Cells. **147**, 255-275 (2016). https://doi.org/10.1016/j.solmat.2015.12.025.

[25] Z. Zhu, C.C. Chueh, N. Li, C. Mao, A.K.Y. Jen, Realizing efficient lead-free formamidinium tin triiodide perovskite solar cells via a sequential deposition route. Adv. Mater. **30**, 1703800 (2018). https://doi.org/10.1002/adma.201703800.

[26] F. Jiang, D. Yang, Y. Jiang, T. Liu, X. Zhao, Y. Ming, B. Luo, F. Qin, J. Fan, H. Han, L. Zhang, Y. Zhou, Chlorine-incorporation-induced formation of the layered phase for antimony-based lead-free perovskite solar cells. J. Am. Chem. Soc. **140**, 1019-1027 (2018). https://doi.org/10.1021/jacs.7b10739.

[27] K.M. Boopathi, P. Karuppuswamy, A. Singh, C. Hanmandlu, L. Lin, S.A. Abbas, C.C. Chang, P.C. Wang, G. Li, C.W. Chu, Solution-processable antimony-based light-absorbing materials beyond lead halide perovskites. J. Mater. Chem. A. **5**, 20843-20850 (2017). https://doi.org/10.1039/C7TA06679A.

[28] T. Krishnamoorthy, H. Ding, C. Yan, W.L. Leong, T. Baikie, Z. Zhang, M. Sherburne, S. Li, M. Asta, N. Mathews, S.G. Mhaisalkar, Lead-free germanium iodide perovskite materials for photovoltaic applications. J. Mater. Chem. A. **3**, 23829-23832 (2015). https://doi.org/10.1039/C5TA05741H.

[29] M. Lyu, J.-H. Yun, P. Chen, M. Hao, L. Wang, Addressing toxicity of lead: Progress and applications of low-toxic metal halide perovskites and their derivatives. Adv. Energy Mater. **7**, 1602512 (2017). https://doi.org/10.1002/aenm.201602512.

[30] N.K. Noel, S.D. Stranks, A. Abate, C. Wehrenfennig, S. Guarnera, A.-A. Haghighirad, A. Sadhanala, G.E. Eperon, S.K. Pathak, M.B. Johnston, Lead-free organic–inorganic tin halide perovskites for photovoltaic applications. Energy Environ. Sci. **7**, 3061-3068 (2014). https://doi.org/10.1039/C4EE01076K.

[31] I. Kopacic, B. Friesenbichler, S.F. Hoefler, B. Kunert, H. Plank, T. Rath, G. Trimmel, Enhanced performance of germanium halide perovskite solar cells through compositional engineering. ACS Appl. Energy Mater. . **1**, 343-347 (2018). https://doi.org/10.1021/acsaem.8b00007.

[32] C.N. Savory, A theoretical exploration of emerging solar absorber materials. 2018, UCL (University College London).

[33] F. De Angelis, Modeling materials and processes in hybrid/organic photovoltaics: From dye-sensitized to perovskite solar cells. Acc. Chem. Res. **47**, 3349-3360 (2014). https://doi.org/10.1021/ar500089n.

[34] K. Sobayel, M. Akhtaruzzaman, K. Rahman, M. Ferdaous, Z.A. Al-Mutairi, H.F. Alharbi, N.H. Alharthi, M.R. Karim, S. Hasmady, N. Amin, A comprehensive defect study of tungsten disulfide (WS_2) as electron transport layer in perovskite solar cells by numerical simulation. Results Phys. **12**, 1097-1103 (2019). https://doi.org/10.1016/j.rinp.2018.12.049.

[35] F. Jahantigh, M.J. Safikhani, The effect of HTM on the performance of solid-state dye-sanitized solar cells (SDSSCs): A SCAPS-1D simulation study. J. Appl. Phys A. **125**, 276 (2019). https://doi.org/10.1007/s00339-019-2582-0.

[36] B. Nath, P.C. Ramamurthy, G. Hegde, D. Roy Mahapatra, Role of electrodes on perovskite solar cells performance: A review. ISSS j. micro smart syst. **11**, 61-79 (2022). https://doi.org/10.1007/s41683-021-00089-y.

[37] V.H. Nguyen, D.T. Papanastasiou, J. Resende, L. Bardet, T. Sannicolo, C. Jiménez, D. Muñoz-Rojas, N.D. Nguyen, D. Bellet, Advances in flexible metallic transparent electrodes. Small. **18**, 2106006 (2022). https://doi.org/10.1002/smll.202106006.

[38] F. Azri, A. Meftah, N. Sengouga, A. Meftah, Electron and hole transport layers optimization by numerical simulation of a perovskite solar cell. Sol. Energy. **181**, 372-378 (2019). https://doi.org/10.1016/j.solener.2019.02.017.

[39] B.K. Korir, J.K. Kibet, S.M. Ngari, Computational simulation of a highly efficient hole transport-free dye-sensitized solar cell based on titanium oxide (TiO_2) and zinc oxysulfide (ZnOS) electron transport layers. J. Electron. Mater. **50**, 7259-7274 (2021). https://doi.org/10.1007/s11664-021-09250-7.

[40] N. Rono, A.E. Merad, J.K. Kibet, B.S. Martincigh, V.O. Nyamori, Optimization of hole transport layer materials for a lead-free perovskite solar cell based on formamidinium tin iodide. Energy Technol. **9**, 2100859 (2021). https://doi.org/10.1002/ente.202100859.

[41] B. Wang, X. Xiao, T. Chen, Perovskite photovoltaics: A high-efficiency newcomer to the solar cell family. Nanoscale. **6**, 12287-12297 (2014). https://doi.org/10.1039/C4NR04144E.

[42] R. Taheri-Ledari, K. Valadi, A. Maleki, High-performance HTL-free perovskite solar cell: An efficient composition of ZnO NRs, RGO, and $CuInS_2$ QDs, as electron-transporting layer matrix. Prog. Photovolt. **28**, 956-970 (2020). https://doi.org/10.1002/pip.3306.

[43] A. Gheno, S. Vedraine, B. Ratier, J. Bouclé, π-Conjugated materials as the hole-transporting layer in perovskite solar cells. Metals. **6**, 21 (2016). https://doi.org/10.3390/met6010021.

[44] I. Hussain, H.P. Tran, J. Jaksik, J. Moore, N. Islam, M.J. Uddin, Functional materials, device architecture, and flexibility of perovskite solar cell. Emergent mater. **1**, 133-154 (2018). https://doi.org/10.1007/s42247-018-0013-1.

[45] Z. Song, S.C. Watthage, A.B. Phillips, M.J. Heben, Pathways toward high-performance perovskite solar cells: review of recent advances in organo-metal halide perovskites for photovoltaic applications. J. Photonics Energy. **6**, 022001 (2016). https://doi.org/10.1117/1.JPE.6.022001.

[46] S. Huang, Q. Dong, Y. Lu, L. Duan, D. Zhang, Outstanding performance of electron-transport-layer-free perovskite solar cells using a novel small-molecule interlayer modified FTO substrate. J. Chem. Eng. **422**, 130001 (2021). https://doi.org/10.1016/j.cej.2021.130001.

[47] L. Huang, X. Sun, C. Li, R. Xu, J. Xu, Y. Du, Y. Wu, J. Ni, H. Cai, J. Li, Z. Hu, J. Zhang, Electron transport layer-free planar perovskite solar cells: Further performance enhancement perspective from device simulation. Sol. Energy Mater Sol. Cells. **157**, 1038-1047 (2016). https://doi.org/10.1016/j.solmat.2016.08.025.

[48] Z. Zhou, S. Pang, Highly efficient inverted hole-transport-layer-free perovskite solar cells. J. Mater. Chem. A. **8**, 503-512 (2020). https://doi.org/10.1039/C9TA10694D.

[49] S. Li, T. Guo, Y. Li, S. Yun, H. Xu, H. Li, A. Huang, Construction of nanostructured $CH_3NH_3PbI_3$ layer for high-performance perovskite solar cells by Ar plasma etching. Mater. Res. Bull. **147**, 111666 (2022). https://doi.org/10.1016/j.materresbull.2021.111666.

[50] F. Li, C. Ma, H. Wang, W. Hu, W. Yu, A.D. Sheikh, T. Wu, Ambipolar solution-processed hybrid perovskite phototransistors. Nat. Commun. **6**, 8238 (2015). https://doi.org/10.1038/ncomms9238.

[51] F. Di Giacomo, V. Zardetto, G. Lucarelli, L. Cinà, A. Di Carlo, M. Creatore, T.M. Brown, Mesoporous perovskite solar cells and the role of nanoscale compact layers for remarkable all-round high efficiency under both indoor and outdoor illumination. Nano Energy. **30**, 460-469 (2016). https://doi.org/10.1016/j.nanoen.2016.10.030.

[52] Y. Xia, S. Dai, Review on applications of PEDOTs and PEDOT:PSS in perovskite solar cells. J. Mater. Sci.: Mater. Electron. **32**, 12746-12757 (2021). https://doi.org/10.1007/s10854-020-03473-w.

[53] J. Niu, D. Yang, X. Ren, Z. Yang, Y. Liu, X. Zhu, W. Zhao, S. Liu, Graphene-oxide doped PEDOT:PSS as a superior hole transport material for high-efficiency perovskite solar cell. Org. Electron. **48**, 165-171 (2017). https://doi.org/10.1016/j.orgel.2017.05.044.

[54] S. Nair, S.B. Patel, J.V. Gohel, Recent trends in efficiency-stability improvement in perovskite solar cells. Mater. Today Energy. **17**, 100449 (2020). https://doi.org/10.1016/j.mtener.2020.100449.

[55] J. Yan, T.J. Savenije, L. Mazzarella, O. Isabella, Progress and challenges on scaling up of perovskite solar cell technology. Sustain. Energy Fuels. **6**, 243-266 (2022). https://doi.org/10.1039/D1SE01045J

[56] R. Chen, Y. Feng, L. Jing, M. Wang, H. Ma, J. Bian, Y. Shi, Low-temperature sprayed carbon electrode in modular HTL-free perovskite solar cells: A comparative study on the choice of carbon sources. J. Mater. Chem. C. **9**, 3546-3554 (2021). https://doi.org/10.1039/D0TC05528J.

[57] A.U. Duha, M.F. Borunda, Optimization of a Pb-free all-perovskite tandem solar cell with 30.85% efficiency. Opt. Mater. **123**, 111891 (2022). https://doi.org/10.1016/j.optmat.2021.111891.

[58] A. Marti, G.L. Araújo, Limiting efficiencies for photovoltaic energy conversion in multigap systems. Sol. Energy Mater. Sol. Cells. **43**, 203-222 (1996). https://doi.org/10.1016/0927-0248(96)00015-3.

[59] A.U. Duha, M.F. Borunda, Optimization of a Pb-free all-perovskite tandem solar cell with 30.85% efficiency. Optical Materials. **123**, 111891 (2022). https://doi.org/10.1016/j.optmat.2021.111891.

[60] L. Liu, P. Liu, S. Ullah, S.-E. Yang, H. Guo, L. Wang, X. Wang, Y. Chen, The optimization of $CsPbIBr_2$ top sub-cells for the application in monolithic all-perovskite tandem solar cells. Sol. Energy. **228**, 274-281 (2021). https://doi.org/10.1016/j.solener.2021.08.023.

[61] B. Farhadi, M. Ciprian, F. Zabihi, A. Liu, Influence of contact electrode and light power on the efficiency of tandem perovskite solar cell: Numerical simulation. Sol Energy. **226**, 161-172 (2021). https://doi.org/10.1016/j.solener.2021.08.043.

[62] J. Chen, N.G. Park, Causes and solutions of recombination in perovskite solar cells. J. Adv. Mater. **31**, 1803019 (2019). https://doi.org/10.1002/adma.201803019.

[63] K. Lu, Y. Lei, R. Qi, J. Liu, X. Yang, Z. Jia, R. Liu, Y. Xiang, Z. Zheng, Fermi level alignment by copper doping for efficient ITO/perovskite junction solar cells. J. Mater. Chem. A. **5**, 25211-25219 (2017). https://doi.org/10.1039/C7TA07828E.

[64] J. Bisquert, E.J. Juarez-Perez, The causes of degradation of perovskite solar cells. J. Phys. Chem. Lett. . **10**, 5889-5891 (2019). https://doi.org/10.1021/acs.jpclett.9b00613.

[65] N.H. Tiep, Z. Ku, H.J. Fan, Recent advances in improving the stability of perovskite solar cells. Adv. Energy Mater. **6**, 1501420 (2016). https://doi.org/10.1002/aenm.201501420.

[66] A. Le Bris, J.-F. Guillemoles, Hot carrier solar cells: Achievable efficiency accounting for heat losses in the absorber and through contacts. Appl. Phys. Lett. **97**, 113506 (2010). https://doi.org/10.1063/1.3489405

[67] J. Kim, A. Ho-Baillie, S. Huang, Review of Novel Passivation Techniques for Efficient and Stable Perovskite Solar Cells. Sol. RRL. **3**, 1800302 (2019). https://doi.org/10.1002/solr.201800302.

[68] Y. Tu, X. Yang, R. Su, D. Luo, Y. Cao, L. Zhao, T. Liu, W. Yang, Y. Zhang, Z. Xu, Diboron-assisted interfacial defect control strategy for highly efficient planar perovskite solar cells. Adv. Mater. **30**, 1805085 (2018). https://doi.org/10.1002/adma.201805085.

[69] J.P.C. Baena, L. Steier, W. Tress, M. Saliba, S. Neutzner, T. Matsui, F. Giordano, T.J. Jacobsson, A.R.S. Kandada, S.M. Zakeeruddin, Highly efficient planar perovskite solar cells through band alignment engineering. Energy Environ. Sci. **8**, 2928-2934 (2015). https://doi.org/10.1039/C5EE02608C

[70] J. Peng, Y. Wu, W. Ye, D.A. Jacobs, H. Shen, X. Fu, Y. Wan, T. Duong, N. Wu, C. Barugkin, H.T. Nguyen, D. Zhong, J. Li, T. Lu, Y. Liu, M.N. Lockrey, K.J. Weber, K.R. Catchpole, T.P. White, Interface passivation using ultrathin polymer–fullerene films for high-efficiency perovskite solar cells with negligible hysteresis. Energy Environ. Sci. **10**, 1792-1800 (2017). https://doi.org/10.1039/C7EE01096F.

[71] L. He, Z. Lv, H. Jiang, X. Ma, F. Wang, L. Fan, M. Wei, J. Yang, L. Yang, H. Liu, Sandwich-like electron transporting layer to achieve highly efficient perovskite solar cells. J. Power Sources. **453**, 227876 (2020). https://doi.org/10.1016/j.jpowsour.2020.227876.

[72] P. Liu, Y. Sun, S. Wang, H. Zhang, Y. Gong, F. Li, Y. Shi, Y. Du, X. Li, S.-s. Guo, Q. Tai, C. Wang, X.-Z. Zhao, Two dimensional graphitic carbon nitride quantum dots modified perovskite solar cells and photodetectors with high performances. J. Power Sources. **451**, 227825 (2020). https://doi.org/10.1016/j.jpowsour.2020.227825.

[73] K.J. Xu, R.T. Wang, A.F. Xu, J.Y. Chen, G. Xu, Hysteresis and instability predicted in moisture degradation of perovskite solar cells. ACS Appl. Mater. Interfaces. **12**, 48882-48889 (2020). https://doi.org/10.1021/acsami.0c17323.

[74] M. Salado, L. Contreras-Bernal, L. Caliò, A. Todinova, C. López-Santos, S. Ahmad, A. Borras, J. Idígoras, J.A. Anta, Impact of moisture on efficiency-determining electronic processes in perovskite solar cells. J. Mater. Chem. A. **5**, 10917-10927 (2017). https://doi.org/10.1039/C7TA02264F.

[75] R.K. Misra, S. Aharon, B. Li, D. Mogilyansky, I. Visoly-Fisher, L. Etgar, E.A. Katz, Temperature- and component-dependent degradation of perovskite photovoltaic materials under concentrated sunlight. J. Phys. Chem. Lett. **6**, 326-330 (2015). https://doi.org/10.1021/jz502642b.

[76] A. Wincukiewicz, J.B. Jasinski, M. Tokarczyk, R. Pietruszka, M. Godlewski, M. Kaminska, The effects of doping and coating on degradation kinetics in perovskites. Sol. Energy Mater Sol. Cells. **230**, 111142 (2021). https://doi.org/10.1016/j.solmat.2021.111142.

[77] J. Troughton, K. Hooper, T.M. Watson, Humidity resistant fabrication of $CH_3NH_3PbI_3$ perovskite solar cells and modules. Nano Energy. **39**, 60-68 (2017). https://doi.org/10.1016/j.nanoen.2017.06.039.

[78] S.K. Gupta, S. Banerjee, A. Singh, L.S. Pali, A. Garg, Modeling of degradation in normal and inverted OSC devices. Sol. Energy Mater Sol. Cells. **191**, 329-338 (2019). https://doi.org/10.1016/j.solmat.2018.11.039.

[79] C. Aranda, A. Guerrero, J. Bisquert, Crystalline clear or not: Beneficial and harmful effects of water in perovskite solar cells. ChemPhysChem. **20**, 2587-2599 (2019). https://doi.org/10.1002/cphc.201900393.

[80] Z.Q. Lin, H.W. Qiao, Z.R. Zhou, Y. Hou, X. Li, H.G. Yang, S. Yang, Water assisted formation of highly oriented $CsPbI_2Br$ perovskite films with the solar cell efficiency exceeding 16%. J. Mater. Chem. A. **8**, 17670-17674 (2020). https://doi.org/10.1039/D0TA05118G.

[81] S. Ruan, M.-A. Surmiak, Y. Ruan, D.P. McMeekin, H. Ebendorff-Heidepriem, Y.-B. Cheng, J. Lu, C.R. McNeill, Light induced degradation in mixed-halide perovskites. J. Mater. Chem. C. **7**, 9326-9334 (2019). https://doi.org/10.1039/C9TC02635E.

[82] M. Anaya, J.F. Galisteo-López, M.E. Calvo, J.P. Espinós, H. Míguez, Origin of light-induced photophysical effects in organic metal halide perovskites in the presence of oxygen. J. Phys. Chem. Lett. **9**, 3891-3896 (2018). https://doi.org/10.1021/acs.jpclett.8b01830.

[83] Z. Zhang, Y. Liu, P. Zhang, Y. Mao, Natural passivation of the perovskite layer by oxygen in ambient air to improve the efficiency and stability of perovskite solar cells simultaneously. Org. Electron. **88**, 106007 (2021). https://doi.org/10.1016/j.orgel.2020.106007.

[84] D. Bryant, N. Aristidou, S. Pont, I. Sanchez-Molina, T. Chotchunangatchaval, S. Wheeler, J.R. Durrant, S.A. Haque, Light and oxygen induced degradation limits the operational stability of methylammonium lead triiodide perovskite solar cells. Energy Environ Sci. **9**, 1655-1660 (2016). https://doi.org/10.1039/C6EE00409A

[85] N. Aristidou, C. Eames, I. Sanchez-Molina, X. Bu, J. Kosco, M.S. Islam, S.A. Haque, Fast oxygen diffusion and iodide defects mediate oxygen-induced degradation of perovskite solar cells. Nat. Commun. **8**, 15218 (2017). https://doi.org/10.1038/ncomms15218.

[86] C. Wang, F. Gu, Z. Zhao, H. Rao, Y. Qiu, Z. Cai, G. Zhan, X. Li, B. Sun, X. Yu, B. Zhao, Z. Liu, Z. Bian, C. Huang, Self-repairing tin-based perovskite solar cells

with a breakthrough efficiency over 11%. Adv. Mater. **32**, 1907623 (2020). https://doi.org/10.1002/adma.201907623.

[87] S. Ma, G. Yuan, Y. Zhang, N. Yang, Y. Li, Q. Chen, Development of encapsulation strategies towards the commercialization of perovskite solar cells. Energy Environ. Sci., (2022). https://doi.org/10.1039/D1EE02882K.

[88] M. Mohammadi, S. Gholipour, M. Malekshahi Byranvand, Y. Abdi, N. Taghavinia, M. Saliba, Encapsulation strategies for highly stable perovskite solar cells under severe stress testing: Damp heat, freezing, and outdoor illumination conditions. ACS Appl. Mater. Interfaces. **13**, 45455-45464 (2021). https://doi.org/10.1021/acsami.1c11628.

[89] C.-Y. Chang, B.-C. Tsai, Y.-C. Hsiao, M.-Z. Lin, H.-F. Meng, Solution-processed conductive interconnecting layer for highly-efficient and long-term stable monolithic perovskite tandem solar cells. Nano Energy. **55**, 354-367 (2019). https://doi.org/10.1016/j.nanoen.2018.10.014.

[90] E. Cuddihy, C. Coulbert, A. Gupta, R. Liang, Electricity from photovoltaic solar cells: Flat-plate solar array project final report. volume VII: Module encapsulation. (1986). https://resolver.caltech.edu/JPLpub86-31-volumeVII.

[91] J.A. Schwenzer, T. Hellmann, B.A. Nejand, H. Hu, T. Abzieher, F. Schackmar, I.M. Hossain, P. Fassl, T. Mayer, W. Jaegermann, U. Lemmer, U.W. Paetzold, Thermal stability and cation composition of hybrid organic–inorganic perovskites. ACS Appl. Mater. Interfaces. **13**, 15292-15304 (2021). https://doi.org/10.1021/acsami.1c01547.

[92] C. Wang, F. Gu, Z. Zhao, H. Rao, Y. Qiu, Z. Cai, G. Zhan, X. Li, B. Sun, X. Yu, B. Zhao, Z. Liu, Z. Bian, C. Huang, Self-Repairing Tin-Based Perovskite Solar Cells with a Breakthrough Efficiency Over 11%. **32**, 1907623 (2020). https://doi.org/10.1002/adma.201907623.

[93] W. Ke, M.G. Kanatzidis, Prospects for low-toxicity lead-free perovskite solar cells. Nat. Commun. **10**, 965 (2019). https://doi.org/10.1038/s41467-019-08918-3.

[94] W. Cao, Z. Hu, Z. Lin, X. Guo, J. Su, J. Chang, Y. Hao, Defects and doping engineering towards high performance lead-free or lead-less perovskite solar cells. J. Energy Chem. **68**, 420-438 (2022). https://doi.org/10.1016/j.jechem.2021.12.002.

[95] Y. Zheng, R. Su, Z. Xu, D. Luo, H. Dong, B. Jiao, Z. Wu, Q. Gong, R. Zhu, Perovskite solar cell towards lower toxicity: A theoretical study of physical lead reduction strategy. Sci. Bull. **64**, 1255-1261 (2019). https://doi.org/10.1016/j.scib.2019.06.006.

[96] A.H. Slavney, R.W. Smaha, I.C. Smith, A. Jaffe, D. Umeyama, H.I. Karunadasa, Chemical approaches to addressing the instability and toxicity of lead–halide

perovskite absorbers. Inorg. Chem. **56**, 46-55 (2017). https://doi.org/10.1021/acs.inorgchem.6b01336.

[97] J. Cao, F. Yan, Recent progress in tin-based perovskite solar cells. Energy Environ. Sci. **14**, 1286-1325 (2021). https://doi.org/10.1039/D0EE04007J.

[98] E. Jokar, C.-H. Chien, C.-M. Tsai, A. Fathi, E.W.-G. Diau, Robust tin-based perovskite solar cells with hybrid organic cations to attain efficiency approaching 10%. Adv. Mater. **31**, 1804835 (2019). https://doi.org/10.1002/adma.201804835.

[99] W. Ke, C.C. Stoumpos, M.G. Kanatzidis, "Unleaded" perovskites: Status quo and future prospects of tin-based perovskite solar cells. Adv. Mater. **31**, 1803230 (2019). https://doi.org/10.1002/adma.201803230.

[100] E.W.-G. Diau, E. Jokar, M. Rameez, Strategies to improve performance and stability for tin-based perovskite solar cells. ACS Energy Lett. **4**, 1930-1937 (2019). https://doi.org/10.1021/acsenergylett.9b01179.

[101] E. Jokar, C.-H. Chien, C.-M. Tsai, A. Fathi, E.W.-G. Diau, Robust Tin-Based Perovskite Solar Cells with Hybrid Organic Cations to Attain Efficiency Approaching 10%. **31**, 1804835 (2019). https://doi.org/10.1002/adma.201804835.

[102] T. Wang, F. Zheng, G. Tang, J. Cao, P. You, J. Zhao, F. Yan, 2D WSe_2 flakes for synergistic modulation of grain growth and charge transfer in tin-based perovskite solar cells. Adv. Sci. **8**, 2004315 (2021). https://doi.org/10.1002/advs.202004315.

[103] H. Zhang, W. Liu, R. Li, M. Zhang, M. Guo, Lead-less mesoscopic perovskite solar cells with enhanced photovoltaic performance by strontium chloride substitution. Ceram. Int. **44**, 18863-18870 (2018). https://doi.org/10.1016/j.ceramint.2018.07.121.

[104] N. Soleimanioun, M. Rani, S. Sharma, A. Kumar, S.K. Tripathi, Binary metal zinc-lead perovskite built-in air ambient: Towards lead-less and stable perovskite materials. Sol. Energy Mater. Sol. Cells. **191**, 339-344 (2019). https://doi.org/10.1016/j.solmat.2018.11.021.

[105] A. Hima, A. Khechekhouche, I. Kemerchou, N. Lakhdar, B. Benhaoua, F. Rogti, I. Telli, A. Saadoun, GPVDM simulation of layer thickness effect on power conversion efficiency of $CH_3NH_3PbI_3$ based planar heterojunction solar cell. Int. J. Energetica. **3** (2018). https://www.ijeca.info.

[106] A. Hima, N. Lakhdar, B. Benhaoua, A. Saadoune, I. Kemerchou, F. Rogti, An optimized perovskite solar cell designs for high conversion efficiency. Superlattices Microstruct. **129**, 240-246 (2019). https://doi.org/10.1016/j.spmi.2019.04.007.

[107] J. Gong, S. Krishnan, Chapter 2 - Mathematical modeling of dye-sensitized solar cells, in *Dye-Sensitized Solar Cells*, M. Soroush and K.K.S. Lau, Editors. 2019, Academic Press: New York, USA. p. 51-81.

[108] N.F. Ramli, S. Sepeai, N.F.M. Rostan, N.A. Ludin, M.A. Ibrahim, M.A.M. Teridi, S.H. Zaidi. Model development of monolithic tandem silicon-perovskite solar cell by SCAPS simulation. in *AIP Conf. Proc.* 2017. AIP Publishing LLC. https://doi.org/10.1063/1.4982178.

[109] S. Michael, A novel approach for the modeling of advanced photovoltaic devices using the SILVACO/ATLAS virtual wafer fabrication tools. Sol. Energy Mater. Sol. Cells. **87**, 771-784 (2005). https://doi.org/10.1016/j.solmat.2004.07.050.

[110] S. Yaşar, S. Kahraman, S. Çetinkaya, Ş. Apaydın, İ. Bilican, İ. Uluer, Numerical thickness optimization study of CIGS based solar cells with wxAMPS. Optik. **127**, 8827-8835 (2016). https://doi.org/10.1016/j.ijleo.2016.06.094.

[111] M. Burgelman, K. Decock, A. Niemegeers, J. Verschraegen, S. Degrave, SCAPS manual. (2016). Version 8-4-2021, https://scaps.elis.ugent.be/SCAPS%20manual%20most%20recent.pdf, accessed on 4 November 2021.

[112] A.-A. Kanoun, M.B. Kanoun, A.E. Merad, S. Goumri-Said, Toward development of high-performance perovskite solar cells based on $CH_3NH_3GeI_3$ using computational approach. Sol. Energy. **182**, 237-244 (2019). https://doi.org/10.1016/j.solener.2019.02.041.

[113] A. Kumar, S. Singh, Numerical modeling of lead-free perovskite solar cell using inorganic charge transport materials. Mater. Today, (2020). https://doi.org/10.1016/j.matpr.2020.02.545.

[114] S.J. Fonash, Solar cell device physics. Elsevier. 2010, Academic press INC: New York, USA.

[115] Y. Liu, Y. Sun, A. Rockett, A new simulation software of solar cells—wxAMPS. Sol. Energy Mater. Sol. Cells. **98**, 124-128 (2012). https://doi.org/10.1016/j.solmat.2011.10.010.

[116] J. Smucker, J. Gong, A comparative study on the band diagrams and efficiencies of silicon and perovskite solar cells using wxAMPS and AMPS-1D. Sol. Energy. **228**, 187-199 (2021). https://doi.org/10.1016/j.solener.2021.09.066.

[117] Y. Liu, D. Heinzel, A. Rockett, A new solar cell simulator: WxAMPS. Conf. Rec. IEEE Photovolt. Spec. Conf., 002753-002756 (2011). https://doi.org/10.1109/PVSC.2011.6186517.

[118] R. MacKenzie, V. Balderrama, S. Schmeisser, R. Stoof, S. Greedy, J. Pallarès, L. Marsal, A. Chanaewa, E. Von Hauff, Loss mechanisms in high efficiency polymer solar cells. Adv. Energy Mater. **6**, 1501742 (2016). https://doi.org/10.1002/aenm.201501742.

[119] S. international, ATLAS User's manual. **5** (2008). https://www.eng.buffalo.edu/~wie/silvaco/atlas_user_manual.pdf, accessed on 27 January 2023.

[120] M. Mehrabian, S. Dalir, Numerical simulation of highly efficient dye sensitized solar cell by replacing the liquid electrolyte with a semiconductor solid layer. Optik. **169**, 214-223 (2018). https://doi.org/10.1016/j.ijleo.2018.05.059.

[121] S. Michael, A.D. Bates, M.S. Green. Silvaco ATLAS as a solar cell modeling tool. in *Conf. Rec. IEEE Photovolt. Spec. Conf.* 2005. https://doi.org/10.1109/PVSC.2005.1488232.

[122] S. Zandi, M. Razaghi, Finite element simulation of perovskite solar cell: A study on efficiency improvement based on structural and material modification. Sol. Energy. **179**, 298-306 (2019). https://doi.org/10.1016/j.solener.2018.12.032.

[123] R. Stangl, C. Leendertz, General principles of solar cell simulation and introduction to AFORS-HET, in *Physics and Technology of Amorphous-Crystalline Heterostructure Silicon Solar Cells*, W.G.J.H.M. van Sark, L. Korte, and F. Roca, Editors. 2012, Springer Berlin Heidelberg: Berlin, Heidelberg. p. 445-458.

[124] S. Zandi, P. Saxena, N.E. Gorji, Numerical simulation of heat distribution in RGO-contacted perovskite solar cells using COMSOL. Sol. Energy. **197**, 105-110 (2020). https://doi.org/10.1016/j.solener.2019.12.050.

[125] P.A. Basore, D.A. Clugston. PC1D version 4 for Windows: From analysis to design. in *Conference record of the twenty fifth IEEE PHOTOVOLTAIC SPECIALISTS CONFERENCE - 1996*. 1996. New York. https://doi.org/10.1109/PVSC.1996.564023.

[126] M.I. Hossain, F.H. Alharbi, N. Tabet, Copper oxide as inorganic hole transport material for lead halide perovskite based solar cells. Sol. Energy. **120**, 370-380 (2015). https://doi.org/10.1016/j.solener.2015.07.040.

[127] S. Abdelaziz, A. Zekry, A. Shaker, M. Abouelatta, Investigating the performance of formamidinium tin-based perovskite solar cell by SCAPS device simulation. Opt. Mater. **101**, 109738 (2020). https://doi.org/10.1016/j.optmat.2020.109738.

[128] P.K. Patel, Device simulation of highly efficient eco-friendly $CH_3NH_3SnI_3$ perovskite solar cell. Sci. Rep. **11**, 3082 (2021). https://doi.org/10.1038/s41598-021-82817-w.

[129] D. Jayan K, V. Sebastian, J. Kurian, Simulation and optimization studies on $CsPbI_3$ based inorganic perovskite solar cells. Sol. Energy. **221**, 99-108 (2021). https://doi.org/10.1016/j.solener.2021.04.030.

[130] Y. Raoui, H. Ez-Zahraouy, N. Tahiri, O. El Bounagui, S. Ahmad, S. Kazim, Performance analysis of $MAPbI_3$ based perovskite solar cells employing diverse charge selective contacts: Simulation study. Sol. Energy. **193**, 948-955 (2019). https://doi.org/10.1016/j.solener.2019.10.009.

[131] F. Behrouznejad, S. Shahbazi, N. Taghavinia, H.-P. Wu, E. Wei-Guang Diau, A study on utilizing different metals as the back contact of $CH_3NH_3PbI_3$ perovskite

solar cells. J. Mater. Chem. A. **4**, 13488-13498 (2016). https://doi.org/10.1039/C6TA05938D.

[132] K. Deepthi Jayan, V. Sebastian, Comprehensive device modelling and performance analysis of $MASnI_3$ based perovskite solar cells with diverse ETM, HTM and back metal contacts. Sol. Energy. **217**, 40-48 (2021). https://doi.org/10.1016/j.solener.2021.01.058.

[133] Q. Luo, H. Ma, F. Hao, Q. Hou, J. Ren, L. Wu, Z. Yao, Y. Zhou, N. Wang, K. Jiang, H. Lin, Z. Guo, Carbon nanotube based inverted flexible perovskite solar cells with all-inorganic charge contacts. Adv. Funct. Mater. **27**, 1703068 (2017). https://doi.org/10.1002/adfm.201703068.

[134] Q. Meng, Y. Chen, Y.Y. Xiao, J. Sun, X. Zhang, C.B. Han, H. Gao, Y. Zhang, H. Yan, Effect of temperature on the performance of perovskite solar cells. J. Mater. Sci.: Mater. Electron. **32**, 12784-12792 (2021). https://doi.org/10.1007/s10854-020-03029-y.

CHAPTER EIGHT

Optical and Quantum Electronics (2022) 54:317
https://doi.org/10.1007/s11082-022-03737-1

Simulation of the photovoltaic performance of a perovskite solar cell based on methylammonium lead iodide

Nicholas Rono[1] · Abdelkrim E. Merad[2] · Joshua K. Kibet[3] · Bice S. Martincigh[1] · Vincent O. Nyamori[1]

Received: 7 August 2021 / Accepted: 8 April 2022

Abstract

Herein, we report a numerical simulation of a model perovskite solar cell whose architectural design is: glass/FTO/IGZO/$CH_3NH_3PbI_3$/spiro-OMeTAD/Au. The main goal was to optimize the performance of the device utilizing indium gallium zinc oxide (IGZO) as the electron transport layer. The performance of the device was explicitly compared with similar devices fabricated experimentally and theoretically. Although IGZO has attractive properties, it has not been widely utilized. The simulation was performed with the solar cell capacitance simulator software. In this model, the effects of varying several parameters on the overall solar cell performance were critically examined. These parameters include the thickness of the solar absorber (methylammonium lead iodide), hole transport and electron transport layers; doping densities of the hole transport and electron transport layers; density of defects of the absorber layer; back-contact metal work function and operational temperature. The simulation results showed that the performance of the device can be enhanced by optimizing the thickness of the absorber and its defect density, and also the thickness and doping densities of the hole transport and electron transport layers. It was found that an absorber interface with higher defect density resulted in poorer performance of the device. Additionally, it was noted that the cell operated best at low temperatures. Also, metallic back contacts, made of nickel, platinum or lead, gave similar results as gold. Therefore, these metals can be used as alternatives to gold since they are relatively cheaper. With the optimal conditions of the solar cell in place, the following photovoltaic characteristics were obtained: the power conversion efficiency PCE was 19.95%, short circuit current density (Jsc) was 25.55 mA cm-2, open circuit voltage (V_{oc}) was 5.32 V and fill factor FF was 14.68%. This PCE value is higher than for comparable solar cells devices that have been examined either computationally or experimentally. These insights will prove useful in the fabrication and advancement of high-performance perovskite solar cells for large-scale applications.

✉ Abdelkrim E. Merad
aemerad@gmail.com

[1] School of Chemistry and Physics, University of KwaZulu-Natal, Westville Campus, Private Bag x54001, Durban 4000, South Africa

[2] Solid State Physics Team, Theoretical Physics Laboratory, Faculty of Sciences, A Belkaid University, Box 119, 13000 Tlemcen, Algeria

[3] Chemistry Department, Egerton University, Njoro Campus, P.O. Box 536, Egerton 20115, Kenya

Published online: 30 April 2022

CHAPTER EIGHT

Simulation of the photovoltaic performance of a perovskite solar cell based on methylammonium lead iodide

Nicholas Rono[a], Abdelkrim E. Merad[b]*, Joshua K. Kibet[c], Bice S. Martincigh[a] and Vincent O. Nyamori[a]

[a]School of Chemistry and Physics, University of KwaZulu-Natal, Westville Campus, Private Bag x54001, Durban, 4000, South Africa

[b]Solid State Physics Team, Theoretical Physics Laboratory, Faculty of Sciences, A Belkaid University, Box 119, 13000, Tlemcen, Algeria

[c]Chemistry Department, Egerton University, Njoro Campus, P.O. Box 536-20115, Egerton, Kenya

*Corresponding author: E-mail: aemerad@gmail.com, Tel: +213554702391

Abstract

Herein, we report a numerical simulation of a model perovskite solar cell whose architectural design is: glass/FTO/IGZO/$CH_3NH_3PbI_3$/spiro-OMeTAD/Au. The main goal was to optimise the performance of the device utilising indium gallium zinc oxide (IGZO) as the electron transport layer (ETL). The performance of the device was explicitly compared with similar devices fabricated experimentally and theoretically. Although IGZO has attractive properties, it has not been widely utilised. The simulation was performed with the solar cell capacitance simulator (SCAPS) software. In this model, the effects of varying several parameters on the overall solar cell performance were critically examined. These parameters include the thickness of the solar absorber (methylammonium lead iodide), hole transport and electron transport layers; doping densities of the hole transport and electron transport layers; density of defects of the absorber layer; back-contact metal work function and operational temperature. The simulation results showed that the performance of the device can be enhanced by optimising the thickness of the absorber and its defect density, and also the thickness and doping densities of the hole transport and electron transport layers. It was found that an absorber interface with higher defect density resulted in poorer performance of the device.

Additionally, it was noted that the cell operated best at low temperatures. Also, metallic back contacts, made of nickel, platinum or lead, gave similar results as gold. Therefore, these metals can be used as alternatives to gold since they are relatively cheaper. With the optimal conditions of the solar cell in place, the following photovoltaic characteristics were obtained: the power conversion efficiency PCE was 19.95%, short-circuit current density (J_{sc}) was 25.55 mA cm^{-2}, open-circuit voltage (V_{oc}) was 5.32 V and fill factor FF was 14.68%. This PCE value is higher than for comparable solar cells devices that have been examined either computationally or experimentally. These insights will prove useful in the fabrication and advancement of high-performance perovskite solar cells for large-scale applications.

Keywords: Numerical simulation; HTL; ETL; SCAPS; perovskite; solar cell.

8.1 Introduction

Much research time and effort has been devoted towards the modification of architectural designs of perovskite solar cells from both experimental and theoretical perspectives in order to enhance the power conversion efficiency (PCE) [1]. Theoretical investigations such as simulations have become indispensable because they complement experimental work and reduce experimental costs [2]. Recently, the number of publications on simulations of perovskite-based photovoltaic cells have increased exponentially, and the most commonly reported simulation software comprises the solar cell capacitance simulator (SCAPS) [3, 4], SILVACO ATLAS [5], general-purpose photovoltaic device model (GPVDM) [6], and wx-analysis of microelectronic and photonic structures (wxAMPS) [7].

Perovskite solar cells (PSCs) based on inorganic-organic hybrid composites have lately attracted considerable scientific attention due to their low cost [8] and low-temperature processing routes [9], better light absorption coefficients, enhanced carrier lifetimes [10], and relatively high efficiencies [11]. The PCEs for inorganic-organic-based perovskites had risen remarkably from 3.8% to over 23% since 2009 when the first application of these materials in photovoltaic cells was reported [12]. This has been achieved through device modification, such as interface engineering [13], morphological control [14], and optimisation of various parameters, such as the thickness of layers, doping densities, and the nature of the back metallic contacts [15]. In order to enhance the hole extraction mechanism in an inverted PSC, Wang et al. [16] investigated the effect of varying the concentration of methylammonium iodide (MAI) on the PCE of the devices. The MAI was pre-coated on the hole transport layer (HTL), the poly(3,4-ethylenedioxythiophene) polystyrene sulfonate (PEDOT:PSS). The best performing device (with 4 mg/ml MAI concentration) exhibited a PCE of 16.67% compared to pristine with 14.8% and was attributed to the increased short-circuit current density (J_{sc}) 23.52 mA cm-^{2}) and the open-circuit voltage (V_{oc}) (1.01 V). Similarly, defects reduction (either interfacial or bulk defects) is key in enhancing the PCE of the PSCs by reducing the recombination of photogenerated charges. Recently Zhang et al. [17] incorporated potassium sulphate (K_2SO_4) at the interface between electron transport layer i.e. SnO_2 and the perovskite layer, i.e. SnO_2/perovskite interface. The K_2SO_4 assisted in reducing both interfacial defects and bulk defects and more importantly, aided in tuning band alignment.

Ultimately, this modification led to improvement of the PCE from 19.45% to 21.18% in the fabricated devices.

The stability and toxicity of lead are two main issues facing PSCs and limit their commercialisation; thus, a more stable structure and lead-free devices are essential [18]. Accordingly, Zhou et al. [19] computationally investigated the effect of replacing the methylammonium part of the lead-based perovskite materials with super-alkalis such as; Li_3O, Li_2F, and H_5O_2 on the stability of the PSCs. The $H_5O_2MBr_3$ perovskite (where M=Ge, Sn, or Pb) exhibited high stability, and the device with H_5O_2SnBr3 and H_5O_2PbBr3 showed a PCE of 23.17 and 22.83%, respectively. A typical planar perovskite solar cell architecture consists of a hole transport layer (HTL), an absorber perovskite layer, and an electron transport layer (ETL) – all sandwiched by a metallic back contact and a transparent front coated glass window [20]. The HTL materials can be inorganic or organic [4, 21]. For example, inorganic HTL materials include nickel(II) oxide (NiO) [22], copper(I) thiocyanate (CuSCN) [23], copper(I) iodide (CuI) [24], and copper(I) oxide (Cu_2O) [8], while organic materials include poly(3-hexylthiophene) (P3HT) [25], 2,2',7,7'-tetrakis[N,N-di(4-methoxyphenyl)amino]-9,9'-spirobifluorene (spiro-OMeTAD) [26], PEDOT: PSS) [27], and poly(2,5-bis(3-tetradecylthiophen-2-yl)thieno-[3,2-b]thiophene) (D-PBTTT-14) [28].

Similarly, ETL materials can also be classified as organic and comprise substances such as [6,6]-phenyl-C_{61}-butyric acid methyl (PCBM) [29], or inorganic semiconductors such as titanium dioxide (TiO_2) [30], indium gallium zinc oxide (IGZO) [31], tin dioxide (SnO_2) [12], and zinc oxide (ZnO) [32]. Among the ETL materials, TiO_2 and SnO_2 [33] have been extensively used because of their low-temperature processing conditions and high electron transfer capabilities in which photocells based on these materials have attained PCE values above 20% [12]. Although IGZO has scarcely been utilised as an ETL material [34], it shows good potential because of its comparable electron affinity with SnO_2, relatively narrow optical band gap, low-temperature processing routes [35], environmental stability, and high electron mobility (15 $cm^2\ V^{-1}\ s^{-1}$) [31]. Recently, Rao et al. [34] prepared amorphous IGZO via a solution process and incorporated it in a perovskite-based solar cell – the fabricated cell achieved a 17.4% PCE with reasonably good stability. This was attributed to the fact that IGZO has a high charge carrier concentration, high transparency, and high electron mobility [34]. Besides its use in

PCEs, IGZO has also been used in thin-film transistors [36] due to its inherent optoelectronic properties. Generally, the performance of existing PSCs utilising IGZO material as the ETL are still low and can be improved by using different HTL materials, back contacts, and configuration engineering. Recently, Azri et al. [31] tested a configuration of Au/IGZO/$CH_3NH_3PbI_3$/PEDOT:PSS/Au by using SCAPS-1D software and obtained a PCE of a relatively high value (19.51%). Similarly, Lakhdar et al. [37] designed a lead-free perovskite model with the configuration: ITO/PEDOT:PSS/$CH_3NH_3GeI_3$/IGZO/Ag and the model achieved a modest PCE value of 10.16%. Accordingly, changing the layers or even the metallic back contact could result in the improvement of the performance of the device.

This work reports the numerical simulation of a model perovskite solar cell with the following architecture: glass/FTO/IGZO/$CH_3NH_3PbI_3$/spiro-OMeTAD/Au, by making use of SCAPS-1D software. The aim was to propose a model that would give a high PCE compared to other similar cells that have been fabricated experimentally or theoretically. Since IGZO has not been widely investigated, it was interesting to include it as the ETL. Spiro-OMeTAD was chosen as the HTL since it has good band alignment with the absorber. Several parameters of this device have been optimised, and the resulting photovoltaic efficiency has been calculated in this work. In essence, the influence of varying the thickness of the HTL, ETL, and absorber layer, the doping densities of the HTL (N_a) and ETL (N_d) materials, and the absorber defect densities (N_t) were investigated. Furthermore, the effect of changing the metallic back contact and the operating temperature on the overall device performance has also been examined. It is envisaged that the results of this work will be helpful for the future fabrication of highly efficient perovskite solar cells.

8.2 Device architecture and simulation methodology

The device structure of the model perovskite solar cell explored in this work consists of glass/FTO/IGZO/$CH_3NH_3PbI_3$/spiro-OMeTAD/Au as presented in Figure 8.1. The model structure is a planar n-i-p perovskite design; where n is IGZO (ETL), i is the perovskite absorber layer (methylammonium lead iodide, $CH_3NH_3PbI_3$) and p is spiro-OMeTAD (HTL). The corresponding band alignment of the components of the device is shown in Figure 8.1b.

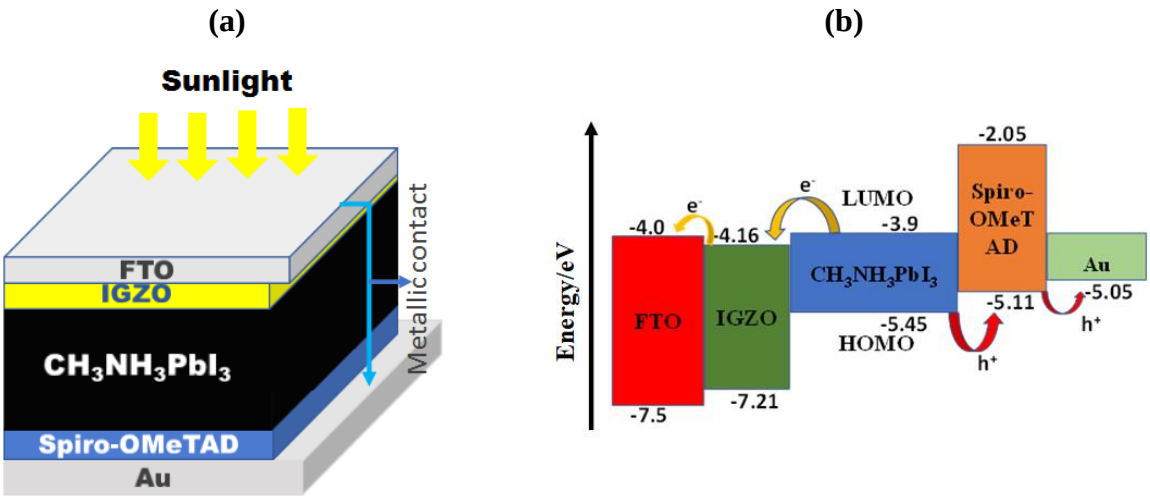

Figure 8.1: (a) Solar cell device architecture and (b) band alignment of the proposed device components

The input parameters of the modelled device were obtained from published reports as listed in Table 8.1. SCAPS-1D simulation software [38] was used for the numerical simulation of the model. For the simulation, the solar spectrum was set at air mass 1.5 global (AM 1.5G), the working temperature was 300 K, and the power density was kept at 100 mW cm^{-2}.

SCAPS software solves the basic semiconductor equations in one dimension under the steady-state conditions and simulates the electric field distribution, generation-recombination profiles, carrier transport processes, and current densities. The Poisson equation showing the relationship between the electric field (E) and space charge density (ρ) is shown in Equation (1).

$$\frac{\partial^2\psi}{\partial^2 x} = -\frac{\partial E}{\partial x} = -\frac{\rho}{\varepsilon_s} = -\frac{q}{\varepsilon_s}[p - n + N_D^+(x) - N_A^-(x) \pm N_{def}(x)] \qquad \text{Equation (1)}$$

where ψ is taken as the electrostatic potential, ε_s is the relative static permittivity of free space, q is the elementary charge, n is the electron density, p is the hole density, N_D^+ is the density of the ionised donors, N_A^- is the density of ionised acceptors, and N_{def} is the defect density of the acceptor or donor.

The continuity equations for electrons and holes are presented as Equations (2) and (3), respectively.

$$\frac{\partial j_n}{\partial x} + G - U_n(n,p) = 0 \qquad \text{Equation (2)}$$

$$-\frac{\partial j_p}{\partial x} + G - U_p(n,p) = 0 \qquad \text{Equation (3)}$$

where j_n is the electron current density, j_p is the hole current density, $U_{n,p}$ is the net recombination rate and G is the generation rate.

The charge carriers move by diffusion and drift, which is expressed in Equations (4) and (5) for the electrons and holes, respectively.

$$j_n = D_n \frac{dn}{dx} + \mu_n n \frac{d\emptyset}{dx} \qquad \text{Equation (4)}$$

$$j_p = D_p \frac{dn}{dx} + \mu_p p \frac{d\emptyset}{dx} \qquad \text{Equation (5)}$$

where D_n is the electron diffusion coefficient, μ_n is the electron mobility, D_p is the hole diffusion coefficient, μ_p is the hole mobility, and $\emptyset$ is the electrostatic potential.

Table 8.1: Input parameters for the simulation of the model solar cell device

Parameter	**FTO**[†]	**IGZO (ETL)**[‡]	**$CH_3NH_3PbI_3$ (perovskite absorber)**[‡]	**Spiro-OMeTAD (HTL)**[†]
Thickness, d/μm	0.05	0.5	0.5	1.0
Bandgap, E_g/eV	3.5	3.05	1.55	3.06
Affinity, χ/eV	4.0	4.16	3.9	2.05
Dielectric Permittivity (relative), ε_r	9.0	10.0	6.5	3.0
Effective density of state at CB, N_c/cm^{-3}	2.2×10^{18}	5.8×10^{18}	2.2×10^{15} *	2.8×10^{19}
Effective density of state at VB, N_v/cm^{-3}	1.8×10^{19}	5.8×10^{18}	2.2×10^{17} *	1.0×10^{19}
Mobility of electrons, μ_n/cm^2 V^{-1} s^{-1}	20.0	15.0	2.0	1.0×10^{-4}
Mobility of holes, μ_p/cm^2 V^{-1} s^{-1}	10.0	0.1	2.0	2.0×10^{-4}
Density of n-type doping, N_d/cm^{-3}	1.0×10^{19}	1.0×10^{18}	5.21×10^{9}	0.0
Density of p-type doping, N_a/cm^{-3}	0.0	0.0	5.21×10^{9}	1.0×10^{18}
Density of defects, N_t/cm^{-3}	0.0	1.0×10^{15}	2.5×10^{13}	1.0×10^{14}

[†]Data from Ref. [39], [‡]Data from Ref. [31], *Data from Ref. [40].

8.3 Results and discussion

The performance of the model perovskite solar cell was optimised by considering the effects of various cell parameters. These included the thickness of the methylammonium lead iodide absorber, hole transport and electron transport layers, the defect density of the absorber, doping densities of the HTL and ETL, the back contact metal work function and the cell operating temperature. The photovoltaic characteristics that were simulated were the PCE, fill factor (FF), short-circuit current density (J_{sc}) open-circuit voltage V_{oc} and quantum efficiency (QE).

8.3.1 Effect of thickness of absorber, hole transport, and electron transport layers

The thickness of each layer of the perovskite solar cell influences the overall performance of the device, especially the absorber layer, therefore, all the layer thicknesses should be optimised. Consequently, to investigate the effects of varying absorber thickness on photovoltaic characteristics, the thickness of the hole transport and electron transport layers was fixed at 1.0 and 0.5 µm, respectively, while the absorber thickness was varied from 0.5 to 1.0 µm. The results obtained for the photovoltaic characteristics as a function of the absorber thickness are presented in Figure 8.2. The results from Figure 8.2a show that the efficiency of the device increases with an increase in absorber thickness. This can be attributed to an increase in electron-hole pair generation due to greater photon absorption. The PCE reached a maximum value at an absorber thickness of 0.9 µm before its performance decreased as the absorber thickness increased.

Similarly, the J_{sc} and FF increased with an increase in absorber thickness (Figure 8.2b); this is because of the increase in the light absorption response and increased electric field, respectively. In contrast, V_{oc} decreased with increased thickness of the absorber due to a possible increase in the recombination of excitons. The V_{oc} value indicates the magnitude of recombination in a device. As can be noted from Equation 6, V_{oc} depends on J_{sc} and the dark saturation current (J_o) [41]:

$$V_{oc} = \frac{nk_BT}{q} \ln\left[\frac{J_{sc}}{J_o} + 1\right] \qquad \text{Equation (6)}$$

where n is a factor, k_B is the Boltzmann constant, T is temperature, q is the elementary charge and J_o is the dark saturation current. The term $\frac{nk_BT}{q}$ is the thermal voltage or flow

of elementary current. Therefore, it follows that V_{oc} decreases as J_o increases. The optimum photovoltaic characteristics at an optimum absorber thickness of 0.9 µm were: PCE = 18.84%, FF = 23.25%, J_{sc} = 24.67 mA cm^{-2} and V_{oc} = 3.28 V.

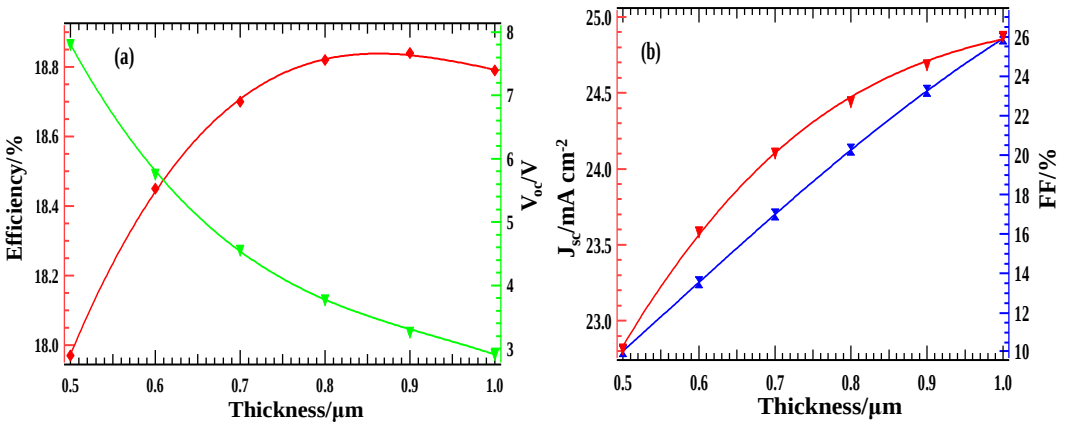

Figure 8.2: Effect of varying the perovskite absorber layer thickness on device performance: (a) efficiency and V_{oc} and (b) J_{sc} and FF

The influence of the thickness of the HTL material on the photovoltaic characteristics was investigated. In this case, the absorber thickness was kept at 0.9 µm and the ETL thickness was fixed at 0.5 µm, while the thickness of the HTL was varied from 1.0 to 0.1 µm at intervals of 0.1 µm. The results obtained are presented in Figure 8.3. The PCE of the device decreased with the increasing thickness (Figure 8.3a) and this could be attributed to the fact that apart from the increase in the path length, there was also an increasing number of holes that were blocked by the thicker HTL from reaching the metallic back contact and, thus, reduced the cell efficiency. The value of FF increased with the HTL thickness as shown in Figure 8.3a. With an increase in the electric field, V_{oc} decreases with an increase in the HTL thickness, as shown in Figure 8.3b, because of the increased recombination of excitons that have a negative implication on device performance. Remarkably, J_{sc} remained constant as depicted in Figure 8.3b. This constant behaviour may be due to the fact that a constant number of charge carriers were generated in the absorber layer, and thus, there was no significant change in the photovoltaic parameters.

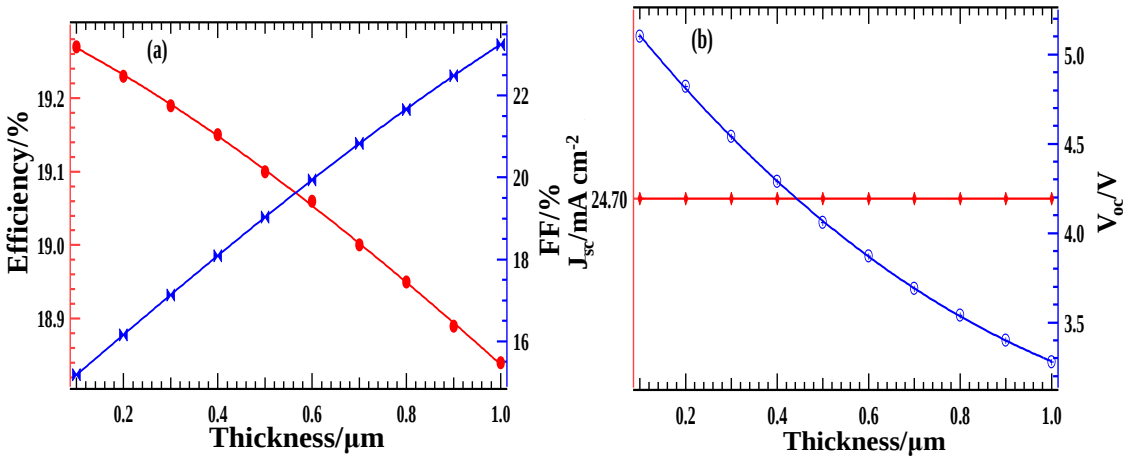

Figure 8.3: Effect of varying the spiro-OMeTAD HTL thickness on device performance: (a) efficiency and FF and (b) J_{sc} and V_{oc}

After optimisation of the absorber and HTL thicknesses (i.e. absorber layer thickness fixed at 0.9 µm and HTL fixed at 0.1 µm), the thickness of the ETL was varied from 0.5 to 0.1 µm and the resulting photovoltaic characteristics are illustrated in Table 8.2. Notably, PCE, V_{oc}, and J_{sc} decreased as the ETL thickness increased. Moreover, the FF decreased slightly before rising again as the ETL thickness increased.

Table 8.2: Photovoltaic parameters of the device with corresponding IGZO layer thickness

Thickness/µm	V_{oc}/V	J_{sc}/mA cm^{-2}	FF/%	PCE/%
0.1	5.33	25.5	14.66	19.92
0.2	5.33	25.33	14.65	19.78
0.3	5.32	25.09	14.67	19.6
0.4	5.32	24.87	14.68	19.43
0.5	5.31	24.7	14.7	19.29

The quantum efficiency (QE) (internal) of the device was also simulated and the results are presented in Figure 8.4. The quantum efficiency was approximately 98% in the wavelength range of 300 to 750 nm. This observation is attributed to the high J_{sc} value witnessed for the optimised device of 25.55 mA cm^{-2}. The QE shown may be the result of the optical absorption of the absorber and ETL because their locations are next to the

front part where direct solar radiation falls, and not the optical absorption of the HTL since it is on the reverse side of the solar radiation and therefore does not a receive significant number of photons. Based on the bandgap values in Table 8.1, the absorber can absorb light of wavelength up to a maximum of about 800 nm while the ETL can absorb a maximum of 406 nm. The photovoltaic characteristics of the device before and after sequential optimisation of the thickness of the absorber layer, HTL and ETL are summarised in Table 8.3. It is evident that after optimisation, the performance of the device was enhanced.

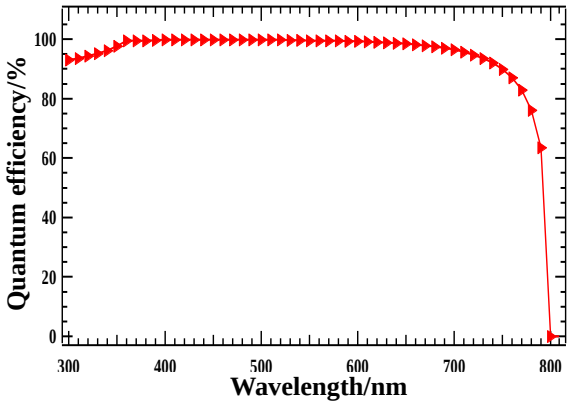

Figure 8.4: Quantum efficiency of the optimised device

Table 8.3: Photovoltaic performance of the device before and after optimisation

Cell:	**glass/FTO/IGZO/$CH_3NH_3PbI_3$/spiro-OMeTAD/Au Cell**			
Parameters		**Starting model**	**Range investigated**	**Optimised model**
Thickness/µm	HTL	1.0	0.1 – 1.0	0.1
	ETL	0.5	0.05 – 0.5	0.05
	Absorber	0.5	0.5 – 1.0	0.9
V_{oc}/V		7.81		5.32
J_{sc}/mA cm^{-2}		22.82		25.55
FF/%		10.07		14.68
PCE/%		17.97		19.95

8.3.2 Effect of density of absorber defects, and HTL and ETL doping densities

In solar cells, the density of the defects in the layer interface is very important as far as photovoltaic performance is concerned [42]. A high defect density can have negative impacts on the performance of perovskite solar cells because it can reduce the quality of the absorber layer by inducing the recombination of excitons that leads to a reduction in cell lifetime. During the deposition of the perovskite absorber material on the surface of the ETL, defects can be introduced on the surface or grain boundaries. It is therefore desirable to utilise methods and materials that reduce this defect density for improved cell performance [43]. At the starting defect density of 2.5×10^{13} $cm^{-3}$the device did not show photovoltaic behaviour, therefore, to investigate the effect of defect density on the absorber performance, the density of defects (N_t) was varied from 2.5×10^{14} to 2.5×10^{18} cm^{-3} and the resulting photovoltaic characteristics are illustrated in Figure 8.5. The PCE decreased sharply from 19.5 to 1.72% with an increase in defect density (Figure 8.5a). This reduced performance possibly arises as a result of the reduced lifetime and increased recombination of electron-hole pairs. Generally, FF, J_{sc}, and V_{oc} (Figure 8.5a and Figure 8.5b) decreased with increasing density of the absorber defects due to increased resistance and recombination. From these results, it is clear that more defects significantly alter the photovoltaic characteristics. The best cell defect density for this model was set to be 2.5×10^{14} cm^{-3}.

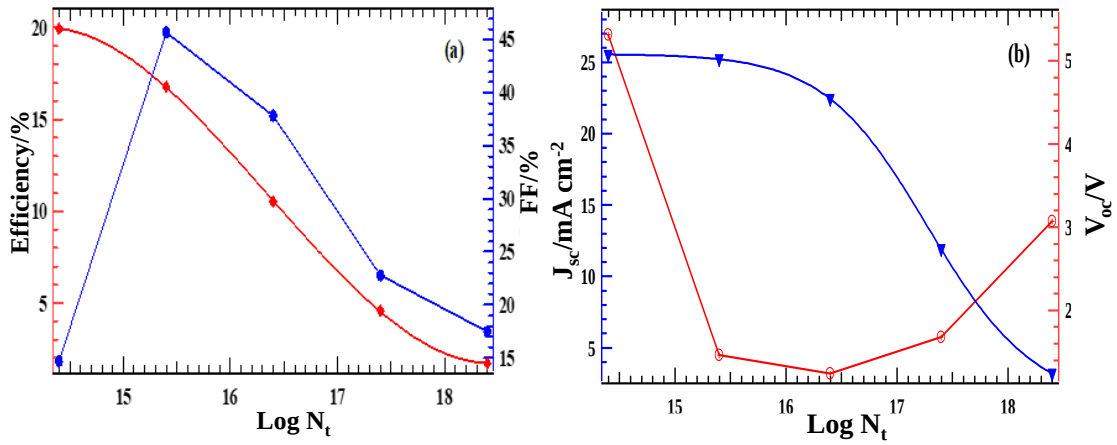

Figure 8.5: Effects on the photovoltaic device performance as a result of changing absorber defect density: (a) efficiency and FF, and (b) J_{sc} and V_{oc}

The effects of doping the HTL and ETL materials were also examined by varying the doping levels from 1.0×10^{14} to 1.0×10^{18} cm^{-3} for both materials. It can be observed

from Figure 8.6 that the PCE, J_{sc}, and V_{oc} increased with increasing donor concentration (N_a), but the FF decreased. This can be credited to the increased conductivity in the device with an increase in doping levels due to increased charge density and hole mobilities. In the case of excess doping levels, the non-carrier acceptor anion concentration will build up, thus lowering hole mobility, and thus best possible doping level is reached. For our case, the best donor doping level was achieved at 1.0×10^{18} cm^{-3} because above this order, the device did not show photovoltaic characteristics.

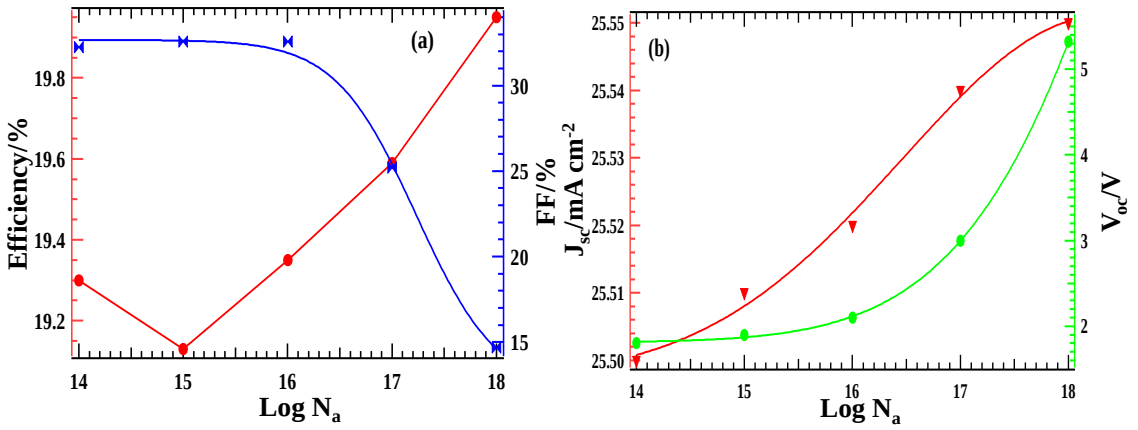

Figure 8.6: Effects of changes in doping density of the HTL on the photovoltaic device performance: (a) efficiency and FF, (b) J_{sc} and V_{oc}

A similar observation was noted for acceptor doping (N_d), as presented in Figure 8.7. Evidently, from Figure 8.7, the device's PCE, J_{sc}, and V_{oc} increased with an increase in doping levels; this is because of an increased charge carrier (electrons) concentration, and thus, the performance is enhanced. The best photovoltaic characteristics were attained when the donor and acceptor's doping concentrations were set at 1.0×10^{18} cm^{-3}. With these best values, the PCE, FF, J_{sc}, and V_{oc} for the device were 19.95 %, 14.68%, 25.58 mA cm^{-2}, and 5.32 V, respectively.

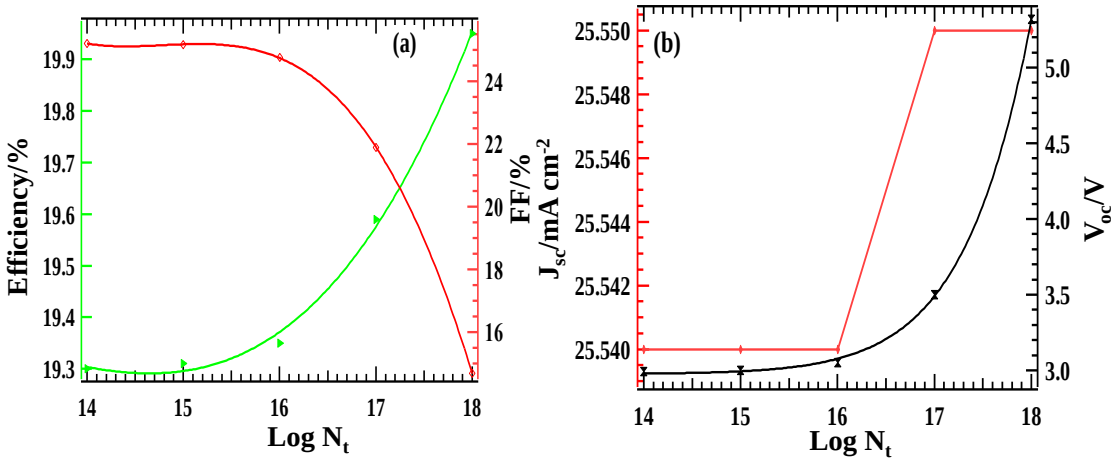

Figure 8.7: Effects of changes in the doping density of ETL on the photovoltaic device performance: (a) efficiency and FF, and (b) J_{sc} and V_{oc}

8.3.3 Influence of metal work function and operating temperature

Different metals with corresponding work functions were tested in the search for better alternatives of metallic back contacts. The work function for gold of 5.05 eV is used as the default in the SCAPS software. This was changed in turn to the following metal work functions: Cu (4.65 eV), Ag (4.7 eV), Ni (5.0 eV), Pd (5.3 eV), and Pt (5.65 eV). Figure 8.8 shows the variation of the photovoltaic characteristics for the device with these different metals. The PCE of the device increases with increasing work function of the metal from 4.65 to 5.0 eV and, thereafter, plateaus, as shown in Figure 8.8a. Similarly, J_{sc} and V_{oc} increase with an increase in the work function (Figure 8b), while FF decreases (Figure 8.8a).

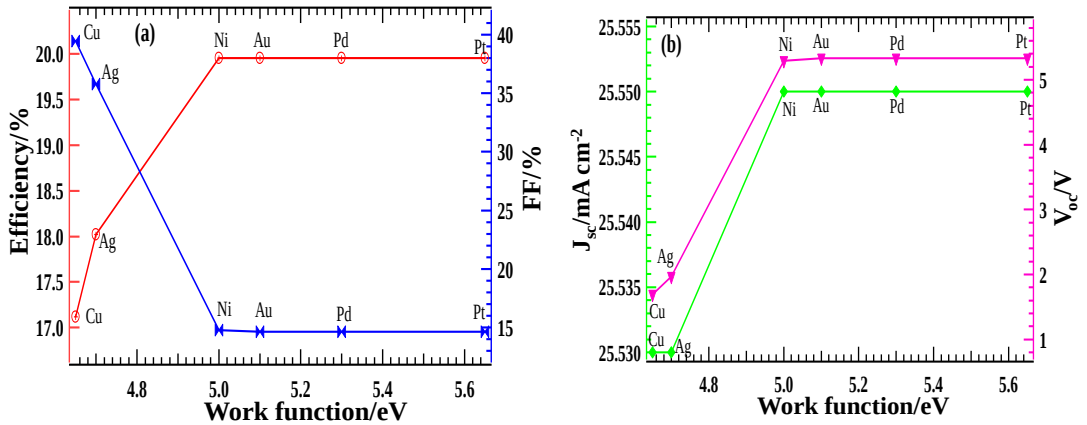

Figure 8.8: Effect on device performance with a change in back metal contact: (a) efficiency and FF, and (b) J_{sc} and V_{oc}

The high performance of Ni, Pt, and Pd can be attributed to their high work functions and V_{oc} and, therefore, they are good candidates for the metal back contact in place of gold which is expensive. Essentially, a metal with a high work function induces a high barrier for electrons to move from the HTL to the metal contact and, thus, enhances performance. Therefore, since Ni, Pt, and Pd gave similar PCE values like that for gold, it can be concluded that they can be used as alternatives to gold [39, 44].

The numerical simulations of the model solar cell investigated in this work were performed at a temperature of 300 K; nonetheless, to determine the effect of operating temperature on the device parameters, the temperature was varied between 260 and 400 K. The primary reason for simulating over this temperature range is because solar cells are conventionally placed outside, on top of buildings. At elevated points and other solar harvesting sites, it exposes them to varying weather conditions and sunlight intensities. Figure 8.9 shows the variation in photovoltaic characteristics as a function of the operating temperature of the solar device.

From Figure 8.9a, the PCE decreased with increasing temperature, an indication that the operation of the cell is affected by temperature changes. This can be explained as follows: at higher temperatures, the band gap is reduced, possibly leading to more recombination of excitons; thus, a decrease in PCE is observed as the operating temperature increases. The FF increased gradually with temperature (Figure 8.9a), and V_{oc} (Figure 8.9b) slightly decreased because of decreasing bandgap [45]. The $J_{sc,}$ on the other hand, remained essentially constant for this device. Parameters such as band gap, electron and hole mobility, and charge carrier concentration are affected by changes in the operating temperature of the electronic device.

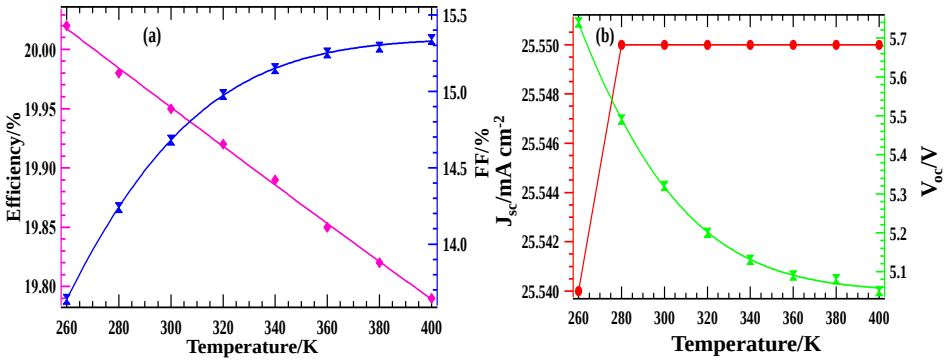

Figure 8.9: Effect on device performance with a change in operating temperature: (a) Efficiency and FF, (b) J_{sc} and V_{oc}

Once all the parameters that affect the device performance were optimised, the final J-V curve for the model cell was simulated. The performance of this model was compared with both experimental and simulated results of other IGZO perovskite-based solar cell designs and is presented in Table 8.4. This model exhibits the highest PCE at 19.95% and compares favourably well with previously reported cells.

Table 8.4: Photovoltaic characteristics of perovskite-based solar cells with IGZO as the ETL

Device architecture	**Experimental/ Simulation**	**V_{oc}/V**	**J_{sc}/mA cm^{-2}**	**FF/%**	**PCE/ %**	**Ref**
Au/IGZO/$CH_3NH_3PbI_3$/PEDOT:PSS/Au	Simulation (SCAPS-1D)	1.27	21.6	71.1	19.51	[31]
ITO/IGZO/Perovskite ($FA_{0.75}MA_{0.25}PbI_{2.5}Br_{0.5}$)/spiro-OMeTAD/Au	Experimental	1.14	27.7	66.8	17.4	[34]
ITO/PEDOT:PSS/$CH_3NH_3GeI_3$/IGZO/Ag	Simulation (SCAPS-1D)	0.81	23.04	54.36	10.16	[37]
FTO/IGZO/$CH_3NH_3PbI_3$/spiro-OMeTAD/Au	Simulation (SCAPS-1D)	5.32	25.55	14.68	19.95	This work

8.4 Conclusion

In this study, the performance of a model perovskite solar cell with the architecture FTO/IGZO/$CH_3NH_3PbI_3$/spiro-OMeTAD/Au was investigated by simulation with SCAPS-1D software. The thickness of the absorber (methylammonium lead iodide), hole transport (spiro-OMeTAD), and electron transport (IGZO) layers were optimised. The optimum values for the absorber, hole transport, and electron transport layers were found to be 0.9, 0.1, and 0.05 µm, respectively. It is evident that the thickness of the layers is important in power conversion efficiency, especially for the absorber. The effect of the defect density of the absorber and the doping concentrations for the HTL and ETL were also examined. For the absorber, a defect density of 2.5×10^{14} cm^{-3} was found to be the

best while a doping concentration of 1.0×10^{18} cm^{-3} was found to be the best possible for both the HTL and ETL materials. This study has also demonstrated that the Au back contact can be replaced with either Ni, Pt, or Pd as back metals since they give similar PCE values and are less expensive than gold, and readily available. The efficiency of the device decreased with increasing operating temperature. Thus, better performance can be achieved at generally lower temperatures. After optimisation, the model cell attained a PCE of 19.95%, with a J_{sc} of 25.55 mA cm^{-2}, V_{oc} of 5.32 V, and FF of 14.68%, which shows an improved efficiency than other similar perovskite solar cells previously reported. This work is envisaged to prove useful for the fabrication of high-performance solar cells. Nonetheless, an experimental approach to the performance of the model photovoltaic cell is highly recommended to complement the theoretical work reported in this study.

Acknowledgments

NR is grateful to the ACADEMY project N° 2017-3052/001-001, for an academic mobility scholarship to the University of Tlemcen, Algeria, where this work was carried out at the Theoretical Physics Laboratory (TPL). AEM is grateful to DGRSDT and MHESR of Algeria for financial support under the PRFU research project N° B00L02UN130120180011. The authors are grateful for the financial support provided by the National Research Foundation (NRF) of South Africa, under grant numbers 103979 and 109580; the University of KwaZulu-Natal (UKZN), the UKZN Nanotechnology Platform, and the Eskom Tertiary Education Support Programme (TESP). The authors are also grateful to Professor Marc Burgelman and his team at the University of Ghent for allowing us to use SCAPS.

References

[1] L.D. Whalley, J.M. Frost, Y.-K. Jung, A. Walsh, Perspective: theory and simulation of hybrid halide perovskites. J. Chem. Phys. **146**, 220901 (2017). https://doi.org/10.1063/1.4984964.

[2] A. Hima, N. Lakhdar, B. Benhaoua, A. Saadoune, I. Kemerchou, F. Rogti, An optimized perovskite solar cell designs for high conversion efficiency. Superlattices Microstruct. **129**, 240-246 (2019). https://doi.org/10.1016/j.spmi.2019.04.007.

[3] N.F. Ramli, S. Sepeai, N.F.M. Rostan, N.A. Ludin, M.A. Ibrahim, M.A.M. Teridi, S.H. Zaidi. Model development of monolithic tandem silicon-perovskite solar cell

by SCAPS simulation. in *AIP Conference Proceedings*. 2017. AIP Publishing LLC. https://doi.org/10.1063/1.4982178.

[4] N. Rono, A.E. Merad, J.K. Kibet, B.S. Martincigh, V.O. Nyamori, A theoretical investigation of the effect of the hole and electron transport materials on the performance of a lead-free perovskite solar cell based on $CH_3NH_3SnI_3$. J. Comput. Electron. **20**, 993-1005 (2021). https://doi.org/10.1007/s10825-021-01673-z.

[5] S. Michael, A novel approach for the modeling of advanced photovoltaic devices using the SILVACO/ATLAS virtual wafer fabrication tools. Sol. Energy Mater. Sol. Cells. **87**, 771-784 (2005). https://doi.org/10.1016/j.solmat.2004.07.050.

[6] A. Hima, A. Khechekhouche, I. Kemerchou, N. Lakhdar, B. Benhaoua, F. Rogti, I. Telli, A. Saadoun, GPVDM simulation of layer thickness effect on power conversion efficiency of $CH_3NH_3PbI_3$ based planar heterojunction solar cell. Int. J. Energetica. **3** (2018). https://www.ijeca.info.

[7] S. Yaşar, S. Kahraman, S. Çetinkaya, Ş. Apaydın, İ. Bilican, İ. Uluer, Numerical thickness optimization study of CIGS based solar cells with wxAMPS. Optik. **127**, 8827-8835 (2016). https://doi.org/10.1016/j.ijleo.2016.06.094.

[8] L. Lin, L. Jiang, P. Li, B. Fan, Y. Qiu, A modeled perovskite solar cell structure with a Cu_2O hole-transporting layer enabling over 20% efficiency by low-cost low-temperature processing. J. Phys. Chem. Solids. **124**, 205-211 (2019). https://doi.org/10.1016/j.jpcs.2018.09.024.

[9] Y. Wang, T. Zhang, F. Xu, Y. Li, Y. Zhao, A facile low temperature fabrication of high performance $CsPbI_2Br$ all-inorganic perovskite solar cells. Sol. Rrl. **2**, 1700180 (2018). https://doi.org/10.1002/solr.201700180.

[10] B. Li, Y. Zhang, L. Zhang, L. Yin, $PbCl_2$-tuned inorganic cubic $CsPbBr_3$ (Cl) perovskite solar cells with enhanced electron lifetime, diffusion length and photovoltaic performance. J. Power Sources. **360**, 11-20 (2017). https://doi.org/10.1016/j.jpowsour.2017.05.050.

[11] C. Liu, W. Li, C. Zhang, Y. Ma, J. Fan, Y. Mai, All-inorganic $CsPbI_2Br$ perovskite solar cells with high efficiency exceeding 13%. J. Am. Chem. Soc. **140**, 3825-3828 (2018). https://doi.org/10.1021/jacs.7b13229.

[12] J. Xie, K. Huang, X. Yu, Z. Yang, K. Xiao, Y. Qiang, X. Zhu, L. Xu, P. Wang, C. Cui, Enhanced electronic properties of SnO_2 via electron transfer from graphene quantum dots for efficient perovskite solar cells. Acs Nano. **11**, 9176-9182 (2017). https://doi.org/10.1021/acsnano.7b04070.

[13] Q. Wang, Development of efficient and stable perovskite solar cells with composition and interface engineering. (2019). https://doi.org/10.17615/tvkj-5s39.

[14] D. Yang, M. Cao, Q. Zhong, P. Li, X. Zhang, Q. Zhang, All-inorganic cesium lead halide perovskite nanocrystals: synthesis, surface engineering and applications. J. Mater. Chem. C. **7**, 757-789 (2019). https://doi.org/10.1039/C8TC04381G.

[15] M.F.M. Noh, C.H. Teh, R. Daik, E.L. Lim, C.C. Yap, M.A. Ibrahim, N.A. Ludin, A.R. bin Mohd Yusoff, J. Jang, M.A.M. Teridi, The architecture of the electron transport layer for a perovskite solar cell. J. Mater. Chem. C. **6**, 682-712 (2018). https://doi.org/10.1039/C7TC04649A.

[16] M. Wang, Z. Zang, B. Yang, X. Hu, K. Sun, L. Sun, Performance improvement of perovskite solar cells through enhanced hole extraction: The role of iodide concentration gradient. Sol. Energy Mater Sol. Cells. **185**, 117-123 (2018). https://doi.org/10.1016/j.solmat.2018.05.025.

[17] C. Zhang, H. Wang, H. Li, Q. Zhuang, C. Gong, X. Hu, W. Cai, S. Zhao, J. Chen, Z. Zang, Simultaneous passivation of bulk and interface defects through synergistic effect of anion and cation toward efficient and stable planar perovskite solar cells. J. Energy Chem. **63**, 452-460 (2021). https://doi.org/10.1016/j.jechem.2021.07.011.

[18] A.H. Slavney, R.W. Smaha, I.C. Smith, A. Jaffe, D. Umeyama, H.I. Karunadasa, Chemical approaches to addressing the instability and toxicity of lead–halide perovskite absorbers. Inorg. Chem. **56**, 46-55 (2017). https://doi.org/10.1021/acs.inorgchem.6b01336.

[19] T. Zhou, M. Wang, Z. Zang, L. Fang, Stable dynamics performance and high efficiency of ABX_3-type super-alkali perovskites first obtained by introducing H_5O_2 cation. Adv. Energy Mater. **9**, 1900664 (2019). https://doi.org/10.1002/aenm.201900664.

[20] S.H. Kang, C. Lu, H. Zhou, S. Choi, J. Kim, H.K. Kim, Pigments, Novel π-extended porphyrin-based hole-transporting materials with triarylamine donor units for high performance perovskite solar cells. Dyes. **163**, 734-739 (2019). https://doi.org/10.1016/j.dyepig.2018.12.065.

[21] M.B. Kanoun, A.-A. Kanoun, A.E. Merad, S. Goumri-Said, Device design optimization with interface engineering for highly efficient mixed cations and halides perovskite solar cells. Results Phys. **20**, 103707 (2021). https://doi.org/10.1016/j.rinp.2020.103707.

[22] Z. Liu, A. Zhu, F. Cai, L. Tao, Y. Zhou, Z. Zhao, Q. Chen, Y.-B. Cheng, H. Zhou, Nickel oxide nanoparticles for efficient hole transport in pin and nip perovskite solar cells. J. Mater. Chem. A. **5**, 6597-6605 (2017). https://doi.org/10.1039/C7TA01593C.

[23] N. Wijeyasinghe, A. Regoutz, F. Eisner, T. Du, L. Tsetseris, Y.H. Lin, H. Faber, P. Pattanasattayavong, J. Li, F. Yan, Copper (I) thiocyanate (CuSCN) hole-transport layers processed from aqueous precursor solutions and their application in thin-film transistors and highly efficient organic and organometal halide perovskite solar cells. Adv. Funct. Mater. **27**, 1701818 (2017). https://doi.org/10.1002/adfm.201701818.

[24] S.Z. Haider, H. Anwar, M. Wang, A comprehensive device modelling of perovskite solar cell with inorganic copper iodide as hole transport material. Semicond. Sci. Technol. **33**, 035001 (2018). https://doi.org/10.1088/1361-6641/aaa596.

[25] E.H. Jung, N.J. Jeon, E.Y. Park, C.S. Moon, T.J. Shin, T.-Y. Yang, J.H. Noh, J. Seo, Efficient, stable and scalable perovskite solar cells using poly (3-hexylthiophene). Nature. **567**, 511-515 (2019). https://doi.org/10.1038/s41586-019-1036-3.

[26] Z. Hawash, L.K. Ono, Y. Qi, Recent advances in Spiro-MeOTAD hole transport material and Its applications in organic–inorganic halide perovskite solar cells. Adv. Mater. **5**, 1700623 (2018). https://doi.org/10.1002/admi.201700623.

[27] C. Zuo, L. Ding, Modified PEDOT layer makes a 1.52 V V_{oc} for perovskite/PCBM solar cells. Adv. Energy Mater. **7**, 1601193 (2017). https://doi.org/10.1002/aenm.201601193.

[28] Z. Tang, Z. Ma, A. Sánchez-Díaz, S. Ullbrich, Y. Liu, B. Siegmund, A. Mischok, K. Leo, M. Campoy-Quiles, W. Li, Polymer: fullerene bimolecular crystals for near-infrared spectroscopic photodetectors. Adv. Mater. **29**, 1702184 (2017). https://doi.org/10.1002/adma.201702184.

[29] L. Zhou, J. Chang, Z. Liu, X. Sun, Z. Lin, D. Chen, C. Zhang, J. Zhang, Y. Hao, Enhanced planar perovskite solar cell efficiency and stability using a perovskite/PCBM heterojunction formed in one step. Nanoscale. **10**, 3053-3059 (2018). https://doi.org/10.1039/C7NR07753J.

[30] A. Möllmann, D. Gedamu, P. Vivo, R. Frohnhoven, D. Stadler, T. Fischer, I. Ka, M. Steinhorst, R. Nechache, F. Rosei, Highly compact TiO_2 films by spray pyrolysis and application in perovskite solar cells. Adv. Eng. Mater. **21**, 1801196 (2019). https://doi.org/10.1002/adem.201801196.

[31] F. Azri, A. Meftah, N. Sengouga, A. Meftah, Electron and hole transport layers optimization by numerical simulation of a perovskite solar cell. Sol. Energy. **181**, 372-378 (2019). https://doi.org/10.1016/j.solener.2019.02.017.

[32] P. Zhang, J. Wu, T. Zhang, Y. Wang, D. Liu, H. Chen, L. Ji, C. Liu, W. Ahmad, Z.D. Chen, Perovskite solar cells with ZnO electron-transporting materials. Adv. Mater. **30**, 1703737 (2018). https://doi.org/10.1002/adma.201703737.

[33] D. Yang, R. Yang, K. Wang, C. Wu, X. Zhu, J. Feng, X. Ren, G. Fang, S. Priya, S.F. Liu, High efficiency planar-type perovskite solar cells with negligible hysteresis using EDTA-complexed SnO_2. Nat. Commun. **9**, 1-11 (2018). https://doi.org/10.1038/s41467-018-05760-x.

[34] Z. Rao, B. Du, C. Huang, L. Shu, P. Lin, N. Fu, S. Ke, Revisit of amorphous semiconductor $InGaZnO_4$: a new electron transport material for perovskite solar cells. J. Alloys Compd. **789**, 276-281 (2019). https://doi.org/10.1016/j.jallcom.2019.02.311.

[35] J.-W. Lee, S.-H. Lee, Y.-H. Kim, S.K. Park, Low-temperature photo-activated inorganic electron transport layers for flexible inverted polymer solar cells. Appl. Phys. A. **116**, 2087-2093 (2014). https://doi.org/10.1007/s00339-014-8407-2.

[36] Z. Wang, Y. Zheng, X. Cao, H. Zhou, C. Liu. Design and fabrication of photo-sensitive thin-film transistors with IGZO and organic photo-absorber. in *2018 International Conference on Electronics Packaging and iMAPS All Asia Conference (ICEP-IAAC)*. 2018. Mie, Japan IEEE. https://doi.org/10.23919/ICEP.2018.8374672.

[37] N. Lakhdar, A. Hima, Electron transport material effect on performance of perovskite solar cells based on $CH_3NH_3GeI_3$. Opt. Mater. **99**, 109517 (2020). https://doi.org/10.1016/j.optmat.2019.109517.

[38] M. Burgelman, K. Decock, A. Niemegeers, J. Verschraegen, S. Degrave, SCAPS manual. 2016, February.

[39] A.-A. Kanoun, M.B. Kanoun, A.E. Merad, S. Goumri-Said, Toward development of high-performance perovskite solar cells based on $CH_3NH_3GeI_3$ using computational approach. Sol. Energy. **182**, 237-244 (2019). https://doi.org/10.1016/j.solener.2019.02.041.

[40] U. Mandadapu, S.V. Vedanayakam, K. Thyagarajan, Simulation and analysis of lead based perovskite solar cell using SCAPS-1D. Indjst. **10**, 65-72 (2017). https://doi.org/10.17485/ijst/2017/v11i10/110721.

[41] M.A. Green, Solar cells: operating principles, technology, and system applications. J Englewood Cliffs, NJ, Prentice-Hall, Inc., . 288 p., (1982). https://ui.adsabs.harvard.edu/abs/1982ph...book.....G/abstract.

[42] F. Zhang, W. Ma, H. Guo, Y. Zhao, X. Shan, K. Jin, H. Tian, Q. Zhao, D. Yu, X. Lu, Interfacial oxygen vacancies as a potential cause of hysteresis in perovskite solar cells. Chem. Mater. **28**, 802-812 (2016). https://doi.org/10.1021/acs.chemmater.5b04019.

[43] F. Wang, S. Bai, W. Tress, A. Hagfeldt, F. Gao, Defects engineering for high-performance perovskite solar cells. npj Flex. **2**, 1-14 (2018). https://doi.org/10.1038/s41528-018-0035-z.

[44] N. Rono, A.E. Merad, J.K. Kibet, B.S. Martincigh, V.O. Nyamori, Optimization of hole transport layer materials for a lead-free perovskite solar cell based on formamidinium tin iodide. Energy Technol. **9**, 2100859 (2021). https://doi.org/10.1002/ente.202100859.

[45] P. Singh, N.M. Ravindra, Temperature dependence of solar cell performance—an analysis. Sol. Energy Mater. Sol. Cells. **101**, 36-45 (2012). https://doi.org/10.1016/j.solmat.2012.02.019.

CHAPTER NINE

Journal of Computational Electronics
https://doi.org/10.1007/s10825-021-01673-z

A theoretical investigation of the effect of the hole and electron transport materials on the performance of a lead-free perovskite solar cell based on $CH_3NH_3SnI_3$

Nicholas Rono[1] · Abdelkrim E. Merad[2] · Joshua K. Kibet[3] · Bice S. Martincigh[1] · Vincent O. Nyamori[1]

Received: 7 August 2020 / Accepted: 12 February 2021

Abstract

This study entails a theoretical investigation of the effect of the hole transport layer (HTL) and electron transport layer (ETL) materials on a lead-free perovskite solar cell based on methylammonium tin iodide ($CH_3NH_3SnI_3$). The simulations of the solar cells were conducted with the aid of the one-dimensional solar cell capacitance simulator, SCAPS-1D. The initial primary cell with the following architectural design: glass/FTO/WS_2/$CH_3NH_3SnI_3$/P3HT/Au, was simulated to yield a modest power conversion efficiency (*PCE*) of 10.47%. In an attempt to improve the *PCE* of this device, several materials were tested as the HTL, and their effects on the *PCE* were simulated. Subsequently, various ETL materials were tested with what were found to be the best possible HTL materials. The *PCE* of the primary device increased from 10.47% to over 16% with the utilization of 2,2′,7,7′-tetrakis [N,N-di(4-methoxyphenyl)amino]-9,9′-spirobifluorene (spiro-OMeTAD), copper(I) oxide (Cu_2O), copper(I) thiocyanate (CuSCN), copper(I) iodide (CuI), and poly(2,5-bis(3-tetradecylthiophen-2-yl)thieno-[3,2-b]thiophene) (D-PBTTT-14) as HTLs. Tungsten disulfide (WS_2) was shown to be the best suitable ETL material. The density of defects of the absorber for the devices with tungsten disulfide as the ETL and Cu_2O, D-PBTTT-4, CuSCN, spiro-OMeTAD, and CuI as the HTLs, was best at 1.5×10^{17} cm^{-3}, while for the primary device, the best value of the density of defects was 1.5×10^{14} cm^{-3}. Furthermore, the energy barriers at the interface for primary and optimum devices was examined. Additionally, the effect of the external operating temperature on the performance of the devices was investigated. The simulation results allow one to propose the best HTL and ETL materials for high performance of lead-free perovskite solar cells, based on tin.

Keywords Simulations · ETL · HTL · Lead-free · Perovskites

1 Introduction

Solar energy has been identified as a source of clean and inexhaustible energy; thus, several advances have been made to harvest and utilize this abundant energy resource [1]. The main challenge in harvesting solar energy is the lack of suitable solar devices with high power conversion efficiency (*PCE*) to convert solar energy to other useful forms of energy [2, 3]. Accordingly, organic–inorganic perovskite solar cells have gained prominence in recent years due to their attractive characteristics. These include ease of fabrication through solution processes, high power conversion efficiency, better light absorption abilities, and long diffusion path lengths of excitons.

The perovskite, methylammonium lead halide, is the most widely investigated perovskite. The solar cell that uses this perovskite material as the absorber, demonstrates a high *PCE* of over 25.2% [4], but it faces significant hurdles for commercial applications because of its poor stability and the threat to the environment, arising from the inherent toxicity exhibited by lead [5]. To mitigate against these challenges, lead-free perovskite solar cells, such as those based on germanium (Ge) [6], antimony (Sb) [7], bismuth (Bi) [8], and

✉ Abdelkrim E. Merad
aemerad@gmail.com

1 School of Chemistry and Physics, University of KwaZulu-Natal, Westville Campus, Private Bag X54001, Durban 4000, South Africa

2 Solid State Physics Team, Theoretical Physics Laboratory, Faculty of Sciences, Abou Bekr Belkaid University, Box 119, 13000 Tlemcen, Algeria

3 Chemistry Department, Egerton University, P.O. Box 536, Njoro CampusEgerton 20115, Kenya

Published online: 03 March 2021

CHAPTER NINE

A theoretical investigation of the effect of the hole and electron transport materials on the performance of a lead-free perovskite solar cell based on $CH_3NH_3SnI_3$

Nicholas Rono,[a] Abdelkrim E. Merad,[b]* Joshua K. Kibet,[c] Bice S. Martincigh[a] and Vincent O. Nyamori[a]

[a]School of Chemistry and Physics, University of KwaZulu-Natal, Westville Campus, Private Bag X54001, Durban, 4000, South Africa

[b]Solid State Physics Team, Theoretical Physics Laboratory, Faculty of Sciences, A Belkaid University, Box 119, 13000, Tlemcen, Algeria

[c]Chemistry Department, Egerton University, Njoro Campus, P.O. Box 536-20115, Egerton, Kenya

*Corresponding author: E-mail: aemerad@gmail.com, Tel: +213554702391

Abstract

This study entails a theoretical investigation of the effect of the hole transport layer (HTL) and electron transport layer (ETL) materials on a lead-free perovskite solar cell based on methylammonium tin iodide ($CH_3NH_3SnI_3$). The simulations of the solar cells were conducted with the aid of the one-dimensional solar cell capacitance simulator, SCAPS-1D. The initial primary cell with the following architectural design: glass/FTO/WS_2/$CH_3NH_3SnI_3$/P3HT/Au, was simulated to yield a modest power conversion efficiency (PCE) of 10.47%. In an attempt to improve the PCE of this device, several materials were tested as the HTL, and their effects on the PCE were simulated. Subsequently, various ETL materials were tested with what were found to be the best possible HTL materials. The PCE of the primary device increased from 10.47% to over 16% with the utilisation of 2,2',7,7'-tetrakis[N,N-di(4-methoxyphenyl)amino]-9,9'-spirobifluorene (spiro-OMeTAD), copper(I) oxide (Cu_2O), copper(I) thiocyanate (CuSCN), copper(I) iodide (CuI), and poly(2,5-bis(3-tetradecylthiophen-2-yl)thieno-[3,2-b]thiophene) (D-PBTTT-14) as HTLs. Tungsten disulfide (WS_2) was shown to be the best suitable ETL material. The density of defects of the absorber for the devices with

WS_2 as the ETL and Cu_2O, D-PBTTT-4, CuSCN, spiro-OMeTAD, and CuI as the HTLs, was best at 1.5×10^{17} cm^{-3}, while for the primary device, the best value of the density of defects was 1.5×10^{14} cm^{-3}. Furthermore, the energy barriers at the interface for primary and optimum devices was examined. Additionally, the effect of the external operating temperature on the performance of the devices was investigated. The simulation results allow one to propose the best HTL and ETL materials for high performance of lead-free perovskite solar cells, based on tin.

Keywords: simulations; ETL; HTL; lead-free; perovskites

9.1 Introduction

Solar energy has been identified as a source of clean and inexhaustible energy; thus, several advances have been made to harvest and utilise this abundant energy resource [1]. The main challenge in harvesting solar energy is the lack of suitable solar devices with high power conversion efficiency (PCE) to convert solar energy to other useful forms of energy [2, 3]. Accordingly, organic-inorganic perovskite solar cells have gained prominence in recent years due to their attractive characteristics. These include ease of fabrication through solution processes, high power conversion efficiency, better light absorption abilities, and long diffusion path lengths of excitons.

The perovskite, methylammonium lead halide, is the most widely investigated perovskite. The solar cell that uses this perovskite material as the absorber, demonstrates a high PCE of over 25.2% [4], but it faces significant hurdles for commercial applications because of its poor stability and the threat to the environment, arising from the inherent toxicity exhibited by lead [5]. To mitigate against these challenges, lead-free perovskite solar cells, such as those based on germanium (Ge) [6], antimony (Sb) [7], bismuth (Bi) [8], and tin (Sn) [9], have been suggested as potential substitutes. In particular, tin-based perovskites are suitable alternatives to lead because they possess similar characteristics, especially since tin and lead fall in the same group in the periodic table. However, tin does exhibit instability problems caused by the oxidation of Sn^{2+} to Sn^{4+} when exposed to air [10]. This problem has been addressed by the addition of tin(II) fluoride (SnF_2) [10] or tin(II) chloride [11], resulting in a compact, stable perovskite material. Consequently, research is ongoing in this field to improve the PCE and stability of lead-free solar cells, since, the performance is still low compared with those of lead-based solar cell designs [12]. Strategies investigated include the selection of suitable hole transport layer (HTL) materials and electron transport layer (ETL) materials, the reduction of defects in the absorber material which entice excitons by acting as Shockley-Read-Hall non-radiative recombination centres, and the addition of dopants, among others.

In order to address stability issues in perovskite solar cells (PSCs), inorganic electron transport layer (ETL) materials, such as, titanium dioxide (TiO_2), indium gallium zinc oxide (IGZO), tin dioxide (SnO_2), zinc oxide (ZnO) and tungsten sulfide (WS_2), have to

be incorporated in solar cells, and this is because the resulting structure is more compact and stable than that of cells with organic-based ETLs such as [6,6]-phenyl-C61-butyric acid methyl (PCBM) [13, 14]. Similarly, organic hole transport layer (HTLs) materials, for example, 2,2',7,7'-tetrakis[N,N-di(4-methoxyphenyl)amino]-9,9'-spirobifluorene (spiro-OMeTAD), have commonly been utilised in perovskite solar cells [15], but, there are other efficient and cheaper materials. Therefore, inorganic HTL materials, such as copper(I) oxide (Cu_2O), copper(I) thiocyanate (CuSCN), and copper(I) iodide (CuI), have also been considered because it makes the device more compact and their efficiencies are appreciable [16]. The inorganic HTL materials are attributed with high electron mobilities, low-cost fabrication methods, and high stabilities; thus, solar cell degeneration is reduced [17]. Moreover, the organic HTL materials, namely, poly(2,5-bis(3-tetradecylthiophen-2-yl)thieno-[3,2-b]thiophene) (D-PBTTT-14) HTL and poly(3-hexylthiophene) (P3HT), have also been tested due to their relatively high hole mobility, although the stability of the cell is low [18].

Recently, the number of papers on the numerical simulation of perovskite solar cells has increased as a result of the availability of numerous 'free' software packages, such as the solar cell capacitance simulator (SCAPS-1D) [19], SILVACO ATLAS [20], general-purpose photovoltaic device model (GPVDM) [21], and wx-analysis of microelectronic and photonic structures (wxAMPS). With the availability of these powerful computational tools, several parameters of the perovskite solar cells can be studied, yielding results consistent with experimental data. Therefore, the overall aim of simulating a photovoltaic material is to assist with the selection of better performing materials for experimental testing in devices.

Herein, we report the numerical simulation and performance optimisation of a tin-based perovskite solar cell whose primary architecture is: glass/FTO/WS_2/$CH_3NH_3SnI_3$/P3HT/Au by making use of the one-dimensional solar cell capacitance simulator (SCAPS-1D) [22]. In essence, several hole- and electron-transport materials were selected and investigated for their efficacy. The hole transport materials included: spiro-OMeTAD, Cu_2O, CuSCN, CuI, and D-PBTTT-14. The electron transport materials examined were TiO_2, IGZO, SnO_2, ZnO and PCBM. The effect of varying the density of defects of the absorber, energy barriers at the interface and, also, the operating temperature on the overall photovoltaic performance of the devices, was investigated.

The results of this work are envisaged to provide direction in future fabrication and engineering of lead-free perovskite solar cells based on tin for possible commercialisation and harvesting of solar energy.

9.2 Computational methodology

In this work, a tin-based perovskite n-i-p device was modelled and numerically simulated with SCAPS-1D software developed by Professor Marc Burgelman and his team at the University of Ghent, Belgium [22]. The model assembly consisted of fluorine-doped tin oxide (FTO) coated glass/ETL/absorber ($CH_3NH_3SnI_3$)/HTL/gold metal back contact, as illustrated in Figure 9.1. The *n* part is the ETL, the *i* part is the absorber ($CH_3NH_3SnI_3$), and the *p* part is the HTL. The SCAPS-1D software numerically solves the basic differential equations that govern semiconductors under steady-state conditions. The differential equations include the Poisson equation, and the equations of continuity of holes and electrons [23]. Therefore, the SCAPS-1D numerical software can simulate the recombination profile, electric field distribution and current densities of a photovoltaic cell. The simulation conditions were: illumination of AM 1.5G, with 100 mW cm^{-2}, a temperature of 300 K, and a working frequency of 1 MHz. The input parameters for the initial primary device (glass/FTO/WS_2/$CH_3NH_3SnI_3$/P3HT/Au) were assembled from published experimental and theoretical data and are summarised in Table 1. The hole and electron thermal velocities were assumed to be a constant and set at 10^7 cm s^{-1} whereas the absorber density of defects, N_t, was set at 1.5×10^{17} cm^{-3}.

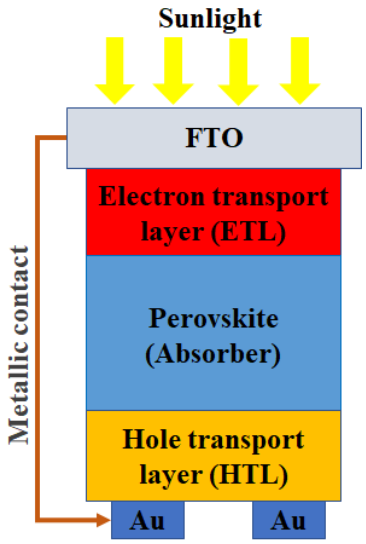

Figure 9.1: Device structure of n-i-p perovskite solar cell investigated in this work

9.3 Results and discussion

As a preliminary step, the simulation of the primary (reference) device with the following architecture: glass/FTO/WS_2/$CH_3NH_3SnI_3$/P3HT/Au, was carried out. The values of the parameters for the main material properties are shown in Table 9.1.

Table 9.1: The values of the primary input parameters for the n-i-p perovskite solar cell components

Parameter	**FTO** [24]	**WS_2 (ETL)** [25]	**$CH_3NH_3SnI_3$ (absorber)** [26]	**P3HT (HTL)** [27]
Band gap, E_g/eV	3.5	1.87	1.31	1.85
Affinity, χ/eV	4.0	4.3	4.17	3.1
Dielectric permittivity (relative), ε_r	9.0	11.9	8.2	3.4
Effective density of state at the conduction band, N_c/cm^{-3}	2.2×10^{18}	1.0×10^{18}	1.0×10^{18}	1.0×10^{22}
Effective density of state at the valence band, N_v/cm^{-3}	1.8×10^{19}	2.4×10^{19}	1.0×10^{18}	1.0×10^{22}
Mobility of electrons, μ_n/cm^2 V^{-1} s^{-1}	20.0	260	1.6	1.0×10^{-4}
Mobility of holes, μ_p/cm^2 V^{-1} s^{-1}	10.0	51	1.6	1.0×10^{-3}
Density of n-type doping, N_D/cm^{-3}	1.0×10^{19}	1.1×10^{19}	0.0	0.0
Density of p-type doping, N_A/cm^{-3}	0.0	0.0	3.3×10^{18} [25]	3.17×10^{13}
Density of defects, N_t/cm^{-3}	0.0	1.2×10^{11}	1.5×10^{17} (varied)	1.0×10^{14}

The resulting photovoltaic performance characteristics, namely, the current density-voltage (J-V) curves and the quantum efficiency-wavelength curves of the device, are presented in Figure 9.2, while the photovoltaic parameters of the primary device, i.e.,

open-circuit voltage (V_{oc}), short-circuit current density (J_{sc}), fill factor (FF), and PCE are illustrated in Figure 9.2a (inset). This device achieved a V_{oc}, J_{sc}, FF and PCE of 0.8299 V, 20.64 mA cm^{-2}, 61.09% and 10.47%, respectively.

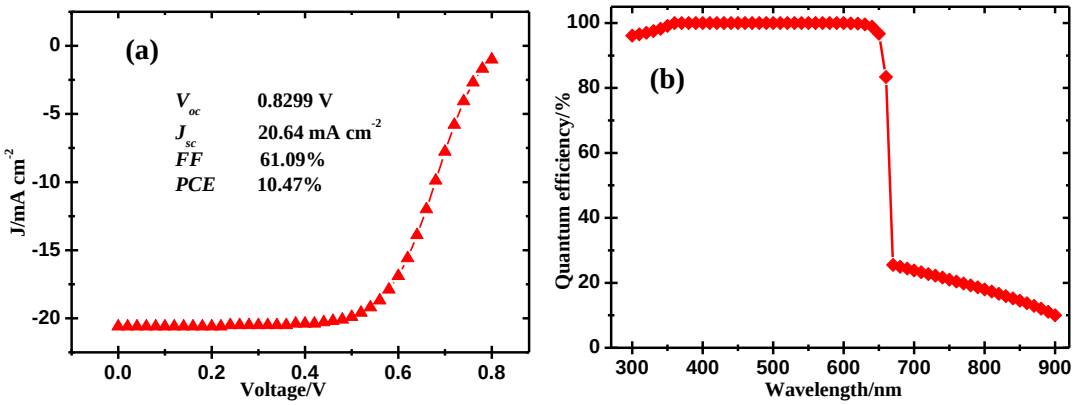

Figure 9.2: Photovoltaic performance characteristics of the primary (reference) n-i-p cell: (a) optimised J-V curve and (b) the quantum efficiency-wavelength curve

Figure 9.2b presents the quantum efficiency (QE) curve obtained, in which the device exhibited a relatively high quantum efficiency of between 95-99% within the visible region of the electromagnetic spectrum (300-640 nm). This could be attributed to the observed modest J_{sc} value of 20.64 mA cm^{-2}. However, the QE curve decreased sharply to about 25% outside the visible region, implying that the absorption of light by the device beyond the visible region breaks down since the ETL has a bandgap of 1.87 eV (663 nm) while the absorber has a bandgap of 1.31 eV (946 nm). Basically, for this cell, the absorber layer can absorb light energy up to a wavelength of 946 nm, whereas the ETL can absorb up to 663 nm. Notably, the optical absorption of the ETL (WS_2) and the absorber have a direct impact on the QE because the ETL is located near the front side of the device and, thus, receives direct illumination from the sun. The absorption of the HTL may be considered negligible because it is located at the rear part of the cell and is blocked by the front layers.

9.3.1 Effect of different hole transport materials

In order to study the effect of different HTL materials on the photovoltaic performance of the primary n-i-p device, several materials were selected, and each was inserted as the hole transport layer. The HTL materials tested included 2,2',7,7'-tetrakis[N,N-di(4-methoxyphenyl)amino]-9,9'-spirobifluorene (spiro-OMeTAD), copper(I) oxide (Cu_2O),

copper(I) thiocyanate (CuSCN), copper(I) iodide (CuI), and poly(2,5-bis(3-tetradecylthiophen-2-yl)thieno-[3,2-b]thiophene) (D-PBTTT-14). Table 9.2 shows the values of the properties that were used as input parameters in the SCAPS-1D software.

Table 9.2: Values of the input parameters for the HTL materials tested

Parameter*	**Spiro-OMeTAD** [28]	**Cu_2O** [24]	**CuSCN** [27]	**CuI** [24]	**D-PBTTT-14** [24]
E_g/eV	3.06	2.17	3.4	3.1	2.16
χ/eV	2.05	3.2	1.9	2.1	3.2
ε_r	3	7.11	10	6.5	10
N_c/cm^{-3}	2.8×10^{19}	2.02×10^{17}	1.7×10^{19}	2.8×10^{19}	2.8×10^{19}
N_v/cm^{-3}	1.0×10^{19}	1.1×10^{19}	2.5×10^{21}	1.0×10^{19}	1.0×10^{19}
μ_n/cm^2 V^{-1} s^{-1}	1.0×10^{-4}	200	1.0×10^{-4}	100	2.83×10^{-3}
μ_p/cm^2 V^{-1} s^{-1}	2.0×10^{-4}	80	1.0×10^{-1}	43.9	2.83×10^{-3}
N_D/cm^{-3}	0.0	0.0	0	0.0	0.0
N_A/cm^{-3}	1.0×10^{18}	1.0×10^{18}	1.0×10^{18}	1.0×10^{18}	1.0×10^{18}
N_t/cm^{-3}	1.0×10^{15} [27]	1.0×10^{14}	1.0×10^{14}	1.0×10^{14}	1.0×10^{14}

*See Table 9.1 for definitions of parameter symbols

Since the thickness of each layer of the device is critical in the overall device performance, the FTO, HTL, absorber and ETL thicknesses for each of the devices with different HTLs were optimised. In essence, optimisation was done sequentially by varying the thickness of a particular layer while keeping the thickness of the remaining layers constant. In this manner, each layer was investigated in turn until a maximum PCE was achieved. For instance, for the primary device, the thickness optimisation was carried out as follows: first, the absorber thickness was varied from 0.08 to 0.3 µm until a maximum PCE was attained, while the thicknesses of the HTL, ETL, and FTO were kept constant at 0.05, 1.3 and 0.05 µm, respectively. The best absorber thickness was determined to be 0.1 µm, after which it was kept constant at this value. The ETL and FTO thicknesses were kept constant, while the thickness of the HTL was varied from

0.002 to 0.005 µm until an optimum value was obtained at 0.003 µm. Similarly, the ETL thickness was varied from 1.3 to 2.3 µm, while the absorber, HTL and FTO thicknesses were kept constant. The optimum ETL thickness was found to be 2.2 µm. Finally, the FTO thickness was optimised by varying its value between 0.05 to 0.03 µm, and the optimum thickness was determined to be 0.04 µm. For all the devices simulated in this work, a similar optimisation procedure was carried out. The optimum thickness values for devices with WS_2 as the ETL and various HTL materials are presented in Table 9.3.

Table 9.3: Optimised layer thicknesses for the devices utilising WS_2 as the ETL, $CH_3NH_3SnI_3$ as the absorber, and different HTL materials

HTM	FTO/µm	ETL/µm	Absorber/µm	HTL/µm
P3HT	0.04	2.2	0.1	0.003
Spiro-OMeTAD	0.05	2.3	0.4	0.01
Cu_2O	0.05	2.5	0.5	0.1
CuSCN	0.02	2.2	0.4	0.01
CuI	0.05	2.3	0.4	0.1
D-PBTTT-14	0.04	2.4	0.7	0.1

Figure 9.3 shows the J-V characteristics and QE (internal) for the devices with a common WS_2 ETL and different HTLs, while Table 9.4 presents the corresponding photovoltaic characteristics. The J-V curve for the device utilising P3HT as the HTL (primary device), rose sharply at a voltage about 5 V, and this could have arisen as a result of the increased series resistance and enhancement in the recombination of excitons that gave a PCE value of 10.47% as observed in Figure 9.3a. On the other hand, the J-V curves for the other devices remain low over the same voltage range of 0 - 0.8 V. Figure 9.3b displays the QE (internal) of the devices employing different HTL materials. It can be seen that the QE curves are apparently the same, implying that the effect of the HTL material on QE, in this case, is inconsequential. In the n-i-p device configuration, the HTL layer material is located near the back contact of the device and, therefore, its optical absorption is

considered insignificant, and this does not affect the QE significantly. Therefore, the observed QE is attributed to the common absorber and ETL material, which are involved in the absorption of light, because they are adjacent to the front contact where direct illumination takes place. The remarkably high QE of approximately 95-99% achieved in the wavelength range of 300 to 640 nm can be attributed to the relatively high J_{sc} of above 20 mA cm^{-2} recorded by the devices.

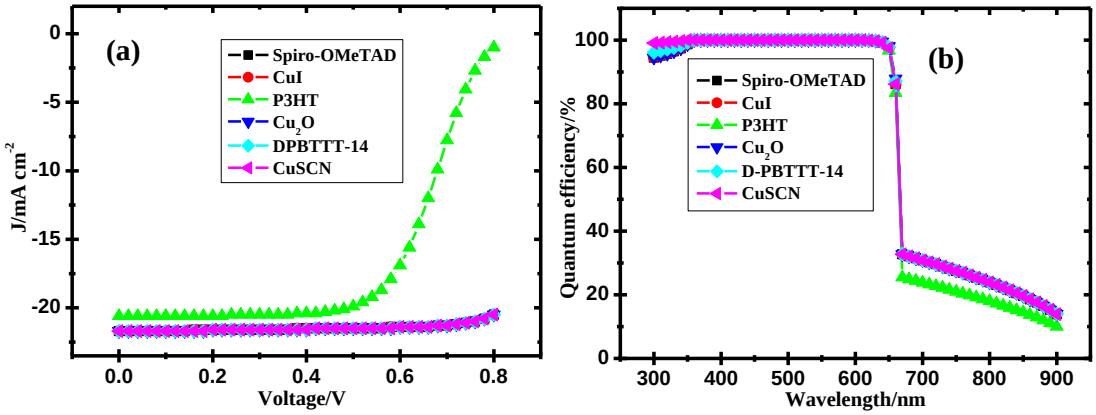

Figure 9.3: Photovoltaic performance characteristics of the n-i-p cells with different HTL materials: (a) J-V characteristics and (b) quantum efficiency as a function of wavelength

From Table 9.4, it can be seen that the J_{sc} and V_{oc} values for all the devices increased relative to those of the reference (primary) device. This suggests that when different HTL materials were used, the recombination rates of charges in the devices decreased, resulting in higher PCE values than for the reference cell. In comparison, spiro-OMeTAD, CuI, CuSCN, and Cu_2O, and D-PBTTT-14 HTLs exhibited PCE percentage improvements of 56.35, 56.45, 56.54, 56.64 and 56.54%, respectively. The highest PCE of 16.40% was exhibited by the device utilising Cu_2O as the HTL. This could be due to proper band alignment with the absorber, as shown in Figure 9.4. In addition, Cu_2O has the highest hole mobility of 80 cm^2 V^{-1} s^{-1} (see Table 9.2). The devices containing either D-PBTTT-14 or CuSCN HTLs, showed similar PCE values of 16.39%, potentially due to the same relative permittivity reported in Table 9.2. Among the organic HTLs, D-PBTTT-14 (16.39%) showed a better PCE than spiro-OMeTAD (10.47%). This can be credited to the fact that D-PBTTT-14 has a higher hole mobility of 2.83×10^{-3} cm^2 V^{-1} s^{-1} than spiro-OMeTAD, that has a hole mobility of 1.0×10^{-4} cm^2 V^{-1} s^{-1} (Table 9.2). Generally, it is evident that the performance of the primary cell was greatly enhanced by inserting

different materials as HTLs. Consequently, because of comparable PCE values, as seen in Table 9.4, Cu_2O, D-PBTTT-14, CuSCN, Spiro-OMeTAD, and CuI HTLs can be considered to be better HTL alternatives to P3HT.

Table 9.4: Photovoltaic characteristics of devices containing WS_2 as the ETL, $CH_3NH_3SnI_3$ as the absorber, and various HTLs

Parameter	P3HT	Spiro-OMeTAD	Cu_2O	CuSCN	CuI	D-PBTTT-14
V_{oc}/V	0.83	2.18	2.21	2.20	2.21	2.19
J_{sc}/mA cm^{-2}	20.64	21.71	21.73	21.72	21.71	21.73
FF/%	61.09	34.53	34.14	34.26	34.17	34.31
PCE/%	10.47	16.37	16.40	16.39	16.38	16.39

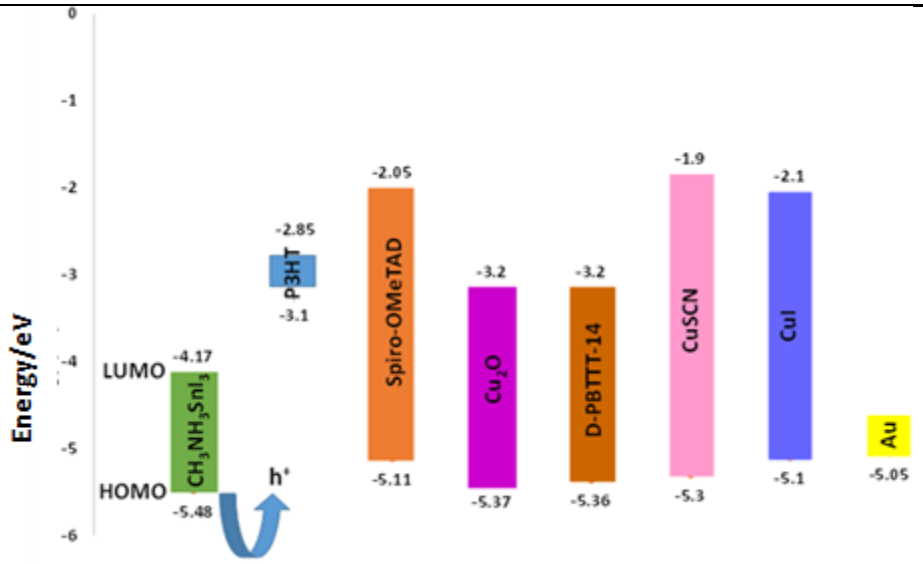

Figure 9.4: Band alignment between the perovskite absorber, the proposed HTLs and the metallic back contact, Au

9.3.2 Effect of absorber density of defects and energy barriers at interfaces

It has been established that the density of defects of the absorber makes a large impact on the photovoltaic characteristics of the device [23]. The presence of defects in a poor-quality absorber induces Shockley-Read-Hall non-radiative recombination centres which delay excitons from reaching the terminals. When this happens, the performance of the

device is significantly affected. In order to explore the best possible density of defects for the simulated cells, the density of defects of the absorber was varied from 1.5×10^{15} to 1.5×10^{21} cm^{-3}. The PCE of the devices sharply decreased as a function of increasing the density of defects, as can be noted in Figure 9.5a. This is because of the increased rate of recombination of charges due to the increased number of defects, leading to a reduction in PCE. Increased recombination reduces both the diffusion path length of the charge carriers and their lifetimes. Except for the primary device, all other devices started showing photovoltaic behaviour at a defect level of 1.5×10^{17} cm^{-3} up to the 21st order, probably due to unfavourable contact between the absorber, ETL and HTL at lower orders. The best possible density of defects was found to be 1.5×10^{17} cm^{-3} with a resulting PCE of approximately 16.40% for all the devices except for the primary P3HT device, which gave a PCE of 10.47%. Remarkably, the device with P3HT can achieve a high PCE value of 17.56% when the density of defects is lowered to 1.5×10^{15} cm^{-3}. However, at the industrial level, the process of regulating the intrinsic density of defects of the absorber is a costly practice and is not usually encouraged. On the other hand, the FF graph (Figure 9.5b) generally decreased as a function of increased density of defects, and this can be credited to the increase in series resistance (R_s) and the shunt conductance (Y). Furthermore, the V_{oc} (Figure 9.5c) and J_{sc} (Figure 9.5d) values generally decreased as the density of defects increased. This is because of the increased recombination of charges.

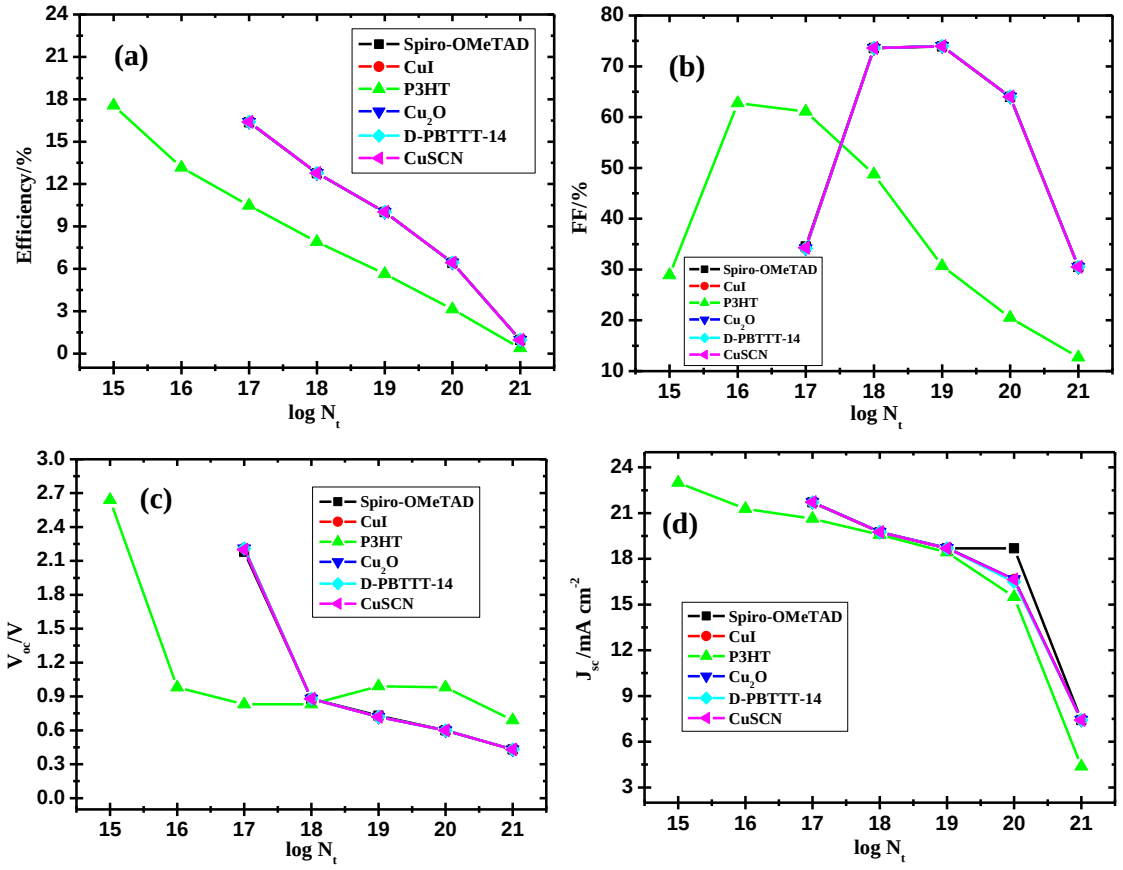

Figure 9.5: Effect of variation of absorber density of defects from 1.5 × 10^{15} cm^{-3} to 1.5 × 10^{21} cm^{-3} on the photovoltaic characteristics of devices with WS_2 as the ETL and different HTLs: (a) quantum efficiency, (b) FF, (c) V_{oc} and (d) J_{sc}

In order to gain more understanding on the energy barriers at the interface, we examined the simulated energy band diagrams of the optimised cell (with Cu_2O as HTL) (Figure 9.6a) and the primary solar cell (Figure 9.6b) devices at equilibrium. Basically, at the junction, there is an energy change at the bottom of the conduction band (ΔEc) and this change is caused by the difference in electron affinities of semiconductors [29, 30]. It follows therefore that that, if the change is positive, it implies that there is no energy barrier and if it is negative, it implies that an energy barrier exists. Similarly, at the junction, an energy change can occur at the top of the valence band (ΔEv) between the two semiconductors materials, and same conventional sign applies, as for energy change at the bottom of the conduction band. Therefore, the energy change on top of the valence band can be expressed as; ΔEv = ΔEc+ΔEg, where $\Delta E_g = Eg_2-Eg_1$ (difference in band gaps of the two materials) [30]. From our simulations, the ΔEc for optimum and primary devices was +0.835 and +0.459 eV, respectively. Although, both values are positive,

implying, that there was no barrier at the interface, to the collection of photogenerated electrons by n-type material in the p-type material, the optimum device exhibited more positive ΔEc than the primary device, thus higher efficiency. Similarly, the ΔEv for optimum and primary device was -1.159 and -0.977 eV, correspondingly. This showed that there was an energy barrier at the interface for collection of photogenerated holes by p-type material in n-type material in both devices.

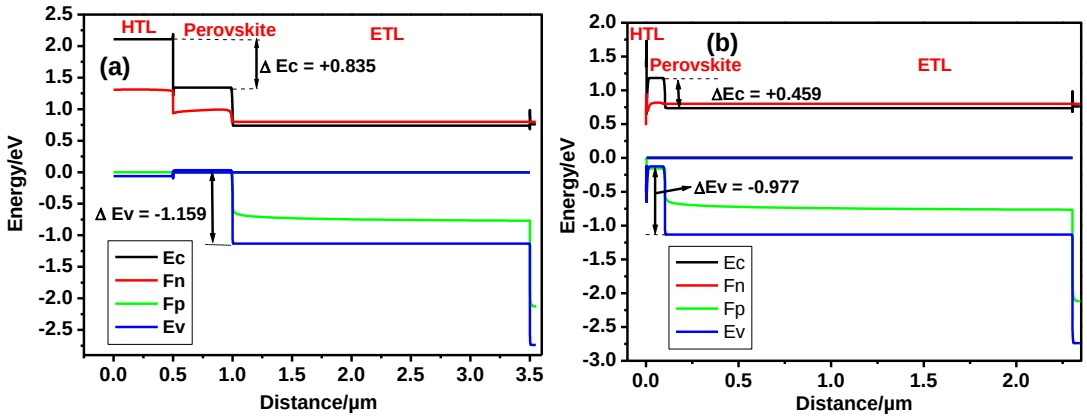

Figure 9.6: Simulated band alignment diagrams for (a) optimum device with Cu_2O as HTL and (b) primary device

9.3.3 Effect of different electron transport materials

So far, in this study, the devices studied utilised WS_2 as the ETL and different HTL materials. In order to examine the effect of different ETL materials on the overall performance of the device, all the selected ETL materials were inserted into each of the three devices with Cu_2O, D-PBTTT-14 and CuSCN as HTLs, since these three materials gave marginally better PCE values. However, for the final selection of an appropriate material for the HTL from these best performing materials, considerations based on cost, toxicity, and stability of the resultant cell structure, play a vital role. For instance, organic D-PBTTT-14 is cheap, but results in a solar cell structure that is not more compact and, thus, unstable compared with inorganic-based HTL materials, such as Cu_2O, and CuSCN, which, result in more compact structures and are more stable. On the other hand, inorganic Cu_2O and CuSCN HTLs are toxic, especially in the aquatic environment while, organic D-PBTTT-14 is not toxic or persistent in the environment. Therefore, organic-based HTLs could be preferred because of their low toxicity and cost.

The ETL materials tested included titanium dioxide (TiO_2), indium gallium zinc oxide (IGZO), tin dioxide (SnO_2), zinc oxide (ZnO) and [6,6]-phenyl-C_{61}-butyric acid methyl (PCBM). The values of the input parameters for various properties of the ETL materials are summarised in Table 9.5.

Table 9.5: Values of the input parameters for the ETL materials tested

Parameter*	**IGZO** [31]	**SnO_2** [31]	**TiO2** [24]	**PCBM** [27]	**ZnO** [31]
E_g/eV	3.05	3.5	3.2	2	3.3
χ/eV	4.16	4	3.9	3.9	4.1
ε_r	10	9	32	3.9	9
N_c/cm^{-3}	5.0×10^{18}	2.2×10^{17}	1.0×10^{19}	2.5×10^{21}	4.0×10^{18}
N_v/cm^{-3}	5.0×10^{18}	2.2×10^{16}	1.0×10^{19}	2.5×10^{21}	1.0×10^{19}
μ_n/cm^2 V^{-1} s^{-1}	15	20	20	0.2	100
μ_p/cm^2 V^{-1} s^{-1}	0.1	10	10	0.2	25
N_D/cm^{-3}	1.0×10^{18}	1.0×10^{17}	1.0×10^{17}	2.93×10^{17}	1.0×10^{18}
N_A/cm^{-3}	0.0	0.0	0.0	0.0	1.0×10^{5}
N_t/cm^{-3}	1.0×10^{15}	1.0×10^{15}	1.0×10^{15} [31]	1.0×10^{15}	2.0×10^{17}

*See Table 9.1 for definitions of parameter symbols

Figure 9.7 shows the J-V characteristic curves and QE curves for the devices with Cu_2O as the HTL material and each of the ETL materials tested. The J-V electrical parameters from Figure 9.7a are presented in Table 9.6, and the optimised thicknesses of various layers are presented in Table 9.7. Unlike for the HTL materials, the different ETL materials exhibited different QEs, as shown in Figure 9.7b; this is due to their different optical absorption properties and the fact that the ETL is located in the front of the device where it receives direct illumination from the sun. The relationship between J_{sc} and QE can be expressed by Equation 1.

$$J_{sc} = q \int \emptyset(\lambda) QE(\lambda) d\lambda \qquad \text{Equation (1)}$$

where J_{sc} is the short-circuit current, q is the electronic charge, $\emptyset(\lambda)$ is the photon flux per wavelength bandwidth unit, and QE is the quantum efficiency.

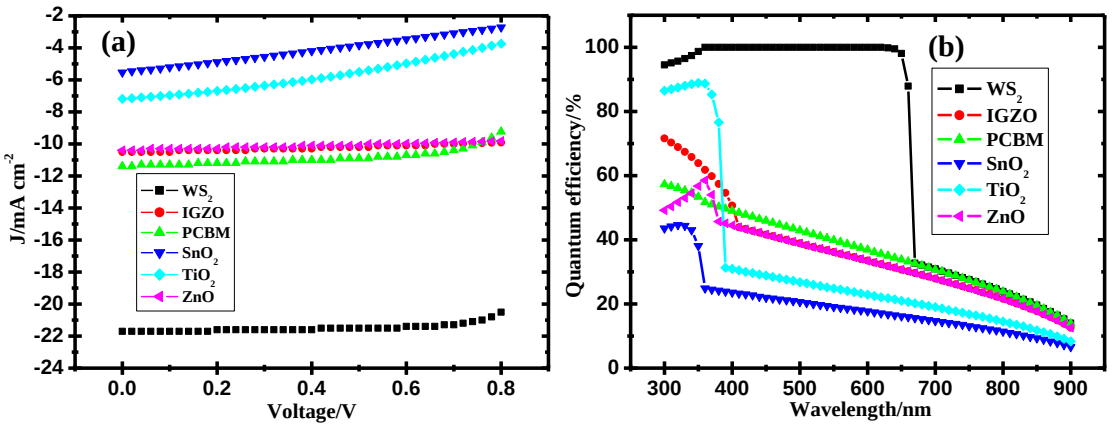

Figure 9.7: Photovoltaic performance characteristics of the cells with Cu_2O as the HTL and different ETL materials: (a) J-V characteristics and (b) quantum efficiency

It follows that as the QE increases, the J_{sc} also increases, and vice versa. From Table 9.6, the device utilising WS_2 as the ETL showed the highest J_{sc} of 21.73 mA cm^{-2}. This high J_{sc} could have contributed to its high QE, as observed in Figure 9.7b. Remarkably, the cell achieved a PCE of 16.40%, which was approximately an 87% PCE enhancement when compared with the most poorly performing device (i.e., with SnO_2 as the ETL). The J_{sc} values for IGZO, PCBM, SnO_2 and ZnO were 10.52, 11.38, 5.52, 7.19 and 10.38 mA cm^{-2}, respectively, as reported in Table 9.6. These values were very low compared to the J_{sc} value obtained with WS_2 as the ETL; thus, the witnessed low QE (Figure 9.7b). Similarly, the PCE values for IGZO, PCBM, SnO_2 and ZnO were 7.93, 7.53, 2.18, 7.56 and 7.85%, respectively. This deviation can be attributed to the high rate of recombination of excitons in these devices and, also, the high series resistance, and thus, low PCE.

Table 9.6: Photovoltaic characteristics of devices with Cu_2O as the HTL and different ETLs

Parameter	**WS_2**	**IGZO**	**PCBM**	**SnO_2**	**TiO_2**	**ZnO**
V_{oc}/V	2.21	9.57	1.28	1.52	1.38	10
J_{sc}/mA cm^{-2}	21.73	10.52	11.38	5.52	7.19	10.34
FF/%	34.14	7.88	51.50	25.94	30.89	7.56
PCE/%	16.40	7.93	7.53	2.18	7.56	7.85

Evidently, the PCE values for IGZO, PCBM, TiO_2 and ZnO were generally similar, and this could be attributed to the almost similar J_{sc} values (see Table 9.6). For TiO_2 which may have been compensated by other properties such as electron mobility, band gap etc. In addition, Figure 9.8 illustrates the band alignment between FTO, different ETLs and the absorber. As can be seen, the conduction bands of these ETL materials (IGZO, PCBM, TiO_2 and ZnO) were all above the LUMO of the absorber, and this could also have contributed to the similar J_{sc} values recorded.

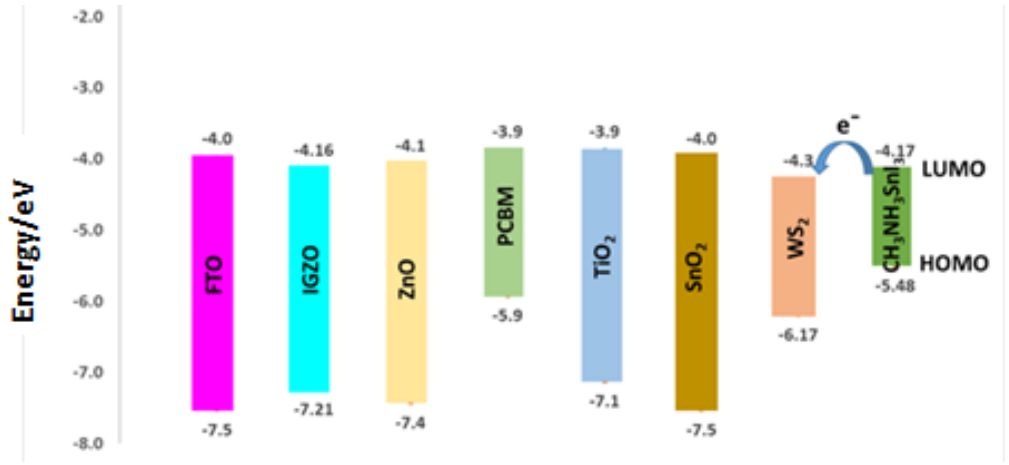

Figure 9.8: Band alignment between FTO, different ETLs and the absorber, $CH_3NH_3SnI_3$

Table 9.7: Optimised layer thicknesses for devices with different ETL materials and Cu_2O as the HTL

ETM	FTO/μm	Cu_2O (HTL)/μm	$CH_3NH_3SnI_3$ (absorber)/μm	ETL/μm
WS_2	0.05	0.1	0.5	2.5
IGZO	0.03	0.05	0.4	0.1
PCBM	0.1	0.05	0.5	0.001
SnO_2	0.03	0.1	0.7	0.5
TiO_2	0.05	0.05	0.4	0.9
ZnO	0.2	0.05	0.7	0.2

Furthermore, for the devices utilising CuSCN and D-PBTTT-14 as the HTLs, optimisation of the layer thicknesses was also carried out, and the values obtained are presented in Table 9.8 and Supporting Information Table S9.1, respectively. Similar observations were made as for the devices with Cu_2O as the HTL. Again, WS_2 as the ETL exhibited better performance than the other ETLs for both sets of devices (Table 9.9 and Supporting Information Table S9.2). As was the case with the Cu_2O HTL, for these sets, SnO_2 as the ETL exhibited the poorest performance. For example, in the CuSCN HTL device, the PCE was 4.7%, and for D-PBTTT-14 as the HTL, the PCE was 4.68%. This can be credited to the low J_{sc} values attained, which show that there was probably more recombination of excitons and, hence, a poor photovoltaic performance. Additionally, there could have been an unfavourable band alignment between the conduction band of SnO_2 and the lowest unoccupied molecular orbital (LUMO) of the perovskite, as can be noted from Figure 9.8.

Table 9.8: Optimised layer thicknesses for devices with different ETL materials and CuSCN as the HTL

ETM/µm	FTO/µm	CuSCN (HTL)/µm	$CH_3NH_3SnI_3$ (absorber)/µm	ETL/µm
WS_2	0.02	0.01	0.4	2.2
IGZO	0.05	0.05	0.7	0.01
PCBM	0.005	0.1	0.4	0.001
SnO_2	0.1	0.05	0.5	0.03
TiO_2	0.003	0.05	0.5	0.004
ZnO	0.2	0.01	0.5	0.2

Table 9.9: Photovoltaic parameters for devices with CuSCN as the HTL and different ETL materials

Parameter	WS_2	IGZO	PCBM	SnO_2	TiO_2	ZnO
V_{oc}/V	2.20	4.69	1.28	1.38	1.39	9.99
J_{sc}/mA cm^{-2}	21.72	10.92	11.39	9.33	11.52	10.37
FF/%	34.26	15.50	51.47	36.72	49.18	7.57
PCE/%	16.39	7.96	7.53	4.70	7.87	7.84

The QEs obtained for devices with CuSCN and D-PBTTT-14 as HTLs, and different ETL materials, are shown in Figure 9.9 and Supporting Information Figure S9.1, respectively. As can be observed, the QE for devices with IGZO, PCBM, SnO_2, TiO_2 and ZnO were all less than 60%, and this was true for both sets of devices. Moreover, the SnO_2 devices had the lowest QE, probably due to poor light absorption of up to about 354 nm (band gap 3.5 eV).

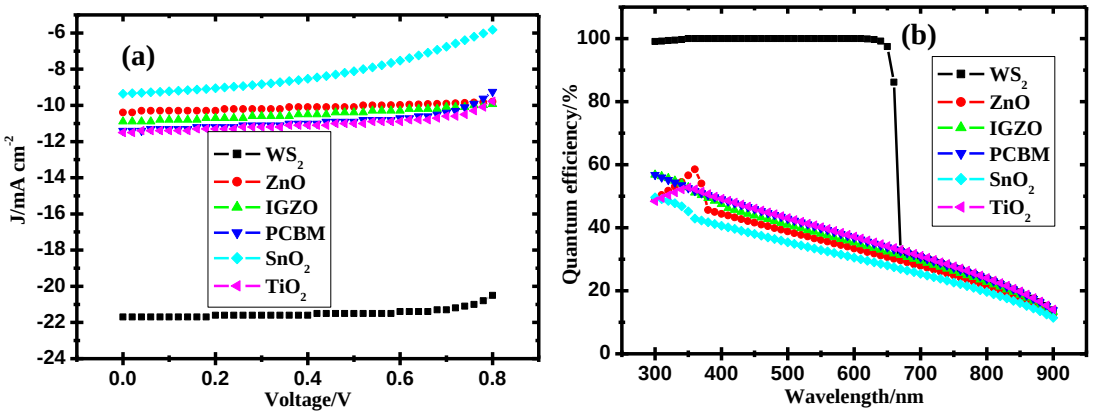

Figure 9.9: Photovoltaic performance characteristics of the cells with CuSCN as the HTL and different ETL materials: (a) J-V characteristics and (b) quantum efficiency

It can be concluded that the theoretical investigation has shown WS_2 to be the best ETL material in all the tested devices. This finding could be associated with the following attributes: high electron mobility of 260 cm^2 V^{-1} s^{-1} (see Table 9.1), a wide range of absorption ability of light (bandgap 1.87 eV) and appropriate band alignment with the absorber (Figure 9.8). Generally, the relationship between the efficiency and photovoltaic parameters of a solar cell can be expressed by Equation 2.

$$\eta = \frac{p_m}{p_{in}} = \frac{(J_{sc} \times V_{oc} \times FF)}{P_{in}} \qquad \text{Equation (2)}$$

where η is the efficiency, J_{sc} is the short-current circuit, V_{oc} is the open-circuit voltage, FF is the fill factor, p_m is the output power, and p_{in} is the input power. Therefore, for WS_2 which exhibited the highest J_{sc} (21.72) value compared with the other ETLs, it showed the highest PCE because, efficiency is directly proportional to J_{sc} as shown in Equation 2. Supplementary Information Table S9.3 shows a summary of PCE values for all the simulated devices.

9.3.4 Effect of temperature

The external operating temperature of a device plays a key role in so far as PCE is concerned. In practice, solar cells are placed outside and are subject to varying weather conditions. Fundamentally, in a solar cell, it has been found that the temperature of the device can be about twofold that of the environment, and this has been found to impede device stability [32]. Figure 9.10 shows the effect of different temperatures on the photovoltaic characteristics of the devices with a common WS_2 ETL, $CH_3NH_3SnI_3$

absorber, and different HTL materials. The PCE and V_{oc} values for devices with HTLs other than P3HT, decreased with increasing temperature, as can be noted in Figures 9.10a and 9.10b. This is occasioned by a decrease in J_{sc} and V_{oc} as the temperature increases, as evidenced by Equation 3.

$$V_{oc} = \frac{nkT}{q} \ln\left[\frac{J_{sc}}{J_o} + 1\right] \qquad \text{Equation (3)}$$

where n is ideality factor, k is the Boltzmann constant, T is the temperature, q is the elementary charge, and J_o is the dark saturation current.

On other hand, the FF for these devices, increased as the temperature increased up to 360 K, and thereafter it remained unchanged for other higher temperatures (Figure 9.10c). For the device with P3HT as the HTL, the PCE, V_{oc} and FF did not significantly change over the tested temperature range, indicating that this device was thermally stable. Moreover, for all devices, the J_{sc} slightly increased as a function of increasing temperature (Figure 9.10d). Meanwhile, the devices containing Cu_2O, CuSCN, D-PBTTT-14, spiro-OMeTAD and CuI as HTLs did not work at temperatures below 260 K, but achieved the best performance at temperatures of 260 and 280 K and, thereafter, the performance declined as the temperature increased. This indicates that these devices are unstable and can degrade at these higher temperatures. However, the cell with P3HT proved to be stable, as evidenced by the seemingly constant PCE over the 260 to 400 K temperature range, although it achieved the lowest PCE.

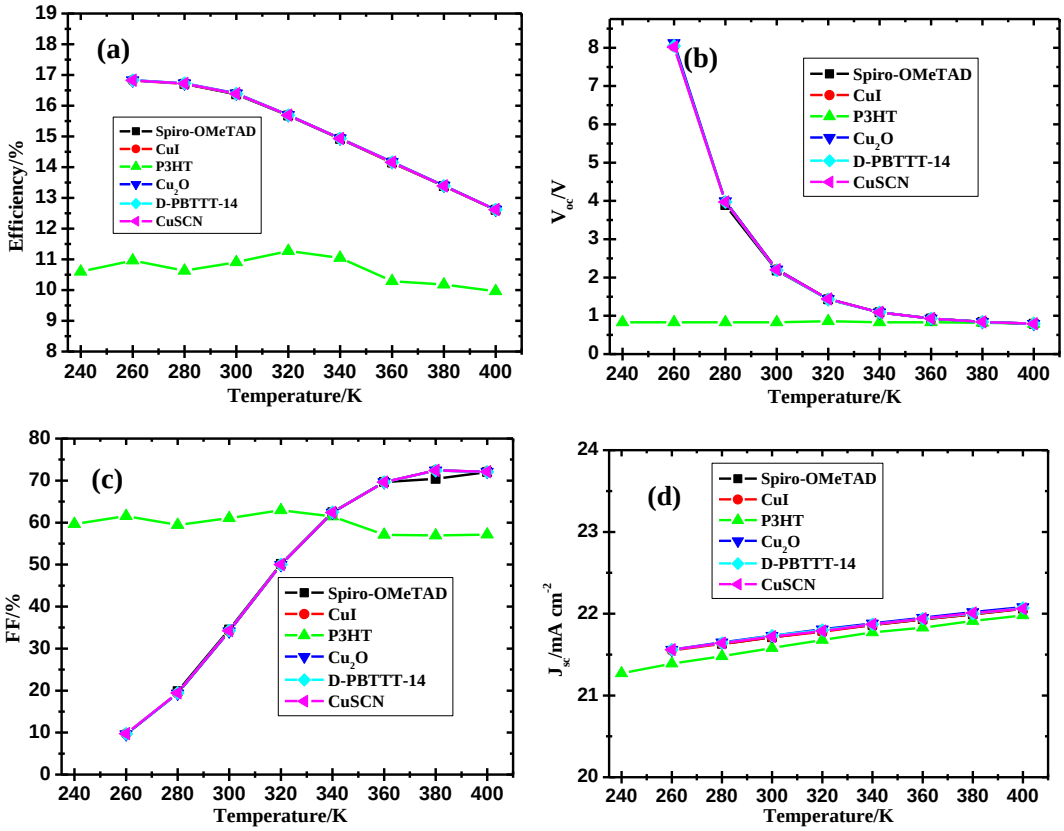

Figure 9.10: Variation of PV performance with operating temperature for devices containing WS_2 as the ETL, $CH_3NH_3SnI_3$ as the absorber, and different HTL materials: (a) quantum efficiency, (b) V_{oc}, (c) FF and (d) J_{sc}

9.4 Conclusion

In this study, a theoretical investigation of a lead-free perovskite solar cell, based on the absorber methylammonium tin iodide ($CH_3NH_3SnI_3$), was conducted by making use of the SCAPS-1D solar simulator. This study has demonstrated that the performance of the device could be greatly improved by inserting suitable materials as the HTL and ETL. The replacement of P3HT in the primary device by one of Cu_2O, CuSCN, D-PBTTT-14, CuI and Spiro-OMeTAD as HTLs, whilst maintaining the same perovskite absorber and WS_2 as the ETL, achieved a PCE of about 16.40% from the initial value of 10.47% (about 56% PCE enhancement). The effect of different HTL materials on the QE was also investigated on devices utilising a common ETL (WS_2), and no significant change was found since the HTL is located at the rear part of the solar cell and does not receive direct illumination. However, different ETLs exhibited different QEs in each device with a common HTL (P3HT). This arises from the different light absorption properties of the

ETL materials that are located in the front part of the device (for n-i-p configuration), and receive light directly. Additionally, the simulations showed that, when various ETLs were inserted in selected devices, i.e., with Cu_2O, CuSCN and D-PBTTT-14 as HTLs, the PCE was enhanced only when WS_2 was used as the ETL. All the tested devices achieved a PCE of about 16.40%, while the other ETLs tested resulted in poorer performances. Furthermore, the absorber density of defects had an impact on the photovoltaic characteristics. The best value was 1.5×10^{17} cm^{-3} for all devices with different HTL materials except for the device with P3HT as the HTL, where a value of 1.5×10^{15} cm^{-3} was optimal. The band alignment for the optimum device allowed effective collection of photogenerated electrons by n-type material in the p-type material, thus highest efficiency. The best operating temperature for the devices was in the 260 – 280 K range; above this, the performance decreased. However, the primary device (with P3HT as the HTL) showed no significant change in performance with increasing temperature but exhibited a low PCE of 10.47%. We envisaged that these simulation results would be useful for the fabrication of lead-free perovskite solar cells and provide an accessible route for their commercialisation. Thus, future work should look towards providing experimental verification of the proposed solar cells to complement the theoretical results obtained here.

Acknowledgements

N.R. is grateful to the ACADEMY project No. 2017-3052/001-001 for an academic mobility scholarship to the University of Tlemcen, Algeria, where this work was carried out at the Theoretical Physics Laboratory. AEM is thankful to DGRSDT and MHESR of Algeria for financial support under the PRFU research project N° B00L02UN130120180011. The authors are appreciative for the research support provided by the National Research Foundation (NRF) of South Africa, under grant numbers 103979 and 109580; the University of KwaZulu-Natal (UKZN), the UKZN Nanotechnology Platform, and the Eskom Tertiary Education Support Programme (TESP).

References

[1] M.H. Ahmadi, M. Ghazvini, M. Alhuyi Nazari, M.A. Ahmadi, F. Pourfayaz, G. Lorenzini, T. Ming, Renewable energy harvesting with the application of

nanotechnology: A review. Int. J. Energy Res. **43**, 1387-1410 (2019). https://doi.org/10.1002/er.4282.

[2] D. Lau, N. Song, C. Hall, Y. Jiang, S. Lim, I. Perez-Wurfl, Z. Ouyang, A. Lennon, Hybrid solar energy harvesting and storage devices: the promises and challenges. Mater. Today Energy. **13**, 22-44 (2019). https://doi.org/10.1016/j.mtener.2019.04.003.

[3] Y. Liang, L. Yu, Development of semiconducting polymers for solar energy harvesting. Polym Rev (Phila Pa). **50**, 454-473 (2010). https://doi.org/10.1080/15583724.2010.515765.

[4] https://www.nrel.gov/pv/assets/pdfs/best-research-cell-efficiencies.20190802.pdf. 04/12/2020].

[5] M. Petrović, V. Chellappan, S. Ramakrishna, Perovskites: solar cells and engineering applications–materials and device developments. Sol. Energy. **122**, 678-699 (2015). https://doi.org/10.1016/j.solener.2015.09.041.

[6] P. Cheng, T. Wu, J. Liu, W.-Q. Deng, K. Han, Lead-free, two-dimensional mixed germanium and tin perovskites. J. Phys. Chem. Lett. **9**, 2518-2522 (2018). https://doi.org/10.1021/acs.jpclett.8b00871.

[7] J.-C. Hebig, I. Kühn, J. Flohre, T. Kirchartz, Optoelectronic properties of $(CH_3NH_3)_3Sb_2I_9$ thin films for photovoltaic applications. ACS Energy Lett. **1**, 309-314 (2016). https://doi.org/10.1021/acsenergylett.6b00170.

[8] M. Lyu, J.-H. Yun, M. Cai, Y. Jiao, P.V. Bernhardt, M. Zhang, Q. Wang, A. Du, H. Wang, G. Liu, Organic–inorganic bismuth (III)-based material: A lead-free, air-stable and solution-processable light-absorber beyond organolead perovskites. Nano Res. **9**, 692-702 (2016). https://doi.org/10.1007/s12274-015-0948-y.

[9] N.K. Noel, S.D. Stranks, A. Abate, C. Wehrenfennig, S. Guarnera, A.-A. Haghighirad, A. Sadhanala, G.E. Eperon, S.K. Pathak, M.B. Johnston, Lead-free organic–inorganic tin halide perovskites for photovoltaic applications. Energy Environ. Sci. **7**, 3061-3068 (2014). https://doi.org/10.1039/C4EE01076K.

[10] S. Gupta, T. Bendikov, G. Hodes, D. Cahen, $CsSnBr_3$, a lead-free halide perovskite for long-term solar cell application: insights on SnF_2 addition. ACS Energy Lett. **1**, 1028-1033 (2016). https://doi.org/10.1021/acsenergylett.6b00402.

[11] C.-M. Tsai, H.-P. Wu, S.-T. Chang, C.-F. Huang, C.-H. Wang, S. Narra, Y.-W. Yang, C.-L. Wang, C.-H. Hung, E.W.-G. Diau, Role of tin chloride in tin-rich mixed-halide perovskites applied as mesoscopic solar cells with a carbon counter electrode. ACS Energy Lett. . **1**, 1086-1093 (2016). https://doi.org/10.1021/acsenergylett.6b00514.

[12] P.V. Kamat, J. Bisquert, J. Buriak, Lead-free perovskite solar cells. ACS Energy Lett. **2**, 904-905 (2017). http://pubs.acs.org/journal/aelccp.

[13] G. Yang, H. Tao, P. Qin, W. Ke, G. Fang, Recent progress in electron transport layers for efficient perovskite solar cells. J. Mater. Chem. A. **4**, 3970-3990 (2016). https://doi.org/10.1039/C5TA09011C.

[14] Y. Chen, Q. Meng, L. Zhang, C. Han, H. Gao, Y. Zhang, H. Yan, SnO_2-based electron transporting layer materials for perovskite solar cells: a review of recent progress. J. Energy Chem. **35**, 144-167 (2019). https://doi.org/10.1016/j.jechem.2018.11.011.

[15] H. Chen, D. Bryant, J. Troughton, M. Kirkus, M. Neophytou, X. Miao, J.R. Durrant, I. McCulloch, One-step facile synthesis of a simple hole transport material for

efficient perovskite solar cells. J. Mater. Chem. A. **28**, 2515-2518 (2016). https://doi.org/10.1021/acs.chemmater.6b00858.
[16] P.K. Kung, M.H. Li, P.Y. Lin, Y.H. Chiang, C.R. Chan, T.F. Guo, P. Chen, A review of inorganic hole transport materials for perovskite solar cells. Adv. Mater. Interfaces. **5**, 1800882 (2018). https://doi.org/10.1002/admi.201800882.
[17] B. Gil, A.J. Yun, Y. Lee, J. Kim, B. Lee, B. Park, Recent progress in inorganic hole transport materials for efficient and stable perovskite solar cells. Electron. Mater. Lett. **15**, 505-524 (2019). https://doi.org/10.1007/s13391-019-00163-6.
[18] R. Singh, P.K. Singh, B. Bhattacharya, H.-W. Rhee, Review of current progress in inorganic hole-transport materials for perovskite solar cells. Appl. Mater. Today. **14**, 175-200 (2019). https://doi.org/10.1016/j.apmt.2018.12.011.
[19] N.F. Ramli, S. Sepeai, N.F.M. Rostan, N.A. Ludin, M.A. Ibrahim, M.A.M. Teridi, S.H. Zaidi. Model development of monolithic tandem silicon-perovskite solar cell by SCAPS simulation. in AIP Conference Proceedings. 2017. AIP Publishing LLC. https://doi.org/10.1063/1.4982178.
[20] S. Michael, A novel approach for the modeling of advanced photovoltaic devices using the SILVACO/ATLAS virtual wafer fabrication tools. Sol. Energy Mater. Sol. Cells. **87**, 771-784 (2005). https://doi.org/10.1016/j.solmat.2004.07.050.
[21] A. Hima, A. Khechekhouche, I. Kemerchou, N. Lakhdar, B. Benhaoua, F. Rogti, I. Telli, A. Saadoun, GPVDM simulation of layer thickness effect on power conversion efficiency of $CH_3NH_3PbI_3$ based planar heterojunction solar cell. Int. J. Energetica. **3** (2018). https://www.ijeca.info.
[22] A. Niemegeers, M. Burgelman, K. Decock, J. Verschraegen, S. Degrave, SCAPS manual. University of Gent (2014).
[23] K. Sobayel, M. Akhtaruzzaman, K. Rahman, M. Ferdaous, Z.A. Al-Mutairi, H.F. Alharbi, N.H. Alharthi, M.R. Karim, S. Hasmady, N. Amin, A comprehensive defect study of tungsten disulfide (WS_2) as electron transport layer in perovskite solar cells by numerical simulation. Results Phys. **12**, 1097-1103 (2019). https://doi.org/10.1016/j.rinp.2018.12.049.
[24] A.-A. Kanoun, M.B. Kanoun, A.E. Merad, S. Goumri-Said, Toward development of high-performance perovskite solar cells based on $CH_3NH_3GeI_3$ using computational approach. Sol. Energy. **182**, 237-244 (2019). https://doi.org/10.1016/j.solener.2019.02.041.
[25] A. Kumar, S. Singh, Numerical modeling of lead-free perovskite solar cell using inorganic charge transport materials. Mater. Today, (2020). https://doi.org/10.1016/j.matpr.2020.02.545.
[26] A. Hima, N. Lakhdar, B. Benhaoua, A. Saadoune, I. Kemerchou, F. Rogti, An optimized perovskite solar cell designs for high conversion efficiency. Superlattices Microstruct. **129**, 240-246 (2019). https://doi.org/10.1016/j.spmi.2019.04.007.
[27] F. Azri, A. Meftah, N. Sengouga, A. Meftah, Electron and hole transport layers optimization by numerical simulation of a perovskite solar cell. Sol. Energy. **181**, 372-378 (2019). https://doi.org/10.1016/j.solener.2019.02.017.
[28] F. Jahantigh, M.J. Safikhani, The effect of HTM on the performance of solid-state dye-sanitized solar cells (SDSSCs): A SCAPS-1D simulation study. J. Appl. Phys A. **125**, 276 (2019). https://doi.org/10.1007/s00339-019-2582-0.
[29] M.B. Kanoun, A.-A. Kanoun, A.E. Merad, S. Goumri-Said, Device design optimization with interface engineering for highly efficient mixed cations and

halides perovskite solar cells. Results Phys. **20**, 103707 (2021). https://doi.org/10.1016/j.rinp.2020.103707.

[30] H.J. Pauwels, G. Vanhoutte, The influence of interface state and energy barriers on the efficiency of heterojunction solar cells. J. Phys. D Appl. Phys. **11**, 649-667 (1978). https://doi.org/10.1088/0022-3727/11/5/009.

[31] N. Lakhdar, A. Hima, Electron transport material effect on performance of perovskite solar cells based on $CH_3NH_3GeI_3$. Opt. Mater. **99**, 109517 (2020). https://doi.org/10.1016/j.optmat.2019.109517.

[32] E. Cuddihy, C. Coulbert, A. Gupta, R. Liang, Electricity from photovoltaic solar cells: flat-plate solar array project final report. Volume VII: Module encapsulation. (1986). https://resolver.caltech.edu/JPLpub86-31-volumeVII.

CHAPTER TEN

Check for updates

RESEARCH ARTICLE

Energy Technology
www.entechnol.de

Optimization of Hole Transport Layer Materials for a Lead-Free Perovskite Solar Cell Based on Formamidinium Tin Iodide

Nicholas Rono, Abdelkrim E. Merad, Joshua K. Kibet, Bice S. Martincigh, and Vincent O. Nyamori*

Recently, lead-based perovskite solar cells have been mainly studied; however, these cells suffer from two main problems: the toxicity of lead and the instability of the devices, which limit their commercialization. Herein, a theoretical investigation of a lead-free perovskite solar cell based on formamidinium tin iodide ($HC(NH_2)_2SnI_3$) with the general architecture glass/FTO/WS_2/$HC(NH_2)_2SnI_3$/HTL/Au is reported. All calculations are performed with the SCAPS-1D solar cell simulator. Two inorganic (CuSCN and Cu_2O) and two organic (P3HT and D-PBTTT-14) hole transport layer (HTL) materials are tested in this model. The effect of the external operating temperature and different metal work functions of the back contact of the cell on the overall performance of the devices is also studied. Simulations showed that, with the introduction of CuSCN, Cu_2O, and P3HT as HTLs, the device can attain a remarkable efficiency of ≈21%. All the modeled devices showed remarkable performance of above 20% at higher temperatures of 380–420 K but degraded slightly when this range is exceeded. Relatively cheaper Pt, Ni, and Pd metals perform better, thus, can replace gold. These simulation results can provide avenues and directions for future advancement of the performance of lead-free perovskite solar cells.

1. Introduction

Photovoltaic technologies have attracted much scientific attention because solar energy is believed to be clean and sustainable.[1–3] Furthermore, the utilization of solar energy can assist in the reduction of environmental pollution arising from fossil fuel consumption, as well as energy supply shortages.[4] Consequently, perovskite solar cells based on organometallic halides have received worldwide attention due to their outstanding properties such as better light absorption,[5] high charge carrier mobilities, low cost,[6] and solution-processable routes.[7,8] In addition, since their first fabrication in 2009, perovskite solar cells have experienced an appreciable increase in power conversion efficiency (PCE) from 3.4 to over 24%.[9,10]

Lead halide-based perovskite solar cells have been widely used due to a number of attractive attributes, such as tunable bandgap,[11,12] better light absorption coefficient, high PCE,[13] and long carrier diffusion lengths.[14] However, despite these qualities and high PCEs of over 20%, lead-based perovskite solar cells face two major drawbacks: device instability and the toxicity of lead.[5,15,16] To circumvent these disadvantages, various advances have been employed; for instance, lead has been completely or partially replaced with other less toxic metals to form lead-free or metal-lead alloyed perovskites, respectively.[17] Recently, Hu et al.[18] constructed a bulk heterojunction absorbing material based on bismuth ($Cs_3Bi_2I_9$–$Ag_3Bi_2I_9$) to replace the lead halide absorber layer. The device achieved a PCE of 3.8% and exhibited improved thermal stability. Similarly, Kanoun et al.[19] theoretically demonstrated the photovoltaic performance of a germanium halide-based perovskite. The device exhibited a remarkable PCE of 21%. The other metal candidates that have been used to replace lead include tin, copper, and antimony.[6,16] Among these lead-free alternatives, tin-based perovskites are the best alternative because of the narrow bandgap, similar chemical properties to those of lead and, also, the PCE values obtained exceeded those of other lead-free perovskites.[16,20]

Although tin-based perovskites have been preferred, these cells still face problems such as instability (because Sn^{2+} can easily be oxidized to Sn^{4+}, when exposed to air),[21] high recombination rates of charge carriers (due to high doped hole concentrations of the order of 10^{19} cm^{-3}),[22] difficulty in controlling morphology during processing (because of rapid reaction

N. Rono, B. S. Martincigh, V. O. Nyamori
School of Chemistry and Physics
University of KwaZulu-Natal
Westville Campus, Private Bag, X54001, Durban 4000, South Africa

A. E. Merad
Solid State Physics Team
Theoretical Physics Laboratory
Faculty of Sciences
A Belkaid University
Box 119, Tlemcen 13000, Algeria
E-mail: abdelkrim.merad@univ-tlemcen.dz

J. K. Kibet
Department of Chemistry
Egerton University
P.O. Box 536, Egerton 20115, Kenya

The ORCID identification number(s) for the author(s) of this article can be found under https://doi.org/10.1002/ente.202100859.

DOI: 10.1002/ente.202100859

CHAPTER TEN

Optimisation of hole transport layer materials for a lead-free perovskite solar cell based on formamidinium tin iodide

Nicholas Rono,[a] Abdelkrim E. Merad,[b]* Joshua K. Kibet,[c] Bice S. Martincigh[a] and Vincent O. Nyamori[a]

[a]School of Chemistry and Physics, University of KwaZulu-Natal, Westville Campus, Private Bag X54001, Durban, 4000, South Africa

[b]Solid State Physics Team, Theoretical Physics Laboratory, Faculty of Sciences, A Belkaid University, Box 119, 13000, Tlemcen, Algeria

[c]Chemistry Department, Egerton University, Njoro Campus, P.O. Box 536-20115, Egerton, Kenya

*Corresponding author: E-mail: aemerad@gmail.com, Tel: +213554702391

Abstract

Recently, lead-based perovskite solar cells have been mainly studied; however, they suffer from two main problems: the toxicity of lead, and the instability, which limit their commercialisation. Herein, we report a theoretical investigation of a lead-free perovskite solar cell based on formamidinium tin iodide ($HC(NH_2)_2SnI_3$) with the general architecture: glass/FTO/WS_2/$HC(NH_2)_2SnI_3$/HTL/Au. All calculations were performed with the SCAPS-1D solar cell simulator. Two inorganic (CuSCN and Cu_2O) and two organic (P3HT and D-PBTTT-14) hole transport layer (HTL) materials were tested in this model. The effect of the external operating temperature and different metal work functions of the back contact of the cell on the overall performance of the devices was also studied. Our simulations showed that, with the introduction of CuSCN, Cu_2O, and P3HT, as HTLs, the device can attain a remarkable efficiency of approximately 21%. All the modelled devices showed remarkable performance of above 20% at higher temperatures of 380 - 420 K, but degraded slightly when this range was exceeded. Relatively cheaper Pt, Ni, and Pd metals performed better, thus, can replace gold. These simulation results can provide avenues and directions for future advancement of the performance of lead-free perovskite solar cells.

Keywords: Perovskite; work function; defects; simulation; HTL; ETL; formamidinium tin iodide

10.1 Introduction

Photovoltaic technologies have attracted much scientific attention because solar energy is believed to be clean and sustainable [1-3]. Furthermore, the utilisation of solar energy can assist in the reduction of environmental pollution arising from fossil fuel consumption as well as energy supply shortages [4]. Consequently, perovskite solar cells based on organometallic halides have received worldwide attention due to their outstanding properties such as better light absorption [5], high charge carrier mobilities, low cost [6], and solution-processable routes [7, 8]. Besides, since their first fabrication in 2009, perovskite solar cells have experienced an appreciable increase in power conversion efficiency (PCE) from 3.4 to over 24% [9, 10].

Lead halide-based perovskite solar cells have been widely used due to a number of attractive attributes, such as tuneable bandgap [11, 12], better light absorption coefficient, high PCE [13], and long carrier diffusion lengths [14]. However, despite these qualities and high PCEs of over 20%, lead-based perovskite solar cells face two major drawbacks: device instability and the toxicity of lead [5, 15, 16]. To circumvent these disadvantages, various advances have been employed; for instance, lead has been completely or partially replaced with other less toxic metals to form lead-free or metal-lead alloyed perovskites, respectively [17]. Recently, Hu et al. [18] constructed a bulk heterojunction absorbing material based on bismuth ($Cs_3Bi_2I_9$–$Ag_3Bi_2I_9$) to replace the lead halide absorber layer. The device achieved a PCE of 3.8% and exhibited improved thermal stability. Similarly, Kanoun et al. [19] theoretically demonstrated the photovoltaic performance of a germanium halide-based perovskite. The device exhibited a remarkable PCE of 21%. The other metal candidates that have been used to replace lead include tin, copper, and antimony [6, 16]. Among these lead-free alternatives, tin-based perovskites are the best alternative because of the narrow bandgap, similar chemical properties to those of lead and, also, the PCE values obtained exceeded those of other lead-free perovskites [16, 20].

Although tin-based perovskites have been preferred, these cells still face problems such as instability (because Sn^{2+} can easily be oxidised to Sn^{4+}, when exposed to air) [21], high recombination rates of charge carriers (due to high doped hole concentrations of the order of 10^{19} cm^{-3}) [22], difficulty in controlling morphology during processing (because of rapid reaction between SnI_2 and ammonium salts) [21, 23], and improper electronic band

alignment between the electron transport layer (ETL), the Sn-based absorber and the hole transport layer (HTL) [21]. Some successful strategies have been introduced to reduce the oxidation of tin. For instance, tin(II) fluoride (SnF_2) has been added to the perovskite material, and this reduced both the instability and the doped hole density, resulting in better performance [24, 25]. Despite $CH_3NH_3SnI_3$ being widely used as the absorber material because of its attractive absorption properties, it faces one peculiar issue of temperature instability, which is linked to the organic $[CH_3NH_3]^+$ cation component [26, 27]. It has been found that when formamidinium $(HC(NH_2)_2)^+$ is used instead of $(CH_3NH_3)^+$, a more compact stable solid perovskite is formed [28]. Notably, the photovoltaic performance of tin-based perovskites is still low compared with lead-based perovskites; [20] thus, there is a need to investigate various parameters of the device architecture in order to enhance the performance.

In this regard, we report the numerical simulation and performance optimisation of a tin-based perovskite solar cell with the following general architecture: glass/FTO/WS_2/$HC(NH_2)_2SnI_3$/HTL/Au, by using the one dimension solar cell capacitance simulator, SCAPS-1D [29]. Different HTL materials were tested in the cell. These hole transport materials comprised of inorganic copper(I) oxide (Cu_2O) and copper(I) thiocyanate (CuSCN), and organic poly(2,5-bis(3-tetradecylthiophen-2-yl)thieno-[3,2-b]thiophene) (D-PBTTT-14) and poly(3-hexylthiophene-2,5-diyl) (P3HT). For each cell with a different HTL, optimisation of the thickness of the absorber, electron transport and hole transport layers, and the HTL and ETL doping densities was carried out. In addition, the effect of varying the density of defects of the absorber on the overall photovoltaic performance of the devices was tested. The effects of changing the back metal contact and operating temperature were also elucidated. Overall, the results of this work are envisaged to aid the future direction of fabricating and engineering lead-free tin-based perovskite solar cells.

10.2 Numerical simulation methodology

The model cell investigated in this work is a tin-based perovskite *p-i-n* device and is illustrated in Figure 10.1a. The general configuration of the cell is: glass/FTO/WS_2/$HC(NH_2)_2SnI_3$/HTL/Au. The *n* part is the ETL, which in this was tungsten disulfide (WS_2), the *i* part is the absorber ($HC(NH_2)_2SnI_3$), and the *p* part is the

HTL. Tungsten disulfide was chosen as the ETL because of the following inherent optoelectronic properties: bandgap between 1.33–2.2 eV, high electron transport mobility (about 260 $cm^2\ V^{-1}\ s^{-1}$), and high transparency [30]. Additionally, formamidinium tin iodide was also considered to be an ideal absorber due to its good light absorption (band gap of 1.41 eV) and relatively high thermal stability [28]. For the hole transport materials, CuSCN and Cu_2O were selected as representatives of inorganic HTL materials. In particular, CuSCN, when used in a solar cell device, results in a more compact structure that enhances stability, it is cheap and has a desirable band alignment with the perovskite absorber, and can quickly be processed via solution methods, it has a high optical transparency, and relatively high hole mobilities of about 0.01 – 0.1 $cm^2\ V^{-1}\ s^{-1}$ [31, 32] while maintaining a high PCE. Similarly, Cu_2O has better band alignment with the perovskite, high hole mobilities (about 80 $cm^2\ V^{-1}\ s^{-1}$) [19], is solution-processable, and has high optical transparency [33]. In addition, the organic HTL illustrative materials, P3HT and D-PBTTT-14, were chosen. P3HT is dopant-free, has relatively high hole mobility, robust stability, and is cheap [34], while the D-PBTTT-14 material is low-cost, nontoxic, and biodegradable [27].

Ideally, when light strikes the device, it is absorbed by the perovskite layer, and electron-hole pairs, also known as excitons, are generated. These charges travel to the electrodes by diffusion-controlled processes: at the boundary of the ETL and perovskite layer, electrons dissociate from holes and are transferred to the metal contact; similarly, at the perovskite and HTL boundary, the holes separate from the electrons and are transferred by the HTL to the back metal contact. It is important to point out that these processes have a significant impact on the PCE of the device [27, 35]. The input parameters describing the device were assembled from published experimental and theoretical data and are summarised in Table 10.1. The hole and electron thermal velocities were assumed to be constant and set at a value of 10^7 cm s^{-1}. The simulations were carried out with SCAPS-1D software [29], under solar illumination of AM 1.5G, with an intensity of 100 mW cm^{-2}, a temperature of 300 K, and a working frequency of 10^6 Hz.

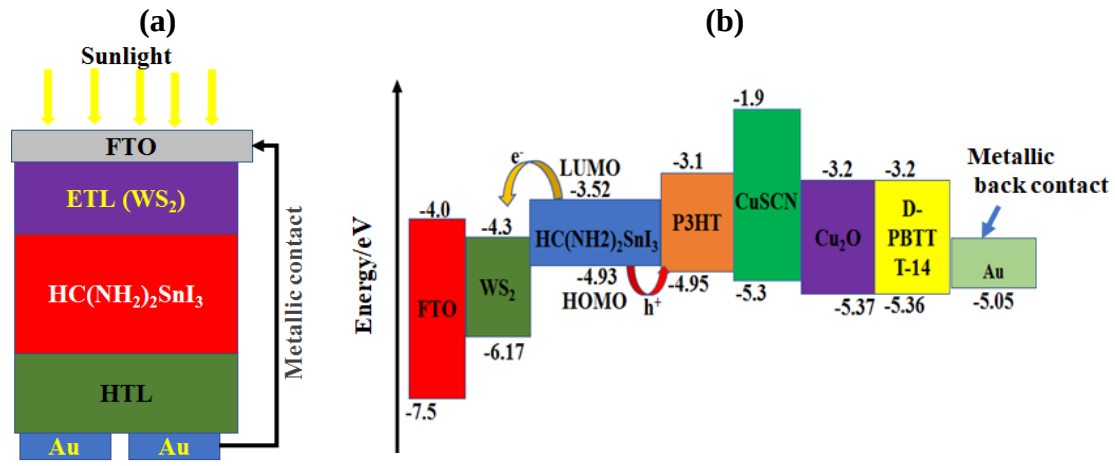

Figure 10.1: (a) Device structure of the *p-i-n* primary perovskite solar cell, and (b) band alignment between the ETL, perovskite, and the proposed HTLs

The SCAPS-1D software numerically solves the basic differential equations that govern semiconductors under a steady-state. It defines the physics of the modelled device such as the recombination profile, electric field distribution, and current densities. The essential semiconductor differential equations are the equations of continuity of holes and electrons, and the Poisson equation [36].

The continuity equations for electrons and holes can be expressed as shown in Equations (1) and (2), respectively.

$$\frac{\partial j_n}{\partial x} + G - U_n(n,p) = 0 \qquad \text{Equation (1)}$$

$$-\frac{\partial j_p}{\partial x} + G - U_p(n,p) = 0 \qquad \text{Equation (2)}$$

where j_n is the electron current density, j_p is the hole current density, $U_{n,p}$ is the net recombination rate and G is the generation rate.

Essentially, the Poisson equation can be used to show the relationship between the electric field (E) and space charge density (ρ), and the relationship between these two physical parameters is indicated in Equation (3).

$$\frac{\partial^2 \psi}{\partial^2 x} = -\frac{\partial E}{\partial x} = -\frac{\rho}{\varepsilon_s} = -\frac{q}{\varepsilon_s}[p - n + N_D^+(x) - N_A^-(x) \pm N_{def}(x)] \qquad \text{Equation (3)}$$

where ψ is the electrostatic potential, ε_s is the relative static permittivity of free space, q is the elementary charge, n is the electron density, p is the hole density, N_D^+ is the density

of the ionised donors, N_A^- is the acceptor density of ionised acceptors, and N_{def} is the defect density of the acceptor or donor.

The charge carrier transport occurs by diffusion and drift, and this phenomenon is expressed by Equations (4) and (5) for the electrons and holes, respectively.

$$j_n = D_n \frac{dn}{dx} + \mu_n n \frac{d\emptyset}{dx} \quad \text{Equation (4)}$$

$$j_p = D_p \frac{dn}{dx} + \mu_p p \frac{d\emptyset}{dx} \quad \text{Equation (5)}$$

where D_n is the electron diffusion coefficient, μ_n is the electron mobility, D_p is the hole diffusion coefficient, μ_p is the hole mobility, and $\emptyset$ is the electrostatic potential.

Table 10.1: Properties of the ETL, absorber, and different HTL materials

Parameter	**FTO** [19]	**WS_2 (ETL)** [37]	**$HC(NH_2)_2SnI_3$ (perovskite absorber)** [38]	**Cu_2O** [19]	**CuSCN** [39]	**D-PBTTT-14** [19]	**P3HT** [39]
Band gap, E_g/eV	3.5	1.87	1.41	2.17	3.4	2.16	1.85
Affinity, χ/eV	4.0	4.3	3.52	3.2	1.9	3.2	3.1
Dielectric permittivity (relative), ε_r	9.0	11.9	8.2	7.11	10	10	3.4
Effective density of state at CB, N_c/cm^{-3}	2.2×10^{18}	1.0×10^{18}	1.0×10^{18}	2.02×10^{17}	1.7×10^{19}	2.8×10^{19}	1.0×10^{22}
Effective density of state at VB, N_v/cm^{-3}	1.8×10^{19}	2.4×10^{19}	1.0×10^{18}	1.1×10^{19}	2.5×10^{21}	1.0×10^{19}	1.0×10^{22}
Mobility of electrons, μ_n/cm^2 V^{-1} s^{-1}	20.0	260	22	200	1.0×10^{-4}	2.83×10^{-3}	1.0×10^{-4}
Mobility of holes, μ_p/cm^2 V^{-1} s^{-1}	10.0	51	22	80	1.0×10^{-1}	2.83×10^{-3}	1.0×10^{-3}
Density of n-type doping, N_d/cm^{-3}	1.0×10^{19}	1.1×10^{19}	0.0	0.0	0	0.0	0.0
Density of p-type doping, N_a/cm^{-3}	0.0	0.0	7.0×10^{16}	1.0×10^{18}	1.0×10^{18}	1.0×10^{18}	3.17×10^{13}
Density of defects, N_t/cm^{-3}	0.0	2.0×10^{11}	2.0×10^{15}	1.0×10^{14}	1.0×10^{14}	1.0×10^{14}	1.0×10^{14}

10.3 Results and discussion

To optimise the photovoltaic performance of the formamidinium tin iodide-based *p-i-n* perovskite solar cell (Figure 10.1a), two inorganic and two organic hole transport materials were tested. These materials were Cu_2O, CuSCN, D-PBTTT-14, and P3HT. The corresponding band alignment between the ETL, perovskite, and the proposed HTLs is given in Figure 10.1b. In the *p-i-n* solar cell, electrons are collected at the FTO transparent conductive electrode and holes are collected at the metal back contact. To simulate the devices, the input parameters listed in Table 10.1 were used. For each device, the photovoltaic characteristics such as the PCE, fill factor (FF), short-circuit current density (J_{sc}), open-circuit voltage (V_{oc}), quantum efficiency (QE) and current density curves (J-V curves) were obtained. In addition, the effect of varying certain device characteristics on the photovoltaic performance was evaluated. The device characteristics investigated include: the thickness of the absorber, electron transport and hole transport layers, the absorber density of defects, doping of device components, the external operating temperature, and the nature of the metallic back contact.

10.3.1 Effect of absorber, ETL and HTL thicknesses

In any perovskite solar cell, optimising the thickness of every layer influences the overall performance of the device, especially that of the absorber [27]. Therefore, in our simulations, the thicknesses of the HTL, absorber, ETL, and FTO for each device with different HTLs were optimised. During this process, the thicknesses of the absorber, ETL, and FTO were kept constant at 0.4 µm, 0.1 µm, and 0.05 µm, respectively, while the thickness of the HTL was varied. Thereafter, the optimised HTL thickness was used together with the fixed absorber thickness of 0.4 µm and fixed FTO thickness of 0.05 µm to obtain the optimum thickness of the ETL. Additionally, the FTO thickness was also varied, while the absorber, ETL and HTL thicknesses were kept fixed accordingly. Finally, the best absorber thickness was obtained by fixing the ETL, HTL and FTO thickness at their optimised values while varying the absorber thickness. The best values for the different layers of the devices are presented in Table 10.2.

Table 10.2: Optimised thicknesses for different layers of devices utilising WS_2 as the ETL, $HC(NH_2)_2SnI_3$ as the absorber, and different hole transport materials

Hole transport material	FTO/μm	ETL/μm	Absorber/μm	HTL/μm
Cu_2O	0.04	1.5	0.8	0.05
CuSCN	0.05	1.5	0.8	0.05
D-PBTTT-4	0.05	1.9	0.4	0.003
P3HT	0.05	1.5	0.9	0.05

To elucidate the influence of the absorber thickness on the photovoltaic parameters, the thickness was varied between 0.1 to 1.2 μm while the HTL, ETL, and FTO thicknesses were kept constant at their optimised values. The results obtained are presented in Figure 10.2. Notably, no photovoltaic parameters were obtained for an absorber thickness between 0.1 - 0.2 μm for devices utilising Cu_2O and CuSCN as HTLs. This is because a thin absorber of such thickness could not absorb a sufficient amount of light to generate excitons. For the other two HTLs (P3HT and D-PBTTT-14), photovoltaic performance was observed in that range of thickness. Evidently, the PCE (Figure 10.2a) of the devices increases with an increase in absorber thickness and reaches a plateau where the increase no longer influences the PCE. As the absorber thickness increases, more excitons are generated; thus, the observed increase in PCE. The gradual decrease in efficiency on reaching the plateau is associated with an increase in the recombination of excitons, since the generated charges now have to travel through longer distances than their diffusion lengths. Similarly, the J_{sc} values increase as the absorber thickens for all the devices and reaches a maximum of about 30 mA cm^{-2} for the CuSCN, P3HT, and Cu_2O cells, and 29.5 mA cm^{-2} for the D-PBTTT-14 cell, at an absorber thickness of 0.8 μm as depicted in Figure 10.2d. This implies that there was less recombination of charges due to reduced series resistance. In the case of the variation of FF with absorber thickness (Figure 10.2b), the FF of the D-PBTTT-14 cell initially rose rapidly from 21 to 43% over a thickness range of 0.1 to 0.2 μm, and then gradually dropped as the absorber thickness increased further. This could be attributed to the increasing series resistance and shunt conductance, thus decreasing the efficiency observed within this range (see Figure 10.2a). Additionally, for other devices, the FF rose gradually (Figure 10.2b). On the other hand, the V_{oc} (Figure 10.2c) decreased as the absorber thickened. This observation was also witnessed by Roy et al. [40] in their simulation study and this could be because of decreased recombination current.

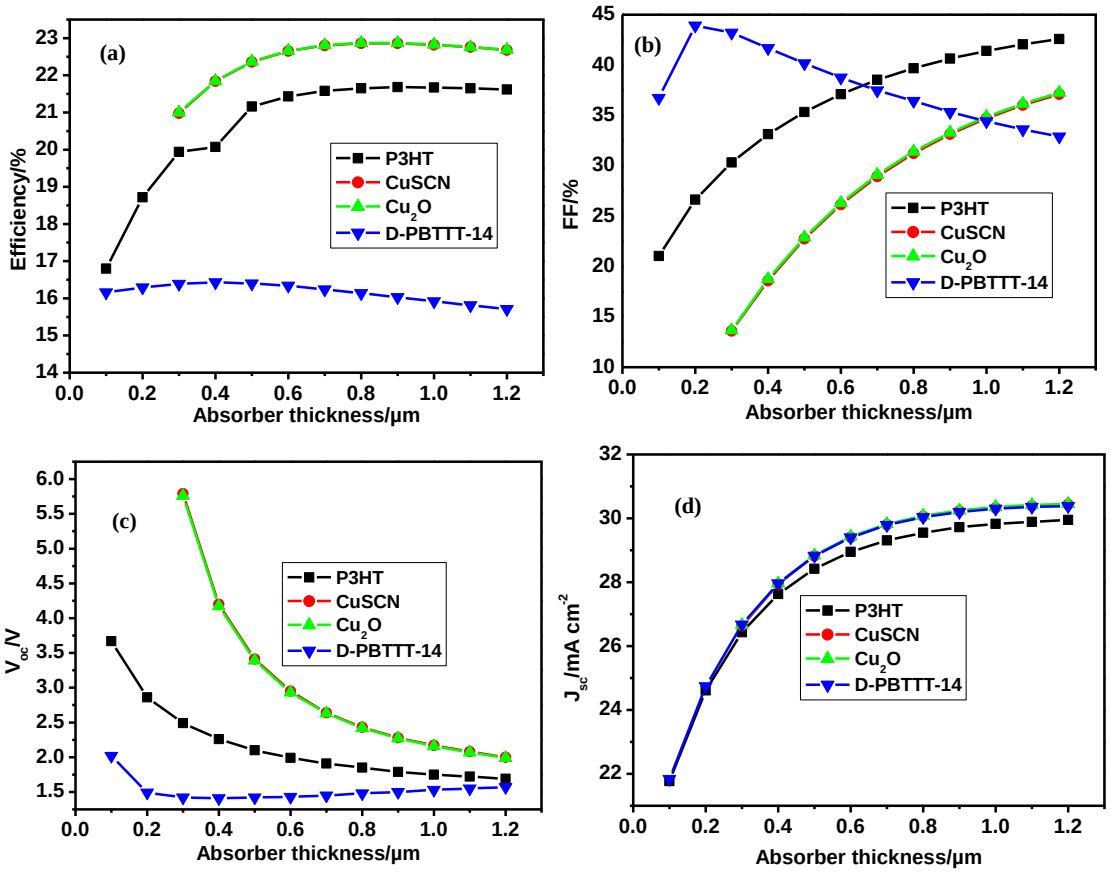

Figure 10.2: Variation of photovoltaic parameters for devices with different HTLs as a function of absorber thickness: (a) Efficiency, (b) FF, (c) V_{oc} and (d) J_{sc}

After the best values for the thickness of each layer were obtained, these values (Table 10.2) were used to obtain the J-V characteristics and quantum efficiency curves for all the modelled devices (with WS_2 as the ETL and different HTLs). The results are depicted in Figure 10.3. As can be seen in Figure 10.3a, the J-V curve for the device utilising D-PBTTT-14, as the HTL, rose sharply at a voltage of about 0.5 V, possibly as a result of increased series resistance and enhancement in the recombination of excitons, to yield the lowest PCE value of 16.43%. On the other hand, the J-V curves for the other devices remain relatively low over the range of 0 - 0.8 V.

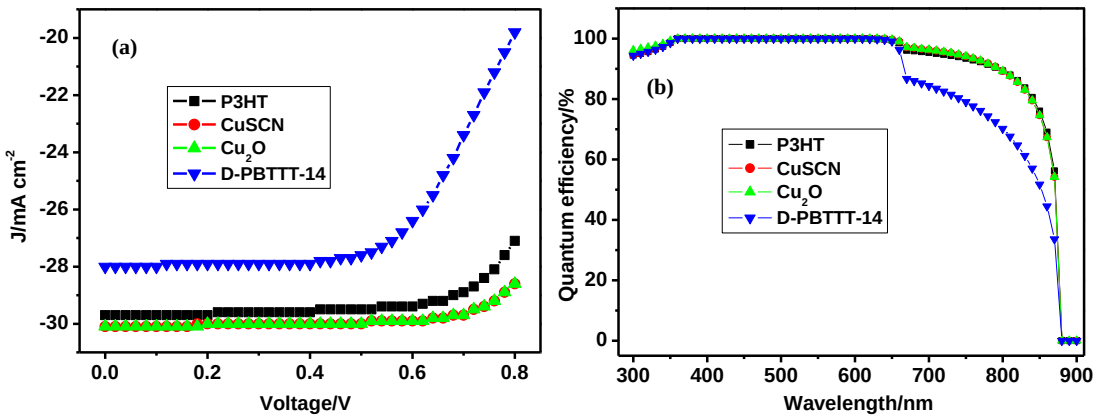

Figure 10.3: (a) J-V characteristics of devices utilising different hole transport materials, and (b) quantum efficiency as a function of wavelength for different hole transport materials

The best PCE values were exhibited by devices utilising inorganic CuSCN (22.88%) and Cu_2O (22.87%) as the HTLs (see Table 10.3). For CuSCN, this high performance could be attributed to proper band alignment with the absorber (Figure 10.1b) despite having a lower hole mobility of 1.0×10^{-1} cm^2 V^{-1} s^{-1} than Cu_2O. In the case of Cu_2O, it can be credited to its high hole mobility of 80 cm^2 V^{-1} s^{-1} (Table 10.1) and also proper band alignment with the absorber. In the class of organic HTLs, the P3HT device showed a PCE value of 21.68%, which was still high compared with the lowest value obtained for the D-PBTTT-14 (16.43%) device. This can be ascribed to the proper band alignment between its highest occupied molecular orbital (HOMO) and the valence band of the perovskite (Figure 10.1b). On the other hand, the D-PBTTT-14 device showed the lowest V_{oc} value of 1.41 V (Table 10.3), which may have contributed to its poor performance. In general, inorganic HTLs performed better than their organic counterparts, probably because of their higher hole mobilities, as reported in Table 10.1.

Table 10.3: Photovoltaic characteristics of devices with WS_2, as the ETL, and different HTLs

Parameter	Cu_2O	CuSCN	D-PBTTT-4	P3HT
V_{oc}/V	2.42	2.44	1.41	1.79
J_{sc}/mA cm^{-2}	30.08	30.07	27.96	29.72
FF/%	31.41	31.23	41.69	40.63
PCE/%	22.87	22.88	16.43	21.68

From Figure 10.3b, it can be seen that the quantum efficiencies (internal) for all the devices are apparently the same. This arises because the HTL material is located near the back contact of the device, and therefore, its optical absorption is considered negligible and does not affect the quantum efficiency. The high quantum efficiency achieved (about 95 - 99%) was attributed to a common WS_2 electron transport material and the absorber used for all the devices. However, the quantum efficiency sharply decreased to about 0% at about 870 – 900 nm, and this was because the device could not absorb much light beyond this region since the absorber has a bandgap of 1.41 eV. It is important to note that the ETL of a *p-i-n* perovskite solar cell configuration (reported in this study) is located next to the front contact where direct illumination takes place; therefore, its optical absorption plays a crucial role as far as quantum efficiency is concerned. Furthermore, at wavelengths longer than 640 nm, the quantum efficiency of the device with D-PBTTTT-14 exhibited a slight drop relative to the other HTLs tested. The relationship between J_{sc} and quantum efficiency can be illustrated by Equation 6.

$$J_{sc} = q \int \emptyset(\lambda) QE(\lambda) d\lambda \qquad \text{Equation (6)}$$

where J_{sc} is the short circuit current, q is the electronic charge, $\emptyset(\lambda)$ is the photon flux per wavelength bandwidth unit, and QE is the quantum efficiency. It follows that as the QE increases, the J_{sc} also increases and *vice versa*.

10.3.2 Effect of absorber density of defects

The level of density of defects of the absorber plays a very important role as far as power conversion is concerned [36]. When a deep level of defects exists in the absorber, the defects act as Shockley-Read-Hall non-radiative centres, which are known to cause a reduced lifetime of minority charge carriers. This causes a significant reduction in V_{oc} values of the solar cell

device [36]. Hence, we investigated the effect of changing the density of defects in the absorber from 2.0×10^{14} to 2.0×10^{19} cm^{-3}. The devices with Cu_2O and CuSCN did not exhibit photovoltaic behaviour when the absorber density of defects was 2.0×10^{15} or less, probably due to unfavourable contact between the absorber and both ETL and HTL (Figure 10.4). Figure 10.4a shows that the PCE of the devices decreased monotonically as a function of increasing density of defects; this can be related to an increased rate of recombination of charges due to the increased number of defects and, thus, the reduction in the observed PCE. Basically, increased recombination reduces the diffusion length of charge carriers and, also, their lifetime. The optimum density of defects for the organic D-PBTTT-14 and P3HT devices was 2.0×10^{14} cm^{-3}, while for the inorganic counterparts (Cu_2O and CuSCN), it was 2.0×10^{15} cm^{-3}. The PCE values attained for the D-PBTTT-14, P3HT, Cu_2O, and CuSCN devices at their optimum absorber density of defects were 19.70, 24.13, 22.87, and 22.88%, respectively. Similarly, the FF values (Figure 10.4b) generally decreased as a function of the increased density of defects, and this can be ascribed to increased series resistance and shunt conductance. From Figure 10.4d, it is seen that the J_{sc} values generally decreased as the density of defects increased. This is ascribed to increased recombination of charges and, thus, the performance decreased. For example, the percentage PCE decrease for D-PBTTT-14 was about 26%, while for P3HT, Cu_2O and CuSCN, it was about 36%. Figure 10.4c shows the effect of density of defects on V_{oc}; generally, there was a sharp decrease in V_{oc} values (from the 14^{th} to 16^{th} order for P3HT, and the 15^{th} to 16^{th} order for Cu_2O and CuSCN) for all devices except for the D-PBTTT-14 device. This is due to increased recombination of photogenerated charges. After that, there was a sharp unexpected increase in V_{oc} as the order of density of defects increased and was in agreement with the result of the device with P3HT in our previous work [27]. It is clear that photovoltaic parameters are very sensitive to the high absorber density of defects in the modelled devices reported in this work. Nonetheless, the density of defects for all devices was fixed at a constant favourable value of 2.0×10^{15} cm^{-3} because of inherent costs in tuning the intrinsic absorber defect density at an industrial level which would be commercially impractical.

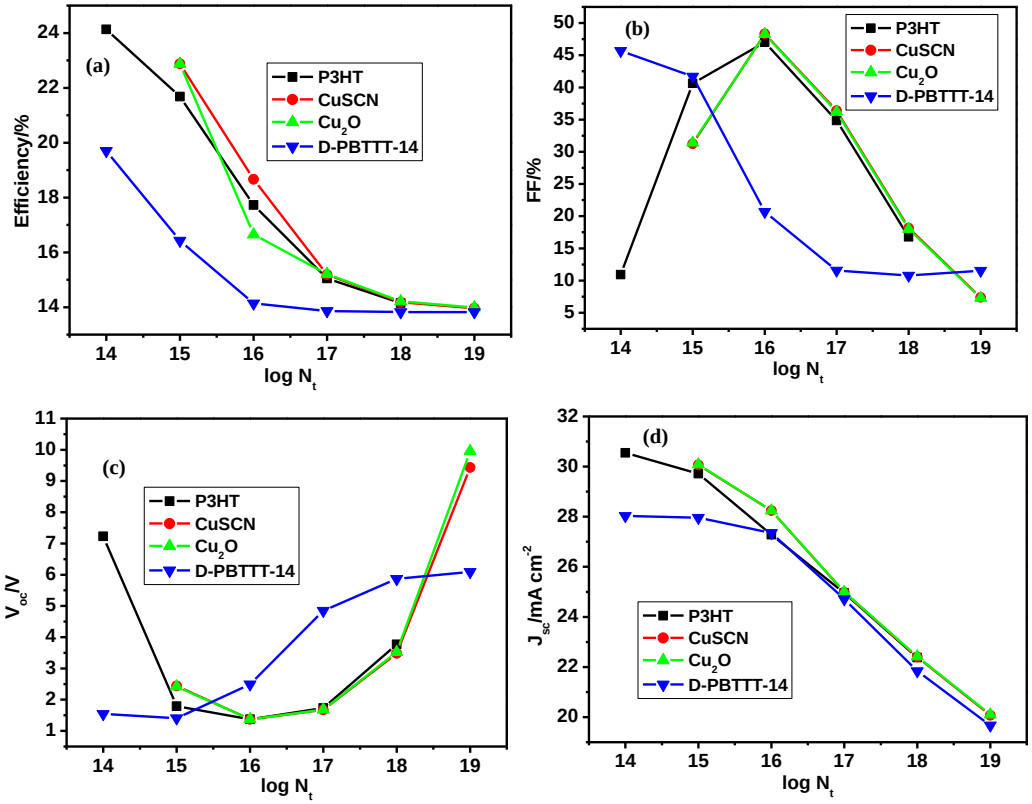

Figure 10.4: Variation of photovoltaic performance by changing the absorber density of defects in the range of 1.5×10^{14} to 1.5×10^{19} cm^{-3} for devices with different hole transport materials: (a) Efficiency, (b) FF, (c) V_{oc} and (d) J_{sc}

10.3.3 Effect of doping various device components

Figure 10.5 shows the effect of dopants on the efficiency of the photovoltaic devices investigated. Figure 10.5a shows the effects of doping the absorber with *p*-type carrier concentrations ranging from 7.0×10^{13} to 7.0×10^{19} cm^{-3}. It can be seen that the efficiency increases with an increase in the dopant concentration up to the 16^{th} order for the Cu_2O and CuSCN devices, and up to the 17^{th} order for the organic D-PBTTT-14 and P3HT devices. Notably, the Cu_2O and CuSCN devices did not show photovoltaic character beyond 7.0×10^{16} cm^{-3}, implying that a larger concentration of dopants was ineffective and may have introduced deep defects causing increased recombination. Additionally, excess doping may have caused the perovskite to change from semiconductor to metallic character, thus, hindering charge transport processes [41].

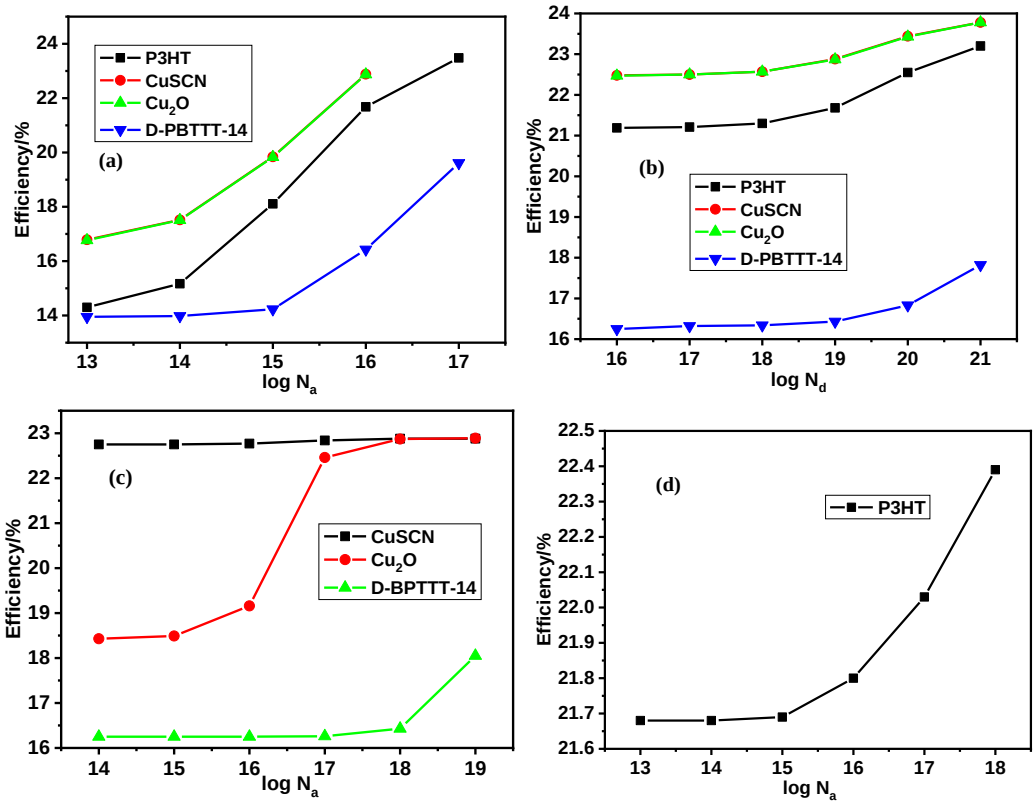

Figure 10.5: Efficiency of devices with different hole transport materials as a result of changes in the dopant concentration in the: (a) absorber, (b) ETL, (c) Cu_2O, CuSCN, D-PBTTT-14 HTLs, and (d) P3HT HTL

Figure 10.5b illustrates the effect of ETL donor concentration (N_d) on performance. The efficiency initially remains constant despite an increase in dopant concentration from 1.1×10^{16} to 1.1×10^{18} cm^{-3}, before it starts rising gradually as the dopant concentration is increased, possibly because of increased conductivity. The maximum dopant concentration was found to be 1.1×10^{18} cm^{-3}. Similarly, the effect of doping in the hole transport material was also studied (acceptor concentration, N_a), and the results are illustrated in Figures 10.5c and 10.5d. For devices with CuSCN, Cu_2O and D-PBTTT-14 HTLs, the concentration was examined from 1.0×10^{14} to 1.1×10^{18} cm^{-3} (Figure 10.5c) and for P3HT from 3.17×10^{13} to 3.17×10^{18} cm^{-3} (Figure 10.5d). From Figure 10.5c, the D-PBTTT-14 device showed no apparent PCE increase as doping changed from 1.1×10^{14} to 1.1×10^{17} cm^{-3}, but above this level, it experiences a slight increase (16.43-18.05%) up to the 19^{th} order, while the PCE for Cu_2O gradually rises from 18.43 to 22.87% as the doping concentration increases from 1.1×10^{14} to 1.1×10^{18} cm^{-3} before reaching saturation at 1.1×10^{19} cm^{-3}. The PCE of CuSCN was not affected by changing the dopant concentration, and this observation may be attributed to the Moss-Burstein effect that was attained at a doping concentration of 1.1×10^{14} cm^{-3} [42]. The efficiency of the P3HT

device increases as the dopant concentration increases from 21.7 to 22.4% because of increased conductivity (Figure 10.5d).

10.3.4 Effect of external operating temperature

During the ordinary operation of solar cells, devices are typically positioned on rooftops and are subject to changing weather conditions, and this affects the stability of the devices. It has been found that the temperature of the device can be about twice that of the environment, and this has posed device stability problems [43]. Figure 10.6 show the variation in the photovoltaic performance as a function of varying temperature from 260 to 420 K. As depicted in Figure 10.6a, the performance of the devices with Cu_2O, CuSCN, and P3HT HTLs slightly increased with increasing temperature from 260 to 380 K before starting to drop at higher temperatures. Remarkably, these devices maintain a PCE of above 20% throughout the temperature range investigated, implying that they can withstand a wide range of temperature conditions without deteriorating. For the D-PBTTT-14 device, the PCE increases from 10.68 to 21.48% with increasing temperature and reaches an apparent plateau at 360 K before dipping slightly. Generally, at temperatures above 360 K, all the devices tested attained comparable PCE values. The decrease in performance at higher temperatures (for our case above 400 K) is attributed to a decrease in the J_{sc} and V_{oc} parameters, and this can be illustrated by Equation 7:

$$V_{oc} = \frac{nkT}{q} \ln\left[\frac{J_{sc}}{J_o} + 1\right] \qquad \text{Equation (7)}$$

where n is ideality factor, k is the Boltzmann constant, T is temperature, q is the elementary charge, and J_o is the reverse saturation current. As shown in Equation 7, when the temperature increases, the J_o also increases, and the overall effect is a decrease in V_{oc}, as observed in our simulation results. Figure 10.6c shows the effect of increasing temperature on V_{oc} for all the solar cells. The V_{oc} gradually rises as a function of increasing temperature and reaches a maximum at 380 K and, thereafter, it decreases. A contrasting observation was made for the FF (Figure 10.6b), where it decreased as the temperature rises to about 380 K before rising again. Moreover, Figure 10.6d shows the effect on $J_{sc,}$ which remains virtually constant for all the modelled devices. From our simulations, the devices with P3HT, Cu_2O, and CuSCN hole transport materials showed better performances (above 20%) at temperatures in the 260 to 420 K window, implying that these devices can withstand a higher temperature range. The D-PBTTT-14 device was shown to work best at temperatures above 380 K, making these devices suitable especially for use in tropical regions.

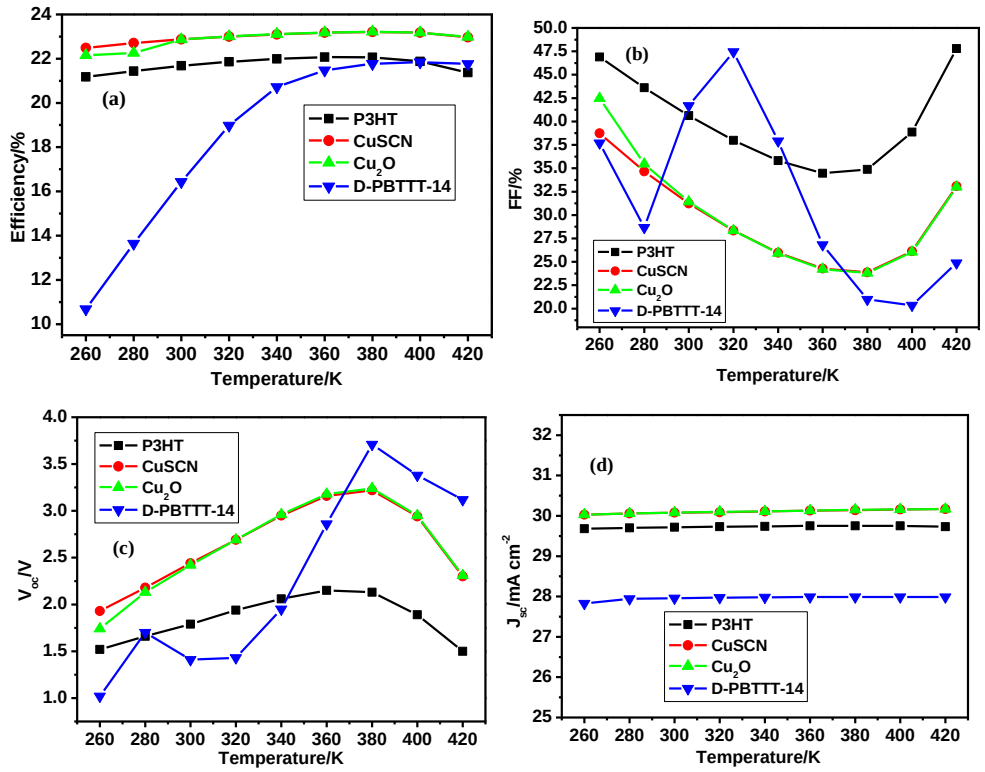

Figure 10.6: Variation of photovoltaic performance with operating temperature for devices with different hole transport materials: (a) Efficiency, (b) FF, (c) V_{oc} and (d) J_{sc}

10.3.5 Effect of metal back contact

Several metal work functions were evaluated to investigate the effect of different metal back contacts on the performance of the solar cells. The tested metals and their work functions included Pt (5.65 eV), Pd (5.3 eV), Ni (5.0 eV), Ag (4.7 eV), Au (5.05 eV), and Cu (4.65 eV). Figure 10.7 shows the variation of photovoltaic parameters with different metal back contacts. Both the PCE, in Figure 10.7a, and V_{oc}, in Figure 10.7c, increase with increasing metal work function, but they reach a plateau at 5.0 eV for all devices except for the P3HT cell, which remains constant for all the metal back contacts tested. Essentially, a high work function metal induces a high barrier for electrons to move from the hole transport material to the metal contact resulting in enhanced cell performance [44]. Generally, the FF values, shown in Figure 10.7b, decrease with increasing metal work function.

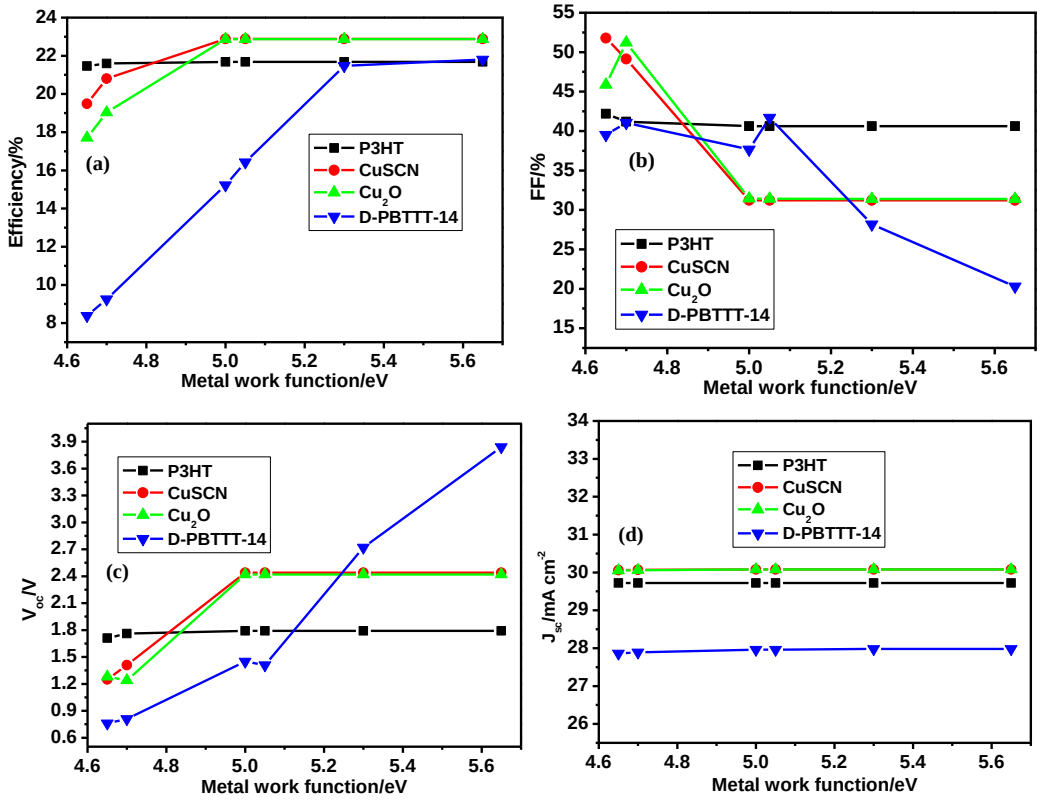

Figure 10.7: Effect of different metal back contacts on the photovoltaic characteristics of devices with different hole transport materials: (a) Efficiency, (b) FF, (c) V_{oc} and (d) J_{sc}

Based on these results, the following metal alternatives can be used as back contacts in place of gold: Pt, Pd, and Ni can be used in devices with Cu_2O and CuSCN hole transport materials since they afford high PCE values. However, for the D-PBTTT-14 device, only Pd and Pt can be used, and for the P3HT device, all the suggested metals can be used to substitute gold. The performance of the selected metal back contacts on the respective devices is summarised in Table 10.4.

Table 10.4: Percentage PCE values for devices utilising different HTLs and metal back-contacts

HTL	Cu	Ag	Ni	Au	Pd	Pt
Cu_2O	17.70	19.03	22.87	22.87	22.87	22.87
CuSCN	19.49	20.82	22.88	22.88	22.88	22.88
D-PBTTT-14	8.38	9.25	15.22	16.43	21.47	21.81
P3HT	21.46	21.60	21.68	21.68	21.68	21.68

10.4 Conclusions

In this paper, the performance of a formamidinium tin iodide-based ($HC(NH_2)_2SnI_3$) perovskite solar cell has been optimised by making use of the SCAPS-1D solar cell simulator. Different hole transport materials were inserted, and their effect on performance was evaluated. The effect of changing the thickness of the absorber, ETL, HTL, and FTO layers, the density of defects, and doping concentration of different components of the devices, were investigated. In addition, the effect of varying the operating temperature conditions and back metal contacts on the device performances was evaluated. Our simulation results showed that the PCE of all the devices increased as the absorber layer thickens. The inorganic-based hole transport materials portrayed better PCE values (CuSCN = 22.88%, Cu_2O = 22.87%) than their organic counterparts (D-PBTTT-14 = 16.43%, P3HT = 21.68%) at a temperature of 300 K. The density of defects and the quality of the film has a significant impact on the PCE of the devices. The PCE of the devices was found to increase with the doping concentrations of the absorber, HTL, and ETL. Nevertheless, the actual process of increasing the doping concentration is expensive to carry out at an industrial level and, consequently, is impractical.

In general, the modelled devices showed a high performance even at elevated temperatures, above 380 K, and can be used in areas such as the tropics. Evidently, cheaper metals, such as Pt, Pd, and Ni, can be used in place of gold because of their high work functions and high PCE values above 20% in all devices. These research findings will be useful for driving future direction in designing and fabrication of perovskite solar cells with high performance.

Acknowledgments

NR is grateful to the ACADEMY project for an academic mobility scholarship to the University of Tlemcen, Algeria, where this work was carried out at the Theoretical Physics Laboratory (TPL). AEM is grateful to DGRSDT and MHESR of Algeria for financial support under the PRFU research project N° B00L02UN130120180011. In addition, the authors are grateful for the financial support provided by the National Research Foundation (NRF) of South Africa, under grant numbers 103979 and 109580; the University of KwaZulu-Natal (UKZN), the UKZN Nanotechnology Platform, and the Eskom Tertiary Education Support Programme (TESP). Finally, the authors are also grateful to Professor Marc Burgelman and his team at the University of Ghent for allowing us to make use of the SCAPS-1D software.

References

[1] N. Rono, J.K. Kibet, B.S. Martincigh, V.O. Nyamori, A review of the current status of graphitic carbon nitride. Crit. Rev. Solid State Mater. Sci. **46**, 189–217 (2021). https://doi.org/10.1080/10408436.2019.1709414.

[2] H. Huang, Solar energy: Ferroelectric photovoltaics. Nat. Photonics. **4**, 134–135 (2010). https://doi.org/10.1038/nphoton.2010.15.

[3] S.K. Mangla, S. Luthra, S. Jakhar, S. Gandhi, K. Muduli, A. Kumar, A step to clean energy-sustainability in energy system management in an emerging economy context. J. Clean. Prod. **242**, 118462 (2020). https://doi.org/10.1016/j.jclepro.2019.118462.

[4] T.-H. Le, Y. Chang, D. Park, Renewable and nonrenewable energy consumption, economic growth, and emissions: International evidence. Energy J. **41** (2020). https://doi.10.5547/01956574.41.2.thle.

[5] J.I. Kwak, S.-H. Nam, L. Kim, Y.-J. An, Potential environmental risk of solar cells: Current knowledge and future challenges. J. Hazard. Mater. **392**, 122297 (2020). https://doi.org/10.1016/j.jhazmat.2020.122297.

[6] G.R. Li, X.P. Gao, Low-cost counter-electrode materials for dye-sensitized and perovskite solar cells. J. Adv. Mater. **32**, 1806478 (2020). https://doi.org/10.1002/adma.201806478.

[7] S.S. Ashrafi, K. Hossain, F. Ahmed, A. Hossain, O. Rahman, Fabrication and characterization of graphene incorporated Cu based perovskite in application of perovskite solar cell under ambient condition. Adv. Mater. Phy. Chem. **10**, 1 (2020). https://doi.org/10.4236/ampc.2020.101001.

[8] H. Zhang, Y. Lu, W. Han, J. Zhu, Y. Zhang, W. Huang, Solar energy conversion and utilization: Towards the emerging photo-electrochemical devices based on perovskite photovoltaics. Chem. Eng. J. **393**, 124766 (2020). https://doi.org/10.1016/j.cej.2020.124766.

[9] A. Kojima, K. Teshima, Y. Shirai, T. Miyasaka, Organometal halide perovskites as visible-light sensitizers for photovoltaic cells. J. Am. Chem. Soc. **131**, 6050-6051 (2009). https://doi.org/10.1021/ja809598r.

[10] J. Xie, K. Huang, X. Yu, Z. Yang, K. Xiao, Y. Qiang, X. Zhu, L. Xu, P. Wang, C. Cui, Enhanced electronic properties of SnO_2 via electron transfer from graphene quantum dots for efficient perovskite solar cells. Acs Nano. **11**, 9176-9182 (2017). https://doi.org/10.1021/acsnano.7b04070.

[11] M.R. Filip, G.E. Eperon, H.J. Snaith, F. Giustino, Steric engineering of metal-halide perovskites with tunable optical band gaps. Nat. Commun. **5**, 1-9 (2014). https://doi.org/10.1038/ncomms6757.

[12] R.J. Sutton, G.E. Eperon, L. Miranda, E.S. Parrott, B.A. Kamino, J.B. Patel, M.T. Hörantner, M.B. Johnston, A.A. Haghighirad, D.T. Moore, Bandgap-tunable cesium lead halide perovskites with high thermal stability for efficient solar cells. Adv. Energy Mater. **6**, 1502458 (2016). https://doi.org/10.1002/aenm.201502458.

[13] H.J. Snaith, Perovskites: The emergence of a new era for low-cost, high-efficiency solar cells. J. Phys. Chem. Lett. **4**, 3623-3630 (2013). https://doi.org/10.1021/jz4020162.

[14] A.A. Zhumekenov, M.I. Saidaminov, M.A. Haque, E. Alarousu, S.P. Sarmah, B. Murali, I. Dursun, X.-H. Miao, A.L. Abdelhady, T. Wu, Formamidinium lead halide perovskite crystals with unprecedented long carrier dynamics and diffusion length. ACS Energy Lett. **1**, 32-37 (2016). https://doi.org/10.1021/acsenergylett.6b00002.

[15] Z. Wang, Q. Lin, F.P. Chmiel, N. Sakai, L.M. Herz, H. Snaith, Efficient ambient-air-stable solar cells with 2D–3D heterostructured butylammonium-caesium-formamidinium lead halide perovskites. Nat. Energy. **2**, 17135 (2017). https://doi.org/10.1038/nenergy.2017.135.

[16] K.M. Boopathi, P. Karuppuswamy, A. Singh, C. Hanmandlu, L. Lin, S.A. Abbas, C.C. Chang, P.C. Wang, G. Li, C.W. Chu, Solution-processable antimony-based light-absorbing materials beyond lead halide perovskites. J. Mater. Chem. A. **5**, 20843-20850 (2017). https://doi.org/10.1039/C7TA06679A.

[17] P.V. Kamat, J. Bisquert, J. Buriak, Lead-free perovskite solar cells. ACS Energy Lett. **2**, 904-905 (2017). https://doi.10.1021/acsenergylett.7b00246.

[18] W. Hu, X. He, Z. Fang, W. Lian, Y. Shang, X. Li, W. Zhou, M. Zhang, T. Chen, Y. Lu, Bulk heterojunction gifts bismuth-based lead-free perovskite solar cells with record efficiency. Nano Energy. **68**, 104362 (2020). https://doi.org/10.1016/j.nanoen.2019.104362.

[19] A.-A. Kanoun, M.B. Kanoun, A.E. Merad, S. Goumri-Said, Toward development of high-performance perovskite solar cells based on $CH_3NH_3GeI_3$ using computational approach. Sol. Energy. **182**, 237-244 (2019). https://doi.org/10.1016/j.solener.2019.02.041.

[20] X. Jiang, F. Wang, Q. Wei, H. Li, Y. Shang, W. Zhou, C. Wang, P. Cheng, Q. Chen, L. Chen, Ultra-high open-circuit voltage of tin perovskite solar cells via an electron transporting layer design. Nat. Commun. **11**, 1-7 (2020). https://doi.org/10.1038/s41467-020-15078-2.

[21] Z. Zhao, F. Gu, Y. Li, W. Sun, S. Ye, H. Rao, Z. Liu, Z. Bian, C. Huang, Mixed-organic-cation tin iodide for lead-free perovskite solar cells with an efficiency of 8.12%. Adv. Sci. **4**, 1700204 (2017). https://doi.org/10.1002/advs.201700204.

[22] B. Wu, Y. Zhou, G. Xing, Q. Xu, H.F. Garces, A. Solanki, T.W. Goh, N.P. Padture, T.C. Sum, Long minority-carrier diffusion length and low surface-recombination velocity in inorganic lead-free $CsSnI_3$ perovskite crystal for solar cells. Adv. Funct. Mater. **27**, 1604818 (2017). https://doi.org/10.1002/adfm.201604818.

[23] F. Hao, C.C. Stoumpos, P. Guo, N. Zhou, T.J. Marks, R.P. Chang, M.G. Kanatzidis, Solvent-mediated crystallization of $CH_3NH_3SnI_3$ films for heterojunction depleted perovskite solar cells. J. Am. Chem. Soc. **137**, 11445-11452 (2015). https://doi.org/10.1021/jacs.5b06658.

[24] M.H. Kumar, S. Dharani, W.L. Leong, P.P. Boix, R.R. Prabhakar, T. Baikie, C. Shi, H. Ding, R. Ramesh, M. Asta, Lead-free halide perovskite solar cells with high photocurrents realized through vacancy modulation. J. Adv. Mater. **26**, 7122-7127 (2014). https://doi.org/10.1002/adma.201401991.

[25] S.J. Lee, S.S. Shin, Y.C. Kim, D. Kim, T.K. Ahn, J.H. Noh, J. Seo, S.I. Seok, Fabrication of efficient formamidinium tin iodide perovskite solar cells through SnF_2–pyrazine complex. J. Am. Chem. Soc. **138**, 3974-3977 (2016). https://doi.org/10.1021/jacs.6b00142.

[26] F. Hao, C.C. Stoumpos, D.H. Cao, R.P. Chang, M.G. Kanatzidis, Lead-free solid-state organic–inorganic halide perovskite solar cells. Nat. Photonics. **8**, 489–494 (2014). https://doi.org/10.1038/nphoton.2014.82.

[27] N. Rono, A.E. Merad, J.K. Kibet, B.S. Martincigh, V.O. Nyamori, A theoretical investigation of the effect of the hole and electron transport materials on the performance of a lead-free perovskite solar cell based on $CH_3NH_3SnI_3$. J. Comput. Electron. **20**, 993-1005 (2021). https://doi.org/10.1007/s10825-021-01673-z.

[28] A. Amat, E. Mosconi, E. Ronca, C. Quarti, P. Umari, M.K. Nazeeruddin, M. Grätzel, F. De Angelis, Cation-induced bandgap tuning in organohalide perovskites: Interplay of spin–orbit coupling and octahedra tilting. Nano Lett. **14**, 3608-3616 (2014). https://doi.doi.org/10.1021/nl5012992.

[29] M. Burgelman, K. Decock, A. Niemegeers, J. Verschraegen, S. Degrave, SCAPS manual. (2016). Version 8-4-2021, https://scaps.elis.ugent.be/SCAPS%20manual%20most%20recent.pdf, accessed on 4 November 2021.

[30] P. Hankare, A. Manikshete, D. Sathe, P. Chate, A. Patil, K. Garadkar, WS_2 thin films: Opto-electronic characterization. J. Alloys Compd. **479**, 657-660 (2009). https://doi.org/10.1016/j.jallcom.2009.01.024.

[31] N.D. Treat, N. Yaacobi-Gross, H. Faber, A.K. Perumal, D.D.C. Bradley, N. Stingelin, T.D. Anthopoulos, Copper thiocyanate: An attractive hole transport/extraction layer for use in organic photovoltaic cells. Appl. Phys. Lett. . **107**, 013301 (2015). https://doi.org/10.1063/1.4926408.

[32] Y. Yang, M.T. Hoang, D. Yao, N.D. Pham, V.T. Tiong, X. Wang, H. Wang, Spiro-OMeTAD or CuSCN as a preferable hole transport material for carbon-based planar perovskite solar cells. J. Mater. Chem. A. **8**, 12723-12734 (2020). https://doi.org/10.1039/D0TA03951A.

[33] Y. Guo, H. Lei, L. Xiong, B. Li, Z. Chen, J. Wen, G. Yang, G. Li, G. Fang, Single phase, high hole mobility Cu_2O films as an efficient and robust hole transporting layer for organic solar cells. J. Mater. Chem. A. **5**, 11055-11062 (2017). https://doi.org/10.1039/C7TA01628J.

[34] P. Zhou, T. Bu, S. Shi, L. Li, Y. Zhang, Z. Ku, Y. Peng, J. Zhong, Y.-B. Cheng, F. Huang, Efficient and stable mixed perovskite solar cells using P3HT as a hole transporting layer. J. Mater. Chem. C. **6**, 5733-5737 (2018). https://doi.org/10.1039/C8TC01345D.

[35] G. Yang, H. Tao, P. Qin, W. Ke, G. Fang, Recent progress in electron transport layers for efficient perovskite solar cells. J. Mater. Chem. A. **4**, 3970-3990 (2016). https://doi.org/10.1039/C5TA09011C.

[36] K. Sobayel, M. Akhtaruzzaman, K. Rahman, M. Ferdaous, Z.A. Al-Mutairi, H.F. Alharbi, N.H. Alharthi, M.R. Karim, S. Hasmady, N. Amin, A comprehensive defect study of tungsten disulfide (WS_2) as electron transport layer in perovskite solar cells by numerical simulation. Results Phys. **12**, 1097-1103 (2019). https://doi.org/10.1016/j.rinp.2018.12.049.

[37] A. Kumar, S. Singh, Numerical modeling of lead-free perovskite solar cell using inorganic charge transport materials. Mater. Today. **26**, 2574-2581 (2020). https://doi.org/10.1016/j.matpr.2020.02.545.

[38] S. Abdelaziz, A. Zekry, A. Shaker, M. Abouelatta, Investigating the performance of formamidinium tin-based perovskite solar cell by SCAPS device simulation. Opt. Mater. **101**, 109738 (2020). https://doi.org/10.1016/j.optmat.2020.109738.

[39] F. Azri, A. Meftah, N. Sengouga, A. Meftah, Electron and hole transport layers optimization by numerical simulation of a perovskite solar cell. J. Sol. Energy. **181**, 372-378 (2019). https://doi.org/10.1016/j.solener.2019.02.017.

[40] P. Roy, N.K. Sinha, S. Tiwari, A. Khare, Influence of defect density and layer thickness of absorption layer on the performance of tin based perovskite solar cell. IOP Conf. Ser.: Mater. Sci. Eng. . **798**, 012020 (2020). https://doi.org/10.1088/1757-899x/798/1/012020.

[41] C.C. Stoumpos, C.D. Malliakas, M.G. Kanatzidis, Semiconducting tin and lead iodide perovskites with organic cations: Phase transitions, high mobilities, and near-infrared photoluminescent properties. Inorg. Chem. **52**, 9019-9038 (2013). https://doi.org/10.1021/ic401215x.

[42] V. Trukhanov, V. Bruevich, D.Y. Paraschuk, Effect of doping on performance of organic solar cells. Phys. Rev. B. **84**, 205318 (2011). https://doi.org/10.1103/PhysRevB.84.205318.

[43] E. Cuddihy, C. Coulbert, A. Gupta, R. Liang, Electricity from photovoltaic solar cells: Flat-plate solar array project final report. volume VII: Module encapsulation. (1986). https://resolver.caltech.edu/JPLpub86-31-volumeVII.

[44] F. Behrouznejad, S. Shahbazi, N. Taghavinia, H.-P. Wu, E.W.-G. Diau, A study on utilizing different metals as the back contact of $CH_3NH_3PbI_3$ perovskite solar cells. J. Mater. Chem. A. **4**, 13488-13498 (2016). https://doi.org/10.1039/C6TA05938D.

CHAPTER ELEVEN

Graphitic carbon nitride doped zinc oxide as an electron transport layer in a lead-free perovskite solar cell: A SCAPS numerical simulation

Nicholas Rono,[a] Abdelkrim E. Merad,[b] Joshua K. Kibet,[c] Bice S. Martincigh[a] and Vincent O. Nyamori[a]*

[a]School of Chemistry and Physics, University of KwaZulu-Natal, Westville Campus, Private Bag X54001, Durban, 4000, South Africa

[b]Solid State Physics Team, Theoretical Physics Laboratory, Faculty of Sciences, A Belkaid University, Box 119, 13000, Tlemcen, Algeria

[c]Chemistry Department, Egerton University, Njoro Campus, P.O. Box 536-20115, Egerton, Kenya

*Corresponding author: E-mail: Nyamori@ukzn.ac.za, Tel: +27312608256

Abstract

In this study, the performance of a lead-free perovskite solar cell (PSC) utilising formamidinium tin iodide ($HC(NH_2)_2SnI_3$) as an absorber layer and with the following configuration: glass/FTO/ETL/$HC(NH_2)_2SnI_3$/CuSCN/Au was numerically simulated. In the device, zinc oxide doped with graphitic carbon nitride (g-C_3N_4/ZnO) was employed as an electron transport layer (ETL). The numerical simulation of the device was carried out by using the one-dimensional solar cell capacitance simulator (SCAPS-1D) software. The effects of changing the g-C_3N_4 dopant concentration, density of defects of the active layer, and the use of diverse metallic back contacts on the overall power conversion efficiency (PCE) of the device were examined. Moreover, the effect of the external operational temperature on the device performance was also investigated. The PCE of the device increased as a function of increasing g-C_3N_4 concentration attributed to the passivation effects of polymeric g-C_3N_4, thus, reducing the recombination of the photogenerated charges at the ETL/absorber boundary. The PCE decreased monotonously as the absorber density of defects increased, and this can be ascribed to an increase in shunt resistance and charge recombination. Relatively cheaper metal back

contacts, such as Ni, Pd, and Pt, showed a similar PCE to that of a Au back contact; thus, can be used in place of Au. It was evident that the performance of the cell was optimal at room temperature but decreased with an increase in temperature. After all the optimisations, the device achieved a PCE of 22.33%. The simulation results are expected to offer directions on the development of PSCs with g-C_3N_4/ZnO as the ETL material for the anticipated commercialisation in the near future.

Keywords: Numerical simulation; electron transport layer; SCAPS-1D; metal work function

11.1 Introduction

Solar energy, as the best alternative energy source, has been considered clean and sustainable because it is inexhaustible and abundant globally compared with for instance, exhaustible fossil fuels [1]. Fossil fuels are expensive and exhaustible and have resulted in detrimental environmental effects such as global warming and pollution [2]. In order to explore better mechanisms of solar harvesting, scientists have devoted much effort in search of better materials that are clean and environmentally benign for the utilisation of the fabrication of solar cells. Recently, perovskite solar cells (PSCs) based on organic-inorganic hybrids have sparked scientific consideration because of their attractive properties, including simple solution-processable routes, considerable long diffusion length, low-cost materials requirement, and better light absorption coefficients [3, 4]. The power conversion efficiency (PCE) of PSCs has risen above 23% since their first inception in 2009 in Japan, because of tremendous advancement in fabrication [5]. The enhancement in PCE towards the theoretical value of 33% according to the Shockley–Queisser efficiency [6] can be attributed to the use of better electron (ETL) and hole transport (HTL) layers, with proper band alignment, and suitable intrinsic properties, for instance, improved light absorption and charge transfer characteristics.

The most commonly used ETL material is titanium dioxide (TiO_2) [7], but this material has a number of shortcomings, such as a high sintering temperature before use, thus, unsuitable for substrates that require low-temperature processing and relatively low electron mobilities [8]. Recently, zinc oxide (ZnO) nanoparticles have been demonstrated to be a suitable alternative to TiO_2 due to their environmentally benign nature, low cost, good optical transparency, straightforward low-temperature preparation routes such as sol-gel [9], ability to be deposited by spin-coating, [10] and better light absorption capabilities [11]. The optical band gap of ZnO has been established to be about 3.3 eV and; thus, it can absorb more sunlight [12]. Moreover, it exhibits a relatively higher electron-transport velocity (about 200 $cm^2\ V^{-1}\ s^{-1}$) [13] than TiO_2 (0.1 – 4 $cm^2\ V^{-1}\ s^{-1}$) [14, 15], which could facilitate faster extraction of electrons from the perovskite absorber material and, hence, its wide application in solar cells as the ETL material [11]. Despite ZnO having these advantages over other metal oxide-based ETLs, there also exist inherent inevitable shortcomings, for instance, the instability of ZnO-based PSCs [14] and surface recombination of excitons, which can be credited to intrinsic defects of ZnO (point

defects) [16]. These defects can lead to the formation of trap states that entice the electrons, especially at the interfaces leading to recombination and poor charge transfer. Recently, interface engineering has been carried out to improve the performance of PSCs through passivation of defects, thus, minimising the fast charge recombination, improving charge transfer mechanisms, and controlling perovskite crystal growth [17, 18]. Graphene [19] and graphitic carbon nitride (g-C_3N_4) [18], which are typical examples of two-dimensional (2D) materials, have been introduced at the interfaces in the solar cells as passivation agents. This has resulted in improved charge transfer characteristics at the interface, and has facilitated the growth of high quality perovskite films [18].

Also, device simulation strategies have lately been used to understand, select appropriate materials, and gain insights into solar cell devices' physical behaviour in an attempt to improve their performances. For instance, Azri et al. [20] computationally studied the effects of various ETL materials in PSC devices. The device with ZnO as ETL exhibited a PCE of 20.64%. The performance enhancement was ascribed to high electron mobilities, better band alignment between the layers and better light absorption. Therefore, simulations are very convenient in PSC performance optimisation. Herein, we report the computational modelling of a lead-free PSC with a basic structure of: glass/FTO/ZnO or ZnO doped with graphitic carbon nitride/$HC(NH_2)_2SnI_3$/CuSCN/Au. The one-dimensional solar cell capacitance simulator (SCAPS-1D) software was employed in the simulation. In this model, the effect on the PCE of doping ZnO with g-C_3N_4 is examined. Furthermore, the impact of varying the absorber defect densities (N_t), using different metallic back contacts, and varying operating temperature conditions, on the device's PCE was explored. It is believed that this work will provide avenues for performance improvement of PSCs utilising ZnO doped with g-C_3N_4 as the ETL material.

11.2 Solar cell configuration and computational approach

The photovoltaic behaviour of the simulated solar cells under investigation was explore with the use of SCAPS-1D simulation code. The SCAPS-1D simulation software was advanced by Professor Marc Burgelman from the University of Ghent, Belgium [21]. The software calculates and resolves the three fundamental semiconductor equations under the steady-state conditions. The calculation is basically in one - dimension and in steady state. Essentially, during the simulation process, the photovoltaic parameters, the output

data on generation-recombination behaviour, electric charge distribution and transport processes and, current densities are generated as reported in our previous work. In essence, the three equations are are: the Poisson and the equations of continuity for electrons and (iii) holes. More details of these equations can be obtained from our previously published works [22, 23].

The device architecture with n-i-p configuration comprised fluorine-doped tin oxide (FTO) glass substrate/ETL, which consisted of g-C_3N_4 doped ZnO/absorber ($HC(NH_2)_2SnI_3$)/HTL (copper(I) thiocyanate (CuSCN))/Au back contact, as shown in Figure 11.1.

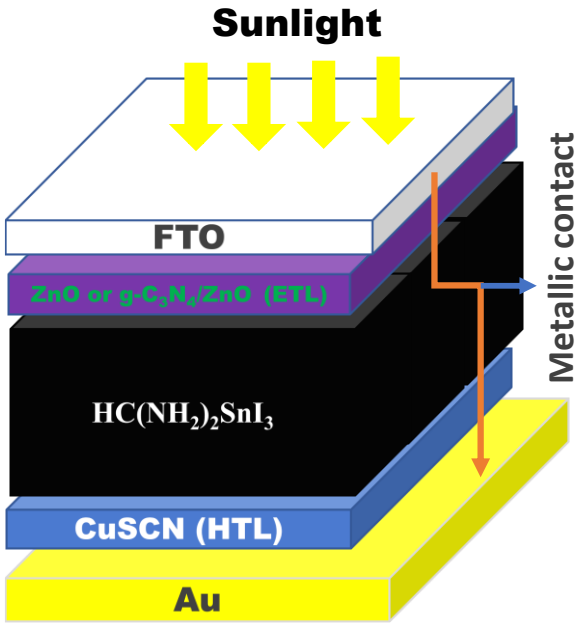

Figure 11.1: The general structure of the modelled device investigated in this study

To simulate the devices, the working conditions for the software were set as described in our previous work in refs [22, 23]. The base parameters for the respective layer components of the cell were collected from theoretical and experimental data previously published and are shown in Table 11.1.

Table 11.1: Material base parameters for simulated device

Parameter	**FTO** [24]	**ZnO (ETL)** [20]	**$HC(NH_2)_2SnI_3$ (perovskite absorber)** [25]	**CuSCN (HTL)** [20]
Thickness, d/μm	0.8	2.0	0.9	0.1
Energy gap, E_g/eV	3.5	Varied	1.41	3.4
Affinity, χ/eV	4.0	4.1	3.52	1.9
Dielectric Permittivity, ε_r	9.0	9	8.2	10
Effective density of state at CB, N_c/cm^{-3}	2.2×10^{18}	4.0×10^{18}	1.0×10^{18}	1.7×10^{19}
Effective density of state at VB, N_v/cm^{-3}	1.8×10^{19}	1.0×10^{19}	1.0×10^{19}	2.5×10^{21}
Electron mobilty, μ_n /cm^2 V^{-1} s^{-1}	20.0	100	22	1.0×10^{-4}
Hole mobility, μ_p/cm^2 V^{-1} s^{-1}	10.0	25	22	1.0×10^{-1}
n-type doping density, N_d/cm^{-3}	1.0×10^{19}	1.0×10^{18}	0	0.0
p-type doping density, N_a/cm^{-3}	0.0	1.0×10^{5}	7.0×10^{16}	1.0×10^{18}
Defects density, N_t/cm^{-3}	0.0	2.0×10^{17}	2.0×10^{15}	1.0×10^{14}

11.3 Results and discussion

In our simulations, the performance of the modelled devices was considered based on parameters such as the PCE, fill factor (FF), short circuit current density (J_{sc}), open circuit voltage V_{oc} and quantum efficiency (QE). Since it is crucial to optimise the thickness of various layers in the device, layer optimisation was carried out systematically as an initial step. After sequential simulation steps, the optimised thickness for FTO, ETL, absorber, and HTL were found to be 0.8, 2.0, 0.9, and 0.1 μm, respectively.

11.3.1 Effect of the doping concentration of graphitic carbon nitride on zinc oxide compact layer

In order to explore the impact of g-C_3N_4 (which is renamed here as CN) as a dopant on the performance of the device with ZnO as the ETL material, the inclusion of different concentrations of CN in ZnO was applied. The different band gap data with corresponding doping levels were gathered from the experimental work of Chetia et al. [26]. Table 11.2 shows the band gap energies of pure ZnO and doped ZnO with different CN dopant ratios. These values were inserted into the respective device during the simulation process, and their effect was examined.

Table 11.2: Input band gap energies of different ETL ZnO materials [26]

Material composition	Band gap energy/eV
ZnO (pure)	3.17
20% CN/ZnO	3.18
33% CN/ZnO	3.19
50% CN/ZnO	3.20
60% CN/ZnO	3.205
67% CN/ZnO	3.21

As depicted in Table 11.2, the band gap of ZnO gradually increased as the doping level of CN increased; this could be due to an electronic modification in the composite between CN and ZnO. From Table 11.3, it can be seen that the PCE of the devices increased as g-C_3N_4 doping levels increases; this could be attributed to the increased band gap energy shown in Table 11.2. The increase in band gap energy could have resulted in better light harvesting capability of the nanocomposites and reduced recombination of photogenerated charges at the interface of the absorber and the ETL material. Basically, CN could act as a passivation agent, thus reducing the number of interfacial defects at the boundary of the ETL and the absorber that could have otherwise enticed photogenerated charges [18]. The device with pristine ZnO registered a low PCE of 22.20% compared with the devices with CN doped ZnO materials. This may be due to the high

recombination of charges at the interface compared with devices that include CN doped ZnO materials. Generally, the impact of CN doping on the PCE of the devices was apparently low and could be directly related to the slight changes in band gap energies as the dopant concentration increased.

Table 11.3: Photovoltaic parameters of devices with the corresponding materials used as the ETLs

Material	**V_{oc}/V**	**J_{sc}/mA cm^{-2}**	**FF/%**	**PCE/%**
ZnO	5.16	28.43	15.12	22.20
20% CN/ZnO	5.16	28.57	15.13	22.32
33% CN/ZnO	5.16	28.57	15.13	22.32
50% CN/ZnO	5.16	28.58	15.13	22.32
60% CN/ZnO	5.16	28.58	15.13	22.32
67% CN/ZnO	5.16	28.58	15.13	22.33

Figure 11.2 shows the devices' quantum efficiency (QE). As can be observed, the QE was above 98% at the wavelength between 400 - 750 nm for all the devices, with a slight difference in the undoped ZnO at the wavelength of about 400 nm. The observed behaviour of the QE can be attributed to the absorption ability of the ETL and the absorber since they are located at the front part of the device, thus, receiving direct illumination. Typically, ETL materials with a band gap above the 3.17 to 3.21 eV range can absorb light over 391.17 nm. Similarly, the absorber can absorb light up to about 800 nm. The high QE of about 98% could also be attributed to an appreciable current density above 15.13 mA cm^{-2} noted by all PSCs as shown in Table 11.3.

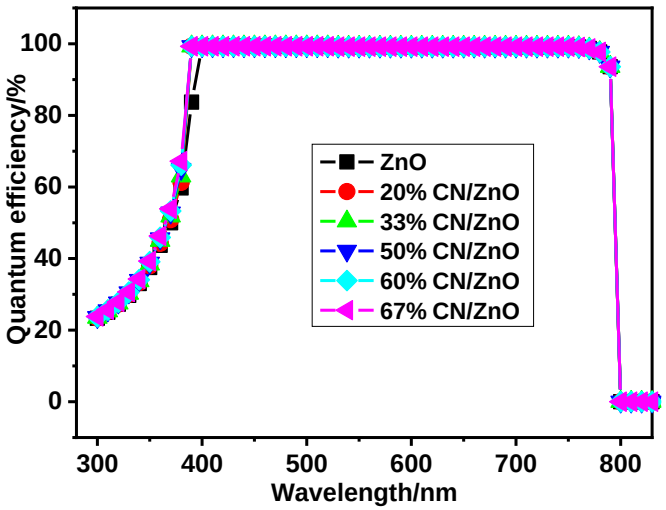

Figure 11.2: Quantum efficiency of the optimised devices

11.3.2 Impacts of varying absorber density of defects

During the fabrication of solar cells, defect formations are inevitable, and this causes a major problem with regard to device perfomance, thus, hampering commercialisation [27]. The defects can be interfacial or may exist within the absorber materials, also referred to as amphoteric defects [28]. Recently, Sobayel et al. [29] showed theoretically that amphoteric defects are more severe than interfacial defects. Therefore, it is important to minimise these defects as much as possible, inorder to avoid recombination of photogenerated charges[22]. Figure 11.3 shows the effect of varying the absorber density of defects on the photovoltaic performance of the devices. The absorber density of defects (N_t) was examined from 2.5×10^{15} to 2.5×10^{19} cm^{-3}. The PCE (Figure 11.3a) of devices decreased monotonically (from 22% to 1.5 %) as a function of the increasing order of defects density. From Figure 11.3b, the FF graph slightly rose and dropped, while the V_{oc} and J_{sc} graphs (Figure 11.3c and Figure 11.3d) also decreased as the defects density increased. This could be as a result of increased recombination of charges which relates to the increased number of defects. Moreover, the shunt and series resistance could also have increased, which severely affected the photovoltaic characteristics of the devices. The effect of CN different doping levels on ZnO was apparently not noticeable because the PCE values were very close. However, the best density of defects was at kept at the 15^{th} order.

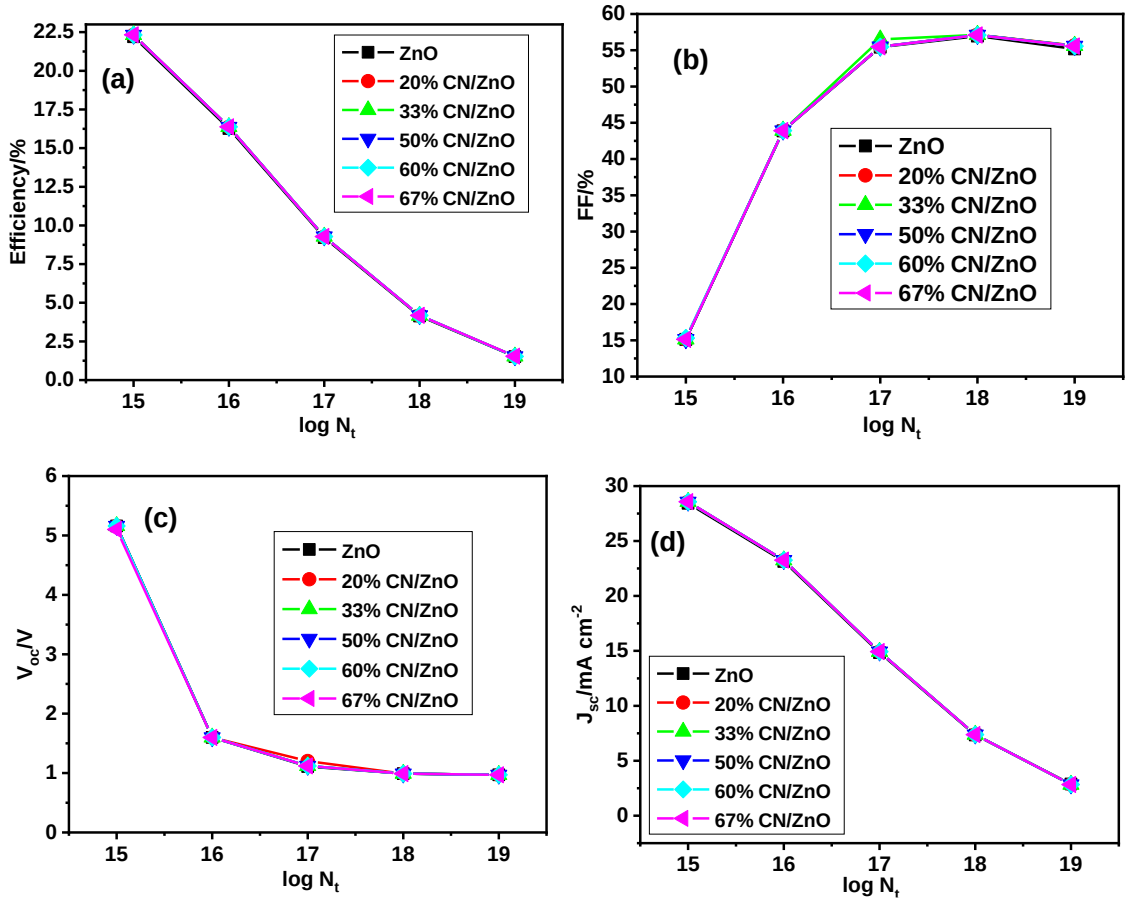

Figure 11.3: Effects of changing absorber defect density on the PSCs performance: (a) efficiency, (b) FF, (c) J_{sc} and (d) V_{oc}

11.3.3 Influence of metal work function

To determine the performance of different metals as back contact anodes, diverse metals with their respective work functions were investigated and compared with the default gold (5.05 eV). The aim here was to search for cost-effective and efficient alternatives to gold. Therefore, the following metals were chosen: Cu (4.65 eV), Ag (4.7 eV), Ni (5.0 eV), Pd (5.3 eV), and Pt (5.65 eV), and their respective work functions were used in the simulation. Figure 11.4 depicts the effects of various metals on the performance of the cells. From Figure 11.4a, the PCE was about 21% for Cu (4.65 eV) and Ag (4.7 eV) metals, and above 22% for Ni (5.0 eV), Au (5.05), Pd (5.3 eV) and Pt (5.65 eV) back contacts.

Similarly, V_{oc} (Figure 11.4c) increased as a function of increasing the metal work function and attained a plateau at 5.0 eV. The FF (Figure 11.4b) decreased and remained constant

at 5.0 eV, while the graph remained apparently constant for J_{sc} (Figure 11.4d). It was observed that metals with high work functions exhibited high performance, which can be attributed to a high open voltage and high work function, thus increasing efficiency [23]. These results show that Ni, Pd, and Pt yielded similar results as gold, thus can replace gold.

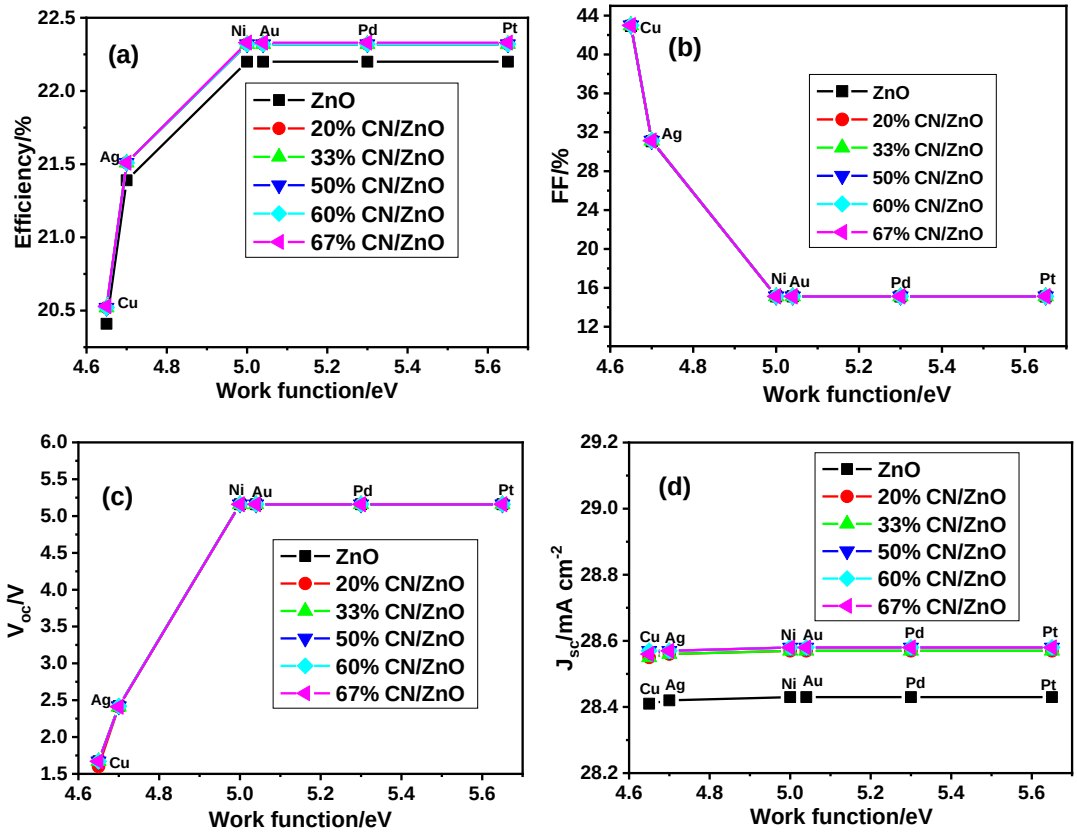

Figure 11.4: Impact of using different metal contacts on the device performance: (a) efficiency, (b) FF, (c) $V_{oc,}$ and (d) J_{sc}

11.3.4 Effect of the operating temperature of the device

Ordinarily, solar cells are left outside on the elevated ground for solar illumination. The conditions outside can severely affect their lifespan and overall performance. So far, we have carried out numerical simulations at an initial temperature of 300 K.

In order to search for optimum operating temperatures, devices were simulated at temperatures between 260 and 440 K. Figure 11.5 shows the impact of temperature on the photovoltaic characteristics. As depicted in Figure 11.5a, the PCE of the devices decreased as the temperature increased. This could result from increased resistance and

recombination; thus, low performance [30]. The FF graphs (Figure 11.5b) increased, while the V_{oc} curves (Figure 11.5c) decreased drastically as the temperature increased. Generally, it has been established that, as the temperature increases, V_{oc} decreases, resulting in low PCE [22, 31]. On the other hand, the J_{sc} slightly increased as the temperature increased; this could be because of the band gap reduction, which led to more electrons reaching the conduction band (CB), thus, causing an increase in the short circuit current. Nonetheless, the optimum operating temperature was established to be about 350 K since the device exhibited the highest PCE at this temperature.

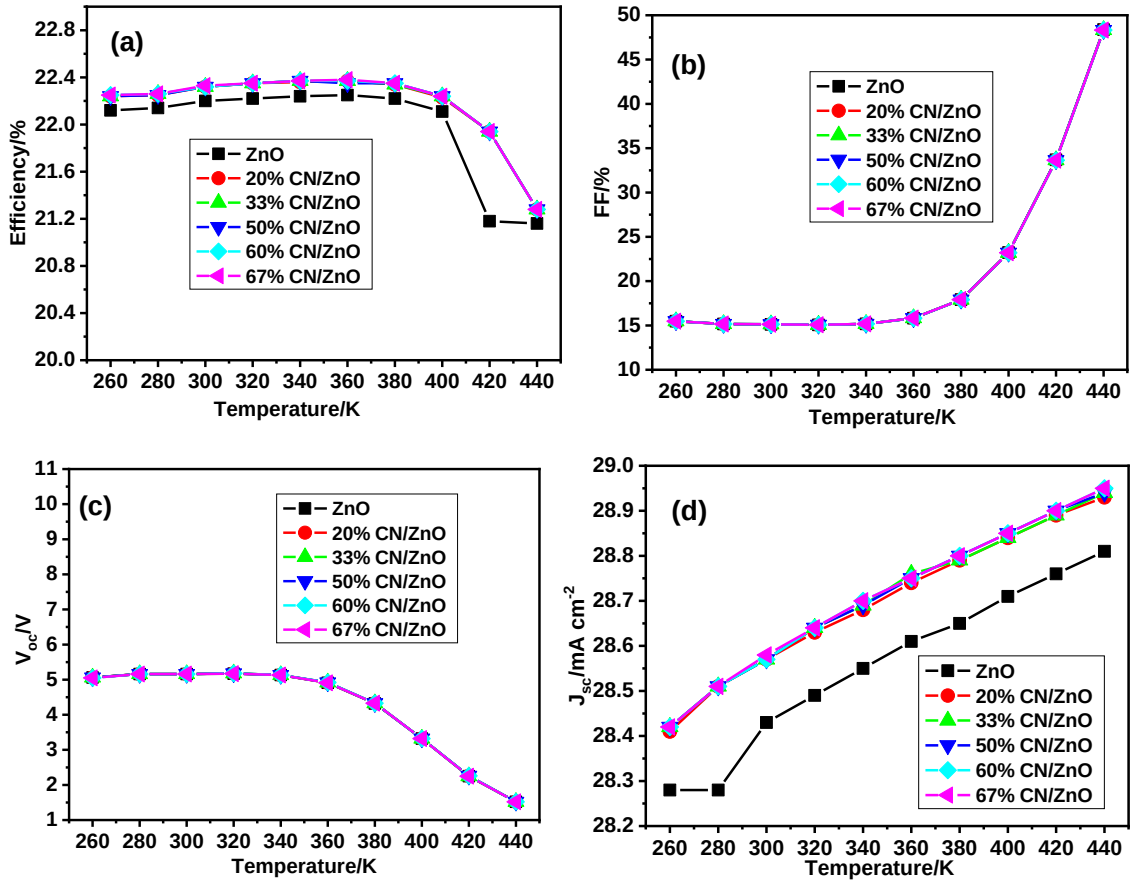

Figure 11.5: Effect of changing the operating temperature on the PSCs performance: (a) Efficiency, (b) FF, (c) $V_{oc,}$ and (d) J_{sc}

11.4 Conclusion

We numerically analysed the performance of a lead-free perovskite solar cell (PSC) with the configuration of; FTO/ZnO/$HC(NH_2)_2SnI_3$/CuSCN/Au using SCAPS-1D software. The effect of doping ZnO with g-C_3N_4 (CN) on the performance of the device was examined. Also, the impact of absorber defect density, the back contact, and the operation

temperature of the device operating on the ultimate power conversion efficeincy (PCE) of the of the device was explored in detail. From the results, it was found that the PCE of the PSCs increased as the doping concentration of g-C_3N_4 increased. This was attributed to the decrease in recombination of charges as g-C_3N_4 passivates the charges in the electron transport layer (ETL) and at the interface between the ETL and the absorber. Additionally, the PCE decreased as the defects density increased due to an increase in the recombination of photogenerated charges. It was also evident that an increase in operational temperature was detrimental to the PCE of the devices since, at high temperatures, the devices degrade, thus, decreasing the PCE. Finally, these findings are believed to guide future experimental fabrication of high-performance solar cell devices.

Acknowledgements

The authors are thankful for the financial support provided by the National Research Foundation (NRF) of South Africa, under grant numbers 103979 and 109580; the University of KwaZulu-Natal (UKZN), the UKZN Nanotechnology Platform, and the Eskom Tertiary Education Support Programme (TESP). The authors are also grateful to Professor Marc Burgelman and his team at the University of Ghent for allowing us to use SCAPS software.

Conflict of interest

The authors declare no conflict of interest.

References

[1] M. Asif, T. Muneer, Energy supply, its demand and security issues for developed and emerging economies. Renew. Sustain. Energy Rev. **11**, 1388-1413 (2007). https://doi.org/10.1016/j.rser.2005.12.004.

[2] M.A. Abdelkareem, K. Elsaid, T. Wilberforce, M. Kamil, E.T. Sayed, A. Olabi, Environmental aspects of fuel cells: A review. Sci. Total Environ. **752**, 141803 (2021). https://doi.org/10.1016/j.scitotenv.2020.141803.

[3] Y. Zheng, B. Ge, L.R. Zheng, Y. Hou, S. Yang, H.G. Yang, Solution-processable nickel–chromium ternary oxide as an efficient hole transport layer for inverted planar perovskite solar cells. J. Mater. Chem. A. **9**, 21792-21798 (2021). https://doi.org/10.1039/D1TA06565C.

[4] T.-T. Li, Y.-B. Yang, G.-R. Li, P. Chen, X.-P. Gao, Two-terminal perovskite-based tandem solar cells for energy conversion and storage. Small. **17**, 2006145 (2021). https://doi.org/10.1002/smll.202006145.

[5] A. Kojima, K. Teshima, Y. Shirai, T. Miyasaka, Organometal halide perovskites as visible-light sensitizers for photovoltaic cells. J. Am. Chem. Soc. **131**, 6050-6051 (2009). https://doi.org/10.1021/ja809598r.

[6] W. Shockley, H.J. Queisser, Detailed Balance Limit of Efficiency of p-n Junction Solar Cells. J. Appl. Phys. **32**, 510-519 (1961). https://doi.org/10.1063/1.1736034.

[7] V.M. Arivunithi, S. Kim, J. Choi, J.H. Sung, H.D. Yoo, E.-S. Shin, Y.-Y. Noh, Y.-S. Gal, H. Lee, S.-H. Jin, Enhanced efficiency and reduced hysteresis by TiO_2 modification in high-performance perovskite solar cells. Org. Electron. **86**, 105922 (2020). https://doi.org/10.1016/j.orgel.2020.105922.

[8] Q. Gao, S. Yang, L. Lei, S. Zhang, Q. Cao, J. Xie, J. Li, Y. Liu, An effective TiO_2 blocking layer for perovskite solar cells with enhanced performance. Chem. Lett. **44**, 624-626 (2015). https://doi.org/10.1246/cl.150049.

[9] S. Jurablu, M. Farahmandjou, T.P. Firoozabadi, Sol-gel synthesis of zinc oxide (ZnO) nanoparticles: Study of structural and optical properties. J. Sci. Islam. Repub. **26**, 281-285 (2015). https://jsciences.ut.ac.ir/article_55316.html.

[10] K. Mahmood, A. Khalid, S.W. Ahmad, M.T. Mehran, Indium-doped ZnO mesoporous nanofibers as efficient electron transporting materials for perovskite solar cells. Surf. Coat. Technol. **352**, 231-237 (2018). https://doi.org/10.1016/j.surfcoat.2018.08.039.

[11] A. Al-Kahlout, ZnO nanoparticles and porous coatings for dye-sensitized solar cell application: Photoelectrochemical characterization. Thin Solid Films. **520**, 1814-1820 (2012). https://doi.org/10.1016/j.tsf.2011.08.095.

[12] M.K. Debanath, S. Karmakar, Study of blueshift of optical band gap in zinc oxide (ZnO) nanoparticles prepared by low-temperature wet chemical method. Mater. Lett. **111**, 116-119 (2013). https://doi.org/10.1016/j.matlet.2013.08.069.

[13] S.J. Pearton, D.P. Norton, K. Ip, Y.W. Heo, T. Steiner, Recent advances in processing of ZnO. J. Vac. Sci. Technol. B. **22**, 932-948 (2004). https://doi.org/10.1116/1.1714985.

[14] P. Zhang, J. Wu, T. Zhang, Y. Wang, D. Liu, H. Chen, L. Ji, C. Liu, W. Ahmad, Z.D. Chen, S. Li, Perovskite solar cells with ZnO electron-transporting materials. Adv. Mater. **30**, 1703737 (2018). https://doi.org/10.1002/adma.201703737.

[15] H.S. Jung, N.-G. Park, Perovskite solar cells: From materials to devices. Small. **11**, 10-25 (2015). https://doi.org/10.1002/smll.201402767.

[16] Y. Cao, J. Luo, W. Huang, Y. Ling, J. Zhu, W.-X. Li, F. Yang, X. Bao, Probing surface defects of ZnO using formaldehyde. J. Chem. Phys. **152**, 074714 (2020). https://doi.org/10.1063/1.5138372.

[17] X. Sun, M. Li, Q. Qiu, J. Song, L. Zhu, Y. Qiang, Charge transfer enhancement of TiO_2/perovskite interface in perovskite solar cells. J. Mater. Sci.: Mater. Electron. **32**, 22936-22943 (2021). https://doi.org/10.1007/s10854-021-06778-6.

[18] J. Chen, H. Dong, L. Zhang, J. Li, F. Jia, B. Jiao, J. Xu, X. Hou, J. Liu, Z. Wu, Graphitic carbon nitride doped SnO_2 enabling efficient perovskite solar cells with PCEs exceeding 22%. J. Mater. Chem. A. **8**, 2644-2653 (2020). https://doi.org/10.1039/C9TA11344D.

[19] J. Xie, K. Huang, X. Yu, Z. Yang, K. Xiao, Y. Qiang, X. Zhu, L. Xu, P. Wang, C. Cui, D. Yang, Enhanced electronic properties of SnO_2 via electron transfer from graphene quantum dots for efficient perovskite solar cells. ACS Nano. **11**, 9176-9182 (2017). https://doi.org/10.1021/acsnano.7b04070.

[20] F. Azri, A. Meftah, N. Sengouga, A. Meftah, Electron and hole transport layers optimization by numerical simulation of a perovskite solar cell. J. Sol. Energy. **181**, 372-378 (2019). https://doi.org/10.1016/j.solener.2019.02.017.

[21] M. Burgelman, K. Decock, A. Niemegeers, J. Verschraegen, S. Degrave, SCAPS manual. (2016). Version 8-4-2021, https://scaps.elis.ugent.be/SCAPS%20manual%20most%20recent.pdf, accessed on 4 November 2021. .

[22] N. Rono, A.E. Merad, J.K. Kibet, B.S. Martincigh, V.O. Nyamori, Simulation of the photovoltaic performance of a perovskite solar cell based on methylammonium lead iodide. Quantum Electron. **54**, 317 (2022). https://doi.org/10.1007/s11082-022-03737-1.

[23] N. Rono, A.E. Merad, J.K. Kibet, B.S. Martincigh, V.O. Nyamori, Optimization of hole transport layer materials for a lead-free perovskite solar cell based on formamidinium tin iodide. Energy Technol. **9**, 2100859 (2021). https://doi.org/10.1002/ente.202100859.

[24] A.-A. Kanoun, M.B. Kanoun, A.E. Merad, S. Goumri-Said, Toward development of high-performance perovskite solar cells based on $CH_3NH_3GeI_3$ using computational approach. J. Sol. Energy. **182**, 237-244 (2019). https://doi.org/10.1016/j.solener.2019.02.041.

[25] S. Abdelaziz, A. Zekry, A. Shaker, M. Abouelatta, Investigating the performance of formamidinium tin-based perovskite solar cell by SCAPS device simulation. Opt. Mater. **101**, 109738 (2020). https://doi.org/10.1016/j.optmat.2020.109738.

[26] T.R. Chetia, M.S. Ansari, M. Qureshi, Graphitic carbon nitride as a photovoltaic booster in quantum dot sensitized solar cells: A synergistic approach for enhanced charge separation and injection. J. Mater. Chem. A. **4**, 5528-5541 (2016). https://doi.org/10.1039/C6TA00761A.

[27] F. Zhang, W. Ma, H. Guo, Y. Zhao, X. Shan, K. Jin, H. Tian, Q. Zhao, D. Yu, X. Lu, Interfacial oxygen vacancies as a potential cause of hysteresis in perovskite solar cells. Chem. Mater. **28**, 802-812 (2016). https://doi.org/10.1021/acs.chemmater.5b04019.

[28] F. Wang, S. Bai, W. Tress, A. Hagfeldt, F. Gao, Defects engineering for high-performance perovskite solar cells. npj Flex Electron. **2**, 22 (2018). https://doi.org/10.1038/s41528-018-0035-z.

[29] K. Sobayel, M. Akhtaruzzaman, K.S. Rahman, M.T. Ferdaous, Z.A. Al-Mutairi, H.F. Alharbi, N.H. Alharthi, M.R. Karim, S. Hasmady, N. Amin, A comprehensive defect study of tungsten disulfide (WS_2) as electron transport layer in perovskite solar cells by numerical simulation. Results in Phys. **12**, 1097-1103 (2019). https://doi.org/10.1016/j.rinp.2018.12.049.

[30] P. Singh, N.M. Ravindra, Temperature dependence of solar cell performance—an analysis. Sol. Energy Mater. Sol. Cells. **101**, 36-45 (2012). https://doi.org/10.1016/j.solmat.2012.02.019.

[31] M.A. Green, Solar cells: operating principles, technology, and system applications. J Englewood Cliffs, NJ, Prentice-Hall, Inc., 288 p., (1982). https://ui.adsabs.harvard.edu/abs/1982ph...book.....G/abstract.

CHAPTER TWELVE

Conclusions and future work

12.1 Conclusions

The performance and stability of organic solar cells (OSCs) and perovskite solar cells (PSCs) are still low compared with commercially available silicon-based solar cells. Therefore, focused studies to improve their performance are necessary to unlock their potential for commercialisation. Thus, this work investigated solar harvesting materials and devices experimentally and computationally.

Graphitic carbon nitride (g-C_3N_4) material was of key interest in this study because of its desirable properties, such as a tuneable band gap of about 2.7 eV, chemical and physical stability, environmentally benign nature, and, more importantly, better light-harvesting ability. Therefore, g-C_3N_4 material and its composites were investigated and incorporated into solar cells. Bulk graphitic carbon nitride (B-g-C_3N_4) was synthesised by conventional polycondensation of a nitrogen-rich melamine precursor. This bulk material was exfoliated into nanosheets by two techniques, namely, thermal etching and liquid exfoliation techniques. In order to improve the properties of the nanosheet, a CdS dopant was prepared by a precipitation method. Composites of the two materials were prepared via a mechanochemical approach. The fundamental characterisation techniques investigated the optical absorption, electrical conductivity, morphological characteristics, thermal stability, chemical composition, and structural properties of the as-prepared materials. These techniques included TEM, HR-TEM, SEM, XRD, TGA, BET, EIS, FTIR, UV-Vis, elemental analysis, Raman spectroscopy, and photoluminescence (PL) spectroscopy.

Density functional theory (DFT) calculations performed using the Wien2k code on heptazine-based g-C_3N_4 showed that the material was slightly transparent. Also, its optical absorption and conductivity were maximum in the visible region of the electromagnetic spectrum. The Tran–Blaha modified Becke-Johnson (mBJ) exchange-correlation potential was more accurate than the generalised gradient approximation of the Perdew-Burke-Ernzerhof (PBE) (GGA-PBE) potential in calculating the electronic band structure. The thermal etching exfoliation method, when applied to B-g-C_3N_4,

produced nanosheets (CNNS-TE) with enhanced optoelectronic properties (lower band gap), a porous structure, and improved light harvesting ability than those obtained by the liquid exfoliation approach. When these CNNS-TE nanosheets were doped with cadmium sulfide (CdS/CNNS-TE), the resulting composites exhibited lower band gap energies than the pristine CNNS-TE or CdS materials, and the PL experiments indicated that the introduction of the CdS dopant assisted in reducing the recombination of photogenerated charges.

When the synthesised materials were incorporated in the active layer with P3HT:$PC_{61}BM$ blends of bulk heterojunction organic solar cells (BHJ-OSCs), the device with 5% CdS/CNNS-TE yielded the highest PCE (2.21%). The introduction of the dopant in the active layer of the OSC led to high J_{sc} and improved PCE in all the tested devices. The improvement of PCE was credited to better light harvesting, reduced recombination rates of photogenerated charges, and enhanced charge transfer characteristics in the device as a result of the introduction of dopants. Moreover, graphitic carbon nitride nanosheets (CNNS-CB) from the chemical blowing method of exfoliation of B-g-C_3N_4 were composited with CdS nanoparticles to form CdS/CNNS-CB heterostructures. When the composites were introduced as dopants in the active layer (with P3HT:$PC_{61}BM$ polymer blend) of an OSC, the best device with 10% CdS/CNNS-CB yielded a PCE of 3.45%, which was about 183% power conversion enhancement when compared with the pristine device. Comparatively, the CNNS-CB and its composites showed better performance than CNNS-TE-based (with 50% performance enhancement) materials. The best performance exhibited by CNNS-CB-based materials was attributed to relatively more structural defects created by heat and escaping blowing gases, which could possibly lead to improved cross-plane diffusion plane paths, thus facilitating the charge transfer process more than CNNS-TE-based materials.

A second class of third-generation solar cells, namely, perovskite solar cells, were investigated computationally by numerical simulation with the SCAPS-1D computational code. A typical configuration of a PSC entails glass/FTO/IGZO/$CH_3NH_3PbI_3$/spiro-OMeTAD/Au. However, herein we introduced (IGZO) because of its desirable properties such as low band gap, high thermal and chemical stability, and relatively high electron mobility of about 15 $cm^2\ V^{-1}\ s^{-1}$. The numerical simulation of the PSC device with the configuration glass/FTO/IGZO/$CH_3NH_3PbI_3$/spiro-OMeTAD/Au showed that the layer

thickness, density of defects of the absorber, and operational temperature impacted the overall performance of the device. A lower density of absorber defects was preferable since the rate of recombination of photogenerated charges could be impaired with a high density of defects. In an effort to avoid the use of toxic Pb, a lead-free device was investigated. The effects of different electron transport layer (ETL) and hole transport layer (HTL) materials on the performance of this lead-free device showed WS_2 to be a better ETL material due to its high electron transport mobility of about 260 $cm^2\ V^{-1}\ s^{-1}$. On the other hand, spiro-OMeTAD, Cu_2O, CuSCN, CuI, and D-PBTTT-14 showed appreciable PCE above 16% when utilised as HTL materials. Also, the device with formamidinium, instead of methyl ammonium, component in the perovskite absorber showed relatively high thermal stability. The formamidinium part resulted in the formation of a more compact structure that could withstand high operational temperatures. Also, cheaper alternatives than gold as the metal back contact, such as Ni, Pt, and Pb, could be utilised since they exhibited comparable PCEs to Au in all the tested devices. The introduction of g-C_3N_4 to the ZnO ETL in PSC devices led to better light harvesting and, thus, a high J_{sc} and improved PCE. Precisely, this study showed that the performance of lead-free devices could be optimised (to over 22 %), and they can outperform their lead-based counterparts.

In general, this study showed that the performance of OSC and PSC devices could be enhanced by incorporating better light harvesting materials, such as g-C_3N_4, with improved charge transport characteristics and suppressed recombination of photogenerated charges. Further, numerical simulation of PSC devices allowed the study of experimentally elusive aspects of the devices that aid in performance optimisation. Thus, this study has provided strategies for performance enhancement of OSC and PSC devices from computational and experimental perspectives.

12.2 Future work

Despite the various research strategies presented in this work for improving the performance of OSC and PSC devices, there are still a number of aspects that could be addressed, for instance:

1. The effects of heteroatom doping or composite formation on the optoelectronic properties of g-C_3N_4 should be further explored with regard to solar harvesting applications both computationally and experimentally.
2. While this study concentrated on g-C_3N_4 nanosheets (2D) and some composites, other dimensions, such as nanorods (1D), quantum dots (0D), nanotubes (1D), and 3-D g-C_3N_4, as well as their composites, should be investigated to broaden the potential use of g-C_3N_4 in OSC and PSC devices.
3. The actual fabrication of the simulated PSC devices should be carried out in order to evaluate their performance experimentally. In particular, the devices with the following proposed configurations are proposed:
    - glass/FTO/ZnO/g-C_3N_4/$CH_3NH_3PbI_3$/CuSCN/Au
    - glass/FTO/WS_2/$CH_3NH_3SnI_3$/CuSCN/Au and WS_2/g-C_3N_4 as ETL
    - glass/FTO/WS_2/$HC(NH_2)_2SnI_3$/CuSCN/Au and also with WS_2/g-C_3N_4 as ET

APPENDICES

Appendix A: Supporting information for chapter five

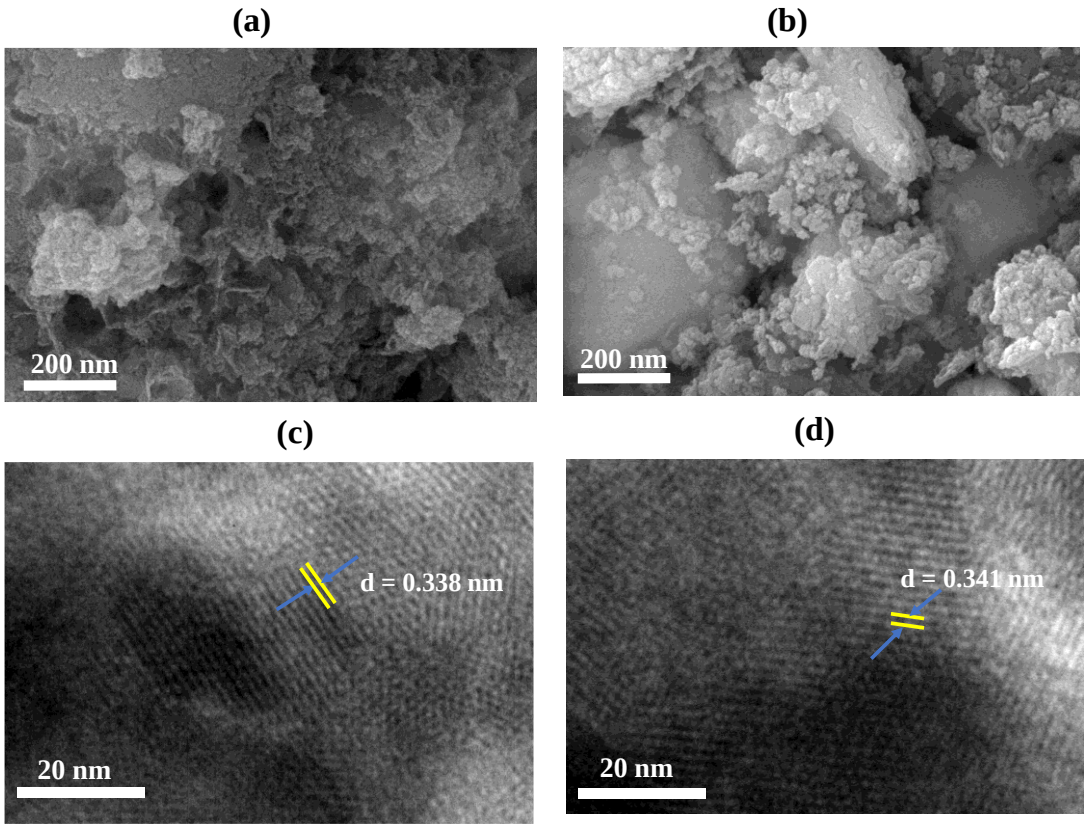

Figure 5.S1: SEM images of (a) 10% CdS/CNNS-TE and (b) 20% CdS/CNNS-TE samples, and HRTEM images of (c) 10% CdS/CNNS-TE and (d) 20% CdS/CNNS-TE

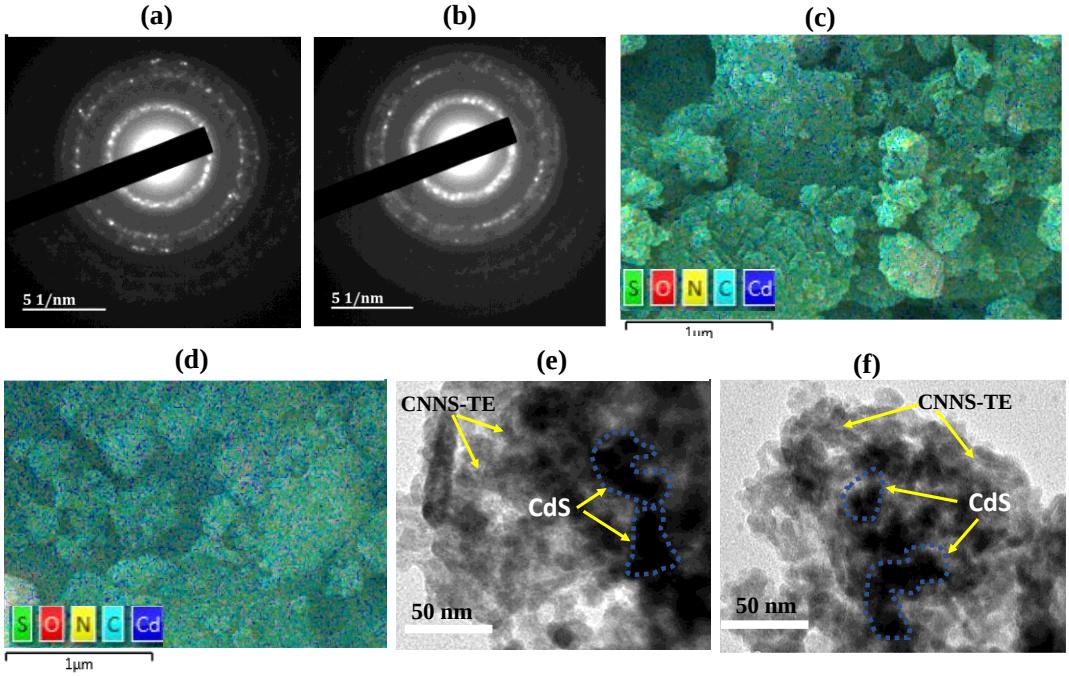

Figure 5.S2: SAED images for (a) 10% CdS/CNNS-TE and (b) 20% CdS/CNNS-TE samples. SEM-EDX mapping for (c) 10% CdS/CNNS-TE and (d) 20% CdS/CNNS-TE. TEM images for (e) 10% CdS/CNNS-TE and (f) 20% CdS/CNNS-TE samples

Appendix B: Supporting information for chapter six

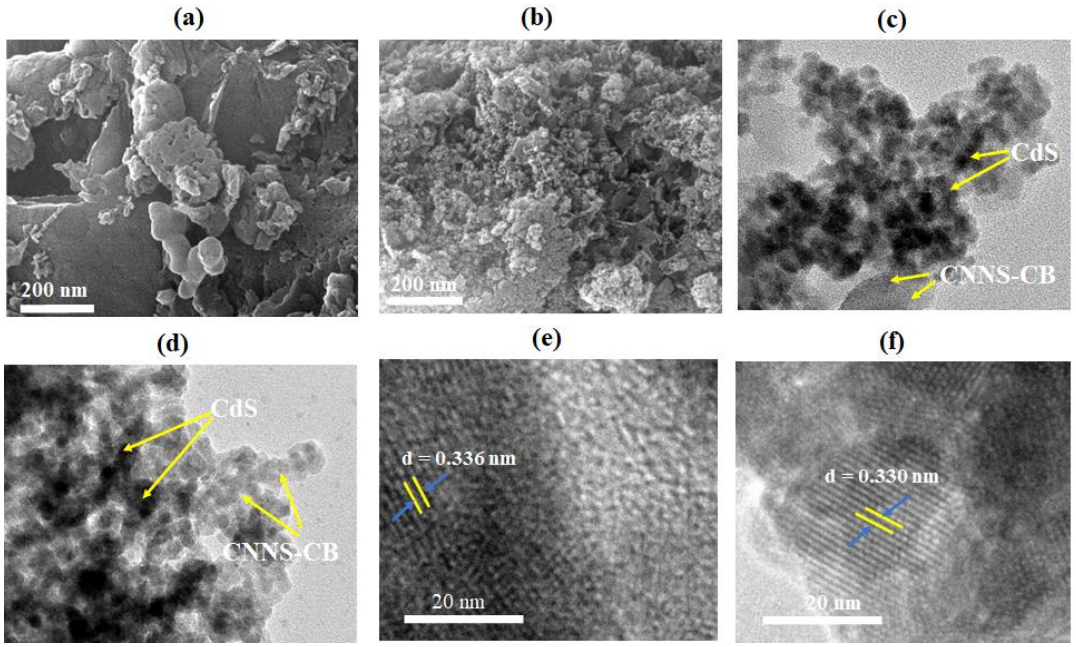

Figure S6.1: SEM images of (a) 5% CdS/CNNS-CB and (b) 20% CdS/CNNS-CB samples. TEM images of (c) 5% CdS/CNNS-CB and (d) 20% CdS/CNNS-CB. HRTEM images of (e) 5% CdS/CNNS-CB, and (f) 20% CdS/CNNS-CB

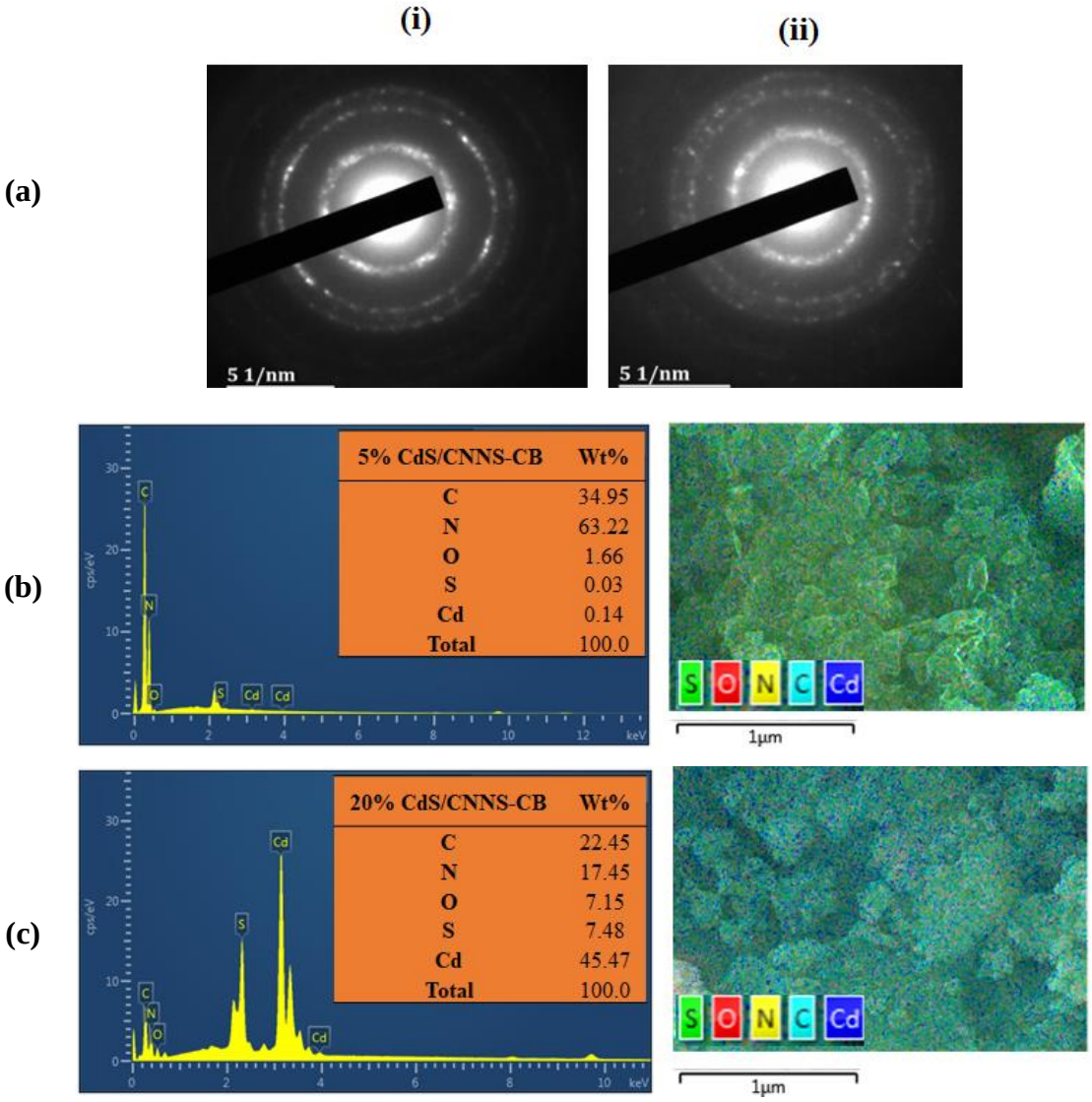

Figure S6.2: (a) HRTEM-SAED images for (i) 5% CdS/CNNS-CB and (ii) 20% CdS/CNNS-CB samples. SEM-EDX elemental composition graph, composition table (inset), and the corresponding mapping images for (b) 5% CdS/CNNS-CB and (c) 20% CdS/CNNS-CB samples

Appendix C: Supporting information for chapter nine

Table S9.1: Optimised layer thicknesses for devices with D-PBTTT-14 as the HTL and different ETL materials

ETL	FTO/µm	D-PBTTT-14 (HTL)/µm	$CH_3NH_3SnI_3$ (absorber)/µm	ETL/µm
WS_2	0.04	0.1	0.7	2.4
IGZO	0.03	0.03	0.5	0.01
PCBM	0.05	0.002	0.2	0.002
SnO_2	0.3	0.02	0.2	0.03
TiO_2	0.05	0.05	0.4	0.004
ZnO	0.1	0.05	0.4	0.1

Table S9.2: Photovoltaic parameters of devices with D-PBTTT-14 as the HTL and various ETL materials

Parameter	WS_2	IGZO	PCBM	SnO_2	TiO_2	ZnO
V_{oc}/V	2.19	4.71	1.28	1.38	1.43	9.99
J_{sc}/mA cm^{-2}	21.73	10.92	11.23	9.24	11.46	10.38
FF/%	34.31	15.48	51.71	36.76	48.02	7.57
PCE%	16.39	7.96	7.41	4.68	7.86	7.86

Table S9.3: A summary of PCE values of all the simulated devices

ETL	HTL					
	P3HT	**Spiro-OMeTAD**	**Cu_2O**	**CuSCN**	**CuI**	**D-PBTTT-14**
WS_2	10.47	16.37	16.40	16.39	16.38	16.39
IGZO			7.93	7.96		7.96
PCBM			7.53	7.53		7.41
SnO_2			2.18	4.70		4.68
TiO_2			7.56	7.87		7.86
ZnO			7.85	7.84		7.86

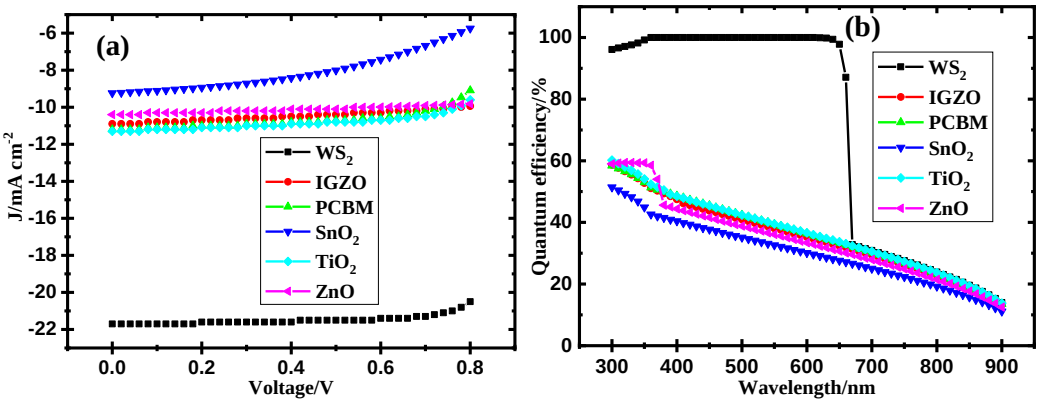

Figure S9.1: Photovoltaic performance characteristics of cells with D-PBTTT-14 as the HTL and different ETL materials: (a) J-V characteristics and (b) quantum efficiency